PSL UNIVERSITÉ PARIS

**THÈSE DE DOCTORAT**

DE L'UNIVERSITÉ PSL

Préparée à MINES ParisTech

# Strain localization and ductile fracture in single crystals: application to irradiated austenitic stainless steels

~

# Localisation de la déformation et rupture ductile dans les monocristaux : application aux aciers austénitiques inoxydables irradiés


Soutenue par

**Jean-Michel SCHERER**

Le 19 octobre 2020



École doctorale n°621

**Ingéniérie des Systèmes, Matériaux, Mécanique, Énergétique**

Spécialité

**Mécanique**


Composition du jury :

| | |
|---|---|
| Jacques BESSON<br>Mines ParisTech CNRS | *Président* |
| Lorenzo BARDELLA<br>Università degli Studi di Brescia | *Rapporteur* |
| Stefanie REESE<br>RWTH Aachen University | *Rapporteur* |
| Éric LORENTZ<br>EDF R&D | *Examinateur* |
| Renaud MASSON<br>CEA Cadarache | *Examinateur* |
| Thomas PARDOEN<br>Université catholique de Louvain | *Examinateur* |
| Samuel FOREST<br>Mines ParisTech CNRS | *Directeur de thèse* |
| Benoît TANGUY<br>CEA Saclay | *Directeur de thèse* |
| Jérémy HURE<br>CEA Saclay | *Invité* |

MINES ParisTech | PSL

*To my teachers*

# Acknowledgements

Dear reader, thank you for opening my PhD dissertation. I hope it will be useful to you. Please join me in acknowledging the participation of all the people who have made the following pages come true.

I express my greatest gratitude to the members of my PhD committee. I would like to acknowledge the devotion of Prof. Stefanie Reese and Prof. Lorenzo Bardella who kindly accepted to review my manuscript. I am also grateful for the thorough reading and enlightening comments of Prof. Thomas Pardoen, Eric Lorentz and Renaud Masson. Thank you for having accepted to recognise me as worthy of becoming a researcher in your community. I promise to do my best to honour this unique opportunity you have given me.

Je voudrais ensuite remercier Jérémy Hure, Benoît Tanguy, Samuel Forest et Jacques Besson de m'avoir guidé, conseillé et encouragé avec bienveillance tout au long de ces trois années. Chacun à votre manière vous m'avez transmis vos expériences et votre savoir avec enthousiasme et passion. Ensemble vous avez œuvré pour que je puisse toujours progresser dans les meilleures conditions. Merci pour la confiance que vous avez placé en moi, je vous en suis infiniment redevable.

J'adresse mes remerciements aux nombreuses personnes avec qui j'ai eu la chance de discuter et travailler au cours de ma thèse. Tout d'abord j'aimerais remercier l'ensemble des membres du Service d'Études des Matériaux Irradiés du CEA de Saclay pour leur accueil chaleureux. J'aimerais particulièrement saluer Philippe Grange pour son aide précieuse sans laquelle de sublimes expériences n'auraient probablement pas vu le jour. Merci également à Didier Bossu et Arnaud Courcelle pour leur disponibilité et les nombreux services qu'ils m'ont rendus. Je remercie aussi tous les stagiaires et doctorants qui se sont succédés au sein du service. Je souhaite bon courage à Rachma Azihari, Alice Bermont, Pierrick François et aussi David Siedel dans la poursuite de leur thèse et à Cédric Sénac dans sa recherche du meilleur dessert de la cantine. Enfin je remercie du fond du cœur Mohamed Shokeir, Ahmed Zouari et Kamila Wilczýnska pour les discussions enflammées et les bons moments que nous avons partagés ensemble.

Je voudrais également remercier toutes les personnes que j'ai rencontré au Centre des Matériaux de l'École des Mines de Paris. Tout d'abord, merci à René Cluzet d'avoir su multiplier les éprouvettes comme certains multiplient les pains... Je remercie Vikram Phalke, Chao Ling, Anna Ask, Aldo Marano, Tobias Kaiser, Moubine Al Kotob, Clément Ribart, Yazid Madi, Matti Lindroos, Gilles Rousselier et bien sûr Jonathan Champagne avec qui j'ai pu partager des discussions scientifiques extrêmement enrichissantes. Un grand merci également à Chloé Varenne, Rossen Tchakalov, Lenny Jacquinot d'avoir bien

voulu m'accepter à leur table et de m'avoir offert le café, souvent, malgré mes absences et mes retards répétés. Many thanks to Harris Farooq for his humour and for being such a true friend. Merci à Bastien Fosse d'avoir partagé avec moi sa passion pour la nature. J'aimerais enfin dire spécialement merci à Juan Manuel Garcìa et Clément Bertaux. Vous êtes d'une générosité sans pareil, merci pour tout ce que nous avons partagé ensemble.

À tous, trois années auront été bien trop courtes pour que je puisse profiter du temps passé avec vous autant que je l'aurais souhaité. J'espère sincèrement que nos chemins se recroiseront à l'avenir.

J'aimerais maintenant saluer et remercier du fond du cœur les personnes qui m'ont soutenu tout au long de cette aventure. Les bières d'afterwork n'auraient pas eu la même saveur sans Clément Faul, Jacques Jotz, Fanny Stark et Amélie Siegrist. Les week-end au vert n'auraient pas été aussi riches en souvenirs sans Valentin Krebs, Anthony Spina, Ael Ragonnet et Étienne Scholly. Merci à Pauline Bozo pour tous les bons moments passés ensemble. Enfin, un immense merci à mes parents Anne et Thierry et à mes frères Louis, Antoine et Sébastien. Vous avez été d'un soutient sans faille depuis le tout début. Absolument aucune des pages qui suivent n'aurait existé sans vous. Merci !

# Table of contents

# Nomenclature

Einstein's summation convention is adopted such that, repeated indices are summed up, if not otherwise stated.

**Tensors**

| | |
|---|---|
| $\mathcal{R} = \{\underline{\boldsymbol{e}}_1, \underline{\boldsymbol{e}}_2, \underline{\boldsymbol{e}}_2\}$ | orthonormal basis |
| $x$ | scalar (order 0) |
| $\underline{\boldsymbol{x}} = x_i \underline{\boldsymbol{e}}_i$ | vector (order 1) |
| $\underset{\sim}{\boldsymbol{X}} = X_{ij} \underline{\boldsymbol{e}}_i \otimes \underline{\boldsymbol{e}}_j$ | second order |
| $\underset{\approx}{\boldsymbol{X}} = X_{ijkl} \underline{\boldsymbol{e}}_i \otimes \underline{\boldsymbol{e}}_j \otimes \underline{\boldsymbol{e}}_k \otimes \underline{\boldsymbol{e}}_l$ | fourth order |
| $\underset{\sim}{\boldsymbol{X}}^T = X_{ji} \underline{\boldsymbol{e}}_i \otimes \underline{\boldsymbol{e}}_j$ | transposed second order tensor |
| $\underset{\sim}{\boldsymbol{X}}^{-1} = X_{ij}^{-1} \underline{\boldsymbol{e}}_i \otimes \underline{\boldsymbol{e}}_j$ | inversed second order tensor |
| $\underset{\sim}{\boldsymbol{X}}^{-T} = X_{ji}^{-1} \underline{\boldsymbol{e}}_i \otimes \underline{\boldsymbol{e}}_j$ | transposed inversed second order tensor |
| $\dot{x}$, $\dot{\underline{\boldsymbol{x}}}$, $\dot{\underset{\sim}{\boldsymbol{X}}}$ | time derivatives of tensors |
| $\mathrm{tr}\,(\underset{\sim}{\boldsymbol{X}}) = X_{ii}$ | trace of second order tensor |
| $\det(\underset{\sim}{\boldsymbol{X}})$ | determinant of second order tensor |

**Contractions / Products**

| | |
|---|---|
| $\underline{\boldsymbol{x}} . \underline{\boldsymbol{y}} = x_i y_i$ | scalar product |
| $\underset{\sim}{\boldsymbol{X}} . \underset{\sim}{\boldsymbol{Y}} = X_{ij} Y_{jk}$ | simple contraction |
| $\underset{\sim}{\boldsymbol{X}} : \underset{\sim}{\boldsymbol{Y}} = X_{ij} Y_{ij}$ | first double contraction |
| $\underset{\approx}{\boldsymbol{X}} : \underset{\sim}{\boldsymbol{Y}} = X_{ijkl} Y_{kl}$ | second double contraction |
| $\underline{\boldsymbol{x}} \otimes \underline{\boldsymbol{y}} = x_i y_j \underline{\boldsymbol{e}}_i \otimes \underline{\boldsymbol{e}}_j$ | dyadic product on vectors |
| $\underset{\sim}{\boldsymbol{X}} \otimes \underset{\sim}{\boldsymbol{Y}} = X_{ij} Y_{kl} \underline{\boldsymbol{e}}_i \otimes \underline{\boldsymbol{e}}_j \otimes \underline{\boldsymbol{e}}_k \otimes \underline{\boldsymbol{e}}_l$ | first dyadic product on tensors |
| $\underset{\sim}{\boldsymbol{X}} \overline{\otimes} \underset{\sim}{\boldsymbol{Y}} = X_{il} Y_{jk} \underline{\boldsymbol{e}}_i \otimes \underline{\boldsymbol{e}}_j \otimes \underline{\boldsymbol{e}}_k \otimes \underline{\boldsymbol{e}}_l$ | second dyadic product on tensors |
| $\underset{\sim}{\boldsymbol{X}} \underline{\otimes} \underset{\sim}{\boldsymbol{Y}} = X_{ik} Y_{jl} \underline{\boldsymbol{e}}_i \otimes \underline{\boldsymbol{e}}_j \otimes \underline{\boldsymbol{e}}_k \otimes \underline{\boldsymbol{e}}_l$ | third dyadic product on tensors |

**Particular quantities**

| | |
|---|---|
| $D_0$ | material (sub-)domain in the initial configuration |
| $D$ | material (sub-)domain in the current configuration |
| $\partial D_0$ | boundary of material (sub-)domain in the initial configuration |
| $\partial D$ | boundary of material (sub-)domain in the current configuration |
| $\underline{\boldsymbol{X}}$ | position of a material point in $D_0$ |
| $\underline{\boldsymbol{x}}$ | position of a material point in $D$ |
| $\underline{\boldsymbol{u}} = \underline{\boldsymbol{x}} - \underline{\boldsymbol{X}}$ | displacement field |
| $\underset{\sim}{\mathbf{1}} = \delta_{ij}\underline{\boldsymbol{e}}_i \otimes \underline{\boldsymbol{e}}_j$ | second order identity tensor |
| $\underset{\approx}{\mathbf{1}} = \frac{1}{2}\left(\delta_{ik}\delta_{jl} + \delta_{il}\delta_{jk}\right)\underline{\boldsymbol{e}}_i \otimes \underline{\boldsymbol{e}}_j \otimes \underline{\boldsymbol{e}}_k \otimes \underline{\boldsymbol{e}}_l$ | fourth order identity tensor on symmetric second order tensors |
| $\underset{\sim}{\boldsymbol{F}} = \dfrac{\partial \underline{\boldsymbol{x}}}{\partial \underline{\boldsymbol{X}}}$ | deformation gradient |
| $\underset{\sim}{\boldsymbol{E}}$ | elastic part of $\underset{\sim}{\boldsymbol{F}}$ |
| $\underset{\sim}{\boldsymbol{P}}$ | plastic part of $\underset{\sim}{\boldsymbol{F}}$ |
| $\underset{\sim}{\boldsymbol{E}}^e_{GL} = \frac{1}{2}(\underset{\sim}{\boldsymbol{E}}^T.\underset{\sim}{\boldsymbol{E}} - \underset{\sim}{\mathbf{1}})$ | elastic Green-Lagrange strain tensor |
| $\underset{\sim}{\boldsymbol{\sigma}}$ | Cauchy stress tensor |
| $\underset{\sim}{\boldsymbol{\Pi}}^e = \det\left(\underset{\sim}{\boldsymbol{E}}\right)\underset{\sim}{\boldsymbol{E}}^{-1}.\underset{\sim}{\boldsymbol{\sigma}}.\underset{\sim}{\boldsymbol{E}}^{-T}$ | Piola (or second Piola-Kirchhoff) stress tensor w.r.t. the intermediate configuration |
| $\underset{\sim}{\boldsymbol{S}} = \det\left(\underset{\sim}{\boldsymbol{F}}\right)\underset{\sim}{\boldsymbol{\sigma}}.\underset{\sim}{\boldsymbol{F}}^{-T}$ | Boussinesq (or first Piola-Kirchhoff) stress tensor |
| $\underset{\sim}{\boldsymbol{\Pi}}^M = \underset{\sim}{\boldsymbol{E}}^T.\underset{\sim}{\boldsymbol{E}}.\underset{\sim}{\boldsymbol{\Pi}}^e$ | Mandel stress tensor |

**Acronyms / Abbreviations**

| | |
|---|---|
| 2D | two-dimensional |
| 3D | three-dimensional |
| BCC | body-centered cubic |
| BF | bright field |
| BWR | boiling water reactor |
| CMOD | crack mouth opening displacement |
| CRSS | critical resolved shear stress |
| CT | compact tension |

| | |
|---|---|
| CW | cold worked |
| DDD | discrete dislocation dynamics |
| DF | dark field |
| DIC | digital image correlation |
| dpa | displacement per atom |
| EBSD | electron backscatter diffraction |
| FCC | face-centered cubic |
| FFT | fast Fourier transform |
| FNR | fast neutron reactor |
| GND | geometrically necessary dislocations |
| GSM | generalized standard materials |
| HCP | hexagonal close-packed |
| HFIR | high flux isotope reactor |
| HHO | hybrid high-order |
| IPF | inverse pole figure |
| LWR | light water reactor |
| NT | notch tensile |
| PIS | plastic instability stress |
| PKA | primary knock-on atom |
| PWR | pressurized water reactor |
| RIS | radiation induced segregation |
| RVE | representative volume element |
| SA | solution annealed |
| SED | secondary electron detector |
| SEM | scanning electron microscope |
| SENT | single-edge-notch tension |
| SRCT | synchrotron radiation-computed tomography |
| SSD | statistically stored dislocations |
| SVE | statistical volume element |
| TEM | transmission electron microscopy |
| WWER | water-water energetic reactor |

# 1
# Introduction


## Résumé

Cette thèse s'inscrit dans le contexte général de l'amélioration continue de la sécurité des installations nucléaires. Elle s'intéresse plus particulièrement au comportement des matériaux se trouvant à proximité du cœur d'un réacteur. Elle s'appuie pour cela sur de précédentes études menées afin de comprendre, modéliser et prédire la chute de ténacité des aciers austénitiques inoxydables utilisés comme matériaux des structures internes de réacteurs nucléaires. Ces structures portantes sont soumises à des doses d'irradiation importantes au cours de leur durée de vie. Or il a été montré que de tels niveaux d'irradiation induisent une évolution des propriétés microstructurales et *de facto* des propriétés mécaniques de ces matériaux. La création de défauts à l'échelle cristallographique sous irradiation a été identifiée comme origine de la dégradation de ces propriétés. La compréhension fine des effets de l'irradiation sur l'écrouissage et les propriétés à rupture de ces matériaux nécessite donc de faire appel à des outils adaptés à cette échelle. La caractérisation mécanique des aciers austénitiques à l'échelle cristalline n'a été que très rarement étudiée d'un point de vue expérimental. Les modèles de plasticité cristalline reposent donc sur des paramètres matériaux dont les valeurs numériques couramment utilisées sont issues d'identifications faites à une échelle supérieure, celle du polycristal. De plus, les modèles de plasticité cristalline prenant en compte l'endommagement ductile ne sont qu'à leurs débuts. Des études plus approfondies sont donc nécessaires afin de pouvoir les mettre en œuvre dans des calculs de structures. Les objectifs de cette thèse sont ainsi triples. Nous réaliserons d'une part l'identification de certains paramètres d'une loi de comportement mécanique de plasticité cristalline à partir de résultats expérimentaux obtenus sur monocristaux d'aciers austénitiques inoxydables. D'autre part nous nous attacherons à développer et implanter dans un code de calcul aux éléments finis, un modèle numériquement efficace de plasticité cristalline à gradient. Ce dernier sera exploité pour étudier le phénomène de localisation de la déformation plastique observé dans de nombreux matériaux irradiés. Enfin, nous présenterons un modèle innovant utilisant le formalisme à gradient pour la simulation de la rupture ductile de monocristaux poreux.

# Contents

## 1.1 Historical context

The successive discovery of chemical chain reactions, existence of the neutron and nuclear fission during the first half of the twentieth century made of nuclear power a promising source of energy. However, the first artificial nuclear reactor Chicago Pile-1, reaching criticality on 2 December 1942, was described by one of its designers Enrico Fermi as *"a crude pile of black bricks and wooden timbers"*. Ever since tremendous efforts have been put not only into enhancing efficiency but also into improving safety of such installations. Nevertheless global aging of the existing fleet of nuclear power plants and prevention of nuclear accidents require a continuing effort in order to maintain nuclear security. For that purpose, material science and in particular fracture mechanics is a cornerstone. Understanding the effects of temperature, pressure and radiations conditions on the behaviour and strength of materials is essential for the design and lifetime prediction of nuclear reactors. Furthermore, discoveries made in the context of nuclear materials do not only benefit to the sector of nuclear energy, but also enrich the knowledge about materials which have many other potential applications.

Back in the early twentieth century fracture mechanics involved essentially thorough experimental investigations and observations of crack propagation in materials. Standardized mechanical tests were proposed in order to measure toughness, *i.e.* the resistance of a material with respect to crack propagation. A few decades later emerged theoretical work on failure by crack propagation in brittle materials first, then in ductile materials. During the second half of last century the theoretical and experimental study of the effects of voids in the ductile fracture mechanism has thrived. Today's available computing power allows to use refined extensions of these models in order to simulate numerically crack propagation in specimens and even structures with accuracy. Now, in keeping with advances in the field of materials sciences for nuclear industry applications, the experimental, theoretical and numerical work presented hereafter aims at contributing to the improvement of nuclear installations' safety. It falls within the same scope as and continues several PhD thesis works conducted at the *Laboratoire de Comportement Mécanique des Matériaux Irradiés* (LCMI) from CEA Saclay in cooperation with Centre des Matériaux of Mines ParisTech. The studies carried out by Han (2012), Ling (2017) and Barrioz (2019) constitute the main foundation on which the progress made during this work is built. Han (2012) developed, implemented and identified a crystal plasticity model that accounts for irradiation induced Frank loops. He also formulated the first homogenized yield criterion for porous single crystals. Ling (2017) extended the latter criterion to finite strains and proposed a first model of ductile failure in single crystals which he validated upon comparison to porous unit-cell simulations. He also developed a reduced strain gradient model for single crystals based on the micromorphic approach. Barrioz (2019) investigated the influence of irradiation induced defects, in particular nano-voids, on the ductile failure mechanisms from an experimental perspective. He also proposed new criteria to predict void coalescence in highly swollen irradiated materials. This work continues their efforts and aims at modeling and simulating strain localization and void-driven ductile fracture in austenitic stainless steels used in the nuclear industry.

## 1.2 Industrial interest

Inside a nuclear reactor vessel, *internals* are structures designed to *support*, *align* and *guide* the core components; *set the path* for the coolant fluid; and *direct* and *support* the in-core instrumentation. Any accident occurring during operation or any hazardous external event such as a high magnitude earthquake would lead to the transfer of the loads imposed on the fuel assemblies to the upper and lower support structures. In a Pressurized Water Reactor (PWR) as depicted in Figure 1.1, the lower core support structures consist in the core barrel, the core baffles, the lower core plate and support columns, the neutron shields pads and the lower core support plate. The upper core structures, providing support to the fuel assemblies, rod cluster control assembly (RCCA) and in-core instrumentation, consist in an upper support assembly, upper support columns, RCCAs guide columns, thermocouple columns and the upper core plate.

In Fast Neutron Reactors (FNR) such as the sodium cooled FNR shown in Figure 1.2, hot and cold internals as well as fuel claddings and the reactor vessel are made of austenitic stainless steel.

In nuclear reactors most internals are made of austenitic stainless steel alloys. Excellent mechanical properties, combined with a high resistance to corrosion and irradiation at relatively low costs make such alloys among the best candidates for the functions described above. The nominal conditions of operation of these structures are indeed extremely harsh. In conventional Light Water Reactors (LWR) temperature of lower internals lies around 300 – 370 °C. In the mean time, the neutron flux is about $10^{14} - 10^{15}$ neutrons/cm$^2$/s and the coolant flow rate about $10^4$ kg s$^{-1}$. The combination of these conditions can collectively degrade the integrity of reactor internals. During unit outages, visual and ultrasound controls are performed on critical parts and some of them such as springs, bolts or guides can be replaced if their integrity is corrupted. However, other parts such as the core shroud or the upper guide structure would have a strong impact on the economical and technical operation in case of replacement and their integrity assessment is based on ageing studies of the materials. In FNR fuel claddings temperature can rise above 600 °C and irradiation dose levels which are reached can provoke a macroscopic swelling by cavity nucleation.

To date, in LWR, in-core failures observed in iron- and nickel-based stainless alloys are mainly due to a degradation process referred to as irradiation-assisted stress-corrosion cracking (IASCC). IASCC corresponds to an enhancement of susceptibility to corrosion and stress corrosion cracking induced by irradiation. It has detrimental effects on the mechanical properties, in particular susceptibility regarding crack initiation and propagation. Notwithstanding the fact that IASCC is one of the main mode of degradation observed in LWR's internals, there remain other possible failure mechanisms which were observed in irradiated austenitic stainless steel specimens. In FNR the macroscopic swelling caused by irradiation induced nano-void nucleation can be responsible for a quasi-brittle behaviour of austenitic stainless steels. It is all the more important that these mechanisms can be understood and predicted to the extent that an increase in the lifetime of existing reactors is envisaged. With such lifetime extensions, irradiation dose levels seen by reactor internals will inevitably rise. It will be shown later how irradiation doses can cause formation of irradiation-induced defects such as dislocation Frank loops and nano-sized voids. The former can cause strain localization and thus be responsible for an important loss of ductility, while the latter can affect void-driven ductile fracture. Therefore, the forthcoming study is devoted to the investigation of strain localization and void-driven ductile failure mechanisms in irradiated austenitic stainless steels.

## 1.3 Scientific interest

Models to describe plasticity in single crystals are widespread in the literature. However, experimental data on single crystals available to calibrate such models for austenitic steels are very scarce. Therefore, material parameters involved in these models are mostly identified on experiments performed at a larger scale, namely at the polycrystal scale. Other parameters are also determined from simulations performed at smaller scales such as discrete dislocations dynamics simulations. All in all it appears particularly interesting to obtain experimental data at the single crystal scale in order to inform more reliably models designed to describe mechanisms taking place at that scale.

Furthermore, irradiation-induced defects can severely affect the deformation mechanisms of irradiated materials. Gliding dislocations can indeed swipe out these defects in their motion and cause local softening, which in turn leads to strain localization in narrow bands called channels. Yet, modeling strain localization phenomena is a thriving topic in the current literature. Several models are indeed available, including models developed in the context of crystal plasticity. Strain localization occurring in irradiated austenitic steels can therefore serve as a practical case study for such models. It can help to identify their limitations and give insight on how to introduce more physics in their formulation.

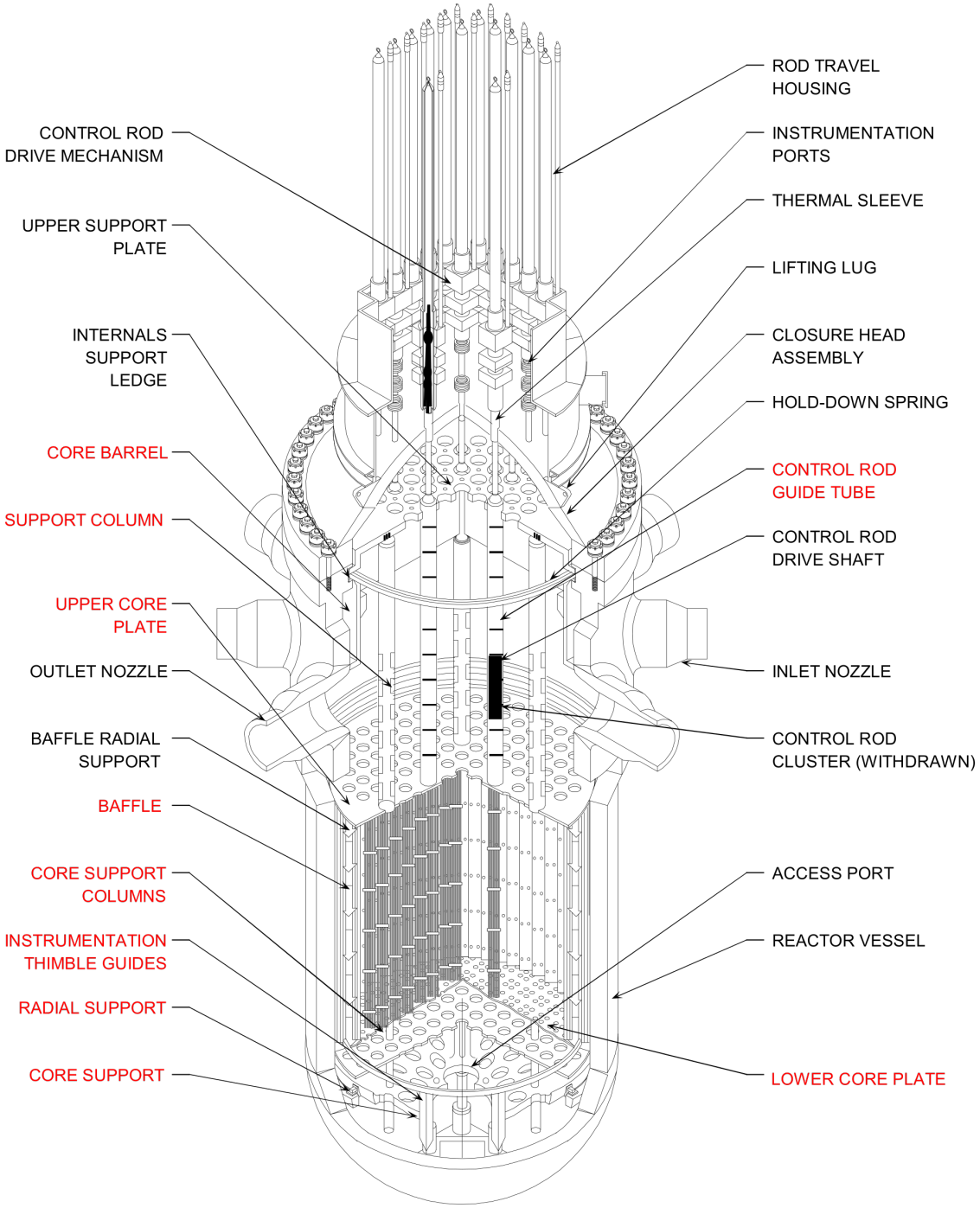


Figure 1.1 Cutaway view of a Pressurized Water Reactor vessel (USNRC, 2020). Internal structures made of austenitic stainless steel are depicted in red color.

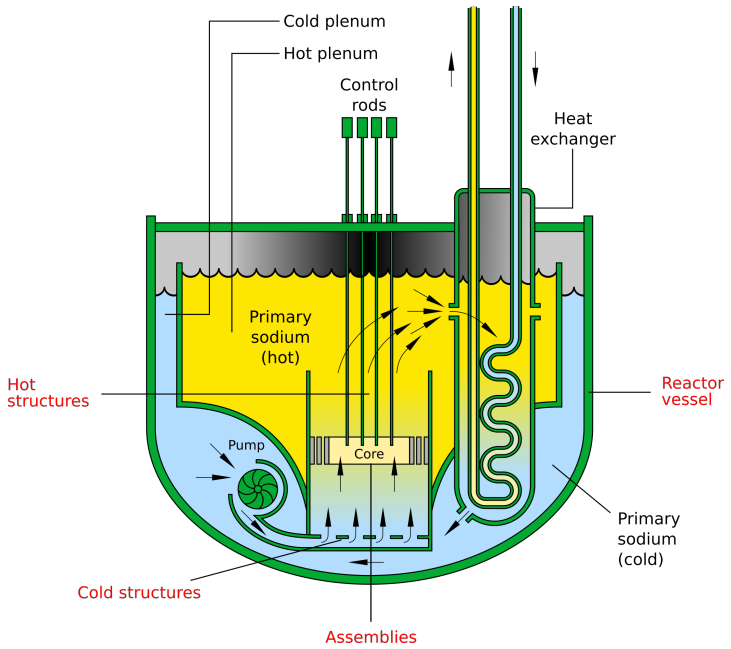


Figure 1.2 Cutaway view of a sodium cooled Fast Neutron Reactor vessel (Beao, 2014). Structures made of austenitic stainless steel are depicted in red color.

Moreover, in a wide range of conditions, the failure of irradiated austenitic steels is governed by void-driven ductile fracture mechanisms. Models describing nucleation, growth and coalescence of voids to simulate ductile fracture are also widespread in the literature. Nevertheless, models accounting for anisotropy due to crystal plasticity are still in their infancy. Further developments are required in order to be able to study ductile failure at the crystal scale in structures.

## 1.4 Objectives

The objectives of the present work are thereby threefold:

- calibrate a crystal plasticity material law suitable for unirradiated and irradiated austenitic stainless steels.
- develop and implement a numerically efficient non-local, gradient-enhanced model appropriate for modeling strain localization phenomena observed in irradiated materials.
- elaborate and deploy a regularized model of void-driven ductile fracture in single crystals.

## 1.5 Methodology

First of all, forefront experimental methods are employed in order to perform, monitor and analyze tensile tests on stainless steel single crystal specimens. Data acquired during these tests are used to calibrate an existing model of crystal plasticity for which to date some parameters remain imprecisely known.

Furthermore, light is shed on limitations of existing strain-gradient plasticity models used in the literature to address the problem of strain localization in nuclear materials. It is shown on the basis of analytical derivations how such restrictions are inherent to a general feature common to these models. A remedy is then proposed in order to enhance their capabilities and thus deal with the initial objective of simulating localization occurring in irradiated materials.

In addition, interest is given to the computational cost of the finite element implementation of such a model. It is shown how alternative approaches can significantly improve the numerical performance to the expense of relatively low additional implementation effort. Particular attention is devoted to demonstrate to which extent consistence with prior results is kept.

Finally, focus is set on developing a model first of this kind, suited to the simulation of regularized crack propagation in single- and polycrystals. First, a reconciliation of ductile fracture models at hand in the literature is attempted and the thermodynamical framework which ensues serves as a foundation for further developments. Building blocks of such a model available in the literature are then gathered together and complemented with innovative ideas on void coalescence. Simulations of fracture in single crystals are performed eventually to demonstrate the strengths and weaknesses of the final model.

Each of the above paragraphs gives rise to a different chapter of the present work. Each chapter is presented in the form of a scientific article, and complemented with additional relevant information.

## 1.6 Outline

The outline of the present work is as follows. In Chapter 2 the main knowledge concomitantly justifying and serving as a basis for the next chapters is presented in the form of a literature review. The synthesis describing the effect of irradiation on microstructural and mechanical properties of austenitic stainless steels will serve as a motivation for the two main topics of this work, namely strain localization and ductile fracture in single crystals.

In Chapter 3 experimental results obtained on austenitic stainless steels single crystals are presented. First, attention is drawn on experimental conditions and methods. Then, results are described in detail. Eventually, experimental data are exploited in order to identify material parameters of a standard crystal plasticity law available in the literature.

Chapter 4 is devoted to the enhancement of a strain gradient plasticity model. Inherent limitations regarding models involving constant material length scales are put in evidence. Improvements by consideration of an evolving characteristic length are proposed. The major benefit of this extension is then demonstrated in the context of modeling strain localization phenomena occurring in single crystals, as observed in irradiated materials.

In Chapter 5 several approaches available in the literature to interpret and implement a strain gradient crystal plasticity model are discussed and compared. Details of the finite element implementation of a numerically efficient Lagrange multiplier based formulation are presented. Differences and similarities between these settings are highlighted upon comparison of numerical simulation results.

Chapter 6 is dedicated to the presentation of a comprehensive model of ductile fracture for single crystals. A thermodynamical foreword is given in a first step in order to recast available models in a unique formalism. The latter is then employed so as to derive an homogenized model of porous single crystals accounting for growth and coalescence of voids. Finally the model is employed to simulate crack propagation in single crystal structures.

Concluding remarks and opening to future developments are finally presented in Chapter 7.

*If I have seen further it is by standing on the shoulders of Giants.*

Isaac Newton

# 2
# Literature review


## Résumé

Dans ce chapitre est présenté l'état de l'art en matière d'observations expérimentales des propriétés des aciers austénitiques inoxydables irradiés utilisés en conditions des réacteurs à eau légère et des réacteurs à neutrons rapides. Les effets de l'irradiation sur la nano-structure de ces matériaux seront tout d'abord exposés. Puis, l'incidence des évolutions micro- et nano-structurales sur les mécanismes de déformations sera abordée. Nous verrons ensuite comment les propriétés mécaniques sont affectées par l'irradiation. D'une part, nous verrons comment, sous certaines conditions, les modes de déformations peuvent être modifiés par l'existence de défauts d'irradiation. Nous nous appuierons pour cela sur des observations faites par microscopie électronique à balayage et en transmission permettant de révéler la présence d'hétérogénéités intenses de déformation dans les matériaux irradiés. D'autre part, nous nous intéresserons aux propriétés mécaniques macroscopiques des aciers irradiés. En particulier nous discuterons des conséquences de l'irradiation sur leurs propriétés à rupture. Ensuite, nous verrons quelles sont les conditions propices à l'apparition de zones de localisation de la déformation. Nous examinerons comment la mécanique des milieux continus généralisés peut servir de cadre théorique à la modélisation et la simulation de telles hétérogénéités de déformations induites par des instabilités de natures diverses. Nous analyserons plusieurs méthodes disponibles dans la littérature et comment elles peuvent être mises en œuvre pour modéliser les phénomènes de localisation observés dans certains aciers irradiés. Enfin, nous nous intéresserons aux mécanismes à l'origine de la rupture ductile gouvernée par l'évolution de cavités telles que celles pouvant exister dans les aciers irradiés. Nous verrons comment des méthodes d'homogénéisation périodique permettent de modéliser la rupture ductile des milieux poreux. Les modèles les plus avancés visant à prévoir le comportement des monocristaux poreux seront enfin abordés et comparés.

# Contents

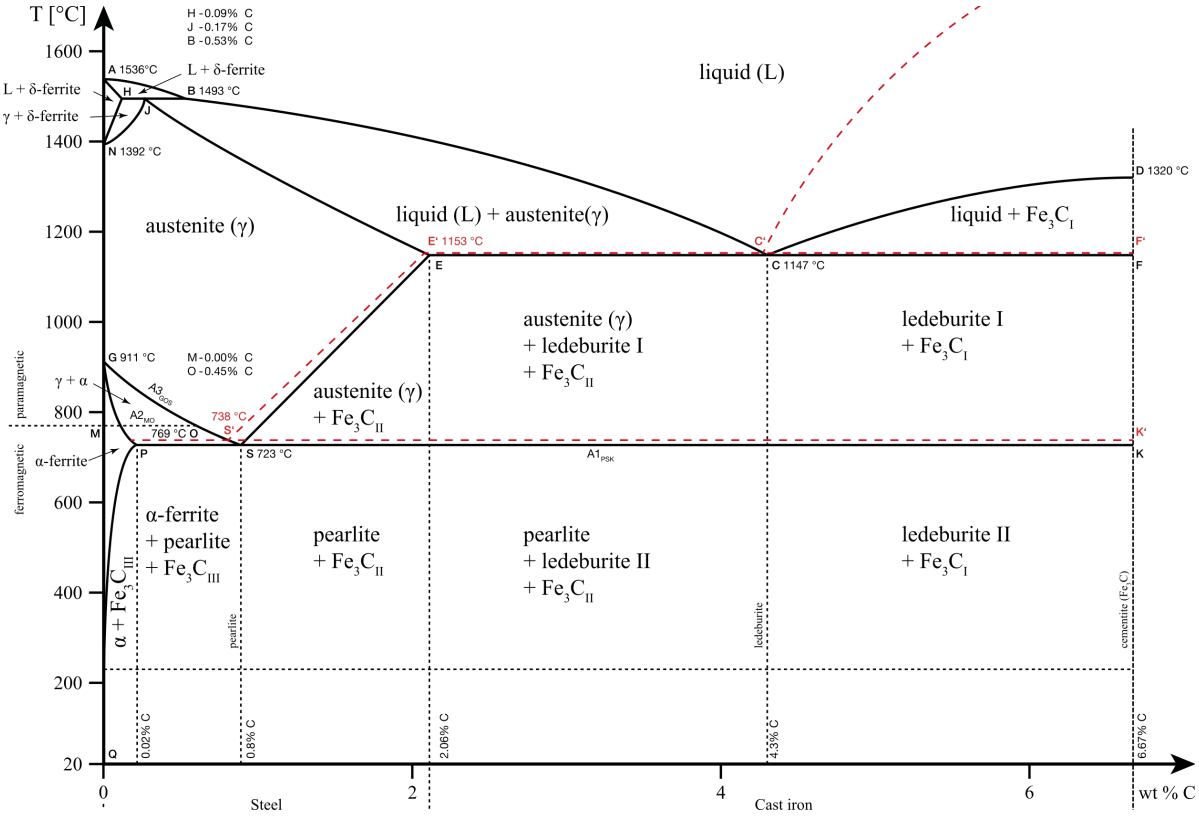


Figure 2.1 Stable (solid black lines) and metastable (dashed red lines) binary Iron-Carbon phase diagrams (Caesar, 2019).

## 2.1 Mechanical behaviour of nuclear austenitic stainless steels

### 2.1.1 Micro and nano-structure of undamaged and radiation-damaged austenitic stainless steels

#### 2.1.1.1 Austenitic stainless steels

Austenite, named after metallurgist Sir William Chandler Roberts-Austen (1843–1902), is an allotrope of iron or solid solution of iron with an alloying element. Also known as gamma-phase iron ($\gamma$-Fe), austenite is obtained by austenitization of an iron-based alloy, where the alloy is heated to a temperature such that the crystal structure transforms from body-centered cubic (BCC) ferrite into the more open and prone to alloying element dissolution face-centered cubic (FCC) austenite. In austenitic stainless steels the alloying element is carbon. As shown in the stable (solid black lines) iron-carbon phase diagram Figure 2.1, austenite exists in steels above the critical eutectoid temperature of 723 °C. However addition of certain alloying elements, such as manganese and nickel can stabilize the austenitic structure. High levels of alloying elements can even make austenite stable at room temperature. On the other hand elements such as silicon, molybdenum and chromium destabilize the austenite structure and therefore raise the eutectoid temperature. However significant amount of chromium is introduced in stainless steels to induce a thin chromium oxide layer at their surface which is responsible for their stainless character. Figure 2.2 shows several families of steels with respect to their respective nickel and chromium amount. This study focuses on the mostly used austenitic stainless steels in the nuclear industry, namely grade 304 and 316 stainless steels. Chemical requirements for such steels are presented in Table 2.1. Some observations will also be given about advanced austenitic stainless steels developed for FNR irradiation conditions. Table 2.1 gathers the chemical composition of these steels as defined in (ASTM Standard A240/A240M, 2012) specifications.

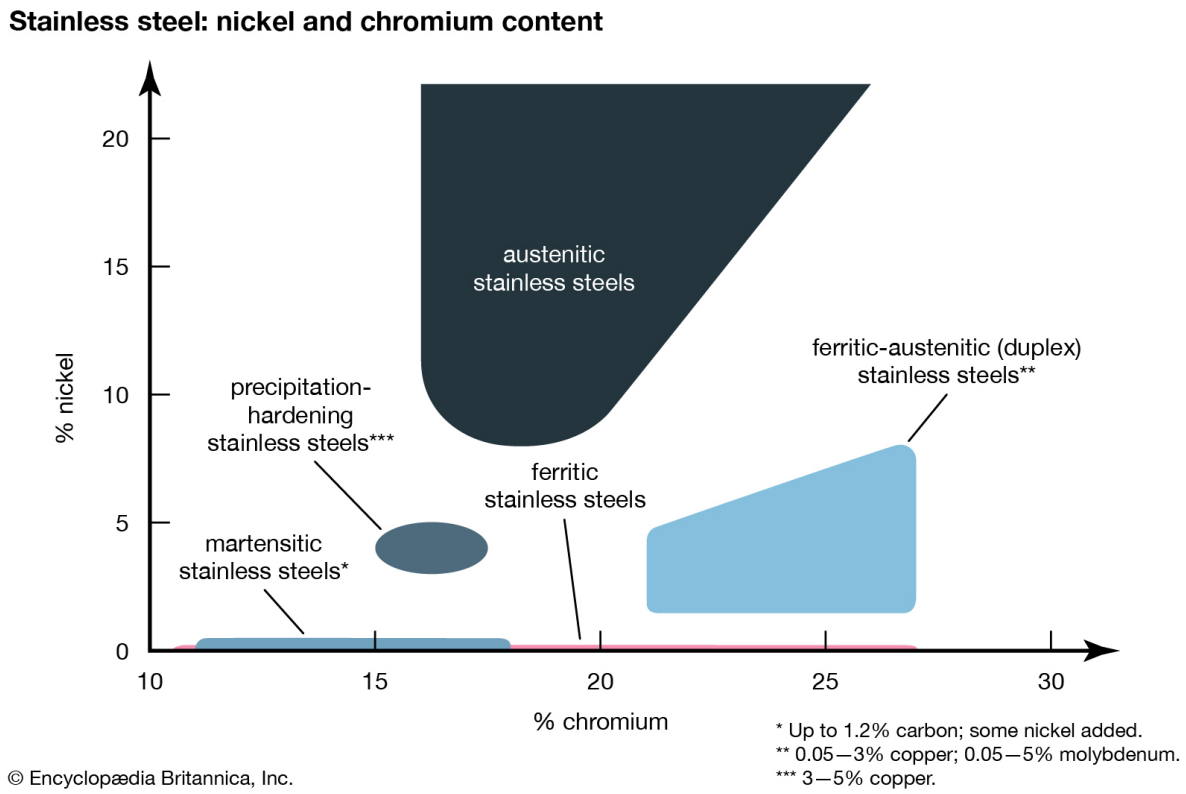


Figure 2.2 Domains of several stainless steel classes as a function of nickel and chromium contents (Encyclopædia Britannica, 2019).

Table 2.1 Chemical composition requirements (weight %[1]) for 304, 304L, 316, 316L austenitic stainless steels according to ASTM Standard A240/A240M (2012) specifications.

| Type | C | Mn | P | S | Si | Cr | Ni | Mo | N | Fe |
|---|---|---|---|---|---|---|---|---|---|---|
| 304 | 0.07 | 2.00 | 0.045 | 0.030 | 0.75 | 17.5-19.5 | 8.0-10.5 | .. | 0.10 | balance |
| 304L[2] | 0.030 | 2.00 | 0.045 | 0.030 | 0.75 | 17.5-19.5 | 8.0-12.0 | .. | 0.10 | balance |
| 316 | 0.08 | 2.00 | 0.045 | 0.030 | 0.75 | 16.0-18.0 | 10.0-14.0 | 2.00-3.00 | 0.10 | balance |
| 316L[2] | 0.030 | 2.00 | 0.045 | 0.030 | 0.75 | 16.0-18.0 | 10.0-14.0 | 2.00-3.00 | 0.10 | balance |

The FCC crystal structure is schematized in Figure 2.3a. Black disks represent atomic sites of the crystal lattice. Blue arrows indicate the highest atomic density directions ($\langle 110 \rangle$ directions) which are also the preferential slip directions for dislocations. One out of the four highest atomic density planes ($\{111\}$ planes) is filled in grey. Also known as slip planes, they correspond to the slipping planes associated to dislocation motion. Figure 2.3b displays an electron backscatter diffraction (EBSD) map, obtained by scanning electron microscopy (SEM), of a solution annealed (SA) 316L stainless steel. The color map represents the crystal orientation of the material. It can be observed that the microstructure of the material is organized in grains of uniform crystal orientation. For low nickel alloys (304 and 304L), a significant amount of ferrite is also observed. The main population of defects in the crystal structure of these grains

[1]Maximum, unless range or minimum is indicated.

[2]L stands for "low-carbon" for which carbon analysis should be reported to nearest 0.001% as compared to 0.01% for other steels

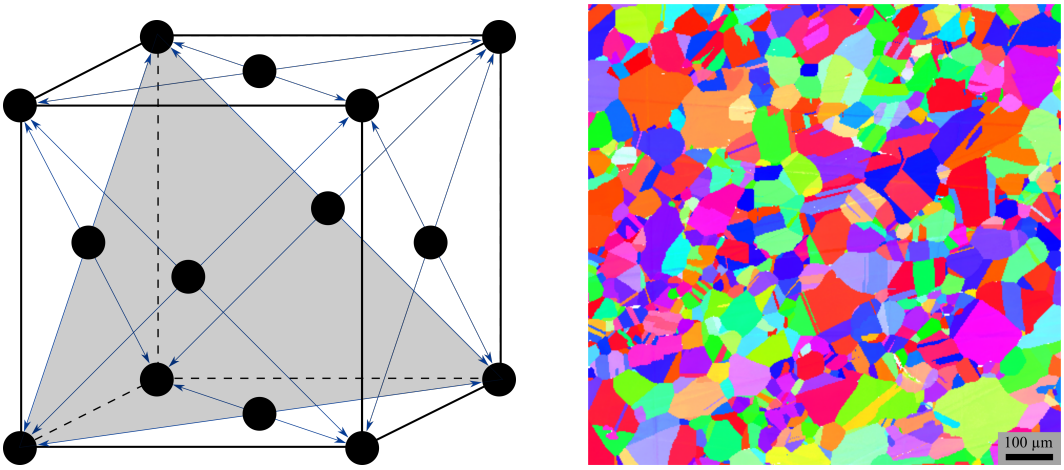


(a) (b)

Figure 2.3 (a) FCC crystal lattice showing ⟨110⟩ slip directions (blue arrows) and one of the four {111} slip plane (grey triangle). (b) EBSD map of a SA 304 stainless steel (courtesy of A. Courcelle) where colors denote crystal orientations.

are linear discontinuities called dislocations. The concept of dislocation was first theorized and studied by Volterra (1907). They were illustrated within soap bubble rafts first imagined and studied by Bragg and Nye (1947) as shown in Figure 2.4a. With the advent of electron microscopy dislocations can nowadays be imaged in metallic alloys by transmission electron microscopy (TEM) as shown in Figure 2.4b. Although this work focuses mainly on perfect dislocations and a few kinds of irradiation induced defects presented in next section, many other types of defects can also exist inside the crystal structure of austenitic stainless steels. As discussed by de Bellefon and Van Duysen (2016), perfect dislocations belonging to one of the twelve $\{111\}a/2\langle 110\rangle$ slip systems, under some circumstances, can split to form Shockley partial dislocations of type $a/6\langle 112\rangle$ in order to reduce their overall strain energy. These are known to be at the origin of deformation twinning and martensite formation processes in FCC crystals which are also observed in steels.

#### 2.1.1.2 Defects in radiation damaged austenitic stainless steels

This section is a non-exhaustive summary of the literature review by Etienne (2009). Focus is made on the main aspects concerning the phenomena studied in this work. In nuclear power plants neutrons emitted during the nuclear reaction may exit the fission material and interact with surrounding structural materials and in particular stainless steels used for internals. The neutron ballistic interaction with an atom of the steel can lead to the formation of an elementary defect called Frenkel pair constituted of a vacancy and an interstitial atom. The energy needed for the formation of such a pair is about 40 eV in $\alpha$-iron (ASTM Standard E521-96, 2009). Since this value is unknown in $\gamma$-iron the same value is often used for this allotrope. If the energy transmitted by the incident neutron to the primary knock-on atom (PKA) is sufficient, the latter can in turn become a projectile and impact an other atom to create a Frenkel pair. It follows a cascade of displacements by collision (lasting about 1 ps) and recombination (lasting about 10 ps). Irradiation dose is therefore often measured in terms of displacements per atom (dpa). After collision and recombination point defects may remain free or agglomerated in clusters inside the material. It is the accumulation of these defects during irradiation which are responsible for microstructure evolution of radiation-damaged steels and the properties changes which ensues. Three main mechanisms are identified as origin of microstructure evolutions: diffusion and precipitation accelerated by irradiation, radiation induced segregation (RIS) and

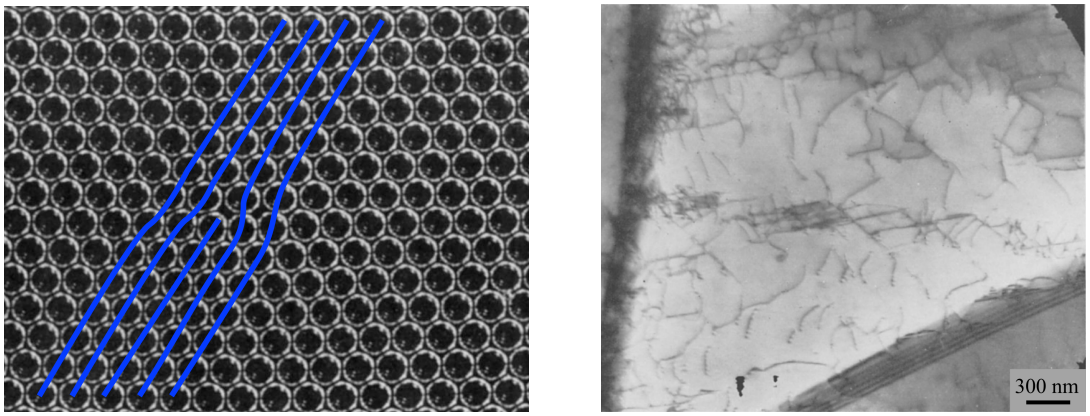


(a) (b)

Figure 2.4 (a) Bubble raft illustration of the concept of dislocation. The bubbles diameter is 1.9 mm (Bragg and Nye, 1947). (b) Transmission electron micrography of dislocations in a rolled stainless steel (Whelan et al., 1957).

clustering of defects. For the purpose of this work defect clusters will be described in details respectively for LWR and FNR temperature conditions.

In LWR conditions, nominal temperature is close to 300 °C. Under these circumstances interstitial clusters can turn into dislocation loops. Interstitial dislocation loops are either perfect prismatic loops (Burgers vector $\underline{\boldsymbol{b}} = (a/2)\langle 100\rangle$) which are glissile, or faulted (Burgers vector $\underline{\boldsymbol{b}} = (a/3)\langle 111\rangle$) which are sessile. The latter, known as Frank loops, are energetically more favorable than the former when their diameter is smaller than a critical radius. Therefore Edwards et al. (2003) reported that interstitial loops formed under irradiation are essentially Frank loops. Most works consider interstitial Frank loops, but vacancies Frank loops are also possible. The maximum density of dislocation loops is attained between 300 °C and 400 °C (Zinkle et al., 1993). Saturation of the density (above $10^{23}\,\mathrm{m}^{-3}$) is reached between 1 and 5 dpa (Bruemmer et al., 1999), but the radius increases with the dose until saturation. Therefore as the dose increases the radius of Frank loops can reach the critical radius for which perfect prismatic glissile loops are more favorable. Frank loops can then unfault and merge into the dislocation network (Garnier, 2009; Pokor, 2002). Still under LWR conditions and at high doses, the production of helium in the transmutation reaction of nickel is responsible for the formation of bubbles Zinkle et al. (1993). These bubbles have typically a diameter of 2-3 nm and their density is close to $10^{23}\,\mathrm{m}^{-3}$ at 35 dpa and 350 °C. Under some circumstances, bubbles can grow and reach a critical diameter at which they are no more filled with helium and are thus designated as cavities. Frank loops, dislocation network and helium bubbles are the main irradiation defects observed in LWR conditions, but other irradiation-induced features are observed such as small ($\sim$ 1 nm) clusters known as black dots, or precipitates.

In FNR conditions, *e.g.* in sodium fast reactor, austenitic stainless steels are used for fuel cladding for which nominal temperature is in the range 400 °C - 650 °C and irradiation doses up to and even higher than 100 dpa. Under these circumstances a radiation induced dislocation network can be formed. Dislocations formed under irradiation are attributed to the transition of faulted sessile Frank loops to perfect prismatic glissile loops. At high doses, the main irradiation defect is nano-voids, first reported by Cawthorne and Fulton (1967), with typical diameters up to few tens of nanometers. The porosity associated with the presence of these nano-voids can be very high, up to 10%. Since the formation of such voids is associated to an augmentation of the overall volume of the material, this phenomenon is referred to as irradiation induced swelling. Figure 2.5 shows a variety of defects which can be observed in an irradiated SA 316 stainless steel.

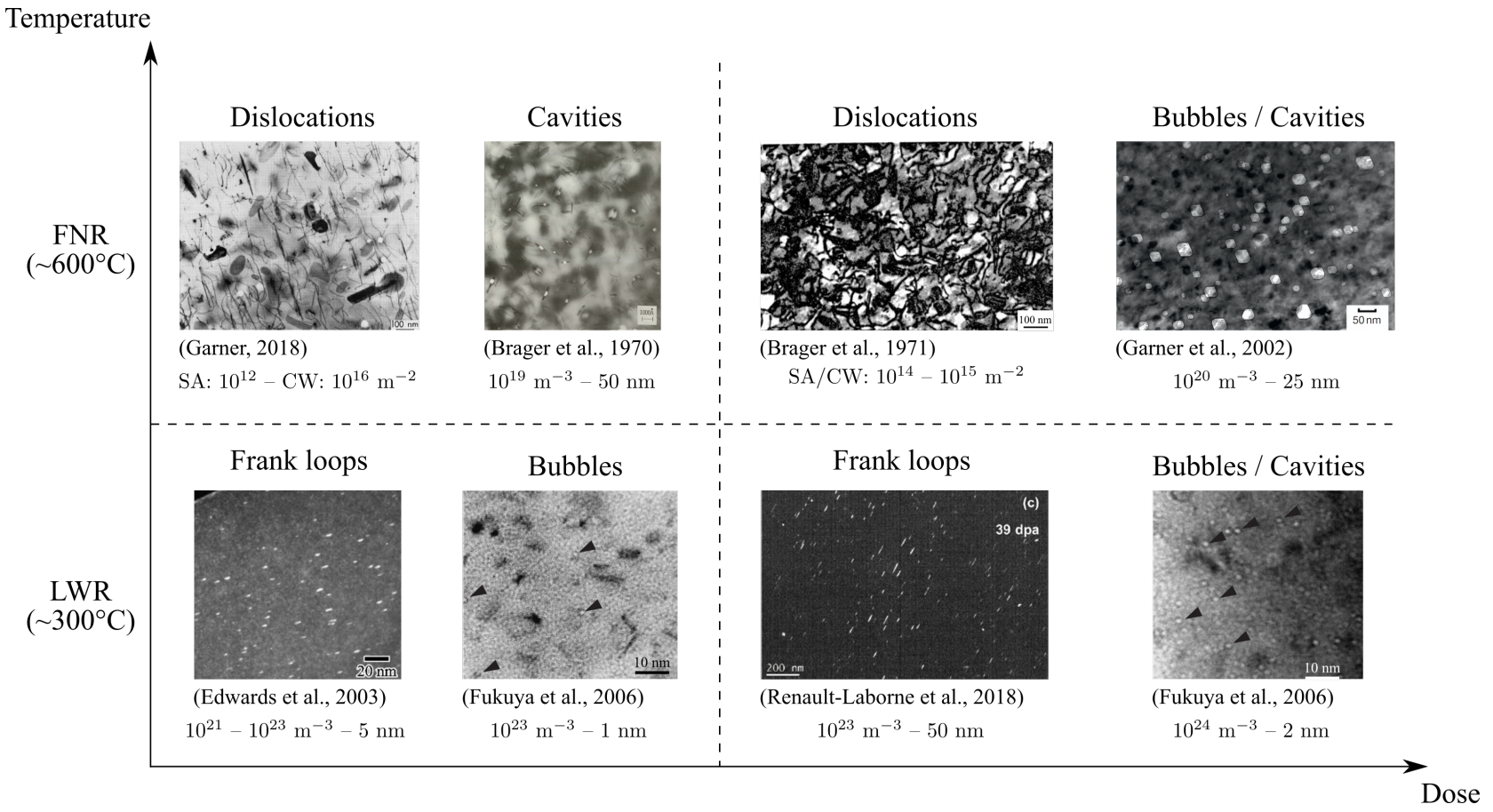


Figure 2.5 Main defects types as a function of dose and temperature of irradiation in austenitic stainless steels. Order of magnitudes for measured densities and sizes are reported under each kind of defect. Bright field (dislocations, cavities and bubbles) and dark field (Frank loops) transmission electron micrographs are taken from (Brager et al., 1971; Edwards et al., 2003; Fukuya et al., 2006; Garner, 2018; Garner et al., 2002; Renault-Laborne et al., 2018).

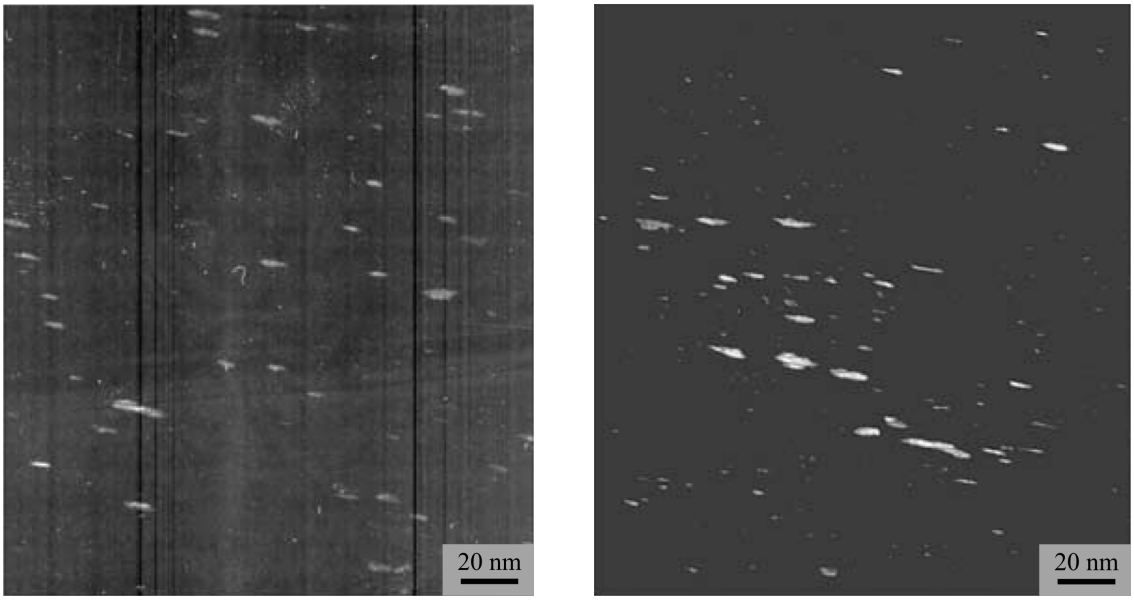


(a) (b)

Figure 2.6 Frank loops in a 316 stainless steel after (a) neutron irradiation at 2.9 dpa and (b) proton irradiation at 3.0 dpa displaying similar densities and sizes (Gan and Was, 2001).

Many limitations are associated with neutron irradiations to study radiation-induced defects. Amongst these difficulties are the irradiation duration (and associated cost), the neutron activation of the target (mainly due to isotopic transmutation of nickel), the difficult monitoring of parameters (flux, dose, temperature). Therefore ions are commonly used as irradiation particles.

Protons ($H^+$) are often used to reproduce the defects populations obtained in LWR conditions. Gan and Was (2001) indeed have shown that, under some circumstances, defect microstructures produced by protons irradiations are similar to neutrons irradiations as seen in Figure 2.6 for Frank loops. They characterized the dependence of the number density and size of dislocation loops and voids upon irradiation dose, temperature and chemical composition. They showed that proton-irradiated 304 and 316 stainless steels at 1 dpa display similar loop diameter distributions as neutron irradiated 304 (at 0.7 dpa) and 316 (at 1.1 dpa) stainless steels (see Figure 2.7). Not only loop diameters are similar but also the faulted loop density evolution with respect to irradiation dose. It can be observed on Figure 2.8a that loop density evolution with the dose for steels proton-irradiated at 360 °C almost superimposes with loop density evolution in steels neutron-irradiated at 300 °C, the difference in irradiation temperature compensating the difference in irradiation flux. The trends of loops diameter and density evolution with irradiation temperature are also very similar for neutron and proton irradiations. Void density evolution with respect to the dose are in the same order of magnitude at 400 °C for neutron- and proton-irradiated stainless steels (see Figure 2.8b).

Heavy ions, such as iron, copper, silicon, nickel, etc, are often used to simulate high fluence neutron irradiations in FNR conditions (Kulcinski et al., 1971; Nelson et al., 1970). Pre-implantation or co-implantation of helium can be carried out in order to mimic the presence of helium due to nickel transmutation during neutron irradiation (Choyke et al., 1979; Packan and Farrell, 1983). As it can be observed in Figure 2.9, heavy ions mainly allow to produce a population of nano-cavities similar in density and size to the cavities produced in FNR conditions. The different kind of defect populations described in this section are responsible for drastic modifications in the deformation mechanisms observed in irradiated steels. For instance, as it will be discussed in next section, radiation induced Frank loops can trigger intense localization of plastic flow. As a consequence the mechanical behaviour is greatly affected by irradiation as will be discussed in a second step.

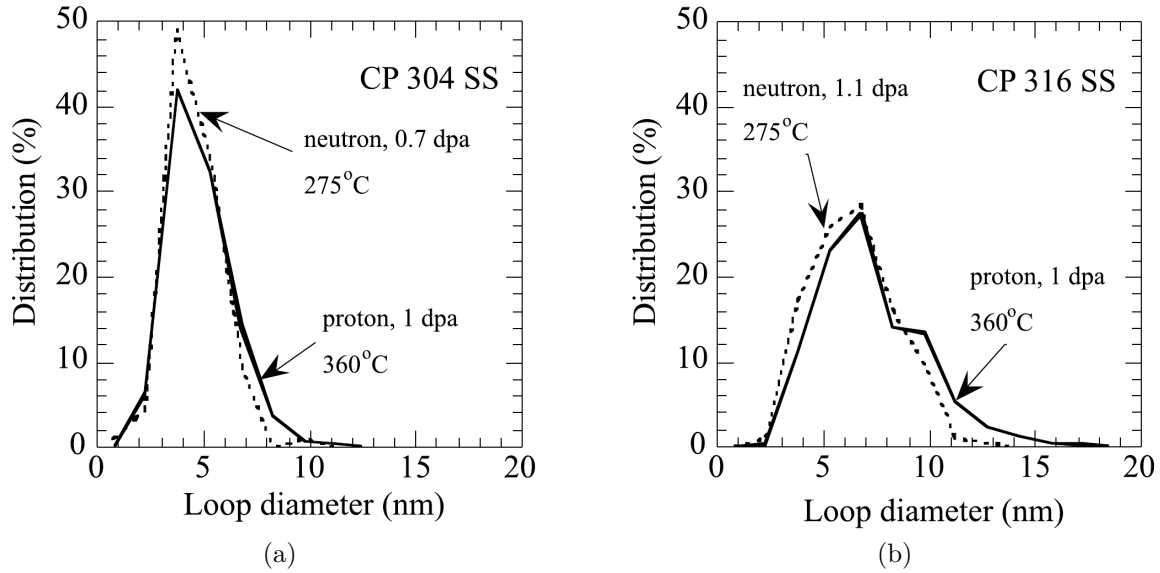


(a) (b)

Figure 2.7 (a) Comparison of loop size distribution between 0.7 dpa (275 °C, dashed line) neutron-irradiated and 1 dpa (360 °C, solid line) proton-irradiated 304 stainless steel (b) Comparison of loop size distribution between 1.1 dpa (275 °C, dashed line) neutron-irradiated and 1 dpa (360 °C, solid line) proton-irradiated 316 stainless steel (Gan and Was, 2001).

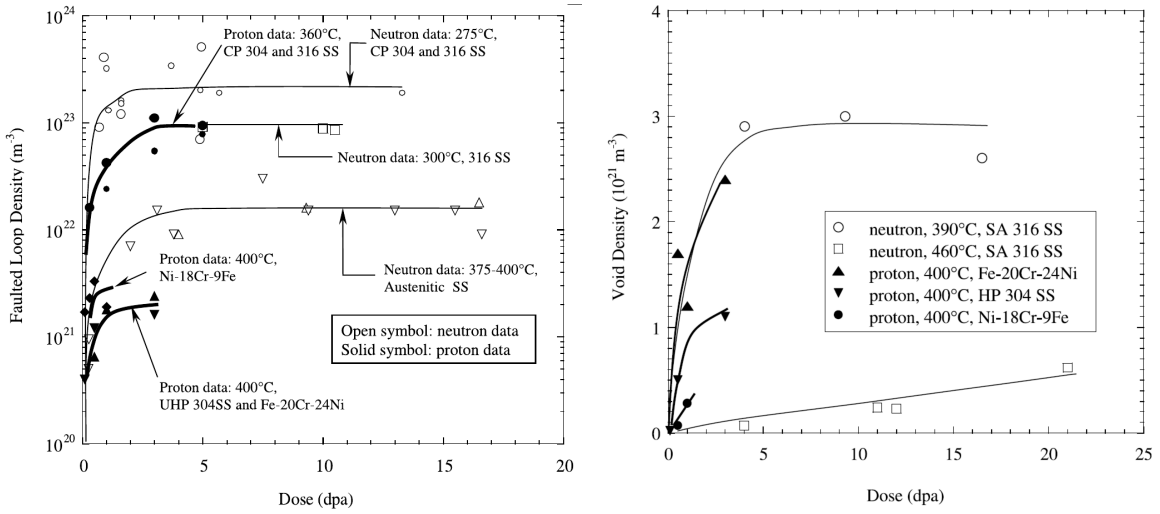


(a) (b)

Figure 2.8 (a) Evolution of faulted loop density with respect to irradiation dose for (270-400 °C, open symbols) neutron- and (400 °C, solid symbols) proton-irradiated Fe-Cr-Ni alloys. (b) Evolution of void density with respect to irradiation dose for (390-460 °C, open symbols) neutron- and (400 °C, solid symbols) proton-irradiated Fe-Cr-Ni alloys (Gan and Was, 2001).

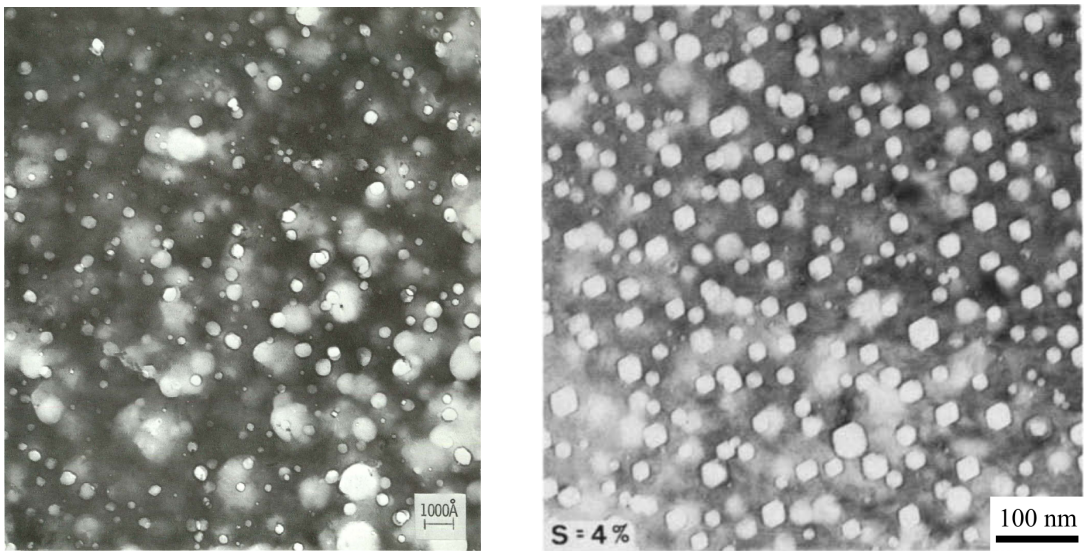


(a) (b)

Figure 2.9 Cavities formed at high doses by (a) fast neutron irradiation at 595 °C (Brager et al., 1971) (b) nickel ions with helium pre-implantation at 630 °C (Lewis et al., 1979).

### 2.1.2 Strain localization in radiation damaged austenitic stainless steels

With the advent of electron microscopy in the 1960s first observations of evidences of strain localization in neutron-irradiated copper were made by Greenfield and Wilsdorf (1961). Comparison of deformed unirradiated and irradiated copper showed that irradiation induces a more heterogeneous deformation mode. While deformation appears homogeneous in unirradiated copper (see Figure 2.10a) channels of intense deformation appear in irradiated copper (see Figure 2.10b). Formation of these deformation channels is commonly explained by the dislocation channeling mechanism. Dislocation channeling consists in localization of dislocation glide inside thin channels (typically 100 nm wide). These channels can appear when hardening defects are swiped out by gliding dislocations. The hardening defects being removed, dislocation glide becomes easier in the wake of previous dislocations. Dislocation channeling can be seen as a local softening behaviour. For dislocation channeling to occur sessile defect clusters (such as black dots and Frank dislocation loops), which are obstacles to dislocations, need to be present inside the bulk of the material (Wechsler, 1973; Zinkle and Matsukawa, 2004). Therefore dislocation channeling was observed in:

1. **irradiated metals**: in copper (Dai and Victoria, 1996; Essmann and Seeger, 1964; Greenfield and Wilsdorf, 1961; Sharp, 1974), zirconium (Farrell et al., 2003; Wei et al., 2007), niobium (Tucker et al., 1969; Wechsler et al., 1969), molybdenum (Mastel et al., 1963) and steels (Byun et al., 2006; Chaouadi, 2008; Farrell et al., 2003, 2004; Fish et al., 1973; Gussev et al., 2015; Hashimoto and Byun, 2007; Jiao and Was, 2010; Kacher et al., 2012; Renault-Laborne et al., 2018; Smidt Jr, 1970a,b)

2. **quenched hardened metals**: in gold due to stacking fault tetraedra (Bapna et al., 1968), aluminum due to vacancy loops (Essmann and Seeger, 1964; Mori and Meshii, 1969; Shin and Meshii, 1963), aluminum-magnesium (Greenfield and Crivelli-Visconti, 1966)

3. **predeformed metals**: in molybdenum due to dislocation tangles (Luft et al., 1975)

Dislocation channeling is responsible for the macroscopic decrease in ductility observed in irradiated materials discussed in 2.1.3.

Figure 2.11 shows TEM micrographs of irradiated SA 316 stainless steels displaying dislocation channels. Dislocation channels appear as clear bands in TEM because they are depleted

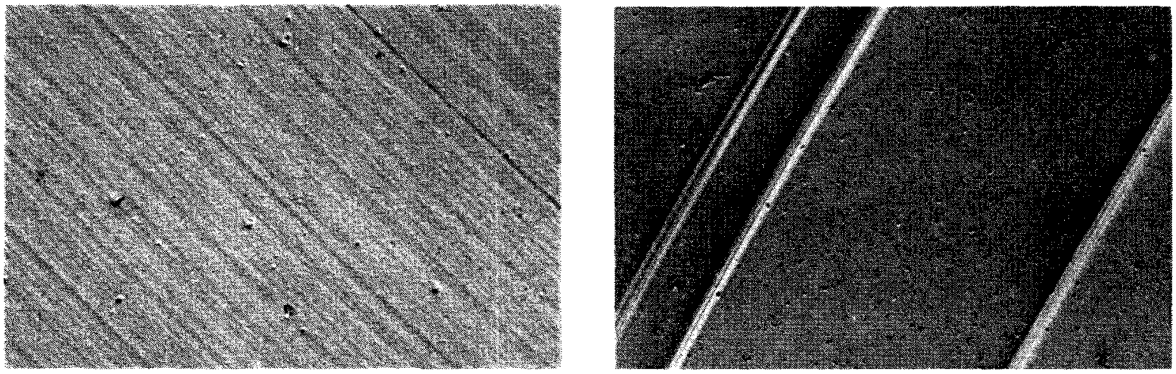

(a) (b)

Figure 2.10 Electron micrography of copper displaying (a) elementary structure in unirradiated copper; 20000X (b) clustered-structure characteristic of easy glide in neutron-irradiated copper; 6000X (Greenfield and Wilsdorf, 1961).

in defect clusters which appear as small black zones. It can be seen from 2.11a that dislocation channels can have different orientations in a single grain and therefore interact with each other. When irradiation is carried out in conditions for bubbles and voids to nucleate, dislocation channels may interact with these defect as well. Fish and Hunter (1976) showed how irradiation voids were significantly sheared inside a 50 nm wide dislocation channel. Garner (2012) measured a shear deformation of 100-200% inside this channel by comparing the shape of voids outside and inside of the channel.

Byun et al. (2006) proposed a microscale deformation mode map (see Figure 2.12) for 316 and 316LN stainless steels irradiated at low temperatures (60-100 °C) and tensile-tested at room temperature. The deformation map is given in terms of irradiation dose and maximum applied true stress. The zones where channel deformation occurs are located above 1000 MPa of maximum applied true stress or above 0.1 dpa irradiation dose.

Cui et al. (2018); Nogaret et al. (2008) investigated the formation of single dislocation channels by discrete dislocation dynamics (DDD) simulations. They performed numerical tensile tests experiments on low-dose and high-dose irradiated iron single crystals. They defined a deformation localization index (DLI) which corresponds to the percent of the volume with plastic strain that is lower than the volume average. They found (see Figure 2.13a) that this index increases with irradiation dose. For overall plastic strains lower than 1% the DLI decreases for both irradiation dose considered. However for the larger dose the DLI increases notably above 1% overall plastic strain, while it is almost constant for the lowest irradiation dose. Fig 2.13b shows that at higher dose, the increase of the DLI is associated to a transition from a multiple slip mode to a single slip mode. On the contrary, at low dose, no such a transition occurs (see Fig 2.13c).

Arsenlis et al. (2012) studied by DDD how the irradiation-induced defect density affects channeling localization in irradiated BCC iron. They showed that below defect densities of $3.61 \times 10^{21}\,\mathrm{m}^{-3}$ no dislocation channels are formed in a tensile test along a $\langle 001 \rangle$ loading direction. However at defect densities larger than $8.15 \times 10^{21}\,\mathrm{m}^{-3}$ dislocation channels are formed under the same loading conditions. Therefore it exists a critical defect density which triggers dislocation channeling which is in accordance with Cui et al. (2018) findings. Arsenlis et al. (2012) also showed that channel initiation and size are mediated by Frank loop coalescence resulting from elastic interactions with moving dislocations.

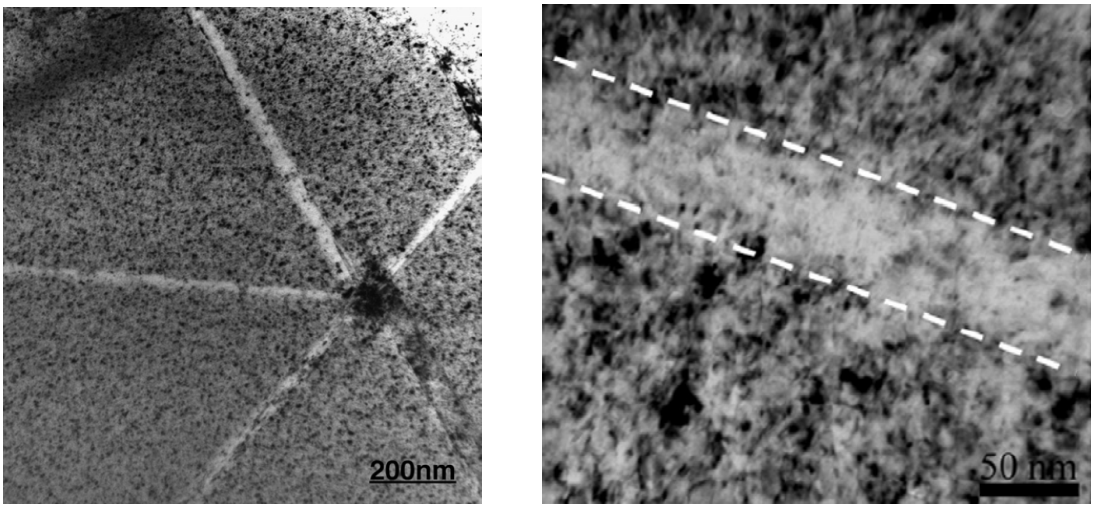


(a) (b)

Figure 2.11 (a) TEM micrography of dislocation channels in a SA 316 stainless steel neutron-irradiated at 65-100 °C to 0.78 dpa and tested at room temperature to an initial specimen strain rate of $10^{-3}\,s^{-1}$ (Hashimoto and Byun, 2007) (b) TEM micrography of a dislocation channel in a stainless steel proton-irradiated at 360 °C to 5 dpa and tested at 288 °C to 7% in argon (Jiao and Was, 2010).

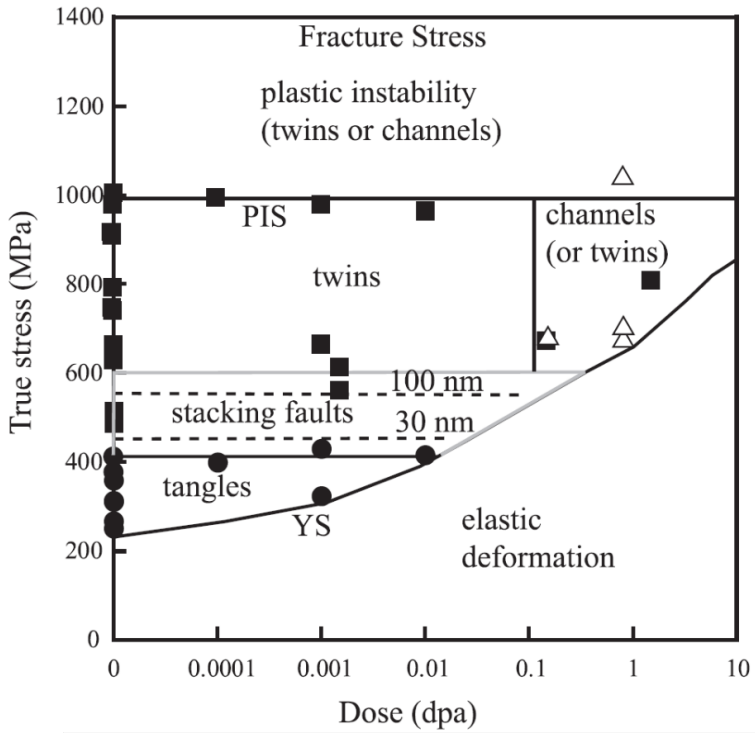


Figure 2.12 Deformation modes map with respect to irradiation dose and true stress for 316 and 316 LN stainless steels irradiated in a high flux isotope reactor (HFIR) at low temperatures (60-100 °C) and tested at room temperature. Plastic instability stress (PIS) is defined by the true stress at the onset of necking (Byun et al., 2006).

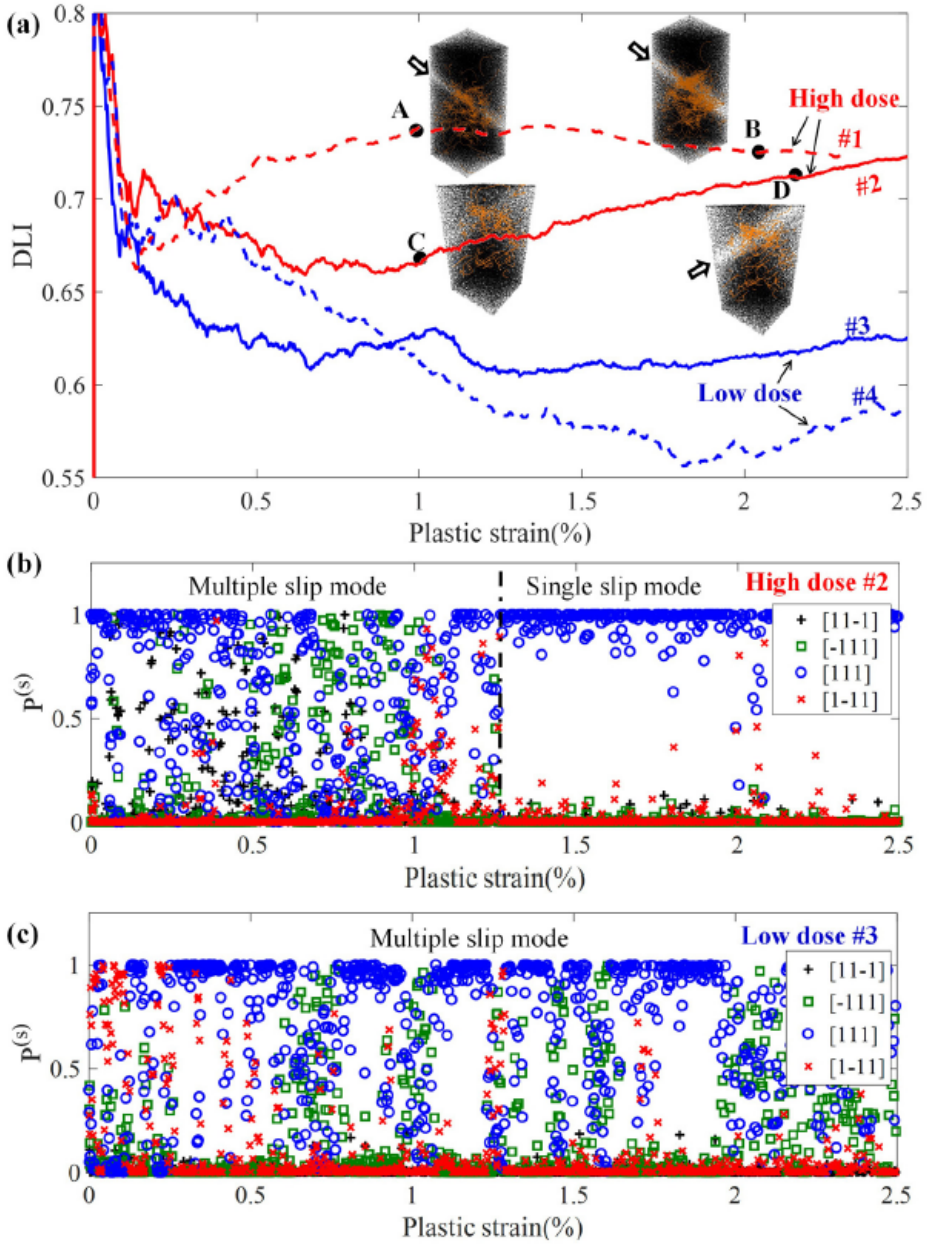


Figure 2.13 Discrete dislocation dynamics results of tensile tests on iron single crystal pillars of diameter 1.5 µm loaded along a ⟨001⟩ crystal direction. (a) Deformation Localization Index (DLI) evolution with respect to plastic strain (insets show irradiation defects (dark dots) distribution and dislocation network (orange lines), open arrows point at dislocation channels). (b-c) Plastic strain rate fractions induced by dislocations on different slip planes for high- and low-dose configurations (Cui et al., 2018).

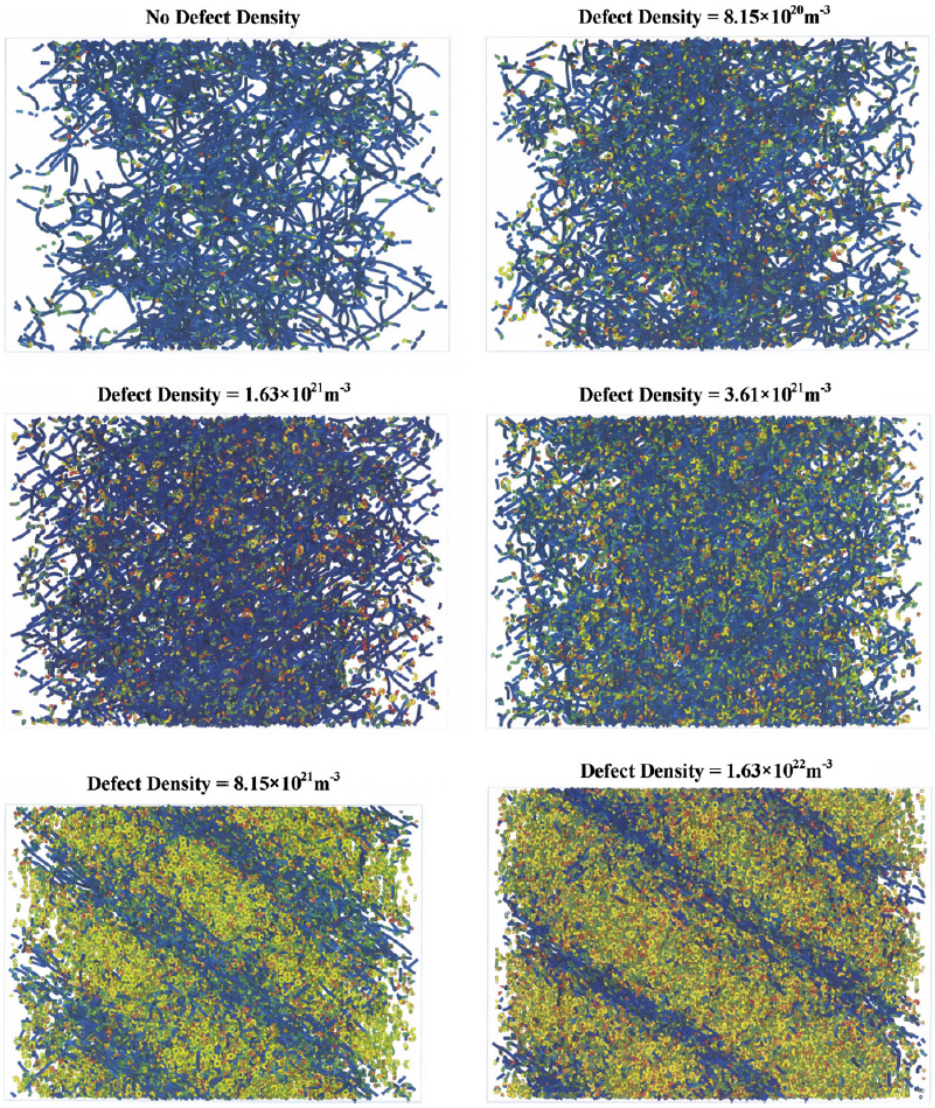


Figure 2.14 Transition from homogeneous to heterogeneous deformation as the defect density increases in irradiated BCC iron obtained by dislocation dynamics (DD) simulations. Green and yellow tones represent a high density of dislocation loops. Blue tones correspond to network dislocations (Arsenlis et al., 2012).

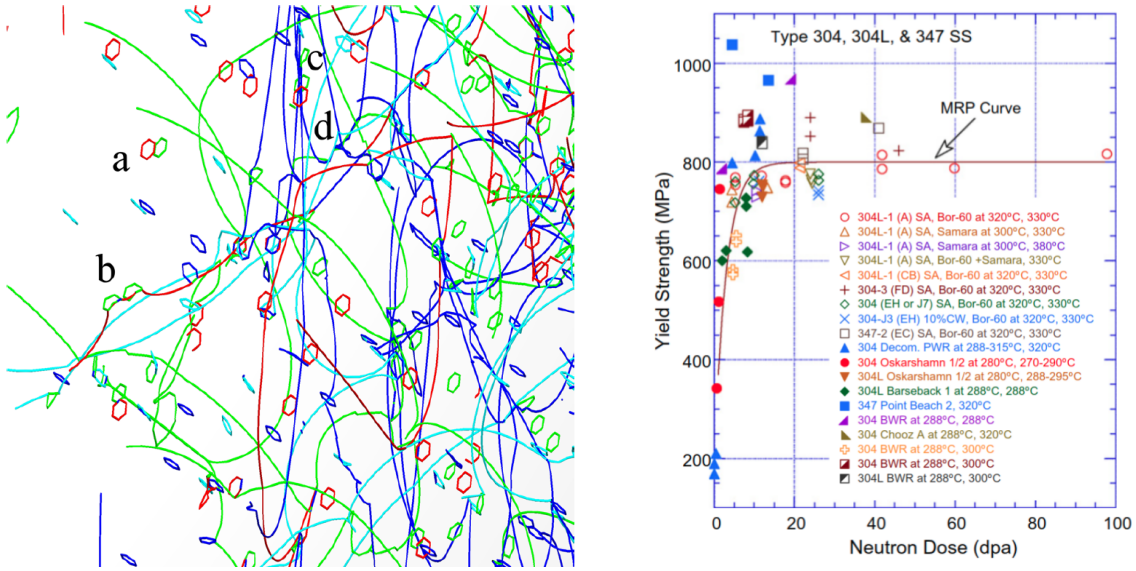


(a) (b)

Figure 2.15 (a) Dislocation – Frank loop Orowan interactions in DDD simulations of irradiated iron (Lehtinen et al., 2018). Frank loops appear as small closed ringlets, while dislocations correspond to elongated curved and entangled lines. (b) Yield strength evolution with respect to neutron dose for SA grade 304, 304L, 316L and 347 stainless steels at 270-380 °C (Chopra and Rao, 2011a).

### 2.1.3 Mechanical properties of undamaged and radiation damaged austenitic stainless steels

The mechanical properties in tension and crack propagation experiments on undamaged and radiation-damaged austenitic stainless steels are presented. These properties will be related to deformation mechanisms presented in section 2.1.2 and will be connected to the analysis of fracture modes proposed in section 2.1.4.

#### 2.1.3.1 Mechanical properties in tension

Four main features are observed when comparing tensile test macroscopic measurements on undamaged and radiation-damaged stainless steels irradiated in LWR and FNR conditions:

1. **A significant increase of the yield strength** is obtained after irradiation in LWR and FNR conditions. Pokor et al. (2004b) quantified this strengthening induced by irradiation for three different stainless steel grades, each of them irradiated in a different reactor, at 330 and 375 °C. The yield stresses of unirradiated SA 304 and CW 316 are respectively 380 MPa and 650 MPa. They both display an almost linear increase of the yield stress in the 0-10 dpa irradiation dose range with a quick saturation at about 500-600 MPa yield stress increase above 10 dpa. Increase of yield strength with irradiation dose in stainless steels were also reported and quantified in (Bagley et al., 1987; Bailat et al., 2000; Byun and Hashimoto, 2006; Chopra and Rao, 2011a; Garnier, 2009; Holmes and Straalsund, 1977; Renault-Laborne et al., 2018) and also in (Fish and Hunter, 1976; Garner et al., 1981; Hamilton et al., 1982; Odette and Lucas, 1989) where the dependence on irradiation temperature was studied. Such a strengthening is due to the presence of irradiation defects that act as barriers for dislocation motion. This Orowan-like mechanism is materialized in Figure 2.15a taken from a DDD simulation of irradiated iron (Lehtinen et al., 2018). Evolution of yield strength with neutron dose is depicted in Figure 2.15b.

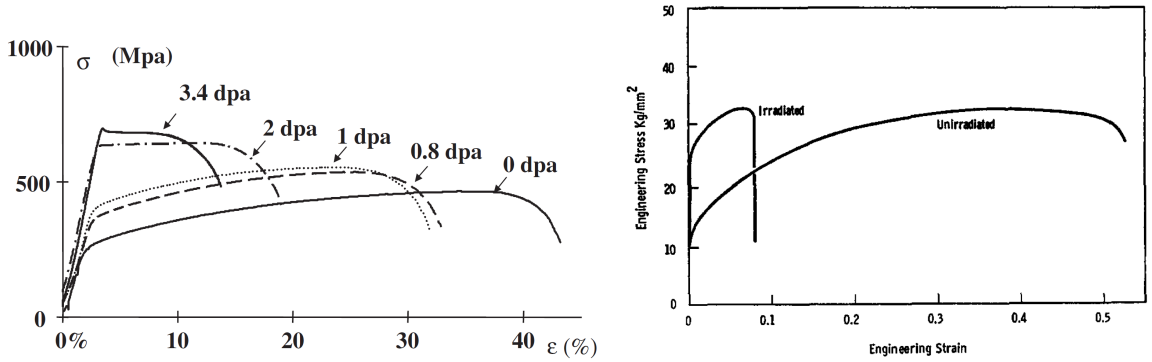


(a) (b)

Figure 2.16 (a) Tensile stress-strain curves obtained at 330 °C on a SA 304 stainless steels irradiated to different doses in OSIRIS reactor at about 330 °C (Pokor et al., 2004a). (b) Tensile stress-strain curves obtained at 600 °C on a 304 stainless steels irradiated in reactor EBR-II to $1.1\times10^{22}$ n/cm$^2$ at 540±50 °C (Holmes et al., 1969).

2. **An important decrease of the strain hardening capability** is induced by irradiation. Pokor et al. (2004a) performed tensile test experiments on SA 304L stainless irradiated up to 3.4 dpa in mixed spectrum OSIRIS reactor. As depicted in Figure 2.16a, they illustrated the rapid drop of the strain hardening capability with irradiation dose. At 2 dpa almost no strain hardening occurs. At 3.4 dpa a small stress drop is observed after the yield point and is followed by a stress plateau until striction and final failure. Decrease of hardening capability with irradiation dose in stainless steels was also reported and quantified in Byun and Hashimoto (2006); Pokor et al. (2004b); Renault-Laborne et al. (2018). A parallel between irradiation and pre-deformation can in fact be drawn as suggested by Byun and Farrell (2004b) and depicted in Figure 2.17a.

3. **An increase in the ultimate strength** is observed after irradiation. Even though the hardening capability decreases drastically with irradiation dose, the paramount augmentation of yield strength after irradiation is responsible for the increase of ultimate strength after irradiation. Evolution of ultimate strength with irradiation dose in stainless steels was reported and quantified in (Bagley et al., 1987; Byun and Hashimoto, 2006; Garnier, 2009; Holmes and Straalsund, 1977; Pokor et al., 2004a,b; Renault-Laborne et al., 2018).

4. **A sharp decrease of ductility** is exhibited after irradiation. Tensile experiments performed by Pokor et al. (2004a) show that the total elongation plummets with irradiation dose. As shown in Figure 2.16a, the total elongation is about 42% at 0 dpa and plunges to less than 15% at 3.4 dpa. Figure 2.16b displays the ductility reduction which can be observed in FNR conditions for a grade 304 stainless steel. Under such circumstances, at high fluences, even a macroscopic brittle-like behaviour can be observed. Figure 2.17b displays the evolution of total elongation with neutron dose in different stainless steels. Decrease of ductility with irradiation dose in stainless steels was also reported and quantified in Bagley et al. (1987); Garnier (2009); Pokor et al. (2004b); Renault-Laborne et al. (2018) and also in (Fish and Hunter, 1976; Hamilton et al., 1982) where the dependence on irradiation temperature was studied. Ductility loss is in fact a direct outcome of the strain hardening capability decrease. Considère's global instability criterion (Considère, 1885) predicting onset of necking ($\mathrm{d}F/\mathrm{d}\varepsilon \leq 0$ or $\mathrm{d}\sigma/\mathrm{d}\varepsilon \leq \sigma$) is met earlier when the macroscopic strain hardening slope is reduced. If the macroscopic ductility is notably affected by irradiation, nevertheless, locally, large strain levels can be reached in the vicinity of the neck.

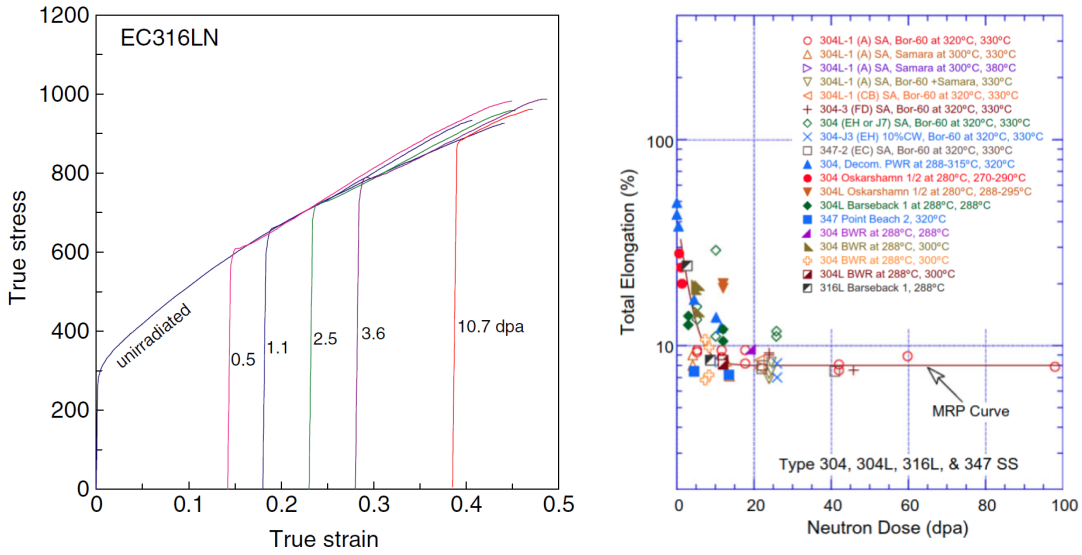


(a) (b)

Figure 2.17 (a) Equivalence between irradiation and pre-deformation for true stress-true strain tensile curves of a 316LN stainless steel irradiated to different doses. Curves of irradiated specimen were positively shifted by 0.14, 0.18, 0.23, 0.28, and 0.385 horizontally in order to match the unirradiated specimen curve. Increase in yield stress induced by irradiation equals 305, 358, 421, 485, and 587 MPa respectively (Byun and Farrell, 2004b). (b) Total elongation evolution with respect to neutron dose for SA grade 304, 304L, 316L and 347 stainless steels at 270-380 °C (Chopra and Rao, 2011a).

#### 2.1.3.2 Mechanical properties for crack propagation

Fracture toughness is a measure of a material's resistance to the propagation of a crack. Experiments conducted at several neutron doses and irradiation temperatures on compact tension (CT) specimens show a significant decrease of toughness when increasing irradiation dose (Alexander et al., 1996; Chopra and Rao, 2011a,b; Chopra and Shack, 2008; Clarke et al., 1990; Hamilton et al., 1987; Jitsukawa et al., 1999; Krug and Shogan, 2005; Little, 1986; Michel and Gray, 1987; Mills, 1988; Rodchenkov et al., 2009; Torimaru et al., 2010; Xu and Fyfitch, 2004). Figure 2.18a and 2.18b exhibit a sharp, almost linear, plunge of fracture energy $J_{Ic}$ in the 0-10 dpa range, followed by a quick saturation to a plateau value above 10 dpa. It can be seen that similar trends are observed in LWR and FNR irradiations conditions. In fact it is well established that fracture toughness is strongly positively correlated to the yield strength and even more so to the hardening capability of a material (Pardoen and Hutchinson, 2003). Therefore increase of yield strength and decrease of hardening capability, observed when increasing dose in radiation-damaged materials, are opposite driving forces regarding the fracture toughness of nuclear stainless steels. In addition depending on irradiation conditions precipitation and swelling (by cavity formation) may occur. Both are known to have a detrimental impact on fracture toughness when the fracture is governed by nucleation, growth and coalescence of voids. As a consequence, as their time in reactor increases (thus their neutron exposure increases), structural integrity of austenitic stainless steels with respect to crack propagation should be closely monitored. In that respect, understanding the underlying fracture mechanisms associated with this property is of paramount importance. To that extent, the following section is dedicated to the whys and wherefores of aforementioned fracture properties.

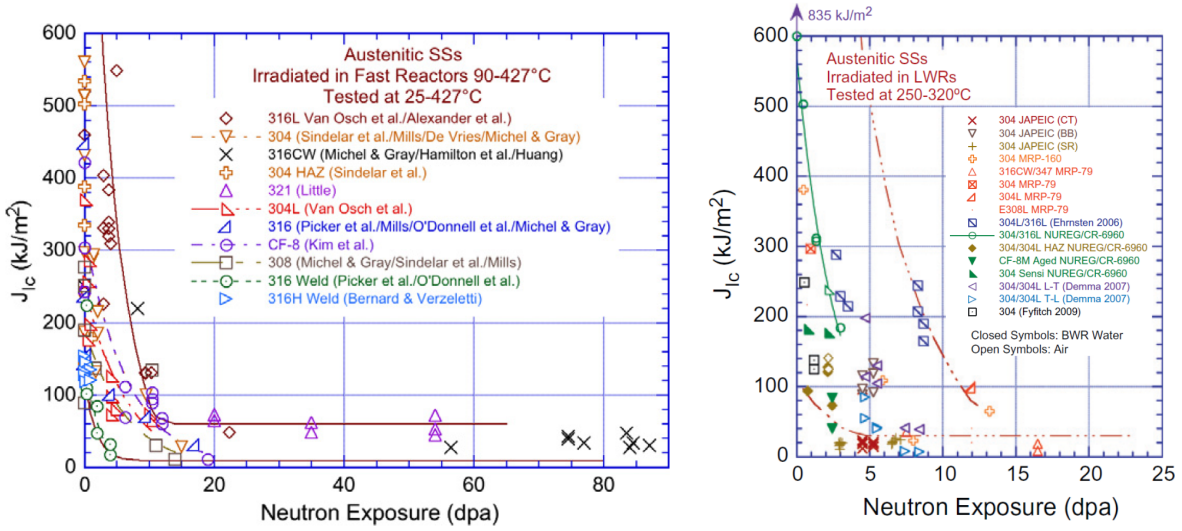


(a) (b)

Figure 2.18 (a) Fracture energy $J_{Ic}$ with respect to neutron exposure for different stainless steels grades irradiated in FNR at 90-427 °C and tested at 25-427 °C (a) and LWR and tested at 250-320 °C (Chopra and Rao, 2011b).

### 2.1.4 Fracture mode in radiation damaged austenitic stainless steels

Despite alteration of mechanical properties due to irradiation, the major fracture mode of radiation-damaged austenitic stainless steels remains mostly ductile through void growth to coalescence mechanisms in a wide range of temperatures, loading rates and neutron fluences when tested outside a corrosive environment. Nevertheless fracture toughness plummets when irradiation dose increases as discussed in section 2.1.3. Therefore there is a particular interest in looking into the effect of irradiation on the mechanisms of void-driven ductile failure.

Krug and Shogan (2005) and Conermann (2005) investigated the void-driven ductile fracture mechanisms of stainless steels irradiated in LWR conditions. As shown in 2.19, in absence of irradiation a classical dimpled fracture surface is observed. These dimples are the outcome of coalescence of micrometric voids. Interestingly, when irradiation dose increases the fracture surfaces remain predominantly composed of dimples similar to those observed at 0 dpa. These observations, combined with the loss of ductility previously discussed, raise the question of how the deformation mechanisms influence nucleation, growth and coalescence of such micrometric voids. In particular, understanding the interaction between strain localization inside channels and evolution of intragranular voids could help explain more precisely the loss of toughness due to irradiation.

Hunter et al. (1972) analyzed the ductile fracture surfaces of 304 SA stainless steels irradiated between 0 and 54 dpa in FNR conditions. Figure 2.19 shows the fracture surfaces observed at 0 dpa, 14 dpa and 54 dpa. A classical ductile fracture surface exhibiting dimples is observed at 0 dpa. At 14 dpa dimpled regions are still visible, but flat transgranular facets are also clearly apparent. At 54 dpa the fracture surface is mainly composed of transgranular facets. Similar observations were made by Gurovich et al. (2015); Margolin et al. (2016) on 18Cr-10Ni-Ti austenitic stainless steel tensile specimen fracture surfaces. Their samples were taken from BOR-60 reactor shield assemblies irradiated at temperatures which vary along the assemblies from 320 to 450 °C which cover a wide range of radiation-induced swelling values. Irradiation doses vary from 30 to 150 dpa and the samples were tested at 290 °C. The authors were able to correlate the amount of dimpled area and transgranular facets on the fracture surface to the swelling level induced by irradiation. In addition they reported a third kind of fracture surface morphology, composed of nano-dimples, which appears at large swelling levels. Nano-dimples were also observed after high doses irradiations in FNR Phenix as shown in Figure 2.19 at 90

dpa. In the literature a different ductile fracture mechanism is associated to each fracture surface morphology:

1. **classical void-driven ductile fracture** by nucleation, growth and coalescence of micrometric voids. It is characterized by presence of micrometric dimples on fracture surfaces and occurs at low irradiation doses.

2. **channel fracture** induced by intense localization of plastic deformation (so-called channel deformation). It is characterized by presence of transgranular, often terraced, flat facets on fracture surfaces. Channel fracture was reported in irradiated austenitic stainless steels in (Bloom, 1976; Fish et al., 1973; Fukuya et al., 2008; Hamilton et al., 1987; Hojná, 2017; Huang, 1984, 1992; Hunter et al., 1972; Little, 1986; Margolin et al., 2016; Mills, 1988, 1997; Odette and Lucas, 1991). It occurs at intermediate to high irradiation doses.

3. **nanovoid-driven ductile fracture** by growth and coalescence of vacancy voids. It is characterized by presence of unstructured zones composed of nano-dimples on fracture surfaces. Nano-dimpling was reported in irradiated austenitic stainless steels in (Courcelle et al., 2018; Gurovich et al., 2015; Neustroev and Garner, 2009). It occurs at very high doses, when irradiation induced swelling is considerable.

These fracture modes may coexist, hence fracture surfaces may be a composite of micro-dimples, flat facets and nano-dimples. Margolin et al. (2016) measured the fracture mode portion as a function of swelling for two different shield assemblies (see Figure 2.20). Classical ductile fracture dominate at swelling levels below 2%. The channel fracture mode, characterized by flat facets, covers a wide range of swelling levels for the BM-7 shield assembly irradiated between 30-46 dpa. However for higher dose levels (100-150 dpa for E-65 shield assembly) nanovoid-driven ductile failure already predominates above 3.5% swelling. The TEM micrography by Fish et al. (1973) in Figure 2.21 showing how vacancy voids are sheared inside a dislocation channel might give some insight of the underlying mechanisms of channel fracture and/or nanovoid-driven fracture. Although heavily irradiated materials exhibit, macroscopically, very low ductility, they display, microscopically, a very high ductility inside dislocation channels. This drastically heterogeneous deformation mode affects how material fails. A characteristic length can be associated to this heterogeneity. Instead of favouring failure by nucleation, growth and coalescence of voids bigger in size, it promotes failure by growth/shearing of voids smaller in size than this characteristic length.

In this section the radiation-induced microstructure evolutions were introduced. In particular, defects formed under LWR and FNR irradiation conditions were presented. Existence of a localized deformation mechanism and the conditions prone for its appearance were then investigated. Irradiation was shown to have a detrimental effect on mechanical properties and more specifically on toughness. In order to get some insight on the link between mechanical characteristics and microstructural properties and deformation mechanisms, attention was given to fracture surfaces and information they give on fracture mechanisms. Two tracks of investigation can readily be identified and constitute the topics of the next two sections. First of all a succinct overview of strain localization modeling is presented. Then, existing models for void-driven ductile fracture and their extension to crystal plasticity are introduced.

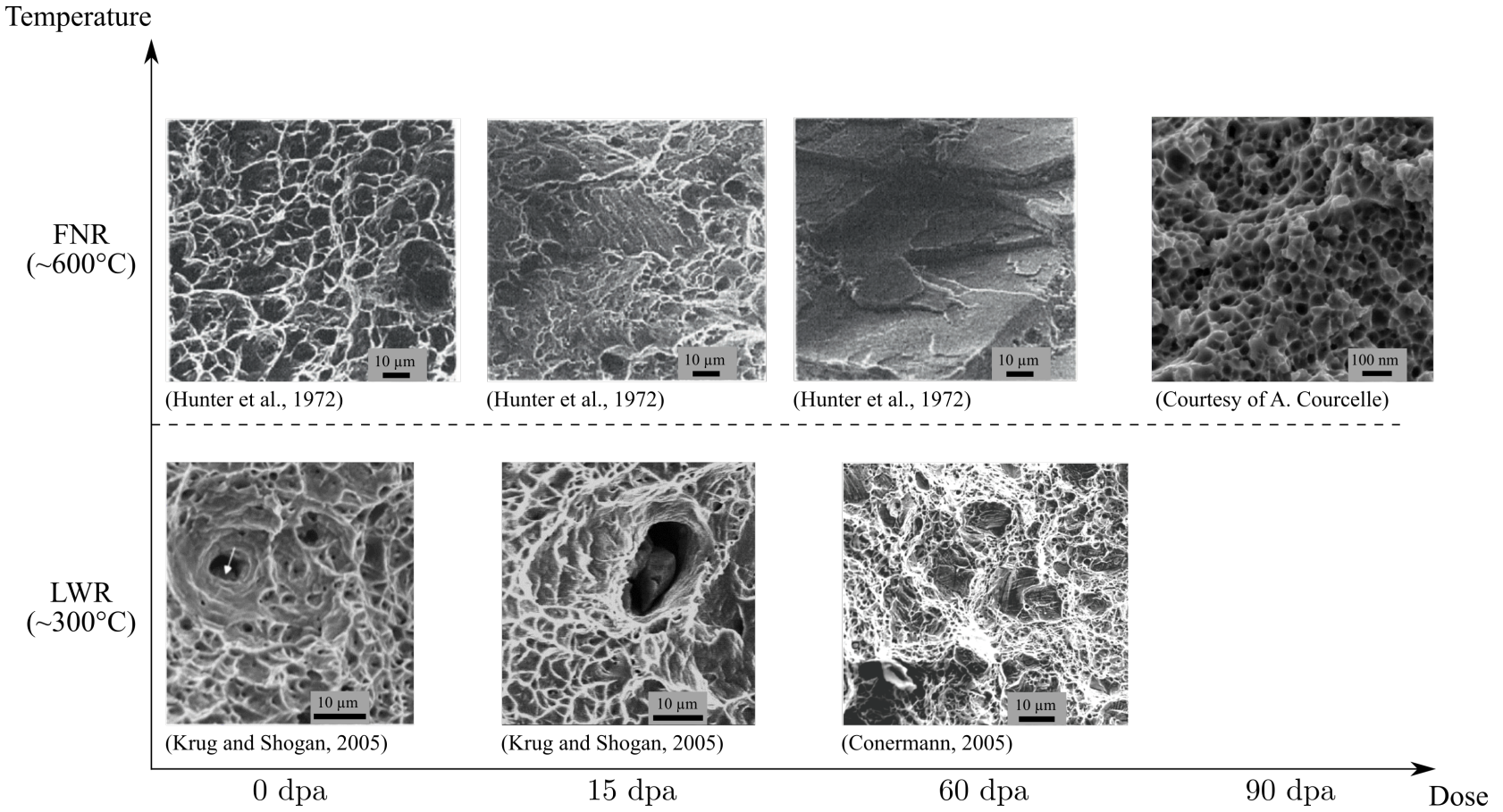


Figure 2.19 Fracture surfaces as a function of dose and temperature of irradiation in austenitic stainless steels. Scanning electron micrographs are taken from (Conermann, 2005; Garner, 2012; Hojná, 2017; Hunter et al., 1972; Krug and Shogan, 2005).

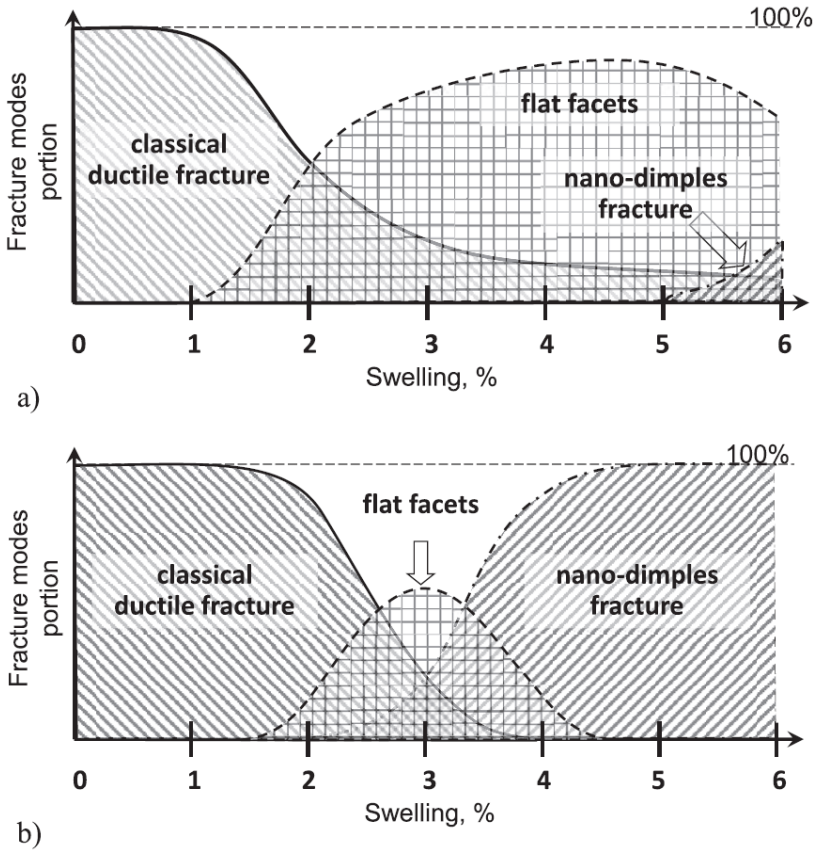


Figure 2.20 Fracture modes evolution with respect to swelling for (a) BM-7 shield assembly irradiated between 320-450 °C to 30-46 dpa and (b) E-65 shield assembly irradiated between 320-370 °C to 100-150 dpa of Russian water-water energetic reactor (WWER) BOR-60 (Margolin et al., 2016).

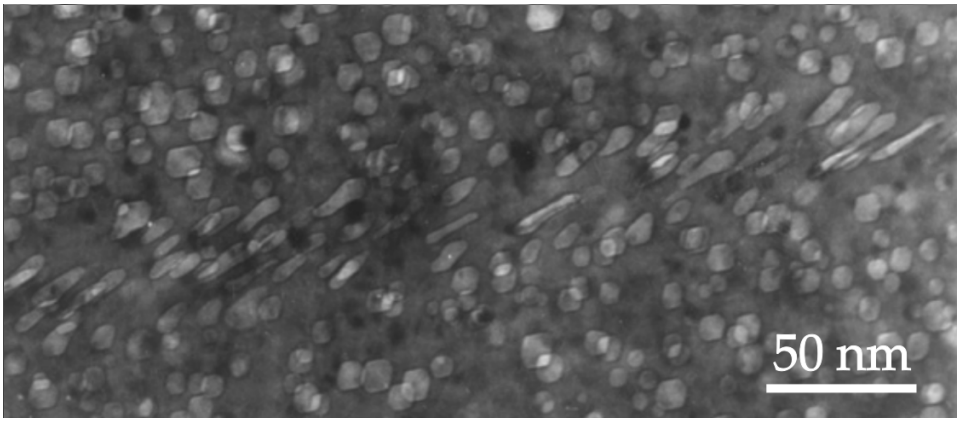


Figure 2.21 304 steel tensile specimen neutron-irradiated to 40 dpa at 400 °C and tested at 370 °C. Elongation of voids suggests a strain of 100–200% in the ~50 nm wide deformation band (Fish et al., 1973).

## 2.2 Strain localization phenomena in metallic materials

In the forthcoming section the origins of strain localization phenomena are discussed. Then, the advantages of non-local models to describe such mechanisms are introduced.

### 2.2.1 Conditions to strain localization

In the literature strain localization phenomena are recognized to be caused by:

1. **global instabilities** which were first theorized by Considère (1885) and later generalized and linked to the loss of uniqueness of the solution to the rate boundary value problem by Hill (1958). These instabilities are reputed to be responsible for localization phenomena such as diffused necking, but also for buckling as illustrated in Figure 2.22. Intervoid necking, which consists in necking of the ligament separating two voids and commonly considered as onset of void coalescence, is regarded as playing a major role in ductile failure by void growth and coalescence and also belongs to this class. Mathematically, such instabilities are associated with the instability criterion $\det\left(\underset{\approx}{\boldsymbol{\mathcal{L}}}\right) = 0$ where $\underset{\approx}{\boldsymbol{\mathcal{L}}}$ is the tangent operator.

2. **material instabilities** such as strain softening or dynamic strain aging. These instabilities, which can be predicted by the criterion derived in (Rice, 1976) and its extensions, are reputed to be responsible for localization phenomena such as shear banding, Lüders bands and Portevin-Le Chatelier effect. This criterion states that there might be a jump in strain rates (*i.e.* strain localization) if $\det\left(\underline{\boldsymbol{N}}.\underset{\approx}{\boldsymbol{\mathcal{L}}}.\underline{\boldsymbol{N}}\right) = 0$, where $\underline{\boldsymbol{N}}$ is the unit normal to the surface discontinuity. Slip and kink bands observed in single crystals (see Figure 2.23) are common occurrences of such instabilities (Asaro and Rice, 1977). Dislocation channels observed in irradiated metals also belong to this class.

### 2.2.2 Modeling of strain localization phenomena

In the context of nuclear materials, Marano et al. (2019) investigated the formation of dislocation channels at the polycrystal level using a continuum crystal plasticity model in Fast Fourier Transform (FFT) simulations. In order to trigger strain localization the authors considered a phenomenological exponential softening for the critical resolved shear stress of each slip system. They showed that several parallel channels of intense deformation appear in each grain. These bands are either parallel (slip bands) or orthogonal (kink bands) to the preferential slip plane of

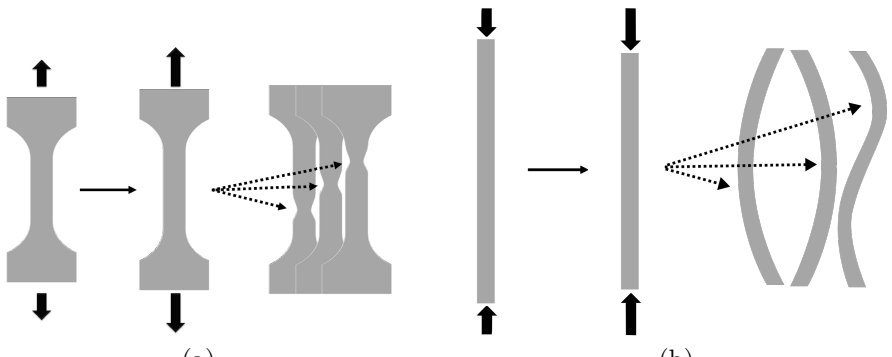


Figure 2.22 (a) Schematic of necking in a tensile experiment (Al Kotob, 2019) (b) Schematic of buckling in a compression experiment.

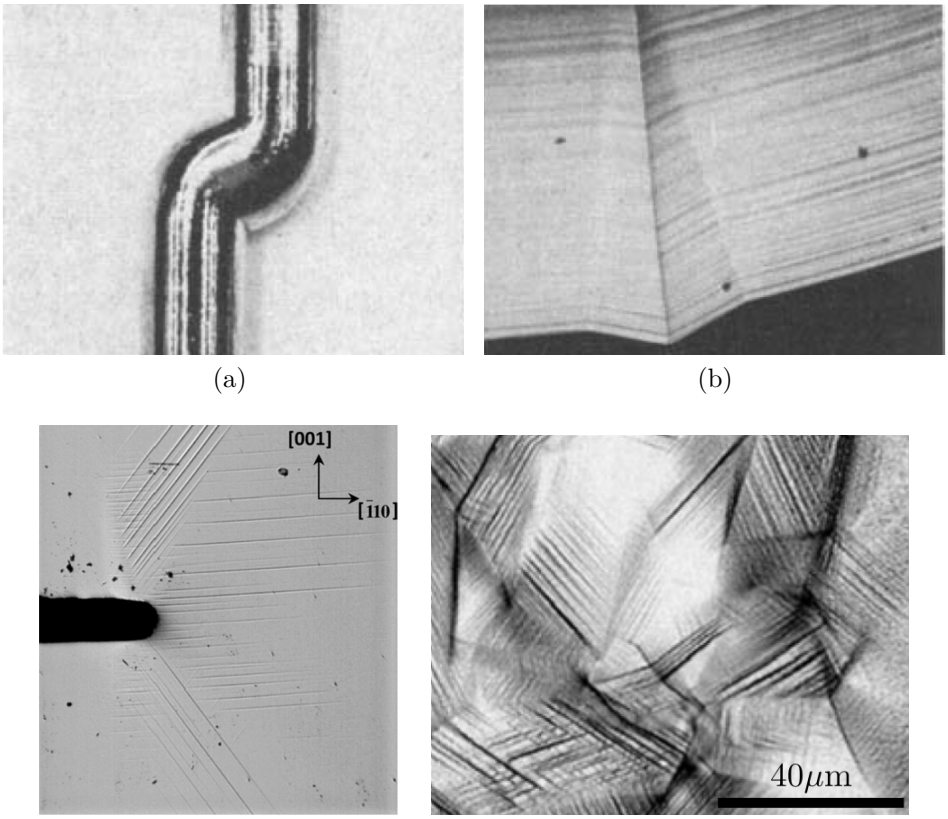


(a) (b)

(c) (d)

Figure 2.23 Compressive (a) ortho- and (b) para-kink bands in zinc single crystals after loading in compression (Gilman, 1954). (c) SEM micrography of slips bands at a crack tip in deformed Nickel-based superalloy single crystal CT-specimen (Sabnis et al., 2012). (d) Digital Image Correlation (DIC) strain map obtained after 7% macroscopic strain of a 304L stainless steel polycrystal tensile specimen (Di Gioacchino and Quinta da Fonseca, 2013).

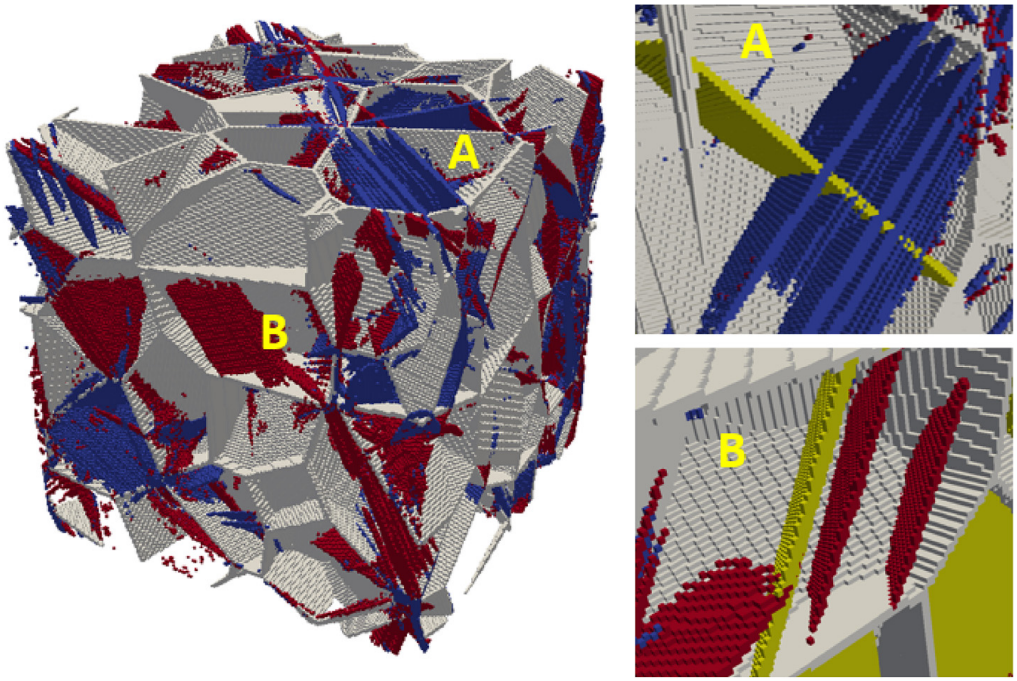


Figure 2.24 Fast Fourier Transform (FFT) crystal plasticity simulation results of a 3D FCC polycrystal displaying localization slip (red) and kink (blue) bands. Grain boundaries and activated slip planes are respectively plotted grey and yellow (Marano et al., 2019).

the grain they belong to as originally predicted by Asaro and Rice (1977). The authors argued that kink bands, which are responsible for large crystal lattice curvature, are never observed in practice in irradiated materials. Therefore they used a strain gradient extension of their model in order to penalize lattice rotations and were able to replace kink bands by bundles of slip bands in their simulations. However, as pointed out by the authors, due to the softening behaviour which is considered and despite the regularization technique they use to cancel kink bands, their simulations are mesh size dependent. This kind of mesh dependencies is a regular issue in the context of softening behaviour.

Modeling strain localization phenomena with conventional plasticity generally entails dependency of the results on the spatial discretization used to solve the underlying differential equations. In the context of finite element analysis, results may then depend on element type, element size, element orientation, etc. For example, absence of convergence when element size is reduced (see Fig 2.26a) is often encountered when localization occurs. The root of this issue is the loss of ellipticity of partial differential equations for example when softening comes into play. The loss of stability causes softening and localization to be a self-perpetuating phenomenon. One solution to deal with absence of mesh convergence is to treat the mesh size as a material parameter (Achouri et al., 2013; Xue et al., 2010). Therefore this parameter can then be identified on experimental data. However this approach is not fully satisfactory because it requires to know *a priori* where localization will occur. Another approach to deal with strain localization is to take advantage of so called non-local models. These theories involve regularization techniques based on integral or gradient operators. A proposition of classification of the generalized continuum theories is given in Figure 2.25 by Forest (2006). The key idea shared by such models is to consider that the behaviour of a given material point depends not only on its own state but also on the state of its neighbours. Therefore material length scales naturally arise and will serve as parameters to be linked to the characteristic length of plastic deformation mechanisms involved during localization processes. For a more detailed comparison of several non-local formulations the reader is referred to (Chen, 2019). Figure 2.26 shows how a gradient-based non-local model allows to alleviate mesh dependency results when softening-induced strain localization occurs. Similarly, Figure 2.27 demonstrates how an integral non-local formulation allows to solve mesh

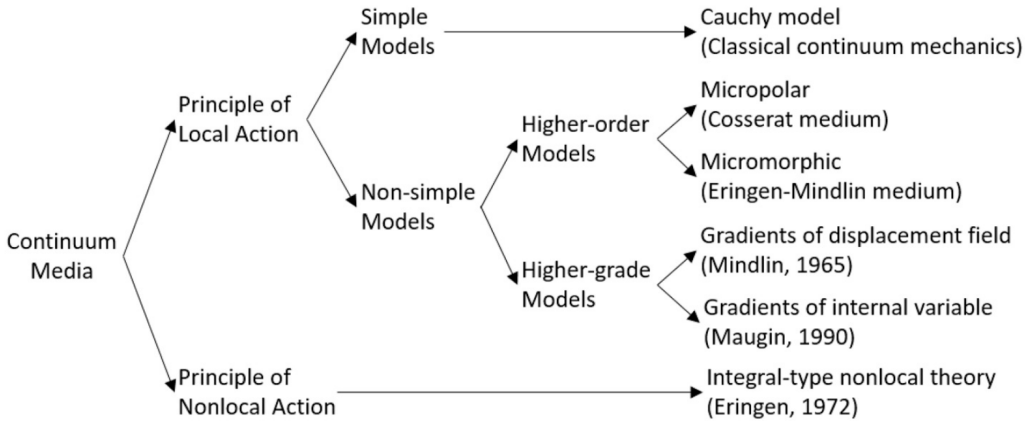


Figure 2.25 Proposition of classification of the mechanics of generalized continuum media (Forest, 2006).

dependency when softening is induced by damage. Other techniques, such as phase field methods have recently been used in order to treat efficiently non-localities (Ask et al., 2018; Miehe et al., 2010).

For the purpose of this work focus is set on strain gradient continuum plasticity theories, because they present the advantage of being easier to implement in numerical solvers. A thorough review on theoretical, numerical and experimental aspects of these theories was recently published by Voyiadjis and Song (2019). The idea of these formulations is to introduce the second gradient of displacement or the gradient of a strain measure into the framework. Several approaches were pursued in the literature. Nye (1953) proposed the first gradient-enhanced plasticity theory in order to predict measured size effects by accounting for the geometrically necessary dislocations (GND) density tensor. The probably most general and ambitious gradient theories were then developed for elasticity in (Eringen and Suhubi, 1964; Mindlin, 1964, 1965; Toupin, 1962) and plasticity in (Forest and Sievert, 2003; Gudmundson, 2004; Hutchinson and Fleck, 1997). Forest (2009) reviewed several strain gradient approaches to the elasticity, plasticity, damage, and diffusion in solids. The author showed how these theories relate to one another and can be cast into the unifying micromorphic approach. For crystal plasticity models in the setting of gradient plasticity, three classes can be identified. A family of models is based on the GND density tensor (Cordero et al., 2010; Gurtin, 2002). Another is based on scalar measures of statistically stored dislocation (SSD) and GND densities on each slip system (Evers et al., 2004; Svendsen and Bargmann, 2010). The last, proposed by Wulfinghoff and Böhlke (2012), is based on a single accumulated plastic strain measure.

In order to guaranty that these theories do not violate the fundamental laws of thermodynamics, several thermodynamical formulations were developed in the literature. The method pursued by Forest et al. (2002); Frémond and Nedjar (1996); Gurtin and Anand (2009); Hutchinson and Fleck (1997) of enriching the power density of internal forces and of contact forces is presented briefly. The cornerstone of the enriched internal power formulation is the idea that introduction of mechanical gradient effects should lead to an extension of the power of internal and contact forces entering the principle of virtual power. For sake of simplicity and the purpose of this work the gradient of a single scalar accumulated plastic strain variable, noted $p$, is considered. In the context of small strains, the enriched power of internal and contact forces is introduced as

$$\mathcal{P}^{(i)} = \underset{\sim}{\boldsymbol{\sigma}} : \underset{\sim}{\dot{\boldsymbol{\varepsilon}}} + a\dot{p} + \underline{\boldsymbol{b}} . \nabla \dot{p} \qquad \mathcal{P}^{(c)} = \underline{\boldsymbol{t}} . \underline{\dot{\boldsymbol{u}}} + a^c \dot{p} \tag{2.1}$$

where $\underset{\sim}{\boldsymbol{\sigma}}$ is the Cauchy stress tensor, $\underset{\sim}{\dot{\boldsymbol{\varepsilon}}}$ the total strain rate tensor, $a$ and $\underline{\boldsymbol{b}}$ generalized scalar and vector stresses, $\underline{\boldsymbol{t}}$ the surface traction vector, $\underline{\dot{\boldsymbol{u}}}$ the displacement rate and $a^c$ a generalized

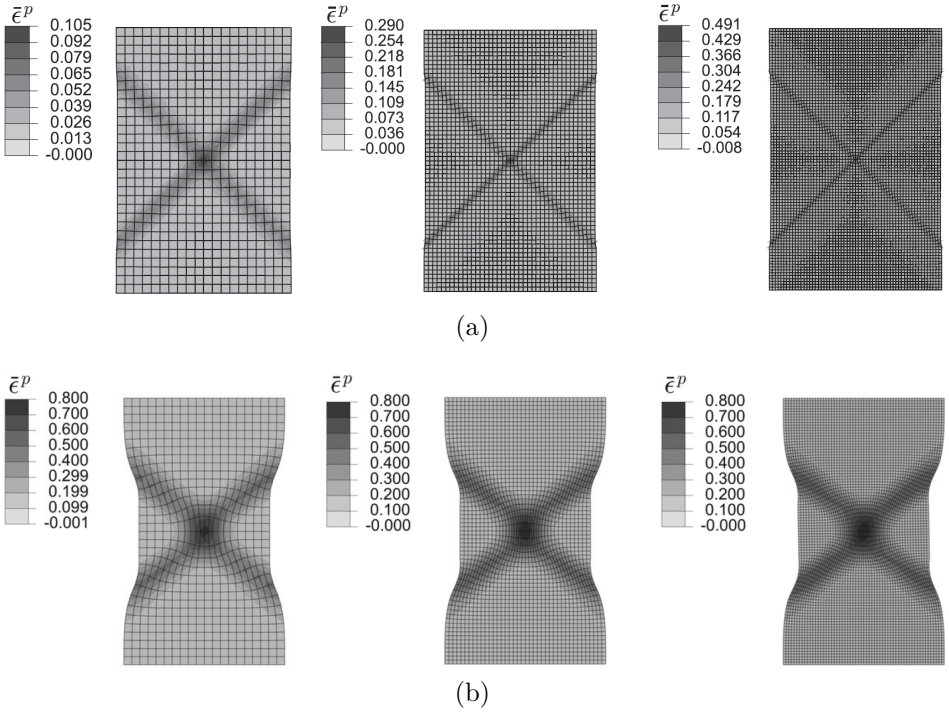


Figure 2.26 (a) Softening-induced localization in shear bands without gradient-regularization displaying mesh dependence. (b) Softening-induced localization in shear bands with gradient-regularization displaying mesh convergence (Anand et al., 2012).

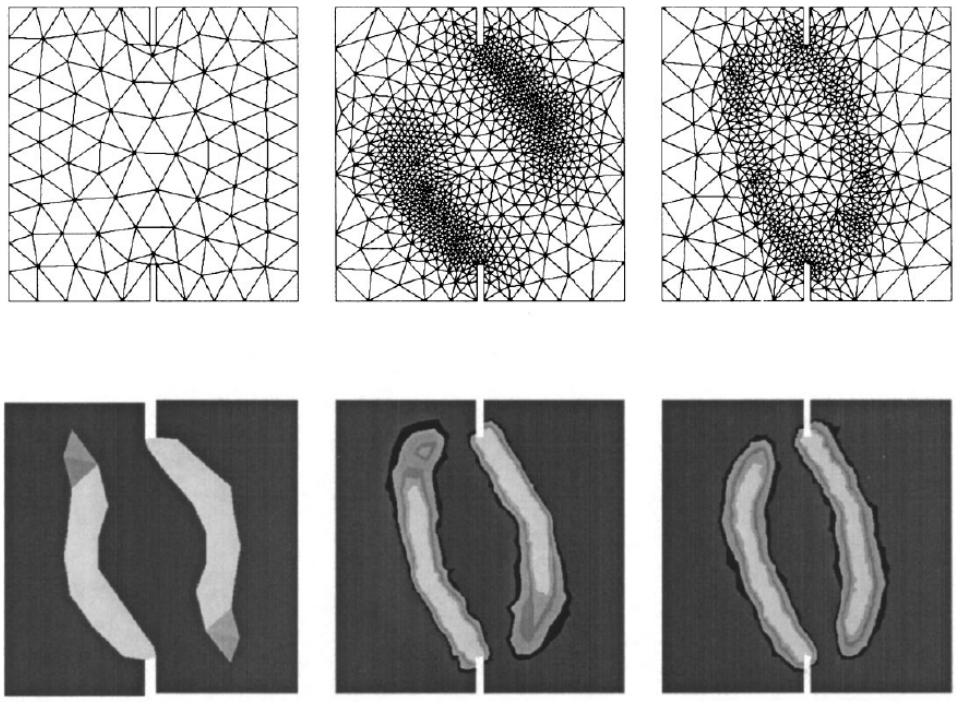

Figure 2.27 Regularized curved crack propagation in a double-edge notched specimen obtained with an integral non-local formulation by (Bažant and Jirásek, 2002).

contact stress scalar. The generalized principle of virtual power which ensues states that *the stress and acceleration field in a material body, verify the local equations of dynamics if and only if the power of the internal, remote and contact forces balances the power of the acceleration field in any virtual motion and for any sub-domain, under the hypothesis of continuity of the fields involved.* Neglecting the contribution of inertia effects and remote forces it gives for any sub-domain $D$

$$\int_D (\underset{\sim}{\boldsymbol{\sigma}} : \dot{\underset{\sim}{\boldsymbol{\varepsilon}}} + a\dot{p} + \underline{\boldsymbol{b}} . \nabla \dot{p}) \, \mathrm{d}V = \int_{\partial D} (\underline{\boldsymbol{t}} . \underline{\dot{\boldsymbol{u}}} + a^c \dot{p}) \, \mathrm{d}S \tag{2.2}$$

where $\partial D$ represents the surface boundary of sub-domain $D$. Applying the divergence theorem results in the following generalized balance equations and Neumann boundary conditions

$$\begin{aligned}
\mathrm{div}\,(\underset{\sim}{\boldsymbol{\sigma}}) &= \underline{\mathbf{0}} \quad \forall \underline{\boldsymbol{x}} \in D && (2.3)\\
\mathrm{div}\,(\underline{\boldsymbol{b}}) &= a \quad \forall \underline{\boldsymbol{x}} \in D && (2.4)\\
\underline{\boldsymbol{t}} &= \underset{\sim}{\boldsymbol{\sigma}} . \underline{\boldsymbol{n}} \quad \forall \underline{\boldsymbol{x}} \in \partial D && (2.5)\\
a^c &= \underline{\boldsymbol{b}} . \underline{\boldsymbol{n}} \quad \forall \underline{\boldsymbol{x}} \in \partial D && (2.6)
\end{aligned}$$

where $\underline{\boldsymbol{n}}$ denotes the outward surface normal unit vector. The first law of thermodynamics then states that *the variation of internal and kinetic energy of any sub-domain of a material body in the current configuration is due to mechanical power and heat input.* In absence of heat transfers it gives in the local form

$$\mathcal{P}^{(i)} = \rho \dot{e} \tag{2.7}$$

where $e$ is the specific internal energy density and $\rho$ the volumetric mass density. An additive decomposition of the strain tensor in an elastic and a plastic part $\underset{\sim}{\boldsymbol{\varepsilon}} = \underset{\sim}{\boldsymbol{\varepsilon}}^e + \underset{\sim}{\boldsymbol{\varepsilon}}^p$ is considered. The Helmholtz specific free energy density, $\psi = e - Ts$, where $T$ is the temperature and $s$ the specific entropy density, is assumed to depend on the set of state variables $\{\underset{\sim}{\boldsymbol{\varepsilon}}^e, p, \nabla p\}$. The second law of thermodynamics states that the global amount of entropy increases. Therefore in absence of entropy flux and source, the specific dissipation density $d$ is positive

$$d = T\dot{s} = \dot{e} - \dot{\psi} \geq 0 \tag{2.8}$$

Combining the first and second laws of thermodynamics Eq. (2.7) and (2.8) it comes

$$\rho d = \left( \underset{\sim}{\boldsymbol{\sigma}} - \rho \frac{\partial \psi}{\partial \underset{\sim}{\boldsymbol{\varepsilon}}^e} \right) : \dot{\underset{\sim}{\boldsymbol{\varepsilon}}}^e + \left( a - \rho \frac{\partial \psi}{\partial p} \right) \dot{p} + \left( \underline{\boldsymbol{b}} - \rho \frac{\partial \psi}{\partial \nabla p} \right) . \nabla \dot{p} + \underset{\sim}{\boldsymbol{\sigma}} : \dot{\underset{\sim}{\boldsymbol{\varepsilon}}}^p \geq 0 \tag{2.9}$$

The following state laws are then postulated

$$\begin{aligned}
\underset{\sim}{\boldsymbol{\sigma}} &= \rho \frac{\partial \psi}{\partial \varepsilon^e} && (2.10)\\
a &= \rho \frac{\partial \psi}{\partial p} - \overline{H} && (2.11)\\
\underline{\boldsymbol{b}} &= \rho \frac{\partial \psi}{\partial \nabla p} && (2.12)
\end{aligned}$$

where it has been assumed for sake of simplicity that no dissipation is associated with the generalized stress $\underline{\boldsymbol{b}}$, whereas $-\overline{H}$ is the dissipative part of the generalized stress a. This approach allows to recover the Aifantis (1984, 1987) gradient theory which involves a single internal length.

The residual mechanical dissipation is then

$$\rho d = \underset{\sim}{\boldsymbol{\sigma}} : \dot{\underset{\sim}{\varepsilon}}^p - \overline{H}\dot{p} \quad \geq \quad 0 \tag{2.13}$$

At this stage a dissipation pseudo-potential $\Omega$, function of the thermodynamic forces $-\underset{\sim}{\boldsymbol{\sigma}}$ and $\overline{H}$, can be defined in order to determine the evolution of the state variables. This potential must guaranty that for any possible process Eq. (2.13) is satisfied. It is worth noting that according to state laws Eqs. (2.11), (2.12) and balance equation Eq. (2.4) it comes

$$\overline{H} = \rho\frac{\partial\psi}{\partial p} - a = \rho\frac{\partial\psi}{\partial p} - \operatorname{div}\left(\underline{\boldsymbol{b}}\right) = \rho\frac{\partial\psi}{\partial p} - \operatorname{div}\left(\rho\frac{\partial\psi}{\partial\nabla p}\right) \tag{2.14}$$

The choice of the Helmholtz free energy potential $\psi$ and the dissipation pseudo-potential $\Omega$ entirely determine the gradient-enhanced material behaviour. The last term in equation (2.14) is the non-local dissipative stress which will regularize the strain localization phenomena. In practice a supplementary hardening will be induced by existing gradients of $p$. A typical result associated to strain gradient models is the coupling of nonlinearity and nonlocality which arises in the material behaviour. This coupling can become an issue when solving the governing differential equations, because they cannot be solved directly in a pointwise manner as in conventional plasticity. Relaxation methods have been developed, such as the micromorphic approach (Forest, 2009) or a Lagrange multiplier approach (Zhang et al., 2018), in order to deal with this difficulty. These two methods will be extensively presented and used in next chapters.

## 2.3 Ductile failure in metallic materials

Ductile failure gathers together several failure modes which are regularly encountered in metallic materials at moderate/high temperatures and moderate/slow loading rates. Noell et al. (2018) proposed a taxonomy of ductile failure modes reported in the literature. Figure 2.28 synthesizes and illustrates seven taxa of ductile failure. As reported in section 2.1.4, void-driven ductile failure is the predominant fracture mechanism observed in irradiated austenitic stainless steels in a wide variety of irradiation conditions. Therefore, as this work proceeds focus is made on void-driven ductile fracture mechanisms.

### 2.3.1 Experimental investigation of void-driven ductile fracture mechanisms

Void-driven ductile fracture is commonly decomposed into three major mechanisms:

1. **Void nucleation** consists in emergence of voids within the material. Voids typically nucleate at defects in the crystal lattice such as inclusions, precipitates, grain boundaries, etc. These defects are obstacles for dislocation glide and therefore they are responsible for stress concentrations which eventually lead either to their decohesion (Avramovic-Cingara et al., 2009; Xu and Needleman, 1993) or to their cracking (Shabrov et al., 2004). The X-ray tomography scans performed by Babout et al. (2004) on aluminum alloys in Figure 2.29 display the mechanisms of debonding and cracking. In the context of nuclear materials it is important to remind that voids and bubbles can also be induced by irradiation. Irradiation induced voids are typically three orders of magnitude smaller than voids nucleated at defects, but may still be responsible for failure if irradiation-induced swelling is important as confirmed by the observations of fracture surfaces.

2. **Void growth** corresponds to the increase of voids' volume. After void nucleation the mechanical loading may result in the expansion of their volume. High-resolution 3D tomography scans on nuclear pressure vessel steel by Daly et al. (2017) shown in Figure

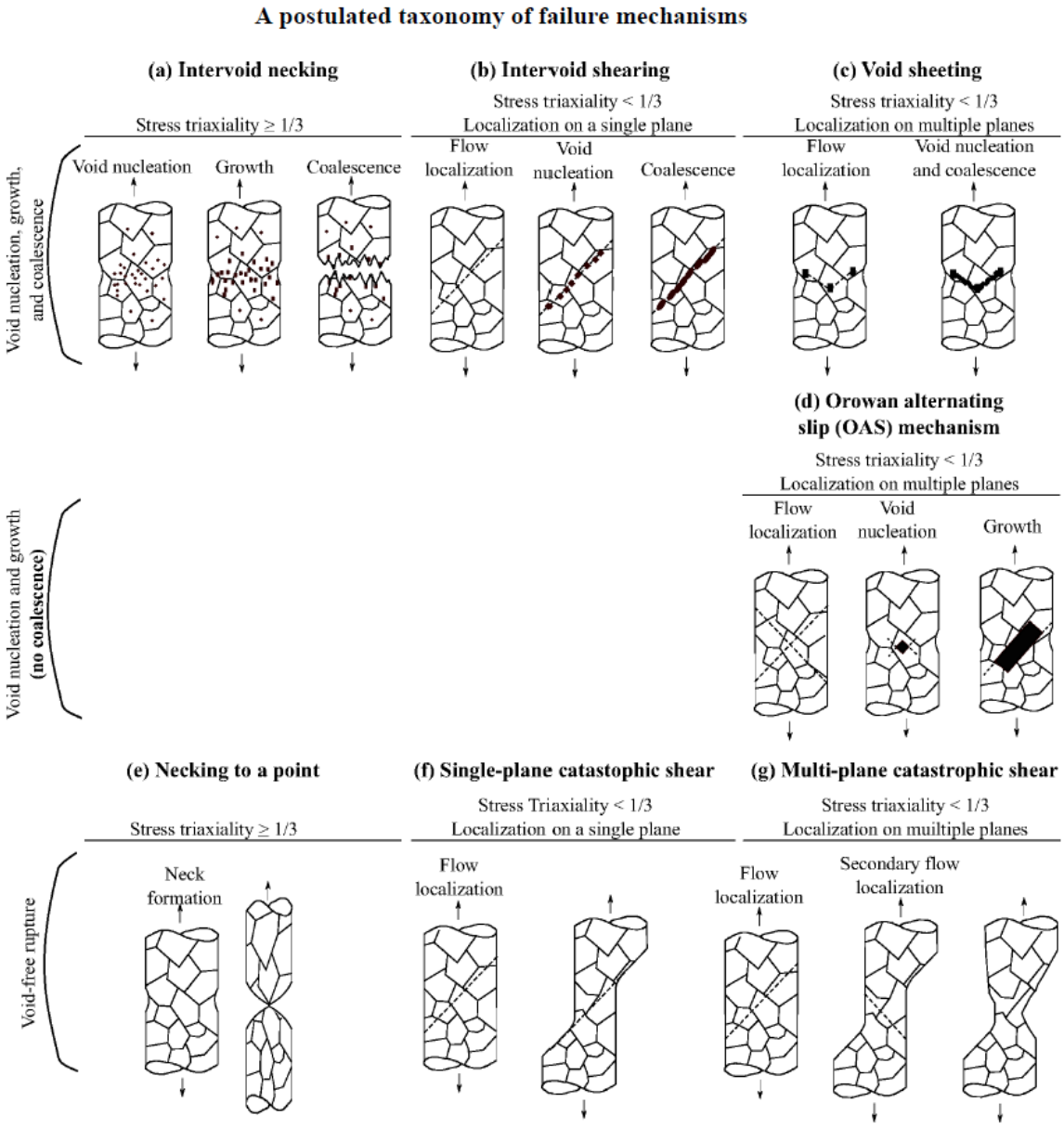


Figure 2.28 Schematic of ductile failure mechanisms which may coexist and interact (Noell et al., 2018).

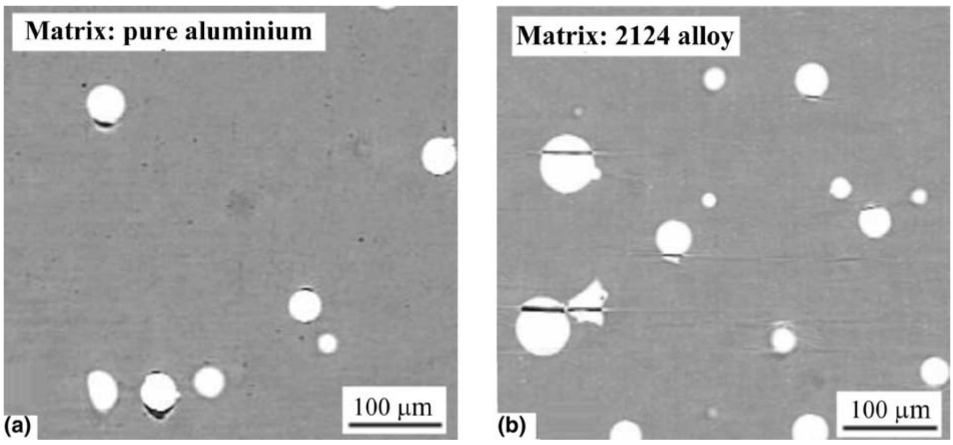


Figure 2.29 X-ray computed tomography of (a) debonding and (b) cracking of $ZrO_2/SiO_2$ spherical particles in aluminum alloys (Babout et al., 2004).

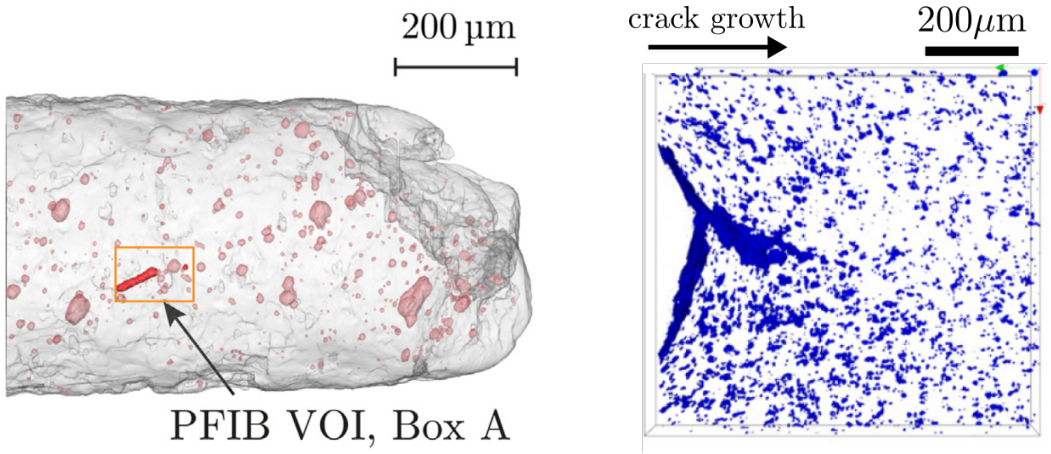


(a) (b)

Figure 2.30 (a) High-resolution 3D X-ray computed tomography of a nuclear pressure vessel steel. The tomography core was extracted near the crack tip of a deformed CT specimen. Segmented voids are displayed in red (Daly et al., 2017). (b) Laminography of a 2139 Al–Cu alloy CT specimen displaying segmented voids in blue around the notch (left) close to the specimen mid-plane (Morgeneyer et al., 2011).

2.30a exhibit that the void volume fraction is significantly larger near the fracture surface. The laminography images on aluminum-copper alloy by Morgeneyer et al. (2011) in Figure 2.30b display how voids gradually grow in front of a crack. Voids close to the notch are larger in size than voids further away from the notch. Voids growth corresponds to a regime during which voids grow without directly interacting with each other.

3. **Void coalescence** sets on when voids start to interact with each other. During coalescence strain localizes in the intervoid ligaments for example by necking or shearing. Coalescence of voids eventually leads to formation of cracks which will ultimately lead to failure. Morgeneyer and Besson (2011) showed experimentally how switching from intervoid necking into void shearing can lead to a flat to slant transition during crack propagation (see Figure 2.31).

Void-driven ductile fracture can often easily be identified by fractography analyses. When fracture is due to void nucleation, growth and coalescence the fracture surface displays crevices known as dimples. At the bottom of dimples can sometimes be observed the defects which

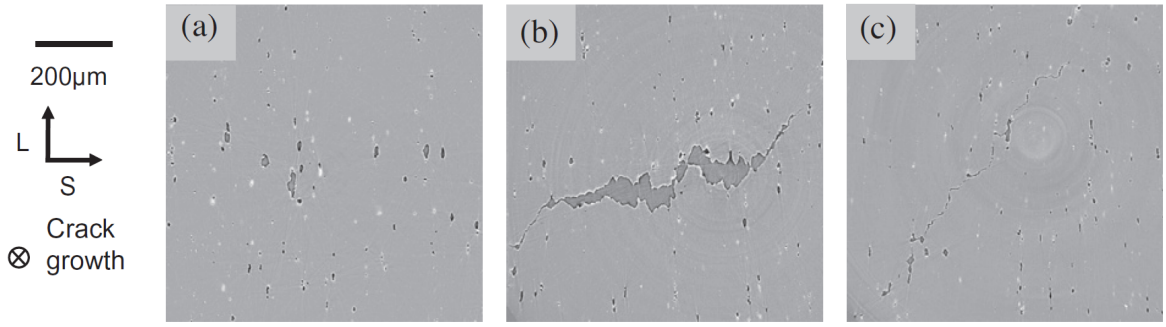


Figure 2.31 2D Synchrotron radiation-computed tomography (SRCT) images at (a) peak load (b) flat to slant transition (c) slant propagation during a Kahn tear test of an Aluminum AA2139 alloy (Morgeneyer and Besson, 2011).

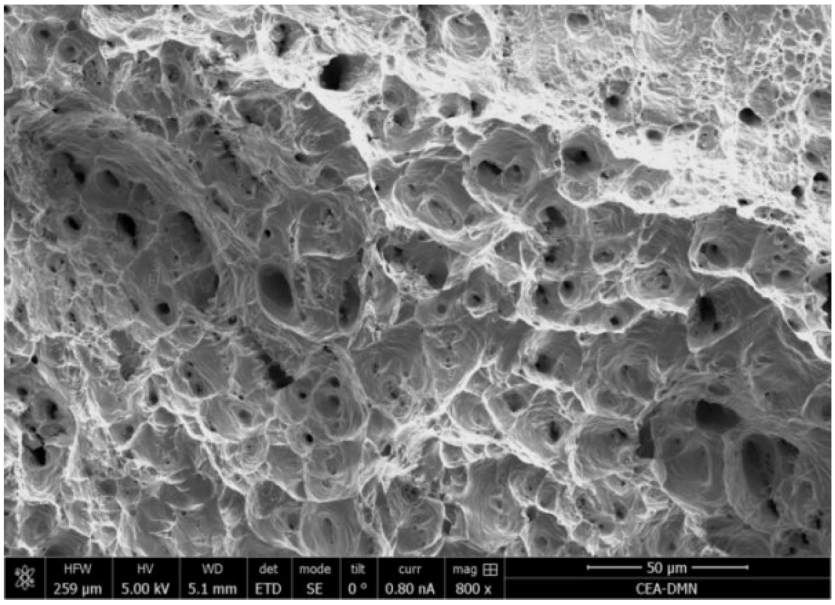


Figure 2.32 SEM micrography of a 304L stainless steel fracture surface displaying micrometric dimples (Barrioz et al., 2019).

served to void nucleation. Figure 2.32 shows a typical SEM micrography of a 304L stainless steel fracture surface.

### 2.3.2 Homogenization of porous materials applied to ductile fracture

Modeling and simulating accurately void-driven ductile failure is of paramount importance in mechanics of materials, because it makes possible proper design of structures. In the context of nuclear materials it is even more vital. Recent literature reviews by Benzerga and Leblond (2010); Besson (2010); Pineau et al. (2016) have established the state of the art concerning the 'local approach to fracture' and, in particular but not only, prediction of porous metals behaviour up to failure based on micromechanical modeling. They addressed nucleation, growth and coalescence of voids by homogenization techniques. Homogenization is based on the statistical or representative volume element techniques (SVE or RVE) in order to estimate effective properties of a micro-structured material. For the purpose of this work, focus is set on homogenized models of porous materials in the growth and coalescence regime. It should be noted that models developed by McClintock (1968); Rice and Tracey (1969) prior to homogenized models, or thermodynamical approaches (Rousselier, 1981), as well as variational methods (Danas and Castañeda, 2009) are other possible alternatives to describe and predict ductile failure.

#### 2.3.2.1 Void growth models

Gurson (1977) laid a milestone by conducting the theoretical and numerical limit analysis of a spherical hollow sphere. The author developed the yield loci and flow rule of a simplified ductile porous material made of a rigid perfect-plastic matrix material following the von Mises yield criterion. In the past four decades this model has extensively been enhanced in order to improve its accuracy and to take into account more and more physical phenomena:

1. **Accuracy improvements** were obtained by Tvergaard and Needleman (1984) to better fit porous unit-cell simulations and experimental results.
2. **Shear dominated failure** modifications were proposed by Nahshon and Hutchinson (2008).
3. **Void shape** effects were introduced in the model by Gologanu et al. (1993).
4. **Interfacial stresses** effects were supplemented by Dormieux and Kondo (2010).
5. **Inhomogeneous boundary strain rate** effects were studied by Gologanu et al. (1997).
6. **Isotropic and kinematic hardening** effects were respectively introduced by Leblond et al. (1995) and Mear and Hutchinson (1985).
7. **Hill, Tresca, Mohr-Coulomb and Schmid yield criteria** were used instead of von Mises criterion for the matrix material respectively by Benzerga and Besson (2001), Cazacu et al. (2014), Anoukou et al. (2016) and Han et al. (2013).
8. **Strain gradients** effects in the matrix material were accounted for by Wen et al. (2005).

Gurson's yield function in its simplest, yet general form, can be written

$$\phi^g(\underset{\sim}{\boldsymbol{\Sigma}}, \sigma_0, \alpha_i) = A(\alpha_i)\left(\frac{\mathcal{F}(\underset{\sim}{\boldsymbol{\Sigma}})}{\sigma_0}\right)^2 + B(\alpha_i)\cosh\left(C(\alpha_i)\frac{\mathcal{G}(\underset{\sim}{\boldsymbol{\Sigma}})}{\sigma_0}\right) + D(\alpha_i) \tag{2.15}$$

where $\underset{\sim}{\boldsymbol{\Sigma}} = 1/V\int_V \underset{\sim}{\boldsymbol{\sigma}}\mathrm{d}V$ is the macroscopic Cauchy stress tensor, $\sigma_0$ the matrix material yield stress and $\alpha_i$ a set of internal variables describing voids' state such as the void volume fraction, voids' aspect ratio, orientation, etc. $\mathcal{F}$ and $\mathcal{G}$ denote scalar valued equivalent stresses, which respectively reduce to the von Mises equivalent stress and the hydrostatic mean stress in the original formulation by Gurson. $A$, $B$, $C$ and $D$ are scalar valued function which depend on voids' state only. In the original formulation $A = 1$, $B = 2f$, $C = 3/2$ and $D = -(1 + f^2)$, where $f$ is the void volume fraction. Besson (2010) argued that the yield function Eq. 2.15 can instead be interpreted as an implicit definition of some effective stress $\sigma_g^*$ inside the matrix material such that $\phi^g(\underset{\sim}{\boldsymbol{\Sigma}}, \sigma_g^*, \alpha_i) = 0$. The yield function then becomes simply

$$\tilde{\phi}^g = \sigma_g^* - \sigma_0 \tag{2.16}$$

The interest of such a procedure is that the definition of $\sigma_g^*$ can be easily modified without further formal modifications of the constitutive equations. This is of particular interest for numerical implementation of material behaviours. Gurson complemented the yield function 2.15 with a flow rule by proving that the normality rule holds, hence

$$\dot{\underset{\sim}{\boldsymbol{\varepsilon}}}^p = \dot{\Lambda}\frac{\partial\phi^g}{\partial\underset{\sim}{\boldsymbol{\Sigma}}} \tag{2.17}$$

where $\dot{\underset{\sim}{\boldsymbol{\varepsilon}}}^p$ is the plastic strain tensor at small strains and $\dot{\Lambda}$ a macroscopic so-called plastic multiplier. Closure of the model is obtained by giving evolution equations for the internal

variables $\alpha_i$. When $\alpha_i$ reduces to the void volume fraction $f$, the commonly accepted evolution equation, in absence of void nucleation, is based on mass conservation

$$\dot{f} = (1-f)\mathrm{tr}\ (\underset{\sim}{\dot{\varepsilon}}^p) \tag{2.18}$$

This evolution law is based on some underlying homogenization hypothesis which will be discussed further in Chapter 6.

Thermodynamical approaches followed by Rousselier (1981, 1987, 2001) or variational methods followed by Castañeda (1991) led to different, yet closely related homogenized models of porous materials.

#### 2.3.2.2 Void coalescence models

Thomason (1985) performed a limit-load analysis at incipient failure for a porous solid containing square-prismatic voids. The author derived the maximum stress which can bear the intervoid ligament separating voids before necking. Once this critical stress is reached localization of plastic deformation will occur inside the ligament. Thomason's criterion characterizes the onset of void coalescence by intervoid necking. However it can also be seen as a yield criterion (Benzerga et al., 2001). With this point of view, void growth and void coalescence are two plastic mechanisms which can be chosen to be activated either separately or possibly simultaneously. Extensions of Thomason's criterion of intervoid necking has been extensively generalized in order to improve its accuracy and to take into account more physical phenomena:

1. **Strict upper-boundedness** of maximum limit loads were developed in Benzerga and Leblond (2014); Morin et al. (2015).

2. **Shear dominated** coalescence was supplemented by Scheyvaerts et al. (2011); Tekoğlu et al. (2012); Torki et al. (2015).

3. **Matrix plastic anisotropy** effects were developed by Keralavarma and Chockalingam (2016); Morin (2015).

4. **Interfacial stresses** effects were introduced by Gallican and Hure (2017).

5. **Hardening** effects were introduced by Pardoen and Hutchinson (2000); Scheyvaerts et al. (2011).

6. **Secondary population of voids** were considered in Fabrègue and Pardoen (2008).

Thomason's criterion in its simplest, yet general form, can be written in absence of shear loading:

$$\phi^c(\underset{\sim}{\Sigma}, \sigma_0, \alpha_i) = \frac{\Sigma_{33}}{\sigma_0} - (1-\chi_p^2)\mathcal{C}(\alpha_i) \tag{2.19}$$

where it is assumed that coalescence occurs in the plane with normal $\underline{\boldsymbol{e}}_3$. $\sigma_0$ still represent the yield stress of the matrix material and $\mathcal{C}$ is a concentration factor depending on voids' state. In its original form $\mathcal{C}(\chi_p, W) = \left[0.1\left((1/\chi_p - 1)/W\right)^2 + 1.2\sqrt{1/\chi_p}\right]$ where $\chi_p$ is the size of square-prismatic voids, normalized by the homogenization cell size and $W$ is the aspect ratio of the square-prismatic voids. Thomason's model was developed for square-prismatic cells and voids. However, in the literature, the model is assessed on orthorombic unit-cells containing spheroidal voids. Therefore, $\chi_p$ is not appropriate to characterize the intervoid distance since the latter evolves along the height of the void. Torki et al. (2015) proposed to define an equivalent intervoid distance for spheroidal voids $\chi_s$ such that two cells having the same porosity inside the material band containing the void will have the same intervoid distance. To satisfy this condition one can prove that $\chi_s = \sqrt{\pi/6}\chi_p$ . Closure of the model is obtained by giving evolution equations

for the internal variables $\alpha_i$. When $\alpha_i$ reduces to the normalized intervoid distance and the void aspect ratio, geometrical considerations, for prismatic cells with spheroidal voids, give

$$\dot{W} = \frac{9}{4}\frac{\lambda}{\chi_s}\left[1 - \frac{2}{\pi\chi_s^2}\right]\dot{\varepsilon}_{eq}^p \qquad \dot{\lambda} = \frac{3}{2}\lambda\dot{\epsilon}_{eq}^p \qquad \chi_s = \left(\frac{6f\lambda}{\pi W}\right)^{\frac{1}{3}} \tag{2.20}$$

Following again the procedure proposed in Besson (2010), Eq. (2.19) can be interpreted as an implicit definition of an effective stress $\sigma_c^*$ inside the matrix material such that $\phi^c(\underset{\sim}{\boldsymbol{\Sigma}}, \sigma_c^*, \alpha_i) = 0$. It follows that the yield function then becomes

$$\tilde{\phi}^c = \sigma_c^* - \sigma_0 \tag{2.21}$$

#### 2.3.2.3 Extensions into the framework of crystal plasticity

Most of the aforementioned models were developed in the framework of von Mises or Hill plasticity. Nevertheless, in metallic alloys, voids, cavities or bubbles, which have been described earlier, are often intragranular defects. Therefore each void is surrounded, locally, by a single crystal. It is thus a motivation to consider crystal plasticity in the homogenization procedure. The pioneering analytical work of (Hori and Nemat-Nasser, 1988a,b) demonstrated the prominent effect of crystal plasticity on the evolution of void shapes in FCC and BCC crystals.

Experimental studies dedicated to quantify the effect of crystal plastic anisotropy on void growth and coalescence are still scarce. Crépin et al. (1996) investigated the fast cavity growth and rupture by prismatic slip in $\beta-$treated zirconium. They showed how lath forces plastic slip to localize at their boundaries, causing a preferential growth of tubular voids parallel to their orientation. Ultimately cracks propagate along the dotted path formed by cavities. Gan et al. (2006) studied the deformation and crystal rotation patterns surrounding cylindrical holes in aluminum. Crystal plasticity finite element simulations were validated upon comparison with analytical slip line theory and experimental results. They highlighted existence of discontinuities of activated slip systems and lattice rotation, confirming existence of slip sectors as predicted by the slip line theory. Recently Barrioz et al. (2019) studied the effect of dislocation channeling, induced by irradiation defects, on the behaviour of holes drilled in the middle of grains of tensile 304L stainless steel polycrystal specimens. They evidenced a strong modification of void evolution at low strains in the irradiated material as compared to the pristine material. The dislocation channels which are formed interact strongly with voids. However as the strain increases, activation of secondary dislocation channels lead to a more and more homogeneous deformation mode.

Numerical studies have also contributed to qualify the effect of plastic anisotropy of crystals in the context of ductile failure. Periodic porous unit-cells frequently used to assess the effective behaviour of porous materials up to failure were used. Typical fields of accumulated plastic slip observed in single crystal porous unit-cell simulations are depicted in Figure 2.33 for several crystal orientations. The main findings obtained from finite element simulations of voids embedded in a crystal matrix can be listed as follows.

1. Void growth rate is strongly affected by crystal orientation. Influence of crystal orientation on void growth decreases with stress triaxiality (Ha and Kim, 2010; Ling et al., 2016; Potirniche et al., 2006a; Selvarajou et al., 2019; Yerra et al., 2010). Potirniche et al. (2006a), for example, reported that, for uniaxial loadings, voids grow, in a [111] orientation, twice as fast as in a [100] orientation. For highly anisotropic orientations, porous crystals can exhibit an almost incompressible behaviour because only a few slip systems are active (Ling et al., 2016; Mbiakop et al., 2015a,b).

2. Crystal orientation influences the evolution of the shape of voids. For low symmetry crystal orientations and small stress triaxialities voids tend to rotate along with the lattice (Potirniche et al., 2006a). Ha and Kim (2010), reported for example, that while the cross

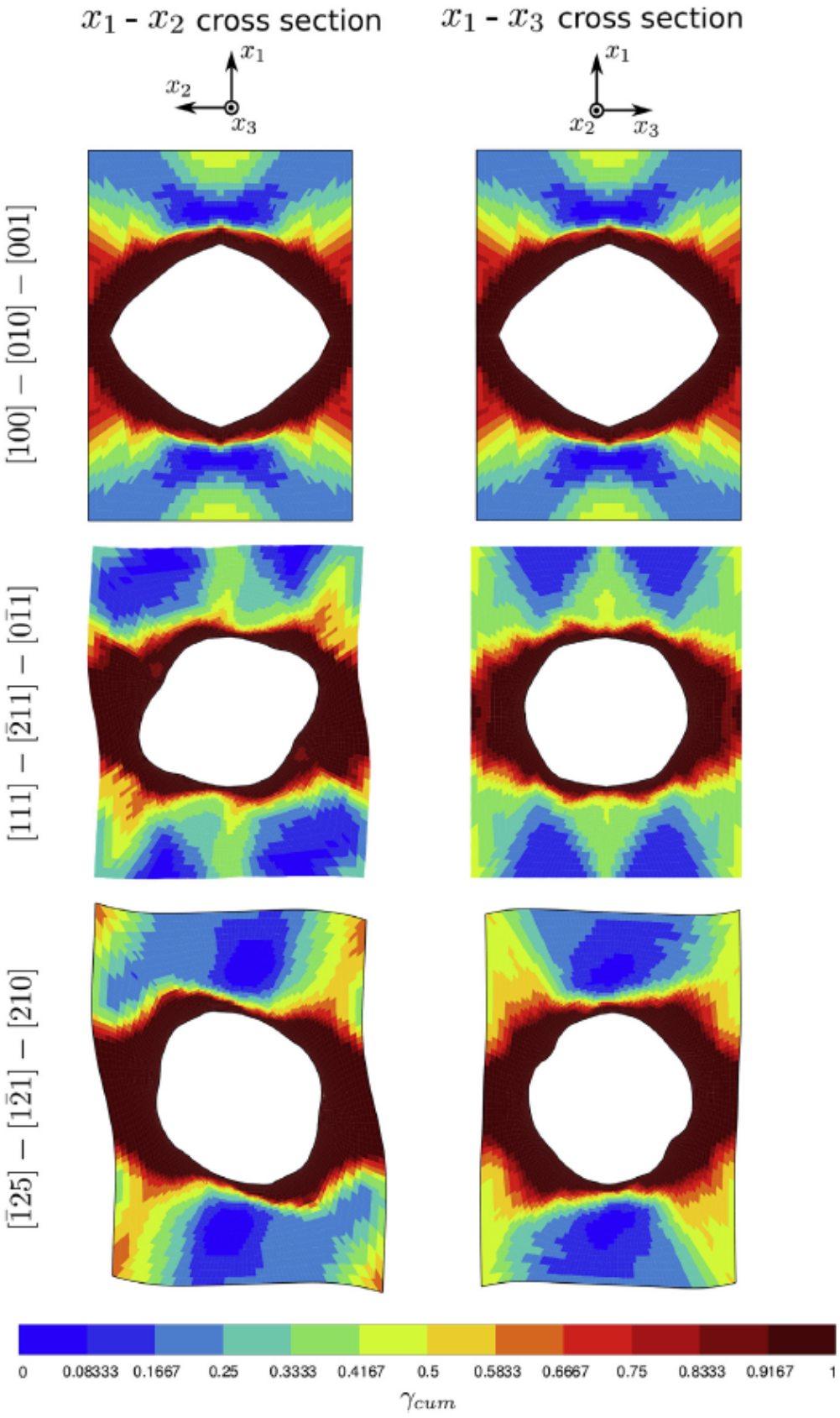


Figure 2.33 Accumulated plastic slip fields plotted in cross-sections of periodic single crystal porous unit-cell simulations with an imposed stress triaxiality $T = 3$ obtained for a initial porosity $f_0 = 0.01$ and at a strain such that $f = 0.1$. Fields are reproduced from (Ling et al., 2016).

section of voids becomes elliptic when loaded in a [110] direction, loading along a [$\bar{1}$23] orientation produces corners which are due to combined rotation and stretching of voids.

3. For some crystal orientations, void-induced hardening can be observed as compared to pristine void-free material because the presence of voids changes the local stress state as compared to the remotely applied one (Selvarajou et al., 2019).

4. The overall effect of crystal orientation is larger for small initial void volume fractions (Ha and Kim, 2010; Ling et al., 2016).

5. Void volume fraction at coalescence is strongly influenced by the crystal orientation while it is almost independent of the stress triaxiality (Ling et al., 2016; Yerra et al., 2010). Crystal orientation affects more void coalescence velocity at low stress triaxiality (Liu et al., 2012).

6. Broader multiple slip regions are observed when a strain gradient crystal matrix is considered (Borg and Kysar, 2007). In this context, smaller voids are responsible for a localized deformation mode inside regions which intersect the void surface and are parallel to the active slip system. Smaller voids are also responsible for larger maximum mean stresses and reduced void growth (Borg et al., 2008; Hussein et al., 2008; Shu, 1998). In addition strain gradient effects tend to smooth out the geometry of voids as their size decreases.

Meanwhile, other authors focused on more local mechanisms. Chang et al. (2013); Potirniche et al. (2006b); Traiviratana et al. (2008) studied void growth in single crystal by large scale 2D and 3D molecular dynamics. They investigated the behaviour of single crystals containing voids with radius of 1 to 100 nm. They showed that plastic deformation in the vicinity of voids is triggered by nucleation of dislocations at atomic steps on voids' surface. For nano-voids (radius $\leq 10$ nm), the stress necessary to nucleate dislocations increases when the void radius is decreased (at a given void volume fraction). According to the authors, no size effect could be observed on void growth rate for voids with radii smaller than 50 nm. Recently, Hure et al. (2020) investigated experimentally the behaviour of nanovoids in conditions relevant for low stress triaxiality and large strain conditions. They were able to demonstrate a possible existence, though limited, of void growth size effect for very small voids (radius $\leq 10$ nm). Furthermore, Segurado and Llorca (2009); Segurado and LLorca (2010) investigated the mechanism of void growth by DDD for void radii greater than 100 nm. For such voids growth is triggered by nucleation of dislocations in the bulk. The authors were able to show that larger voids grow more rapidly than smaller voids. To summarize, for very small voids (radius $\leq 10$ nm) a 'smaller is stronger' size effect can be expected, while for larger voids (radius $\geq 100$ nm) a 'larger is faster' size-effect can be anticipated. In addition, according to their experimental observations, Hure et al. (2020) argued that even at the nanoscale continuum mechanics modeling of plasticity could still remain relevant to describe the behaviour of voids.

A few homogenized models describing the growth of voids in porous single crystals were developed in the past decade. These models do not account for any size effects, thus limiting their scope to void sizes at least greater than 10 nm. Han et al. (2013) proposed the first yield function for single crystals containing voids. Based on a variational formulation due to Castañeda and Suquet (1997) the authors formulated a small strain Gurson's like yield criterion for each slip system of the single crystal. The resulting yield function can be seen as an extension of Schmid's law to porous crystals, the plastic behavior of which is sensitive to the hydrostatic pressure. The model was later generalized to finite deformations and extended with a flow rule by Ling et al. (2016). Following the same procedure as in previous section, the implicit definition of

the effective resolved shear stress inside the crystal matrix $\tau_s^*$ for $s$-th slip system can be written

$$\begin{aligned}\phi^s(\underset{\sim}{\mathbf{\Pi}}^M, \tau_s^*, \alpha_i) = A(\alpha_i)\left(\frac{\mathcal{F}(\underset{\sim}{\mathbf{\Pi}}^M)}{\tau_s^*}\right)^2 + B(\alpha_i)\left(\frac{\mathcal{G}(\underset{\sim}{\mathbf{\Pi}}^M)}{\tau_s^*}\right)^2 \\ + C(\alpha_i)\cosh\left(D(\alpha_i)\frac{\mathcal{H}(\underset{\sim}{\mathbf{\Pi}}^M)}{\tau_s^*}\right) + E(\alpha_i)\end{aligned} \tag{2.22}$$

where $\underset{\sim}{\mathbf{\Pi}}^M$ is Mandel's stress related to each resolved shear stress $\tau_s$ by $\underset{\sim}{\mathbf{\Pi}}^M : (\underline{\boldsymbol{m}}_s \otimes \underline{\boldsymbol{n}_s}) = \tau_s$ where $\underline{\boldsymbol{m}}_s$ is the unit vector in the gliding direction and $\underline{\boldsymbol{n}}_s$ is the unit vector normal to the slip plane. In (Han et al., 2013; Ling et al., 2016), $\alpha_i$ reduces to the void volume fraction $f$, and one has

$$A = 1 \qquad B = \alpha f \tfrac{2}{45} \qquad C = 2q_1 f \qquad D = q_2\sqrt{\tfrac{3}{20}} \qquad E = -(1 + (q_1 f)^2) \tag{2.23}$$

$$\mathcal{F}(\underset{\sim}{\mathbf{\Pi}}^M) = \tau_s \qquad \mathcal{G}(\underset{\sim}{\mathbf{\Pi}}^M) = \sqrt{\tfrac{3}{2}\underset{\sim}{\mathbf{\Pi}}^{M'} : \underset{\sim}{\mathbf{\Pi}}^{M'}} \qquad \mathcal{H}(\underset{\sim}{\mathbf{\Pi}}^M) = \Pi_m^M \tag{2.24}$$

where $\underset{\sim}{\mathbf{\Pi}}^M = \underset{\sim}{\mathbf{\Pi}}^{M'} + \Pi_m^M \underset{\sim}{\mathbf{1}}$. The parameters $\alpha$, $q_1$ and $q_2$ are to be fitted by comparison with RVE simulations. The values identified by Ling et al. (2016) are $\alpha = 5.69$, $q_1 = 1.60$ and $q_2 = 1.19$. Then, the yield function on each system is simply

$$\tilde{\phi}^s = \tau_s^* - \tau_s^c \tag{2.25}$$

Hardening is therefore readily accounted for in the critical resolved shear stress $\tau_s^c$ of the pristine void-free single crystal. A few other models of porous single crystals have been proposed in the literature. One is due to Paux et al. (2015). It is based on a modification of Gurson's model to account for the crystallographic nature of the matrix material. The modifications consist in replacing $\sigma_0$ by $\tau_0$ the critical resolved shear stress in absence of hardening in Eq. (2.15) and changing the definition of $\mathcal{F}$ and $C$

$$\mathcal{F}(\underset{\sim}{\mathbf{\Sigma}}) = \left(\sum_{s=1}^{N} |\underset{\sim}{\mathbf{\Sigma}} : (\underline{\boldsymbol{m}}_s \otimes \underline{\boldsymbol{n}}_s)|^n\right)^{\frac{1}{n}} \qquad C = \kappa' \simeq 0.506 \tag{2.26}$$

where $N$ is the number of slip systems and $n$ a positive regularization exponent. When $n$ goes to infinity $\mathcal{F}(\underset{\sim}{\mathbf{\Sigma}})$ converges towards the largest term in the sum over $s$. The model can be seen as a regularized Schmid law (Arminjon, 1991; Gambin, 1992) extended to account for the effect of the hydrostatic pressure. This model was then extended in order to take into account hardening in (Paux et al., 2018). The second is due to Mbiakop et al. (2015a,b). It is based on the modified variational (MVAR) method established by Danas and Aravas (2012). The authors argued that the effective (macroscopic) strain rate tensor $\underset{\sim}{\boldsymbol{D}}$ is given by

$$\underset{\sim}{\boldsymbol{D}} = \frac{\partial \tilde{U}}{\partial \underset{\sim}{\mathbf{\Sigma}}} \tag{2.27}$$

where the effective potential of a porous medium $\tilde{U}(\underset{\sim}{\mathbf{\Sigma}}, \alpha_i) = (1-f) \min_{\underset{\sim}{\boldsymbol{\sigma}} \in S(\underset{\sim}{\mathbf{\Sigma}})} \langle U(\underset{\sim}{\boldsymbol{\sigma}}) \rangle$ is given by the MVAR model

$$\tilde{U}_{mvar}(\underset{\sim}{\mathbf{\Sigma}}) = (1-f)^{-n} \sum_{s=1}^{N} \frac{\dot{\gamma}_0^s (\tau_0^s)^{-n}}{n+1} \left(\underset{\sim}{\mathbf{\Sigma}}.\underset{\approx}{\boldsymbol{S}}^{mvar,s}.\underset{\sim}{\mathbf{\Sigma}}\right)^{\frac{n+1}{2}} \tag{2.28}$$

It has the advantage to include the void shape and orientation effects, which are not accounted for neither by Ling et al. (2016) nor Paux et al. (2018). Figure 2.34 compares the yield loci

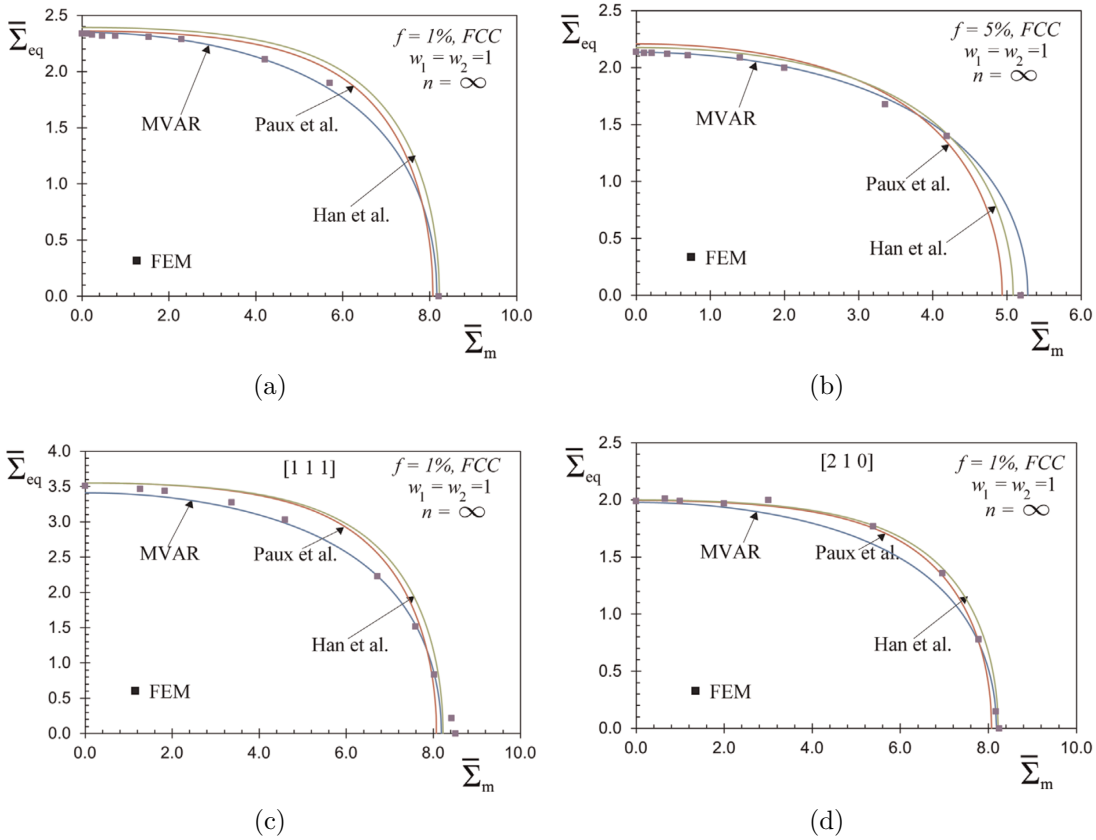


Figure 2.34 Comparison of yield loci obtained with the model by Han et al. (2013), Paux et al. (2015) and Mbiakop et al. (2015a). In (a) and (b) crystal orientation is [100]-[010]-[001] and porosity equal to 1% and 5% respectively. In (c) and (d) porosity is 1% and crystal orientation is [111]-[$\bar{2}$11]-[0$\bar{1}$1] and [210]-[$\bar{1}$20]-[001] respectively. Corresponding porous unit-cell numerical limit analysis results are also reported. Graphs are reproduced from (Mbiakop et al., 2015a).

predicted by the three porous single crystal void growth criteria presented above. It can be seen that all of them predict very similar elastic domains for different porosities and crystal orientations. On the same graphs are also plotted the results obtained from numerical limit analysis simulations performed on porous unit-cells by Han et al. (2013). A quite good agreement between homogenized models and limit analysis simulations can also be observed. Recently Joëssel (2018) proposed alternative effective properties of voided cubic crystals under hydrostatic loading. He followed two distinct approaches to derive upper bounds of the effective flow stress $\tilde{\sigma}_h$ of porous single crystals. The first method is based on the Hollow-sphere assemblages (HSA) Gurson-like technique, while the second follows the infinite-rank sequential laminates (LAM) method (Idiart, 2008). Both approaches lead to the following expression

$$\tilde{\sigma}_h = \alpha(n) n (f^{-\frac{1}{n}} - 1) \tag{2.29}$$

where $n$ is the creep exponent and $\alpha(n)$ depends on the chosen homogenization technique. The authors obtained the following expressions of $\alpha_{HSA}$ and $\alpha_{LAM}$

$$\alpha_{HSA} = \left\langle \underset{\underset{\sim}{\boldsymbol{\sigma}}_d \in \mathcal{T}_d}{\text{Sup}} \frac{|\underline{\boldsymbol{\xi}} \cdot \underset{\sim}{\boldsymbol{\sigma}}_d \cdot \underline{\boldsymbol{\xi}}|^{\frac{n}{n+1}}}{\left(\sum_{k=1}^{N} \tau_0^{(k)-n} |\underset{\sim}{\boldsymbol{\sigma}}_d \cdot (\underline{\boldsymbol{m}}_s \otimes \underline{\boldsymbol{n}}_s)|^{n+1}\right)^{\frac{1}{n}}} \right\rangle \tag{2.30}$$

$$\alpha_{LAM} = \left\langle \underset{\underset{\sim}{\boldsymbol{\sigma}}_d \in \mathcal{T}_{\parallel}(\underline{\boldsymbol{\xi}})}{\text{Sup}} \frac{|\underline{\boldsymbol{\xi}} \cdot \underset{\sim}{\boldsymbol{\sigma}}_d \cdot \underline{\boldsymbol{\xi}}|^{\frac{n}{n+1}}}{\left(\sum_{k=1}^{N} \tau_0^{(k)-n} |\underset{\sim}{\boldsymbol{\sigma}}_d \cdot (\underline{\boldsymbol{m}}_s \otimes \underline{\boldsymbol{n}}_s)|^{n+1}\right)^{\frac{1}{n}}} \right\rangle \tag{2.31}$$

$\underline{\boldsymbol{\xi}}$ denotes the normalized position vector relative to the center of the sphere, $\mathcal{T}_d$ represents the set of symmetric deviatoric stresses and $\mathcal{T}_{\parallel}(\underline{\boldsymbol{\xi}}) = \{\underset{\sim}{\boldsymbol{\sigma}}_d \in \mathcal{T}_d : \underset{\sim}{\boldsymbol{\sigma}}_d \cdot \underline{\boldsymbol{\xi}} \parallel \underline{\boldsymbol{\xi}}\}$. The authors were able to obtain quite a good agreement with porous unit-cell results under hydrostatic loadings for several porosities, creep exponents and crystal anisotropies.

Homogenized models describing coalescence of voids in single crystals are even more scarce. A first criterion was built by Yerra et al. (2010) in order to be able to predict onset of void coalescence in single crystals. The authors proposed an extension to Thomason's criterion given in Eq. (2.19) suited to incorporate hardening and crystal plasticity effects. The criterion writes

$$\phi^c(\underset{\sim}{\boldsymbol{\Sigma}}, \sigma_0, \alpha_i) = \frac{\Sigma_{eq}}{\sigma_y^{loc}} + \frac{3}{2}\frac{\Sigma_m}{\sigma_y^{loc}} - (1 - \chi_p^2)\frac{3}{2}\mathcal{C}(\alpha_i) \tag{2.32}$$

where $\sigma_y^{loc}$ is a measure of material strength in the vicinity of the void in the coalescence plane. In order to estimate this quantity Yerra et al. (2010) proposed to perform an ancillary computation of a single crystal which orientation is given by the crystal orientation in the vicinity of the void. The applied loading is equibiaxial straining which is representative of the loading in the coalescence plane. $\sigma_y^{loc}$ is then the equivalent stress reached by this single crystal when the equivalent plastic strain equals an estimation of the local plastic strain in the vicinity of the void extrapolated from the average applied strain tensor. The authors showed that such a criterion allows to give a satisfactory prediction of the equivalent strain at onset of void coalescence. More recently Hure (2019) derived a coalescence criterion for porous single crystals by extending to the crystal plasticity framework the coalescence criterion in tension and shear developed by Torki et al. (2015). The coalescence criterion relies on three average Taylor factors $M_1$, $M_2$ and $M_3$ which are numerically computed by integrating over the intervoid ligament local Taylor factors obtained by Taylor's minimum shear principle. The criterion writes

$$\begin{cases} \dfrac{\left(|\Sigma_{33}| - t(W,\chi_p)\Sigma^{surf}\right)^2}{b^2\Sigma^{vol^2}} + 4\dfrac{\Sigma_{sh}^2}{T^2} - 1 = 0 \quad \text{for} \quad |\Sigma_{33}| \geq \Sigma^{surf} \\ 4\dfrac{\Sigma_{sh}^2}{T^2} - 1 = 0 \quad \text{for} \quad |\Sigma_{33}| \leq \Sigma^{surf} \end{cases} \tag{2.33}$$

where one has

$$t(W,\chi) = \frac{W(-0.84 + 12.9\chi_p)}{1 + W(-0.84 + 12.9\chi_p)} \qquad b = 0.9 \tag{2.34}$$

$$\Sigma^{surf} = \tau_0 M_1 \left[\frac{\chi_p^3 - 3\chi_p + 2}{3\sqrt{3}W\chi_p}\right] \tag{2.35}$$

$$\Sigma^{vol} = \tau_0 M_2 \frac{2}{\sqrt{3}}\left[2 - \sqrt{1 + 3\chi_p^4} + \ln\left(\frac{1 + \sqrt{1 + 3\chi_p^4}}{3\chi^2}\right)\right] \tag{2.36}$$

$$T = \tau_0 \frac{2M_3}{\sqrt{3}}(1 - \chi_p^2) \tag{2.37}$$

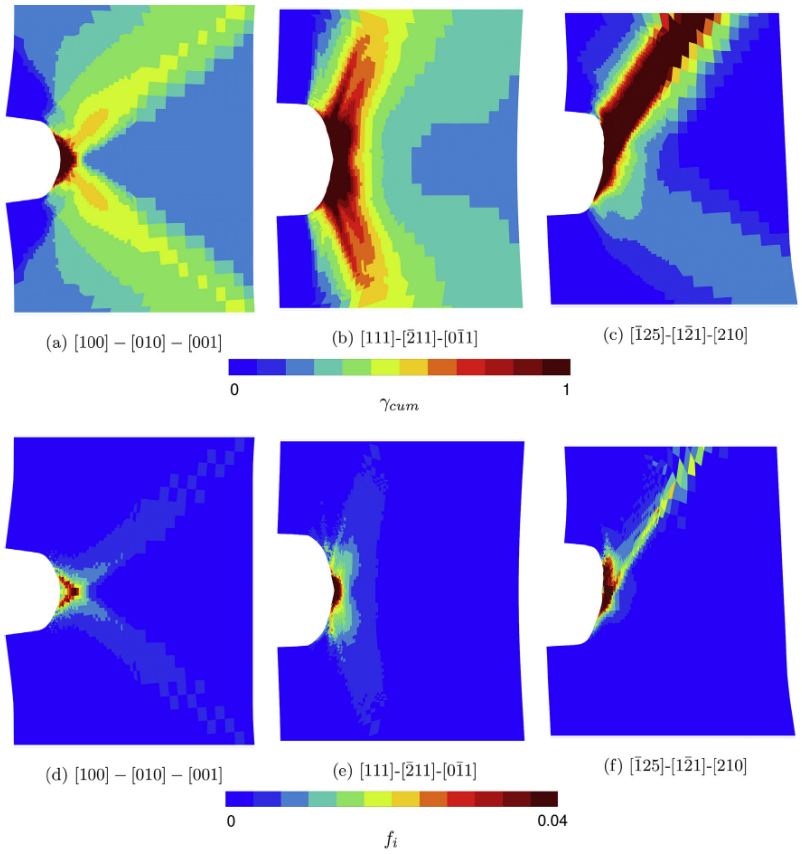


Figure 2.35 Accumulated plastic slip fields (a-c) and porosity fields (d-f) in the vicinity of the notch of a single crystal SENT specimen for three different crystal orientations (Ling et al., 2016).

Hure (2019) showed with numerical limit analysis performed by FFT on cylindrical and cubic unit-cells that the semi-analytical coalescence criterion is in very good agreement with the numerical yield loci for both FCC and hexagonal close-packed (HCP) single crystals. Effects of the set of slip systems, crystal orientation, void shape and volume were assessed. The strong coupling, at low applied stress triaxiality, between crystal and void lattice orientation on the coalescence stress was also demonstrated.

To the author's knowledge, the only applications of such models of porous single crystals to the simulation of structures were performed by Ling et al. (2016) on a single-edge-notch tension specimen. Figure 2.35 displays the accumulated plastic slip and porosity fields obtained for three different crystal orientations. These results were obtained with a model accounting for void growth only. In addition, they suffer from the well known issue of mesh-dependency associated to damage induced softening and related instability.

## 2.4 Conclusions

A state of the art was reported in order to address the study of *strain localization and ductile fracture in the context of irradiated austenitic stainless steels modeling* with the most recent knowledge and tools at hand in the literature. Focus was made on experimental results and modeling methods.

First of all, a description of the material at the center of this study was provided. The crystallographic nature of austenitic stainless steels was shown to be the scene of great evolutions induced by neutron radiations produced by fission reactions. The nature, as well as the conditions (temperature, dose, flux spectrum) of apparition of the defects produced by radiation-damage

were described. It was also discussed how proton irradiation can serve as an effective and advantageous tool to mimic a neutron irradiation induced defect microstructure. For the purpose of this work the main point to remember is that dislocation Frank loops, voids and bubbles can be formed under irradiation. The consequences caused by these defects on the mechanical behaviour of irradiated austenitic stainless steels were outlined. The main features caused by radiation-induced defects are an increase of yield and ultimate strength and a loss of hardening capability and ductility. As a result the fracture toughness of austenitic stainless steels endures a dramatic decrease when irradiation dose increases. Although these properties are well assessed in the literature at the polycrystal level, very few experimental data are available at the single crystal level. Consequently, for purposes of modeling the local intragranular behaviour of austenitic stainless steels, experimental investigations of unirradiated and irradiated single crystals are necessary.

Then, the link between irradiation-induced defects and observed material properties was characterized. Comments on how instabilities may arise from material properties or geometrical conditions and result in strain localization phenomena were given. Dislocation Frank loops, responsible for strengthening of irradiated austenitic stainless steels, can in turn lead to material instabilities. Their elimination in the path of gliding dislocations provokes local softening and therefore easier glide for the forthcoming dislocations resulting in dislocation channeling. Dislocation channels are widely observed in (irradiation)-hardened metals and are the bridging link between strengthening and loss of hardening capability and ductility. Modeling strain localization phenomena requires specific means in order to thwart ill-posedness of conventional theories in this context. Strain gradient plasticity is an efficient tool to incorporate length scales dependencies into material models and thus ensure uniqueness of the solution in simulation of strain localization. Nevertheless the non-local coupling terms which arise in strain gradient plasticity models are responsible for an increased complexity in the resolution of the differential equations governing the material behaviour. Tremendous numerical efforts are hence necessary in order to compute the behaviour of large structures. Efficient numerical treatment and implementation of strain gradient models are therefore required.

Last, mechanisms of ductile failure in metallic materials are presented. Focus is made on void-driven ductile fracture which is typically decomposed into void nucleation, void growth and void coalescence. In radiation-damaged materials two distinct population of voids can simultaneously coexist and be responsible for failure. Micrometric voids nucleate by inclusion rupture or decohesion and nanometric voids formed by clustering of vacancies induced by irradiation. Both populations are affected and interact with the heterogeneous deformation mode induced by dislocation channeling. Ductile failure of irradiated stainless steels can occur by growth and coalescence of micro- and nano-metric voids. Modeling the behaviour of porous materials up to failure can be performed with homogenized models. Homogenization techniques provide approximations of effective properties of representative volume elements. Recently homogenization of porous single crystals were carried out in order to be able to predict ductile failure accounting for crystal plasticity anisotropies effects. However, to the author's knowledge, a complete, regularized ductile failure model of porous single crystals has not yet been proposed.

This synthesis provides the guidelines of the present work:

1. produce experimental data on austenitic stainless steels single crystals to inform and validate existing continuum crystal plasticity models

2. enhance representativeness of simulated strain localization in single crystals

3. improve computational efficiency of existing strain gradient plasticity models

4. formulate a full and regularized model of ductile failure for porous single crystals

In Chapter 3 the methods and results of tensile tests carried out on austenitic stainless steel single crystals are presented. These experimental data are used to calibrate the parameters of a continuum crystal plasticity material model. Chapter 4 deals with a reduced micromorphic

crystal plasticity model at finite strains. Analytical solutions of a case study are derived and compared to finite element resolutions. The model is enhanced in order to better predict strain localization when softening saturates. In Chapter 5 a Lagrange multiplier based relaxation method is compared to the micromorphic approach. The computational efficiency of the method is highlighted on 3D finite element simulations. Chapter 6 presents a regularized continuum crystal plasticity model suited for the prediction of ductile fracture. The model is applied to simulate failure of single crystal specimens.

# 3

# Mechanical behaviour of austenitic stainless steel single crystals at 300 °C


## Résumé

Dans ce chapitre nous nous intéressons au comportement mécanique en traction à 300 °C de monocristaux d'un acier austénitique inoxydable 316L. Des essais de traction avec mesure de champs de déplacements par corrélation d'images numériques sont réalisés afin de caractériser le comportement de ce matériau suivant différentes directions cristallographiques. Des hétérogénéités de déformation sous forme de bandes sont observées en surface des éprouvettes. L'orientation de ces bandes semble coïncider avec la trace des plans de glissement actifs prédits par le critère de Schmid. Par ailleurs, une dépendance significative du seuil de plasticité et de l'écrouissage à l'orientation cristalline est mise en évidence. Les courbes de tractions expérimentales sont ensuite comparées aux résultats de simulations par éléments finis de ces mêmes essais. Une loi de plasticité cristalline standard dans la littérature est utilisée. Différents ensembles de paramètres matériaux disponibles dans la littérature sont examinés. Les comparaisons des résultats de simulations avec les résultats expérimentaux montrent qu'aucun des ensembles de paramètres proposés dans de précédentes études ne conduit à un accord satisfaisant entre les expériences et les simulations. Une identification des paramètres matériaux est donc proposée afin de réconcilier les prévisions des simulations de plasticité cristalline avec les résultats expérimentaux d'essais de tractions sur monocristaux.

## Contents

## 3.1 Introduction

Due to their excellent mechanical properties at relatively low cost, austenitic stainless steels are widely used as structural materials in engineering applications (Marshall, 1984). For instance, their mechanical behaviour in the range of temperatures and pressures operating inside nuclear pressure vessels makes them suitable for internal structural use. These qualities have led to an extensive literature aiming at measuring, understanding and leveraging the origin of these particularly interesting properties. Experimental as well as numerical studies were carried out in order to investigate the underlying mechanisms at scales spanning over several orders of magnitude. Microscopical analyses based on electron micrography are widely used to characterize and link mechanical properties to microstructural features such as grain size, grain morphology, crystallographic morphology, presence of precipitates, etc. Microstructural characterization of steels are mostly performed at subcrystalline level, while most mechanical tests are performed on polycrystalline specimens, thus averaging the behaviour of numerous grains. The reason for the striking gap between the scales of microstructural observation and mechanical characterization is twofold. First, most applications of steels do involve pieces composed of a large number of grains and therefore do not necessarily require measuring the mechanical behaviour of individual grains. Second, mechanical testing of individual grains is challenging for steels due to relatively small grain size obtained during elaboration, typically a few tens of micrometers.

Nevertheless filling this gap could have substantial benefits. Elementary mechanisms of plasticity and fracture occur indeed often at scales below the grain size. Furthermore, models of material behaviours have become more and more refined. For instance, continuum theory of crystal plasticity is a modeling tool of utmost importance for bridging subgrain features to macroscopic mechanical behaviour. However crystal plasticity models rely on material parameters which remain, for some, imprecisely known in austenitic stainless steels due to the lack of experimental work at this scale. To some extent, evaluation of these parameters can be carried out by inverse identification on polycrystals experiments or by coarse-graining results obtained by numerical simulations performed at smaller scales (*e.g.* discrete dislocation dynamics (DDD) simulations). Yet, an experimental investigation of the mechanical behaviour of austenitic stainless steel single crystals would help validating or if not amending numerical values of material parameters used in the literature. The present work aims at performing this task.

Several techniques exist in order to grow millimeter-sized (or even larger) metallic single crystals such as the Bridgman–Stockbarger method or the Czochralski method. They can thus be used in order to produce ingots from which single crystal specimens can be machined while controlling the orientation of the crystal lattice within the sample geometry. Experiments on pure metallic single crystals were performed for instance on aluminum (Taylor and Elam, 1925), copper (Cuitino and Ortiz, 1996; Demir and Raabe, 2010), magnesium (Syed et al., 2012) and $\alpha-$iron (Keh and Nakada, 1967). Experiments on metallic alloys single crystals are more scarce since their elaboration is often more sophisticated. Available studies focus predominantly on nickel-based superalloys (Hanriot et al., 1991; Raffaitin et al., 2007) or Hadfield steels (Canadinc et al., 2005; Karaman et al., 2000). Some experimental techniques do not require large grains, such as for instance mircropillar compression or nanoindentation. Such methods were respectively used by Paccou et al. (2019) and Weaver et al. (2017) to characterize virgin and irradiated 304 stainless steel. However, small scale experimental techniques often come with the difficulty of assessing the dependency of the results to the size of the samples. This question is raised because the scale of the sample becomes of the same order of magnitude as the scale of the deformation processes. When possible, experimental methods which do not involve that kind of issues should be preferred, at least for first investigations. To the authors' knowledge a single study performed by Karaman et al. (2001) reports tensile test results on 316L stainless steel millimeter-sized single crystals. Their tensile experiments were carried out on nitrogen-free and nitrogen-strengthened steels at room temperature with a strain rate of $5\times10^{-5}\,\mathrm{s}^{-1}$ and with the tensile directions oriented along <111>, <001> and <123> crystal directions. At these temperature and strain rates, slip and twinning mechanisms coexist and interact. In order to isolate and analyze only one plastic mechanism it is more convenient to study the behaviour of

316L stainless steel at a higher temperature where slip predominates. For light water nuclear reactor applications the temperature of structural internals made out of 316L stainless steel neighbours 300-350 °C, therefore a temperature of 300 °C is chosen in the present study.

If experiments on metallic single crystals are seldom in the literature, in contrast, many crystal (elasto-)plasticity models are available and used in numerical simulations. A common feature shared by most models is to consider a set of yield criteria in order to account for several inelastic mechanisms, such as plastic slip on different slip systems. Some differences between available models stem from their either phenomenological or more physical foundation. For instance (Méric et al., 1991) consider a phenomenological crystal plasticity theory. On the other hand a variety of dislocation-based crystal plasticity theories were formulated (Kuhlmann-Wilsdorf, 1999). Some models account for the edge or screw nature of dislocations (Gurtin, 2006), while others introduce size dependencies by accounting for the presence of geometrically necessary dislocations (Gurtin, 2008). In addition, formulations with a critical stress (threshold) to activate plastic slip (Méric et al., 1991) and formulations without a critical stress (threshold-free) (Kothari and Anand, 1998) are available. Furthermore, rate-independent settings (Anand and Kothari, 1996; Forest and Rubin, 2016; Schmidt-Baldassari, 2003) and viscoplastic frameworks (Méric et al., 1991; Rashid and Nemat-Nasser, 1992) were concurrently proposed. All in all, a wide variety of models are at hand in the literature. More often than not, their parameters are obtained from inverse identification on polycrystals or by upscaling numerical results from DDD or molecular dynamics (MD) simulations rather than from direct calibration on single crystal tests.

The objectives of the present chapter are threefold. First tensile tests are performed on austenitic stainless steel single crystal specimens at 300 °C. Tensile tests are carried out along directions close to <111> and <110> crystal orientations. Digital image correlation analysis is applied in order to measure displacement and strain fields. Then, experimental data are confronted to theoretical modeling of single crystals. First of all, the correct prediction of activated slip systems by Schmid's criterion is assessed. Thereafter, finite element simulations, are performed in order to calibrate a crystal plasticity model available in the literature. Eventually, a review of enhanced crystal plasticity constitutive equations to account for irradiation induced defects is presented. Thereafter, preliminary experimental results for a prospective study on proton-irradiated austenitic single crystals are presented.

The chapter is organized as follows. In Section 3.2 the material and experimental techniques used for this study are presented. Section 3.3 gathers experimental results obtained from *ex situ* tensile tests. In Section 3.4 the identification procedure of material parameters of a crystal plasticity model is explained and comparison to experimental data are presented. A review of crystal plasticity models relevant for irradiated austenitic steels and preliminary results on proton-irradiated stainless steels are presented in section 3.5. Concluding remarks and prospects are given in Section 3.6.

## 3.2 Experimental methods

### 3.2.1 Material and instruments

A $25 \times 25 \times 2$ mm 316L grade austenitic stainless steel plate composed of mainly two millimeter-sized weakly-misoriented grains was purchased from Princeton Scientific Corporation (Princeton Scientific Corporation, 2020). An EBSD map of the plate showing the two grains is given in Appendix A. The chemical compositions as provided by the supplier is given in Table 3.1. Electrical-discharge machining with a $\phi = 100$ µm wire was used in order to obtain two $25 \times 25 \times 0.9$ mm sized plates by cutting through the thickness of the initial plate. The same machining technique was then used to cut tensile specimens inside single- or bi-crystal regions of the plate. The geometry design and dimensions were optimized in order to maximize the number of specimens to be machined from the plates while remaining compatible with the available testing equipment described in Section 3.2.2. A sketch of the tensile specimen geometry and

Table 3.1 Supplier provided chemical compositions (weight %) of the 316L austenitic stainless steel plate.

| C | Mn | P | S | Si | Cr | Ni | Mo | N | Fe |
|---|---|---|---|---|---|---|---|---|---|
| ≤ 0.060 | 2.00 | 0.045 | 0.030 | 0.75 | 17.0 | 12.0 | 2.5 | 0.10 | balance |

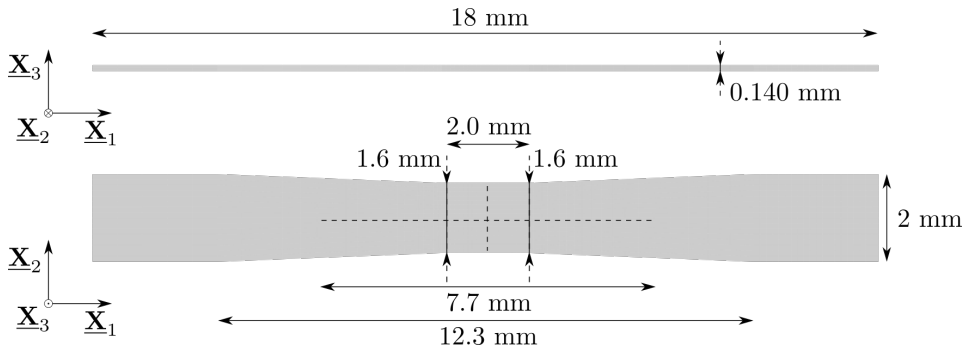


Figure 3.1 Sketch of the geometry and dimensions of the tensile specimens. Horizontal and vertical profile dashed lines correspond to the major axes of the rectangular region of interest used for digital image correlation analysis.

dimensions is presented in Figure 3.1. The lowest cross section area located in the center of the specimen is 1.6 mm wide, over a length of 2 mm. The sampling plans of the recto (denoted R) and verso (denoted V) side of the initial plate are presented in Appendix A. The specimens were mechanically polished in order to reach a thickness of 140 µm and a mirror finish on both sides. That thickness was chosen in order to be able to maintain the grip between the specimen and the clumping jaws of the micro-tensile machine. The last polishing stage was achieved with a standard 0.25 µm colloidal silica suspension from Struers (Struers, 2020) in order to remove the polishing-induced hardened layers. More details on the specimen preparation procedure are given in Appendix B.1.

A JEOL JSM-IT300 scanning electron microscope (SEM) equipped with an Oxford NordlysMax$^3$ EBSD (Electron Backscatter Diffraction) detector was used to make EBSD maps of single crystals tensile specimens and perform fractography analyses.

### 3.2.2 Tensile testing and temperature control

Tensile experiments were performed on a Proxima tension micromachine purchased from MicroMecha (MicroMecha, 2020) compatible with *ex situ* and SEM *in situ* testing. The machine was operated by imposing a constant 1 µm /s displacement rate to the mobile crosshead. A Sensy (Sensy, 2020) loading cell (model 2962) with a maximum capacity of 200 N was used to measure the applied traction force. Calibration of the loading cell was performed once before all the tests were carried out.

Temperature of the specimen was imposed through a 8 × 8 mm wide heating unit in contact with the surface of the specimen. An in house spring-controlled device was used in order to prevent any bending deflection to be imposed by the heating unit on the specimen while maintaining an optimal contact. Temperature regulation is calibrated by imposing a control temperature to the thermocouple welded to the heating unit and measuring the temperature by another thermocouple welded on the surface of a sacrificial specimen. Using sacrificial samples allows to control the temperature without damaging real samples. Because the specimens are very thin a gradient of about 20 °C is repeatably measured *ex situ* between the control and

measured temperatures. A uniform temperature profile was measured by infrared thermography on the region facing the surface in contact with the heating unit. A gradient of approximately -60 °C /mm along the tensile direction was measured on both sides of the heated region. More details on the temperature gradient measurement are given in Appendix C.

### 3.2.3 Digital Image Correlation field measurements

For *ex situ* tensile tests a paint speckle pattern is used for Digital Image Correlation (DIC) measurements. A random pattern is obtained by laying first a thin layer of white paint. In a second step droplets of black paint are disposed on the white surface by using an airbrush with very thin aperture in order to minimize the black spots diameter. A mean diameter of about 20 µm is obtained. A heat resistant paint (HI-TEMP from KBS Coatings (KBS, 2020)) is used to make the DIC pattern. A Canon MP-E 65mm f/2.8 1-5x lens mounted on a Canon Mark IV digital camera is utilized for optical image acquisition. A maximum image definition of $6720 \times 4480$ pixels is used to take pictures every 10 s during the tests. For all the tests the pixel size varies between 1.78 µm/pixel and 2.53 µm/pixel. The MATLAB software Ncorr (Blaber et al., 2015) is used to perform image correlations and fields post-processing. A correlation area of length $L_0$=7.7 mm and width $W_0$=1.5 mm centered in the middle of the specimen is used. The correlation window radius is equal to 50 µm and the spacing between correlation windows is 25 µm. Ncorr is also used to compute the local in plane deformation gradient $\underset{\sim}{\boldsymbol{F}} = \partial \underline{\boldsymbol{x}} / \partial \underline{\boldsymbol{X}}$. In order to compute strains, an optimal length over which displacements evolution can reasonably be considered as linear must be defined. If this distance is chosen too large, deformations will be smoothed out and information is lost. If on the contrary it is chosen too small, noise in the displacements measurements are amplified and strain fields are unrealistically oscillating. In our case an optimal length of 100 µm was found after several tests. Furthermore, the out-of plane components of $\underset{\sim}{\boldsymbol{F}}$ cannot be directly measured with the two-dimensional image correlation technique used in this study. However, according to Papasidero et al. (2015), a three-dimensional equivalent strain can be defined as follows. First, a two-dimensional Hencky strain tensor is defined as

$$\underset{\sim}{\boldsymbol{H}}^{2D} = \frac{1}{2} \log \left( \underset{\sim}{\boldsymbol{F}}^T . \underset{\sim}{\boldsymbol{F}} \right) = \begin{pmatrix} H_{11} & H_{12} \\ H_{12} & H_{22} \end{pmatrix} \tag{3.1}$$

From $\underset{\sim}{\boldsymbol{H}}^{2D}$, in-plane principal strain components $H_I^{2D}$ and $H_{II}^{2D}$ can be determined. Then, assuming small elastic strains and using plastic incompressibility the third principal Hencky strain can be estimated as $H_{III} = -H_I^{2D} - H_{II}^{2D}$ . Finally, the von Mises norm can be used to define a scalar equivalent strain measure

$$H_{eq}^{3D} = \sqrt{\frac{2}{3} \left( (H_I^{2D})^2 + (H_{II}^{2D})^2 + H_{III}^2 \right)} = \frac{2}{\sqrt{3}} \sqrt{(H_I^{2D})^2 + (H_{II}^{2D})^2 + H_I^{2D} H_{II}^{2D}} \tag{3.2}$$

## 3.3 Experimental results

### 3.3.1 Microstructure of tensile specimens

The austenitic stainless steel plate used in this study was sold by Princeton Scientific Corporation as a single crystal with $\langle 111 \rangle$ and $\langle 1\bar{1}0 \rangle$ crystal directions parallel to the long edges of the plate. However, as mentioned earlier, the plate was actually composed of mainly two millimeter-sized weakly-misoriented grains. The presence of a grain boundary crossing the middle of the plate was detected when performing an EBSD map covering the whole surface of the plate (see Appendix A). The misorientation between the two grains (later denoted G1 and G2) is about 10°. As far as possible tensile specimens were taken from one or the other grain, hence avoiding the presence of the grain boundary in their minimum cross section area. In Table 3.2, the notations used to

Table 3.2 Notations used to denote the tensile specimen and their respective crystal orientation.

| Notation | Grain | $[\phi_1, \Phi, \phi_2]$ | Tensile $\underline{\boldsymbol{X}}_1$ | Transverse $\underline{\boldsymbol{X}}_2$ | Normal $\underline{\boldsymbol{X}}_3$ |
|---|---|---|---|---|---|
| R4 | G1 | [98°, 35°, 38°] | [111] | $[1\bar{1}0]$ | $[11\bar{2}]$ |
| R2, R3 | G2 | [308°, 59°, 40°] | $[1\bar{1}0]$ | [111] | $[\bar{1}\bar{1}2]$ |

denote the tensile specimen, the grain they were taken from and their corresponding average Euler angles (given with the Bunge convention ZXZ) are presented. For practical purposes the closest crystallographic orientations are given for the principal axes of each specimen. It is important to note that these crystallographic orientations are not exactly aligned with the specimen axes, but are used to have an informative approximate orientation of the crystal inside the specimens. In the forthcoming numerical analysis in Section 3.4, as-measured orientations will be used by assigning average Euler angles to the whole specimen. For two different specimens, each one taken from one of the two grains composing the initial plate, a large scale EBSD map covering the whole surface is performed. These EBSD maps are presented in Figure 3.2 along with their corresponding Inverse Pole Figures (IPF). From Figures 3.2a and 3.2b it can be seen that the specimen R4 is weakly misoriented (about 3°) from the announced crystal orientation. On the contrary in Figures 3.2c and 3.2d a misorientation of about 10° can be observed between the orientation of specimen R2 and the announced orientation. This is due to the fact that specimen R2 was taken from grain G2 which was known to be slightly misoriented with respect to G1. On the EBSD maps, white regions are BCC-indexed zones which correspond to elongated ferrite inclusions. The presence of these defects is probably due to the elaboration process of the millimeter-sized grains. As this work proceeds, their influence on the mechanical behaviour will be neglected for the sake of simplicity.

### 3.3.2 *Ex situ* tensile results

#### 3.3.2.1 DIC measurements

As presented in Section 3.2.3 the software Ncorr is used to compute displacement fields by digital image correlations. These fields are then post-processed in order to extract an equivalent Hencky strain $H_{eq}^{3D}$ defined at Eq. (3.2). Figure 3.3 displays, for each orientation, the corresponding fields of equivalent strain at two different macroscopic tensile strains defined as $\Delta L/L_0$. $\Delta L$ denotes the variation in length of the correlation zone which initial length is $L_0 = 7.7\,\text{mm}$. In Figures 3.3a and 3.3c $\Delta L/L_0 = 0.05$ and on in Figures 3.3b and 3.3d $\Delta L/L_0 = 0.10$. At a macroscopic strain level of 0.05, equivalent strain fields are already significantly heterogeneous. For each orientation narrow bands appear in the whole correlation area and are not restricted to the lowest cross section region located at the center. Overall their width is lower than approximately 200 µm. These bands are collectively oriented along preferential directions. For each specimen essentially two preferential directions can be observed and several parallel bands are visible for each of them. In specimen R4, the bands are approximately symmetrically inclined at ±15° with respect to the tensile direction. In specimen R2, the bands are approximately inclined at −58° and 30° with respect to the tensile direction. The local maximum equivalent strain reaches up to 0.2 in almost all bands, while outside of the bands a strain lower than 0.05 is always observed. In specimen R4 all bands have mostly the same intensity in terms of equivalent strain. On the contrary, in specimen R2, one band located in the middle of the specimen appears almost twice stronger as all others. At a macroscopic strain level of 0.1, the heterogeneity of equivalent strain field persists for both specimens and the same narrow bands remain visible. For both orientations all the bands observable at $\Delta L/L_0 = 0.10$ were already noticeable at $\Delta L/L_0 = 0.05$. While their

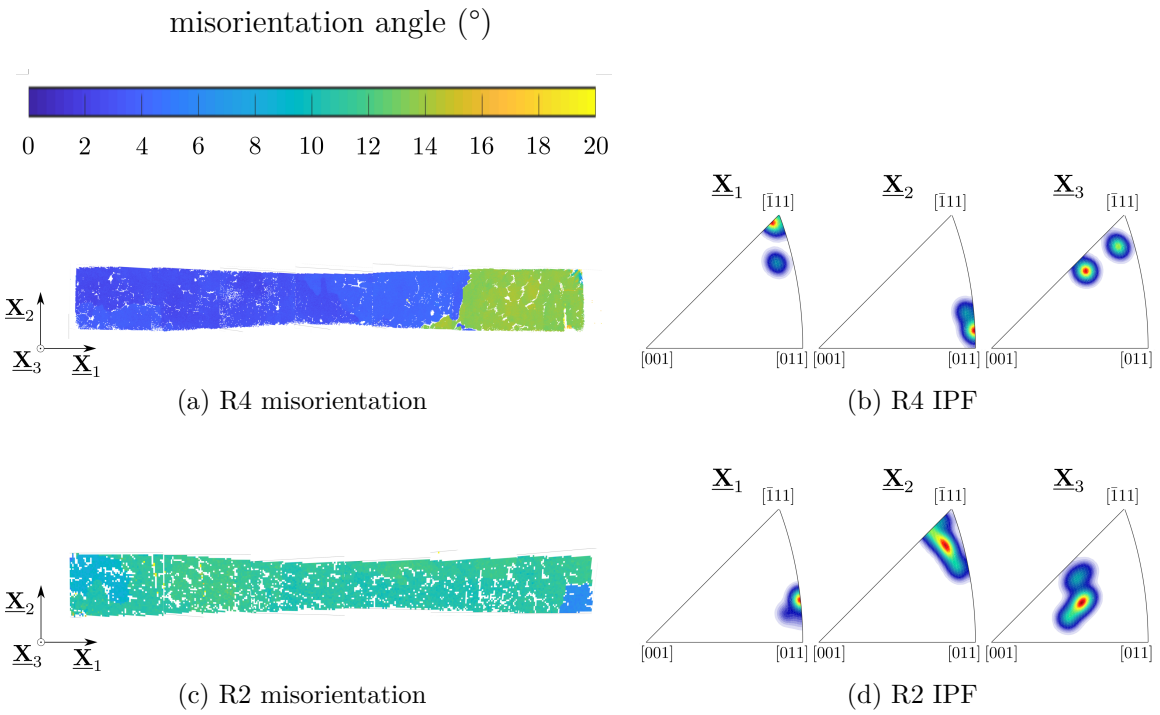


(a) R4 misorientation

(b) R4 IPF

(c) R2 misorientation

(d) R2 IPF

Figure 3.2 (a) and (c) EBSD measured misorientation angle of crystal orientation in specimen R4 and R2 with respect to theoretical orientation (b) and (d) Inverse Pole Figure for $\underline{\boldsymbol{X}}_1$, $\underline{\boldsymbol{X}}_2$ and $\underline{\boldsymbol{X}}_3$ directions in specimen R4 and R2.

number does not increase, their intensity has been however clearly strengthened. Most bands display indeed a maximum equivalent strain close to 0.3. These maxima are often located at the intersection of non-parallel bands. Their intensity not only is enhanced, but also their width is slightly expanded. The orientation of the bands with respect to the tensile direction does not seem to have evolved significantly. The equivalent strain field outside the bands also increased appreciably and reaches about 0.1 for both specimens.

#### 3.3.2.2 Activated slip systems

Tensile tests were performed up to fracture and post-mortem analysis of specimens surface were conducted by SEM. Secondary Electron Detector (SED) images of the specimens surface taken at locations of intense local straining are shown in Figure 3.4. Figure 3.4a displays the main features which were observed in specimen R4, namely three groups of slip lines bundles. Many slip lines can indeed be observed as straight parallel lines crossing the whole picture. These lines are oriented along three principal directions. It is worth noting that two of these directions are respectively symmetrically inclined with angles of about ±18° with respect to the tensile direction represented by the white vertical arrow. These two directions coincide remarkably well with the directions of the more macroscopic bands observed on DIC equivalent strain fields. Therefore the narrow bands described in previous section are most probably caused by the formation of slip lines bundles like the ones depicted in Figure 3.4a. A third family of slip lines emerges at approximately 81° with respect to the tensile direction. Figure 3.4b displays the main features which were observed in specimen R2, namely several groups of slip lines bundles. The direction of the slip lines are inclined at about 50° with respect to the tensile direction. This direction does not exactly coincide with the narrow band direction observed on DIC equivalent strain fields, but does not fall too far either. One probable explanation to this discrepancy is the existence of lattice rotation between the moment at which the picture in Figure 3.3d was taken (at $\Delta L/L_0 = 0.10$) and the moment at which the picture in Figure 3.4b was taken (after

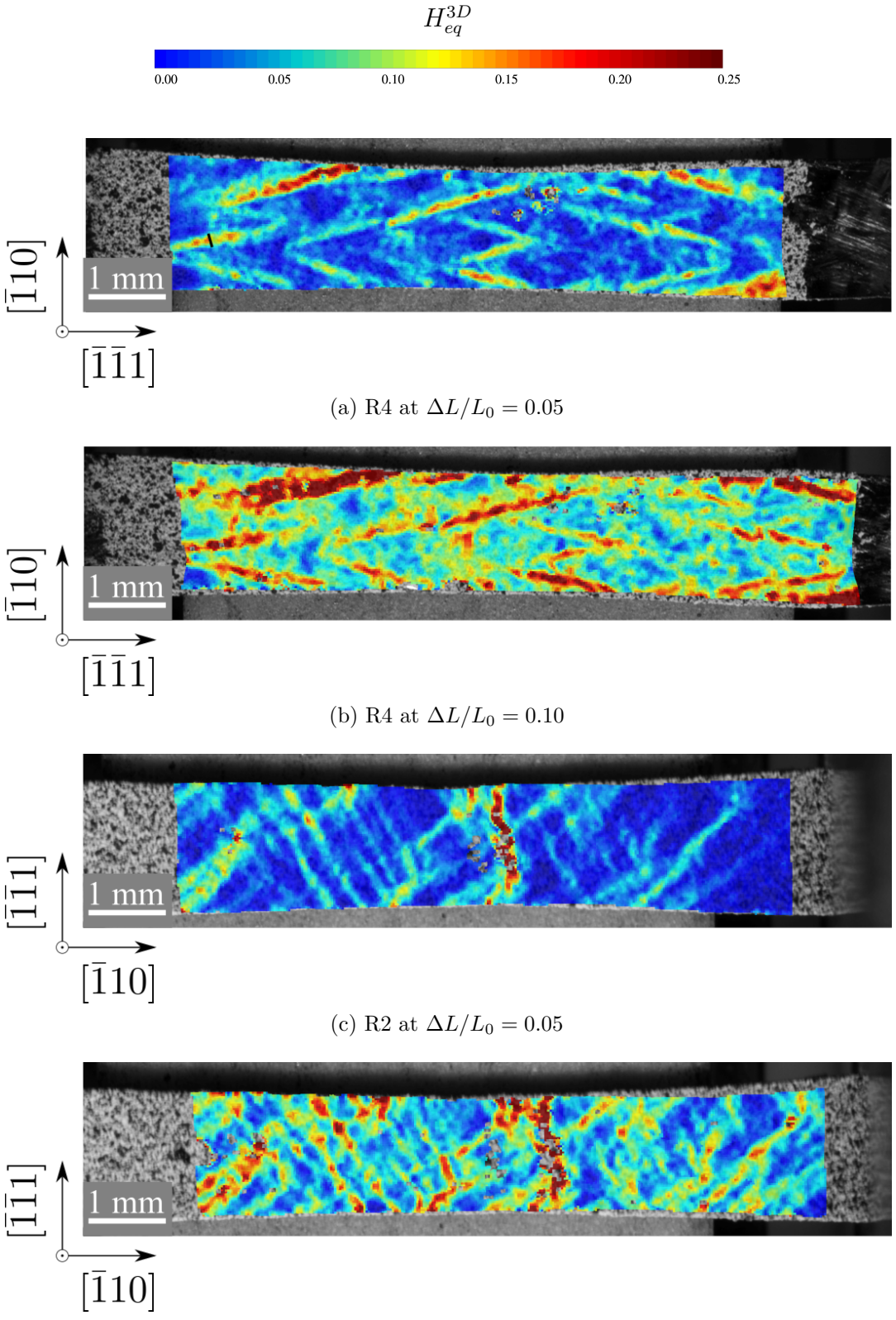


(a) R4 at $\Delta L/L_0 = 0.05$

(b) R4 at $\Delta L/L_0 = 0.10$

(c) R2 at $\Delta L/L_0 = 0.05$

(d) R2 at $\Delta L/L_0 = 0.10$

Figure 3.3 DIC measured three-dimensional equivalent Hencky strain fields at macroscopic strain of $\Delta L/L_0 = 0.05$ in (a) and (c) and $\Delta L/L_0 = 0.10$ in (b) and (d). The closest crystal directions aligned with the tensile and transverse direction are depicted.

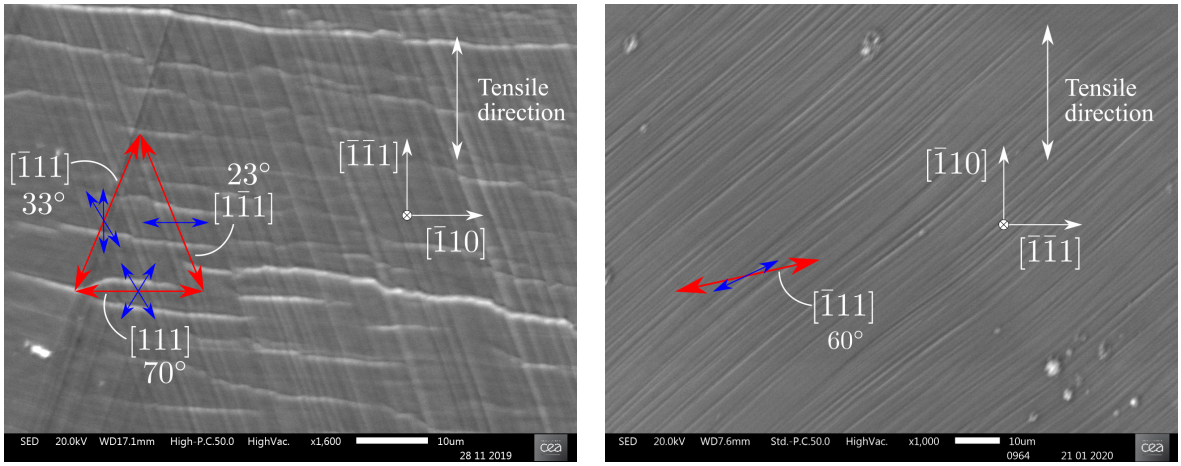


(a) R4 (b) R2

Figure 3.4 Slip lines observed by SEM on post-mortem specimen's surface. Red arrows (resp. blue arrows) indicate the slip plane trace (resp. slip direction) of activated slip systems predicted by the Schmid criterion.

fracture). Figures 3.4a and 3.4b show the directions of slip traces (red arrows) and slip directions (blue arrows) projected in the specimen surface plane of the FCC slip systems having the highest Schmid factors. For each slip plane of normal $\underline{\boldsymbol{n}}^s$, the outlet angle with respect to the specimen surface normal $\underline{\boldsymbol{N}}$ is computed as $\theta = \text{acos}\,(\underline{\boldsymbol{n}}^s.\underline{\boldsymbol{N}})$ and presented in Figure 3.4. An outlet angle of 0° means that the slip plane and the specimen surface coincide, while an angle of 90° means that the slip plane is orthogonal to the specimen surface. It can be noted that for specimen R4 the slip lines directions are very well predicted by the Schmid criterion. Red arrows are indeed almost perfectly aligned with the observed slip lines. This observation is more mitigated for specimen R2. The predicted slip trace orientation does not match precisely the slip lines orientation observed. This observation corroborates the possible existence of significant rotation of the crystal lattice between its initial and post-mortem state in specimen R2. A progressive alignment of the active slip planes traces with the tensile direction seems to occur, which is in agreement with the crystal plasticity theory. A further discussion on this point will be given on the basis of numerically predicted lattice rotation for both orientations in Section 3.4.3.3.

#### 3.3.2.3 Stress-strain behaviour

The engineering stress is defined as $F/S_0$, where $F$ denotes the force measured by the loading cell and $S_0$ the initial smallest cross section ($1.6\times0.140\,\text{mm}$). Figure 3.5a shows the evolution of the unfiltered measure of engineering stress against the imposed crosshead displacement. Figure 3.5b gives the evolution of engineering stress against the DIC measured macroscopic strain $\Delta L/L_0$. Note that DIC measurements are made every 50 s, or equivalently every increment of 50 µm crosshead displacement. Therefore Figure 3.5b is smoothed as compared to Figure 3.5a. In addition curves are truncated in Figure 3.5b because image correlations failed at large strains due to paint speckle pattern cracking and decohesion.

First of all a striking difference in initial yield stress, hardening behaviour and ductility can be noticed between specimen R4 and specimens R2 and R3. Notwithstanding these differences in both cases a remarkably linear hardening behaviour is observed. Also noteworthy is the repeatability of the results obtained with specimen R2 and R3 which display almost an identical yield stress and an overlapping hardening behaviour. A yield stress of about $\sigma_0^{R4} = 105\,\text{MPa}$ is measured for specimen R4, while it reaches only about $\sigma_0^{R2} = 65\,\text{MPa}$ and $\sigma_0^{R3} = 70\,\text{MPa}$ in specimen R2 and R3 respectively. The ratio of yield stresses is close to the ratio of maximum Schmid factors which are respectively equal to $m_{R4} = 0.29$ in specimen R4 and $m_{R2,R3} = 0.39$ in

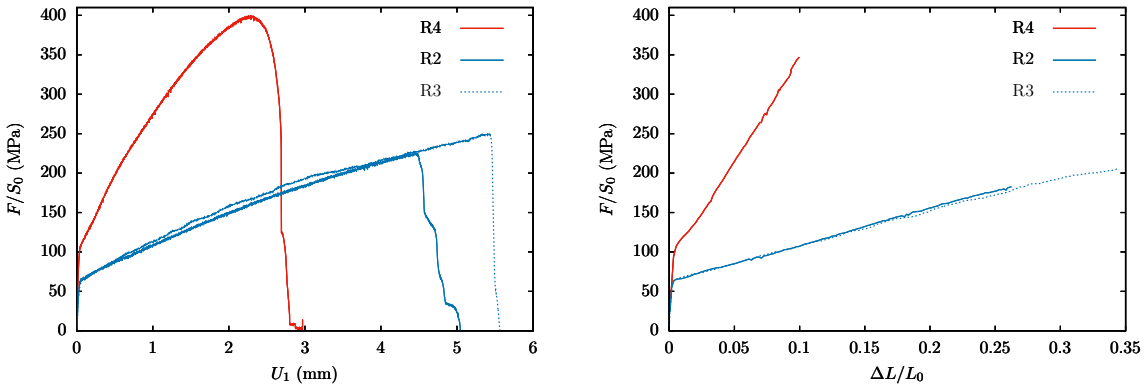


(a) (b)

Figure 3.5 Experimental engineering stress *vs* (a) crosshead displacement (b) DIC measured macroscopic strain. In (b) curves are smoothed out because DIC measurements are done every 0.05 mm crosshead displacement and also truncated because DIC fails at large strains due to paint speckle pattern cracking and decohesion.

specimen R2 and R3. One has indeed $\sigma_0^{R2}/\sigma_0^{R4} \simeq 0.62$ and $\sigma_0^{R3}/\sigma_0^{R4} \simeq 0.66$ to be compared to $m_{R4}/m_{R2,R3} \simeq 0.74$. In Figure 3.5b, the almost linear hardening behaviour for specimen R4 is characterized by a slope of $H_{R4} = 2575$ MPa, while a slope of $H_{R2} = H_{R3} = 465$ MPa is obtained with specimen R2 and R3. For all the tests the linear hardening regime is preceded by a limited hardening regime which lasts for about 1 % of macroscopic strain after the purely elastic regime. It probably corresponds to an easy glide period, during which single slip is essentially operating locally without much forest dislocations interactions. The second plastic stage lasts until failure of the specimen which occurs almost without significant strain after the ultimate tensile strength. Failure occurs indeed by propagation of a crack starting from one long-edge side and reaching rapidly the other long-edge side of the specimen.

## 3.4 Numerical identification of crystal plasticity material parameters

### 3.4.1 Crystal plasticity law

The tensile experiments presented in previous section are used in order to identify the material parameters of a crystal plasticity model often used in the literature. The model is essentially composed of yield criteria, flow rules, hardening laws and dislocation density evolution laws defined per slip system.

The usual Schmid yield criterion defined per slip system is used. It states that plastic slip is active on a given slip system $s$ if and only if the resolved shear stress $\tau^s$ applied on this system reaches a critical value noted $\tau_c^s$. In the context of finite strains, $\tau^s$ is often defined with respect to Mandel's stress tensor $\underset{\sim}{\boldsymbol{\Pi}}^M$ by $\tau^s = \underset{\sim}{\boldsymbol{\Pi}}^M : (\underline{\boldsymbol{m}}^s \otimes \underline{\boldsymbol{n}}^s)$, where $\underline{\boldsymbol{m}}^s$ and $\underline{\boldsymbol{n}}^s$ refer to the slip direction and normal to slip plane unit vectors in the undistorted configuration of system $s$ respectively. Mandel's stress is defined with respect to Cauchy's stress $\underset{\sim}{\boldsymbol{\sigma}}$ by $\underset{\sim}{\boldsymbol{\Pi}}^M = \det(\underset{\sim}{\boldsymbol{E}})\, \underset{\sim}{\boldsymbol{E}}^T . \underset{\sim}{\boldsymbol{\sigma}} . \underset{\sim}{\boldsymbol{E}}^{-T}$, where a multiplicative elastic-plastic decomposition of the deformation gradient is assumed ($\underset{\sim}{\boldsymbol{F}} = \underset{\sim}{\boldsymbol{E}} . \underset{\sim}{\boldsymbol{P}}$). The yield criteria therefore read

$$f^s = |\tau^s| - \tau_c^s \tag{3.3}$$

Several approaches exist in order to define flow rules per slip system. From a numerical point of view one major difficulty arises, because of the possible indeterminacy of active slip systems. In order to alleviate this obstacle viscoplastic flow rules are often used (Busso and Cailletaud, 2005; Peirce et al., 1983). In this work following flow rules are utilized in the form

$$\dot{\gamma}^s = \text{sign}\left(\tau^s\right) \dot{\gamma}_0 \left\langle \frac{f^s}{\tau_0} \right\rangle^n \tag{3.4}$$

The hardening laws are expressed as functions of the scalar dislocation densities $\rho^s$ per slip system $s$ defined as the length of dislocation lines per unit volume on system $s$. The hardening laws account therefore for lattice friction and dislocations interactions. Following Franciosi et al. (1980), the critical resolved shear stress (CRSS) is taken as

$$\tau_c^s = \tau_0 + \mu b \sqrt{\sum_{u=1}^{N} a^{su} \rho^u} \tag{3.5}$$

where $\tau_0$ is the thermal component of the CRSS due to lattice friction, $b$ is the norm of the dislocation Burgers vector $\underline{\boldsymbol{b}}$, $\mu$ is the shear modulus and $a^{su}$ is a matrix describing interactions between dislocations. For FCC metals, it usually takes the form of a $12 \times 12$ matrix composed for symmetry reasons of only 6 independent coefficients noted $a_1$ to $a_6$. These coefficients can be regarded as Taylor factors describing the possible dislocation junctions or dipoles formations (Bassani and Wu, 1991; Devincre et al., 2006; Franciosi, 1985; Kubin et al., 2008; Madec et al., 2003), namely self-hardening interactions ($a_1$), coplanar interactions ($a_2$), Hirth locks ($a_3$), colinear interactions ($a_4$), glissile junctions ($a_5$), and Lomer locks ($a_6$) can exist.

$$[a^{su}] = \begin{array}{c} \begin{array}{cccccccccccc} A2 & A3 & A6 & B2 & B4 & B5 & C1 & C3 & C5 & D1 & D4 & D6 \end{array} \\ \left[\begin{array}{cccccccccccc} a_1 & a_2 & a_2 & a_4 & a_5 & a_5 & a_3 & a_5 & a_6 & a_3 & a_6 & a_5 \\ & a_1 & a_2 & a_5 & a_3 & a_6 & a_5 & a_4 & a_5 & a_6 & a_3 & a_5 \\ & & a_1 & a_5 & a_6 & a_3 & a_6 & a_5 & a_3 & a_5 & a_5 & a_4 \\ & & & a_1 & a_2 & a_2 & a_3 & a_6 & a_5 & a_3 & a_5 & a_6 \\ & & & & a_1 & a_2 & a_6 & a_3 & a_5 & a_5 & a_4 & a_5 \\ & & & & & a_1 & a_5 & a_5 & a_4 & a_6 & a_5 & a_3 \\ & & & & & & a_1 & a_2 & a_2 & a_4 & a_5 & a_5 \\ & & & & & & & a_1 & a_2 & a_5 & a_3 & a_6 \\ & & & & & & & & a_1 & a_5 & a_6 & a_3 \\ & & & & & & & & & a_1 & a_2 & a_2 \\ & & & & & & & & & & a_1 & a_2 \\ & & & & & & & & & & & a_1 \end{array}\right] \end{array} \begin{array}{c} A2 \\ A3 \\ A6 \\ B2 \\ B4 \\ B5 \\ C1 \\ C3 \\ C5 \\ D1 \\ D4 \\ D6 \end{array} \tag{3.6}$$

Several atomistic and DDD studies were carried out in order to determine numerically appropriate values for the $a_i$ coefficients (Devincre et al., 2006; Madec et al., 2003; Monnet et al., 2009). It appears that colinear interactions ($a_4$) display the strongest interaction. On the contrary Hirth locks ($a_3$) seem to induce a less significant hardening. In between, Lomer locks ($a_6$), self-hardening ($a_1$), coplanar interactions ($a_2$) and glissile junctions ($a_5$) have similar importance on the hardening behaviour. Furthermore, DDD simulations performed on single crystal copper by Devincre et al. (2006) have shown that intensity of interactions between dislocations varies with the total density of dislocations. This property is attributed to the modification of the line tension by Monnet and Mai (2019). The latter authors also argued that other kinds of defects, such as dislocation loops which will be discussed in next section, do also contribute to the modification of the line tension. Therefore, they proposed the following identification from DDD simulations for the dependence of the interaction matrix coefficients upon the total

obstacle density $\rho_{obs}$

$$a^{su} = a^{su}_{ref}\left(0.2 + 0.8\frac{\ln\left(0.35b\sqrt{\rho_{obs}}\right)}{\ln\left(0.35b\sqrt{\rho_{ref}}\right)}\right)^2 \tag{3.7}$$

If $\rho_{obs} = \rho_{ref}$, then $a^{su} = a^{su}_{ref}$. In addition $a^{su}$ is a decreasing function of $\rho_{obs}$ in the domain of interest $10^9$–$10^{15}\,\mathrm{m}^{-2}$. Variations with respect to $a^{su}_{ref}$ become non-negligible when $\rho_{obs}$ differs from $\rho_{ref}$ by one or several orders of magnitudes. Such a situation can occur in case of intense hardening by dislocation multiplication (or also when dislocation loops are annihilated in the context of irradiated materials). A diminution of about a factor 2 is obtained when $\rho_{obs}$ becomes large ($\sim 10^{15}\,\mathrm{m}^{-2}$). Unless otherwise stated, evolution of matrix interaction coefficients will be neglected throughout this work.

An identification of the material parameters of the crystal plasticity law is sought. As long as DDD results have shown that self-hardening, coplanar interactions, glissile junctions and Lomer locks have similar influence on hardening, the following approximation will be used to reduce the number of independent parameters from 6 to only 3

$$A_1 = a_1 \simeq a_2 \simeq a_5 \simeq a_6 \qquad A_2 = a_3 \qquad A_3 = a_4 \tag{3.8}$$

It should be remarked that, when going to large deformations, the interaction matrix is used outside its identification domain where little is known about its evolution.

Furthermore, the scalar dislocation densities evolution equations are generally composed of at least two contributions (Devincre et al., 2006; Mecking and Kocks, 1981; Tabourot et al., 1997; Teodosiu, 1975). A positive contribution that accounts for storage governed by multiplication of dislocations by interactions with other systems based on Orowan's relation. This term is characterized by an estimation of the number of obstacles $\kappa$ a dislocation can cross before being pinned. Magnitude of the interactions between systems is characterized in FCC materials by a $12\times12$ interaction matrix $b^{su}$. For the sake of simplicity it is assumed that $b^{su} = 1-\delta^{su}$ where $\delta^{su}$ is Kronecker's delta. In that manner dislocations in each system do not interact with dislocations among the same system, but interact with the dislocations in all others system with the same intensity. In addition a negative contribution describes annihilation of dislocations dipoles in a given system in order to account for dynamical recovery. This mechanism is characterized by an annihilation distance $bG_c$, where $b$ is the norm of Burgers vector and $G_c$ a proportionality factor. The standard dislocation density evolution on system $s$ is therefore

$$\dot{\rho}^s = \frac{|\dot{\gamma}^s|}{b}\left(\frac{1}{\kappa}\sqrt{\sum_{u=1}^{N} b^{su}\rho^u} - bG_c\rho^s\right) \tag{3.9}$$

A sensitivity analysis to the values of crystal plasticity hardening parameters $\kappa$, $G_c$ and $A_i$ is presented in Appendix D in order to show how each parameter influences the hardening behaviour.

## 3.4.2 Parameters identification procedure

### 3.4.2.1 Hardening parameters

The scope of the present study is mainly to identify the hardening behaviour of austenitic stainless steel single crystals at 300 °C and low loading rates. The elastic constants and viscosity parameters will be considered as known from the literature. In addition some hardening parameters are known with accuracy from experiments available in the literature. The friction stress $\tau_0$ can be identified reasonably from tensile tests on polycrystals as pointed out by Monnet and

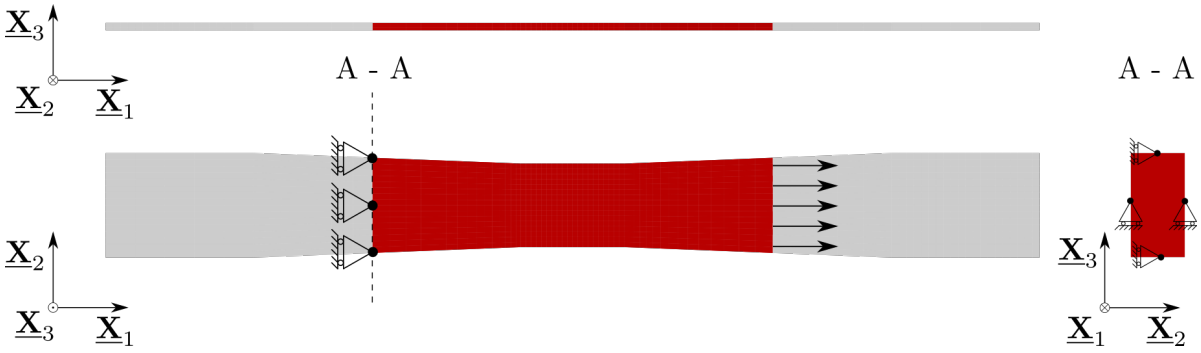


Figure 3.6 Sketch of the tensile specimen geometry with the simulated part marked in red.

Mai (2019). It can be related indeed to the initial yield stress of solution annealed (low or moderate effect of the initial density of dislocations on the yield stress) polycrystals by the following relation

$$\tau_0 = \tau_\infty + \frac{\mu}{\mu(300\text{K})} \frac{K}{M\sqrt{d}} \tag{3.10}$$

where the first term $\tau_\infty$ is size independent and the second term accounts for the grain size Hall-Petch effect. According to Monnet and Mai (2019) the evolution with temperature of $\tau_\infty$ can be obtained from polycrystals tensile tests (Pawel et al., 1996)

$$\tau_\infty = 43 - 0.055T \qquad (\tau_\infty \text{ in MPa and } T \text{ in } K) \tag{3.11}$$

In Eq. (3.10) $\mu$ and $\mu(300\text{K})$ denote the shear modulus at current temperature and 300 K respectively. $M$ is Taylor's factor (equal to 3.06 in the FCC structure) and $d$ represents the average grain size. $K$ is a material parameter equal to 1.0 – 1.15 MPa$\sqrt{\text{m}}$ in austenitic stainless steels (Feaugas and Haddou, 2003; Rao et al., 1975). The shear modulus and its evolution with temperature is known from the literature (Ghosh and Olson, 2002)

$$\mu = -3 \times 10^{-5} T^2 - 5.6 \times 10^{-3} T + 88 \qquad (\mu \text{ in GPa and } T \text{ in } K) \tag{3.12}$$

The norm of the Burgers vector is well known from the literature (Ridley et al., 1971). The remaining parameters are the initial densities of dislocations per slip system $\rho_0^s$, the three hardening matrix parameters $A_i$ defined in previous section and the parameters $\kappa$ and $G_c$ involved in the evolution equations of dislocation densities.

### 3.4.2.2 Geometry, boundary conditions and identification procedure

In order to identify these parameters, finite element simulations are performed with the crystal plasticity model presented in Section 3.4.1 which was implemented in the finite element software Z-set (Z–set package, 2020). These simulations are performed by prescribing the measured DIC displacement $U_1$ along the tensile direction to a finite element mesh having the same geometry as the correlation area. The geometry of the simulated area is depicted in red in Figure 3.6. The prescribed displacement boundary conditions are also presented. Note that a uniform $U_1$ displacement is prescribed on the right–hand side short face. The geometry is meshed with 180 elements in the length, 30 in the width and 5 in the thickness. Quadratic elements with 8 Gauss points reduced integration are used. Convergence of the results with respect to mesh size was verified. Since specimens R2 and R3 display very similar behaviour, identification is only carried out with experimental results obtained on specimens R2 and R4. The same weight is given to each orientation in the optimization procedure. Identification of the hardening parameters is done in three steps. First the initial dislocation density is identified by minimizing the mismatch

Table 3.3 Numerical values of material parameters for single crystal simulations as used in the literature and as obtained from optimization. Identified parameters are displayed in bold font.

| Parameter | Ling (2017) | Monnet and Mai (2019) | Fit | Unit |
|---|---|---|---|---|
| Elastic constants | | | | |
| $C_{11}$ | 200000 | 200000 | 200000 | [MPa] |
| $C_{12}$ | 136000 | 136000 | 136000 | [MPa] |
| $C_{44}$ | 105000 | 105000 | 105000 | [MPa] |
| Viscosity parameters | | | | |
| $\dot{\gamma}_0$ | $10^{29}$ | $10^{29}$ | $10^{29}$ | [$s^{-1}$] |
| $n$ | 15 | 15 | 15 | - |
| Hardening parameters | | | | |
| $\tau_\infty$ | 42.8 | 10.0 | 10.0 | [MPa] |
| $\tau_0$ | 88 | 55.2 | - | [MPa] |
| $\mu$ | 65600 | 73800 | 73800 | [MPa] |
| $\rho_0^s$ | $8.34 \times 10^8$ | $2 \times 10^{12}$ | $\mathbf{3.17 \times 10^{11}}$ | [$m^{-2}$] |
| $b$ | $2.54 \times 10^{-10}$ | $2.54 \times 10^{-10}$ | $2.54 \times 10^{-10}$ | [m] |
| $\kappa$ | 42.8 | 12.0 | **29.0** | - |
| $G_c$ | 10.4 | 3.9 | **0.01** | - |
| $A_1$ | 0.124 | 0.124 | **0.087** | - |
| $A_2$ | 0.070 | 0.070 | **0.297** | - |
| $A_3$ | 0.625 | 0.625 | **0.579** | - |

of experimental and numerical yield points. In a second step $\kappa$, $G_c$ are optimized in order to describe the hardening part of the experimental curve. Finally, $A_i$ from Eq. (3.8) are identified in order to minimize also the mismatch of the hardening part of the experimental and numerical stress-strain curves. For identification of $\kappa$, $G_c$ and $A_i$ only the part up to $U_1 = 1$ mm of the hardening curve in Figure 3.5a is used for optimization. This crosshead displacement corresponds to a macroscopic DIC measured strain of $\Delta L/L_0 = 0.075$ for specimen R4 and $\Delta L/L_0 = 0.10$ for specimen R2 in Figure 3.5b.

Parameters obtained after optimization as well as the values used in the literature are listed in Table 3.3. Results of the optimization procedure are displayed in bold font. Other material parameters which were not optimized are also presented for completeness. Note that $\tau_0$ is left empty for the proposed identification since the grain size effect is not relevant for the present experiments conducted on single crystals.

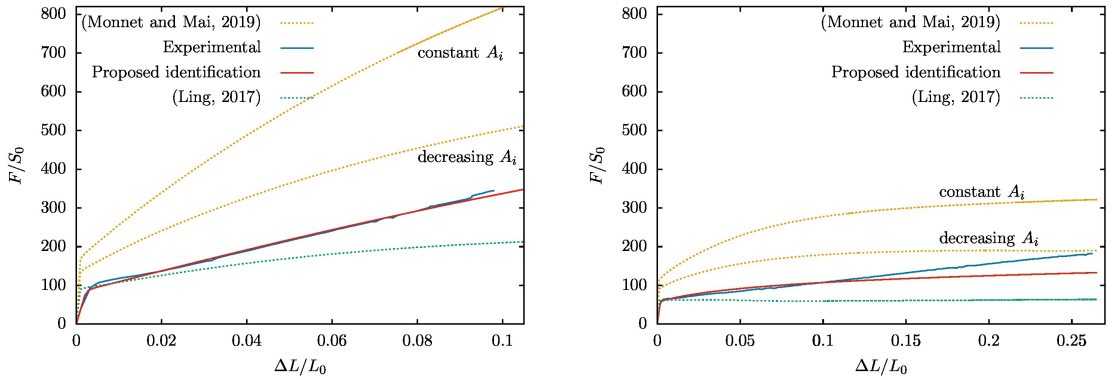


(a) R4 (b) R2

Figure 3.7 Comparison of experimental and numerical engineering stress *vs* DIC measured displacement with the simulation parameters presented in Table 3.3 for specimen R4 in (a) and specimens R2 and R3 in (b).

## 3.4.3 Comparison with experimental results

### 3.4.3.1 Macroscopic stress-strain behaviour

Ling (2017) and Monnet and Mai (2019) calibrated the crystal plasticity material parameters on tensile experiments performed on SA 304L polycrystals by Pokor et al. (2004a). Note that tensile tests presented in this study are conducted on 316L stainless steel which has a slightly different chemical composition (see Table 2.1). The fact that two different sets of material parameters were found to fit the same experiment is a proof that additional experiments were necessary in order to get confidence in one or the other set of parameters. A new set of material parameters was therefore identified on single crystal tensile experiments and compared to the prediction obtained with the sets available in the literature. Figure 3.7 shows the stress-strain curves obtained with the new optimized parameters set. Numerical simulations with parameters sets available in the literature are also presented. Figure 3.7a displays the comparison of experimental and numerical curves for specimen R4, while Figure 3.7b displays the same comparison for specimen R2 and R3. First of all a blatant discrepancy between experimental results and results obtained numerically with the parameters available in the literature can be observed. With the set of parameters used in (Ling, 2017) the yield stress is satisfyingly reproduced, but predicted hardening is weaker than experimentally measured. With the set of material parameters used in (Monnet and Mai, 2019), the yield stress is not well reproduced, because of the relatively high initial dislocation density considered. In addition a much stronger hardening is predicted numerically in this case, which fails to reproduce the experimental observations. To summarize, two different sets of material parameters available in the literature produce results that are bounding the actual behaviour.

The set of optimized parameters is capable of fitting very accurately the experimental data on single crystals. The yield point is well predicted thanks to the fit of the initial dislocation density per system $\rho_0^s$. The hardening slope is precisely reproduced thanks to the fit of $\kappa$, $G_c$ and $A_i$. Yet, there is no guarantee that the proposed numerical values are unique in order to match the experimental curves. The material parameters resulting from the identification procedure on single crystals experiment were therefore used in large FFT and FEM simulations of a periodic polycrystal. FFT simulations are performed with AMITEX (Gélébart, 2020) on a cubic cell composed of 600 Voronoï grains. The cubic cell is discretized with $101 \times 101 \times 101$ cubic voxels. FEM simulations are performed with Z-set on a cubic cell composed of 512 cubic grains which are each discretized with 27 quadratic finite elements with reduced integration. In both FFT and FEM simulations a tensile loading is prescribed with periodic boundary conditions imposed in the three directions. Results not displayed here have shown that numerically predicted results are converged in terms of number of grains and in terms of mesh size. Figure 3.8 shows the

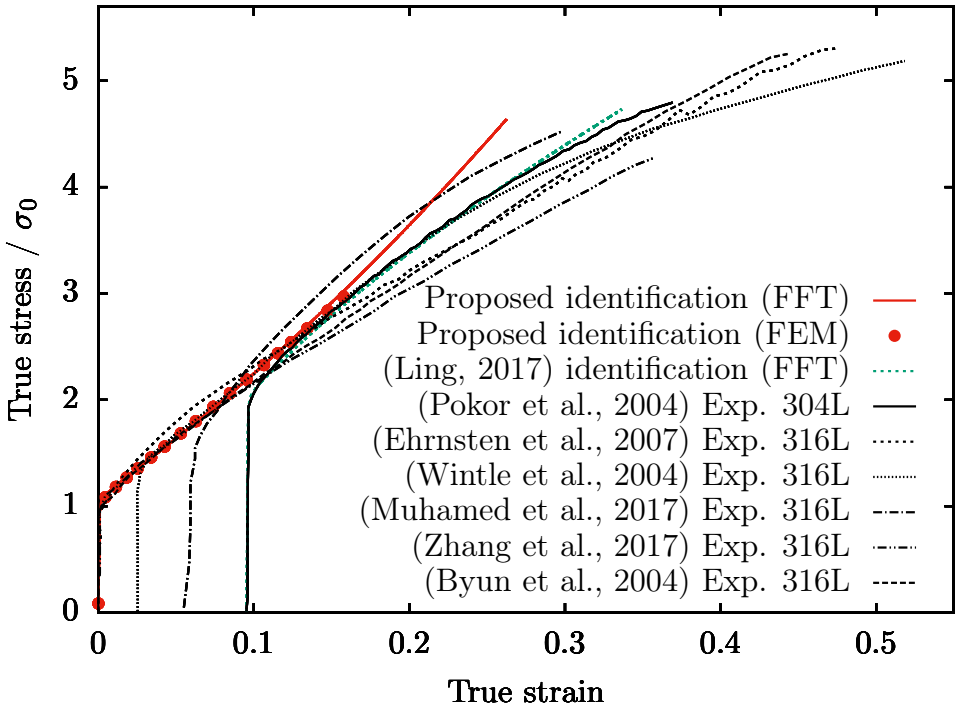


Figure 3.8 Comparison of numerical (FFT and FEM) and experimental normalized true stress *vs* true strain curves on 304L and 316L stainless steels polycrystals. Experimental data are reproduced from Byun and Farrell (2004a); Ehrnstén et al. (2007); Muhamed et al. (2017); Pokor et al. (2004a); Wintle et al. (2004); Zhang et al. (2017). ($\sigma_0 = 140\,\text{MPa}$)

true stress *vs* true strain curves obtained numerically with the proposed identification. On the same graph are also plotted the numerical FFT curve obtained with the parameters identified by Ling (2017) and experimental curves on 304L and 316L stainless steels at ∼300 °C from the literature. Since experiments were performed on different stainless steel grades and on materials having uncommunicated, but most likely different initial dislocation density, some experimental curves were shifted along the true strain axis in such a way that their yield point falls onto the curve with the lowest yield stress $\sigma_0 = 140\,\text{MPa}$. First of all, although the underlying numerical implementation of the crystal plasticity model is different, FEM and FFT simulations display an excellent agreement. Then, Ling's identification fits very well the experimental curve obtained by Pokor et al. (2004a) as expected. Although some variability exist among experimental data, the overall beam of experimental curves remains relatively narrow. In order to normalize the numerical true stress obtained with the proposed identification, a value of the material parameter $\tau_0$ was to be defined (i.e a grain size $d$ chosen). $\tau_0$ was worked out in such a way that normalizing the numerical curve by $M\tau_0$, where $M$ is the Taylor factor equal to 3.06 in the FCC structure, results in a normalized yield stress of 1. It was found that the value of $\tau_0$ satisfying this condition is equal to 68 MPa. With $\tau_\infty = 10.0\,\text{MPa}$, it corresponds to a grain size of $d = 30\,\mu\text{m}$ which is the size measured by Byun et al. (2004) on their 316L stainless steels tensile specimens. The parameters identified on single crystal tensile experiments result in a remarkably satisfying agreement with tensile experiments on polycrystals without further calibration than the grain size. All in all, the proposed identification results in a adequate fit to experimental results obtained on single- and polycrystals.

### 3.4.3.2 Local strain fields and profiles

In order to verify that the crystal plasticity law is capable of matching not only macroscopic quantities, but also local quantities, experimental and numerical local strain fields are compared.

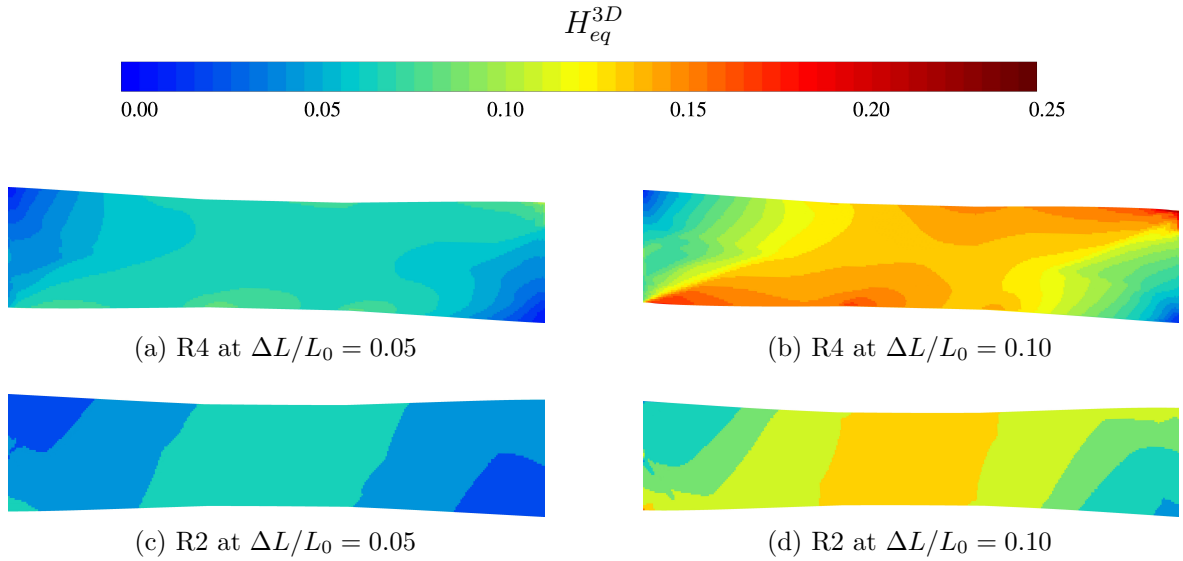


(a) R4 at $\Delta L/L_0 = 0.05$

(b) R4 at $\Delta L/L_0 = 0.10$

(c) R2 at $\Delta L/L_0 = 0.05$

(d) R2 at $\Delta L/L_0 = 0.10$

Figure 3.9 Numerically computed equivalent Hencky strain fields at macroscopic strain of $\Delta L/L_0 = 0.05$ in (a) and (c) and $\Delta L/L_0 = 0.10$ in (b) and (d). The closest crystal directions aligned with the tensile and transverse direction are depicted.

To do so, numerical simulations are post-processed in order to compute the equivalent Hencky strain defined at Eq. (3.2). Experimental equivalent Hencky strain fields obtained by DIC were plotted in Figure 3.3. Their numerical counterpart obtained with the set of optimized crystal plasticity parameters are plotted in Figure 3.9. It can be observed that computed equivalent strain fields are overall much more homogeneous than experimentally measured fields. However, in an average sense numerical results agree rather well with experimental data.

To confirm this observation profiles of equivalent strain along $\underline{\boldsymbol{X}}_1$ and $\underline{\boldsymbol{X}}_2$ directions are plotted in Figure 3.10 at $\Delta L/L_0 = 0.05$ and Figure 3.11 at $\Delta L/L_0 = 0.10$. Profile lines are plotted along horizontal and vertical symmetry axes of the specimen (dashed lines in Figure 3.6). Since a finer discretization is used for DIC measurements than for numerical simulations, raw experimental profiles (light blue) are smoothed out (deep blue) on a grid composed of the same number of nodes as the finite element mesh. In addition raw DIC measurements (light blue) are plotted as thick curves in order to evidence potential errors due to the DIC method. The thickness of the curve along the y-axis of the graphs represents the maximum error which was observed on DIC measurements in case of a rigid body motion. That error was shown to be always lower than or equal to $H_{eq}^{3D,\text{error}} = 0.005$. Numerical profiles obtained with the several sets of material parameters described in Table 3.3 are displayed. The heterogeneity of the experimental equivalent strain field depicted in Figure 3.3 translates into the presence of several local minima and maxima in the profile curves. On the other hand, smoothness of numerical results depicted in Figure 3.9 are characterized by smooth equivalent strain profiles. Peaks observed on the experimental profile are more numerous along $\underline{\boldsymbol{X}}_1$, because the correlation area is wider along that direction. In the same manner, for numerical results, a greater discrepancy between minimum and maximum equivalent strain is observed along $\underline{\boldsymbol{X}}_1$ than along $\underline{\boldsymbol{X}}_2$ because the simulated area is wider along the former direction. As already stated above, in an average sense numerical results agree well with experimental observations. The reasons why the crystal plasticity simulations do not predict intense heterogeneities as the ones observed experimentally are at least twofold. First of all, numerical samples have homogeneous material properties, which might be a crude assumption for instance in terms of initial dislocation densities. Then, a non-negligible hardening is predicted for both orientations considered. Therefore, any area where plastic strain would become more intense would also rapidly become much harder by dislocation multiplication. As a result, plastic slip would in turn be activated in the neighbourhood of such an area leading to smoothing of the initial intensely deformed region. As non-negligible hardening

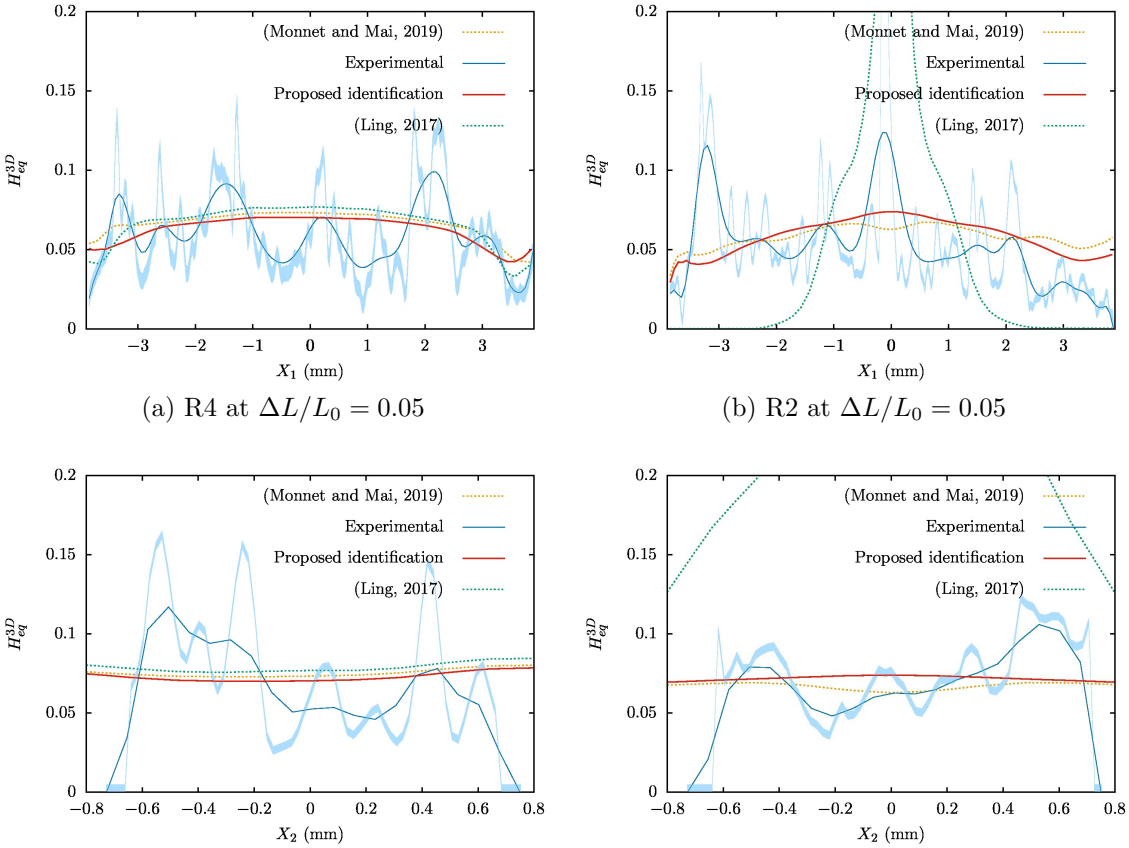


(a) R4 at $\Delta L/L_0 = 0.05$

(b) R2 at $\Delta L/L_0 = 0.05$

(c) R4 at $\Delta L/L_0 = 0.05$

(d) R2 at $\Delta L/L_0 = 0.05$

Figure 3.10 Horizontal (a,b) and vertical (c,d) equivalent Hencky strain profile lines at $\Delta L/L_0 = 0.05$ in specimens with crystal orientation close to R4 in (a,c) and R2 in (b,d) obtained by DIC and finite element simulations with the parameters presented in Table 3.3.

behaviours are also observed experimentally, the origin of observed plastic heterogeneities could be linked to material properties heterogeneities. Other explanations could be the presence of geometrical heterogeneities caused by specimen machining and preparation or wrinkling due to the small thickness of the specimens (140 µm). In Appendix E the effect of hard inclusions on the local strain behaviour is investigated. It is shown that a few numbers of hard inclusions can be responsible for a much more heterogeneous strain pattern than without inclusions. Ferrite inclusions could potentially play the role of hard inclusions and cause the heterogeneities observed in DIC strain fields.

#### 3.4.3.3 Fields of lattice rotation

The crystal plasticity formulation at finite strains used in this work is based on a multiplicative decomposition of the deformation gradient $\underset{\sim}{\boldsymbol{F}}$ into an elastic part $\underset{\sim}{\boldsymbol{P}}$ and a plastic part $\underset{\sim}{\boldsymbol{E}}$. While $\underset{\sim}{\boldsymbol{P}}$ accounts for plastic slip and is thus lattice rotation free, $\underset{\sim}{\boldsymbol{E}}$ describes rotation and stretching of the crystal lattice. The polar decomposition $\underset{\sim}{\boldsymbol{E}} = \underset{\sim}{\boldsymbol{R}}.\underset{\sim}{\boldsymbol{U}}$ gives thereby the rotation tensor $\underset{\sim}{\boldsymbol{R}}$ and the stretch tensor $\underset{\sim}{\boldsymbol{U}}$. From the rotation tensor a rotation angle $\phi$ can be defined as

$$\phi = \arccos\left(\frac{1}{2}(\mathrm{trace}\,(\underset{\sim}{\boldsymbol{R}}) - 1)\right) \tag{3.13}$$

The magnitude of $\phi$ indicates how much the crystal lattice has rotated with respect to its initial configuration. In Figure 3.12, the fields of lattice rotation $\phi$ computed numerically for specimen

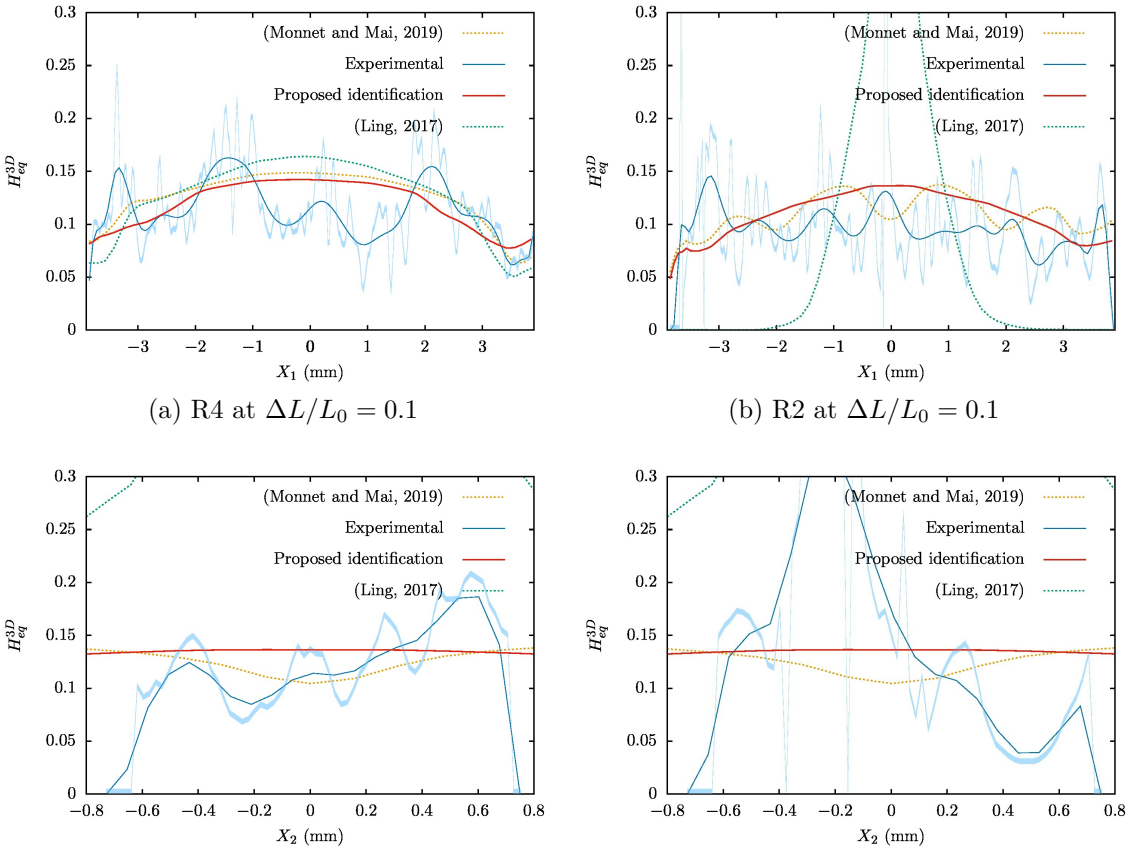


(a) R4 at $\Delta L/L_0 = 0.1$

(b) R2 at $\Delta L/L_0 = 0.1$

(c) R4 at $\Delta L/L_0 = 0.1$

(d) R2 at $\Delta L/L_0 = 0.1$

Figure 3.11 Horizontal (a,b) and vertical (c,d) equivalent Hencky strain profile lines at $\Delta L/L_0 = 0.1$ in specimens with crystal orientation R4 in (a,c) and R2 in (b,d) obtained by DIC and finite element simulations with the parameters presented in Table 3.3.

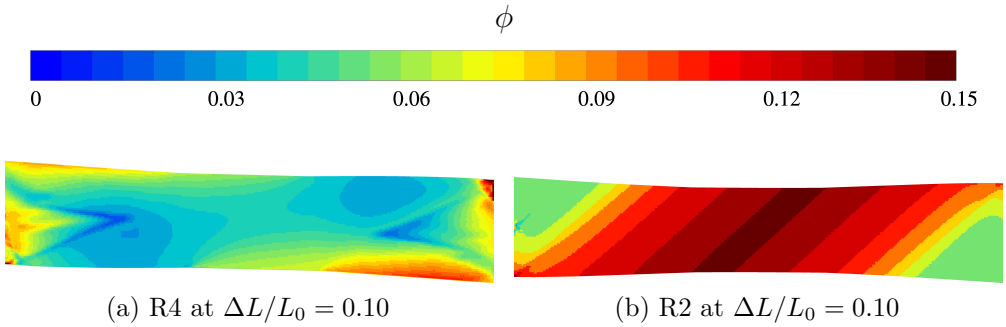


(a) R4 at $\Delta L/L_0 = 0.10$ (b) R2 at $\Delta L/L_0 = 0.10$

Figure 3.12 Crystal lattice rotation $\phi$ at $\Delta L/L_0 = 0.10$ in specimens with crystal orientation R4 in (a) and R2 in (b) obtained by finite element simulations with the fitted parameters presented in Table 3.3.

R4 and R2 are plotted at $\Delta L/L_0 = 0.10$. In the area of reduced cross section, the lattice rotation computed for specimen R2 is significantly larger than for specimen R4. This result supports the argument given to explain the discrepancy observed between the direction of observed slip traces in Figure 3.4b and the theoretical direction predicted in the initial configuration of the crystal lattice.

## 3.5 Mechanical behaviour of irradiated austenitic stainless steel single crystals

### 3.5.1 Crystal plasticity laws accounting for irradiation defects

As discussed in Chapter 2, the main population of defects generated under Light Water Reactor (LWR) conditions in austenitic stainless steels are dislocation Frank loops. Theses defects are responsible for pinning dislocations, hence to some extent preventing their motion and thus increasing the yield stress of irradiated steels. Several constitutive equations were proposed in the literature to account for Frank loop induced hardening and already reviewed to some extent by Han (2012).

#### 3.5.1.1 Dispersed barrier hardening model

The modified dispersed barrier model (Li et al., 2014; Monnet, 2015; Seeger, 1958) accounts for the volumetric density of dislocation loops (unit $\mathrm{m}^{-3}$) $\rho_L$ by introducing an additional contribution into the critical resolved shear stress

$$\tau_c^s = \tau_0 + \mu b \sqrt{\sum_{u=1}^{12} a^{su} \rho^u} + \alpha_L \mu b_L \sqrt{\phi_L \rho_L} \tag{3.14}$$

where $\alpha_L$ is a weighting factor, $b_L$ is the norm of the Burgers vector of Frank loops of type $(a/3)<111>$ and $\phi_L$ is the Frank loop diameter. Monnet and Mai (2019) noted that the hardening due to Frank loops decreases when the density of other defects (dislocations, solute clusters) increases. They proposed the following fit for the weighting factor $\alpha_L$

$$\alpha_L = 0.16 - 0.068 \ln\left(0.35 b \sqrt{\rho_{obs}}\right) \tag{3.15}$$

where $\rho_{obs}$ is the density of all kinds of defects, namely $\rho_{obs} = \sum_{u=1}^{12} a^{su} \rho^u + \phi_L \rho_L$. In the domain of interest for $\rho_{obs}$, $\alpha_L$ decreases from 1 to about 0.2. Li et al. (2014) proposed as an extension to replace the exponent 0.5 over $\phi_L \rho_L$ by an exponent $n$ which can be identified from DDD

simulations. Recently, Monnet (2018) argued that a more relevant expression of the dispersed barrier model in presence of several kinds of defects would be to consider the following quadratic combination of their contribution into the critical resolved shear stress

$$\tau_c^s = \tau_0 + \sqrt{(\mu b)^2 \sum_{u=1}^{12} a^{su}\rho^u + (\alpha_L \mu b_L)^2 \phi_L \rho_L} \tag{3.16}$$

Since dislocations interact with Frank loops, modifications of the dislocation density evolution were proposed. If Eq. (3.14) is adopted, then a natural extension of Eq. (3.9) is

$$\dot{\rho}^s = \frac{\dot{\gamma}^s}{b}\left(\frac{1}{\kappa}\sqrt{\sum_{u=1}^{12} b^{su}\rho^u} + \frac{1}{\kappa}\sqrt{k_{dl}\phi_L\rho_L} - bG_c\rho^s\right) \tag{3.17}$$

where $k_{dl}$ is a weighting factor characterizing intensity of dislocation-dislocation loop interactions. Such an expression can be interpreted as follows. The first term on the right-hand side corresponds to the inverse of the mean free path $L_D$ between dislocations, while the second term can be interpreted as the inverse of the mean free path $L_L$ between Frank loops. Therefore the sum of the two first terms corresponds to an harmonic average of mean free paths between different kinds of defects. On the other hand, if Eq. (3.16) is adopted, then a natural extension of Eq. (3.9) becomes

$$\dot{\rho}^s = \frac{\dot{\gamma}^s}{b}\left(\frac{1}{\kappa}\sqrt{\sum_{u=1}^{12} b^{su}\rho^u + k_{dl}\phi_L\rho_L} - bG_c\rho^s\right) \tag{3.18}$$

A single mean free path is established in Eq. (3.18). Monnet and Mai (2019) argued that forest dislocations and dislocation loops can indeed be considered in the same mean free path, because gliding dislocations need to cut through both kinds of defects. However, the authors also noted that forest and coplanar dislocation interactions are different in nature. Therefore, they proposed to separate both contributions and to introduce a second mean free path weighted by $\kappa_c$ for coplanar dislocation interactions. In addition, they proposed an heuristic dependence of dislocation densities evolutions to grain size in order to account for the dislocation storage at grain boundaries. The evolution equations for dislocation densities is then finally written as

$$\dot{\rho}^s = \frac{\dot{\gamma}^s}{b}\left(\frac{1}{d} + \frac{1}{\kappa}\sqrt{\sum_{u\in\text{forest}} b^{su}\rho^u + k_{dl}\phi_L\rho_L} + \frac{1}{\kappa_c}\sqrt{\sum_{u\in\text{coplanar}(s)} b^{su}\rho^u} - bG_c\rho^s\right) \tag{3.19}$$

$$= \frac{\dot{\gamma}^s}{b}\left(\frac{1}{d} + \frac{1}{L^s} - bG_c\rho^s\right) \tag{3.20}$$

where $L^s$ is the average mean free path for system $s$. However, Eq. (3.20) does not reduce to the conventional evolution equation of dislocations densities when the density of Frank loops vanishes. Note that other authors (Barton et al., 2013; Song et al., 2015) do not account for the influence of Frank loops in the mean free path calculation, thus keeping the original Kocks-Mecking dislocation evolution equation unchanged.

Regarding evolution of dislocation loop densities, geometrical considerations made by Barton et al. (2013) led to the evolution equations used in Monnet and Mai (2019), namely

$$\dot{\rho}_L = -\lambda_L \frac{\phi_L}{b}\rho_L \sum_{s=1}^{12} |\dot{\gamma}^s| \tag{3.21}$$

where $\lambda_L$ is a dimensionless parameter that controls the rate at which dislocation loops are swept out in the wake of gliding dislocations.

#### 3.5.1.2 Extension of the dispersed barrier hardening model

A refinement of the dispersed barrier model was proposed in (Song et al., 2015). Dislocation Frank loops are mainly lying in <111> planes of the FCC lattice. The families or populations of dislocation loops can therefore be described by four scalar fields $\rho_L^k$ corresponding to their respective volumetric density (unit $m^{-3}$) on each <111> plane. Eqs. (3.14) or (3.16) remain unchanged provided that

$$\rho_L = \sum_{k=1}^{4} \rho_L^k \tag{3.22}$$

The main idea behind such a refinement is to have a framework capable of describing the bifurcation from an homogeneous deformation mode towards an heterogeneous deformation mode in which dislocation channeling predominates (Arsenlis et al., 2012). A faster reduction of loop density in a given plane could indeed trigger apparition of a predominant slip system which is known to be correlated to dislocation channel formation (Cui et al., 2018) (see Figure 2.13).

Evolution equations for dislocation Frank loops densities per slip plane were proposed in the literature. A model by Krishna and De (2011); Krishna et al. (2010) suggests that dislocation loop densities evolution equations can be expressed as

$$\dot{\rho}_L^k = -\frac{\phi_L}{b} \left\langle \rho_L^k - \rho_L^{sat} \right\rangle \left( \sum_{s=1}^{12} \rho^s \right) \left( \sum_{s \in \text{coplanar}(k)} A_L^s |\dot{\gamma}^s| \right) \tag{3.23}$$

where $A_L^s$ is the annihilation area defined by $A_L^s = 2 d_L L^s + \pi d_L^2$, with $d_L$ is the standoff distance for dislocation loop annihilation. Eq. (3.23) is to a large extent analogous to Eq. (3.21). Mainly three differences can be noticed. First the annihilation area depends upon the dislocation mean free path $L^s$. Second, a lower bound saturation value $\rho_L^{sat}$ is introduced in order to depict the fact that debris of dislocation loops can remain in the material. Third, only coplanar dislocation glide can contribute to dislocation loop density evolution.

Based on an original formulation by Barton et al. (2013), Song et al. (2015) proposed a tensorial formulation of the dispersed barrier model in which Eq. (3.14) becomes

$$\tau_c^s = \tau_0 + \mu b \sqrt{\sum_{u=1}^{12} a^{su} \rho^u} + \alpha_L \mu b_L \sqrt{\sum_{k=1}^{4} \underset{\sim}{\boldsymbol{G}}_s : \underset{\sim}{\boldsymbol{H}}^k} \tag{3.24}$$

where for slip system $s$ the tensor $\underset{\sim}{\boldsymbol{G}}_s = \underline{\boldsymbol{n}}^s \otimes \underline{\boldsymbol{n}}^s$. Tensor $\underset{\sim}{\boldsymbol{H}}^k$ is a so-called damage descriptor tensor inspired by Barton et al. (2013). It represents the density of dislocation loops belonging to the loop family of habit plane $k$. Double contraction between $\underset{\sim}{\boldsymbol{G}}_s$ and $\underset{\sim}{\boldsymbol{H}}^k$ represents the interaction between a dislocation gliding in slip system $s$ with a dislocation loop in plane $k$. The definition of the damage descriptor is $\underset{\sim}{\boldsymbol{H}}^k = 3\phi_L \rho_L^k \underset{\sim}{\boldsymbol{M}}^k$, with $\underset{\sim}{\boldsymbol{M}}^k = \underset{\sim}{\boldsymbol{1}} - \underline{\boldsymbol{n}}^k \otimes \underline{\boldsymbol{n}}^k$ the tangential projection tensor onto the habit plane $k$. An alternative to Eq. (3.24) would be to consider the quadratic formulation proposed by Monnet (2018) that leads to a similar expression of the critical resolved shear stress as in Eq. (3.16). To complement Eq. (3.24) with evolution laws, Song et al. (2015) proposed the following tensorial evolution equations

$$\dot{\underset{\sim}{\boldsymbol{H}}}^k = -\eta \sum_{s=1}^{N} \left( |\dot{\gamma}^s| \underset{\sim}{\boldsymbol{G}}_s : \underset{\sim}{\boldsymbol{H}}^k \right) . \underset{\sim}{\boldsymbol{M}}^k \tag{3.25}$$

where $\eta$ characterizes the annihilation efficiency similarly to $\lambda_L$ in Eq. (3.21). As in previous formulation, the loop density evolution depends on the intensity of plastic slip through $|\dot{\gamma}^s|$. The fact that the direction of $\dot{\underset{\sim}{\boldsymbol{H}}}^k$ coincide with $\underset{\sim}{\boldsymbol{M}}^k$ reflects the fact that gliding dislocations do not interact with dislocation loops lying in a plane parallel to their gliding plane (Barton et al., 2013; Song et al., 2015).

#### 3.5.1.3 Cascade induced source hardening model

It was noted from DDD simulations that an underestimation of the strengthening resulting from irradiation can occur when only dislocation Frank loops are accounted for (Tanguy et al., 2013). Han (2012) argued that the mechanism of cascade induced source hardening can add up to the dispersed barrier hardening mechanism and explain this discrepancy. The model, originally proposed by Trinkaus et al. (1997a,b), describes the effect of dislocation Frank loops in the same way as a Cottrell atmosphere that pins glissile dislocations. The mechanism of dislocation unpinning then leads to an additional softening, which Han (2012); Tanguy et al. (2013) proposed to model by a phenomenological exponential decrease of the critical resolved shear stress when plastic slip increases. If the form of the dispersed barrier hardening model defined at Eq. (3.14) is used, then its extension by the cascade induced source hardening model leads to the following definition of the critical resolved shear stress

$$\tau_c^s = \tau_0 + \mu b \sqrt{\sum_{u=1}^{12} a^{su}\rho^u} + \alpha_L \mu b_L \sqrt{\phi_L \rho_L} + \tau_a \exp\left(-\frac{|\gamma^s|}{\gamma_0}\right) \tag{3.26}$$

where $\tau_a$ and $\gamma_0$ are material parameters which determine the additional strengthening induced by dislocation pinning and the rate of dislocation unpinning respectively.

### 3.5.2 Proton-irradiation of austenitic stainless steel single crystals

Modeling of irradiation-induced hardening at the single crystal level comes along with an additional set of material parameters. For irradiated austenitic stainless steels identification of these parameters is usually based on fitting experimental tensile curves by performing polycrystal simulations. This task was for example carried out by Han et al. (2013); Hure et al. (2016); Monnet and Mai (2019). In line with the motivations of this chapter, performing mechanical tests on irradiated stainless steel single crystals would be of great interest in order to validate or amend the sets of material parameters available in the literature. In order to be able to carry out such tests in a near future, the preliminary task of performing irradiation of austenitic stainless steel single crystals was achieved. For the purpose of keeping track of this work the irradiation experiment is described below.

#### 3.5.2.1 Material

The same austenitic stainless steel single crystal plate used for the tensile tests on virgin material described above was used for irradiation. As depicted in Appendix A, a 20×18×0.9 mm slab was cut with an electron discharge machine with a brass wire of diameter 100 µm. In the context of this experiment, the main limitation for the slab geometry was the size of the sample holder which was used for irradiation. Of course, this geometry needed also to be compatible with available material and prospective tensile specimen geometry compatible with the tensile machine. Pictures of the sample holder and of the slab mounted onto the sample holder are shown in Figure 3.13. One face of the slab was mirror polished and a final polishing step with a colloidal silica suspension was performed in order to remove the polishing-induced hardened layer. Note that white spots visible on the specimen surface in Figure 3.13 do not correspond to scratches, but are in fact caused by ferrite inclusions.

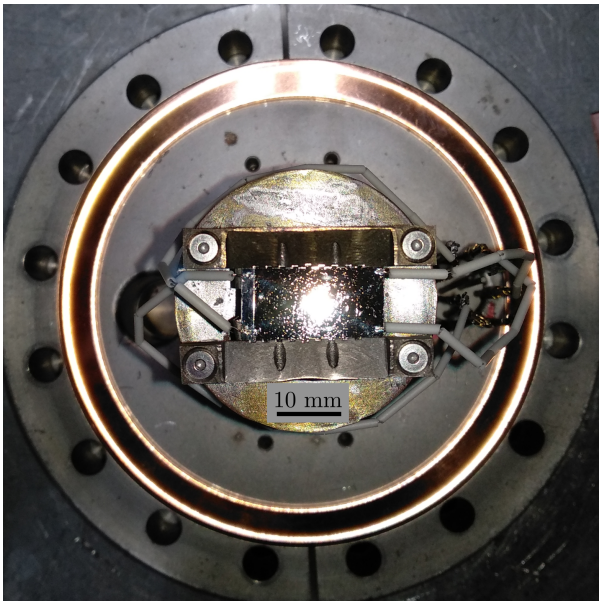


Figure 3.13 Austenitic single crystal slab mounted onto the irradiation sample holder viewed from above. Four thermocouples were welded in two corners of the slab (right) and a separate plate contiguous to the plate (left). Bright spots on the slab surface are caused by ferrite inclusions.

#### 3.5.2.2 Irradiation facility and conditions

Proton irradiation of the single crystal plate was performed at the Michigan Ion Beam Laboratory (MIBL). The Wolverine Beamline ♯2 was used to accelerate protons up to an energy of 3.0 MeV. During irradiation temperature can rise because of the high energy particles impacts. In order to prevent such heating of the plate an indium layer is placed on its bottom face (contact between the plate and the sample holder). The indium layer becomes liquid above 156 °C and thus allows to efficiently draw out the excess of heat from the material. During the experiment the temperature of the target was kept at 350 °C within a ±10 °C range. This temperature was chosen on the basis of the equivalence between neutron and proton irradiation induced defect populations by Gan and Was (2001). As shown in Figure 2.7 and 2.8a, the authors attested that proton irradiations at 360 °C yielded similar dislocation Frank loop sizes and densities as neutron irradiations at 275 °C in 304 and 316 grade stainless steels. Such irradiation conditions are relevant for LWR conditions. Temperature monitoring was made by infrared thermography during irradiation. Before irradiation, calibration of thermal imaging was performed by measuring temperature through four thermocouples welded on the specimen surface and on a separate plate contiguous to the specimen as shown in Figure 3.13. The separate plate was used in order to avoid wasting expensive single crystal material which could have been damaged by the welding process. The pressure inside the irradiation chamber was kept constant below $10^{-7}$ torr, or equivalently $1.3 \times 10^{-5}$ Pa which corresponds to an advanced secondary vaccuum. An average total current of ∼32 µA was measured during the whole 90 h long irradiation process. The experiment resulted in a total integrated fluence of $3.5 \times 10^{19}$ ions/cm$^2$ on an irradiated area covering 18×10 mm$^2$. In order to cover the whole area a rastering technique was used. The rastering method was preferred over defocusing because it was shown to produce more homogeneous distributions of defects when using protons as irradiation particles in previous studies. Irradiation conditions are summarized in Table 3.4.

#### 3.5.2.3 Results

As noted above and in Table 3.4, the irradiation experiment resulted in an integrated fluence of $3.5 \times 10^{19}$ ions/cm$^2$. However this figure does not provide precise information on the distribution

Table 3.4 Proton irradiation conditions in MIBL's Wolverine Beamline ♯2.

| Ions | Energy | Temp. | Stage pressure | Current | Beam hours | Fluence |
|---|---|---|---|---|---|---|
| $H^+$ | 3.0 MeV | 350 °C | $1.3 \times 10^{-5}$ Pa | 32 µA | 90 h | $3.5 \times 10^{19}$ ions/cm$^2$ |

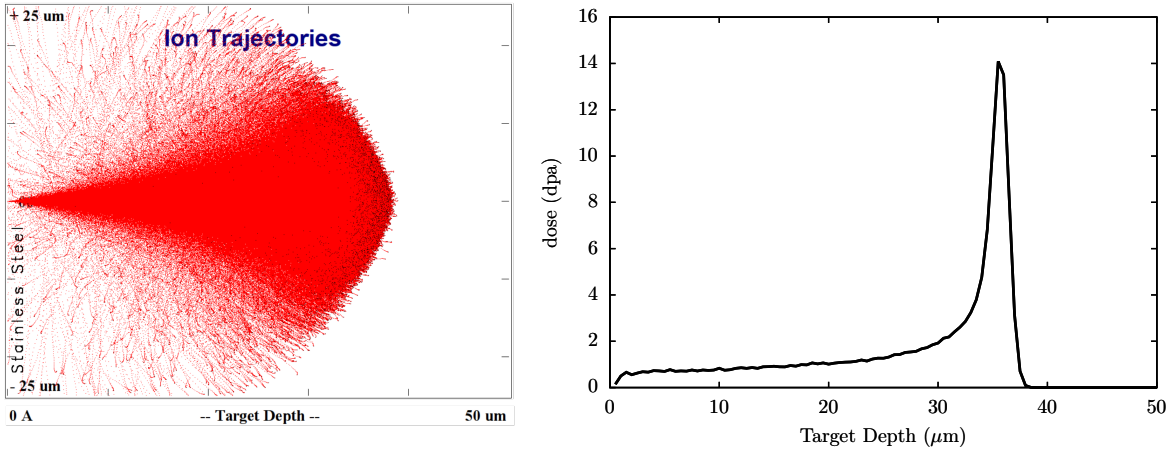


(a) (b)

Figure 3.14 (a) Cross-section of hydrogen ions trajectories in stainless steel for 3.0 MeV incident energy. (b) Dose profile across the depth of the irradiated stainless steel specimen.

of defects generated in the material. The latter depends also on the beam energy, 3.0 MeV, and the composition of the material in Table 3.1. Nevertheless the distribution which results from these parameters can be simulated with the software SRIM (Ziegler et al., 2010). The result of the SRIM simulation of the hydrogen beam interaction with stainless steel is presented in Figure 3.14a. The beam hits perpendicularly the specimen surface at the origin on the horizontal axis. Hydrogen ions can then be deviated from their initially horizontal direction. Individual ions paths are depicted by red dots. It can be seen that the majority of ions trajectories are contained in a cone which revolution axis coincides with the incident direction of the beam. Furthermore it can be noted that, with the incident energy considered and the thickness of the sample, all ions are stopped within the material. With the parameters of the irradiation experiment, hydrogen ions were simulated to not travel deeper than 38 µm in the specimen. As a consequence irradiation-induced defects cannot be expected to exist deeper than the surface layer of 38 µm. In order to characterize the distribution of damage induced across the irradiated layer, the dose profile in displacements per atom (dpa) is plotted in Figure 3.14b. Displacements per atom are calculated by summing vacancies created by incident ions and vacancies created by recoils. SRIM output quantities are expressed in vacancies/Å/ion and can thus be converted into dpa by multiplying them to the integrated fluence and dividing the result by the atomic density of the material. The profile displays mainly three distinct regions. Between 0 and 30 µm depth the dose increases with depth with a relatively low gradient of ∼0.04 dpa/µm. In this region irradiation dose can therefore be reasonably considered as constant and equal to ∼1 dpa. In the range 25-38 µm depth the dose increases dramatically and then plummets down to almost zero. A maximum of more than 14 dpa is reached at a depth of ∼35 µm. Above 38 µm depth irradiation dose can be considered as negligible since hydrogen ions never reach that far in the material.

One possible consequence of irradiation by energetic particles is the radioactive activation of the target. Such an activation depends upon the incident energy of the ion beam and on the cross

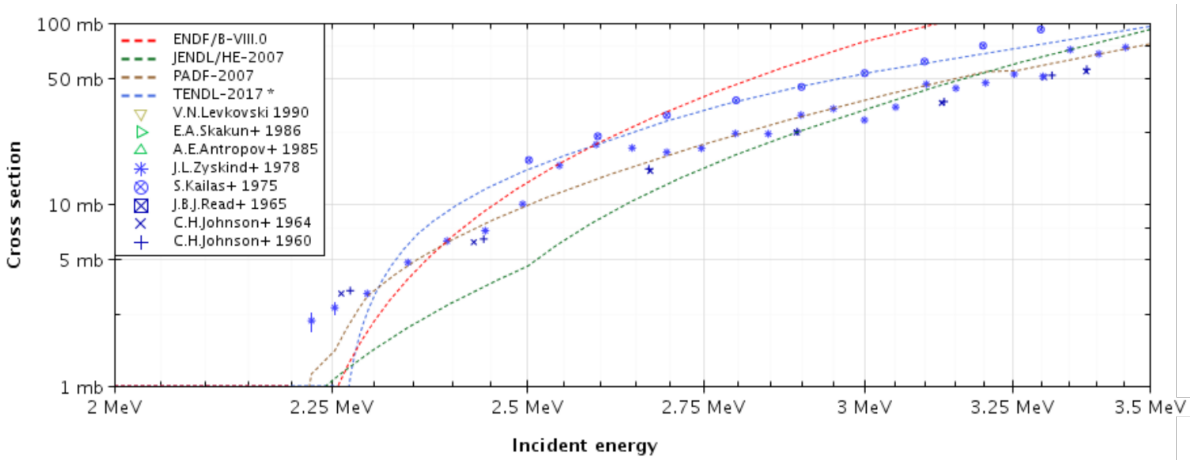


Figure 3.15 Evolution of the cross sectional area of $^{54}$Cr with the incident energy of hydrogen ions.

sectional area of the incident particle interaction with the chemical elements which composes the target. The cross section, expressed in barns[1], is a measure of probability that a specific process will take place in a collision of two particles. In the present experiment, incident ions are hydrogen ions and target elements are the main constituents of stainless steel listed in Table 3.1. Many interactions between incident protons and isotopes of elements present in steel can produce radioactive elements. Most of these products have very short half-lifes (a few seconds or less). However, $^{54}$Mn which can be formed in the interaction between a proton and $^{54}$Cr or $^{57}$Fe has a half-life of $T_{1/2} = 312.19$ days. Therefore if the energy of incident protons is sufficient for this interactions to take place, the irradiated target can become radioactive. Simulations and experimental data of the evolution of the cross section between hydrogen ions and $^{54}$Cr with respect to the incident energy are plotted in Figure 3.15. It can be observed that the cross section, *i.e.* the probability of an interaction, increases by two orders of magnitudes for incident energies between 2.25 and 3.5 MeV. Since our irradiation experiment was conducted with an incident energy of 3.0 MeV this interaction is likely to occur and therefore presence of $^{54}$Mn, which is a by-product of the interaction, can be expected. As a consequence the radioactive decay of the irradiated sample is expected to follow in the best case scenario an exponential decay with the half-life of $^{54}$Mn. The measured decay of the sample is plotted in Figure 3.16 against the exponential decay which would result from $^{54}$Mn. The correspondence between the measured decay and the exponential decay of $^{54}$Mn confirms that $^{54}$Mn is responsible for the radioactive activity of the sample.

[1] 1 barn = $10^{-28}$ m$^{-2}$

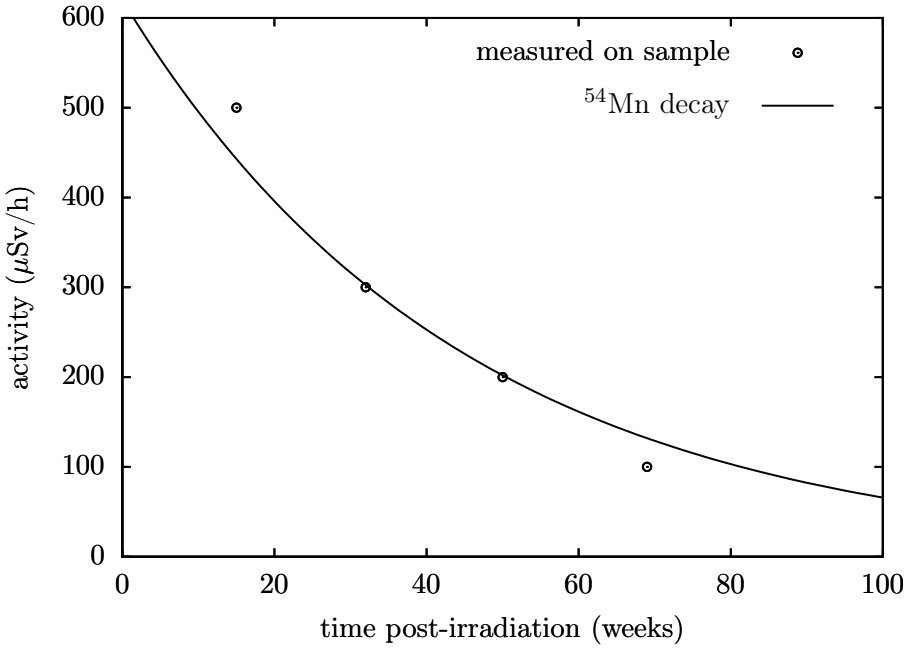


Figure 3.16 Activity decay as measured on proton-irradiated sample compared to exponential decay of radioactive $^{54}$Mn isotope.

## 3.6 Conclusions

The outcomes of this chapter can be summarized as follows.

- An experimental protocol was established in order to carry out tensile tests on 316L austenitic stainless steel single crystals. EBSD maps of the specimen surface were carried out in order to characterize the misorientation with the orientation announced by the supplier. Temperature monitoring was shown to be achievable by controlling only the temperature of the heating unit. A DIC setup based on optical acquisition of paint speckle pattern deposited on specimen surface turned up to be the most practicable solution to measure displacements fields.

- Tensile experiments were performed in two different directions of the FCC stainless steel single crystal. The DIC measured displacements fields were post-processed in order to compute a scalar Hencky equivalent plastic strain field. Persistent heterogeneities of strain could be observed for both orientations. These heterogeneities are materialized by mainly two groups of thin bands which are parallel to one another for each crystal orientation tested. The orientations of the bands with respect to the tensile direction were shown to correspond to the most favorable slip systems traces according to Schmid's law. At a smaller scale, electron microscopy revealed that each band was in fact composed of bundles of slip lines.

- Force measurements showed the significant discrepancy in terms of hardening that is due to the crystal anisotropy. The <111> orientation displayed the highest yield strength and the greatest strain-hardening slope as compared to the <110> orientation. In both cases almost linear hardening curves were obtained with a satisfying repeatability.

- Experimental stress-strain curves were compared to finite element simulations with a crystal plasticity constitutive behaviour. Material parameters available in the literature were shown to give unsatisfying predictions of the hardening behaviour. Therefore, an identification of material parameters was proposed in order to obtain a better agreement between experimental data and numerical results. The equivalent strain fields obtained numerically

agree well, in an average sense, with DIC measurements. However heterogeneities of strain were not predicted with the crystal plasticity model used. Possible roots of experimentally measured strain heterogeneities are for instance material properties heterogeneities or geometrical imperfections, both of which were not accounted for in the simulations.

- A review of available crystal plasticity hardening models accounting for irradiation-induced dislocation Frank loops was proposed. Several formulations of the dispersed barrier hardening model are available in the literature. The key ingredients to these are the addition of one or several internal variables characterizing the density of dislocation Frank loops. As obstacles to dislocations' motion, dislocation loops participate to the critical resolved shear stress and possibly to the mean free path of gliding dislocations. As internal variables, dislocation loop densities are assigned evolution laws which in essence describe how they can be annihilated by gliding dislocations.

- A synthesis of the proton-irradiation experiment on a 316L single crystal carried out at MIBL was made. Irradiation conditions were chosen in order to produce a microstructure of defects comparable to what could be seen in LWR conditions for a dose of 1 dpa. A future study will focus on performing mechanical tests on the irradiated layer in order to be able to validate or amend sets of material parameters proposed in the literature for the dispersed barrier hardening crystal plasticity model.

*One shall sleep well only if a simulation is running.*

S. F.

# 4

# Strain gradient crystal plasticity with evolving length scale

This chapter was published in the European Journal of Mechanics - A/Solids as:
Scherer, J. M., Besson, J., Forest, S., Hure, J., & Tanguy, B. (2019). Strain gradient crystal plasticity with evolving length scale: Application to voided irradiated materials. European Journal of Mechanics-A/Solids, 77, 103768.

## Résumé

Un modèle de plasticité cristalline micromorphe basé sur un formalisme en grandes transformations est utilisé pour simuler la localisation de la déformation plastique au sein d'une bande de glissement. L'exemple d'un monocristal possédant un unique système de glissement et soumis à chargement de cisaillement simple est étudié dans un premier temps. Des solutions analytiques sont obtenues pour le glissement simple dans le cas d'un écrouissage positif, nul et négatif. L'écrouissage négatif linéaire, c'est-à-dire l'adoucissement linéaire, entraîne une largeur de bande de localisation constante, tandis que l'adoucissement non linéaire avec saturation entraîne une largeur de bande croissante. Un tel comportement adoucissant avec saturation est parfois rencontré dans les aciers irradiés. Une amélioration du modèle est donc proposée afin de maintenir une largeur de bande de localisation limitée lorsque l'on envisage un comportement comportant un adoucissement exponentiel. Des solutions analytiques approchées sont utilisées pour valider les résultats obtenus par éléments finis dans le cas du cisaillement simple. Le modèle étendu de plasticité cristalline micromorphe est ensuite appliqué pour prédire l'interaction entre bandes de glissement localisées et cavités pouvant par exemple être rencontrées dans les matériaux irradiés poreux exhibant pour certains un comportement adoucissant. Pour cela, des cellules unitaires poreuses périodiques à cavités cylindriques sont sollicitées en cisaillement simple. Les résultats des simulations montrent un accord qualitativement satisfaisant entre les prédictions numériques et les observations expérimentales vis-à-vis de la forme et de l'orientation des cavités.

## Contents

## 4.1 Introduction

Strain localization is commonly encountered in experiments involving a wide range of materials at scales spanning over multiple orders of magnitude and are referred to as necking, shear bands, Lüders bands, Portevin-Le Chatelier effect. The pioneering works of Considère (1885); Hadamard (1903); Hill (1962); Mandel (1966); Rice (1976); Thomas (1961) set the general framework for predicting strain localization as a result of a mechanical instability involving either geometric or material imperfections. In metals, a material-based instability may for example originate from a porosity growth induced softening behaviour leading to shear-banding, while necking in a tensile test is an example of a geometry-based instability (Audoly and Hutchinson, 2019; Hart, 1967). In single crystals slip bands and kink bands described in (Gilman, 1954; Jaoul, (1965, 2008); Neuhäuser, 1988) are common occurrences of material induced strain localization phenomena. Characteristic length scales arise naturally in strain localization phenomena observed in experiments, but conventional material models are however size-independent and therefore cannot provide satisfying predictions for strain localization. In addition when aiming at modeling softening mechanisms, numerical simulations using conventional theories display spurious mesh dependent dissipated energy due to the loss of ellipticity of the underlying partial differential equations (see e.g. Bažant et al. (1984); Germain et al. (2007); Lorentz and Benallal (2005)). As a remedy, regularization methods such as Cosserat, integral and gradient models (see (Forest, 2005) and references quoted therein) have been developed extensively in the past few decades also motivated by size effects observed in experiments. In particular, observations suggest that some size effects in metals are related to Geometrically Necessary Dislocations (GND) (Fleck and Hutchinson, 1997; Stelmashenko et al., 1993). Hence strain gradient plasticity (SGP) theories have been extended to frameworks suited to (sub-)crystalline scales, as for instance continuum crystal plasticity ((Bardella, 2006; Cordero et al., 2010; Fleck and Hutchinson, 1997; Forest et al., 2000; Niordson and Kysar, 2014) and references quoted therein).

For metallic single crystals strain localization induced by material softening generally results in the formation of slip bands. These thin bands are parallel to the primary slip plane and their thickness is directly related to the defect density and softening mechanism involved. In contrast, kink bands are localization zones of finite thickness that are perpendicular to the slip direction. Kink bands are known to occur when strain incompatibility arises and if not enough slip systems are available. Asaro and Rice (1977) have performed a bifurcation analysis of plastic slip localization for crystals undergoing single slip. Their theoretical analysis shows that slip and kink bands are equally probable single slip localization modes in that conditions. Asaro and Rice's bifurcation analysis is based on standard crystal plasticity. More advanced crystal plasticity models incorporate the dislocation density tensor as a hardening variable in addition to scalar dislocation densities (statistically stored dislocations) (Gurtin, 2002; Wulfinghoff et al., 2015). Dislocation pile-ups are known to induce a back-stress and associated kinematic hardening (Cordero et al., 2010; Forest, 2008; Steinmann and Stein, 1996). As a result localization in kink bands can be superseded by slip bands that do not induce any lattice curvature as proved by the bifurcation analysis in (Forest, 1998). Strain gradient plasticity introduces length scales in the continuum models and can therefore provide physically-relevant regularization properties. It appears that strain gradient plasticity regularizes kink bands, meaning that simulated kink bands have a finite thickness (Forest et al., 2001). In contrast the finite element simulation of slip bands is mesh–dependent (they are one element (in fact one Gauss point) thick) because they can develop in the absence of accumulation of GND. The recent simplified strain gradient plasticity model developed by Ling et al. (2018), following the approach from Wulfinghoff et al. (2013); Wulfinghoff and Böhlke (2012), displays the unique feature of regularizing both slip and kink bands. This is because it involves the full gradient of an accumulated slip variable instead of the dislocation density tensor or individual GND densities. This model is acknowledged to be too crude to control independently the intensity of slip and kink bands. The regularization effect on slip bands is of phenomenological nature, it has no precise physical background in contrast to kink bands which are controlled by the formation of polarized dislocation walls represented by

GND densities. It is a necessary feature for a model to be used in mesh–objective finite element simulations of slip banding in crystals.

Although it is of particular importance when investigating flow localization, only a few works mention the evolution of the length scale during straining and how it is linked to the hardening/softening behaviour. In an early work Zbib and Aifantis (1988) highlighted the slip band narrowing arising when considering a parabolic hardening/softening behaviour in a strain gradient framework. In the different but closely related context of non-local damage models, Geers et al. (1998); Simone et al. (2004) evidenced spurious spreading of damage over continuously wider regions. Recently Poh and Sun (2017) and Vandoren and Simone (2018) proposed to use a damage-dependent length scale respectively in micromorphic and integral non-local damage models to address this unwanted phenomenon. Dislocations motion mechanisms motivated Forest and Sedláček (2003) to propose evolving length scales depending on the dislocation density. Dahlberg and Boasen (2019) provided a strain gradient framework incorporating an evolution law for the constitutive length scale parameter which is also physically based and directly related to the dislocation density. Evolving length scales are also present in the newly developed SGP model by Petryk and Stupkiewicz (2016). Also, to the authors' knowledge, the case of saturating softening behaviour has received little attention in the literature. This is particularly important when aiming at simulating ductile failure at large local strains of materials exhibiting softening. It will be shown in the present work that the saturated regime in most existing SGP models leads to unwanted broadening of the localization zone. This feature will be analyzed and a remedy will be proposed.

One example of intense flow localization is the mechanism of dislocation channel deformation (DCD). It consists in a highly heterogeneous deformation mode at the grain scale. Abundant observations of this deformation mode have been made in quenched (Bapna et al., 1968; Mori and Meshii, 1969; Wechsler, 1973), predeformed (Luft et al., 1975) and irradiated (Farrell et al., 2003; Fish et al., 1973; Gussev et al., 2015; Jiao and Was, 2010; Smidt Jr, 1970b; Tucker et al., 1969; Wechsler, 1973) metals. Such channels initiate when the first moving dislocations are clearing a path of isolated sessile obstacles, for example Frank dislocation loops, leading to a reduced defect density inside channels. They are also called clear bands due to their contrast in electron microscopy (Lee et al., 2001). The induced softening along that path is the precursor to flow localization. It has been shown experimentally in (Farrell et al., 2003) and numerically in (Arsenlis et al., 2012; Barton et al., 2013; Cui et al., 2018) that deformation localization in irradiated steels is simultaneously accompanied by a loss of dislocation interactions and activation of fewer slip systems. The thickness of dislocation channels is typically measured in a 10 nm to 100 nm range in irradiated materials (Farrell et al., 2003). Dislocation channels are known to have a strong influence on macroscopic mechanical properties of nuclear materials. Dislocation channels may indeed interact with grain boundaries and favor the mechanism of Irradiation Assisted Stress Corrosion Cracking (IASSC) (McMurtrey et al., 2011). Moreover the Transmission Electron Microscope (TEM) observations of deformed radiation-damaged stainless steels in Figures 4.1a and 4.1b suggest that dislocation channels may also interact with other irradiation induced defects such as nanometric voids or bubbles. Elongated voids inside channels indicate possible large local strains.

In this study a reduced finite strain micromorphic single crystal plasticity model is used to describe slip band localization in single crystals. The novelty of the approach lies first in the analytical derivation of closed form solutions obtained from a micromorphic crystal plasticity theory in case of single slip associated to linear hardening and softening behaviours. It is demonstrated that this kind of model predicts an increasing and unbounded localization slip band width when a saturation of softening is reached. Second, an enhanced micromorphic crystal plasticity model, involving an evolving length scale, is then proposed that predicts a bounded localization slip band width for realistic saturating softening behaviours. Finally, the enhanced model is applied to study the interaction between localization slip bands and voids that may exist or nucleate in irradiated materials. For that purpose a 2D plane strain periodic

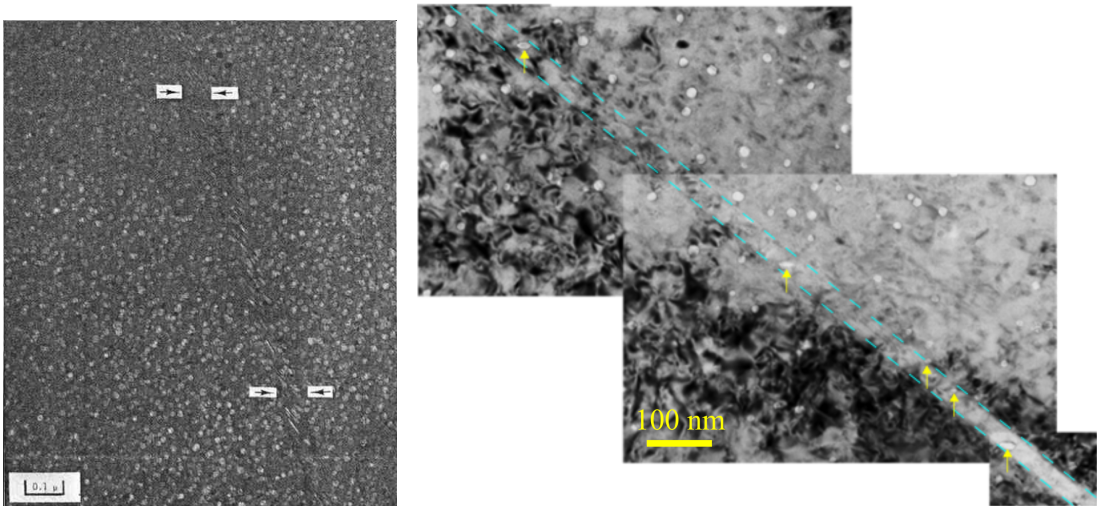


(a) (b)

Figure 4.1 (a) Dislocation channeling observed by TEM in a highly irradiated ($7.5 \times 10^{22}$ n/cm$^2$, $E > 0.1$ MeV) deformed tension specimen tested (stainless steel 316) at 370 °C (reproduced from (Fish et al., 1973)) displaying peanut-like void shapes (b) Deformed neutron irradiated stainless steel 316 at 340 °C displaying sheared and elongated irradiation voids (pointed out with yellow arrows) inside a dislocation channel (bounded by cyan dashed lines) (reproduced from (Renault-Laborne et al., 2018)).

porous unit-cell containing one void is loaded in simple shear with the shearing direction parallel to the single slip direction. A simple exponential softening behaviour is used in order to model softening due to irradiation defects clearing by the DCD mechanism. The relative influence on localization of the intrinsic length scale of the micromorphic crystal plasticity model and of the void size and effective void volume fraction inside the localization slip band are assessed.

The paper is outlined as follows. In Section 4.2 the main features of the micromorphic crystal plasticity model are presented and analytical reference solutions for single crystals under simple shear are derived, assuming single slip and linear hardening behaviour. An analytical solution for linear softening is established showing constant slip band width. An enhanced model is then proposed in order to keep a bounded localization slip band width for non-linear softening behaviour in Section 4.3. In Section 4.2 and 4.3, numerical solutions are compared to the analytical solutions. Finite element predictions of void / localization band interactions are presented and discussed in Section 4.4 for 2D plane strain periodic porous unit-cells. Concluding remarks follow in Section 4.5.

## 4.2 Simple shear in the cases of linear hardening and perfect plasticity

The model used in the next sections is taken from (Ling et al., 2018) and synoptically recalled hereafter. It is based on initial formulations by Erdle and Böhlke (2017); Wulfinghoff and Böhlke (2012) and finite deformation extensions from (Forest, 2016b). Underline $\underline{A}$ and under-wave bold $\underset{\sim}{\boldsymbol{A}}$ symbols refer to vectors and second-order tensors, respectively. Scalar product, outer product, double contraction and tensorial product are respectively written $\underline{\boldsymbol{A}}.\underline{\boldsymbol{B}}$, $\underline{\boldsymbol{A}} \wedge \underline{\boldsymbol{B}}$, $\underset{\sim}{\boldsymbol{A}} : \underset{\sim}{\boldsymbol{B}}$ and $\underline{\boldsymbol{A}} \otimes \underline{\boldsymbol{B}}$. Transposition, inversion, inversion followed by transposition and time derivation are respectively written $\underset{\sim}{\boldsymbol{A}}^T$, $\underset{\sim}{\boldsymbol{A}}^{-1}$, $\underset{\sim}{\boldsymbol{A}}^{-T}$, $\dot{\underset{\sim}{\boldsymbol{A}}}$.

### 4.2.1 A reduced micromorphic single crystal plasticity model at finite deformations

Let us consider a crystalline continuum for which each material point can uniquely be defined by a position vector $\underline{\boldsymbol{X}}$ in the reference configuration $D_0$ and a position vector $\underline{\boldsymbol{x}}$ in the current configuration $D$. Following the micromorphic approach of (Forest, 2016b; Germain, 1973), at time $t$, the degrees of freedom (DOF) of the material point are described by the field of displacement vector $\underline{\boldsymbol{u}}\,(\underline{\boldsymbol{X}}\,,t)$ and an additional microslip scalar field $\gamma_\chi(\underline{\boldsymbol{X}}\,,t)$. This additional field of degrees of freedom $\gamma_\chi$, which comes in addition to usual constitutive internal variables, is introduced to refine the kinematical description at a given material point $\underline{\boldsymbol{X}}$

$$\text{DOF} = \{\underline{\boldsymbol{u}}\,, \gamma_\chi\} \tag{4.1}$$

In the present work, the micromorphic variable $\gamma_\chi$ is akin to a cumulative plastic slip variable within the micromorphic approach (Forest, 2016b). It will serve as an auxiliary variable for a convenient numerical implementation of strain gradient plasticity.

The Lagrangian gradients of the degrees of freedom are

$$\underset{\sim}{\boldsymbol{H}}(\underline{\boldsymbol{x}}\,,t) = \frac{\partial \underline{\boldsymbol{u}}}{\partial \underline{\boldsymbol{X}}} = \text{Grad}\,\underline{\boldsymbol{u}} \tag{4.2}$$

$$\underline{\boldsymbol{K}}\,(\underline{\boldsymbol{x}}\,,t) = \frac{\partial \gamma_\chi}{\partial \underline{\boldsymbol{X}}} = \text{Grad}\,\gamma_\chi \tag{4.3}$$

where the displacement gradient $\underset{\sim}{\boldsymbol{H}}$ is directly related to the deformation gradient $\underset{\sim}{\boldsymbol{F}}$ by $\underset{\sim}{\boldsymbol{F}} = \underset{\sim}{\boldsymbol{1}} + \underset{\sim}{\boldsymbol{H}}$, and $\underline{\boldsymbol{K}}$ is referred to as the microslip gradient vector. The following stresses are introduced

$$\underset{\sim}{\boldsymbol{S}} = \frac{\rho_0}{\rho}\underset{\sim}{\boldsymbol{\sigma}}.\underset{\sim}{\boldsymbol{F}}^{-T} \tag{4.4}$$

$$\underline{\boldsymbol{M}} = \frac{\rho_0}{\rho}\underset{\sim}{\boldsymbol{F}}^{-1}.\underline{\boldsymbol{m}} \tag{4.5}$$

$$S = \frac{\rho_0}{\rho}s \tag{4.6}$$

where $\underset{\sim}{\boldsymbol{S}}$ is the Boussinesq (or first Piola-Kirchhoff) stress tensor which generates mechanical power with $\dot{\underset{\sim}{\boldsymbol{F}}}$ and $\underset{\sim}{\boldsymbol{\sigma}}$ the Cauchy stress tensor which generates power with $\dot{\underset{\sim}{\boldsymbol{F}}}.\underset{\sim}{\boldsymbol{F}}^{-1}$. The vectors $\underline{\boldsymbol{M}}$ and $\underline{\boldsymbol{m}}$ are generalized stresses with respect to the reference and current configuration, respectively. They are respectively conjugate to $\dot{\underline{\boldsymbol{K}}}$ and $\dot{\underline{\boldsymbol{K}}}\,.\underset{\sim}{\boldsymbol{F}}^{-1}$ in the power of internal forces, see (Ling et al., 2018). Similarly, $S$ and $s$ are generalized stresses in the reference and current configurations which generate power with $\dot{\gamma}_\chi$. The balance laws for momentum and generalized momentum take the form

$$\text{Div}\,\underset{\sim}{\boldsymbol{S}} = \underline{\boldsymbol{0}}\,, \quad \forall \underline{\boldsymbol{X}} \in D_0 \tag{4.7}$$

$$\text{Div}\,\underline{\boldsymbol{M}} - S = 0, \quad \forall \underline{\boldsymbol{X}} \in D_0 \tag{4.8}$$

where $D_0$ is the reference configuration of the body. The associated boundary conditions read

$$\underline{\boldsymbol{T}} = \underset{\sim}{\boldsymbol{S}}.\underline{\boldsymbol{n}}_0, \quad \forall \underline{\boldsymbol{X}} \in \partial D_0 \tag{4.9}$$

$$M = \underline{\boldsymbol{M}}\,.\underline{\boldsymbol{n}}_0, \quad \forall \underline{\boldsymbol{X}} \in \partial D_0 \tag{4.10}$$

where $\underline{\boldsymbol{T}}$ is the surface traction vector which generates power over $\dot{\underline{\boldsymbol{u}}}$. $M$ is the generalized surface traction which generates power over $\dot{\gamma}_\chi$. Vector $\underline{\boldsymbol{n}}_0$ is the outward unit normal to the surface element of the boundary $\partial D_0$ of the body. The multiplicative decomposition of the

deformation gradient $\underset{\sim}{\boldsymbol{F}}$ is adopted

$$\underset{\sim}{\boldsymbol{F}} = \underset{\sim}{\boldsymbol{E}}.\underset{\sim}{\boldsymbol{P}} \tag{4.11}$$

where $\underset{\sim}{\boldsymbol{E}}$ denotes its elastic part and $\underset{\sim}{\boldsymbol{P}}$ its plastic part. The local intermediate configuration $C_\sharp$ consists in the transport of the local reference configuration by the tensor $\underset{\sim}{\boldsymbol{P}}$. The local current configuration $C$ consists in the transport of the reference configuration $C_0$ by $\underset{\sim}{\boldsymbol{F}}$, or equivalently the transport of $C_\sharp$ by $\underset{\sim}{\boldsymbol{E}}$. $\gamma^s$ is the plastic slip on a system $s$ defined by its Schmid tensor $\underset{\sim}{\boldsymbol{N}}^s = \underline{\boldsymbol{m}}^s \otimes \underline{\boldsymbol{n}}^s$ where $\underline{\boldsymbol{n}}^s$ is the normal to the slip plane and $\underline{\boldsymbol{m}}^s$ the slip direction. $\underset{\sim}{\boldsymbol{P}}$ is related to the plastic slips by

$$\dot{\underset{\sim}{\boldsymbol{P}}}.\underset{\sim}{\boldsymbol{P}}^{-1} = \sum_{s=1}^{N} \dot{\gamma}^s \underset{\sim}{\boldsymbol{N}}^s \tag{4.12}$$

where $N$ is the total number of slip systems. The elastic Green-Lagrange strain measure $\underset{\sim}{\boldsymbol{E}}^e_{GL}$ is introduced as

$$\underset{\sim}{\boldsymbol{E}}^e_{GL} = \frac{1}{2}\left(\underset{\sim}{\boldsymbol{E}}^T.\underset{\sim}{\boldsymbol{E}} - \underset{\approx}{\mathbf{1}}\right) \tag{4.13}$$

A plastic accumulated slip measure $\gamma_{cum}$ is now defined as

$$\gamma_{cum} = \int_0^t \sum_{s=1}^{N} |\dot{\gamma}^s| \, \mathrm{d}t \tag{4.14}$$

The relative plastic slip $e$ quantifies the difference between accumulated plastic slip and microslip with

$$e(\underline{\boldsymbol{X}}, t) = \gamma_{cum} - \gamma_\chi \tag{4.15}$$

$\gamma_\chi$ is the micromorphic counterpart of $\gamma_{cum}$, they have identical physical interpretation.
A free energy density function $\psi$ is chosen in the form

$$\rho\psi(\underset{\sim}{\boldsymbol{E}}^e_{GL}, e, \underline{\boldsymbol{K}}, \gamma_{cum}) = \frac{1}{2}\frac{\rho}{\rho_\sharp}\underset{\sim}{\boldsymbol{E}}^e_{GL} : \underset{\approx}{\boldsymbol{C}} : \underset{\sim}{\boldsymbol{E}}^e_{GL} + \frac{1}{2}\frac{\rho}{\rho_0} H_\chi e^2 \tag{4.16}$$

$$+ \frac{1}{2}\frac{\rho}{\rho_0} A \underline{\boldsymbol{K}}^T.\underline{\boldsymbol{K}} + \rho\psi_h(\gamma_{cum}) \tag{4.17}$$

$\underset{\approx}{\boldsymbol{C}}$ is the fourth rank tensor of elastic moduli, $H_\chi$ a penalty modulus, $A$ a higher order modulus and $\rho_0$, $\rho_\sharp$ and $\rho$ are volumetric mass densities in the reference, intermediate and final local configuration respectively. The function $\psi_h(\gamma_{cum})$ is a hardening potential which will take various forms in the following sections. For simplicity a quadratic and isotropic form was assumed for the gradient $\underline{\boldsymbol{K}}$ contribution in the free energy potential, leading to a single higher order modulus $A$. If the penalty modulus $H_\chi$ is large enough, the variable $\gamma_\chi$ is almost equal to $\gamma_{cum}$. In that case, the gradient $\underline{\boldsymbol{K}}$ of $\gamma_\chi$ does not significantly differ from the gradient of the accumulated slip variable $\gamma_{cum}$. In the following sections the following approximation will be used

$$\gamma_\chi \simeq \gamma_{cum}, \quad \frac{\partial\gamma_\chi}{\partial\underline{\boldsymbol{X}}} \simeq \frac{\partial\gamma_{cum}}{\partial\underline{\boldsymbol{X}}}, \quad \frac{\partial^2\gamma_\chi}{\partial\underline{\boldsymbol{X}}^2} \simeq \frac{\partial^2\gamma_{cum}}{\partial\underline{\boldsymbol{X}}^2} \tag{4.18}$$

When the penalty modulus $H_\chi$ takes a high enough value, $\gamma_\chi$ is almost equal to $\gamma_{cum}$. The micromorphic model then reduces to a SGP model (Forest, 2009). The following state laws are postulated, identically fulfilling the second law of thermodynamics

$$\underset{\sim}{\boldsymbol{\Pi}}^e = \underset{\approx}{\boldsymbol{C}} : \underset{\sim}{\boldsymbol{E}}^e_{GL} \tag{4.19}$$

$$S = -H_\chi e \tag{4.20}$$

$$\underline{\boldsymbol{M}} = A\underline{\boldsymbol{K}} \tag{4.21}$$

where the Piola (or second Piola-Kirchhoff) stress tensor $\underset{\sim}{\boldsymbol{\Pi}}^e$ is defined with respect to the intermediate configuration $C_\sharp$ by $\underset{\sim}{\boldsymbol{\Pi}}^e = \frac{\rho_\sharp}{\rho}\underset{\sim}{\boldsymbol{E}}^{-1}.\underset{\sim}{\boldsymbol{\sigma}}.\underset{\sim}{\boldsymbol{E}}^{-T} = \frac{\rho_\sharp}{\rho_0}\underset{\sim}{\boldsymbol{E}}^{-1}.\underset{\sim}{\boldsymbol{S}}.\underset{\sim}{\boldsymbol{P}}^T$. The Mandel stress $\underset{\sim}{\boldsymbol{\Pi}}^M$ is introduced with respect to the intermediate configuration by $\underset{\sim}{\boldsymbol{\Pi}}^M = \underset{\sim}{\boldsymbol{E}}^T.\underset{\sim}{\boldsymbol{E}}.\underset{\sim}{\boldsymbol{\Pi}}^e$, in order to compute the resolved shear stress $\tau^s$ by $\tau^s = \underset{\sim}{\boldsymbol{\Pi}}^M : \underset{\sim}{\boldsymbol{N}}^s$. In contrast to strict strain gradient plasticity, the higher order micromorphic stresses are uniquely defined in the elastic part of the structure. Whereas the slip variable $\gamma$ vanishes in the elastic part, the microslip $\gamma_\chi$ can be different from zero. This occurs close to the boundary with the plastically active domain.
According to the second law of thermodynamics, the residual dissipation inequality is obtained as

$$\sum_{s=1}^{N}\left(|\tau^s| + \frac{\rho_\sharp}{\rho}s - \rho_\sharp\frac{\mathrm{d}\psi_h}{\mathrm{d}\gamma_{cum}}\right)|\dot{\gamma}^s| \geqslant 0 \tag{4.22}$$

Hence the yield function $f^s$ for each slip system $s$ is introduced with

$$f^s = |\tau^s| + \frac{\rho_\sharp}{\rho}s - \rho_\sharp\frac{\mathrm{d}\psi_h}{\mathrm{d}\gamma_{cum}} - \tau_0 = |\tau^s| - \left(\tau_0 - \frac{\rho_\sharp}{\rho}s + \rho_\sharp\frac{\mathrm{d}\psi_h}{\mathrm{d}\gamma_{cum}}\right) \tag{4.23}$$

where $\tau_0$ is the initial critical resolved shear stress, which is assumed for brevity to be the same for all slip systems. For conciseness hardening is here assumed to be a function of $\gamma_{cum}$ only. Noticing that $\rho_\sharp = \rho_0$ due to plastic incompressibility, from Eq. (4.6) one has $\frac{\rho_\sharp}{\rho}s = S$. Accordingly, a rate-dependent law is chosen for the plastic slip rates

$$\dot{\gamma}^s = \mathrm{sign}\,(\tau^s)\,\dot{\gamma}_0\left\langle\frac{|\tau^s| - \left(\tau_0 - S + \rho_\sharp\frac{\mathrm{d}\psi_h}{\mathrm{d}\gamma_{cum}}\right)}{\tau_0}\right\rangle^n \tag{4.24}$$

where $\dot{\gamma}_0$ and $n$ are viscosity parameters.

## 4.2.2 Analytical reference solutions for linear hardening and perfect plasticity

As a simple reference analysis of this model, the problem of a periodic unit-cell loaded in simple shear and undergoing single slip for linear hardening and perfect plasticity behaviours is studied. Predictions of the model are derived analytically in the rate-independent case and used to validate the finite element computations performed with the finite element solver Z–set (Besson and Foerch, 1997; Z–set package, 2020).

### 4.2.2.1 Geometry and boundary conditions

Let us consider the periodic unit-cell of width $W$ in $\underline{\boldsymbol{X}}_1$, length $L$ in $\underline{\boldsymbol{X}}_2$ and thickness $T$ in $\underline{\boldsymbol{X}}_3 = \underline{\boldsymbol{X}}_1 \wedge \underline{\boldsymbol{X}}_2$ directions shown in Figure 4.2. As in (Ling et al., 2018), the problem of simple shear with a unique slip system $(\underline{\boldsymbol{m}}, \underline{\boldsymbol{n}})$ aligned with the shearing direction is considered ($\underline{\boldsymbol{m}} = \underline{\boldsymbol{X}}_1$ and $\underline{\boldsymbol{n}} = \underline{\boldsymbol{X}}_2$). A macroscopic (average) deformation gradient $\overline{\underset{\sim}{\boldsymbol{F}}}$ is applied such that

$$\underline{\boldsymbol{u}} = (\overline{\underset{\sim}{\boldsymbol{F}}} - \underset{\sim}{\boldsymbol{1}}).\underline{\boldsymbol{X}} + \underline{\boldsymbol{v}}(\underline{\boldsymbol{X}}) \tag{4.25}$$

$$\text{with } \overline{\underset{\sim}{\boldsymbol{F}}} = \underset{\sim}{\boldsymbol{1}} + \overline{F}_{12}\underline{\boldsymbol{m}} \otimes \underline{\boldsymbol{n}} \tag{4.26}$$

where $\underline{\boldsymbol{v}}$ is a periodic function of periodicity $W$ in $\underline{\boldsymbol{X}}_1$ direction, $L$ in $\underline{\boldsymbol{X}}_2$ direction and $T$ in $\underline{\boldsymbol{X}}_3$ direction. At origin point $O$ zero displacements are imposed in the three directions such that

$$\underline{\boldsymbol{u}}\,(X_1 = 0, X_2 = 0, X_3 = 0) = \underline{\boldsymbol{0}} \tag{4.27}$$

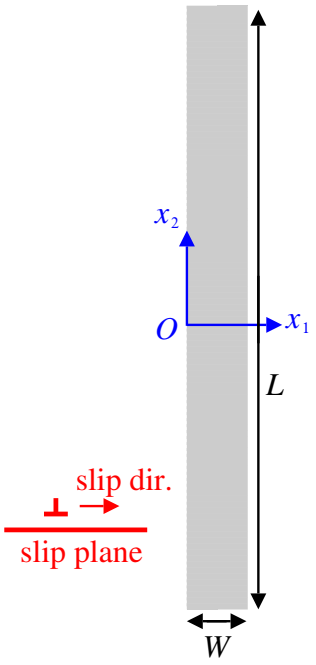


Figure 4.2 Periodic unit-cell of width $W$ along $\underline{\boldsymbol{X}}_1$, length $L$ along $\underline{\boldsymbol{X}}_2$, and thickness $T$ along $\underline{\boldsymbol{X}}_3$.

In order to enforce existence of gradients of the microslip $\gamma_\chi$ along $\underline{\boldsymbol{X}}_2$ and thus evidence the boundary layer formation, Dirichlet boundary conditions along $\underline{\boldsymbol{X}}_2$ are applied while periodic boundary conditions along $\underline{\boldsymbol{X}}_1$ and $\underline{\boldsymbol{X}}_3$ are considered

$$\gamma_\chi\left(X_1=0,X_2,X_3\right) = \gamma_\chi\left(X_1=W,X_2,X_3\right) \tag{4.28}$$

$$\gamma_\chi\left(X_1,X_2=\pm\frac{L}{2},X_3\right) = 0 \tag{4.29}$$

$$\gamma_\chi\left(X_1,X_2,X_3=-\frac{T}{2}\right) = \gamma_\chi\left(X_1,X_2,X_3=\frac{T}{2}\right) \tag{4.30}$$

Analytical solutions are first obtained in the case of linear hardening ($H>0$) and perfect plasticity ($H=0$) corresponding to the following form of the hardening potential:

$$\rho\psi_h(\gamma_{cum}) = \frac{1}{2}\frac{\rho}{\rho_0}H\gamma_{cum}^2 \tag{4.31}$$

where $\gamma_{cum}=|\gamma|$ in the case of monotonic single slip for which the superscript $s$ is dropped, and $H$ is the hardening modulus. In the reference configuration, the equations that need to be satisfied are the balance laws Eqs. (4.7), (4.8) and yielding condition Eq. (4.23). From Eq. (4.12) one has in simple shear with a single slip system that $\underset{\sim}{\boldsymbol{P}}=\underset{\sim}{\mathbf{1}}+\gamma\underline{\boldsymbol{m}}\otimes\underline{\boldsymbol{n}}$. Inspired from the work of (Gurtin, 2000), with $\underset{\sim}{\boldsymbol{F}}=\underset{\sim}{\boldsymbol{E}}.\underset{\sim}{\boldsymbol{P}}$, we make the assumption of small elastic deformations in the absence of lattice rotation expected in the considered slip configuration, *i.e.* $E_{12}\ll 1$ with $\underset{\sim}{\boldsymbol{E}}=\underset{\sim}{\boldsymbol{F}}.\underset{\sim}{\boldsymbol{P}}^{-1}=\underset{\sim}{\mathbf{1}}+E_{12}\underline{\boldsymbol{m}}\otimes\underline{\boldsymbol{n}}$. Hence one obtains

$$\underset{\sim}{\boldsymbol{E}}^e_{GL} \simeq \frac{E_{12}}{2}\left(\underline{\boldsymbol{m}}\otimes\underline{\boldsymbol{n}}+\underline{\boldsymbol{n}}\otimes\underline{\boldsymbol{m}}\right) \tag{4.32}$$

and also $\underset{\sim}{\boldsymbol{\Pi}}^e=\underset{\approx}{\boldsymbol{C}}:\underset{\sim}{\boldsymbol{E}}^e_{GL}\simeq\Pi^e_{12}\left(\underline{\boldsymbol{m}}\otimes\underline{\boldsymbol{n}}+\underline{\boldsymbol{n}}\otimes\underline{\boldsymbol{m}}\right)$ where $\underset{\approx}{\boldsymbol{C}}$ is the elasticity tensor. It follows from the definition of Mandel's stress $\underset{\sim}{\boldsymbol{\Pi}}^M=\underset{\sim}{\boldsymbol{E}}^T.\underset{\sim}{\boldsymbol{E}}.\underset{\sim}{\boldsymbol{\Pi}}^e$ and the small elastic strain assumption

that $\underset{\sim}{\mathbf{\Pi}}^M \simeq \underset{\sim}{\mathbf{\Pi}}^e$, and thus, dropping the superscript for the unique system $s$, one has

$$\tau = \underset{\sim}{\mathbf{\Pi}}^M : (\underline{\boldsymbol{m}} \otimes \underline{\boldsymbol{n}}) \simeq \underset{\sim}{\mathbf{\Pi}}^e : (\underline{\boldsymbol{m}} \otimes \underline{\boldsymbol{n}}) \tag{4.33}$$

Hence one obtains $\Pi^e_{12} \simeq \tau$. The assumption of small elastic deformations yields also $\underset{\sim}{\boldsymbol{S}} \simeq \underset{\sim}{\mathbf{\Pi}}^e.\underset{\sim}{\boldsymbol{P}}^{-T}$. Note that $\underset{\sim}{\boldsymbol{P}}$ is of the form $\underset{\sim}{\boldsymbol{P}} = \underset{\sim}{\mathbf{1}} + \gamma \underline{\boldsymbol{m}} \otimes \underline{\boldsymbol{n}}$, hence $\underset{\sim}{\boldsymbol{P}}^{-T} = \underset{\sim}{\mathbf{1}} - \gamma \underline{\boldsymbol{n}} \otimes \underline{\boldsymbol{m}}$ and the balance equation (4.7) rewrites

$$\mathrm{Div}\,(\underset{\sim}{\mathbf{\Pi}}^e - \gamma \underset{\sim}{\mathbf{\Pi}}^e.(\underline{\boldsymbol{n}} \otimes \underline{\boldsymbol{m}})) = \underline{\mathbf{0}} \tag{4.34}$$

which yield, when projected along $\underline{\boldsymbol{X}}_1$ and $\underline{\boldsymbol{X}}_2$

$$\frac{\partial \tau}{\partial X_2} - \frac{\partial (\gamma \tau)}{\partial X_1} = 0 \tag{4.35}$$

$$\frac{\partial \tau}{\partial X_2} = 0 \tag{4.36}$$

From the periodic boundary conditions Eqs. (4.28) and (4.30), and arbitrariness of the width $W$ and thickness $T$, invariant solutions along $\underline{\boldsymbol{X}}_1$ and $\underline{\boldsymbol{X}}_3$ will be sought, *i.e.* $\gamma_\chi(X_1, X_2, X_3) = \gamma_\chi(X_2)$. Similarly, from Eq. (4.18) $\gamma$ is also invariant along $\underline{\boldsymbol{X}}_1$ and $\underline{\boldsymbol{X}}_3$. As a consequence equations (4.35) and (4.36) give respectively that $\tau$ is invariant along $\underline{\boldsymbol{X}}_1$ and $\underline{\boldsymbol{X}}_2$. Since the periodic unit-cell can be considered arbitrarily thin along $\underline{\boldsymbol{X}}_3$ without loss of generality, $\tau$ is also invariant along $\underline{\boldsymbol{X}}_3$. Hence $\tau$ is uniform in the periodic unit-cell:

$$\tau(X_1, X_2, X_3) = \tau \tag{4.37}$$

Combining Eqs. (4.20) and (4.21) with Eq. (4.8) leads to the differential equation governing the microslip

$$A \frac{\mathrm{d}^2 \gamma_\chi}{\mathrm{d}X_2^2} = H_\chi (\gamma_\chi - \gamma) \tag{4.38}$$

From the homogeneity of the shear stress in the unit-cell, when yielding occurs the whole unit-cell becomes plastic and the yield condition Eq. (4.23) leads to $f = |\tau| - (\tau_0 + H\gamma + H_\chi(\gamma - \gamma_\chi)) = 0$. Combined with Eq. (4.38) one obtains another form of the differential equation governing the microslip

$$A \frac{\mathrm{d}^2 \gamma_\chi}{\mathrm{d}X_2^2} - \frac{H H_\chi}{H + H_\chi} \gamma_\chi + \frac{H_\chi}{H + H_\chi} (|\tau| - \tau_0) = 0 \tag{4.39}$$

Since the shear stress $\tau$ is uniform in the unit-cell, the differential equation (4.39) governing the microslip is a second-order, linear, inhomogeneous differential equation with constant coefficients. It is elliptic if $H > 0$ and parabolic if $H = 0$.

#### 4.2.2.2 Linear hardening ($H > 0$)

In the case of linear hardening Eq. (4.39) takes the form

$$\frac{\mathrm{d}^2 \gamma_\chi}{\mathrm{d}X_2^2} - \left(\frac{2\pi}{\lambda_0}\right)^2 \gamma_\chi = -\left(\frac{2\pi}{\lambda_0}\right)^2 \kappa \tag{4.40}$$

where $\lambda_0$ and $\kappa$ are constants defined by:

$$\lambda_0 = 2\pi\sqrt{\frac{A(H+H_\chi)}{|H|H_\chi}}, \text{ assuming } H+H_\chi \geq 0 \tag{4.41}$$

$$\kappa = \left(\frac{\lambda_0}{2\pi}\right)^2 \frac{H_\chi(|\tau|-\tau_0)}{A(H+H_\chi)} \tag{4.42}$$

Note that for large values of the penalty parameter $H_\chi$, one has $H_\chi \gg H$ and the intrinsic length $\lambda_0 \simeq 2\pi\sqrt{A/H}$, which is the expression for the strain gradient plasticity model. For a strictly positive linear hardening, the solutions of Eq. (4.40) are of the form

$$\gamma_\chi(X_2) = \alpha\cosh\left(2\pi\frac{X_2}{\lambda_0}\right) + \beta\sinh\left(-2\pi\frac{X_2}{\lambda_0}\right) + \kappa \tag{4.43}$$

where $\alpha$ and $\beta$ are integration constants. For symmetry reasons $\gamma_\chi(X_2) = \gamma_\chi(-X_2)$ which leads to $\beta = 0$ and $\alpha$ is uniquely determined from boundary condition Eq. (4.29)

$$\alpha = -\frac{\kappa}{\cosh\left(\frac{2\pi}{\lambda_0}\frac{L}{2}\right)} \tag{4.44}$$

which finally leads to

$$\gamma_\chi = \kappa\left(1 - \frac{\cosh\left(\frac{2\pi}{\lambda_0}X_2\right)}{\cosh\left(\frac{2\pi}{\lambda_0}\frac{L}{2}\right)}\right) \tag{4.45}$$

Since $\underset{\sim}{\boldsymbol{F}} = \underset{\sim}{\boldsymbol{E}}.\underset{\sim}{\boldsymbol{P}} = (\underset{\sim}{\mathbf{1}} + E_{12}(\underline{\boldsymbol{m}} \otimes \underline{\boldsymbol{n}})).(\underset{\sim}{\mathbf{1}} + \gamma(\underline{\boldsymbol{m}} \otimes \underline{\boldsymbol{n}})) \simeq (\underset{\sim}{\mathbf{1}} + (E_{12}+\gamma)(\underline{\boldsymbol{m}} \otimes \underline{\boldsymbol{n}}))$ from Eqs. (4.32) and (4.37) one has

$$\tau = \Pi^e_{12} = 2C_{44}E^e_{GL,12} = \frac{2C_{44}}{L}\int_{-\frac{L}{2}}^{\frac{L}{2}}\left(\frac{F_{12}-\gamma}{2}\right)\mathrm{d}X_2 \tag{4.46}$$

where $C_{44}$ denotes the elastic shear modulus. From yielding condition Eq. (4.23) $\gamma$ can be replaced by $\dfrac{|\tau|-\tau_0+H_\chi\gamma_\chi}{H+H_\chi}$ in Eq. (4.46) and the integration provides an expression of $\tau$ as a function of the applied macroscopic (average) shear $\overline{F}_{12}$ and material parameters

$$\tau = \frac{\overline{F}_{12} + \frac{\tau_0}{Z_h}}{\frac{1}{C_{44}} + \frac{1}{Z_h}} \tag{4.47}$$

$$\text{where } \frac{1}{Z_h} = \frac{1}{H} - \frac{2H_\chi\tanh\left(\frac{2\pi}{\lambda_0}\frac{L}{2}\right)}{L\frac{2\pi}{\lambda_0}H(H+H_\chi)} \tag{4.48}$$

#### 4.2.2.3 Perfect plasticity ($H = 0$)

For the case of perfect plasticity, $H = 0$, the same periodic and Dirichlet type boundary value problem as in the previous section is studied. In that case the differential equation (4.39) becomes

$$\frac{\mathrm{d}^2\gamma_\chi}{\mathrm{d}X_2^2} + \frac{|\tau|-\tau_0}{A} = 0 \tag{4.49}$$

Table 4.1 Numerical values of material and unit-cell parameters.

| $C_{11}$ | $C_{12}$ | $C_{44}$ | $\tau_0$ | A | $H_\chi$ | n | $\dot{\gamma}_0$ | $L$ |
|---|---|---|---|---|---|---|---|---|
| 200 GPa | 136 GPa | 105 GPa | 10 MPa | 1 N | $10^5$ MPa | 15 | $10^{17}\,\mathrm{s}^{-1}$ | 1 mm |

The analytical reference solution in case of perfect plasticity is thus of polynomial form

$$\gamma_\chi(X_2) = \frac{\tau_0 - |\tau|}{2A} X_2^2 + \alpha X_2 + \beta \tag{4.50}$$

where $\alpha$ and $\beta$ are integration constants, which are uniquely determined from boundary conditions

$$\alpha = 0 \quad \text{and} \quad \beta = -\frac{\tau_0 - |\tau|}{8A} L^2 \tag{4.51}$$

which finally leads to

$$\gamma_\chi(X_2) = \frac{\tau_0 - |\tau|}{2A} \left( X_2^2 - \left(\frac{L}{2}\right)^2 \right) \tag{4.52}$$

This solution is also obtained when computing the Taylor expansion at order two of Eq. (4.45) with $H$ going to zero, *i.e.* $\lambda_0$ going to infinity and $X_2/\lambda_0$ going to 0. Using the uniformity of the shear stress in the unit-cell, equation (4.46) leads now to

$$\tau = \frac{\overline{F}_{12} + \frac{\tau_0}{Z_p}}{\frac{1}{C_{44}} + \frac{1}{Z_p}} \tag{4.53}$$

$$\text{where } \frac{1}{Z_p} = \frac{1}{H_\chi} + \frac{L^2}{12A} \tag{4.54}$$

which is also obtained with the Taylor expansion of Eq. (4.48) when $H$ goes to zero. In the case of strictly positive linear hardening a boundary layer solution is obtained. The size of the boundary layer depends on the ratio between the material length scale $\lambda_0$ and the size $L$ of the unit-cell. In the case of perfect plasticity, it appears that the size of the plastic zone, or in other words the radius of curvature of the parabola, depends not only on the higher order modulus $A$ but also on the size $L$ of the unit-cell.

The analytical solutions Eqs. (4.45) and (4.52) are used to validate the finite element solution of the same boundary value problem. The unit-cell is discretized regularly in 101 elements (reduced integration with eight Gauss points). The interpolation is quadratic for the displacements $\underline{\boldsymbol{u}}$ and linear for $\gamma_\chi$. Cubic elasticity is considered and $C_{11}$, $C_{12}$ and $C_{44}$ denote the elasticity moduli. Table 4.1 gathers the material parameters that have been used for validation in case of linear hardening $H = 1000\,\mathrm{MPa}$ and perfect plasticity $H = 0\,\mathrm{MPa}$. Figure 4.3 shows the finite element and analytical solutions at $\overline{F}_{12} = 1\%$. Viscosity parameters $\dot{\gamma}_0$ and $n$ have been chosen such that the response is almost rate-independent. The viscous part of the stress is equal to $\tau_0(\dot{\gamma}/\dot{\gamma}_0)^{1/n}$. With the chosen values of the parameters, it is more than 20 times lower than the critical resolved shear stress in the range of strain rates considered here. A perfect agreement is also obtained for any other value of $\overline{F}_{12}$.

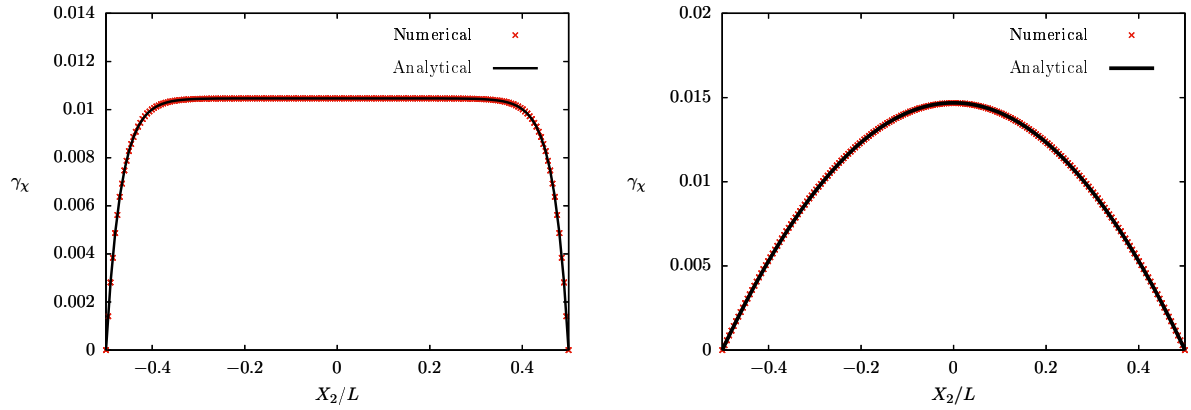


(a) (b)

Figure 4.3 Analytical (black line) and finite element (red crosses) solutions of differential equation (4.39) with: (a) a strictly positive linear hardening ($H = 1000\,\text{MPa}$) and (b) perfect plasticity ($H = 0\,\text{MPa}$) at $\overline{F}_{12} = 1\%$.

## 4.3 Simple shear in the case of softening behaviour

This section is dedicated to the prediction of the micromorphic crystal plasticity model for softening behaviour and in particular to the formation of localization slip bands. As mentioned in the introduction strain gradient models can be used to regularize strain localization phenomena by introducing one or several characteristic lengths. It is shown here how the model presented in Section 4.2 incorporates an intrinsic length that, in case of single slip and linear softening, is related to the localization slip band width. Then non-linear saturating softening behaviour are shown to trigger an increasing slip localization band width. An enhanced model is then proposed in order to bound the localization band width and thus confine the localization zone when the softening behaviour tends toward perfect plasticity.

### 4.3.1 Linear softening ($H < 0$)

Let us now consider a linear softening behaviour ($H < 0$ in the hardening potential Eq. (4.31)). The same boundary conditions Eqs. (4.28), (4.29) and (4.30) as in previous section are kept. Because of the material softening a plastic instability is expected. Therefore a solution with localized plastic deformation over a width $\lambda$ along $\underline{\boldsymbol{X}}_2$ and centered at $O$ is sought for. In the plastic zone the yield condition is satisfied while $\dot{\gamma}$ is zero in the elastic zone

$$f = 0 \qquad \forall X_2 \in \left[-\tfrac{\lambda}{2}; \tfrac{\lambda}{2}\right] \tag{4.55}$$

$$\dot{\gamma} = 0 \quad \forall X_2 \in \left[-\tfrac{L}{2}; -\tfrac{\lambda}{2}\right] \cup \left[\tfrac{\lambda}{2}; \tfrac{L}{2}\right] \tag{4.56}$$

The differential equation (4.39) governing $\gamma_\chi$ is only valid in the region $X_2 \in \left[-\frac{\lambda}{2}; \frac{\lambda}{2}\right]$ and the solutions are of the form

$$\gamma_\chi(X_2) \quad = \quad \alpha \cos\left(2\pi \frac{X_2}{\lambda_0}\right) + \beta \sin\left(2\pi \frac{X_2}{\lambda_0}\right) + \kappa \tag{4.57}$$

For symmetry reasons $\gamma_\chi(X_2) = \gamma_\chi(-X_2)$, hence $\beta = 0$. Out of the plastic zone $\gamma(X_2) = 0$ and at the elastic/plastic interfaces, *i.e.* at $X_2 = \pm\frac{\lambda}{2}$, continuity of microslip $\gamma_\chi$ and of generalized

stress normal to the interface $\underline{\boldsymbol{M}}.\underline{\boldsymbol{X}}_2$ must hold, hence

$$\gamma_\chi\left(\pm\frac{\lambda}{2}\right) \simeq \gamma\left(\pm\frac{\lambda}{2}\right) = 0 \tag{4.58}$$

$$\underline{\boldsymbol{M}}\left(\pm\frac{\lambda}{2}\right).\underline{\boldsymbol{X}}_2 = A\frac{\mathrm{d}\gamma_\chi}{\mathrm{d}X_2}\Big|_{X_2=\pm\frac{\lambda}{2}} = 0 \tag{4.59}$$

Combining Eqs. (4.58) and (4.59) with Eq. (4.57) one gets

$$\alpha = \frac{|\tau| - \tau_0}{H} \tag{4.60}$$

$$\lambda = \lambda_0 \tag{4.61}$$

Hence it is shown that, for $H_\chi \gg H$, the material parameters $H$ and $A$ fully determine the width $\lambda = \lambda_0 \simeq 2\pi\sqrt{A/H}$ of the localization slip band that arises in single slip with a linear softening behaviour. This is in contrast to the parabolic case of the previous section for which the plastic zone size depends on the length of the unit-cell. From Eq. (4.46) the uniform shear stress writes

$$\tau = \frac{\overline{F}_{12} + \frac{\tau_0}{Z_e}}{\frac{1}{C_{44}} + \frac{1}{Z_e}} \tag{4.62}$$

$$\text{where } \frac{1}{Z_e} = \frac{\lambda_0}{HL} \tag{4.63}$$

In the case of strictly negative linear softening the localized solution obtained is a cosine profile. The period of the cosine function is a material parameter and it is equal to the width of the localization band. If the length $L$ of the unit-cell is larger than $\lambda_0$ the period of the cosine function is then equal to $L$.

Numerically, in order to trigger the localization instability in the center of the periodic unit-cell, a defect is introduced in its middle. It consists in a single element having an initially slightly lower critical resolved shear stress $\tau_0^{defect}$ taken equal to 99% of $\tau_0$. The analytical solution Eq. (4.57) is used to validate the finite element solution of the same boundary value problem using the same mesh as in Section 4.2. Figure 4.4 shows both solutions at $\overline{F}_{12} = 1\%$. A perfect agreement is also obtained for any other value of $\overline{F}_{12}$.

### 4.3.2 Non-linear softening and localization slip band widening

A linear softening behaviour is useful to establish analytical reference solutions, but is of limited interest for modeling softening in real materials at large deformations. In order to model any given saturating softening behaviour, for example the clearing of Frank dislocation loops inside dislocation channels relevant for irradiated materials, it is proposed to introduce in Eq. (4.16) a non-linear exponential softening by means of the hardening potential

$$\rho\psi_h = -\frac{\rho}{\rho_0}\tau_a\gamma_0\exp\left(-\frac{\gamma_{cum}}{\gamma_0}\right) \tag{4.64}$$

This kind of softening is similar to the phenomenological dislocation unpinning model proposed by Ling et al. (2017). The goal of the present subsection is to evidence the broadening of the localization band when such a non-linear softening behaviour is adopted inside the formulation presented in Section 4.2. An enhanced model is then proposed in order to bound *a priori* the localization slip band width when considering linear and non-linear softening behaviours. (Zbib and Aifantis, 1988) evidenced the narrowing of localization shear bands by adopting a concave parabolic hardening. However, parabolic softening is unrealistic at large strains and is not used

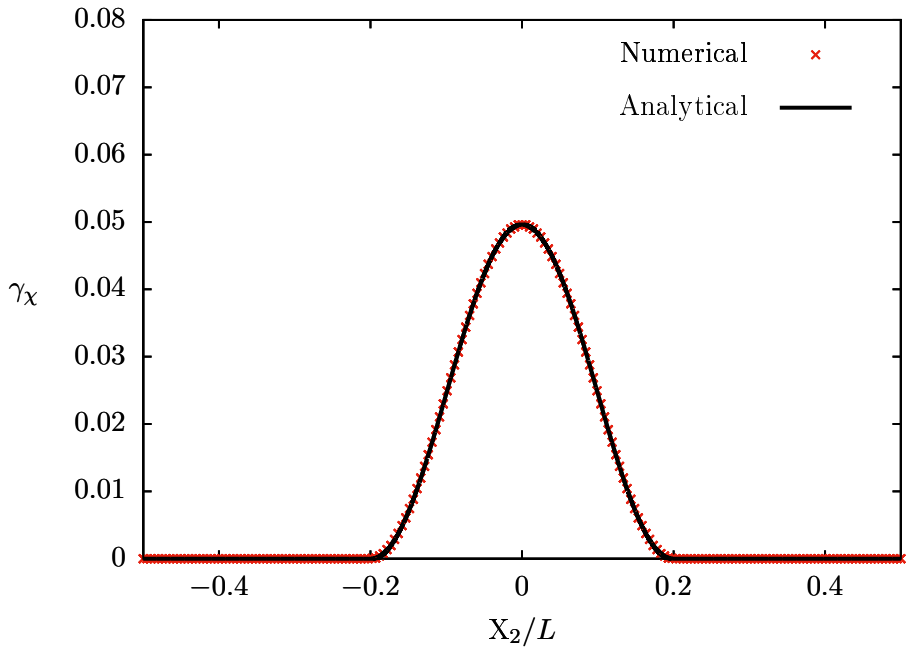


Figure 4.4 Analytical (black line) and finite element (red crosses) solutions of differential equation (4.39) with a linear negative hardening ($H = -250\,\mathrm{MPa}$) at $\overline{F}_{12} = 1\%$.

in the present work. As shown in the previous subsection, for simple shear in single slip, a constant band width is obtained in case of a linear softening. Hence a slip band width widening is expected to occur due to the increase of the (negative) tangent softening modulus of the softening proposed in equation (4.64). The yield condition Eq. (4.23) in the particular case of a non-linear exponential hardening writes:

$$f^s = |\tau^s| - \left(\tau_0 - H_\chi(\gamma_\chi - \gamma_{cum}) + \tau_a \exp\left(-\frac{\gamma_{cum}}{\gamma_0}\right)\right) = 0 \tag{4.65}$$

The solution in terms of $\gamma_{cum}$ for yielding condition Eq. (4.65) involves the Lambert $\mathcal{W}$ function[1]. Finally $\gamma_{cum}$ is eliminated from the differential equation (4.38) which provides

$$A\frac{\mathrm{d}^2\gamma_\chi}{\mathrm{d}X_2^2} + H_\chi\gamma_0\mathcal{W}\left(-\frac{\tau_a}{H_\chi\gamma_0}\exp\left(\frac{\tau_0 - |\tau| - H_\chi\gamma_\chi}{H_\chi\gamma_0}\right)\right) = \tau_0 - |\tau| \tag{4.66}$$

This differential equation cannot be solved analytically, however a local analysis in the neighbourhood of a given point $\underline{\boldsymbol{X}} = \underline{\boldsymbol{X}}^0$ suffices to prove the widening of the localization band. The function $\dfrac{\mathrm{d}\psi_h}{\mathrm{d}\gamma_{cum}}$ is then approximated by its Taylor expansion in $\underline{\boldsymbol{X}}^0$ with

$$\frac{\mathrm{d}\psi_h}{\mathrm{d}\gamma_{cum}}(\gamma_{cum}) \simeq H_T^0(\gamma_{cum} - \gamma_{cum}(X_2^0)) + \frac{\mathrm{d}\psi_h}{\mathrm{d}\gamma_{cum}}(\gamma_{cum}(X_2^0)), \tag{4.67}$$

$$\text{with } H_T^0 = \frac{\mathrm{d}^2\psi_h}{\mathrm{d}\gamma_{cum}^2}(\gamma_{cum}(X_2^0)) \tag{4.68}$$

[1]For $z \in \mathbb{C}$, and the function $f : z \mapsto ze^z$, the Lambert $\mathcal{W}$ function is defined as the inverse function of $f$, i.e. such that for $z \in \mathbb{C}$, $z = f^{-1}(ze^z) = \mathcal{W}(ze^z)$

This expression can be substituted in Eq. (4.23) and the same analysis as in previous subsection leads then to a local characteristic length scale $\lambda$ which is similar to the case of linear softening

$$\lambda \quad = \quad 2\pi\sqrt{\frac{A(H_T^0+H_\chi)}{|H_T^0|H_\chi}} \simeq 2\pi\sqrt{\frac{A}{|H_T^0|}} \tag{4.69}$$

$|H_T^0|$ decreases when $\gamma_{cum}(X_2^0)$ increases and ranges in $\left]0;\frac{\tau_a}{\gamma_0}\right]$. $\gamma_{cum}$ reaches its maximum at the center of the defect ($X_2^0=0$), so $\lambda$ is maximum at $X_2^0=0$ and goes to infinity when softening saturates, *i.e.* when $\gamma_{cum}(X_2^0)$ goes to infinity and $|H_T^0|$ goes to 0. Finally this proves that the localization band width tends to increase when increasing $\overline{F}_{12}$. This result has been verified by computing the finite element solution of the $\gamma_\chi$ profile for the exponential softening potential Eq. (4.64). Figure 4.5 shows the numerical solution obtained for different values of $\overline{F}_{12}$. Eventually

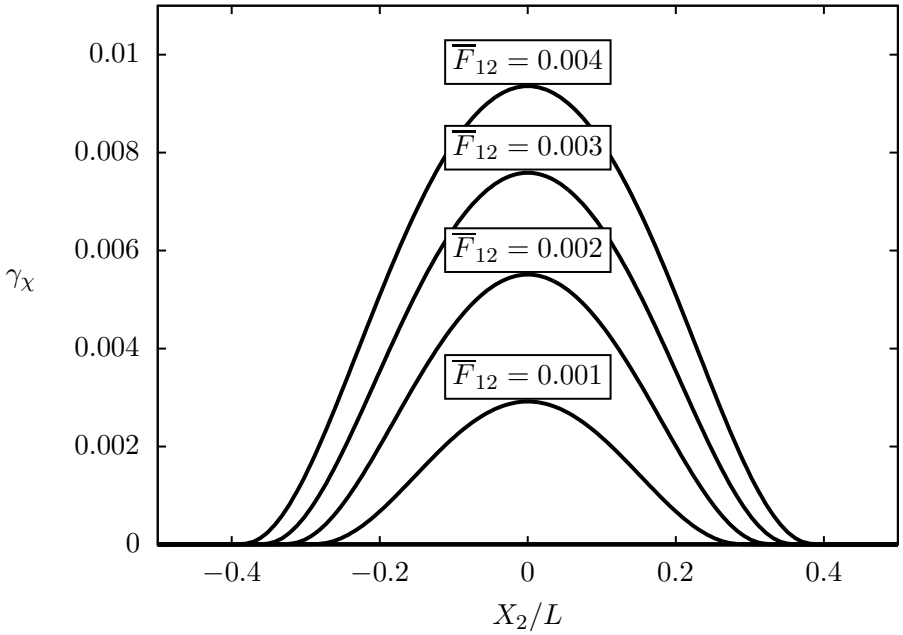


Figure 4.5 Finite element solution of equation (4.38) for an exponential softening behaviour displaying localization band width widening.

for large values of $\gamma_{cum}$ the localization slip band edges reach the boundary of the periodic unit-cell and plastic deformation tends to become homogeneous. This feature of localization slip band broadening is not acceptable when trying to simulate continuing localization at plastic strains much greater than the softening saturating strain ($\gamma_{cum} \gg \gamma_0$).

### 4.3.3 An enhanced model for a bounded localization slip band width

An enhanced micromorphic crystal plasticity model is therefore proposed in order to bound *a priori* the localization slip band width when solving the problem of simple shear in single slip. Up to now $A$ was taken as a constant material parameter, while hardening was taken into account with the hardening potential $\psi_h(\gamma_{cum})$. Here a dependence of the higher order modulus $A$ with respect to $\gamma_{cum}$ is introduced in the form

$$A(\gamma_{cum}) \quad = \quad -\left(\frac{\Lambda_0}{2\pi}\right)^2 \rho_\sharp \frac{\mathrm{d}^2\psi_h}{\mathrm{d}\gamma_{cum}^2} \tag{4.70}$$

where $\Lambda_0$ has the dimension of a length. The corresponding Lagrangian potential Eq. (4.16) writes:

$$\rho\psi = \frac{1}{2}\frac{\rho}{\rho_\sharp}\underset{\sim}{\boldsymbol{E}}^e_{GL} : \underset{\approx}{\boldsymbol{C}} : \underset{\sim}{\boldsymbol{E}}^e_{GL} + \frac{1}{2}\frac{\rho}{\rho_0}H_\chi e^2 + \frac{1}{2}\frac{\rho}{\rho_0}A(\gamma_{cum})\underline{\boldsymbol{K}}^T.\underline{\boldsymbol{K}} + \rho\psi_h(\gamma_{cum}) \tag{4.71}$$

By virtue of the second law of thermodynamics the state laws Eqs. (4.19) and (4.20) still hold and Eq. (4.21) becomes

$$\underline{\boldsymbol{M}} \quad = \quad A(\gamma_{cum})\underline{\boldsymbol{K}} \tag{4.72}$$

The residual dissipation inequality is now

$$\sum_{s=1}^{N}\left(|\tau^s| + \frac{\rho_\sharp}{\rho}s - \rho_\sharp\frac{\mathrm{d}\psi_h}{\mathrm{d}\gamma_{cum}} - \frac{1}{2}\frac{\mathrm{d}A}{\mathrm{d}\gamma_{cum}}\underline{\boldsymbol{K}}^T.\underline{\boldsymbol{K}}\right)|\dot{\gamma}^s| \geqslant 0 \tag{4.73}$$

An enhanced yield function is proposed in the form

$$f^s = |\tau^s| - \left(\tau_0 - \frac{\rho_\sharp}{\rho}s + \rho_\sharp\frac{\mathrm{d}\psi_h}{\mathrm{d}\gamma_{cum}} + \frac{1}{2}\frac{\mathrm{d}A}{\mathrm{d}\gamma_{cum}}\underline{\boldsymbol{K}}^T.\underline{\boldsymbol{K}}\right) \tag{4.74}$$

It can be seen that the introduction of an evolving higher order modulus induces additional apparent hardening in the expression of the effective critical resolved shear stress. For the problem of single slip considered here superscript $s$ is dropped and combining Eq. (4.72) with the balance equation (4.8) and yielding condition Eq. (4.74) one obtains the general differential equation inside the plastic zone $[-\frac{\lambda}{2};\frac{\lambda}{2}]$

$$A(\gamma_{cum})\frac{\mathrm{d}^2\gamma_\chi}{\mathrm{d}X_2^2} \quad = \quad \frac{1}{2}\frac{\mathrm{d}A}{\mathrm{d}\gamma_{cum}}\left(\frac{\mathrm{d}\gamma_\chi}{\mathrm{d}X_2}\right)^2 - \frac{\mathrm{d}A}{\mathrm{d}\gamma_{cum}}\frac{\mathrm{d}\gamma_{cum}}{\mathrm{d}X_2}\frac{\mathrm{d}\gamma_\chi}{\mathrm{d}X_2} + \tau_0 + \rho_\sharp\frac{\mathrm{d}\psi_h}{\mathrm{d}\gamma_{cum}} - |\tau| \tag{4.75}$$

At this step it is straightforward to show that Eqs. (4.74) and (4.75) reduce respectively to Eqs. (4.23) and (4.40) in case of a linear hardening/softening behaviour ($\psi_h(\gamma_{cum}) = \frac{1}{2}H\gamma_{cum}^2$). In that case $\Lambda_0 = \lambda$ and the solutions of this equation have been detailed in Sections 4.2.2.2, 4.2.2.3 and 4.3.1. For an exponential softening behaviour of the type proposed in Eq. (4.64) one has

$$\rho_\sharp\frac{\mathrm{d}\psi_h}{\mathrm{d}\gamma_{cum}} = \tau_a\exp\left(-\frac{\gamma_{cum}}{\gamma_0}\right) \quad \text{and} \quad A(\gamma_{cum}) = \left(\frac{\Lambda_0}{2\pi}\right)^2\frac{\tau_a}{\gamma_0}\exp\left(-\frac{\gamma_{cum}}{\gamma_0}\right) \tag{4.76}$$

Note that $A(\gamma_{cum}) \geq 0$ such that the free energy potential is convex with respect to the microslip gradient. Two approximations allow us to derive an approximate closed form solution to differential equation (4.75).

### Approximation 1

At initiation of plastic slip, gradients along $\underline{\boldsymbol{X}}_2$ of accumulated plastic slip and microslip are close to zero. Therefore the first and second terms of the right-hand side of differential equation (4.75) that involve quadratic terms of these gradients can be neglected. The approximate differential equation becomes

$$A(\gamma_{cum})\frac{\mathrm{d}^2\gamma_\chi}{\mathrm{d}X_2^2} \quad = \quad \tau_0 + \rho_\sharp\frac{\mathrm{d}\psi_h}{\mathrm{d}\gamma_{cum}} - |\tau| \tag{4.77}$$

### Approximation 2

The analytical solutions are derived in the limit case of SGCP, *i.e.* when the penalty factor $H_\chi$ of the micromorphic model is large enough. Therefore combining Eq. (4.76) with approximated differential equation (4.77) and approximations Eq. (4.18), one gets

$$\left(\frac{\Lambda_0}{2\pi}\right)^2 \frac{\tau_a}{\gamma_0} \exp\left(-\frac{\gamma_{cum}}{\gamma_0}\right) \frac{\mathrm{d}^2\gamma_{cum}}{\mathrm{d}X_2^2} = \tau_0 + \tau_a \exp\left(-\frac{\gamma_{cum}}{\gamma_0}\right) - |\tau| \tag{4.78}$$

With the variable substitution

$$\Gamma = \exp\left(-\frac{\gamma_{cum}}{\gamma_0}\right) \tag{4.79}$$

the derivatives with respect to $X_2$ are rewritten as

$$\frac{\mathrm{d}\Gamma}{\mathrm{d}X_2} = -\frac{1}{\gamma_0} \exp\left(-\frac{\gamma_{cum}}{\gamma_0}\right) \frac{\mathrm{d}\gamma_{cum}}{\mathrm{d}X_2}, \tag{4.80}$$

$$\text{and } \frac{\mathrm{d}^2\Gamma}{\mathrm{d}X_2^2} = \frac{1}{\gamma_0^2} \exp\left(-\frac{\gamma_{cum}}{\gamma_0}\right) \left(\frac{\mathrm{d}\gamma_{cum}}{\mathrm{d}X_2}\right)^2 - \frac{1}{\gamma_0} \exp\left(-\frac{\gamma_{cum}}{\gamma_0}\right) \frac{\mathrm{d}^2\gamma_{cum}}{\mathrm{d}X_2^2} \tag{4.81}$$

$$\simeq -\frac{1}{\gamma_0} \exp\left(-\frac{\gamma_{cum}}{\gamma_0}\right) \frac{\mathrm{d}^2\gamma_{cum}}{\mathrm{d}X_2^2} \tag{4.82}$$

where quadratic terms of the gradient of accumulated plastic slip are again neglected. The differential equation governing $\Gamma$ is then derived from Eq. (4.78) as

$$\frac{\mathrm{d}^2\Gamma}{\mathrm{d}X_2^2} + \left(\frac{2\pi}{\Lambda_0}\right)^2 \Gamma = \left(\frac{2\pi}{\Lambda_0}\right)^2 \frac{|\tau| - \tau_0}{\tau_a} \tag{4.83}$$

Its solutions are of the form

$$\Gamma(X_2) = \alpha \cos\left(2\pi \frac{X_2}{\Lambda_0}\right) + \beta \sin\left(2\pi \frac{X_2}{\Lambda_0}\right) + \frac{|\tau| - \tau_0}{\tau_a} \tag{4.84}$$

where $\alpha$ and $\beta$ are integration constants. Inserting the latter result into the yield condition $f = 0$ one has

$$\gamma_\chi(X_2) = \frac{\tau_0 - |\tau|}{H_\chi} + \frac{\tau_a}{H_\chi}\Gamma(X_2) - \gamma_0 \ln(\Gamma(X_2)) \tag{4.85}$$

For symmetry reasons $\gamma_\chi(X_2) = \gamma_\chi(-X_2)$, hence $\beta = 0$. Combining Eqs. (4.58) and (4.59) one obtains

$$\lambda = \Lambda_0 \tag{4.86}$$

$$\alpha = \frac{|\tau| - (\tau_0 + \tau_a)}{\tau_a} \tag{4.87}$$

The approximated analytical solution Eq. (4.85) is compared to the finite element solution of the same boundary value problem using the full model and using the same mesh as in Section 4.2. Figure 4.6 shows both solutions at $\overline{F}_{12} = 0.05\%$ and $\overline{F}_{12} = 0.1\%$. Since approximation 1 is only valid close to initiation of plastic slip, agreement between analytical and numerical results deteriorates when $\overline{F}_{12}$ increases. Nevertheless one should notice that close to the elastic/plastic interfaces a good agreement is obtained because gradients of accumulated plastic slip and microslip remain small in these regions. As a consequence the width of the localization zone

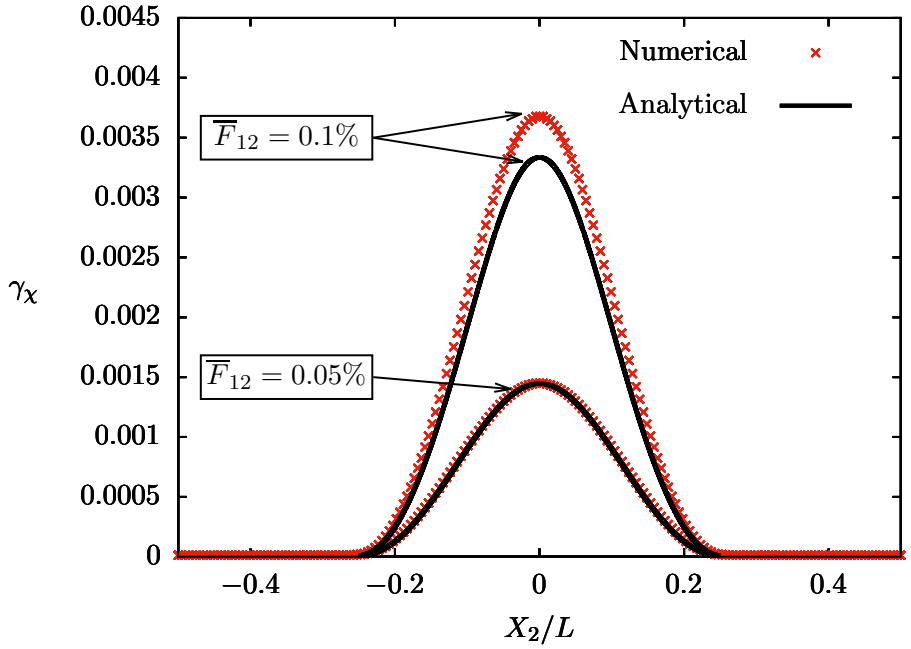


Figure 4.6 Analytical (black line) and finite element (red crosses) solutions of differential equation governing $\gamma_\chi$ at $\overline{F}_{12} = 0.05\%$ and $\overline{F}_{12} = 0.1\%$, when considering the non-linear softening behaviour Eq. (4.64) and the constitutive function Eq. (4.70) for $A(\gamma_{cum})$.

obtained numerically remains bounded and close to the one derived analytically and given by Eq. (4.86). Figure 4.7 displays in dashed lines the finite element solution obtained with the expression of $A(\gamma_{cum})$ expressed at Eq. (4.70) in case of an exponential softening for different values of $\overline{F}_{12}$ ($\overline{F}_{12} \in \{0.001, 0.002, 0.003, 0.004\}$). The solid curves on Figure 4.7 are the one plotted in Figure 4.5 used to show localization band widening when a constant value of $A$ is taken.

The proposed expression of $A(\gamma_{cum})$ allows to bound the localization band width at any strain when considering an exponential softening[2]. However it can be observed from Figure 4.7 that while the size of the region where plastic slip occurred is fixed, the size of the region of continuing plastic flow decreases for further straining $\overline{F}_{12}$. The latter region becomes vanishingly thin since its size is proportional to the square root of higher order modulus $A$ which, according to Eq. (4.76), tends to zero for increasing plastic slip. This means that the classical crystal plasticity model, without regularization, is retrieved. To that extent, the band width becomes close to the mesh size in the finite element simulation.

## 4.4 Application to irradiated voided crystals: void/slip band interaction

As shown in (Fish et al., 1973) and on Figure 4.1b, irradiation induced nanovoids may be heavily sheared inside dislocation channels during straining. The objective here is to study the possible interactions between these voids and such localization bands from a continuum mechanical perspective. It is shown experimentally in (Farrell et al., 2003) and numerically in (Cui et al., 2018) that essentially one single slip system is active inside such a dislocation channel. Therefore a single slip system is considered in the following. A periodic distribution of voids in a plate is considered for simplicity. Interactions between voids and localization bands are

[2]Results not shown here indicate that a bounded localization band width is obtained also when considering a bi-linear (softening followed by a plateau) behaviour.

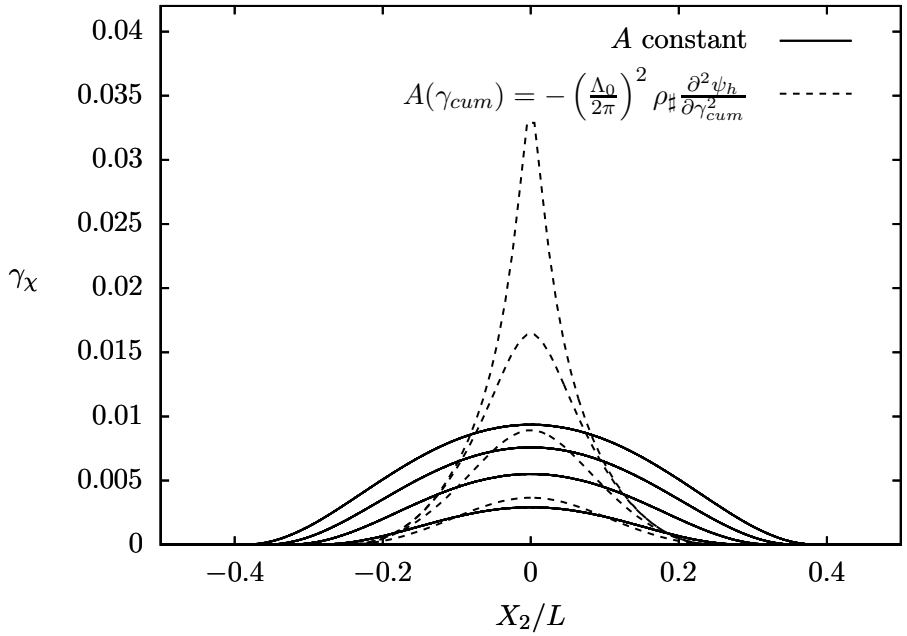


Figure 4.7 Finite element solutions of differential equation governing $\gamma_\chi$ for $A$ constant displaying localization band width widening (solid line) and for $A(\gamma_{cum})$ inducing a bounded localization band width (dashed line).

analyzed in the finite element simulation of a single unit-cell with appropriate periodic boundary conditions.

### 4.4.1 Finite element meshes, loading and boundary conditions

The periodic unit-cell is made of a one-element thick square plate of width and height $L$ in direction $\underline{\boldsymbol{X}}_1$ and $\underline{\boldsymbol{X}}_2$ and thickness $T$ along $\underline{\boldsymbol{X}}_3$. A cylindrical hole of radius $R$ is located at the center, see Figure 4.8. Regular meshes consist of hexahedral elements which are quadratic in displacements $\underline{\boldsymbol{u}}$ and linear in $\gamma_\chi$ (reduced integration with eight integration points). In the same way as in previous section, an average deformation gradient $\overline{F}_{12}$ is prescribed to the unit-cell with fully periodic boundary conditions. This corresponds to the same macroscopic simple glide deformation field Eq. (4.26) as in the previous section. The microslip variable $\gamma_\chi$ is taken periodic along all three directions. A unique slip system $(\underline{\boldsymbol{m}}, \underline{\boldsymbol{n}})$ aligned with the shearing direction 1 is considered ($\underline{\boldsymbol{m}} = \underline{\boldsymbol{X}}_1$ and $\underline{\boldsymbol{n}} = \underline{\boldsymbol{X}}_2$). An exponential softening behaviour of type Eq. (4.64) is used and Eq. (4.70), and more precisely Eq. (4.76), are adopted for the evolution of the higher order modulus $A(\gamma_{cum})$. Cubic elasticity is considered and Table 4.2 gathers the numerical values of fixed material parameters used for all the simulations.

### 4.4.2 Choice of geometrical and material parameters

The initial void volume fraction is defined as

$$f_0^{\text{band}} = \frac{\pi R^2 T}{2RLT} = \frac{\pi R}{2L} \tag{4.88}$$

which represents the ratio between the volume of the cylindrical hole to the volume of the box of edge length $L$ along $\underline{\boldsymbol{X}}_1$ and $2R$ along $\underline{\boldsymbol{X}}_2$ as plasticity is expected to localize in that region.

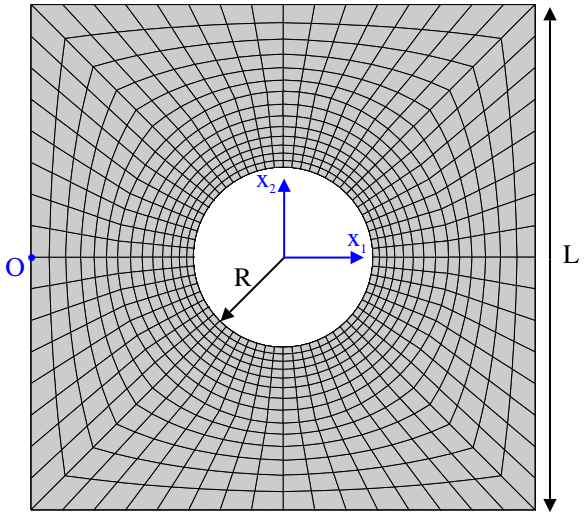


Figure 4.8 Periodic unit-cell mesh with a cylindrical hole (width and height $L$ and thickness $T$).

Table 4.2 Numerical values of material parameters for the simulation of periodic porous unit-cells.

| $C_{11}$ | $C_{12}$ | $C_{44}$ | $\tau_0$ | $\tau_a$ |
|---|---|---|---|---|
| 200 GPa | 136 GPa | 105 GPa | 235 MPa | 35 MPa |

| $\gamma_0$ | $\Lambda_0$ | $H_\chi$ | $n$ | $\dot{\gamma_0}$ |
|---|---|---|---|---|
| 0.1 | 100 nm | $10^6$ MPa | 15 | $10^{20}\,\mathrm{s}^{-1}$ |

Table 4.3 Discrete values of parameters of interest in the simulation of slip band/void interactions.

| $\chi_0 = 2R/L$ | $q_0 = R/\Lambda_0$ |
|---|---|
| $[0.2, 0.4]$ | $[1/18, 1/12, 1/9, 1/6, 1/3]$ |

In fact this void volume fraction is proportional to the intervoid spacing ratio $\chi_0$ defined as

$$\chi_0 = \frac{2R}{L} \tag{4.89}$$

The ratio $q_0$ of the intrinsic length to void size is defined as

$$q_0 = \frac{R}{\Lambda_0} \tag{4.90}$$

where the constitutive intrinsic length $\Lambda_0$ enters Eq. (4.70). For convenience purposes in the following $\chi_0$ will referred to as the porosity and $q_0$ as the normalized void size.

Throughout all simulations $\Lambda_0$ is fixed to 100 nm which corresponds to an upper bound of the dislocation channels width observed in irradiated steels. Noting that according to (Farrell et al., 2003), the greater the irradiation dose the wider and the fewer the dislocation channels. Such a size is at the limit of continuum mechanical modeling. It is therefore assumed that there are enough dislocation sources in these bands for strain gradient continuum crystal plasticity to be applicable. Table 4.3 gathers the discrete values retained for the parameters $\chi_0$ and $q_0$ in the following simulations.

### 4.4.3 Results

Figure 4.9 shows the results obtained for a macroscopic shear strain $\overline{F}_{12} = 0.15$. Very large strains are reached inside the localization band in accordance with the large deformation setting of the theory and finite element implementation. It is important to note that local strains may significantly exceed the maximum value of the accumulated plastic strain $\gamma_{cum}$ of the legend bar. Also for visualization purposes all unit-cells are displayed with the same size for a given void volume fraction, even though the actual hole and cell sizes are varied.

In order to measure the influence of $q_0$ and $\chi_0$ on the localization phenomenon, the localization slip band thickness is defined as

$$\lambda = \max_{x_1=0,x_2,x_3=0} \left( x_2^b - x_2^a, \Delta\gamma_{cum}(x_2^a) > \Delta\gamma_{cum}^{max}/15 \text{ and } \Delta\gamma_{cum}(x_2^b) > \Delta\gamma_{cum}^{max}/15 \right) \tag{4.91}$$

$$\text{where } \Delta\gamma_{cum}^{max} = \max_{x_1=0,x_2,x_3=0} (\Delta\gamma_{cum}(x_2)) \tag{4.92}$$

In other words, the band thickness is measured at 1/15 of the peak strain value. Figures 4.10 and 4.11 display the evolution of $\lambda$ with the macroscopic strain for three values of $q_0$ at $\chi_0 = 0.2$ and $\chi_0 = 0.4$ respectively. For the two Figures the dashed lines correspond to the limit where $\lambda$ reaches four times the initial size along $\underline{\boldsymbol{X}}_2$ of the largest element inside the localization band. Therefore, results above this line can be considered as mesh independent, while it is considered mesh dependent when it goes below it. For both Figures the top dashed line corresponds to $q_0 = 1/3$, the middle dashed line to $q_0 = 1/6$ and the bottom dashed line corresponds to $q_0 = 1/18$. Figure 4.12 shows the evolution of $\lambda$ with $q_0$ at $\overline{F}_{12} = 2.5\%$ for two values of $\chi_0$.

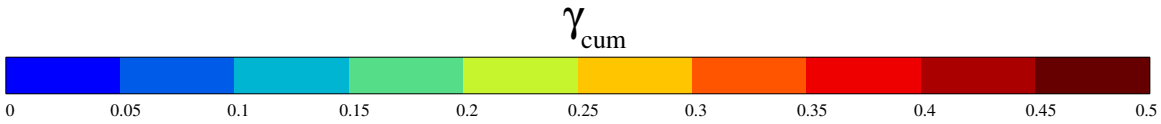


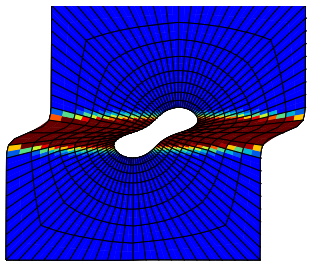

(a) $\chi_0 = 0.2$ and $q_0 = 1/3$

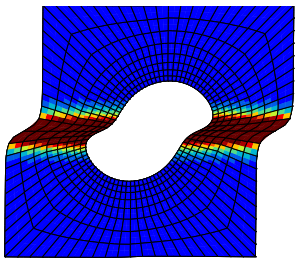

(b) $\chi_0 = 0.4$ and $q_0 = 1/3$

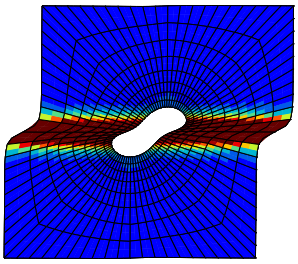

(c) $\chi_0 = 0.2$ and $q_0 = 1/6$

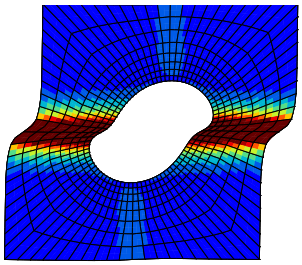

(d) $\chi_0 = 0.4$ and $q_0 = 1/6$

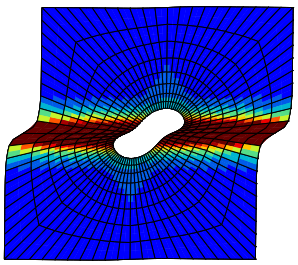

(e) $\chi_0 = 0.2$ and $q_0 = 1/9$

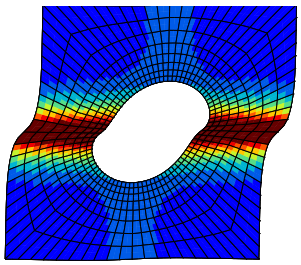

(f) $\chi_0 = 0.4$ and $q_0 = 1/9$

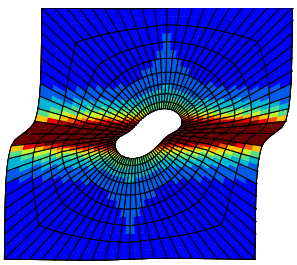

(g) $\chi_0 = 0.2$ and $q_0 = 1/12$

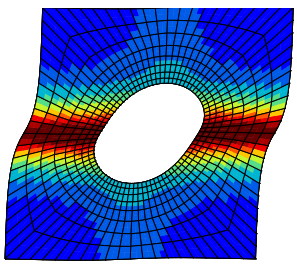

(h) $\chi_0 = 0.4$ and $q_0 = 1/12$

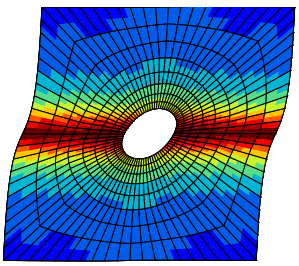

(i) $\chi_0 = 0.2$ and $q_0 = 1/18$

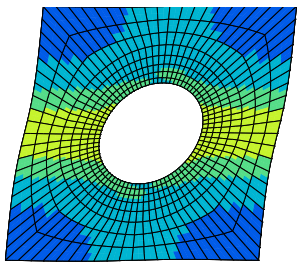

(j) $\chi_0 = 0.4$ and $q_0 = 1/18$

Figure 4.9 Finite element results showing the interaction of a slip band and a void in a unit-cell under average shear at $\overline{F}_{12} = 0.15$.

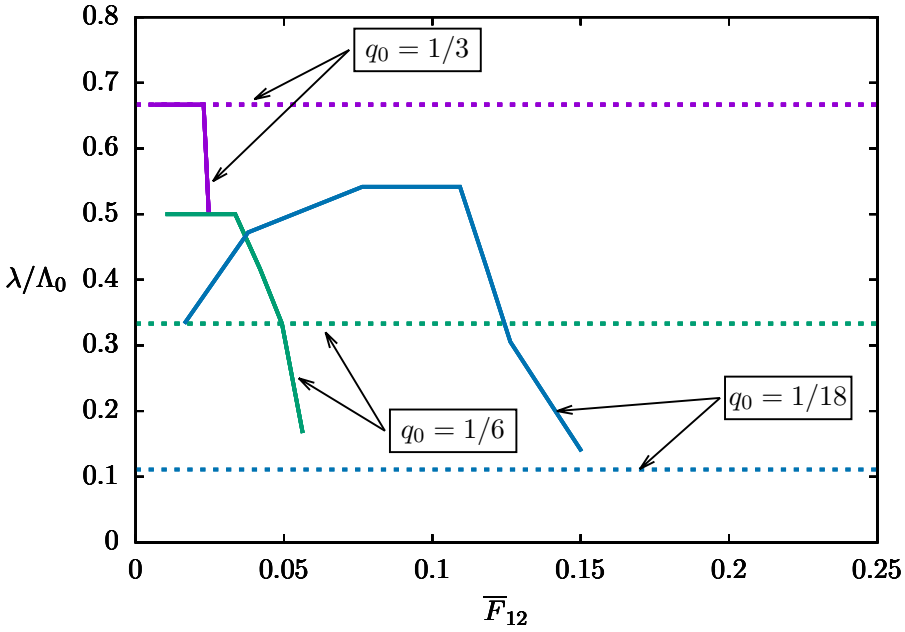


Figure 4.10 Normalized localization slip band width $\lambda$ as a function of $\overline{F}_{12}$ for three different values of parameter $q_0$ and for $\chi_0 = 0.2$. Dashed lines represent the normalized width equal to four times the initial mesh size.

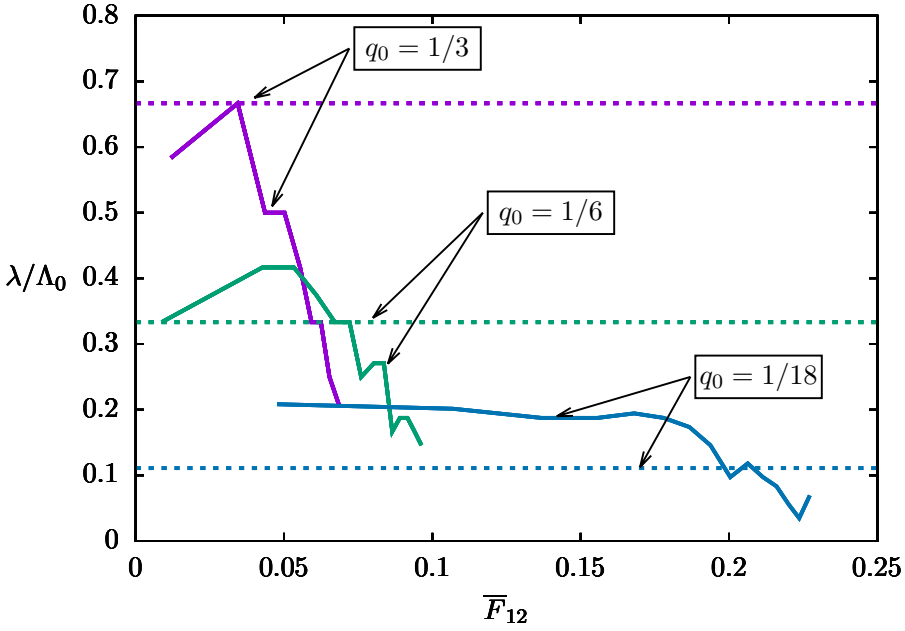


Figure 4.11 Normalized localization slip band width $\lambda$ as a function of $\overline{F}_{12}$ for three different values of parameter $q_0$ and for $\chi_0 = 0.4$. Dashed lines represent the normalized width equal to four times the initial mesh size.

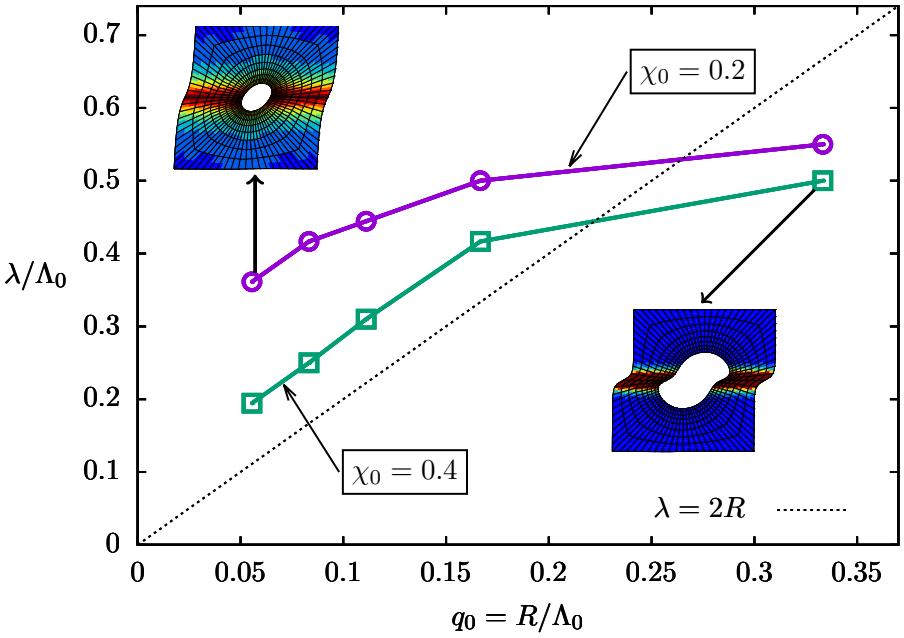


Figure 4.12 Normalized localization slip band width $\lambda$ as a function of $q_0$ for two different void volume fractions at the overall shear value $\overline{F}_{12} = 0.025$. Insets correspond to snapshots of Figure 4.9i (left) and 4.9b (right) at $\overline{F}_{12} = 0.15$.

## 4.4.4 Discussion

### 4.4.4.1 Effect of intrinsic length and hole size on void shape

Figure 4.9 shows that void shape is significantly impacted both by $q_0$ and $\chi_0$. For the lowest values of $q_0$, *i.e.* the lowest normalized void sizes, the holes remain elliptical, while they take peanut-like shapes when their size increases and become comparable with the intrinsic length scale. In addition increasing the porosity $\chi_0$ induces preservation of elliptical void shapes for larger normalized void sizes. Eventually even for large void volume fractions peanut-like shapes are obtained. Peanut-like void shapes are in good agreement with those observed inside dislocation channels (see Figure 4.1a and 4.1b). However this agreement is for now only qualitative, and one must note that similar void shapes can be obtained with standard J2 flow theory.

### 4.4.4.2 Effect of intrinsic length and hole size on localized slip band width

Figure 4.10 and 4.11 show that, at a given porosity $\chi_0$, larger values of normalized void size $q_0$ induce thicker localization slip bands. In addition increasing the porosity $\chi_0$, for a given normalized void size $q_0$, decreases the localization slip band width.

Figure 4.12 shows more precisely that at a low macroscopic shear strain, larger normalized void sizes and/or smaller porosities induce thicker localization slip bands. The effect of the normalized void size can be understood as follows. When the void radius is much lower than $\Lambda_0$ the width of the localization zone is mainly governed by the void size. Hence, for small values of $q_0$, $\lambda$ strongly depends on $q_0$. However when the void radius is of the order of magnitude of the intrinsic material length scale $\Lambda_0$ the width of the localization band is mainly governed by the latter parameter. Therefore a saturation of the localization band width is observed as $q_0$ increases. The effect of the porosity can be understood as follows. For a low porosity $\chi_0$ the localization band width $\lambda$ is expected to be close to the one of the sound material which has been shown in previous section to be equal to the intrinsic material length scale $\Lambda_0$. When increasing porosity $\chi_0$, with void radii always smaller than the intrinsic material length scale

($q_0 = R/\Lambda_0 < 1$), voids are responsible of more intense flow localization and therefore localization bands are thinner than in the case of the sound material.

#### 4.4.4.3 Effect of intrinsic length and hole size on the selection of slip and kink band modes

It can be seen in Figure 4.9 that slip and kink bands, respectively parallel and perpendicular to the slip direction, initiate where the sheared material cross-section is reduced due to the presence of the void. In the simulations performed, kink bands were found to have a lower intensity than slip bands. It was proven by (Asaro and Rice, 1977) that slip and kink bands are equivalently probable at initiation of plastic slip for the problem considered. In the post-bifurcation simulations, the results clearly show that slip bands dominate at least for the considered configurations. This is probably due to the fact that, in contrast to slip band, kink bands are associated to strong lattice rotation and curvature so that their structure evolves rapidly with further overall straining Forest (1998); Forest et al. (2001). The present simulations show that the relative intensity of kink bands decreases when the macroscopic strain increases. As expected and according to (Ling et al., 2018) it is found that when decreasing the normalized void size $q_0$ the regularization power of the gradient model affects both kink and slip bands. For a given porosity $\chi_0$ it is observed that the larger the normalized void size, the lower is the relative intensity of the kink band compared to the slip band. In addition it can be observed that, for a given normalized void size, the relative intensity of the kink band increases when increasing the porosity. It should be emphasized that the present model incorporates the effect of the spatial derivatives of the microslip both along and perpendicular to the slip plane. Gradient effects along the slip direction are related to the densities of geometrically necessary dislocations which are known to be responsible for significant size effects. This contribution plays an essential role in the thickness of kink bands (Forest et al., 2001). In contrast gradient effects perpendicular to the slip planes are less explored even though they could be related to cross-slip (or climb at higher temperatures) of dislocations contributing to the finite thickness of slip band bundles (Neuhäuser, 1983). The present model is isotropic with respect to the gradient of slip vector which essentially leads to the same finite thickness for slip and kink bands (see Ling et al. (2018)). A more elaborate formulation should introduce anisotropy and include a smaller length scale for slip bands than for kink bands.

## 4.5 Conclusions

The main findings of the present work can be summarized as follows:

1. The predictions of a micromorphic crystal plasticity model in case of single slip linear hardening for a periodic unit-cell in simple shear have been established analytically. These analytical solutions have been used to validate the finite element implementation. Three cases were distinguished: linear hardening, perfect plasticity and linear softening. A fixed localization band width was shown to emerge in case of linear softening directly related to the higher order modulus of the micromorphic model.

2. A localization band widening has been observed in the finite element simulations at large strains when a non-linear saturating softening and a constant higher order modulus are considered. This band broadening has not been mentioned in the previous literature on plastic strain localization because most of the results in the literature are limited to linear softening and do not consider the saturating regime. It has been observed in the case of damage localization and cracking for some gradient damage model simulations. Such a broadening of plastic bands is not relevant for the simulation of continuing localization in slip bands observed for instance in irradiated materials.

3. An enhanced model is proposed in order to preserve a bounded localization band width when a non-linear saturating softening behaviour is used. It is based on a non-constant higher order modulus which varies with the accumulated plastic slip. Finite element results at large strains and an approximate analytical solution using such an evolving length scale confirm the absence of widening of the localization slip band in simple shear. The proposed constitutive function $A(\gamma_{cum})$ is decreasing toward zero which leads to a vanishingly small slip band width in the saturated regime. This is similar to existing gradient damage models based on an evolving and vanishing intrinsic length scale at fracture.

4. The enhanced model was applied to the study of void and slip band interaction. The effects of normalized void size and porosity versus intrinsic material length scale on the shape of deformed void, the localization band width, and the localized deformation pattern were illustrated by systematic micromorphic finite element simulations at large strains. Void shape was shown to evolve from elliptical towards peanut-like shape when increasing normalized void size or decreasing void volume fraction which correspond to the experimental observation (see Figure 4.1a). This model applied to a porous material has shown that the localization band width depends simultaneously on the intrinsic material length scale and the void size. Kink bands and slip bands are always observed at initiation of plastic slip and the relative intensity of slips bands compared to kink bands increases when increasing the macroscopic shear strain.

Future work will be dedicated to quantify the influence of several other physical parameters like the tensile versus shear stress ratio (*i.e.* stress biaxiality), the slip system orientation and the number of active slip systems.

*Les bugs c'est comme les cacahuètes... on s'arrête lorsqu'il n'y en a plus.*

J. B.

# 5

# Lagrange multiplier based *vs* micromorphic gradient-enhanced rate-(in)dependent crystal plasticity modeling and simulation

This chapter was accepted for publication in the journal *Computer Methods in Applied Mechanics and Engineering* as:
Scherer, J. M., Phalke, V., Besson, J., Forest, S., Hure, J., & Tanguy, B. (2020). Lagrange multiplier based *vs* micromorphic gradient-enhanced rate-(in)dependent crystal plasticity modeling and simulation.

---

## Résumé

Une théorie de plasticité cristalline à gradient impliquant le gradient d'un seul champ scalaire est présentée. Des formalismes de plasticité cristalline dépendant et indépendant de la vitesse de déformation sont considérés. Le modèle est ensuite reformulé en suivant d'abord l'approche micromorphe, puis en suivant une approche basée sur un multiplicateur de Lagrange. L'implémentation numérique dans le cadre d'une résolution par éléments finis est détaillée pour cette dernière. L'efficacité numérique de l'approche à multiplicateur de Lagrange est mise en évidence dans un exemple impliquant la régularisation d'une bande de localisation. Il est montré que l'amélioration des performances numériques atteint jusqu'à deux ordres de grandeur dans l'accélération du temps de calcul. Ensuite, les effets de taille prévus par les formulations micromorphe et à multiplicateur de Lagrange sont évalués. Tout d'abord, des comparaisons numériques sont effectuées sur des cylindres monocristallins en torsion. La saturation des effets de taille induits par l'approche micromorphe et l'absence de saturation avec l'approche à multiplicateur de Lagrange lorsque la taille de l'échantillon est réduite sont démontrées. La formulation à multiplicateur de Lagrange est finalement appliquée pour caractériser les effets de taille prévus pour la croissance ductile de cellules unitaires poreuses sous triaxialité des contraintes imposée. Un excellent accord avec les résultats micromorphes est obtenu.

---

## Contents

## 5.1 Introduction

The anisotropic elasto-plastic deformation of crystalline aggregates including shape change, crystallographic texture, and strain hardening can be predicted by classical continuum crystal plasticity (Cailletaud et al., 2003; Roters et al., 2010). The classical continuum crystal plasticity formulation can be enhanced in order to predict experimentally observed size effects such as precipitate or grain size effects, for instance based on the introduction of the dislocation density tensor and associated constitutive length scales (Fleck and Hutchinson, 1997; Forest, 1998; Gurtin, 2000).

Experimental evidence of size effects can be found in different mechanical tests such as micro-torsion (Fleck and Hutchinson, 1997; Gao and Huang, 2001; Guo et al., 2017; Liu et al., 2012), micro-compression (Greer et al., 2005; Uchic et al., 2004), micro-bending (Gao and Huang, 2001; Haque and Saif, 2003; Stölken and Evans, 1998) and micro-indentation (Gao and Huang, 2001; Liu and Ngan, 2001; Nix and Gao, 1998) of crystalline materials. Size–dependent crystal plasticity modeling is required when the specimen or grain size becomes comparable to the intrinsic lengths of the underlying plastic deformation mechanisms (Fleck and Hutchinson, 1997; Kocks and Mecking, 2003). The gradient of shear strain results in the development of the dislocation density tensor which can be described in terms of the storage of geometrically necessary dislocations (GND) (Acharya and Bassani, 2000; Ashby, 1970; Bardella, 2006; Cordero et al., 2012a; Gurtin, 2002). The GND density controls the material strain hardening together with the usual scalar dislocation densities, also called statistically stored dislocations (SSD).

The strain gradient plasticity approach can also be used to regularize the simulation of shear band formation in crystalline solids. Strain softening results in a narrow band of intense shearing. The possible loss of ellipticity of partial differential equations in strain softening materials results in an ill-posed boundary value problem and classically shows dependency on mesh size or density. The shear band dependency on the mesh size or density can be overcome by introducing intrinsic material length scale in conventional plasticity (Anand et al., 2012; Kaiser and Menzel, 2019b; Needleman, 1988; Peerlings et al., 2002; Vignjevic et al., 2018; Voyiadjis and Al-Rub, 2005) and in crystal plasticity (Kaiser and Menzel, 2019a; Ling et al., 2018; Petryk and Stupkiewicz, 2016). Furthermore, the difficulties in assessment of active slip systems within the crystal plasticity framework can be overcome by rate-dependent (Busso and Cailletaud, 2005) or rate-independent (Forest and Rubin, 2016; Kaiser and Menzel, 2019a) formulations.

Implementation of strain gradient crystal plasticity in a finite element code is a challenging task that has been performed for example by Bardella et al. (2013); Borg et al. (2008); Nellemann et al. (2017, 2018); Panteghini and Bardella (2016); Shu (1998); Yalcinkaya et al. (2012) at small strains and by Kaiser and Menzel (2019a); Lewandowski and Stupkiewicz (2018); Ling et al. (2018); Niordson and Kysar (2014) at finite deformations. An efficient method to implement strain gradient plasticity models is to resort to the micromorphic approach proposed by Forest (2009) at small strains and Forest (2016a) at finite deformation, as demonstrated by Anand et al. (2012); Brepols et al. (2017) for conventional plasticity and by Aslan et al. (2011); Cordero et al. (2010); Ryś et al. (2020) for crystal plasticity based on the dislocation density tensor. According to this approach, additional plastic microdeformation degrees of freedom, in the sense of Eringen and Suhubi (1964), are introduced at each node and the curl part of the microdeformation tensor is assumed to expend work with a conjugate couple stress tensor. A penalty parameter, which can be interpreted as a higher order elasticity modulus, is used to constrain the plastic microdeformation to be as close as possible to the usual plastic deformation. As a consequence, the curl of the microdeformation tensor almost coincides with the dislocation density tensor.

The computational cost of finite element simulation based on strain gradient or micromorphic crystal plasticity is rather high due to the number of additional degrees of freedom and the strong nonlinearities of the problem. A reduced micromorphic crystal plasticity model was proposed by (Erdle and Böhlke, 2017; Ling et al., 2018; Scherer et al., 2019; Wulfinghoff et al., 2013; Wulfinghoff and Böhlke, 2012). It is limited to a single scalar additional degree of freedom, called microslip variable which is bounded to remain close to the cumulative plastic slip by means of the penalty parameter. The gradient of the microslip is then assumed to be an argument of the

Helmholtz free energy density function. This approach can be compared to the relaxation of the strain gradient plasticity model by a Lagrange multiplier based formulation recently proposed by (Zhang et al., 2018) for isotropic materials. As in the micromorphic approach, one hardening variable is duplicated in two separate instances. One instance of the variable is dedicated to nonlocality and the other to nonlinearity, see (Zhang et al., 2018). The equivalence between both variables is weakly enforced by a Lagrange multiplier, instead of a penalty term. The Lagrange term is added to the free energy function and treated as an additional field variable. This strong coupling scheme was shown to reduce the computational cost drastically compared to previous algorithms. Details of finite element implementation of micromorphic strain gradient rate-dependent crystal plasticity based on Newton-Raphson method to integrate the differential equations can be found in (Ling et al., 2018). The numerical implementation of a Lagrange multiplier based strain gradient isotropic plasticity model was presented in (Zhang et al., 2018)

The objective of the present work is to compare the computational performances and predictions of reduced micromorphic crystal plasticity and a new Lagrange multiplier based implementation of strain gradient plasticity. The novelty of the work lies, first, in this new formulation of strain gradient plasticity with a Lagrangian function and, second, in the comparison of the predictions of the two models. The computational performance and physical relevance of both models are also assessed. Three distinct physical situations are considered. First, regularization of strain localization in a periodic bar undergoing strain-softening is investigated. Then, the size and orientation dependent torsion of FCC single crystal wires is investigated showing that both models coincide at intermediate wire diameters but differ in their asymptotic behaviour. Further, the numerically efficient Lagrange multiplier based constitutive framework is used to study the ductile growth and coalescence of voids in porous unit-cells. The results are compared to data obtained with the micromorphic approach that are already available in the literature.

The outline of the paper is as follows. In section 5.2, a thermodynamically consistent formulation of reduced strain gradient crystal plasticity is presented in the rate-dependent and rate-independent cases. In section 5.3 the constitutive framework of reduced micromorphic and Lagrange multiplier approaches are described. The numerical implementation of the latter is presented in section 5.4. Numerical examples of a sheared periodic bar, a cylinder in torsion and a porous unit-cell under axisymmetric triaxial loading are provided in section 5.5. Concluding remarks follow in section 5.6.

The notations used in the paper are as follows. Underlined bold $\underline{\boldsymbol{a}}$ and under-wave bold $\underset{\sim}{\boldsymbol{A}}$ stand respectively for first and second rank tensors. The transpose, inverse, transpose of inverse and time derivative are denoted by $\underset{\sim}{\boldsymbol{A}}^T$, $\underset{\sim}{\boldsymbol{A}}^{-1}$, $\underset{\sim}{\boldsymbol{A}}^{-T}$ and $\dot{\underset{\sim}{\boldsymbol{A}}}$ respectively. The single and double contractions are written as $\underset{\sim}{\boldsymbol{A}}.\underline{\boldsymbol{b}} = A_{ij}b_j\underline{\boldsymbol{e}}_i$ and $\underset{\approx}{\boldsymbol{A}} : \underset{\sim}{\boldsymbol{B}} = A_{ijkl}B_{kl}\underline{\boldsymbol{e}}_i \otimes \underline{\boldsymbol{e}}_j$ respectively. The following tensor products are used: $\underline{\boldsymbol{a}} \otimes \underline{\boldsymbol{b}} = a_ib_j\underline{\boldsymbol{e}}_i \otimes \underline{\boldsymbol{e}}_j$, $\underset{\sim}{\boldsymbol{A}} \otimes \underset{\sim}{\boldsymbol{B}} = A_{ij}B_{kl}\underline{\boldsymbol{e}}_i \otimes \underline{\boldsymbol{e}}_j \otimes \underline{\boldsymbol{e}}_k \otimes \underline{\boldsymbol{e}}_l$, $\underset{\sim}{\boldsymbol{A}} \underline{\otimes} \underset{\sim}{\boldsymbol{B}} = A_{ik}B_{jl}\underline{\boldsymbol{e}}_i \otimes \underline{\boldsymbol{e}}_j \otimes \underline{\boldsymbol{e}}_k \otimes \underline{\boldsymbol{e}}_l$ and $\underset{\sim}{\boldsymbol{A}} \overline{\otimes} \underset{\sim}{\boldsymbol{B}} = A_{il}B_{jk}\underline{\boldsymbol{e}}_i \otimes \underline{\boldsymbol{e}}_j \otimes \underline{\boldsymbol{e}}_k \otimes \underline{\boldsymbol{e}}_l$, where $\underline{\boldsymbol{e}}_i$ refers to an orthonormal base vector.

## 5.2 A reduced strain gradient crystal plasticity theory

### 5.2.1 Thermodynamical formulation

A reduced strain gradient crystal plasticity theory is adopted in which only the gradient of a scalar effective quantity is considered in keeping with (Aifantis, 1984). Based on the work by Wulfinghoff and Böhlke (2012) the accumulated plastic slip $\gamma_{cum}$, defined as

$$\gamma_{cum} = \int_0^t \sum_{s=1}^{N} |\dot{\gamma}^s| \, \mathrm{d}t \tag{5.1}$$

is chosen to be the thermodynamic variable carrying gradient effects. $\dot{\gamma}^s$ denotes the plastic slip rate on the $s-$th slip system. In the finite strain setting, the deformation gradient $\underset{\sim}{\boldsymbol{F}}$, with

components $F_{ij} = \partial x_i / \partial X_j$, is multiplicatively split into an elastic part $\underset{\sim}{\boldsymbol{E}}$ and a plastic part $\underset{\sim}{\boldsymbol{P}}$ such that $\underset{\sim}{\boldsymbol{F}} = \underset{\sim}{\boldsymbol{E}}.\underset{\sim}{\boldsymbol{P}}$. The plastic velocity gradient $\underset{\sim}{\boldsymbol{L}}^p$ is related to the slip rates on each slip system by

$$\underset{\sim}{\boldsymbol{L}}^p = \dot{\underset{\sim}{\boldsymbol{P}}}.\underset{\sim}{\boldsymbol{P}}^{-1} = \sum_{s=1}^{N} \dot{\gamma}^s (\underline{\boldsymbol{m}}^s \otimes \underline{\boldsymbol{n}}^s) \quad \text{with} \quad \underset{\sim}{\boldsymbol{L}} = \dot{\underset{\sim}{\boldsymbol{F}}}.\underset{\sim}{\boldsymbol{F}}^{-1} = \dot{\underset{\sim}{\boldsymbol{E}}}.\underset{\sim}{\boldsymbol{E}}^{-1} + \underset{\sim}{\boldsymbol{E}}.\underset{\sim}{\boldsymbol{L}}^p.\underset{\sim}{\boldsymbol{E}}^{-1} \tag{5.2}$$

where $\underline{\boldsymbol{m}}^s$ and $\underline{\boldsymbol{n}}^s$ refer to the gliding direction and direction normal to the slip plane respectively. In the reference configuration, upon neglecting body forces, following (Fleck and Hutchinson, 1997; Gurtin and Anand, 2009) the principle of virtual power, for all material subsets $D_0$ of the body, can be written as

$$\int_{D_0} \left( \underset{\sim}{\boldsymbol{S}} : \dot{\underset{\sim}{\boldsymbol{F}}} + S\dot{\gamma}_{cum} + \underline{\boldsymbol{M}} . \dot{\underline{\boldsymbol{K}}} \right) \mathrm{d}V_0 = \int_{\partial D_0} (\underline{\boldsymbol{T}} . \dot{\underline{\boldsymbol{u}}} + M\dot{\gamma}_{cum}) \, \mathrm{d}S_0 \qquad \forall \dot{\underline{\boldsymbol{u}}}, \quad \forall \dot{\gamma}_{cum}, \quad \forall D_0 \tag{5.3}$$

where $\underset{\sim}{\boldsymbol{S}}$ is the Boussinesq (or nominal 1-st Piola-Kirchhoff) stress tensor related to the Cauchy stress tensor $\underset{\sim}{\boldsymbol{\sigma}}$ by $\underset{\sim}{\boldsymbol{S}} = (\rho_0/\rho) \underset{\sim}{\boldsymbol{\sigma}}.\underset{\sim}{\boldsymbol{F}}^{-T}$ with $\rho_0$ (respect. $\rho$) the volumetric mass density in the reference configuration (respect. current configuration). Vector $\underline{\boldsymbol{T}}$ is the traction vector and $\dot{\underline{\boldsymbol{u}}}$ is an arbitrary velocity field. $S$ and $\underline{\boldsymbol{M}}$ are higher order stresses and $M$ a higher order traction scalar. $\underline{\boldsymbol{K}}$ is the Lagrangian gradient of the accumulated plastic slip, $\underline{\boldsymbol{K}} = \mathrm{Grad}\, \gamma_{cum}$. From Eq. (5.3) it can be derived that, within any subset $D_0$ of the body, the stresses satisfy the equilibrium relations

$$\mathrm{Div}\, \underset{\sim}{\boldsymbol{S}} = \underline{\boldsymbol{0}} \quad \forall \underline{\boldsymbol{X}} \in D_0 \tag{5.4}$$

$$\mathrm{Div}\, \underline{\boldsymbol{M}} - S = 0 \quad \forall \underline{\boldsymbol{X}} \in D_0 \tag{5.5}$$

in the absence of body forces and in the static case. As a result of Eq. (5.3), on the surface of the subset $\partial D_0$ the stresses $\underset{\sim}{\boldsymbol{S}}$ and $\underline{\boldsymbol{M}}$ are in equilibrium with the traction vector $\underline{\boldsymbol{T}}$ and scalar $M$ according to

$$\underline{\boldsymbol{T}} = \underset{\sim}{\boldsymbol{S}}.\underline{\boldsymbol{n}}_0 \quad \forall \underline{\boldsymbol{X}} \in \partial D_0, \tag{5.6}$$

$$M = \underline{\boldsymbol{M}} . \underline{\boldsymbol{n}}_0 \quad \forall \underline{\boldsymbol{X}} \in \partial D_0 \tag{5.7}$$

where $\underline{\boldsymbol{n}}_0$ refers to the outward unit surface normal. In order to formulate a complete thermodynamic theory of reduced strain gradient crystal plasticity a free energy potential $\psi$ needs to be defined. The specific free energy potential $\psi$ is chosen to depend on the elastic Green-Lagrange strain measure $\underset{\sim}{\boldsymbol{E}}^e_{GL} = (1/2) \left( \underset{\sim}{\boldsymbol{E}}^T.\underset{\sim}{\boldsymbol{E}} - \underset{\sim}{\boldsymbol{1}} \right)$, the accumulated plastic slip $\gamma_{cum}$, its Lagrangian gradient $\underline{\boldsymbol{K}}$ and hardening variables $r^s$ left to be defined.

$$\psi \left( \underset{\sim}{\boldsymbol{E}}^e_{GL}, \gamma_{cum}, r^s, \underline{\boldsymbol{K}} \right) = \frac{1}{2\rho_\sharp} \underset{\sim}{\boldsymbol{E}}^e_{GL} : \underset{\approx}{\boldsymbol{C}} : \underset{\sim}{\boldsymbol{E}}^e_{GL} + \psi_h(r^s, \gamma_{cum}) + \frac{A}{2\rho_0} \underline{\boldsymbol{K}} . \underline{\boldsymbol{K}} \tag{5.8}$$

where $\rho_\sharp$ refers to the volumetric mass density in the intermediate configuration (*i.e.* the configuration resulting from the transport of the reference configuration by $\underset{\sim}{\boldsymbol{P}}$). The contribution of the accumulated plastic slip gradient is weighed by the strictly positive material parameter, so called higher order modulus, $A$. The Clausius-Duhem inequality (isothermal case) resulting from 1-st and 2-nd principles of thermodynamics enforces

$$\frac{\underset{\sim}{\boldsymbol{S}}}{\rho_0} : \dot{\underset{\sim}{\boldsymbol{F}}} + \frac{S}{\rho_0} \dot{\gamma}_{cum} + \frac{\underline{\boldsymbol{M}}}{\rho_0} . \dot{\underline{\boldsymbol{K}}} - \dot{\psi} \geq 0 \tag{5.9}$$

The first term on left-hand side of Eq. (5.9) can be decomposed into an elastic contribution and a plastic contribution

$$\frac{\underset{\sim}{\boldsymbol{S}}}{\rho_0} : \dot{\underset{\sim}{\boldsymbol{F}}} = \frac{\underset{\sim}{\boldsymbol{\Pi}}^e}{\rho_\sharp} : \dot{\underset{\sim}{\boldsymbol{E}}}^e_{GL} + \frac{\underset{\sim}{\boldsymbol{\Pi}}^M}{\rho_\sharp} : \left(\dot{\underset{\sim}{\boldsymbol{P}}}.\underset{\sim}{\boldsymbol{P}}^{-1}\right) \tag{5.10}$$

where $\underset{\sim}{\boldsymbol{\Pi}}^e$ is the second Piola-Kirchhoff stress tensor defined by $\underset{\sim}{\boldsymbol{\Pi}}^e = (\rho_\sharp/\rho)\underset{\sim}{\boldsymbol{E}}^{-1}.\underset{\sim}{\boldsymbol{\sigma}}.\underset{\sim}{\boldsymbol{E}}^{-T} = (\rho_\sharp/\rho_0)\underset{\sim}{\boldsymbol{E}}^{-1}.\underset{\sim}{\boldsymbol{S}}.\underset{\sim}{\boldsymbol{P}}^T$ with respect to the intermediate configuration and $\underset{\sim}{\boldsymbol{\Pi}}^M$ is the Mandel stress tensor defined by $\underset{\sim}{\boldsymbol{\Pi}}^M = \underset{\sim}{\boldsymbol{E}}^T.\underset{\sim}{\boldsymbol{E}}.\underset{\sim}{\boldsymbol{\Pi}}^e$. The residual dissipation in Eq. (5.9) then writes

$$\begin{aligned}\left(\frac{\underset{\sim}{\boldsymbol{\Pi}}^e}{\rho_\sharp} - \frac{\partial\psi}{\partial\underset{\sim}{\boldsymbol{E}}^e_{GL}}\right) : \dot{\underset{\sim}{\boldsymbol{E}}}^e_{GL} + \frac{\underset{\sim}{\boldsymbol{\Pi}}^M}{\rho_\sharp} : \left(\dot{\underset{\sim}{\boldsymbol{P}}}.\underset{\sim}{\boldsymbol{P}}^{-1}\right) + \left(\frac{S}{\rho_0} - \frac{\partial\psi_h}{\partial\gamma_{cum}}\right)\dot{\gamma}_{cum} \\ + \left(\frac{\underline{\boldsymbol{M}}}{\rho_0} - \frac{A}{\rho_0}\underline{\boldsymbol{K}}\right).\dot{\underline{\boldsymbol{K}}} - \sum_{s=1}^{N}\frac{\partial\psi_h}{\partial r^s}\dot{r}^s \geq 0\end{aligned} \tag{5.11}$$

Here it is assumed that the higher order stress $S$ has a dissipative part which will be denoted $-\overline{H}$, while $\underline{\boldsymbol{M}}$ is assumed to be non-dissipative. As discussed by Forest and Bertram (2011) it is the most simple assumption to derive Aifantis' model. The following state laws are postulated

$$\underset{\sim}{\boldsymbol{\Pi}}^e = \rho_\sharp\frac{\partial\psi}{\partial\underset{\sim}{\boldsymbol{E}}^e_{GL}} = \underset{\approx}{\boldsymbol{C}} : \underset{\sim}{\boldsymbol{E}}^e_{GL} \tag{5.12}$$

$$S = \rho_0\frac{\partial\psi_h}{\partial\gamma_{cum}} - \overline{H} \tag{5.13}$$

$$\underline{\boldsymbol{M}} = \rho_0\frac{\partial\psi}{\partial\underline{\boldsymbol{K}}} = A\underline{\boldsymbol{K}} \tag{5.14}$$

Finally the residual dissipation reduces to

$$\frac{\underset{\sim}{\boldsymbol{\Pi}}^M}{\rho_\sharp} : \left(\dot{\underset{\sim}{\boldsymbol{P}}}.\underset{\sim}{\boldsymbol{P}}^{-1}\right) - \frac{\overline{H}}{\rho_0}\dot{\gamma}_{cum} - \sum_{s=1}^{N}\frac{\partial\psi_h}{\partial r^s}\dot{r}^s \geq 0 \tag{5.15}$$

The resolved shear stress $\tau^s$ is the energetic counterpart of $\dot{\gamma}^s$ and from Eq. (5.2) it can be deduced that it is related to Mandel stress $\underset{\sim}{\boldsymbol{\Pi}}^M$ by $\tau^s = \underset{\sim}{\boldsymbol{\Pi}}^M : \underset{\sim}{\boldsymbol{N}}^s$ where $\underset{\sim}{\boldsymbol{N}}^s = \underline{\boldsymbol{m}}^s \otimes \underline{\boldsymbol{n}}^s$ is the Schmid tensor. Assuming that the rate of hardening variable $r^s$ is proportional to the slip rate $\dot{\gamma}^s$ (e.g. $\dot{r}^s = g_s(r_s)|\dot{\gamma}^s|$) leads to the following expression of the residual dissipation

$$\sum_{s=1}^{N}\left[|\tau^s| - \frac{\rho_\sharp}{\rho_0}\overline{H} - \rho_\sharp\frac{\partial\psi_h}{\partial r^s}g_s(r_s)\right]|\dot{\gamma}^s| \geq 0 \tag{5.16}$$

where it has been assumed that $\text{sign}\,(\tau^s) = \text{sign}\,(\dot{\gamma}^s)$. Eq. (5.16) motivates the introduction of the yield function of each system defined by

$$f^s = |\tau^s| - \left(\tau_0^s + \frac{\rho_\sharp}{\rho_0}\overline{H} + \rho_\sharp\frac{\partial\psi_h}{\partial r^s}g_s(r_s)\right) = |\tau^s| - \left(\tau_c^s - \frac{\rho_\sharp}{\rho_0}S\right) \tag{5.17}$$

where $\tau_0^s$ is the initial critical resolved shear stress of $s$-th system. The critical resolved shear stress is introduced as $\tau_c^s = \tau_0^s + \rho_\sharp\partial\psi_h/\partial r^s g_s(r_s) + \rho_\sharp\partial\psi_h/\partial\gamma_{cum}$. By combining Eq. (5.5) and Eq. (5.14) one obtains

$$S = \text{Div}\,\underline{\boldsymbol{M}} = \text{Div}\,(A\underline{\boldsymbol{K}}) \tag{5.18}$$

As it can be seen from yield criterion Eq. (5.17), the divergence term induces a coupling between constitutive nonlinearity and spatial nonlocality. Therefore pointwise integration of the differential equation governing the material behaviour over a given domain is precluded. Two different relaxation approaches to deal with this coupling are presented in section 5.3 and compared in terms of computational performance and physical predictions in section 5.5.

### 5.2.2 Rate-dependent and rate-independent formulations

A rate-dependent (viscoplastic) and a rate-independent formulation of crystal plasticity are presented here and used in the next sections.

#### 5.2.2.1 Rate-dependent crystal plasticity

As emphasized in (Busso and Cailletaud, 2005) (and references therein) most rate-independent crystal plasticity theories lead to an ill-conditioned problem regarding the selection of active slip systems. Different methods exist to ensure uniqueness, but their numerical implementation may also play a crucial role in the active slip system selection. One possible way to overcome these issues is to work within a rate-dependent setting. In this framework the slip rates are no longer defined by a rate-independent yield surface, but are governed by a rate-dependent potential surface. Smoothness of viscous potential functions allows one to obtain the direction of the strain increment by the normality rule. Evolution of the plastic slip variables $\gamma^s$ can for example be obtained by considering Norton-type flow rules:

$$\dot{\gamma}^s = \dot{\gamma}_0 \left\langle \frac{f^s}{\tau_0^s} \right\rangle^n \operatorname{sign}(\tau^s) = \dot{\gamma}_0 \Phi_{RD}^s(f^s) \operatorname{sign}(\tau^s) \tag{5.19}$$

where $\dot{\gamma}_0$ and $n$ are material parameters which control the rate sensitivity of the material response. Macauley brackets of a scalar $x$, written $\langle x \rangle$, denote the positive part of $x$ and $\Phi_{RD}^s$ denotes the rate-dependent flow function. High values of the power exponent $n$ and of the reference rate $\dot{\gamma}_0$ lead to a low strain rate sensitivity in a given strain rate range.

#### 5.2.2.2 Rate-independent crystal plasticity

Another possible way to select the active slip systems is to use the rate-independent formulation proposed by Forest and Rubin (2016) and intensively used by Farooq et al. (2020) (later referred to as RubiX formulation). It is characterized by a smooth elastic-plastic transition with no slip indeterminacy. It is based on a strictly rate-independent overstress allowing to remove ill-conditioning of the selection of activated slip systems. The main idea consists in replacing Eq. (5.19) by:

$$\dot{\gamma}^s = \dot{\varepsilon}_{eq} \left\langle \frac{f^s}{R} \right\rangle \operatorname{sign}(\tau^s) = \dot{\varepsilon}_{eq} \Phi_{RI}^s(f^s) \operatorname{sign}(\tau^s) \tag{5.20}$$

where $\dot{\varepsilon}_{eq}$ is a non-negative homogeneous function of degree one in the total velocity gradient $\underset{\sim}{\boldsymbol{L}}$. The rate–independent flow function is noted $\Phi_{RI}^s$ and $\dot{\varepsilon}_{eq}$ is taken here as the total equivalent distortional strain rate:

$$\dot{\varepsilon}_{eq} = \sqrt{\frac{2}{3} \underset{\sim}{\boldsymbol{D}}' : \underset{\sim}{\boldsymbol{D}}'} \qquad \underset{\sim}{\boldsymbol{D}}' = \frac{1}{2}\left(\underset{\sim}{\boldsymbol{L}} + \underset{\sim}{\boldsymbol{L}}^T\right) - \frac{1}{3}(\operatorname{trace} \underset{\sim}{\boldsymbol{L}})\underset{\sim}{\boldsymbol{1}} \tag{5.21}$$

$R$ is a positive constant having the unit of a stress and which controls the amplitude of the rate-independent overstress. As this work proceeds $\dot{\Gamma}$ (resp. $\Phi^s$) will be used indistinguishably to represent either $\dot{\gamma}_0$ or $\dot{\varepsilon}_{eq}$ (resp. $\Phi_{RD}^s$ or $\Phi_{RI}^s$).

### 5.2.3 Summary of constitutive equations

Equilibrium equations, state laws and evolution equations are summarized in Table 5.1.

Table 5.1 Summary of equilibrium equations, state laws and evolutions equations.

| equilibrium equations | state laws | evolution equations |
|---|---|---|
| $\mathrm{Div}\,\underset{\sim}{\boldsymbol{S}} = \underline{\mathbf{0}} \quad \forall \underline{\boldsymbol{X}} \in D_0$ | $\underset{\sim}{\boldsymbol{\Pi}}^e = \underset{\approx}{\boldsymbol{C}} : \underset{\sim}{\boldsymbol{E}}^e_{GL}$ | $\dot{\underset{\sim}{\boldsymbol{E}}} = \dot{\underset{\sim}{\boldsymbol{F}}}.\underset{\sim}{\boldsymbol{F}}^{-1}.\underset{\sim}{\boldsymbol{E}} - \underset{\sim}{\boldsymbol{E}}.\left(\sum_{s=1}^{N}\dot{\gamma}^s\underset{\sim}{\boldsymbol{N}}^s\right)$ |
| $\mathrm{Div}\,\underline{\boldsymbol{M}} - S = 0 \quad \forall \underline{\boldsymbol{X}} \in D_0$ | $\underline{\boldsymbol{M}} = A\underline{\boldsymbol{K}}$ | $\dot{\gamma}^s = \dot{\Gamma}\Phi^s\left(\lvert\tau^s\rvert - \left(\tau_c^s - \frac{\rho_\sharp}{\rho_0}S\right)\right)\mathrm{sign}\,(\tau^s)$ |
| $\underline{\boldsymbol{T}} = \underset{\sim}{\boldsymbol{S}}.\underline{\boldsymbol{n}}_0 \quad \forall \underline{\boldsymbol{X}} \in \partial D_0$ | $S = \rho_0\frac{\partial\psi_h}{\partial\gamma_{cum}} - \overline{H}$ | $\dot{r}^s = g_s(r_s)\lvert\dot{\gamma}^s\rvert$ |
| $M = \underline{\boldsymbol{M}}.\underline{\boldsymbol{n}}_0 \quad \forall \underline{\boldsymbol{X}} \in \partial D_0$ | | $\dot{\gamma}_{cum} = \sum_{s=1}^{N}\lvert\dot{\gamma}^s\rvert$ |

## 5.3 Relaxations of strain gradient plasticity theory

### 5.3.1 Micromorphic approach

Wulfinghoff and Böhlke (2012) and Ling et al. (2018) used the micromorphic approach (Forest, 2009) to tackle the issue of nonlocality and nonlinearity coupling. Their approach is based on the introduction of an additional degree of freedom, denoted $\gamma_\chi$, enriching the kinematic description of the material behaviour. $\gamma_\chi$ is the micromorphic counterpart of $\gamma_{cum}$, and, therefore it bears the same physical interpretation. However $\gamma_{cum}$ and $\gamma_\chi$ are treated independently in the resolution of the equations governing the material behaviour. In this context the principle of virtual power Eq. (5.3) is extended to higher order contributions:

$$\int_{D_0}\left(\underset{\sim}{\boldsymbol{S}} : \dot{\underset{\sim}{\boldsymbol{F}}} + S\dot{\gamma}_\chi + \underline{\boldsymbol{M}}.\mathrm{Grad}\,\dot{\gamma}_\chi\right)\mathrm{d}V_0 = \int_{\partial D_0}\left(\underline{\boldsymbol{T}}.\dot{\underline{\boldsymbol{u}}} + M\dot{\gamma}_\chi\right)\mathrm{d}S_0 \quad \forall\dot{\underline{\boldsymbol{u}}}, \forall\dot{\gamma}_\chi, \forall D_0 \tag{5.22}$$

Using the divergence theorem one can again derive the balance laws in the reference configuration, namely Eq. (5.4) and (5.5),

$$\mathrm{Div}\,\underset{\sim}{\boldsymbol{S}} = 0 \tag{5.23}$$

$$\mathrm{Div}\,\underline{\boldsymbol{M}} - S = 0 \tag{5.24}$$

while on the surface $\partial D_0$ stresses are in equilibrium with the traction vector and scalar

$$\underline{\boldsymbol{T}} = \underset{\sim}{\boldsymbol{S}}.\underline{\boldsymbol{n}}_0 \tag{5.25}$$

$$M = \underline{\boldsymbol{M}}.\underline{\boldsymbol{n}}_0 \tag{5.26}$$

In order to ensure quasi-equality between $\gamma_{cum}$ and $\gamma_\chi$, a penalty term is introduced in the free energy potential penalizing their difference $\gamma_{cum} - \gamma_\chi$, where $H_\chi$ is a penalty modulus which is usually taken large enough so that the results obtained with the model do not depend on the chosen value (typically $H_\chi \sim 10^4 - 10^5$ MPa). With this method the specific free energy density

Eq. (5.8) now writes

$$\begin{aligned}\psi\left(\underset{\sim}{\boldsymbol{E}}^e_{GL}, r^s, \gamma_{cum}, \gamma_\chi, \underline{\boldsymbol{K}}_\chi\right) = \frac{1}{2\rho_\sharp}\underset{\sim}{\boldsymbol{E}}^e_{GL} : \underset{\approx}{\boldsymbol{C}} : \underset{\sim}{\boldsymbol{E}}^e_{GL} + \psi_h(r^s, \gamma_{cum}) \\ + \frac{A}{2\rho_0}\underline{\boldsymbol{K}}_\chi.\underline{\boldsymbol{K}}_\chi + \frac{H_\chi}{2\rho_0}(\gamma_{cum} - \gamma_\chi)^2\end{aligned} \tag{5.27}$$

where $\underline{\boldsymbol{K}}_\chi = \mathrm{Grad}\,\gamma_\chi$. The 1-st and 2-nd principles of thermodynamics now enforce

$$\frac{\underset{\sim}{\boldsymbol{S}}}{\rho_0} : \dot{\underset{\sim}{\boldsymbol{F}}} + \frac{S}{\rho_0}\dot{\gamma}_\chi + \frac{\underline{\boldsymbol{M}}}{\rho_0}.\dot{\underline{\boldsymbol{K}}}_\chi - \dot{\psi} \geq 0 \tag{5.28}$$

The mechanical dissipation therefore becomes

$$\begin{aligned}\left(\frac{\underset{\sim}{\boldsymbol{\Pi}}^e}{\rho_\sharp} - \frac{\partial\psi}{\partial\underset{\sim}{\boldsymbol{E}}^e_{GL}}\right) : \dot{\underset{\sim}{\boldsymbol{E}}}^e_{GL} + \frac{\underset{\sim}{\boldsymbol{\Pi}}^M}{\rho_\sharp} : \left(\dot{\underset{\sim}{\boldsymbol{P}}}.\underset{\sim}{\boldsymbol{P}}^{-1}\right) + \left(\frac{S}{\rho_0} - \frac{\partial\psi}{\partial\gamma_\chi}\right)\dot{\gamma}_\chi - \frac{\partial\psi}{\partial\gamma_{cum}}\dot{\gamma}_{cum} \\ + \left(\frac{\underline{\boldsymbol{M}}}{\rho_0} - \frac{A}{\rho_0}\underline{\boldsymbol{K}}_\chi\right).\dot{\underline{\boldsymbol{K}}}_\chi - \sum_{s=1}^{N}\frac{\partial\psi_h}{\partial r^s}\dot{r}^s \geq 0\end{aligned} \tag{5.29}$$

After selecting non–dissipative contributions, the following state laws are adopted

$$\underset{\sim}{\boldsymbol{\Pi}}^e = \rho_\sharp\frac{\partial\psi}{\partial\underset{\sim}{\boldsymbol{E}}^e_{GL}} \tag{5.30}$$

$$S = \rho_0\frac{\partial\psi}{\partial\gamma_\chi} = -H_\chi(\gamma_{cum} - \gamma_\chi) \tag{5.31}$$

$$\underline{\boldsymbol{M}} = \rho_0\frac{\partial\psi}{\partial\underline{\boldsymbol{K}}_\chi} = A\underline{\boldsymbol{K}}_\chi \tag{5.32}$$

In contrast to the previous section, the constitutive assumption that $S$ is non-dissipative is made here. Therefore the energy dissipated with $\dot{\gamma}_\chi$ vanishes. Yet, a term involving the higher order stress $S$ and conjugate to $\dot{\gamma}_{cum}$ remains. The residual dissipation now writes

$$\frac{\underset{\sim}{\boldsymbol{\Pi}}^M}{\rho_\sharp} : \left(\dot{\underset{\sim}{\boldsymbol{P}}}.\underset{\sim}{\boldsymbol{P}}^{-1}\right) - \sum_{s=1}^{N}\frac{\partial\psi_h}{\partial r^s}\dot{r}^s - \left(\frac{H_\chi}{\rho_0}(\gamma_{cum} - \gamma_\chi) + \frac{\partial\psi_h}{\partial\gamma_{cum}}\right)\dot{\gamma}_{cum} \geq 0 \tag{5.33}$$

which can also be written

$$\sum_{s=1}^{N}\left[|\tau^s| - \frac{\rho_\sharp}{\rho_0}H_\chi(\gamma_{cum} - \gamma_\chi) - \rho_\sharp\frac{\partial\psi_h}{\partial\gamma_{cum}} - \rho_\sharp\frac{\partial\psi_h}{\partial r^s}g_s(r_s)\right]|\dot{\gamma}^s| \geq 0 \tag{5.34}$$

By combining state law Eq. (5.31), equilibrium equation Eq. (5.24) and state law Eq. (5.32) it comes $S = -H_\chi(\gamma_{cum} - \gamma_\chi) = \mathrm{Div}\,\underline{\boldsymbol{M}} = \mathrm{Div}\,(A\underline{\boldsymbol{K}}_\chi)$. Therefore the micromorphic approach is a relaxation[1] of the strict strain gradient formulation from section 5.2 in the sense that no spatial derivatives are explicitly involved for the non-local contribution in Eq. (5.34). The plastic slip rates now are

$$\dot{\gamma}^s = \dot{\Gamma}\Phi^s\left(|\tau^s| - \left(\tau_c^s + \tfrac{\rho_\sharp}{\rho_0}H_\chi(\gamma_{cum} - \gamma_\chi)\right)\right)\mathrm{sign}\,(\tau^s) \tag{5.35}$$

[1]Relaxation is meant here in a sense different from Neff et al. (2014), where this terminology was used to describe a "linear micromorphic model with symmetric Cauchy force stresses" which is put in contrast to "the classical Mindlin-Eringen model for micromorphic media with intrinsically non-symmetric force stresses".

The main drawback of this method, in the context of viscoplasticity, lies in the necessity of taking a large value for $H_\chi$ in order to assure quasi-equality between $\gamma_\chi$ and $\gamma_{cum}$. In the limit case of almost rate insensitivity the viscoplastic parameters $n$ and $\dot{\gamma}_0$ are such that the nonlinear system of equation governing activation of slip systems is very stiff and thus extremely sensitive to the errors that are made during the iterative process (typically an Euler-backward scheme) used to solve them. As a consequence small time steps are necessary in order to achieve convergence. One possible way to tackle this issue and allow the use of large time steps with the micromorphic approach is to use a rate-independent crystal plasticity setting such as the one proposed by Forest and Rubin (2016) and presented in section 5.2.2.2.

### 5.3.2 Lagrange multiplier approach

Alternatively, the Lagrange multiplier method proposed by Fortin and Glowinski (1983) and successfully applied in (Zhang et al., 2018) can be used. This approach is described here for relaxing the theory presented in section 5.2.1. The main ideas of the method are first to duplicate the variable upon which the nonlinear-nonlocal coupling is acting and second to enforce equality between both variables through a Lagrangian function. In the context of the model presented in section 5.2.1 the non-local instance of the coupling variable will be denoted $\gamma_\chi$ while its local instance is $\gamma_{cum}$. Similarly to the micromorphic approach, $\underline{\boldsymbol{K}}_\chi = \mathrm{Grad}\,\gamma_\chi$ is regarded as a state variable. Enforcing equality between $\gamma_\chi$ and $\gamma_{cum}$ is achieved using a Lagrange multiplier $\lambda$. It turns out that the previous free energy density in Eq. (5.8) becomes a Lagrangian function

$$\begin{aligned}\mathcal{L}\left(\underset{\sim}{\boldsymbol{E}}^e_{GL}, \gamma_{cum}, r^s, \gamma_\chi, \underline{\boldsymbol{K}}_\chi, \lambda\right) = \frac{1}{2\rho_\sharp}\underset{\sim}{\boldsymbol{E}}^e_{GL} : \underset{\approx}{\boldsymbol{C}} : \underset{\sim}{\boldsymbol{E}}^e_{GL} + \psi_h(r^s, \gamma_{cum}) \\ + \frac{A}{2\rho_0}\underline{\boldsymbol{K}}_\chi.\underline{\boldsymbol{K}}_\chi + \frac{\lambda}{\rho_0}(\gamma_\chi - \gamma_{cum}) + \frac{\mu_\chi}{2\rho_0}(\gamma_\chi - \gamma_{cum})^2\end{aligned} \tag{5.36}$$

where $\mu_\chi$ is a Lagrangian penalization modulus. The 1-st and 2-nd principles of thermodynamics still require to verify Eq. (5.28), where $\dot{\psi}$ is now replaced by $\dot{\mathcal{L}}$, and the mechanical dissipation is written as in Eq. (5.29). The postulated state laws are now

$$\underset{\sim}{\boldsymbol{\Pi}}^e = \rho_\sharp \frac{\partial \psi}{\partial \underset{\sim}{\boldsymbol{E}}^e_{GL}} \tag{5.37}$$

$$S = \rho_0 \frac{\partial \psi}{\partial \gamma_\chi} = \lambda + \mu_\chi(\gamma_\chi - \gamma_{cum}) = \Delta_\chi - \mu_\chi \gamma_{cum} \tag{5.38}$$

$$\underline{\boldsymbol{M}} = \rho_0 \frac{\partial \psi}{\partial \underline{\boldsymbol{K}}_\chi} = A\underline{\boldsymbol{K}}_\chi \tag{5.39}$$

Similarly to the micromorphic approach, the constitutive assumption that $S$ is non-dissipative is made. Therefore the energy dissipated with $\dot{\gamma}_\chi$ vanishes. Yet, a term involving the higher order stress $S$ and conjugate to $\dot{\gamma}_{cum}$ remains. For convenience the scalar stress $\Delta_\chi = \lambda + \mu_\chi \gamma_\chi$ is introduced. By definition $\partial\mathcal{L}/\partial\lambda$ must vanish when the constraint $\gamma_{cum} = \gamma_\chi$ is met

$$\frac{\partial \mathcal{L}}{\partial \lambda}\dot{\lambda} = (\gamma_\chi - \gamma_{cum})\frac{\dot{\lambda}}{\rho_0} = 0 \tag{5.40}$$

and therefore the residual mechanical dissipation becomes

$$\frac{\underset{\sim}{\boldsymbol{\Pi}}^M}{\rho_\sharp} : \left(\dot{\underset{\sim}{\boldsymbol{P}}}\underset{\sim}{\boldsymbol{P}}^{-1}\right) - \sum_{s=1}^{N}\frac{\partial \psi_h}{\partial r^s}\dot{r}^s - \left(\frac{\mu_\chi \gamma_{cum} - \Delta_\chi}{\rho_0} + \frac{\partial \psi_h}{\partial \gamma_{cum}}\right)\dot{\gamma}_{cum} \geq 0 \tag{5.41}$$

which can also be written

$$\sum_{s=1}^{N}\left[|\tau^s| - \frac{\rho_\sharp}{\rho_0}\left(\mu_\chi\gamma_{cum} - \Delta_\chi\right) - \rho_\sharp\frac{\partial\psi_h}{\partial\gamma_{cum}} - \rho_\sharp\frac{\partial\psi_h}{\partial r^s}g_s(r_s)\right]|\dot{\gamma}^s| \geq 0 \tag{5.42}$$

By combining state law Eq. (5.38), equilibrium Eq. (5.24) and state law Eq. (5.39) it comes $S = \Delta_\chi - \mu_\chi\gamma_{cum} = \mathrm{Div}\,\underline{\boldsymbol{M}} = \mathrm{Div}\left(A\underline{\boldsymbol{K}}_\chi\right)$. Therefore the Lagrange multiplier approach is a relaxation of the strict strain gradient formulation from section 5.2 in the sense that no spatial derivative is explicitly involved in the non-local contribution in Eq. (5.42). The plastic slip rates now are

$$\dot{\gamma}^s = \dot{\Gamma}\Phi^s\left(|\tau^s| - \left(\tau_c^s + \frac{\rho_\sharp}{\rho_0}\left(\mu_\chi\gamma_{cum} - \Delta_\chi\right)\right)\right)\mathrm{sign}\left(\tau^s\right) \tag{5.43}$$

## 5.4 Numerical implementation

The numerical implementation in a finite element setting of the Lagrange multiplier approach is described. Details on the implementation of the micromorphic formulation can be found in (Ling et al., 2018).

### 5.4.1 Integration of constitutive equations

The sets of degrees of freedom (DOF), input variables (IN), output variables (OUT) and integration variables (INT) are:

$$\text{DOF: } \{\underline{\boldsymbol{u}}, \gamma_\chi, \lambda\} \quad \text{IN: } \{\underset{\sim}{\boldsymbol{F}}, \Delta_\chi\} \quad \text{OUT: } \{\underset{\sim}{\boldsymbol{S}}, \gamma_M\} \quad \text{INT: } \{\underset{\sim}{\boldsymbol{E}}, \gamma^s, r^s, \gamma_{cum}\} \tag{5.44}$$

where $\gamma_M$ is merely a copy of $\gamma_{cum}$ obtained at the end of the constitutive integration. Integrating the constitutive equations consists, for known values of all variables at a given time step $n$, in computing the evolution of the output and internal variables at next time step $n+1$ knowing the evolution laws of the input variables. At the global level the output variables need to satisfy the weak form of the balance equations Eqs. (5.23), (5.24), (5.25) and Eq. (5.26). It can be noted that

$$\underset{\sim}{\boldsymbol{S}} = J\underset{\sim}{\boldsymbol{\sigma}}.\underset{\sim}{\boldsymbol{F}}^{-T} = \frac{1}{2}\frac{J}{J_e}\underset{\sim}{\boldsymbol{E}}.\left(\underset{\approx}{\boldsymbol{C}} : \left(\underset{\sim}{\boldsymbol{E}}^T.\underset{\sim}{\boldsymbol{E}} - \underset{\sim}{\boldsymbol{1}}\right)\right).\underset{\sim}{\boldsymbol{E}}^T.\underset{\sim}{\boldsymbol{F}}^{-T} \tag{5.45}$$

where state law Eq. (5.30) has been used along with the elastic free energy used in Eq. (5.36) and $J = \det\left(\underset{\sim}{\boldsymbol{F}}\right)$ and $J_e = \det\left(\underset{\sim}{\boldsymbol{E}}\right)$. The evolution of $\underset{\sim}{\boldsymbol{S}}$ depends on evolutions of $\underset{\sim}{\boldsymbol{E}}$ and $\underset{\sim}{\boldsymbol{F}}$. Within the Lagrange multiplier approach the set of equations to be solved at the local level are similar to evolution equations in Table 5.1 and can be reformulated incrementally as the problem of finding the solution of the following system of equations $\mathcal{R}(\Delta\underset{\sim}{\boldsymbol{E}}, \Delta\gamma^s, \Delta r^s, \Delta\gamma_{cum})$:

$$\mathcal{R} = \begin{cases} \mathcal{R}_{\underset{\sim}{\boldsymbol{E}}} = \Delta\underset{\sim}{\boldsymbol{E}} - \Delta\underset{\sim}{\boldsymbol{F}}.\underset{\sim}{\boldsymbol{F}}^{-1}.\underset{\sim}{\boldsymbol{E}} - \underset{\sim}{\boldsymbol{E}}.\left(\sum_{s=1}^{N}\Delta\gamma^s\underset{\sim}{\boldsymbol{N}}^s\right) = 0 \\ \mathcal{R}_{\gamma^s} = \Delta\gamma^s - \Delta\Gamma\Phi^s\left(|\tau^s| - \left\langle\tau_c^s - \frac{\rho_\sharp}{\rho_0}\left(\Delta_\chi - \mu_\chi\gamma_{cum}\right)\right\rangle\right)\mathrm{sign}\left(\tau^s\right) = 0 \\ \mathcal{R}_{r^s} = \Delta r^s - g_s(r_s)|\Delta\gamma^s| = 0 \\ \mathcal{R}_{\gamma_{cum}} = \Delta\gamma_{cum} - \sum_{s=1}^{N}|\Delta\gamma^s| = 0 \end{cases} \tag{5.46}$$

where $\Delta\Gamma = \Delta\varepsilon_{eq}$ in the rate-independent formulation and $\Delta\Gamma = \dot{\gamma}_0 \Delta t$ in the rate-dependent formulation. Note that it may happen that $\tau_c^s - (\rho_\sharp/\rho_0)(\Delta_\chi - \mu_\chi \gamma_{cum}) < 0$. In that case this value is replaced by 0 in the computation. Note also that Eq. (5.46) does not guarantee that plastic incompressibility is satisfied. In order to fulfill this condition, the tensor $\underset{\sim}{\boldsymbol{E}}$ is corrected at the beginning of each iteration of the Newton algorithm used to solve Eq. (5.46). This correction amounts to replace $\underset{\sim}{\boldsymbol{E}}$ by $(J/J_e)^{1/3}\underset{\sim}{\boldsymbol{E}}$. As a result, the corrected tensor $\underset{\sim}{\boldsymbol{P}}$ verifies $\det(\underset{\sim}{\boldsymbol{P}}) = 1$, which corresponds to the plastic incompressibility condition. Solving $\mathcal{R}(\Delta\underset{\sim}{\boldsymbol{E}}, \Delta\gamma^s, \Delta r^s, \Delta\gamma_{cum}) = 0$ is performed using a Newton algorithm with an Euler backward (implicit) scheme which requires computation of the Jacobian matrix $\mathcal{J} = \partial\mathcal{R}/\partial\Delta v_{\text{int}}$ (or some approximation of it). The analytical Jacobian matrix for the resolution of Eq. (5.46) is given in Appendix F.

### 5.4.2 Finite element formulation

The model is implemented in the finite element software Z-set using a 3D total Lagrangian formulation following (Besson and Foerch, 1998; Z–set package, 2020). The principle of virtual power in the context of the Lagrange multiplier method combines Eqs. (5.23), (5.24), (5.25), (5.26), and in addition Eq. (5.40) must be satisfied

$$\begin{cases} \forall \underline{\dot{\boldsymbol{u}}} & \displaystyle\int_{D_0} \underset{\sim}{\boldsymbol{S}} : \dot{\underset{\sim}{\boldsymbol{F}}} \mathrm{d}V_0 = \int_{\partial D_0} \underline{\boldsymbol{T}} . \underline{\dot{\boldsymbol{u}}} \, \mathrm{d}S_0 & (5.47) \\ \forall \dot{\gamma}_\chi & \displaystyle\int_{D_0} A\underline{\boldsymbol{K}}_\chi . \dot{\underline{\boldsymbol{K}}}_\chi + (\Delta_\chi - \mu_\chi \gamma_M)\dot{\gamma}_\chi \mathrm{d}V_0 = \int_{\partial D_0} M\dot{\gamma}_\chi \mathrm{d}S_0 & (5.48) \\ \forall \dot{\lambda} & \displaystyle\int_{D_0} (\gamma_\chi - \gamma_M)\dot{\lambda} \mathrm{d}V_0 = 0 & (5.49) \end{cases}$$

The finite element problem is solved by a monolithic iterative method. The material body occupies the domain $D_0$ in its reference configuration, the decomposition of this body in $n$ finite elements raises

$$\begin{cases} \forall \underline{\dot{\boldsymbol{u}}} & \displaystyle\sum_{e=1}^{n} \int_{D_0^e} \underset{\sim}{\boldsymbol{S}} : \dot{\underset{\sim}{\boldsymbol{F}}} \mathrm{d}V_0^e = \sum_{e=1}^{n_S} \int_{\partial D_0^e} \underline{\boldsymbol{T}} . \underline{\dot{\boldsymbol{u}}} \, \mathrm{d}S_0^e & (5.50) \\ \forall \dot{\gamma}_\chi & \displaystyle\sum_{e=1}^{n} \int_{D_0^e} A\underline{\boldsymbol{K}}_\chi . \dot{\underline{\boldsymbol{K}}}_\chi + (\Delta_\chi - \mu_\chi \gamma_M)\dot{\gamma}_\chi \mathrm{d}V_0^e = \sum_{e=1}^{n_S} \int_{\partial D_0^e} M\dot{\gamma}_\chi \mathrm{d}S_0^e & (5.51) \\ \forall \dot{\lambda} & \displaystyle\sum_{e=1}^{n} \int_{D_0^e} (\gamma_\chi - \gamma_M)\dot{\lambda} \mathrm{d}V_0^e = 0 & (5.52) \end{cases}$$

The boundary $\partial D_0$ is discretized into $n_S$ surface elements $\partial D_0^e$ for the application of surface tractions. As this section proceeds tensors are written with index notations. Within the volume of each element the degrees of freedom $u_i$, $\gamma_\chi$ and $\lambda$ are interpolated by their values at $p$ nodes for the displacements ($\tilde{u}_i^a$ for $a \in [1;p]$) and $q$ nodes for Lagrange multiplier $\lambda$ and the microslip $\gamma_\chi$ ($\widetilde{\lambda}^b$ and $\tilde{\gamma}_\chi^b$ for $b \in [1;q]$)

$$u_i = \sum_{a=1}^{p} {}^{u}N^a \tilde{u}_i^a \qquad \gamma_\chi = \sum_{b=1}^{q} {}^{\chi}N^b \tilde{\gamma}_\chi^b \tag{5.53}$$

$$\lambda = \sum_{b=1}^{q} {}^{\chi}N^b \widetilde{\lambda}^b \quad \text{thus} \quad \Delta_\chi = \sum_{b=1}^{q} {}^{\chi}N^b \left(\widetilde{\lambda}^b + \mu_\chi \tilde{\gamma}_\chi^b\right) \tag{5.54}$$

where ${}^{u}N^{a}$ and ${}^{\chi}N^{b}$ are shape functions, the superscripts denoting the element node number. The deformation gradient $F_{ij}$ and the Lagrangian gradient of microslip $K_i$ are given by

$$F_{ij} = \sum_{a=1}^{p} {}^{u}B_j^a \widetilde{u}_i^a \qquad K_{\chi i} = \sum_{b=1}^{q} {}^{\chi}B_i^b \widetilde{\gamma}_\chi^b \tag{5.55}$$

with ${}^{u}B_j^a = \partial {}^{u}N^a / \partial X_j$ and ${}^{\chi}B_i^b = \partial {}^{\chi}N^b / \partial X_i$. Using these relations in Eqs. (5.50), (5.51) and (5.52) leads to

$$\begin{cases} \displaystyle\sum_{e=1}^{n} \int_{D_0^e} S_{ij} \sum_{a=1}^{p} {}^{u}B_j^a \dot{\widetilde{u}}_i^a \mathrm{d}V_0^e = \sum_{e=1}^{n_S} \int_{\partial D_0^e} T_i \sum_{a=1}^{p} {}^{u}N^a \dot{\widetilde{u}}_i^a \mathrm{d}S_0^e & (5.56) \\ \displaystyle\sum_{e=1}^{n} \int_{D_0^e} A \sum_{b=1}^{q} {}^{\chi}B_i^b \widetilde{\gamma}_\chi^b \sum_{b=1}^{q} {}^{\chi}B_i^b \dot{\widetilde{\gamma}}_\chi^b + \left( \sum_{b=1}^{q} {}^{\chi}N^b \left( \widetilde{\lambda}^b + \mu_\chi \widetilde{\gamma}_\chi^b \right) \right. & \\ \left. - \mu_\chi \gamma_M \displaystyle\sum_{b=1}^{q} {}^{\chi}N^b \dot{\widetilde{\gamma}}_\chi^b \mathrm{d}V_0^e = \sum_{e=1}^{n_S} \int_{\partial D_0^e} M \sum_{b=1}^{q} {}^{\chi}N^b \dot{\widetilde{\gamma}}_\chi^b \mathrm{d}S_0^e \right. & (5.57) \\ \displaystyle\sum_{e=1}^{n} \int_{D_0^e} \left( \sum_{b=1}^{q} {}^{\chi}N^b \widetilde{\gamma}_\chi^b - \gamma_M \right) \sum_{b=1}^{q} {}^{\chi}N^b \dot{\widetilde{\lambda}}^b \mathrm{d}V_0^e = 0 & (5.58) \end{cases}$$

which can be reformulated as

$$\begin{cases} \displaystyle\sum_{e=1}^{n} \sum_{a=1}^{p} \left[ \int_{D_0^e} S_{ij} {}^{u}B_j^a \mathrm{d}V_0^e \right] \dot{\widetilde{u}}_i^a = \sum_{e=1}^{n_S} \sum_{a=1}^{p} \left[ \int_{\partial D_0^e} T_i {}^{u}N^a \mathrm{d}S_0^e \right] \dot{\widetilde{u}}_i^a & (5.59) \\ \displaystyle\sum_{e=1}^{n} \sum_{b=1}^{q} \left[ \int_{D_0^e} A \sum_{k=1}^{q} {}^{\chi}B_i^k \widetilde{\gamma}_\chi^k {}^{\chi}B_i^b + \left( \sum_{k=1}^{q} {}^{\chi}N^k \left( \widetilde{\lambda}^k + \mu_\chi \widetilde{\gamma}_\chi^k \right) - \mu_\chi \gamma_M \right) {}^{\chi}N^b \mathrm{d}V_0^e \right] \dot{\widetilde{\gamma}}_\chi^b = & \\ \displaystyle\sum_{e=1}^{n_S} \sum_{b=1}^{q} \left[ \int_{\partial D_0^e} M {}^{\chi}N^b \mathrm{d}S_0^e \right] \dot{\widetilde{\gamma}}_\chi^b & (5.60) \\ \displaystyle\sum_{e=1}^{n} \sum_{b=1}^{q} \left[ \int_{D_0^e} \left( \sum_{k=1}^{q} {}^{\chi}N^k \widetilde{\gamma}_\chi^b - \gamma_M \right) {}^{\chi}N^b \mathrm{d}V_0^e \right] \dot{\widetilde{\lambda}}^b = 0 & (5.61) \end{cases}$$

According to Eqs. (5.59), (5.60), (5.61) an internal reaction is associated with each degree-of-freedom. $R^a_{\mathrm{int}(u_i,e)}$ refers to the internal reaction related to $u_i$ on node $a$ of element $e$

$$R^a_{\mathrm{int}(u_i,e)} = \int_{D_0^e} S_{ij} {}^{u}B_j^a \mathrm{d}V_0^e \tag{5.62}$$

and to $R^b_{\mathrm{int}(\gamma_\chi,\mathrm{e})}$ (resp. $R^b_{\mathrm{int}(\lambda,e)}$) as the internal reaction related to $\gamma_\chi$ (resp. $\lambda$) on node $b$ of element $e$

$$R^b_{\mathrm{int}(\gamma_\chi,\mathrm{e})} = \int_{D_0^e} A \sum_{k=1}^{q} {}^{\chi}B_i^k \widetilde{\gamma}_\chi^k {}^{\chi}B_i^b + \left( \sum_{k=1}^{q} {}^{\chi}N^k \left( \widetilde{\lambda}^k + \mu_\chi \widetilde{\gamma}_\chi^k \right) - \mu_\chi \gamma_M \right) {}^{\chi}N^b \mathrm{d}V_0^e \tag{5.63}$$

$$R^b_{\mathrm{int}(\lambda,e)} = \int_{D_0^e} \left( \sum_{k=1}^{q} {}^{\chi}N^k \widetilde{\gamma}_\chi^b - \gamma_M \right) {}^{\chi}N^b \mathrm{d}V_0^e \tag{5.64}$$

Analogously, an external reaction is associated to each degree of freedom. $R^a_{\mathrm{ext}(u_i,e)}$, $R^b_{\mathrm{ext}(\gamma_\chi,e)}$, $R^b_{\mathrm{ext}(\lambda,e)}$ refer to the external reactions related to $u_i$ on node $a$, $\gamma_\chi$ and $\lambda$ on node $b$ of element $e$

$$R^a_{\mathrm{ext}(u_i,e)} = \int_{\partial D_0^e} T_i {}^{u}N^a \mathrm{d}S_0^e \qquad R^b_{\mathrm{ext}(\gamma_\chi,e)} = \int_{\partial D_0^e} M {}^{\chi}N^b \mathrm{d}S_0^e \qquad R^b_{\mathrm{ext}(\lambda,e)} = 0 \tag{5.65}$$

With these expressions Eqs. (5.59), (5.60), (5.61) write

$$\begin{cases} \displaystyle\sum_{e=1}^{n}\sum_{a=1}^{p} R^a_{\text{int}(u_i,e)}\dot{\tilde{u}}^a_i = \sum_{e=1}^{n_S}\sum_{a=1}^{p} R^a_{\text{ext}(u_i,e)}\dot{\tilde{u}}^a_i & (5.66)\\ \displaystyle\sum_{e=1}^{n}\sum_{b=1}^{q} R^b_{\text{int}(\gamma_\chi,e)}\dot{\tilde{\gamma}}^b_\chi = \sum_{e=1}^{n_S}\sum_{b=1}^{q} R^b_{\text{ext}(\gamma_\chi,e)}\dot{\tilde{\gamma}}^b_\chi & (5.67)\\ \displaystyle\sum_{e=1}^{n}\sum_{b=1}^{q} R^b_{\text{int}(\lambda,e)}\dot{\tilde{\lambda}}^b = \sum_{e=1}^{n_S}\sum_{b=1}^{q} R^b_{\text{ext}(\lambda,e)}\dot{\tilde{\lambda}}^b & (5.68) \end{cases}$$

This system of equations is solved using Newton's method. The details of the numerical implementation are given in Appendices G and H. As this work proceeds, quadratic (resp. linear) interpolation functions are used for the displacement (resp. microslip and Lagrange multiplier) degrees of freedom.

## 5.5 Numerical examples

### 5.5.1 1D localization band formation

#### 5.5.1.1 Validation of the Lagrange multiplier implementation

Validation of the implementation is done by solving the problem of a periodic bar of length $L$ along $\underline{\boldsymbol{X}}_2$ (see Figure 5.1a) in simple shear with a single slip system and a linear softening behavior ($H < 0$)

$$\tau_c(\gamma) = \tau_0 + H\gamma \tag{5.69}$$

Such a hardening behaviour corresponds to a hardening free energy potential $\psi_h = H\gamma^2/2$. In the reference configuration, the gliding direction $\underline{\boldsymbol{m}}$ is aligned with $\underline{\boldsymbol{X}}_1$, the normal to the slip plane $\underline{\boldsymbol{n}}$ is aligned with $\underline{\boldsymbol{X}}_2$. A macroscopic shear deformation $\overline{\underset{\sim}{\boldsymbol{F}}} = \underset{\sim}{\mathbf{1}} + \overline{F}_{12}\underline{\boldsymbol{m}} \otimes \underline{\boldsymbol{n}}$ is imposed such that the displacement field is given by $\underline{\boldsymbol{u}} = (\overline{\underset{\sim}{\boldsymbol{F}}} - \underset{\sim}{\mathbf{1}}).\underline{\boldsymbol{X}} + \underline{\boldsymbol{v}}(\underline{\boldsymbol{X}})$. Periodic boundary conditions are imposed on the displacement fluctuation $\underline{\boldsymbol{v}}$, micro-slip variable $\gamma_\chi$ and Lagrange multiplier $\lambda$. As discussed in (Scherer et al., 2019) the analytical solution to this problem, in terms of plastic slip, is a localization band following a sine shape within the $[-\lambda_0/2; \lambda_0/2]$ region and no slip elsewhere

$$\gamma(X_2, \overline{F}_{12}) = \begin{cases} \dfrac{|\tau| - \tau_0}{H}\left(\cos\left(2\pi\dfrac{X_2}{\lambda_0}\right) + 1\right) & \text{if} \quad X_2 \in \left[-\dfrac{\lambda_0}{2}; \dfrac{\lambda_0}{2}\right] \\ 0 & \text{if} \quad X_2 \in \left[-\dfrac{L}{2}; -\dfrac{\lambda_0}{2}\right] \cup \left[\dfrac{\lambda_0}{2}; \dfrac{L}{2}\right] \end{cases} \tag{5.70}$$

with the wavelength $\lambda_0 = 2\pi\sqrt{A/|H|}$, where $H$ is the slope of linear softening. It is important to notice that in the context of the Lagrange multiplier approach, when the penalty factor $\mu_\chi = 0$, the Lagrange multiplier $\lambda$, which is a degree of freedom, coincides with the Laplacian of $\gamma$ in this elementary problem. Yet, it can be noted from Eq. (5.70) that the Laplacian of $\gamma$ takes the form

$$\Delta\gamma(X_2, \overline{F}_{12}) = \begin{cases} -\left(\dfrac{2\pi}{\lambda_0}\right)^2 \dfrac{|\tau| - \tau_0}{H}\cos\left(2\pi\dfrac{X_2}{\lambda_0}\right) & \text{if} \quad X_2 \in \left[-\dfrac{\lambda_0}{2}; \dfrac{\lambda_0}{2}\right] \\ 0 & \text{if} \quad X_2 \in \left[-\dfrac{L}{2}; -\dfrac{\lambda_0}{2}\right] \cup \left[\dfrac{\lambda_0}{2}; \dfrac{L}{2}\right] \end{cases} \tag{5.71}$$

which is discontinuous in $\pm\lambda_0/2$. Therefore solving numerically this problem by finite elements with standard continuous shape functions might lead to difficulties. Figure 5.1b and 5.1c show the finite element solutions to this problem in case $\mu_\chi = 0$, for discretizations of respectively $n = 51$ and $n = 201$ elements along the $\underline{\boldsymbol{X}}_2$ direction of the bar and a wavelength $\lambda_0 = L/2$. It is observed that strong oscillations of plastic slip (solid red line) occur around the analytical solution (dashed black line) for both finite element discretizations. These oscillations are caused by abnormal fluctuations of the Lagrange multiplier (solid blue line) also plotted on the same figures. Fluctuations are probably due to poor approximations of the Lagrange multiplier degree of freedom at the discontinuity. This issue can be solved by using the Lagrangian penalization term in Eq. (5.36). The additional penalty term is very similar to the micromorphic penalization, but it bears a completely different meaning. While in the micromorphic approach $H_\chi$ has to be large in order to ensure quasi-equality between $\gamma_{cum}$ and $\gamma_\chi$, in the Lagrange multiplier approach $\mu_\chi$ only helps to provide additional coercivity and can take much lower values in practice. Figure 5.1d and 5.1e show the finite element solution of the periodic bar in simple shear when $\mu_\chi = 50\,\text{MPa}$ for $n = 51$ and $n = 201$. It can be observed that the oscillations almost vanish everywhere, except at $\pm\lambda_0/2$ where their amplitude is much lower and that a smooth solution coinciding with the analytical solution is obtained everywhere else. Another possible alternative to properly account for the discontinuity of the Lagrange multiplier could be to use a discontinuous Galerkin finite element formulation (Cockburn et al., 2012; Hughes et al., 2006).

Another observation can be made on the interdependence between mesh density and the value of $\mu_\chi$ which yields a smooth profile of $\Delta_\chi$. The profiles of $\Delta_\chi$ in a reduced region of the bar for several values of $\mu_\chi$ and the two different mesh densities $n = 51$ and $n = 201$ are plotted in Figure 5.2. It can be seen that if the value of $\mu_\chi$ is not large enough, oscillations of $\Delta_\chi$ are still observed even if $\mu_\chi \neq 0$. Increasing the value of $\mu_\chi$ tends to smooth out the profile of $\Delta_\chi$. In this example, no clear evolution of the profile can be observed for values of $\mu_\chi$ greater than or equal to 10 MPa. The results obtained with $\mu_\chi = 5$ MPa suggest that at a given value of $\mu_\chi$, a finer mesh leads to a smoother profile of the Laplacian term $\Delta_\chi$. In other words, increasing the discretization reduces the value of $\mu_\chi$ required to obtain a smooth profile of $\Delta_\chi$.

#### 5.5.1.2 Computational efficiency

The computational efficiency of both relaxed formulations for the rate-independent and viscous settings are compared in this section. The four possible variants (micromorphic or Lagrange multiplier approach and rate-dependent or rate-independent formulation) are used to solve the localization problem presented above. It can be shown that the shear stress $\tau$ is uniform. In order for the results to be comparable in terms of computational efficiency, the viscous stress $\tau_{vs} = \tau_0(\dot{\gamma}/\dot{\gamma}_0)^{1/n}$, for the rate-dependent setting, and the overstress $\tau_{os} = R(\dot{\gamma}/\dot{\varepsilon}_{eq})$, for the rate-independent setting, need to be calibrated in order for the numerical solution to be close to the rate-independent solution without overstress with a given precision. The macroscopic shear strain rate is chosen to be $\dot{\overline{F}}_{12} = 10^{-2}\ \text{s}^{-1}$. From the analytical expression of $\tau = (\overline{F}_{12} + \tau_0/Z_e)/(1/C_{44} + 1/Z_e)$ with $1/Z_e = \lambda_0/HL$ derived in (Scherer et al., 2019) it follows that the maximum viscous stress is

$$\tau_{vs}^{max} = \tau_0 \left( \frac{2\dot{\overline{F}}_{12}}{\dot{\gamma}_0 H \left( \frac{1}{C_{44}} + \frac{1}{Z_e} \right)} \right)^{1/n} \tag{5.72}$$

while the rate-independent overstress is uniform and given by

$$\tau_{os} = \frac{\sqrt{3}R}{H \left( \frac{1}{C_{44}} + \frac{1}{Z_e} \right)} \tag{5.73}$$

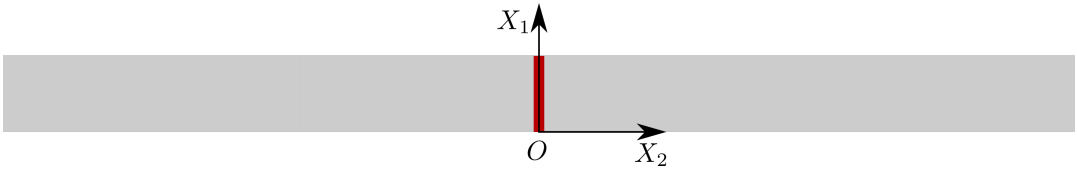


(a)

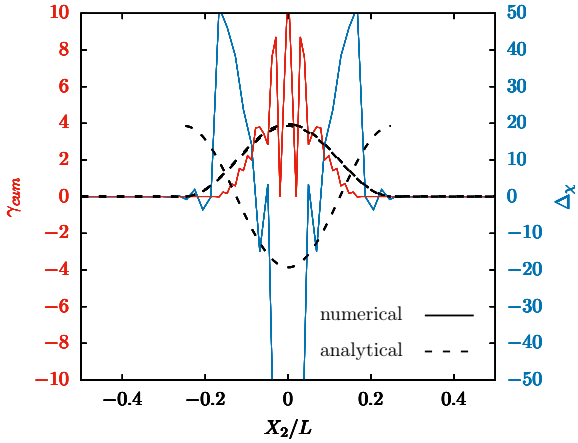


(b) $n = 51$ and $\mu_\chi = 0\,\mathrm{MPa}$

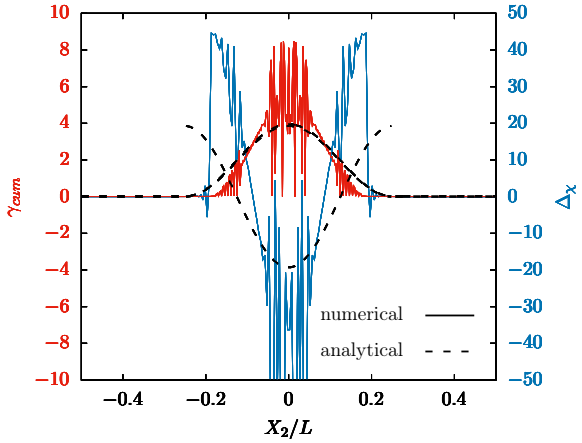


(c) $n = 201$ and $\mu_\chi = 0\,\mathrm{MPa}$

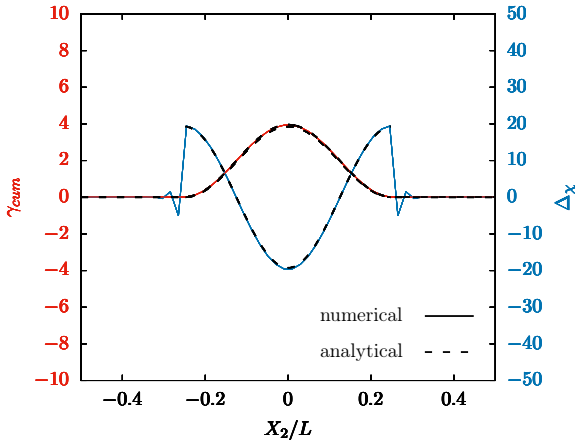


(d) $n = 51$ and $\mu_\chi = 50\,\mathrm{MPa}$

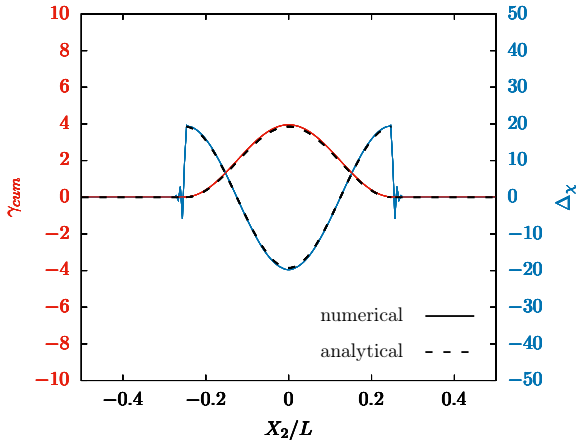


(e) $n = 201$ and $\mu_\chi = 50\,\mathrm{MPa}$

Figure 5.1 (a) Geometry of the periodic bar. (b-e) Analytical (dashed black lines) and numerical (solid blue and red lines) solutions of accumulated plastic slip $\gamma_\chi$ (red) and Laplacian term $\Delta_\chi$ (blue) along a periodic strip in simple shear for a linear softening behaviour (For interpretation of the references to color in this figure caption, the reader is referred to the web version of this paper).

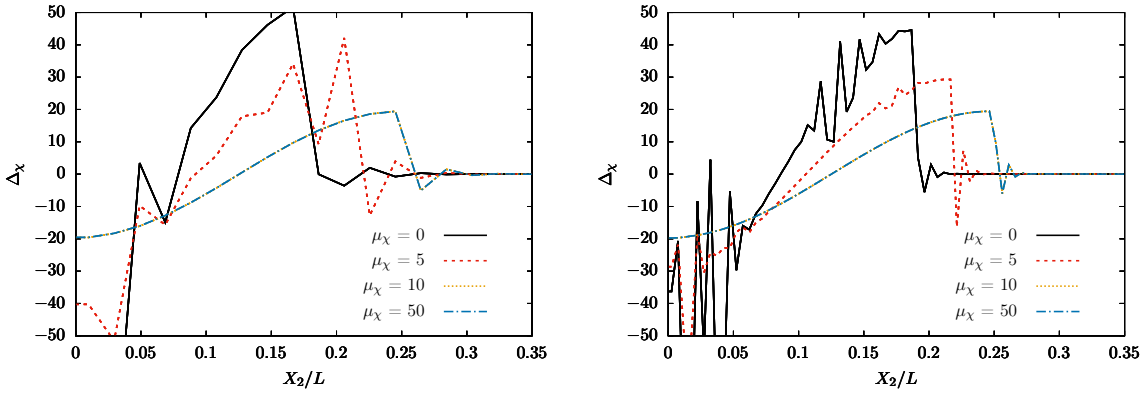


(a) $n = 51$ (b) $n = 201$

Figure 5.2 Numerical solutions of the Laplacian term $\Delta_\chi$ profile along a periodic strip in simple shear for several values of $\mu_\chi$. The discretization is $n = 51$ elements in (a) and $n = 201$ elements in (b).

Table 5.2 Numerical values of material parameters for the comparison of computational efficiencies.

| $C_{44}$ | $\tau_0$ | $H$ | $H_\chi$ | $\mu_\chi$ | $n$ | $\dot{\gamma}_0$ | $R$ |
|---|---|---|---|---|---|---|---|
| 105 GPa | 100 MPa | −10 MPa | $5 \times 10^4$ MPa | 50 MPa | 15 | $10^{30}\,\mathrm{s}^{-1}$ | 0.1 MPa |

$\dot{\gamma}_0$, $n$ and $R$ are chosen such that $\tau_{vs}^{max}$ and $\tau_{os}$ are less than 1% of $\tau_0$. The material parameter used are summarized in Table 5.2. Four different values of $A$ are chosen such that $\lambda_0/L = 2\pi\sqrt{A/|H|}/L$ takes the following values $[0.25; 0.5; 0.75; 1]$. The one-element thick bar is meshed with $n = 201$ quadratic elements with reduced integration (C3D20R). In the micromorphic approach each node has three displacement degrees of freedom and the linear nodes have one additional degree of freedom $\gamma_\chi$. In the Lagrange multiplier approach each node has three displacement degrees of freedom and the linear nodes have two additional degrees of freedom $\gamma_\chi$ and $\lambda$. The number of degrees of freedom in the micromorphic simulations is $n_{DOF} = 4077$, while it is $n_{DOF} = 4485$ with the Lagrange multiplier based formulation. Results not shown here exhibit an overall discrepancy of less than 1% on the predicted numerical $\gamma$ field between the four formulations after a mean shear deformation gradient of $\overline{F}_{12} = 100\%$. All simulations are also in excellent agreement with the analytical solution. Simulations were ran on a single Intel Core i7-7600U CPU. Reference computation time is $T_{ref} = 2316\,\mathrm{s}$ and corresponds to the time needed for the viscous micromorphic formulation to reach $\overline{F}_{12} = 100\%$ with $\lambda_0/L_0 = 0.25$. The relative computation times for the four different values of $\lambda_0/L$ and four different formulations are displayed in Figure 5.3.

First, despite the slightly larger number of degrees of freedom, the computational cost reduction obtained with the Lagrange multiplier based formulation, as compared to the micromorphic approach, is striking. In the rate-dependent setting this speedup ranges from 30 up to almost 200. In the rate-independent setting this speedup ranges between 1.5 and 70. Regarding the micromorphic implementation only, the speedup obtained with the rate-independent setting, as compared to the viscous setting, ranges from more than 2.5 to about 17 as the ratio $\lambda_0/L$ increases. Furthermore, regarding the Lagrange multiplier formulation only, the rate-dependent and rate-independent settings have very similar computational performances. The

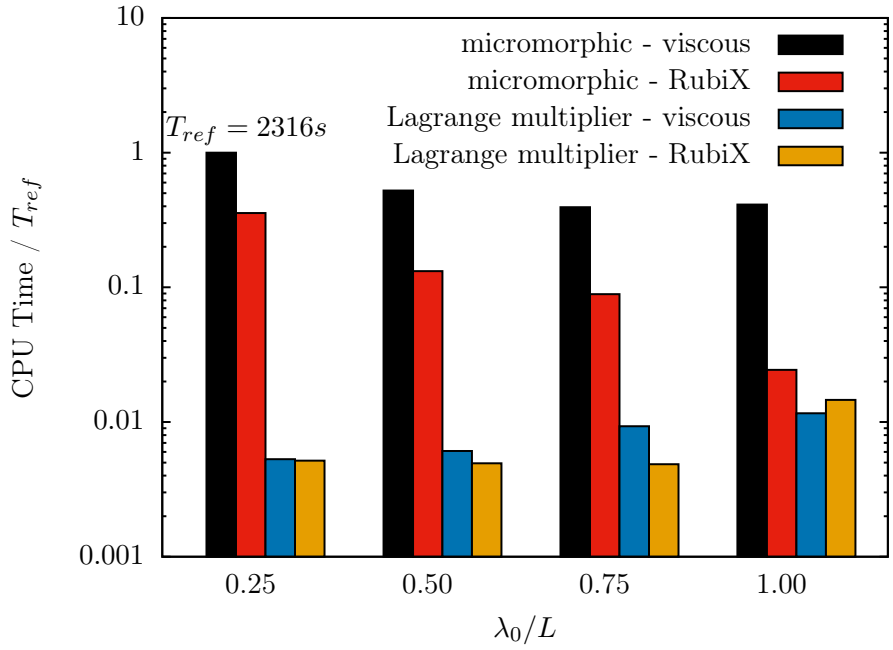


Figure 5.3 Computation times for the finite element resolution of the periodic strip in simple shear and single slip for four different $\Lambda_0/L$ ratios and four different formulations.

rate-independent setting is slightly more efficient for the lowest $\lambda_0/L$ ratios, while on the contrary the rate-dependent formulation performs better at $\lambda_0/L = 1$.

The rate of convergence in the local integration scheme was checked for the micromorphic and Lagrange multiplier approaches. Both methods display a very similar rate of convergence that is very close to the quadratic bound of a Newton scheme. The gap of performances between the two implementations is in fact attributed to the poor conditioning of the local Jacobian matrix when the penalization modulus $H_\chi$ is taken large. Pre-conditioning techniques could be applied in order to enhance the performances of the micromophic approach.

As this work proceeds, the rate-dependent setting is adopted and results obtained with micromorphic and Lagrange multiplier approaches are compared. As already discussed by (Cordero et al., 2010) micromorphic and strict strain gradient formulations, such as the Lagrange multiplier based formulation, are indeed not always strictly equivalent. Therefore the choice of the appropriate formulation should not only be motivated by the computational efficiency but also by the desired scaling law.

### 5.5.2 Size effects in torsion tests

The torsion of single and polycrystal wires has been the subject of intensive experimental and computational research. Nouailhas and Cailletaud (1995) discovered that the torsion of a single crystal bar or tube is characterized by two types of strain gradients: a radial gradient from the center to the outer surface due to the loading, but also a gradient along the outer circumference due to the anisotropic activation of slip systems. This was observed experimentally by means of strain gauges placed along the circumference (Forest et al., 1996). The transition from single to polycrystals for microwires of increasing diameters was computed using finite element crystal plasticity in (Quilici et al., 1998) and more recently in (Bayerschen, 2016). The size–dependent torsion of FCC single crystal bars is investigated below by means of the proposed micromorphic and strain gradient plasticity models.

#### 5.5.2.1 Problem setup

Simulations are performed with a single crystal cylindrical microwire of diameter $D = 2R_0$ meshed with elements that are quadratic for displacements degrees of freedom and linear for $\gamma_\chi$ and $\lambda$. Quadratic shape function are used for displacements degrees of freedom because they are known to provide better interpolation accuracy than linear shape functions. Furthermore, quadratic elements are also known to be less subject to locking issues. However linear shape functions are used for $\gamma_\chi$ and $\lambda$ in order to limit the number of degrees of freedom. It is in fact assumed that plastic deformations vary less rapidly than displacements, in such a way that linear shape functions give sufficient precision to interpolate accumulated plastic slip. With the formalism developed in this work quadratic shape function for $\gamma_\chi$ and $\lambda$ could also have been used. As reduced integration involves a lesser number of integration points than full integration, 20-node brick elements with reduced integration possessing 8 Gauss points (instead of 27 for full integration) are used. Reducing the number of integration points clearly decreases the accuracy of the integration, but it also reduces the computational cost. Furthermore, reduced integrated elements are known to be less stiff than fully integrated elements. Therefore, reduced integration is often recommended in order to avoid the problem of locking and possible oscillations. Yet, reduced integration can lead to hourglassing issues when the element stiffness matrix is zero. In this work methods to prevent hourglass were not used, but no significant hourglass modes could be observed in the simulations which are presented below. Yet, several ways to address hourglassing have been proposed in literature (Belytschko et al., 1984): inserting an artificial stiffness to the hourglass deformation modes, inserting an artificial viscosity, refining the mesh, *etc.* The bottom face of the microwire is clamped while the top surface undergoes a rigid body rotation around the wire axis. The lateral faces are kept traction free, which means that $\underline{\boldsymbol{T}} = 0$ and $M = 0$ from Eq. (5.25) and (5.26). Two orientations of the single crystal are considered: <001> and <111> aligned with the microwire axis. The geometry and the boundary conditions are as shown in Figure 5.4. The Cartesian coordinate system is chosen for the two microwire single crystals (later respectively denoted <001> and <111>) such that

$$\underline{\boldsymbol{X}}_1 = [110] \quad \underline{\boldsymbol{X}}_2 = [1\bar{1}0] \quad \underline{\boldsymbol{X}}_3 = [001] \tag{5.74}$$

and

$$\underline{\boldsymbol{X}}_1 = [\bar{1}\bar{1}2] \quad \underline{\boldsymbol{X}}_2 = [1\bar{1}0] \quad \underline{\boldsymbol{X}}_3 = [111] \tag{5.75}$$

respectively.

Face-centered cubic (FCC) single crystal microwires are simulated. The hardening laws per slip system are based on the evolution of usual scalar dislocation densities. The hardening term accounts for lattice friction and dislocation interactions (Kubin et al., 2008). The critical resolved shear stress (CRSS) is taken as:

$$\tau_c^s = \tau_0 + \mu \sqrt{\sum_{u=1}^{12} a^{su} r^u} \tag{5.76}$$

where $\tau_0$ is the thermal component of the CRSS due to lattice friction, $r^u$ denotes adimensional dislocation density ($r^u/b^2 = \rho^u$ is the usual dislocation density, *i.e.* the length of dislocation lines per unit volume, $b$ is the norm of the dislocation Burgers vector $\underline{\boldsymbol{b}}$), $\mu$ is the shear modulus, and $a^{su}$ is a matrix describing interactions between dislocations. Such an hardening behaviour is standard in the literature, but the link to a free energy potential $\psi_h$ remains an open question. The evolution equation for the adimensional dislocation density $r^s$

$$\dot{r}^s = |\dot{\gamma}^s| \left( \frac{\sqrt{\sum_{u=1}^{12} b^{su} r^u}}{\kappa} - G_c r^s \right) \tag{5.77}$$

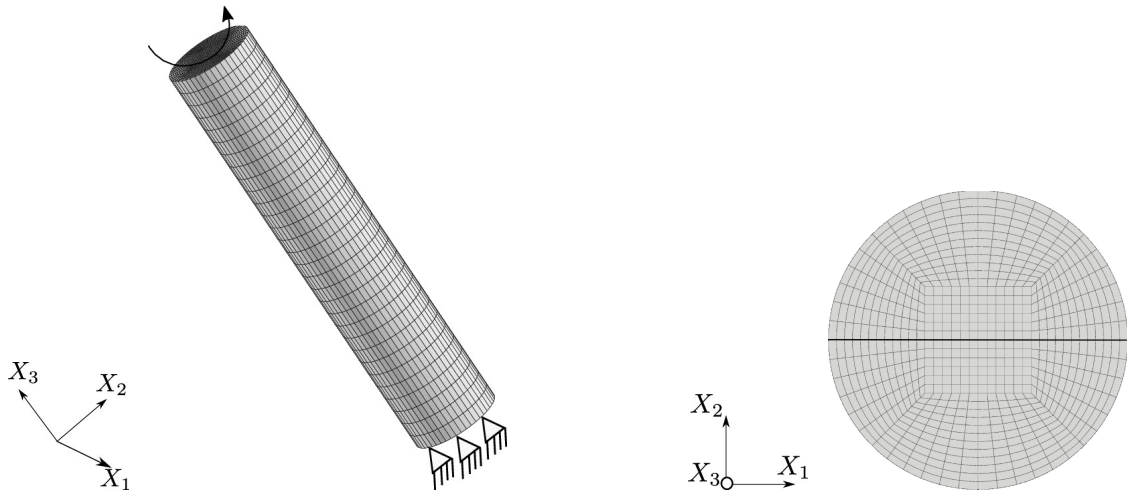


(a) (b)

Figure 5.4 Microwire torsion (a) boundary conditions (b) example mesh from the top side in which the black line represents an initial material line. For the <001> crystal orientation the black line is oriented along a <110> direction. For the <111> crystal orientation it is oriented along a $<11\bar{2}>$ direction.

Table 5.3 Numerical values of material parameters for the simulation of microwires in torsion.

| $C_{11}$ | $C_{12}$ | $C_{44}$ | $\tau_0$ | $n$ | $\dot{\gamma}_0$ | $\mu$ | $G_c$ |
|---|---|---|---|---|---|---|---|
| 259.6 GPa | 179 GPa | 109.6 GPa | 320 MPa | 20 | $10^{33}\,\mathrm{s}^{-1}$ | 77.2 GPa | 10.4 |

| $\kappa$ | $r_0^s$ | $a^{su}$ | $b^{su}$ $(s \neq u)$ | $b^{uu}$ | $H_\chi$ | $\mu_\chi$ |
|---|---|---|---|---|---|---|
| 42.8 | $5.38 \times 10^{-11}$ | 0.124 | 1 | 0 | $10^4$ MPa | $10^3$ MPa |

accounts for multiplication and annihilation of dislocations. The parameter $\kappa$ is proportional to the number of obstacles crossed by a dislocation before being immobilized, $G_c$ is the critical distance controlling the annihilation of dislocations with opposite signs, and $b^{su}$ describes the interactions between dislocations. The structures of the matrices $a^{su}$ and $b^{su}$ are given in (Ling et al., 2018) for FCC crystals. Cubic elasticity is considered. The wrought Inconel 718 material parameters at room temperature used for the numerical simulation are given in Table 5.3. $r_0^s$ denotes the initial value of the adimensional dislocation density, which is assumed to be the same for all slip systems. The various intrinsic length scale to diameter ratios ($\ell/2R_0$) considered in the simulations are given in Table 5.4.

#### 5.5.2.2 Results and discussion

Figure 5.5 and 5.6 show the accumulated plastic strain fields in the deformed configuration for FCC single crystals with wire axis parallel to <001> and <111> respectively. A cross section of each sample is illustrated in Figure 5.5 and 5.6. The radial and circumferential plastic strain gradients are clearly visible. A four-fold pattern is observed for the <001> specimen with maximum plastic strain values along <100> directions. A six-fold pattern is observed for the

Table 5.4 Numerical values of $\ell/2R_0$ ratios for the simulation of microwires in torsion.

| $\ell/2R_0$ <001> | 0.03 | 0.07 | 0.10 | 0.31 | 0.44 | 0.54 |
|---|---|---|---|---|---|---|
| $\ell/2R_0$ <111> | 0.03 | 0.08 | 0.11 | 0.35 | 0.50 | 0.61 |

<111> specimen with maximum plastic strain values along <11$\bar{2}$> directions. The overall curves are presented using normalized torque $T/R_0^3$ as a function of surface strain $\gamma_R$ defined as

$$\gamma_R = kR \tag{5.78}$$

where $k$ is the applied twist per unit length ($\theta/L$). They are given in Figure 5.7 for the two single crystal orientations <001> and <111> using classical crystal plasticity. The <001> crystal orientation is found to be significantly stronger than the <111> wire. The orientation of the crystal to the loading direction causes different slip activity and results in different mechanical responses. The twist angle at the cross-section of the microwire is calculated as $\theta_h = \theta h/L$, where $h$ is the height from the bottom end. The initial material line for <001> and <111> crystal orientation is shown in Figure 5.4b. The rotation of material line with increasing surface strain is as shown in Figure 5.5 and 5.6. The response of the micromorphic wire is also provided in Figure 5.7 for comparison for a given internal length value. In the micromorphic approach, the penalty parameter $H_\chi$ is chosen sufficiently large for $\gamma_{cum}$ and $\gamma_\chi$ to almost coincide. The chosen value of $H_\chi$ in the simulation is $10^4$ MPa. The intrinsic length scale ($\ell$) considered in the simulation is defined as $\ell = \sqrt{A/|H|}$ as proposed in (Ling et al., 2018), where $H$ is the initial equivalent linear hardening modulus. $H$ is estimated by performing uniaxial tensile test on one element as proposed in (Ling, 2017). Its value is given by the ratio of $\tau^s$ and $\gamma^s$ for one activated slip system at the beginning of its activation. Thus the estimated $H$ values for <001> and <111> crystal orientation are 2500 MPa and 2000 MPa respectively. The intrinsic length scale can be varied by varying the constitutive parameter $A$. The various values of $A$ and of the intrinsic length scale to diameter ratio ($\ell/2R_0$) of microwire are given in the Table 5.4. The micromorphic response in Figure 5.7 exhibits a linear hardening of the wire in contrast to the saturated classical crystal plasticity response. The magnitude of the slope depends on the value of the internal length as demonstrated in the following.

The effect of different ratios $\ell/2R_0$ on the size effects in torsion microwires has been studied for the two models considered in this work, namely the micromorphic and strain gradient plasticity formulations. The torque *vs* surface strain curves of the micromorphic model are compared with the Lagrange multiplier based model. The cumulative plastic strain ($\gamma_{cum}$) fields for different $\ell/2R_0$ of microwire ($\ell/2R_0 = 0.03, 0.07, 0.10$ and $0.44$ for <001> and $\ell/2R_0 = 0.03, 0.08, 0.11$ and $0.50$ for <111> crystal orientation) obtained using both models are shown in Figure 5.8 and 5.9. It can be seen that, for low and intermediate values of the ratio $\ell/2R_0$, the two models predict the same accumulated plastic slip fields. In contrast, for the larger value $\ell/2R_0 = 0.31$, the circumferential gradient has almost disappeared according to the Lagrange multiplier based model whereas it is still present in the micromorphic simulation. Increasing the length scale for a fixed wire diameter leads to a strong decrease of the plastic strain gradient. This can be attributed to the fact that the energetic cost of plastic strain gradient increases with $\ell$ and the free energy of the sample is minimum for a limited value of the gradient. These observations are valid for both orientations <001> and <111>. It is remarkable that the four-fold and six-fold patterns disappear for large enough internal length scale values.

The corresponding torque *vs* surface strain curves are provided in Figure 5.10 and 5.11. They clearly show the size-dependent hardening effect for both models. For small and intermediate values of the internal length, the micromorphic and Lagrange multiplier models are found to deliver the same overall responses. This result is expected since the value of penalty parameter

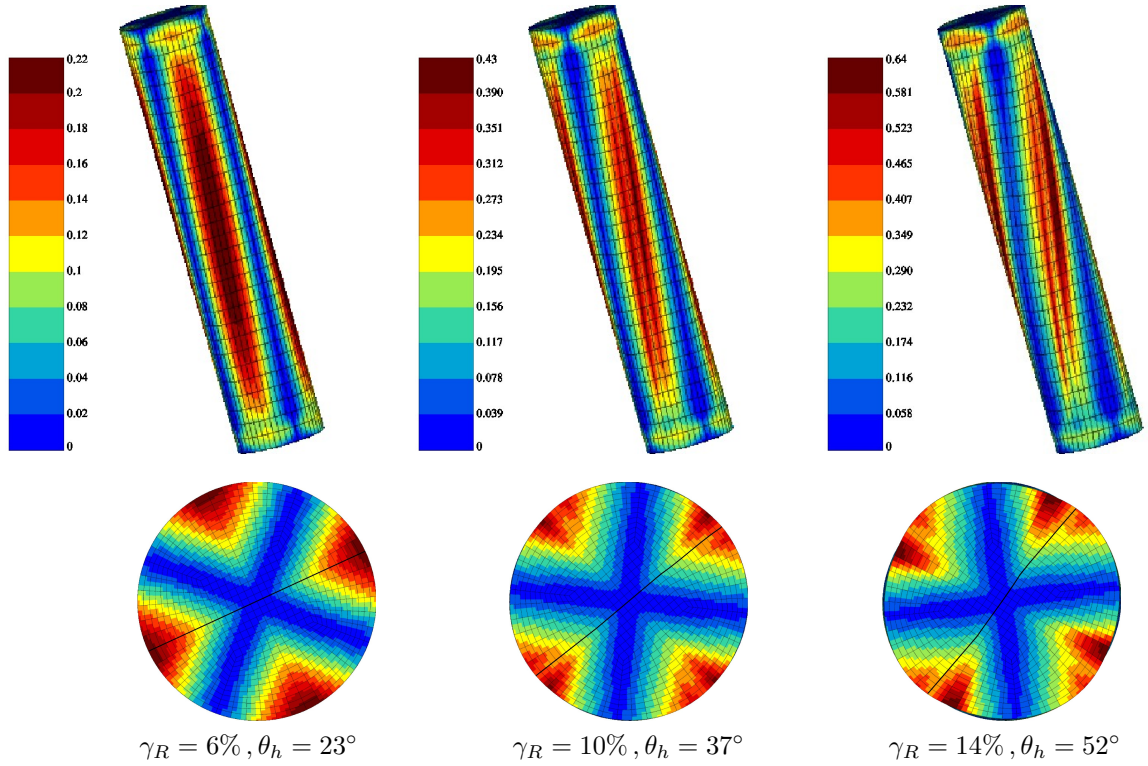


$\gamma_R = 6\% \, , \theta_h = 23^\circ$ $\gamma_R = 10\% \, , \theta_h = 37^\circ$ $\gamma_R = 14\% \, , \theta_h = 52^\circ$

Figure 5.5 Cumulative plastic strain ($\gamma_{cum}$) field in FCC single crystal for <001> crystal orientation in classical crystal plasticity with respect to deformed configuration. The rotation of material line shown in Figure 5.4b with increasing surface strain is shown by a black line on the cross-section.

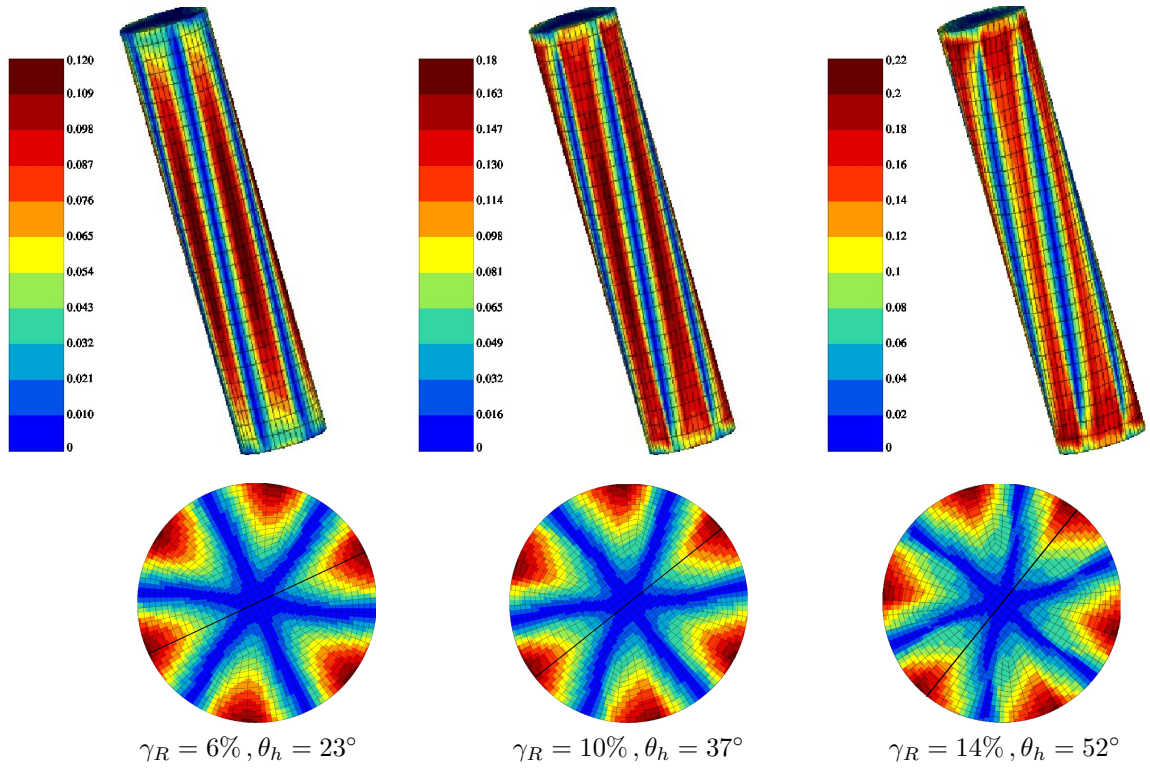


Figure 5.6 Cumulative plastic strain ($\gamma_{cum}$) field in FCC single crystal for <111> crystal orientation in classical crystal plasticity with respect to deformed configuration. The material line shown in Figure 5.4b and its rotation with increasing surface strain are shown by a black line on the cross-section.

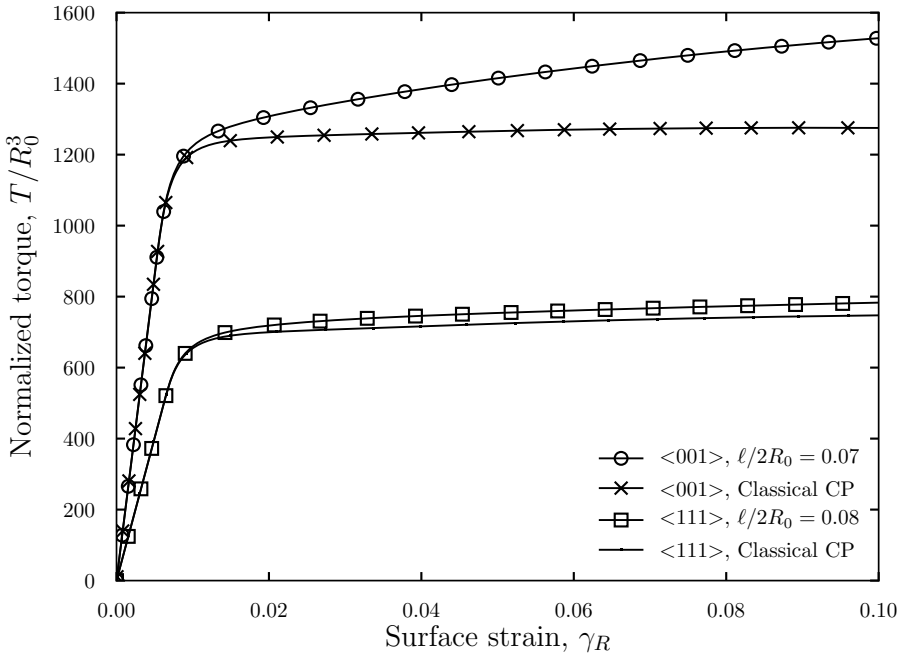


Figure 5.7 Shear stress *vs* surface strain in FCC single crystal wires for <001> and <111> crystal orientation using classical crystal plasticity and micromorphic models.

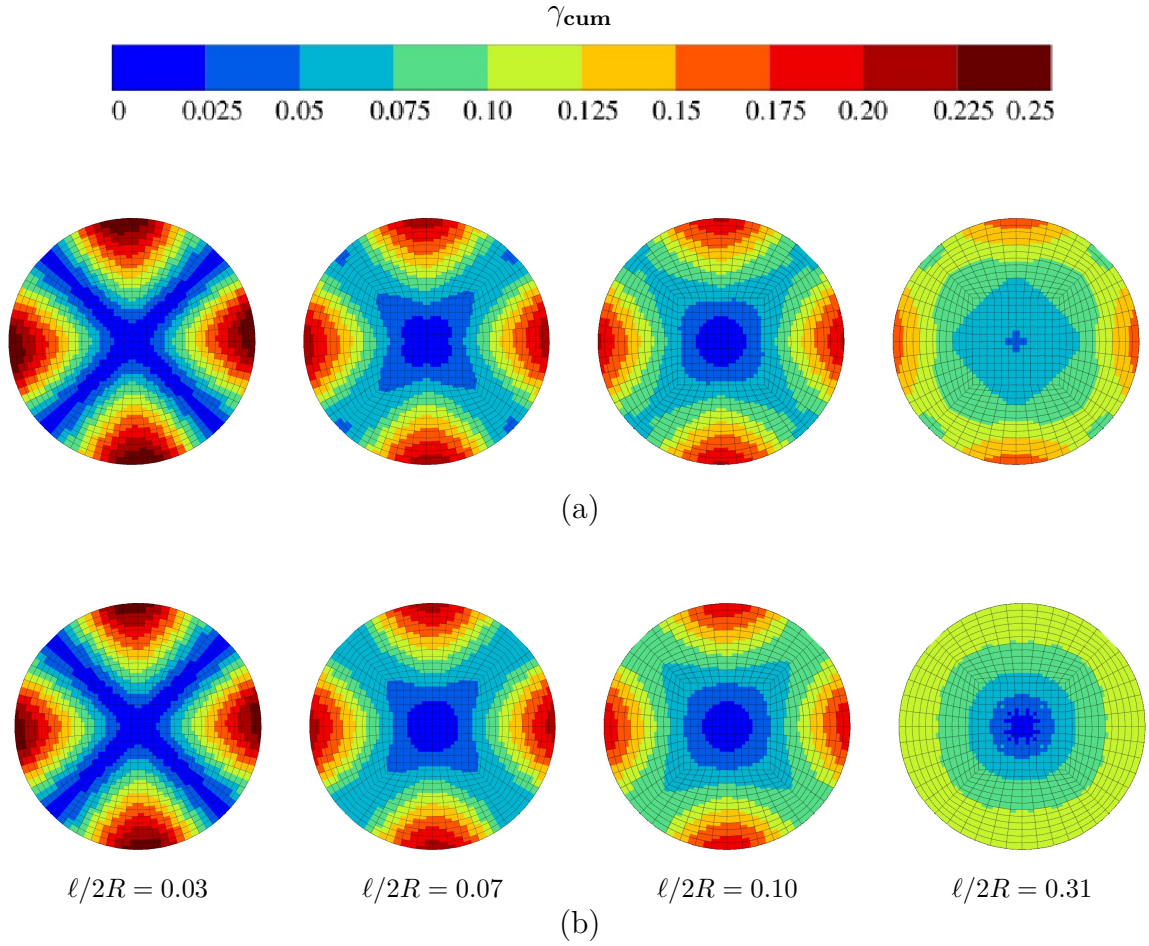


Figure 5.8 Cumulative plastic strain distribution in FCC single crystal for <001> crystal orientation for different values of ratio $\ell/2R_0$ using (a) micromorphic (b) Lagrange multiplier models at surface strain of 0.08 (fields reported on the reference configuration).

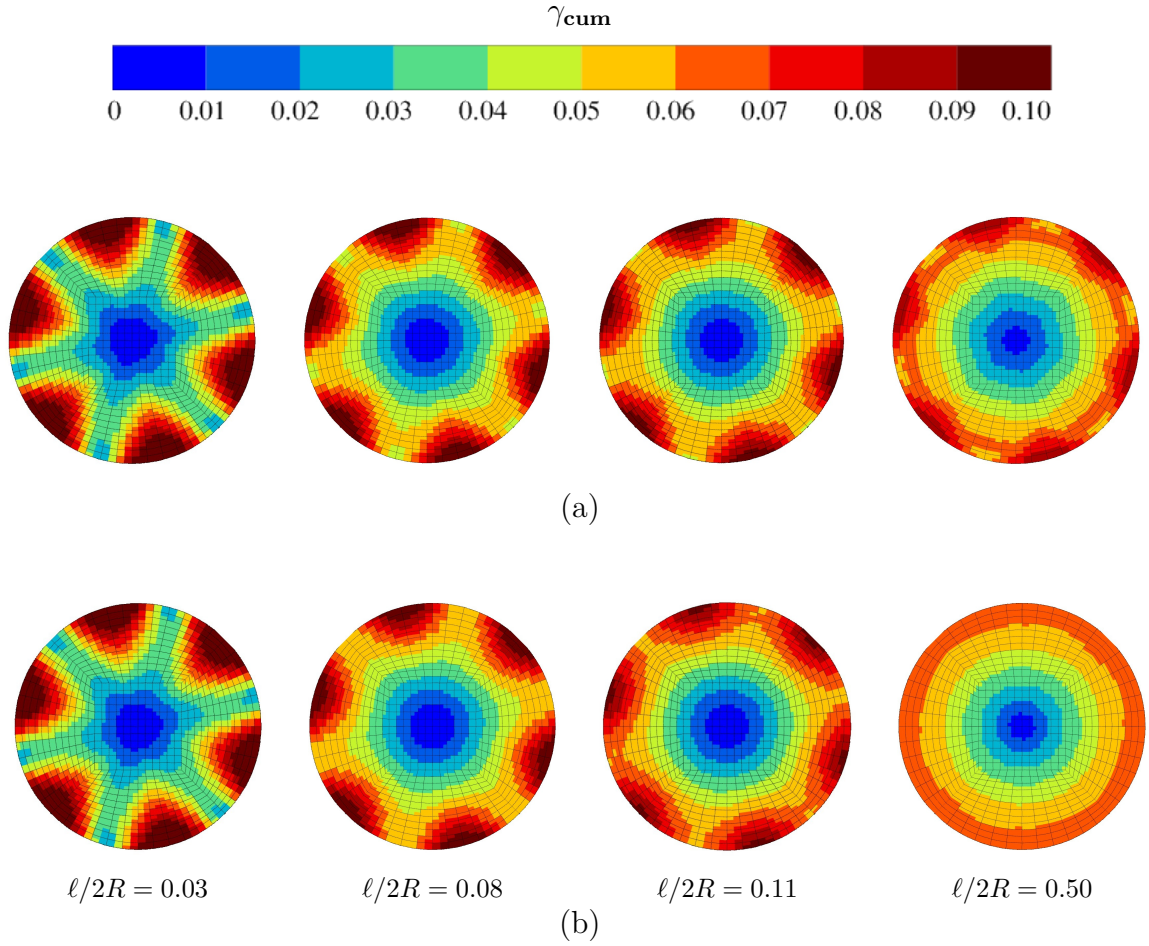


Figure 5.9 Cumulative plastic strain distribution in FCC single crystal for <111> crystal orientation for different values of ratio $\ell/2R_0$ using (a) micromorphic (b) Lagrange multiplier models at surface strain of 0.08 (fields reported on the reference configuration).

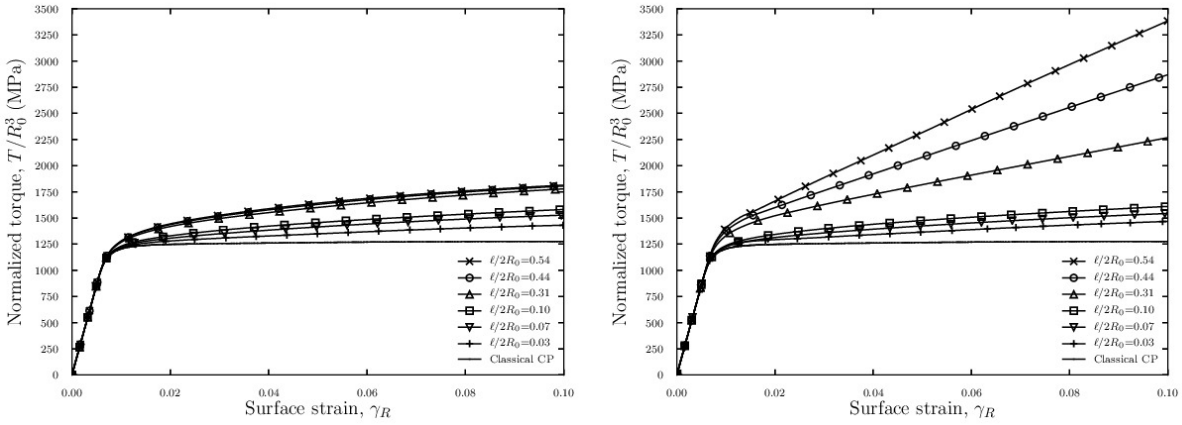


(a) (b)

Figure 5.10 Normalized torque *vs* surface strain curves for FCC <001> crystal orientation for different values of ratio $\ell/2R_0$ using (a) micromorphic (b) Lagrange multiplier models.

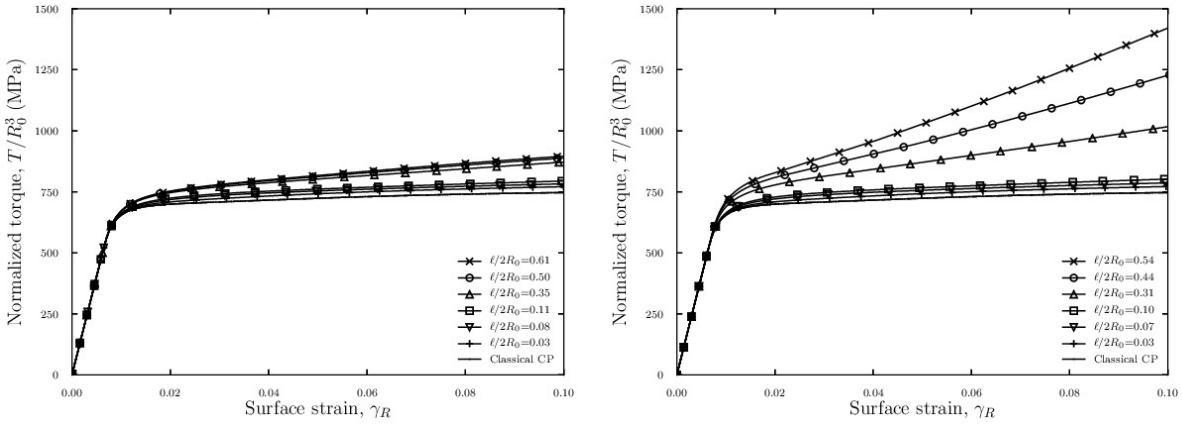


(a) (b)

Figure 5.11 Normalized torque *vs* surface strain curves for FCC <111> crystal orientation for different values of ratio $\ell/2R_0$ using (a) micromorphic (b) Lagrange multiplier models.

in the micromorphic model has been chosen so as to ensure such a correspondence. However, keeping the same value of the penalty parameter $H_\chi$ and increasing the internal length, or equivalently the value of the parameter $A$, leads to a saturation of the torque-shear strain curve for the micromorphic model. In contrast, the Lagrange multiplier based model predicts ever increasing hardening. Figure 5.10a and 5.11a show almost the same micromorphic response for the two largest $\ell/2R_0$ values whereas distinct curves are obtained with the Lagrange multiplier approach, see Figure 5.10b and 5.11b. This saturation of size effects predicted by a micromorphic formulation has already been demonstrated analytically for the microcurl theory by Cordero et al. (2010) in the case of periodic shearing of a laminate at small strains and small rotations. The present new results show that this feature also exists at large strains for torsion. These observations apply to both orientations <001> and <111>. The strongest additional hardening effect is obtained when the internal length takes values comparable to the wire diameter, as expected.

The predictions of the Lagrange multiplier based formulation can be considered in fact as the limit case when the penalty modulus $H_\chi$ goes to infinity in the micromorphic formulation. The predictions obtained with the micromorphic formulation for several values of $H_\chi$ are plotted in Figure 5.12. As $H_\chi$ rises the prediction of the micromorphic formulation goes closer to the

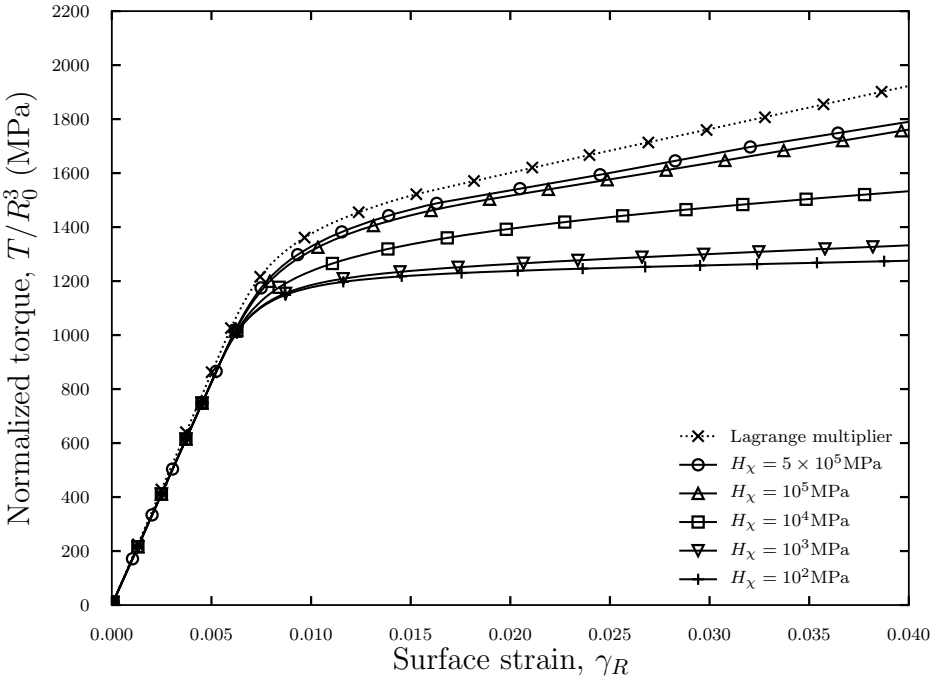


Figure 5.12 Normalized torque *vs* surface strain curves for FCC <001> crystal orientation for different values of $H_\chi$ and for $\ell/2R_0 = 0.44$.

prediction obtained with the Lagrange multiplier based formulation. However increasing $H_\chi$ builds up drastically the computation time since the penalization becomes very stiff. In practice, one could use the penalty term $H_\chi$ in the micromorphic formulation as a parameter to fit the scaling law measured in experiments. This possibility was discussed for micromorphic and Cosserat models in (Cordero et al., 2010). Such a parametrization is however not possible with the Lagrange multiplier based formulation. Nevertheless saturation of the scaling law can also be achieved, with both formulations, by using a more elaborate free energy potential associated to gradient terms. The rather simple quadratic form used in this study can indeed be modified in order to obtain more physically relevant scaling laws.

### 5.5.3 Size effects in ductile fracture: void growth and coalescence

Porous unit-cell simulations are commonly used to assess the mechanisms of void growth and void coalescence which play a major role in the ductile failure of metallic materials. Voids can nucleate at defects such as inclusions and precipitates by cracking or debonding of these defects. Voids may also be induced by other mechanisms such as irradiation in nuclear materials. In all these cases voids are sub-crystalline imperfections. Following the pioneering work of Hori and Nemat-Nasser (1988a,b) recent numerical studies have considered voids embedded in FCC (Ling et al., 2016) and HCP (Selvarajou et al., 2019) single crystals. In addition, Borg et al. (2008); Hussein et al. (2008); Zhao et al. (2009) have analyzed the size effects predicted by strain gradient plasticity, dislocations dynamics and molecular dynamics respectively, in plates containing cylindrical holes. Recently Ling et al. (2018) performed the first size-dependent 3D porous single crystal unit-cell simulations where the micromorphic crystal plasticity formulation presented in Section 5.3.1 was used. Similar unit-cell simulations are reproduced with the Lagrange multiplier based formulation presented in Section 5.3.2 and compared to the results obtained by Ling et al. (2018).

#### 5.5.3.1 Problem setup

An initially spherical void of radius $R_0$ is placed at the center of a cube of size $L_0$ as presented in Figure 5.13a. The matrix material surrounding the void is a FCC single crystal (later denoted <100>) such that

$$\underline{\boldsymbol{X}}_1 = [100] \quad \underline{\boldsymbol{X}}_2 = [010] \quad \underline{\boldsymbol{X}}_3 = [001] \tag{5.79}$$

Therefore, for symmetry reasons only one eighth of the porous unit-cell is considered. Figure 5.13b shows the corresponding finite element mesh for a void volume fraction $f_0 = (4/3)\pi(R_0/L_0)^3 = 1\%$. Quadratic (resp. linear) shape functions are used for the displacement (resp. micro-slip $\gamma_\chi$ and Lagrange multiplier $\lambda$) degrees of freedom. Elements with reduced integration are used. A triaxial axisymmetric loading is applied by prescribing displacement boundary conditions on the inner faces of the cube at $X_1 = 0$, $X_2 = 0$, $X_3 = 0$ and outer faces at $X_1 = L_0/2$, $X_2 = L_0/2$, $X_3 = L_0/2$

$$U_1(X_1 = 0, X_2, X_3) = 0 \qquad U_1(X_1 = L_0/2, X_2, X_3) = U_1(t) \tag{5.80}$$
$$U_2(X_1, X_2 = 0, X_3) = 0 \qquad U_2(X_1, X_2 = L_0/2, X_3) = U_2(t) \tag{5.81}$$
$$U_3(X_1, X_2, X_3 = 0) = 0 \qquad U_3(X_1, X_2, X_3 = L_0/2) = U_3(t) \tag{5.82}$$

External forces $F_1$, $F_2$ and $F_3$ are respectively associated to $U_1$, $U_2$ and $U_3$. The macroscopic stresses $\Sigma_{11}$, $\Sigma_{22}$ and $\Sigma_{33}$ are defined by

$$\Sigma_{11} = \frac{4F_1}{(L_0 + 2U_2)(L_0 + 2U_3)} \tag{5.83}$$
$$\Sigma_{22} = \frac{4F_2}{(L_0 + 2U_1)(L_0 + 2U_3)} \tag{5.84}$$
$$\Sigma_{33} = \frac{4F_3}{(L_0 + 2U_1)(L_0 + 2U_2)} \tag{5.85}$$

A macroscopic strain rate $\dot{\overline{F}}_{11} = 10^{-4}\ \mathrm{s}^{-1}$ is imposed along the $\underline{\boldsymbol{X}}_1$ direction. Displacements $U_2$ and $U_3$ are adjusted following the procedure described in Ling et al. (2016) in order to enforce a constant stress triaxiality $T$ where

$$T = \frac{\Sigma_m}{\Sigma_{eq}} = \frac{1 + \eta_2 + \eta_3}{3\sqrt{1 - \eta_2 - \eta_3 - \eta_2\eta_3 + \eta_2^2 + \eta_3^2}} \tag{5.86}$$

with the relations $\Sigma_{22} = \eta_2\Sigma_{11}$ and $\Sigma_{33} = \eta_3\Sigma_{11}$. For the applied axisymmetric loading considered in this Section, the values $\eta_2 = \eta_3 = 0.625$ were chosen, corresponding to a triaxiality of 2.

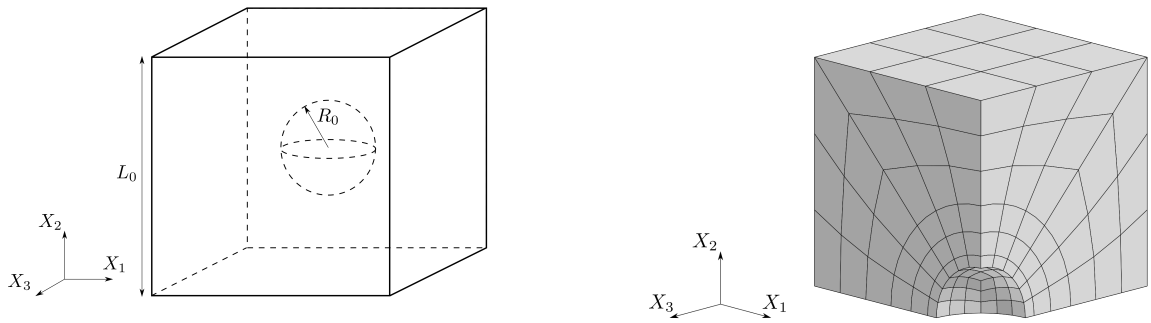


(a) (b)

Figure 5.13 (a) Geometry of a cubic porous unit-cell. (b) 1/8-th of the finite element mesh for $f_0 = 1\%$. Total number of degrees of freedom is $n_{DOF} = 2767$.

The same dislocation density based hardening laws Eq. (5.76) and evolution equations Eq. (5.77) are used. Different material parameters are however considered and listed in Table 5.5 in order to match the material parameters used in Ling et al. (2018). Several values of $A$ are used in order to investigate size effects. As discussed in previous section and by Ling et al. (2018) the intrinsic length scale $\ell = \sqrt{A/H}$ can be considered, where $H$ denotes the linear hardening modulus at initiation of plastic slip in a uniaxial tensile test. The ratio $\ell/L_0$ then governs the predicted size effects. For the material parameters presented in Table 5.5 one obtains $H = 2777\,\text{MPa}$ for the <100> crystal orientation. The numerical values of $\ell/L_0$ used for the simulation of porous unit-cells are: 0, 1/300, 1/90, 1/30 and 1/3. Several values of the penalization modulus $\mu_\chi$ are also considered in order to measure its impact on the macroscopic stress-strain behaviour.

#### 5.5.3.2 Results and discussion

The void volume fraction $f$ is postprocessed from the unit-cell simulations by computing the volume contained in the mesh $V_{mesh}$ (excluding the void) and the total volume contained in the cube $V_{tot} = (L_0 + 2U_1)(L_0 + 2U_2)(L_0 + 2U_3)$ (including the void)

$$f = 1 - \frac{V_{mesh}}{V_{tot}} \tag{5.87}$$

Figure 5.14 plots the evolution of $f$ with the macroscopic deformation $\overline{E}_{11} = 2U_1/L_0$ for the different $\ell/L_0$ ratios considered. The results obtained with the novel Lagrange multiplier based formulation are plotted aside the results presented in (Ling et al., 2018) which were obtained with the micromorphic formulation with the same material parameters, but where the entire unit-cells were computed. It can be noted that when $\ell/L_0$ vanishes, both formulations predict almost exactly the same result. Nevertheless some discrepancies become visible as $\ell/L_0$ increases. This observation can be put in parallel to the discussion made in previous section. The Lagrange multiplier approach corresponds indeed to the limit case of the micromorphic formulation as $H_\chi$ approaches infinity. However in (Ling et al., 2018) for numerical efficiency reasons $H_\chi$ was taken equal to $5 \times 10^4\,\text{MPa}$. Size effects obtained with both formulations are therefore in good qualitative agreement, but turn out to be more pronounced with the Lagrange multiplier setting. These effects are as follows.

With the applied loading the void volume fraction is a monotonically increasing function of $\overline{E}_{11}$. In absence of size effects (*i.e.* $\ell/L_0 = 0$) evolution of the void volume fraction does not depend on the cell size. However as $\ell/L_0$ increases void volume fraction evolution becomes size-dependent. The larger the $\ell/L_0$ ratio is, the slower the void volume fraction rises with

Table 5.5 Numerical values of material parameters for the simulation of porous unit-cells.

| $C_{11}$ | $C_{12}$ | $C_{44}$ | $\tau_0$ | $n$ | $\dot{\gamma}_0$ |
|---|---|---|---|---|---|
| 200 GPa | 136 GPa | 105 GPa | 88 MPa | 15 | $10^{29}\,\mathrm{s}^{-1}$ |

| $\mu$ | $G_c$ | $\kappa$ | $r_0^s$ | $b_{ij}$ $(i \neq j)$ | $b_{ii}$ |
|---|---|---|---|---|---|
| 65.6 GPa | 10.4 | 42.8 | $5.38 \times 10^{-11}$ | 1 | 0 |

| $a_1$, $a_2$ | $a_3$ | $a_4$ | $a_5$ | $a_6$ | $\mu_\chi$ |
|---|---|---|---|---|---|
| 0.124 | 0.07 | 0.625 | 0.137 | 0.122 | $10^2$ ; $10^3$ ; $10^4$ MPa |

macroscopic deformation. This first size effect is due to a more diffuse plastic deformation field when the intrinsic length $\ell$ gets closer to $L_0$. For the three lowest values of the ratio considered, the void volume fraction evolution displays two distinct regimes, while for the two largest ratios only one regime is visible. This two-regime evolution is characteristic of void growth and void coalescence. During the first regime, voids grow rather slowly because of overall yielding of the matrix surrounding them. At some point necking of the ligament separating voids is reached, which leads to a sudden steepening of void growth evolution. This acceleration is due to intense localization of plastic deformation inside the ligament. Onset of void coalescence by intervoid ligament necking is characterized by a transition from a triaxial to a uniaxial straining mode (Koplik and Needleman, 1988). This transition can therefore be detected by computing over time the ratio $|\Delta U_2|/|\Delta U_1|$. Coalescence can be considered to set on as soon as this ratio becomes lower than an arbitrary small critical value, say 5%. Hollow squares are plotted in Figure 5.14 in order to depict the macroscopic strain and void volume fraction at which coalescence begins. For the sake of clarity, coalescence onsets are only displayed for the results obtained by Ling et al. (2018). For a given characteristic length, the micromorphic and Lagrange multiplier formulations predict almost identical strain and void volume fractions at onset of coalescence. The second size effect which appears is that void growth to void coalescence transition is postponed when $\ell/L_0$ is increased. This delay is due to the weaker void volume increase during the growth regime. For the two largest value of $\ell/L_0$ a very flat void growth regime is observed. The quasi-absence of void growth explains why coalescence does not occur in the range of applied deformations. Necking of the intervoid ligament would indeed require larger stresses to be applied. A third size effect which can be observed is a slight increase of the void volume fraction at coalescence when the intrinsic length increases. This additional effect is due to the fact that size effects prevent intense localization of plastic deformation. Therefore void coalescence which occurs by localization of plastic slip in the intervoid ligament requires a larger void volume fraction in order to happen. The macroscopic stress-strain curves obtained with the Lagrange multiplier formulation are plotted in Figure 5.15 aside to the results obtained with the micromorphic formulation presented in Ling et al. (2018). As previously noted for void volume fraction in Figure 5.14, both formulations are also equivalent in terms of stress-strain behaviour when size effects are absent. However the discrepancies between both formulations observed in presence of size effects on void volume fraction evolution are also visible on the stress-strain behaviour. The void volume fraction plays indeed a detrimental role on the macroscopic stress. With low and intermediate intrinsic length scales, voids grow significantly and the material displays a two-regime stress-strain behaviour. During the first regime hardening of the matrix material

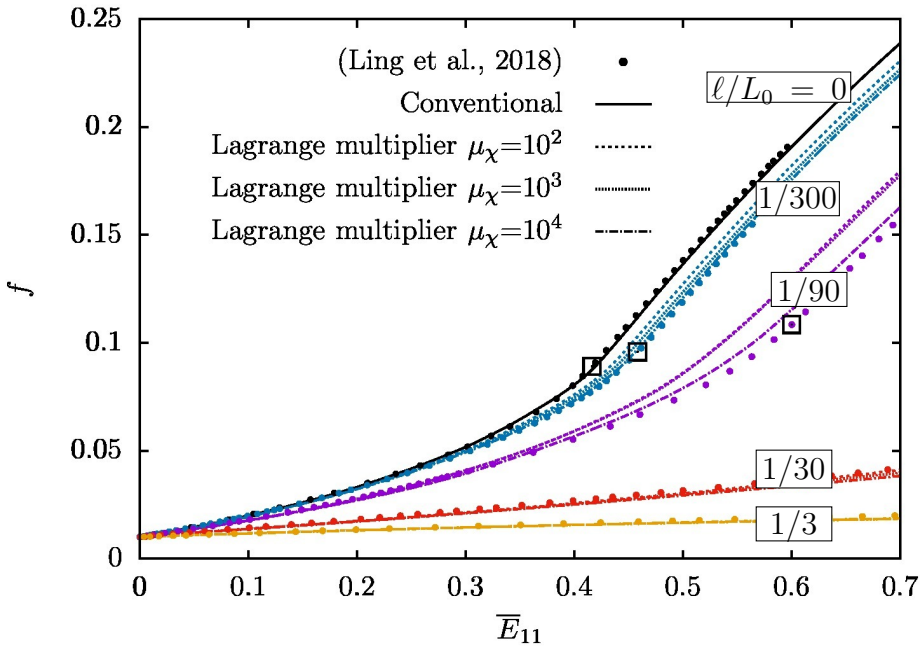


Figure 5.14 Void volume fraction $f$ evolution with respect to macroscopic deformation $\overline{E}_{11}$ for different intrinsic length to cell size ratios $\ell/L_0$ obtained with the micromorphic (solid lines) and the Lagrange multiplier (dashed lines) formulations in porous unit-cell simulations with $f_0 = 0.01$ and material parameters presented in Table 5.5. Hollow squares denote onsets of void coalescence.

dominates over softening induced by void growth. This regime is therefore characterized by an increase of the macroscopic stress despite the augmentation of $f$. In the second regime, softening induced by void growth overcomes the hardening capacity of the matrix leading to a macroscopic softening behaviour. However, for the largest intrinsic length, softening induced by void growth does not overcome hardening of the matrix material, thus the second stress softening regime is not observed. Hollow squares are also plotted on the stress-strain curves in order to depict onset of void coalescence. As discussed earlier, strong size effects postpone the onset of void coalescence, because of impeded void growth. As a collateral effect, it can be noted that the macroscopic stress at coalescence increases notably with $\ell/L_0$. The influence of the penalization modulus $\mu_\chi$ in the Lagrange multiplier formulation is visible in Figure 5.14 and 5.15. For the smallest characteristic length $\mu_\chi$ has a rather weak impact on the void volume fraction evolution and stress behaviour. As the characteristic length increases, the importance of $\mu_\chi$ rises. It can be observed that greater values of $\mu_\chi$ induce a slightly slower void growth and a harder stress-strain behaviour. These effects become more visible at large strains.

The accumulated plastic strain field obtained with the Lagrange multiplier formulation with $\mu_\chi = 10^4$ MPa are displayed in Figure 5.16 at a macroscopic strain $\overline{E}_{11} = 0.3$ for several values of the ratio $\ell/L_0$. These fields are quantitatively in excellent agreement with the results obtained by Ling et al. (2018) with the micromorphic approach. According to conventional crystal plasticity, plastic strains are predominantly localized in the vicinity of the void, in particular where the cross-section area orthogonal to the main tensile direction is minimum. Plastic anisotropy causes the presence of several soft zones, where $\gamma_{cum}$ is maximum and which correspond to regions with highest Schmid factors. As the ratio $\ell/L_0$ is increased the accumulated plastic slip tends to become more homogeneous across the porous unit-cell. Therefore, the maximum local value of $\gamma_{cum}$ drops. In addition, the number of local maxima decreases. Three intense maxima were indeed visible with conventional crystal plasticity, while only two much less intense maxima can be observed when $\ell/L_0 = 30$.

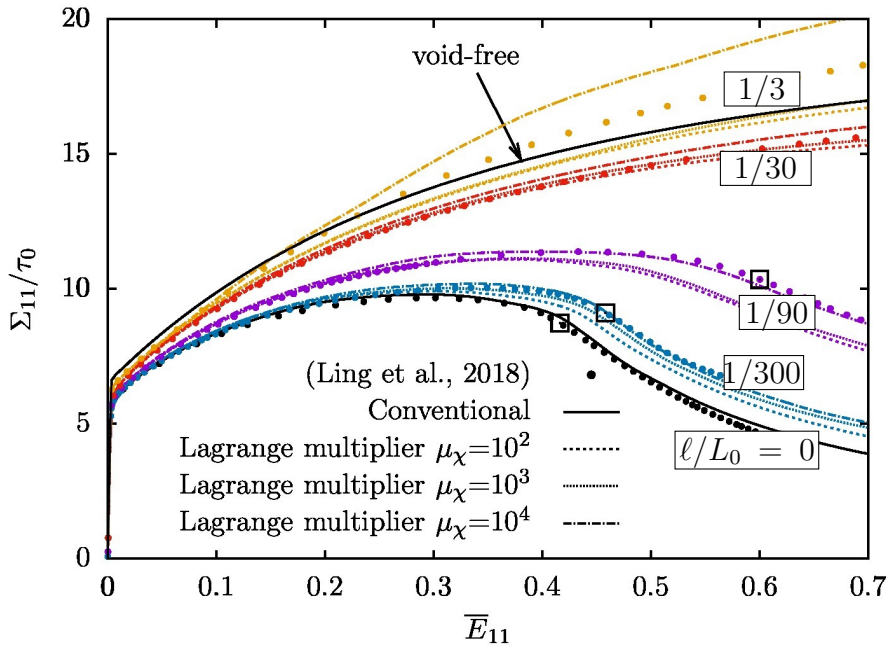


Figure 5.15 Macroscopic stress-strain behaviour for different intrinsic length to cell size ratios $\ell/L_0$ obtained with the micromorphic formulation (dots) by Ling et al. (2018) and the Lagrange multiplier formulation (dashed lines) in porous unit-cell simulations with $f_0 = 0.01$ and material parameters presented in Table 5.5. Hollow squares denote onsets of void coalescence.

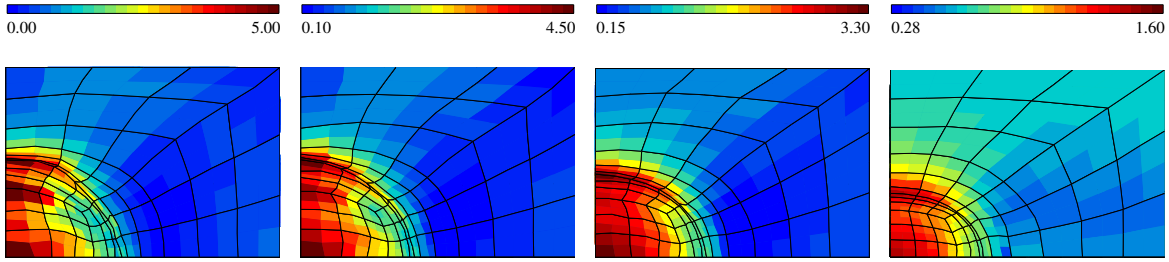


(a) Conventional (b) $\ell/L_0 = 1/300$ (c) $\ell/L_0 = 1/90$ (d) $\ell/L_0 = 30$

Figure 5.16 Cumulative plastic strain fields in porous unit-cells at $\overline{E}_{11} = 0.3$ obtained with the Lagrange multiplier formulation with $\mu_\chi = 10^4$ MPa.

## 5.6 Conclusions

The major outcomes of this study can be stated as follows:

1. A Lagrange multiplier approach accounting for the nonlinearity and nonlocality coupling inherent to strain gradient plasticity was presented. It was compared to the micromorphic approach in the context of crystal plasticity. The main idea of the Lagrange multiplier approach is to enforce weakly equality between local and non-local variables through a Lagrange multiplier.

2. The finite element implementation of the Lagrange multiplier method was detailed. In particular tangent and Jacobian matrices were derived.

3. The computational efficiencies of the micromorphic and Lagrange multiplier formulations were compared. Rate-dependent and rate-independent crystal plasticity settings were used. A significant speedup, reaching a computational time reduction of up to a factor 200, is obtained with the Lagrange multiplier based and rate-dependent formulation compared to the micromorphic and rate-dependent formulation. Important benefits are also displayed with the rate-independent setting as compared to the viscoplastic flow rule, in particular when the micromorphic approach is considered.

4. The prediction of size effects with the micromorphic and Lagrange multiplier approaches were compared for single crystals torsion tests. It was shown that both models provide similar results for small and intermediate internal length scales. However, for larger internal length scales, the hardening due to strain gradients saturates according to the micromorphic approach. A similar saturation effect was observed on the grain size effect on the yield stress in polycrystals using the microcurl model at small strains in (Cordero et al., 2012b). The scaling law is different for the Lagrange multiplier formulation since such a saturation is not observed.

5. Advantage of the Lagrange multiplier numerical efficiency has been taken in order to perform simulations of void growth in porous unit-cells up to void coalescence. Comparison to simulations made previously with the micromorphic formulation displays a very good agreement between both formulations.

Although this model remains computationally rather expensive, the results obtained in this work suggest that simulation of structures, such as real specimens, are now within reach in more reasonable computation times. The work initiated in (Scherer et al., 2019) on the evolution of voids in a softening matrix material will be pursued by performing 3D porous unit-cell simulations by taking advantage of the enhanced computational performance of the Lagrange multiplier formulation. The advances obtained in this paper will also be coupled in a future work to recent extensions of standard crystal plasticity to ductile failure (Ling et al., 2016) and damage (Lindroos et al., 2019).

## Acknowledgements

Part of the research leading to these results (in particular Section 5.5.2) has received funding from the European Union's Horizon 2020 research and innovation programme, Marie Sklodowska-Curie Actions, under grant agreement no. 764979, project "ENABLE", "European Network for Alloys Behaviour Law Enhancement".

# 6

# A strain gradient model for ductile fracture in single crystals


## Résumé

Un modèle complet de rupture ductile pilotée par la croissance et la coalescence de cavités est développé pour les monocristaux. Un formalisme de plasticité cristalline à gradient est adopté comme cadre, afin de régulariser les champs mécaniques locaux. Le modèle est basé sur un cadre thermodynamique original pour les matériaux poreux homogénéisés. Ce dernier unifie et généralise différents cadres thermodynamiques existants. La thermodynamique sert conjointement de ligne directrice d'où découlent naturellement les couplages, mais aussi de garde-fou empêchant la violation des principes fondamentaux. Ce cadre générique est une condition préalable pour, dans un deuxième temps, introduire des contributions non-locales dans une formulation à gradient de déformation plastique. La formulation de plasticité à gradient utilisée est construite à partir d'une relaxation de la plasticité à gradient stricte faisant intervenir un multiplicateur de Lagrange, ainsi qu'un terme de pénalisation dans l'énergie libre. Le modèle de rupture ductile monocristalline établi est basé sur une représentation multisurface de la plasticité des cristaux poreux. Les mécanismes de croissance et de coalescence de cavités sont conjointement pris en compte. Une extension d'une formulation existante est proposée pour la phase de croissance et une nouvelle approche est proposée et validée pour la phase de coalescence. Le modèle obtenu est ensuite mis en œuvre dans des simulations par éléments finis d'un monocristal en déformations planes déformé en traction jusqu'à rupture. La capacité de régularisation et la convergence avec le raffinement du maillage sont démontrées. Des simulations de rupture ductile de structures monocristallines sont ensuite présentées.

## Contents

## 6.1 Introduction

Modeling ductile fracture of metallic alloys is a major topic in the field of mechanical engineering. Multiple mechanisms can spearhead ductile fracture (Noell et al., 2018) that is commonly characterized by significant local inelastic deformation prior to material separation and formation of free surfaces. One main mechanism is related to nucleation, growth and coalescence of voids in the bulk material. The seminal works of Green (1972); Gurson (1977); McClintock (1968); Rice and Tracey (1969); Rousselier (1981); Thomason (1985) paved the way to the establishment of continuum mechanics models of ductile fracture provoked by combined plastic deformation and formation and evolution of voids. The key ingredient of these models consists in introducing a damage scalar variable, related to the volume fraction of voids. The evolution of the damage variable is driven by the local loading state of the material. In order to efficiently reproduce failure after significant plastic deformation these models propose an elegant way to decrease the load bearing capacity of the material when the amount of damage increases. This is accomplished by deriving yield potentials for which the elastic domain shrinks when damage increases. Their approach encompasses two major requirements: (1) to derive the appropriate evolution of the damage variable and (2) to obtain the appropriate dependency of the yield criteria upon damage. In the context of porous plasticity (see the reviews by Benzerga and Leblond (2010); Besson (2010); Pineau et al. (2016)), increase of damage is mainly governed by void nucleation and void growth. Some authors also proposed extensions involving contribution of void shearing (Nahshon and Hutchinson, 2008) in the effective damage variable evolution, although that way the link to void volume fraction is lost. Deriving effective yield criteria of porous solids was conducted by mainly three homogenization techniques. The first, followed by Gurson (1977), involves limit analysis of an idealized porous unit-cell. The second, followed for example by Danas and Castañeda (2009) is based on variational methods. The third followed by Rousselier (1981, 1987, 2001) calls upon thermodynamical considerations (Germain et al., 1983). Early models were extensively enriched to improve their accuracy for instance by introducing fitting parameters (Tvergaard and Needleman, 1984). Extensions were also developed to account for shape (Gologanu et al., 1995), orientation (Cao et al., 2015) or size of voids (Dormieux and Kondo, 2010; Gallican and Hure, 2017). In the homogenization procedure the behaviour of the so-called matrix material that surrounds the voids is of paramount importance. Gurson originally considered an isotropic rigid perfectly plastic matrix material. Gurson's approach was later generalized to take isotropic hardening and kinematic hardening (Besson and Guillemer-Neel, 2003; Mear and Hutchinson, 1985; Morin et al., 2017) into account. Other studies focused on deriving effective yield criteria of porous materials with a plastic anisotropic matrix material (Benzerga and Besson, 2001; Keralavarma and Chockalingam, 2016; Morin et al., 2015).

In most metallic alloys voids nucleate at imperfections such as inclusions or precipitates by debonding or cracking (Babout et al., 2004). These defects can be within the bulk of grains. In this case voids are individually surrounded by single crystals at short distances. Recent experiments were carried out on polycrystal stainless steel tensile specimens containing focused ion beam (FIB) drilled holes inside grains (Barrioz et al., 2019). These showed the importance of crystal orientation on the plastic behaviour surrounding voids. Although anisotropic nature of plasticity in single crystals could be captured to some extent by Hill-type anisotropic yield criteria, single crystal porous unit-cell simulations (Ha and Kim, 2010; Ling et al., 2016; Potirniche et al., 2006a; Selvarajou et al., 2019; Yerra et al., 2010) have shown the strong effect of crystal plasticity on void growth and coalescence. Nevertheless, since the early work by Mori and Meshii (1969), only a few studies were devoted to develop models for porous single crystals up to failure. Single crystal void growth models were settled by Crépin et al. (1996); Han et al. (2013); Ling et al. (2016); Mbiakop et al. (2015a); Paux et al. (2018). Even fewer studies dealt with void coalescence in single crystals (Hure, 2019; Yerra et al., 2010). A comprehensive model combining void growth and void coalescence criteria in porous single crystals is still lacking. The first and foremost objective of the present work is to address the formulation, implementation and application of such a model. The proposed model will be constructed in a finite strain framework on the basis of the void growth model developed in (Ling et al., 2016). An original coalescence

criterion, adapted for intervoid necking in single crystals, is proposed and validated. In keeping with the multi-mechanism plasticity framework proposed by Besson (2009), void growth yield criteria will be combined to void coalescence criterion to obtain a so-called multi-surface model.

Most ductile fracture models predict a softening regime at incipient final failure. Softening occurs in these models on account of damage variable increase which in turn reduces the size of the elastic domain. As a result softening induces localization and localization promotes damage acceleration. Although such a behaviour might be in agreement with underlying physical mechanisms it also entails the major issue of causing ill-posedness of the boundary value problem as reported by Bažant et al. (1984); Lorentz and Benallal (2005). From a numerical point of view, solving these equations, for example by finite elements, results in the absence of convergence of the results when the mesh size is decreased. Localization systematically tends to form the most thin band possible (typically one Gauss point thick). Several approaches were followed to bypass or overcome this issue. In (Achouri et al., 2013; Xue et al., 2010) mesh size is treated as a material parameter used to control the characteristic length of post-localization regime. Another technique used to introduce a material length scale is to deploy the intrinsically size-dependent phase field method as in (Miehe et al., 2016). In another way, theories developed in the context of non-local continua were also successfully applied in order to regularize localization predicted in ductile fracture simulations. Non-local theories, based either on integral or gradient formulations, naturally incorporate one or several length scales. In the context of ductile fracture, these lengths can be used to drive the evolution of damage in the post-localization regime. Size-dependent modeling of ductile fracture not only amounts to the choice of a non-local theory, but also the choice of one or several appropriate non-local variables. Some authors used the damage variable to carry non-local effects (Håkansson et al., 2006; Ramaswamy and Aravas, 1998). Alternatively others used strain quantities as non-local variables such as the volumetric equivalent plastic strain in (Nguyen et al., 2020; Zybell et al., 2014), the equivalent plastic strain in Lorentz et al. (2008); Nguyen et al. (2020); Payet et al. (2012), the strain tensor in Enakoutsa and Leblond (2009) or the matrix equivalent plastic strain in (Nguyen et al., 2020). It is not uncommon that several non-local variables are used. Despite the more important numerical effort it requires, it is mostly necessary in order to be able to regularize localization for any loading path. The present work takes advantage of the strain gradient crystal plasticity model (without damage) developed and compared to the micromorphic approach in Chapter 5. This finite strain formulation of strain gradient plasticity is based on a Lagrange multiplier method already successfully applied by Zhang et al. (2018) for isotropic materials in the context of ductile fracture. For numerical efficiency a single scalar non-local variable is used.

The thermodynamics of continuum damage mechanics is extensively studied in the domain of geophysics and civil engineering, where rocks and soils contain defects (pores, cracks, etc) which may or not be filled with fluids influencing their mechanical behaviour (Chaboche, 1988; Coussy, 2004; Kachanov, 2013). However literature covering thermodynamics of porous metallic alloys remains very scarce. Yet in his seminal work Rousselier (1981) was able to design a mechanical model of ductile failure based on very simple thermodynamical considerations. Furthermore similarities between this model and models derived with other completely different approaches are remarkable. A few other thermodynamical settings were developed in (Besson, 2009), (Enakoutsa et al., 2007) and (Bouby and Kondo, 2017). Building a sound thermodynamical framework for porous plasticity which unifies existing theories will be the third objective of this work. In the same vein as (Nguyen et al., 2020), this framework will work as a prerequisite in order to be able to introduce strain gradient effects and couplings in the constitutive equations of the proposed porous crystal plasticity model.

The new results obtained in this work can be summarized as follows:

1. A thermodynamical framework unifying existing porous plasticity models accounting for void growth and void coalescence is established.

2. A comprehensive finite strain gradient-enhanced model of ductile failure in single crystals is constructed.

3. Simulations of regularized ductile fracture in single crystals, the first of this kind, are reported.

The outline is as follows. In Section 6.2 the thermodynamics of homogenized porous materials is presented. A short literature review serves as an introduction in order to exhibit the limitations of existing models. A unifying thermodynamical framework is then proposed. In Section 6.3 the aforementioned setting is extended to strain gradient crystal plasticity. The chosen gradient enhanced principle of virtual power, free energy potential and dissipation potentials are exposed in details in order to derive an original comprehensive model of ductile fracture in single crystals. The validity of a newly proposed coalescence criterion in single crystals is assessed in Section 6.4. Two different approaches to account for void coalescence are then discussed. In Section 6.5 the ability of the model to regularize ductile fracture is demonstrated. The contribution of the thermodynamical force conjugate to porosity is also investigated. Ductile fracture simulations of single crystal structures are presented in Section 6.6. The outcomes and prospects are listed in Section 6.7.

## 6.2 Thermodynamical framework for homogenized porous materials

The objective of this section is to develop a thermodynamical framework for the modeling of homogenized porous solids. First a brief review of existing thermodynamical settings for homogenized porous solids is presented. Then a framework is set up, which is shown to generalize previous approaches.

### 6.2.1 State of the art

The total volume $V_{tot}$ of a porous solid body is the union of two parts, namely the total volume of empty spaces (or voids ) $V_{voids}$ and the total volume of dense material $V_{mat}$. First and foremost the *void volume fraction* $f_v$ of a porous solid body is defined as the volume of voids divided by the total volume of the body $V_{tot}$

$$f_v = \frac{V_{voids}}{V_{tot}} \tag{6.1}$$

It should be emphasized that there is no universal relation between the macroscopic deformation gradient $\underset{\sim}{\boldsymbol{F}} = \partial \underline{\boldsymbol{x}} / \partial \underline{\boldsymbol{X}}$ and the void volume fraction $f_v$. In fact, any relation between $\underset{\sim}{\boldsymbol{F}}$ and $f_v$ consists in a constitutive assumption related to a homogenization scheme. As a consequence the void volume fraction can be considered in general terms as an independent internal variable. In the forthcoming development the term *porosity* will be used to describe a damage variable which definition might be different from the void volume fraction given at Eq. (6.1). The porosity variable will be noted $f$. Germain et al. (1983); Rousselier (1981) proposed a thermodynamical framework in which the porosity is considered as an independent state variable. A multiplicative decomposition of the deformation gradient $\underset{\sim}{\boldsymbol{F}}$ in an elastic part $\underset{\sim}{\boldsymbol{E}}$ and a plastic part $\underset{\sim}{\boldsymbol{P}}$ is assumed: $\underset{\sim}{\boldsymbol{F}} = \underset{\sim}{\boldsymbol{E}}.\underset{\sim}{\boldsymbol{P}}$. The elastic velocity gradient $\underset{\sim}{\boldsymbol{L}}^e = \dot{\underset{\sim}{\boldsymbol{E}}}.\underset{\sim}{\boldsymbol{E}}^{-1}$ and plastic velocity gradient $\underset{\sim}{\boldsymbol{L}}^p = \dot{\underset{\sim}{\boldsymbol{P}}}.\underset{\sim}{\boldsymbol{P}}^{-1}$ are introduced such that $\underset{\sim}{\boldsymbol{L}} = \dot{\underset{\sim}{\boldsymbol{F}}}.\underset{\sim}{\boldsymbol{F}}^{-1} = \underset{\sim}{\boldsymbol{L}}^e + \underset{\sim}{\boldsymbol{E}}.\underset{\sim}{\boldsymbol{L}}^p.\underset{\sim}{\boldsymbol{E}}^{-1}$. In order to introduce a dependence of the Helmholtz specific free energy potential, noted $\psi$, on the porosity $f$, Rousselier proposed an additive split composed of three parts. The first term $\psi_e$ accounts for elastic energy, the second $\psi_p$ is a hardening potential and the third $\psi_f$ carries the effect of porosity $f$. The Helmholtz specific free energy in the isothermal case is then postulated to take the form

$$\psi(\underset{\sim}{\boldsymbol{E}}, p, f) = \psi_e(\underset{\sim}{\boldsymbol{E}}) + \psi_p(p) + \psi_f(f) \tag{6.2}$$

where $p$ is a hardening variable. In the limit case of $f$ going to one, the specific free energy should vanish. However this is not the case in the Rousselier model since elastic and hardening potentials $\psi_e$ and $\psi_p$ are assumed to be independent of the porosity $f$. This assumption is exact if $f$ is close to zero but deteriorates when $f$ increases. In Rousselier's model $\psi_f$ is obtained by postulating the following form of the dissipation potential $\Omega$ and yield criterion $\phi$

$$\Omega\left(\frac{\underset{\sim}{\boldsymbol{\sigma}}}{\rho}, P, F\right) = \Lambda(\phi) = \Lambda\left(\phi_{eq}\left(\frac{\sigma_{eq}}{\rho}, P\right) + \phi_m\left(\frac{\sigma_m}{\rho}, F\right)\right) \tag{6.3}$$

where $P = \partial\psi_p/\partial p$, $F = \partial\psi_f/\partial f$, $\rho_0 = \rho\det\left(\underset{\sim}{\boldsymbol{F}}\right)$ is the volumetric mass density in the current configuration defined with respect to the volumetric mass density in the initial configuration noted $\rho_0$. The macroscopic Cauchy stress is noted $\underset{\sim}{\boldsymbol{\sigma}}$, with the notations $\sigma_m = \mathrm{tr}\left(\underset{\sim}{\boldsymbol{\sigma}}\right)/3$ and $\sigma_{eq} = \sqrt{3/2\underset{\sim}{\boldsymbol{\sigma}}' : \underset{\sim}{\boldsymbol{\sigma}}'}$ with $\underset{\sim}{\boldsymbol{\sigma}}' = \underset{\sim}{\boldsymbol{\sigma}} - \sigma_m\underset{\sim}{\mathbf{1}}$. Assuming that $\phi_m = g(\sigma_m/\rho)h(F)$ Rousselier showed that there exist a unique possible function $\psi_f(f)$ which satisfies the commonly used evolution equation of the damage variable $f$ (here called porosity)

$$\dot{f} = (1-f)\mathrm{tr}\left(\underset{\sim}{\boldsymbol{L}}^p\right) \tag{6.4}$$

The function $\psi_f$ which satisfies the postulated form of $\phi_m$ and evolution equation (6.4) found by Rousselier writes

$$\psi_f(f) = F^0 f - \frac{\sigma_1}{\rho_0}\left((1-f)\ln(1-f) + f\ln(f)\right) \tag{6.5}$$

This function admits $F^0$ as a limit when $f$ increases in values approaching one. However such a potential imposes the thermodynamic force conjugate to porosity to be

$$F = \frac{\partial\psi}{\partial f} = F^0 - (\sigma_1/\rho_0)\ln(f/(1-f)) \tag{6.6}$$

which diverges when $f$ approaches one. Therefore Rousselier's model should be limited to applications where the porosity is small.
Alternatively Besson (2009) postulates the Helmholtz free energy

$$\psi(\underset{\sim}{\boldsymbol{E}}, p, f) = \psi_e(\underset{\sim}{\boldsymbol{E}}) + (1-f)\psi_p(p) \tag{6.7}$$

The dependence of the elastic energy on $f$ is omitted, in the same manner as in Rousselier's model, because in their model, the stresses (*i.e.* elastic deformations) already decrease due to the fact that the yield surface shrinks when $f$ increases. Unlike Rousselier's model the hardening potential is here multiplied by $(1-f)$ so that $\psi$ vanishes when the porosity reaches one. However the thermodynamic driving force $F = \partial\psi/\partial f = -\psi_p$ was omitted in (Besson, 2009) owing to the fact that according to Eq. (6.4) $f$ and $\underset{\sim}{\boldsymbol{P}}$ are not independent variables. It is therefore interesting to investigate under which hypotheses, the evolution law of $f_v$ coincides with the evolution law of $f$. According to its definition Eq. (6.1), the void volume fraction evolution is

$$\begin{aligned}
\dot{f}_v =& \frac{\dot{V}_{tot} - \dot{V}_{mat}}{V_{tot}} - \frac{(V_{tot} - V_{mat})\dot{V}_{tot}}{V_{tot}^2} = \frac{\dot{V}_{tot}}{V_{tot}} - \frac{\dot{V}_{mat}}{V_{tot}} - \frac{V_{tot} - V_{mat}}{V_{tot}}\frac{\dot{V}_{tot}}{V_{tot}} \\
=& \mathrm{tr}\left(\underset{\sim}{\boldsymbol{L}}\right) - \frac{\dot{V}_{mat}}{V_{tot}} - f_v\mathrm{tr}\left(\underset{\sim}{\boldsymbol{L}}\right) \\
=& (1-f_v)\mathrm{tr}\left(\underset{\sim}{\boldsymbol{L}}^p\right) + \left((1-f_v)\mathrm{tr}\left(\underset{\sim}{\boldsymbol{L}}^e\right) - \frac{\dot{V}_{mat}}{V_{tot}}\right)
\end{aligned} \tag{6.8}$$

Therefore evolutions of $f_v$ and $f$ are the same if and only if

$$\frac{\dot{V}_{mat}}{V_{tot}} = (1 - f_v)\text{tr}\,(\underset{\sim}{\boldsymbol{L}}^e) \quad \text{in other words} \quad \frac{\dot{V}_{mat}}{V_{mat}} = \text{tr}\,(\underset{\sim}{\boldsymbol{L}}^e) \tag{6.9}$$

The aforementioned condition shows the main difference between the void volume fraction and the damage variable called porosity. The void volume fraction incorporates an elastic contribution, while the porosity does not. In fact, Besson (1990) already discussed the fact that an appropriate definition of the porosity must consider a relaxed stress-free state at a reference temperature (*i.e.* a temperature relaxing thermo-elastic strains). Otherwise, (thermo-)elastic strains would contribute to the increase of damage which is not satisfactory. A simple counter-example to prove it is the case of a virtual perfectly dense material, *i.e.* free of voids. If elastic strains are taken into account in the evolution of damage, it means that the application of a any stress would result in the apparition of damage. Moreover, the force conjugate to the porosity $P_f$ defined by Besson (1990) as the *sintering pressure* bears the same physical interpretation as $F$ in Rousselier's model.

Recently Bouby and Kondo (2017) proposed a free energy potential which is similar to the one suggested by Rousselier. Instead of considering $f$ as a state variable, they introduce a so-called Lagrangian porosity $\phi_p = V^t_{void}/V^0_{tot}$. Omitting the dependence on hardening and temperature, they propose to write the free energy as

$$\psi\,(\underset{\sim}{\boldsymbol{E}}, \phi_p) = \psi_e\,(\underset{\sim}{\boldsymbol{E}}) + m(\phi_p) \tag{6.10}$$

No particular expression of $m$ is derived, but the authors argued that the thermodynamic force $P$ conjugate to $\phi_p$ is given by $P = -m'(\phi_p)$ and that it should coincide with the pressure existing inside voids. In their further developments they stated that the effective mean stress seen by the porous material is the sum of the average Cauchy stress and this additional pressure. However to the authors knowledge a proof of such a statement was not yet given. In addition Bouby and Kondo (2017) argued that to retrieve the well known Gurson model the pressure $P$ must be taken equal to zero, for any porosity $\phi_p$. This results in the fact that $m$ is identically zero for any porosity $\phi_p$. With these assumptions the free energy would not depend on the porosity at all.

Another approach was conducted by Enakoutsa et al. (2007) in order to prove that Gurson's model can be cast into the thermodynamical framework of generalized standard materials (GSM) (Halphen and Nguyen, 1975). The authors showed that it is sufficient to assume that porosity is constant in order to satisfy the prerequisite of a GSM theory. As a consequence, with such an assumption, Gurson's model enjoys the following highly advantageous properties:

- non-negativeness of the dissipation
- existence of a solution to the problem of projecting the stress tensor onto the yield surface
- uniqueness of this solution if the free energy is strictly convex with respect to the set of internal variables

Enakoutsa et al. (2007) then argued that, if it is very questionable to consider the porosity fixed over the whole loading path, it is however, from a numerical point of view, reasonable to discretize porosity in an explicit manner. In that way, over a given time increment porosity is treated as a constant, therefore satisfying the GSM conditions and ensuring existence and uniqueness of the sought solution. The main reason why porosity needs to be considered constant in order to satisfy the conditions of the GSM framework is that porosity's evolution equation is not linked by any means to Gurson's criterion (unlike Rousselier's criterion). As a result, porosity does not satisfy an extended normality rule and one needs to remove porosity from the set of state variables, and thus consider it as fixed over time. However, one could also argue that such a condition is a flaw inherent to Gurson's criterion. It is therefore appealing to propose a

modification of Gurson's criterion in order to alleviate the assumption of constant porosity. In the forthcoming section such a modification is proposed in a general setting which is valid for, but not restricted to Gurson's criterion.

## 6.2.2 A unifying thermodynamical framework for porous plasticity

### 6.2.2.1 General formulation

Under isothermal conditions and at finite deformations the state variables are chosen as the elastic Green-Lagrange strain tensor $\underset{\sim}{\boldsymbol{E}}^e_{GL} = (\underset{\sim}{\boldsymbol{E}}^T.\underset{\sim}{\boldsymbol{E}} - \underset{\sim}{\mathbf{1}})/2$ , a hardening variable $p$ and the porosity $f$. The Helmholtz specific free energy density $\psi$ is a scalar valued function of these variables

$$\psi = \psi\left(\underset{\sim}{\boldsymbol{E}}^e_{GL}, p, f\right) \tag{6.11}$$

The following decomposition of the specific free energy density is proposed

$$\psi\left(\underset{\sim}{\boldsymbol{E}}^e_{GL}, p, f\right) = \psi_e\left(\underset{\sim}{\boldsymbol{E}}^e_{GL}, f\right) + \psi_p(p, f) + \psi_f(f) \tag{6.12}$$

which unifies and generalizes the formulations by Rousselier, Besson, Bouby and Kondo. However the constraint that for any $\underset{\sim}{\boldsymbol{E}}^e_{GL}$ and $p$, the functions $\psi_e(\underset{\sim}{\boldsymbol{E}}^e_{GL}, \bullet)$, $\psi_p(p, \bullet)$ and $\psi_f(\bullet)$ go to zero when the porosity $f$ goes to one is imposed. Under isothermal and static conditions, the first and second principle of thermodynamics lead to the well known Clausius-Duhem inequality

$$d = T\dot{s} = \dot{e} - \dot{\psi} \geq 0 \tag{6.13}$$

where $d$ is the specific dissipation density, $T$ the temperature, $\dot{s}$ the rate of specific entropy density and $\dot{e}$ the specific internal power density. In this context, $\dot{e}$ is merely the opposite of the power density of internal forces $p^{(i)} = (\underset{\sim}{\boldsymbol{\sigma}}/\rho) : \underset{\sim}{\boldsymbol{L}}$. It can therefore be written

$$\dot{e} = p^{(i)} = \frac{\underset{\sim}{\boldsymbol{S}}}{\rho_0} : \dot{\underset{\sim}{\boldsymbol{F}}} = \frac{\underset{\sim}{\boldsymbol{\Pi}}^e}{\rho_\sharp} : \dot{\underset{\sim}{\boldsymbol{E}}}^e_{GL} + \frac{\underset{\sim}{\boldsymbol{\Pi}}^M}{\rho_\sharp} : \left(\dot{\underset{\sim}{\boldsymbol{P}}}.\underset{\sim}{\boldsymbol{P}}^{-1}\right) \tag{6.14}$$

$$\text{with} \quad \underset{\sim}{\boldsymbol{\Pi}}^e = \frac{\rho_\sharp}{\rho}\underset{\sim}{\boldsymbol{E}}^{-1}.\underset{\sim}{\boldsymbol{\sigma}}.\underset{\sim}{\boldsymbol{E}}^{-T} \quad \text{and} \quad \underset{\sim}{\boldsymbol{\Pi}}^M = \underset{\sim}{\boldsymbol{E}}^T.\underset{\sim}{\boldsymbol{E}}.\underset{\sim}{\boldsymbol{\Pi}}^e \tag{6.15}$$

where $\underset{\sim}{\boldsymbol{S}}$ is the first Piola-Kirchhoff (Boussinesq) stress tensor related to the Cauchy stress tensor by $\underset{\sim}{\boldsymbol{S}} = (\rho_0/\rho)\underset{\sim}{\boldsymbol{\sigma}}\underset{\sim}{\boldsymbol{F}}^{-T}$. The scalar $\rho_0$ and $\rho_\sharp = \rho_0/\det(\underset{\sim}{\boldsymbol{P}})$ respectively represent the volumetric mass density in the initial and intermediate configuration of the body. The tensor $\underset{\sim}{\boldsymbol{\Pi}}^M$ is the Mandel stress tensor. $\dot{\psi}$ can be decomposed as follows

$$\dot{\psi}\left(\underset{\sim}{\boldsymbol{E}}^e_{GL}, p, f\right) = \frac{\partial\psi}{\partial\underset{\sim}{\boldsymbol{E}}^e_{GL}} : \dot{\underset{\sim}{\boldsymbol{E}}}^e_{GL} + \frac{\partial\psi}{\partial p}\dot{p} + \frac{\partial\psi}{\partial f}\dot{f} \tag{6.16}$$

Inserting Eq. (6.16) into Clausius-Duhem inequality Eq. (6.13) leads to

$$d = \left(\frac{\underset{\sim}{\boldsymbol{\Pi}}^e}{\rho_\sharp} - \frac{\partial\psi}{\partial\underset{\sim}{\boldsymbol{E}}^e_{GL}}\right) : \dot{\underset{\sim}{\boldsymbol{E}}}^e_{GL} + \frac{\underset{\sim}{\boldsymbol{\Pi}}^M}{\rho_\sharp} : \left(\dot{\underset{\sim}{\boldsymbol{P}}}.\underset{\sim}{\boldsymbol{P}}^{-1}\right) - \frac{\partial\psi}{\partial p}\dot{p} - \frac{\partial\psi}{\partial f}\dot{f} \geq 0 \tag{6.17}$$

The following state law is postulated

$$\frac{\underset{\sim}{\boldsymbol{\Pi}}^e}{\rho_\sharp} = \frac{\partial\psi}{\partial\underset{\sim}{\boldsymbol{E}}^e_{GL}} \tag{6.18}$$

The residual dissipation therefore becomes

$$d = \frac{\underset{\sim}{\boldsymbol{\Pi}}^M}{\rho_\sharp} : \left(\dot{\underset{\sim}{\boldsymbol{P}}}.\underset{\sim}{\boldsymbol{P}}^{-1}\right) - \frac{\partial \psi_p}{\partial p}\dot{p} - \left(\frac{\partial \psi_e}{\partial f} + \frac{\partial \psi_p}{\partial f} + \frac{\partial \psi_f}{\partial f}\right)\dot{f} \geq 0 \tag{6.19}$$

Here the thermodynamical forces $R_p/\rho_\sharp = \partial\psi_p/\partial p$ and $R_f/\rho_\sharp = \partial\psi_e/\partial f + \partial\psi_p/\partial f + \partial\psi_f/\partial f$ respectively power conjugate to $\dot{p}$ and $\dot{f}$ are introduced. In addition $-\underset{\sim}{\boldsymbol{\Pi}}^M/\rho_\sharp$ is power conjugate to $\underset{\sim}{\boldsymbol{L}}^p$. In order to define the evolution of internal variables a dissipation (pseudo)-potential $\Omega$ needs to be defined. The chosen dissipation potential must ensure the positivity of the dissipation in Eq. (6.19). It appears here that any choice of $\Omega$ will determine the evolution of $V_{mat}$ *a priori* unknown in Eq. (6.8). For convenience the thermodynamical formulation is cast into the framework of generalized standard materials (Nguyen, 2000), in which the dissipation potential is a function of the thermodynamical forces and the state variables can intervene as parameters

$$\Omega \quad = \quad \Omega\left(-\frac{\underset{\sim}{\boldsymbol{\Pi}}^M}{\rho_\sharp}, \frac{R_p}{\rho_\sharp}, \frac{R_f}{\rho_\sharp}; \underset{\sim}{\boldsymbol{E}}^e_{GL}, p, f\right) \tag{6.20}$$

The evolution equations then formally write

$$\underset{\sim}{\boldsymbol{L}}^p = -\frac{\partial\Omega}{\partial\left(-\frac{\underset{\sim}{\boldsymbol{\Pi}}^M}{\rho_\sharp}\right)} \qquad \dot{p} = -\frac{\partial\Omega}{\partial\left(\frac{R_p}{\rho_\sharp}\right)} \qquad \dot{f} = -\frac{\partial\Omega}{\partial\left(\frac{R_f}{\rho_\sharp}\right)} \tag{6.21}$$

It is further assumed that $\Omega$ depends only on the first and second invariants of the stress tensor $\Pi^M_m$ and $\Pi^M_{eq}$ and the plastic potentials $\phi_{eq}$ and $\phi_m$ are introduced so that

$$\Omega\left(\frac{\Pi^M_{eq}}{\rho_\sharp}, \frac{\Pi^M_m}{\rho_\sharp}, \frac{R_p}{\rho_\sharp}, \frac{R_f}{\rho_\sharp}; \underset{\sim}{\boldsymbol{E}}^e_{GL}, p, f\right) = \Lambda(\phi) = \Lambda\left(\phi_{eq}\left(\frac{\Pi^M_{eq}}{\rho_\sharp}, \frac{R_p}{\rho_\sharp}; f\right) + \phi_m\left(\frac{\Pi^M_m}{\rho_\sharp}, \frac{R_p}{\rho_\sharp}, \frac{R_f}{\rho_\sharp}; f\right)\right) \tag{6.22}$$

The evolution equations Eq. (6.21) become

$$\underset{\sim}{\boldsymbol{L}}^{p'} = -\frac{\mathrm{d}\Lambda}{\mathrm{d}\phi}\frac{\partial\phi_{eq}}{\partial\left(-\frac{\underset{\sim}{\boldsymbol{\Pi}}^{M'}}{\rho_\sharp}\right)} \qquad \mathrm{tr}\left(\underset{\sim}{\boldsymbol{L}}^p\right) = -\frac{\mathrm{d}\Lambda}{\mathrm{d}\phi}\frac{\partial\phi_m}{\partial\left(-\frac{\Pi^M_m}{\rho_\sharp}\right)} \tag{6.23}$$

$$\dot{p} = -\frac{\mathrm{d}\Lambda}{\mathrm{d}\phi}\frac{\partial\phi}{\partial\left(\frac{R_p}{\rho_\sharp}\right)} \qquad \dot{f} = -\frac{\mathrm{d}\Lambda}{\mathrm{d}\phi}\frac{\partial\phi_m}{\partial\left(\frac{R_f}{\rho_\sharp}\right)} \tag{6.24}$$

with $\Pi^M_m = \mathrm{tr}\left(\underset{\sim}{\boldsymbol{\Pi}}^M\right)/3$ and $\underset{\sim}{\boldsymbol{\Pi}}^{M'} = \underset{\sim}{\boldsymbol{\Pi}}^M - \Pi^M_m\underset{\sim}{\mathbf{1}}$. At this point a particular, yet sufficiently general, form for $\phi_m$ is proposed as

$$\phi_m\left(\frac{\Pi^M_m}{\rho_\sharp}, \frac{R_p}{\rho_\sharp}, \frac{R_f}{\rho_\sharp}; f\right) = h\left(\frac{R_f}{\rho_\sharp}; f\right) g\left(\frac{\Pi^M_m}{\rho_\sharp} + k\left(\frac{R_f}{\rho_\sharp}; f\right), \frac{R_p}{\rho_\sharp}; f\right) \tag{6.25}$$

where $h$, $g$ and $k$ are functions to be defined. Such an assumption on the form of $\phi_m$ is a generalization of the form chosen by Rousselier (2001). It is also the key ingredient for modifications of Gurson's potential in order to overcome the necessity of considering a fixed porosity, as done by Enakoutsa et al. (2007), to fit in the GSM framework. In order to satisfy simultaneously Eq.

(6.4) and (6.21) the following equality must be verified

$$\frac{\partial \phi_m}{\partial\left(\frac{R_f}{\rho_\sharp}\right)} = (1-f)\frac{\partial \phi_m}{\partial\left(-\frac{\Pi_m^M}{\rho_\sharp}\right)} \tag{6.26}$$

This equality raises a particular condition on the functions $h$, $g$ and $k$ which needs to be satisfied. That condition can be written as an implication as follows[1]

$$\begin{aligned}
&- h'\left(\frac{R_f}{\rho_\sharp}; f\right) g\left(\frac{\Pi_m^M}{\rho_\sharp} + k\left(\frac{R_f}{\rho_\sharp}; f\right), \frac{R_p}{\rho_\sharp}; f\right) \\
&- h\left(\frac{R_f}{\rho_\sharp}; f\right) k'\left(\frac{R_f}{\rho_\sharp}; f\right) g'\left(\frac{\Pi_m^M}{\rho_\sharp} + k\left(\frac{R_f}{\rho_\sharp}; f\right), \frac{R_p}{\rho_\sharp}; f\right) \\
&= (1-f)h\left(\frac{R_f}{\rho_\sharp}; f\right) \frac{\partial g}{\partial\left(\frac{\Pi_m^M}{\rho_\sharp}\right)}\left(\frac{\Pi_m^M}{\rho_\sharp} + k\left(\frac{R_f}{\rho_\sharp}; f\right), \frac{R_p}{\rho_\sharp}; f\right) \\
&\Rightarrow \dot{f} = (1-f)\mathrm{tr}\left(\underset{\sim}{\boldsymbol{L}}^p\right)
\end{aligned} \tag{6.27}$$

The constitutive formulation of the material behaviour reduces to the choice of free energy potentials $\psi_e$, $\psi_p$, $\psi_f$ and plastic potentials $\phi_{eq}$ and $\phi_m$. The (visco-)plastic multiplier $\dot{\lambda} = \mathrm{d}\Lambda/\mathrm{d}\phi$ is introduced. The dissipation can then be calculated

$$d = \dot{\lambda}\left(-\frac{\underset{\sim}{\boldsymbol{\Pi}}^M}{\rho_\sharp} : \frac{\partial \phi}{\partial\left(-\frac{\underset{\sim}{\boldsymbol{\Pi}}^M}{\rho_\sharp}\right)} + \frac{R_p}{\rho_\sharp}\frac{\partial \phi}{\partial\left(\frac{R_p}{\rho_\sharp}\right)} + \frac{R_f}{\rho_\sharp}\frac{\partial \phi}{\partial\left(\frac{R_f}{\rho_\sharp}\right)}\right) \tag{6.28}$$

Convexity of the potential $\phi$ with respect to its variables is a sufficient condition to ensure positivity of the dissipation.

#### 6.2.2.2 Effective matrix stress

As discussed by Besson (2010), an elegant way to introduce hardening in a flow potential derived by homogenization of porous materials, is to consider this potential $\phi$ as an implicit definition for an effective matrix stress $\sigma_*$. The flow potential then becomes simply a function of the difference between the effective stress and the conventional hardening force. In other words, $\phi$ derived by homogenization is replaced by

$$\left\{\sigma_* \quad | \quad \begin{array}{l} \phi\left(\frac{\underset{\sim}{\boldsymbol{\Pi}}^M}{\rho_\sharp}, \frac{\sigma_*}{\rho_\sharp}, \frac{R_f}{\rho_\sharp}; f\right) \overset{\text{def}}{=} 0 \\ \tilde{\phi}(\sigma_* - R_p; p; f) \end{array}\right. \tag{6.29}$$

$\phi$ is used as an implicit definition of $\sigma_*(\underset{\sim}{\boldsymbol{\Pi}}^M, R_f; f)$. $\tilde{\phi}$ is the effective flow potential. In a particular case, yet still sufficiently general, $\sigma_*$ shall be expressed as an implicit function of the stress $\underset{\sim}{\boldsymbol{\Sigma}}(\underset{\sim}{\boldsymbol{\Pi}}^M, R_f; f) = \underset{\sim}{\boldsymbol{\Pi}}^M - (1-f)R_f\underset{\sim}{\mathbf{1}}$ so that

$$\left\{\sigma_* \quad | \quad \begin{array}{l} \phi\left(\frac{\underset{\sim}{\boldsymbol{\Sigma}}}{\rho_\sharp}, \frac{\sigma_*}{\rho_\sharp}; f\right) \overset{\text{def}}{=} 0 \\ \tilde{\phi}(\sigma_* - R_p; p; f) \end{array}\right. \tag{6.30}$$

[1] The notations $h'$, $g'$ and $k'$ are used as abbreviations for the derivatives of $h$, $g$ and $k$ with respect to their first argument.

An important feature is that if $\sigma_*$ is an homogeneous function of degree $n$ in $\underset{\sim}{\boldsymbol{\Sigma}}$ (*i.e.* $\sigma_*(\alpha\underset{\sim}{\boldsymbol{\Sigma}};f) = \alpha^n\sigma_*(\underset{\sim}{\boldsymbol{\Sigma}};f)$), then Euler's lemma requires

$$\frac{\partial\sigma_*}{\partial\underset{\sim}{\boldsymbol{\Sigma}}} : \underset{\sim}{\boldsymbol{\Sigma}} = n\sigma_* \tag{6.31}$$

The dissipation in Eq. (6.28) can hence be reformulated as

$$\begin{aligned} d &= \dot{\lambda}\left(-\frac{\underset{\sim}{\boldsymbol{\Pi}}^M}{\rho_\sharp} : \frac{\partial\tilde{\phi}}{\partial\left(-\frac{\underset{\sim}{\boldsymbol{\Pi}}^M}{\rho_\sharp}\right)} + \frac{R_p}{\rho_\sharp}\frac{\partial\tilde{\phi}}{\partial\left(\frac{R_p}{\rho_\sharp}\right)} + \frac{R_f}{\rho_\sharp}\frac{\partial\tilde{\phi}}{\partial\left(\frac{R_f}{\rho_\sharp}\right)}\right) \\ &= \dot{\lambda}\left(\frac{\partial\tilde{\phi}}{\partial\sigma_*}\frac{\partial\sigma_*}{\partial\left(\frac{\underset{\sim}{\boldsymbol{\Sigma}}}{\rho_\sharp}\right)}\left(\frac{\partial\left(\frac{\underset{\sim}{\boldsymbol{\Sigma}}}{\rho_\sharp}\right)}{\partial\left(-\frac{\underset{\sim}{\boldsymbol{\Pi}}^M}{\rho_\sharp}\right)} : \left(-\frac{\underset{\sim}{\boldsymbol{\Pi}}^M}{\rho_\sharp}\right) + \frac{\partial\left(\frac{\underset{\sim}{\boldsymbol{\Sigma}}}{\rho_\sharp}\right)}{\partial\left(\frac{R_f}{\rho_\sharp}\right)}\frac{R_f}{\rho_\sharp}\right) + R_p\frac{\partial\tilde{\phi}}{\partial\left(\frac{R_p}{\rho_\sharp}\right)}\right) \\ &= \dot{\lambda}\left(\frac{\partial\tilde{\phi}}{\partial\sigma_*}\frac{\partial\sigma_*}{\partial\left(\frac{\underset{\sim}{\boldsymbol{\Sigma}}}{\rho_\sharp}\right)} : \frac{\underset{\sim}{\boldsymbol{\Sigma}}}{\rho_\sharp} + \frac{R_p}{\rho_\sharp}\frac{\partial\tilde{\phi}}{\partial\left(\frac{R_p}{\rho_\sharp}\right)}\right) \\ &= \dot{\lambda}\left(\frac{\partial\tilde{\phi}}{\partial\sigma_*}n\sigma_* + \frac{R_p}{\rho_\sharp}\frac{\partial\tilde{\phi}}{\partial\left(\frac{R_p}{\rho_\sharp}\right)}\right) \end{aligned} \tag{6.32}$$

#### 6.2.2.3 Link to existing formulations

The framework presented in the previous section unifies several thermodynamical approaches of homogenized porous media. To recover Rousselier's formulation one needs to assume that $\psi_e$ and $\psi_p$ are independent of $f$ in (6.12). It is recalled that this assumption is inconsistent with the fact that $\psi$ should vanish when $f$ goes to one. In Rousselier's model, the function $k$ in Eq. (6.25) vanishes and $h$ and $g$ are chosen such that implication Eq. (6.27) becomes

$$-h'g = (1-f)hg' \Rightarrow \dot{f} = (1-f)\mathrm{tr}\left(\underset{\sim}{\boldsymbol{L}}^p\right) \tag{6.33}$$

Assuming $\phi_{eq} = \Pi^M_{eq}/\rho_\sharp - R_p/\rho_\sharp - R_0/\rho_0$ and solving the differential equation on the left-hand side of Eq. (6.33) implies that

$$h\left(\frac{R_f}{\rho_\sharp};f\right) = f \tag{6.34}$$

$$g\left(\frac{\Pi^M_m}{\rho_\sharp} + k\left(\frac{R_f}{\rho_\sharp};f\right),\frac{R_p}{\rho_\sharp};f\right) = \frac{D\sigma_1}{\rho_0}\exp\left(\frac{\Pi^M_m(1-f_0)}{\sigma_1(1-f)}\right) \tag{6.35}$$

$$\text{with } k\left(\frac{R_f}{\rho_\sharp};f\right) = 0 \tag{6.36}$$

$$\phi = \phi_{eq} + \phi_m = \frac{\Pi^M_{eq}}{\rho_\sharp} - \frac{R_p}{\rho_\sharp} - \frac{R_0}{\rho_0} + \frac{Df\sigma_1}{\rho_0}\exp\left(\frac{\Pi^M_m(1-f_0)}{\sigma_1(1-f)}\right) \tag{6.37}$$

where $D$ and $\sigma_1$ are integration constants and $R_0$ the radius of the initial elastic domain. Note that $h$ coincides with $f$ at $R_f/\rho_\sharp$ only, which does not imply that $h$ is necessarily a constant. Therefore $h'$ does not vanish in general. Besson's formulation can also be recovered by assuming that $\psi_e$ is independent of $f$ and $\psi_f$ is identically zero in (6.12). In addition $\psi_p$ depends on $f$

so that $\psi_p(p,f) = (1-f)\tilde{\psi}_p(p)$. However in Besson's formulation the contribution of $R_f/\rho_\sharp$ was neglected so that $\phi_m = g(\Pi_m^M/\rho_\sharp, R_p/\rho_\sharp; f)$. Lastly, Bouby and Kondo's formulation can be recovered (at small strains where $\phi^p = f$) by assuming that $\psi_e$ is independent of $f$. One can recover the statement made by Bouby and Kondo that the effective mean stress seen by the homogenized materials is a sort of Terzaghi stress, which is the sum of the macroscopic mean stress $\Pi_m^M$ and an additional pressure. Such a formulation is obtained by imposing

$$h\left(\frac{R_f}{\rho_\sharp}\right) = 1 \tag{6.38}$$

$$g\left(\frac{\Pi_m^M}{\rho_\sharp} + k\left(\frac{R_f}{\rho_\sharp}; f\right), \frac{R_p}{\rho_\sharp}; f\right) = 2f\cosh\left(\frac{\frac{\Pi_m^M}{\rho_\sharp} + k\left(\frac{R_f}{\rho_\sharp}; f\right)}{\frac{R_p}{\rho_\sharp}}\right) \tag{6.39}$$

$$\text{with } k\left(\frac{R_f}{\rho_\sharp}; f\right) = -(1-f)\frac{R_f}{\rho_\sharp} \tag{6.40}$$

in Eq. (6.25). With this assumption one has indeed

$$\phi = \phi_{eq}\left(\frac{\Pi_{eq}^M}{\rho_\sharp}, \frac{R_p}{\rho_\sharp}; f\right) + \phi_m\left(\frac{\Pi_m^M - (1-f)R_f}{\rho_\sharp}, \frac{R_p}{\rho_\sharp}\right) \tag{6.41}$$

and more generally

$$\phi = \left(\frac{\underset{\sim}{\mathbf{\Pi}}^M - (1-f)R_f\underset{\sim}{\mathbf{1}}}{\rho_\sharp}, \frac{R_p}{\rho_\sharp}\right) \tag{6.42}$$

where $-(1-f)R_f$ act as a hydrostatic pressure. Here one recognizes the particular form of the stress $\underset{\sim}{\mathbf{\Sigma}} = \underset{\sim}{\mathbf{\Pi}}^M - (1-f)R_f\underset{\sim}{\mathbf{1}}$ described in previous section. Unlike the formulation by Rousselier no additional constraint on $R_f$ is here imposed, thus the dependence of $\psi_e$, $\psi_p$ and $\psi_f$ on $f$ can be chosen freely. In particular one can enforce that the Helmholtz free energy vanishes when $f$ goes to one. As this work proceeds it will therefore be assumed that the general form of the flow potential in Eq. (6.42) holds. Equivalently, as discussed above, one can use Eq. (6.42) as an implicit definition of an effective matrix stress $\sigma_*$ and reformulate the flow potential as

$$\left\{\begin{array}{ll} \sigma_* & \phi\left(\frac{\underset{\sim}{\mathbf{\Pi}}^M - (1-f)R_f\underset{\sim}{\mathbf{1}}}{\rho_\sharp}, \frac{\sigma_*}{\rho_\sharp}, \frac{R_f}{\rho_\sharp}; f\right) \overset{\text{def}}{=} 0 \\ & \tilde{\phi}(\sigma_* - R_p; p; f) \end{array}\right. \tag{6.43}$$

where $\tilde{\phi}$ becomes the effective flow potential of the porous material. Within this formulation, Gurson's flow potential (Gurson, 1977) used by Besson (2009) and Bouby and Kondo (2017) becomes

$$\left\{\begin{array}{ll} \sigma_* & \phi = \left(\frac{\Pi_{eq}^M}{\sigma_*}\right)^2 + 2f\cosh\left(\frac{3}{2}\frac{\Pi_m^M - (1-f)R_f}{\sigma_*}\right) - 1 - f^2 \overset{\text{def}}{=} 0 \\ & \tilde{\phi} = (1-f)(\sigma_* - R_p - R_0) \end{array}\right. \tag{6.44}$$

where it can be noted that $\Pi_{eq}^M = \Sigma_{eq}$, because the von Mises equivalent stress only depends on the deviatoric part of the stress $\underset{\sim}{\mathbf{\Sigma}}$. The particular form of $\tilde{\phi}$ used by Besson (2009) was chosen. The advantage of Gurson's criterion lies in its homogeneity of degree one in $\underset{\sim}{\mathbf{\Sigma}}$. The homogeneity of degree one is indeed the key ingredient in order to satisfy the Hill-Mandel lemma (Besson, 2009). Rousselier's criterion in its original form does not have this property of being homogeneous of degree one in $\underset{\sim}{\mathbf{\Sigma}}$. But one could also, with the same assumptions on functions

$h$, $g$ and $k$, use the extension of Rousselier's criterion by Tanguy and Besson (2001) in order to define an effective matrix stress $\sigma_*$ as

$$\left\{ \sigma_* \quad | \quad \phi = \frac{\Pi^M_{eq}}{\rho_\sharp \sigma_*} + \frac{2}{3} f D_R \exp\left( \frac{q_R}{2} \frac{(\Pi^M_m - (1-f)R_f)(1-f_0)}{\sigma_*(1-f)} \right) \stackrel{\text{def}}{=} 0 \right. \\ \left. \qquad \tilde{\phi} = (1-f)(\sigma_* - R_p - R_0) \right. \tag{6.45}$$

With this definition, $\sigma_*$ is also homogeneous of degree one in $\underset{\sim}{\boldsymbol{\Sigma}}$. Therefore in both cases Euler's lemma Eq. (6.31) can be applied with $n = 1$. In addition, the flow potential $\tilde{\phi}$ chosen in Eq. (6.44) enforces $\dot{\lambda} = \dot{p}$. Eventually, using (6.32) one has

$$d = \frac{\dot{p}}{\rho_\sharp} \left( \tilde{\phi} + (1-f)R_0 \right) \tag{6.46}$$

In order to reduce the thermodynamical framework developed above to its quintessence, a small strain formulation of Gurson's model within this framework is given in Appendix I.

## 6.2.3 Extension to multi-mechanisms plasticity

### 6.2.3.1 General formulation

Extending to finite strains a formulation by Besson (2009) it is considered that multiple plastic deformation mechanisms can coexist so that the overall plastic deformation rate $\underset{\sim}{\boldsymbol{L}}^p = \dot{\underset{\sim}{\boldsymbol{P}}}.\underset{\sim}{\boldsymbol{P}}^{-1}$ is a sum of $K$ plastic deformation rates $\underset{\sim}{\boldsymbol{L}}^p_i$

$$\dot{\underset{\sim}{\boldsymbol{P}}}.\underset{\sim}{\boldsymbol{P}}^{-1} = \sum_{i=1}^{K} \underset{\sim}{\boldsymbol{L}}^p_i \tag{6.47}$$

The internal variables that are now chosen are the elastic Green-Lagrange strain tensor $\underset{\sim}{\boldsymbol{E}}^e_{GL} = (\underset{\sim}{\boldsymbol{E}}^T.\underset{\sim}{\boldsymbol{E}} - \underset{\sim}{\mathbf{1}})/2$, a hardening variable $p_i$ for each deformation mechanism and the porosity $f$. The Helmholtz specific free-energy density is postulated to be of the form

$$\psi\left(\underset{\sim}{\boldsymbol{E}}^e_{GL}, f, p_i\right) = \psi_e(\underset{\sim}{\boldsymbol{E}}^e_{GL}, f) + \sum_{i=1}^{K} \psi^i_p(p_i, f) + \psi_f(f) \tag{6.48}$$

Similarly to previous section the constraint is imposed that for any $\underset{\sim}{\boldsymbol{E}}^e_{GL}$ and $p_i$, the functions $\psi_e(\underset{\sim}{\boldsymbol{E}}^e_{GL}, \bullet)$, $\psi^i_p(p_i, \bullet)$ and $\psi_f(\bullet)$ tend to zero when the porosity $f$ goes to one. The mechanical dissipation then writes

$$\begin{aligned} d = &\left( \frac{\underset{\sim}{\boldsymbol{\Pi}}^e}{\rho_\sharp} - \frac{\partial \psi}{\partial \underset{\sim}{\boldsymbol{E}}^e_{GL}} \right) : \dot{\underset{\sim}{\boldsymbol{E}}}^e_{GL} + \frac{\underset{\sim}{\boldsymbol{\Pi}}^M}{\rho_\sharp} : (\dot{\underset{\sim}{\boldsymbol{P}}}.\underset{\sim}{\boldsymbol{P}}^{-1}) - \sum_{i=1}^{K} \frac{\partial \psi^i_p}{\partial p_i} \dot{p}_i \\ &- \left( \frac{\partial \psi_e}{\partial f} + \sum_{i=1}^{K} \frac{\partial \psi^i_p}{\partial f} + \frac{\partial \psi}{\partial f} \right) \dot{f} \end{aligned} \tag{6.49}$$

The following state law is postulated from Eq. (6.49):

$$\frac{\underset{\sim}{\boldsymbol{\Pi}}^e}{\rho_\sharp} = \frac{\partial \psi}{\partial \underset{\sim}{\boldsymbol{E}}^e_{GL}} \tag{6.50}$$

The thermodynamic forces $R^i_p/\rho_\sharp = \partial \psi^i_p / \partial p_i$ and $R_f/\rho_\sharp = \partial \psi_e/\partial f + \sum_{i=1}^{K} \partial \psi^i_p/\partial f + \partial \psi_f/\partial f$ are respectively conjugate to $\dot{p}_i$ and $\dot{f}$. In addition $-\underset{\sim}{\boldsymbol{\Pi}}^M/\rho_\sharp$ is work conjugate to $\underset{\sim}{\boldsymbol{L}}^p$. The residual

mechanical dissipation therefore becomes

$$d = \frac{\underset{\sim}{\mathbf{\Pi}}^M}{\rho_\sharp} : (\dot{\underset{\sim}{\boldsymbol{P}}}.\underset{\sim}{\boldsymbol{P}}^{-1}) - \sum_{i=1}^{K} \frac{R_p^i}{\rho_\sharp}\dot{p}_i - \frac{R_f}{\rho_\sharp}\dot{f} \geq 0 \tag{6.51}$$

In order to define the evolution of internal variables a dissipation (pseudo)-potential $\Omega_i$ needs to be defined for each plastic deformation mechanism. The chosen dissipation potentials need to ensure the positivity of the dissipation in Eq. (6.51). The dissipation potentials are functions of the thermodynamical forces and the state variables can intervene as parameters

$$\Omega_i = \Omega_i\left(\frac{\underset{\sim}{\mathbf{\Pi}}^M}{\rho_\sharp}, \frac{R_p^i}{\rho_\sharp}, \frac{R_f}{\rho_\sharp}; \underset{\sim}{\boldsymbol{E}}^e_{GL}, p_i, f\right) \tag{6.52}$$

The evolution equations then formally write

$$\dot{\underset{\sim}{\boldsymbol{L}}}^p{}_i = -\frac{\partial\Omega_i}{\partial\left(-\frac{\underset{\sim}{\mathbf{\Pi}}^M}{\rho_\sharp}\right)} \qquad \dot{p}_i = -\frac{\partial\Omega_i}{\partial\left(\frac{R_p^i}{\rho_\sharp}\right)} \qquad \dot{f} = -\sum_{i=1}^{K}\frac{\partial\Omega_i}{\partial\left(\frac{R_f}{\rho_\sharp}\right)} \tag{6.53}$$

For each mechanism the plastic potentials $\phi^i$ is introduced so that

$$\Omega_i\left(\frac{\underset{\sim}{\mathbf{\Pi}}^M}{\rho_\sharp}, \frac{R_p^i}{\rho_\sharp}, \frac{R_f}{\rho_\sharp}; \underset{\sim}{\boldsymbol{E}}^e_{GL}, p_i, f\right) = \Lambda(\phi^i) \tag{6.54}$$

The evolution equations Eq. (6.53) become

$$\underset{\sim}{\boldsymbol{L}}^p_i = -\frac{\mathrm{d}\Lambda}{\mathrm{d}\phi^i}\frac{\partial\phi^i}{\partial\left(-\frac{\underset{\sim}{\mathbf{\Pi}}^M}{\rho_\sharp}\right)} \qquad \dot{p}_i = -\frac{\mathrm{d}\Lambda}{\mathrm{d}\phi^i}\frac{\partial\phi^i}{\partial\left(\frac{R_p}{\rho_\sharp}\right)} \qquad \dot{f} = -\sum_{i=1}^{K}\frac{\mathrm{d}\Lambda}{\mathrm{d}\phi^i}\frac{\partial\phi^i_m}{\partial\left(\frac{R_f}{\rho_\sharp}\right)} \tag{6.55}$$

Taking advantage of the discussion made in previous section a similar potential as in Eq. (6.42) is adopted reminding the implication

$$\begin{aligned}\forall i, \quad \phi^i\left(\frac{\underset{\sim}{\mathbf{\Pi}}^M}{\rho_\sharp}, \frac{R_p^i}{\rho_\sharp}, \frac{R_f}{\rho_\sharp}; \underset{\sim}{\boldsymbol{E}}^e_{GL}, p_i, f\right) = \phi^i\left(\frac{\underset{\sim}{\mathbf{\Pi}}^M - (1-f)R_f\underset{\approx}{\mathbf{1}}}{\rho_\sharp}, \frac{R_p^i}{\rho_\sharp}; \underset{\sim}{\boldsymbol{E}}^e_{GL}, p_i, f\right) \\ \Rightarrow \dot{f} = (1-f)\mathrm{tr}\,(\dot{\underset{\sim}{\boldsymbol{P}}}.\underset{\sim}{\boldsymbol{P}}^{-1})\end{aligned} \tag{6.56}$$

The dependence of $\psi_e$, $\psi_p^i$ and $\psi_f$ on $f$ can therefore be chosen freely. In particular one can enforce that the Helmholtz free energy vanishes when $f$ goes to one. The constitutive formulation of the material behaviour reduces to the choice of free energy potentials $\psi_e$, $\psi_p^i$, $\psi_f$ and plastic potentials $\phi_{eq}^i$ and $\phi_m^i$. The (visco-)plastic multipliers for each deformation mechanism $\dot{\lambda}_i = \mathrm{d}\Lambda/\mathrm{d}\phi^i$ are introduced. The dissipation can than be calculated

$$d = \sum_{i=1}^{K}\dot{\lambda}_i\left(-\frac{\underset{\sim}{\mathbf{\Pi}}^M}{\rho_\sharp} : \frac{\partial\phi^i}{\partial\left(-\frac{\underset{\sim}{\mathbf{\Pi}}^M}{\rho_\sharp}\right)} + \frac{R_p^i}{\rho_\sharp}\frac{\partial\phi^i}{\partial\left(\frac{R_p^i}{\rho_\sharp}\right)} + \frac{R_f}{\rho_\sharp}\frac{\partial\phi^i}{\partial\left(\frac{R_f}{\rho_\sharp}\right)}\right) \tag{6.57}$$

Convexity of the potentials $\phi_i$ is sufficient to ensure the positivity of the dissipation.

#### 6.2.3.2 Effective matrix stresses

The same procedure as in section 6.2.2.2 can be applied to introduce hardening laws for each mechanism by considering the flow potentials $\phi^i$ as implicit definitions for effective matrix stresses $\sigma^i_*$. Flow potentials then become simply the difference between the effective stress and the conventional hardening force. In other words $\phi^i$ derived by homogenization is replaced by

$$\left\{ \sigma^i_* \quad | \quad \begin{array}{l} \phi^i\left(\dfrac{\underset{\sim}{\boldsymbol{\Pi}}^M}{\rho_\sharp}, \dfrac{\sigma^i_*}{\rho_\sharp}, \dfrac{R_f}{\rho_\sharp}; f\right) \overset{\text{def}}{=} 0 \\ \tilde{\phi}^i(\sigma^i_* - R_p; p; f) \end{array} \right. \tag{6.58}$$

$\phi^i$ is used as an implicit definition of $\sigma^i_*(\underset{\sim}{\boldsymbol{\Pi}}^M, R_f; f)$. $\tilde{\phi}^i$ is the effective flow potential. A particular case, yet still general enough, is when $\sigma^i_*$ shall be expressed as an implicit function of a stress $\underset{\sim}{\boldsymbol{\Sigma}}(\underset{\sim}{\boldsymbol{\Pi}}^M, R_f; f) = \underset{\sim}{\boldsymbol{\Pi}}^M - (1-f)R_f\underset{\sim}{\mathbf{1}}$ so that

$$\left\{ \sigma^i_* \quad | \quad \begin{array}{l} \phi^i\left(\dfrac{\underset{\sim}{\boldsymbol{\Sigma}}}{\rho_\sharp}, \dfrac{\sigma^i_*}{\rho_\sharp}; f\right) \overset{\text{def}}{=} 0 \\ \tilde{\phi}^i(\sigma^i_* - R_p; p; f) \end{array} \right. \tag{6.59}$$

An important feature is that if $\sigma^i_*$ is an homogeneous function of degree $n_i$ in $\underset{\sim}{\boldsymbol{\Sigma}}$ (*i.e.* $\sigma^i_*(\alpha\underset{\sim}{\boldsymbol{\Sigma}}; f) = \alpha^{n_i}\sigma^i_*(\underset{\sim}{\boldsymbol{\Sigma}}; f)$), then Euler's lemma requires

$$\frac{\partial \sigma^i_*}{\partial \underset{\sim}{\boldsymbol{\Sigma}}} : \underset{\sim}{\boldsymbol{\Sigma}} = n_i \sigma^i_* \tag{6.60}$$

The dissipation in Eq. (6.57) can hence be reformulated

$$\begin{aligned} d &= \sum_{i=1}^{K} \dot{\lambda}_i \left( -\frac{\underset{\sim}{\boldsymbol{\Pi}}^M}{\rho_\sharp} : \frac{\partial \tilde{\phi}^i}{\partial\left(-\dfrac{\underset{\sim}{\boldsymbol{\Pi}}^M}{\rho_\sharp}\right)} + \frac{R^i_p}{\rho_\sharp}\frac{\partial \tilde{\phi}^i}{\partial\left(\frac{R^i_p}{\rho_\sharp}\right)} + \frac{R_f}{\rho_\sharp}\frac{\partial \tilde{\phi}^i}{\partial\left(\frac{R_f}{\rho_\sharp}\right)} \right) \\ &= \sum_{i=1}^{K} \dot{\lambda}_i \left( \frac{\partial \tilde{\phi}^i}{\partial \sigma^i_*}\frac{\partial \sigma^i_*}{\partial\left(\frac{\underset{\sim}{\boldsymbol{\Sigma}}}{\rho_\sharp}\right)} \left( \frac{\partial\left(\frac{\underset{\sim}{\boldsymbol{\Sigma}}}{\rho_\sharp}\right)}{\partial\left(-\frac{\underset{\sim}{\boldsymbol{\Pi}}^M}{\rho_\sharp}\right)} : \left(-\frac{\underset{\sim}{\boldsymbol{\Pi}}^M}{\rho_\sharp}\right) + \frac{\partial\left(\frac{\underset{\sim}{\boldsymbol{\Sigma}}}{\rho_\sharp}\right)}{\partial\left(\frac{R_f}{\rho_\sharp}\right)}\frac{R_f}{\rho_\sharp} \right) + R^i_p \frac{\partial \tilde{\phi}^i}{\partial\left(\frac{R^i_p}{\rho_\sharp}\right)} \right) \\ &= \sum_{i=1}^{K} \dot{\lambda}_i \left( \frac{\partial \tilde{\phi}^i}{\partial \sigma^i_*}\frac{\partial \sigma^i_*}{\partial\left(\frac{\underset{\sim}{\boldsymbol{\Sigma}}}{\rho_\sharp}\right)} : \frac{\underset{\sim}{\boldsymbol{\Sigma}}}{\rho_\sharp} + \frac{R^i_p}{\rho_\sharp}\frac{\partial \tilde{\phi}^i}{\partial\left(\frac{R^i_p}{\rho_\sharp}\right)} \right) \\ &= \sum_{i=1}^{K} \dot{\lambda}_i \left( \frac{\partial \tilde{\phi}^i}{\partial \sigma^i_*} n_i \sigma^i_* + \frac{R^i_p}{\rho_\sharp}\frac{\partial \tilde{\phi}^i}{\partial\left(\frac{R^i_p}{\rho_\sharp}\right)} \right) \end{aligned} \tag{6.61}$$

## 6.3 Multi-mechanism based strain gradient porous crystal plasticity

The multi-mechanism deformation framework for homogenized porous materials established at finite strain in the previous section is now applied in the context of growth and coalescence of voids in single crystals with non-local gradient effects.

### 6.3.1 Void growth and void coalescence in single crystals

Following the work developed by Ling et al. (2016), a void growth deformation mechanism for each slip system of a single crystal is considered. An additional deformation mechanism is introduced to account for void coalescence. The main argument which motivates not to decompose coalescence in deformation mechanisms on each slip system is that coalescence is a phenomenon which mostly involves activation of many slip systems inside the ligaments separating coalescing voids as discussed by Barrioz et al. (2019). Therefore, for a crystal having $N$ slip systems, the plastic rate is written as

$$\dot{\underset{\sim}{\boldsymbol{P}}}.\underset{\sim}{\boldsymbol{P}}^{-1} = \sum_{s=1}^{N} \underset{\sim}{\boldsymbol{L}}_s^p + \underset{\sim}{\boldsymbol{L}}_c^p \tag{6.62}$$

where the terms in the sum account for plastic slip and void growth on each slip system, and $\underset{\sim}{\boldsymbol{L}}_c^p$ is the plastic rate associated to void coalescence. For each deformation mechanism a scalar deformation rate can be introduced. For void growth they will be denoted $\dot{\gamma}^s$ and $\dot{\gamma}^c$ for void coalescence. Note that $\dot{\gamma}^c$ is not to be interpreted as a slip rate, since void coalescence is not a mechanism decomposed on slip systems. An accumulated plastic deformation variable is introduced as

$$\gamma_{cum} = \int_0^t \left( \sum_{s=1}^{N} |\dot{\gamma}^s| + |\dot{\gamma}^c| \right) \mathrm{d}t \tag{6.63}$$

### 6.3.2 Gradient enhanced principle of virtual power

In the spirit of the model developed by Wulfinghoff and Böhlke (2012) it is assumed that the gradient effects operate on the accumulated plasticity scalar variable $\gamma_{cum}$. In order to treat the nonlocality, a relaxation is used that is based on the duplication of $\gamma_{cum}$ into an auxiliary variable $\gamma_\chi$. Following (Fleck and Hutchinson, 1997; Forest and Sievert, 2003; Gurtin and Anand, 2009), upon neglecting the contribution of body forces, for any material subset $D_0$, an enriched principle of virtual power is stated

$$\int_{D_0} \left( \underset{\sim}{\boldsymbol{S}} : \dot{\underset{\sim}{\boldsymbol{F}}} + S\dot{\gamma}_\chi + \underline{\boldsymbol{M}} \,.\, \dot{\underline{\boldsymbol{K}}}_\chi \right) \mathrm{d}V_0 = \int_{\partial D_0} \left( \underline{\boldsymbol{T}} \,.\, \dot{\underline{\boldsymbol{u}}} + M\dot{\gamma}_\chi \right) \mathrm{d}S_0 \qquad \forall \dot{\underline{\boldsymbol{u}}}\,,\ \forall \dot{\gamma}_{cum},\ \forall D_0 \tag{6.64}$$

Higher order stress scalar $S$ and vector $\underline{\boldsymbol{M}}$ are energetic duals to $\gamma_\chi$ and $\underline{\boldsymbol{K}}_\chi = \mathrm{Grad}\,\gamma_\chi$. Equality of both instances will be ensured by using a Lagrange multiplier in the free energy potential (Zhang et al., 2018). The power of internal forces on the left-hand side of Eq. (6.64) is in equilibrium with the power of contact forces on the right-hand side. The traction vector is $\underline{\boldsymbol{T}}$ and a higher order traction scalar $M$ is dual to $\gamma_\chi$. From Eq. (6.64) one can develop the following balance equations and boundary conditions

$$\mathrm{Div}\,\underset{\sim}{\boldsymbol{S}} = \underline{\boldsymbol{0}} \quad \forall \underline{\boldsymbol{X}} \in D_0 \qquad \text{and} \qquad \underline{\boldsymbol{T}} = \underset{\sim}{\boldsymbol{S}}.\underline{\boldsymbol{n}}_0 \quad \forall \underline{\boldsymbol{X}} \in \partial D_0 \tag{6.65}$$

$$\mathrm{Div}\,\underline{\boldsymbol{M}} - S = 0 \quad \forall \underline{\boldsymbol{X}} \in D_0 \qquad \text{and} \qquad M = \underline{\boldsymbol{M}} \,.\, \underline{\boldsymbol{n}}_0 \quad \forall \underline{\boldsymbol{X}} \in \partial D_0 \tag{6.66}$$

where $\underline{\boldsymbol{n}}_0$ refers to the outward unit surface normal.

### 6.3.3 Gradient enhanced free energy potential

The first step to the definition of the material behaviour is the choice of a specific free energy density potential which depends on the state variables. For the present model the state variables are the elastic Green-Lagrange strain measure $\underset{\sim}{\boldsymbol{E}}^e_{GL}$, the local and non-local accumulated plastic deformation $\gamma_{cum}$ and $\gamma_\chi$, the Lagrangian gradient of the latter $\underline{\boldsymbol{K}}_\chi$, the Lagrange multiplier $\lambda$,

one hardening variables $r^s$ per slip system $s$ and the porosity $f$. A simple acceptable dependence on $f$ of the free energy potential is chosen

$$\psi\left(\underset{\sim}{\boldsymbol{E}}^e_{GL}, \gamma_{cum}, \gamma_\chi, \underline{\boldsymbol{K}}_\chi, r^s, f, \lambda\right) = (1-f)\left(\frac{1}{2\rho_\sharp}\underset{\sim}{\boldsymbol{E}}^e_{GL} : \underset{\approx}{\boldsymbol{C}} : \underset{\sim}{\boldsymbol{E}}^e_{GL} + \psi_h(r^s, \gamma_{cum})\right.$$
$$\left. + \frac{1}{2\rho_0}\underline{\boldsymbol{K}}_\chi.\underset{\sim}{\boldsymbol{A}}.\underline{\boldsymbol{K}}_\chi + \frac{\lambda}{\rho_0}(\gamma_{cum}-\gamma_\chi) + \frac{\mu_\chi}{2\rho_0}(\gamma_{cum}-\gamma_\chi)^2\right) \quad (6.67)$$

which is nothing but the free energy potential of the pristine void-free material weighed by $(1-f)$. The material parameter $\underset{\sim}{\boldsymbol{A}}$ is a second order tensor of higher order moduli. For a material with cubic symmetry $\underset{\sim}{\boldsymbol{A}}$ reduces to $A\underset{\sim}{\boldsymbol{1}}$, where $A$ is the single higher order modulus in this case. $\lambda$ is a Lagrange multiplier which enforces $\gamma_\chi$ and $\gamma_{cum}$ to be equal and $\mu_\chi$ is a Lagrangian penalization modulus enhancing coercivity of the model. From the 1-st and 2-nd principle of thermodynamics the Clausius-Duhem inequality is written

$$d = \frac{\underset{\sim}{\boldsymbol{S}}}{\rho_0} : \dot{\underset{\sim}{\boldsymbol{F}}} + \frac{S}{\rho_0}\dot{\gamma}_\chi + \frac{\underline{\boldsymbol{M}}}{\rho_0}.\dot{\underline{\boldsymbol{K}}}_\chi - \dot{\psi} \geq 0 \quad (6.68)$$

The first term of equation Eq. (6.68) can be decomposed into elastic and plastic contributions as in Eq. (6.14). The mechanical dissipation therefore becomes

$$d = \left(\frac{\underset{\sim}{\boldsymbol{\Pi}}^e}{\rho_\sharp} - \frac{\partial\psi}{\partial\underset{\sim}{\boldsymbol{E}}^e_{GL}}\right) : \dot{\underset{\sim}{\boldsymbol{E}}}^e_{GL} + \frac{\underset{\sim}{\boldsymbol{\Pi}}^M}{\rho_\sharp} : \left(\dot{\underset{\sim}{\boldsymbol{P}}}.\underset{\sim}{\boldsymbol{P}}^{-1}\right) + \left(\frac{S}{\rho_0} - \frac{\partial\psi}{\partial\gamma_\chi}\right)\dot{\gamma}_\chi + \left(\frac{\underline{\boldsymbol{M}}}{\rho_0} - \frac{\partial\psi}{\partial\underline{\boldsymbol{K}}_\chi}\right).\dot{\underline{\boldsymbol{K}}}_\chi$$
$$- (1-f)\sum_{s=1}^{N}\frac{\partial\psi_h}{\partial r^s}\dot{r}^s - \frac{\partial\psi}{\partial\gamma_{cum}}\dot{\gamma}_{cum} - \frac{\partial\psi}{\partial f}\dot{f} - \frac{\partial\psi}{\partial\lambda}\dot{\lambda} \geq 0 \quad (6.69)$$

The following state laws are adopted

$$\underset{\sim}{\boldsymbol{\Pi}}^e = \rho_\sharp\frac{\partial\psi}{\partial\underset{\sim}{\boldsymbol{E}}^e_{GL}} = (1-f)\underset{\approx}{\boldsymbol{C}} : \underset{\sim}{\boldsymbol{E}}^e_{GL} \quad (6.70)$$

$$S = \rho_0\frac{\partial\psi}{\partial\gamma_\chi} = (1-f)\left(\lambda - \mu_\chi(\gamma_{cum}-\gamma_\chi)\right) = (1-f)\left(\Delta_\chi - \mu_\chi\gamma_{cum}\right) \quad (6.71)$$

$$\underline{\boldsymbol{M}} = \rho_0\frac{\partial\psi}{\partial\underline{\boldsymbol{K}}_\chi} = (1-f)A\underline{\boldsymbol{K}}_\chi \quad (6.72)$$

For convenience the scalar stress $\Delta_\chi = \lambda + \mu_\chi\gamma_\chi$ is introduced. By definition $\partial\psi/\partial\lambda$ must vanish when the constraint $\gamma_{cum} = \gamma_\chi$ is met therefore

$$\frac{\partial\psi}{\partial\lambda}\dot{\lambda} = (1-f)(\gamma_{cum}-\gamma_\chi)\frac{\dot{\lambda}}{\rho_0} = 0 \quad (6.73)$$

and the residual mechanical dissipation follows

$$d = \frac{\underset{\sim}{\boldsymbol{\Pi}}^M}{\rho_\sharp} : \left(\dot{\underset{\sim}{\boldsymbol{P}}}\underset{\sim}{\boldsymbol{P}}^{-1}\right) - (1-f)\sum_{s=1}^{N}\frac{\partial\psi_h}{\partial r^s}\dot{r}^s \quad (6.74)$$

$$- (1-f)\left(\frac{\mu_\chi\gamma_{cum} - \Delta_\chi}{\rho_0} + \frac{\partial\psi_h}{\partial\gamma_{cum}}\right)\dot{\gamma}_{cum} - \frac{\partial\psi}{\partial f}\dot{f} \geq 0 \quad (6.75)$$

Here it is postulated that rates of hardening variables are proportional to slip rates on each slip system, *i.e.* $\dot{r}^s = a(r^s)|\dot{\gamma}^s|$. The thermodynamic forces are defined as

$$\frac{R_s}{\rho_\sharp} = \frac{\partial \psi_h}{\partial r^s} a(r^s) \tag{6.76}$$

$$\frac{R_{cum}}{\rho_\sharp} = \frac{\partial \psi_h}{\partial \gamma_{cum}} \tag{6.77}$$

$$\frac{R_f}{\rho_\sharp} = \frac{\partial \psi_f}{\partial f} = -\left( \frac{1}{2\rho_\sharp} \underset{\sim}{\boldsymbol{E}}^e_{GL} : \underset{\approx}{\boldsymbol{C}} : \underset{\sim}{\boldsymbol{E}}^e_{GL} + \psi_h(r^s, \gamma_{cum}) + \frac{A}{2\rho_0} \underline{\boldsymbol{K}}_\chi . \underline{\boldsymbol{K}}_\chi + \frac{\lambda}{\rho_0}(\gamma_{cum} - \gamma_\chi) + \frac{\mu_\chi}{2\rho_0}(\gamma_{cum} - \gamma_\chi)^2 \right) \tag{6.78}$$

### 6.3.4 Gradient enhanced dissipation potentials

In the present framework the dissipation potentials are a function of thermodynamical forces and the state variables can intervene as parameters. For the void growth and void coalescence mechanisms the individual potentials for the mechanisms $i = 1..K$ are

$$\Omega_i = \Omega_i \left( \frac{\underset{\sim}{\boldsymbol{\Pi}}^M}{\rho_\sharp}, \frac{R_i}{\rho_\sharp}, \frac{R_{cum}}{\rho_\sharp}, \frac{R_f}{\rho_\sharp}; \underset{\sim}{\boldsymbol{E}}^e_{GL}, r_i, \gamma_{cum}, \gamma_\chi, \lambda, f \right) \tag{6.79}$$

As discussed earlier and expressed at Eq. (6.56), a sufficient condition to fulfill $\dot{f} = (1-f)\mathrm{tr}\left(\dot{\underset{\sim}{\boldsymbol{P}}} . \underset{\sim}{\boldsymbol{P}}^{-1}\right)$ is to consider flow rules $\phi^i$ such that

$$\phi^i = \phi^i \left( \frac{\underset{\sim}{\boldsymbol{\Pi}}^M - (1-f)R_f \underset{\sim}{\boldsymbol{1}}}{\rho_\sharp}, \frac{R_s}{\rho_\sharp}, \frac{R_{cum}}{\rho_\sharp}; \underset{\sim}{\boldsymbol{E}}^e_{GL}, r_s, \gamma_{cum}, \gamma_\chi, \lambda, f \right) \tag{6.80}$$

#### 6.3.4.1 Void growth

For void growth mechanisms an extension of the implicit definition of effective resolved shear stresses $\tau^s_*$ established at small strains for porous single crystals by Han et al. (2013) and extended to finite strains by Ling et al. (2016) is adopted

$$\phi^s = \left(\frac{\tau^s}{\tau^s_*}\right)^2 + \alpha \frac{2}{45} f \left(\frac{\Pi^M_{eq}}{\tau^s_*}\right)^2 + 2q_1 f \cosh\left( q_2 \sqrt{\frac{3}{20}} \frac{\Pi^M_m - (1-f)R_f}{\tau^s_*} \right) - 1 - (q_1 f)^2 \overset{\text{def}}{=} 0 \tag{6.81}$$

where $\tau^s = (\underset{\sim}{\boldsymbol{\Pi}}^M - (1-f)R_f \underset{\sim}{\boldsymbol{1}}) : (\underline{\boldsymbol{m}}^s \otimes \underline{\boldsymbol{n}}^s)$ with $\underline{\boldsymbol{m}}^s$ and $\underline{\boldsymbol{n}}^s$ respectively the gliding direction and normal to slip plane for system $s$. With this definition, the effective stresses $\tau^s_*$ are positive. The flow potentials are then chosen as

$$\tilde{\phi}^s = (1-f)\left( \tau^s_* - R_s - R_{cum} - \frac{\rho_\sharp}{\rho_0}(\mu_\chi \gamma_{cum} - \Delta_\chi) - \tau^s_0 \right) \tag{6.82}$$

where $\tau^s_0$ in the initial critical resolved shear stress of system $s$. The contribution $R_s$ and $R_{cum}$ correspond to conventional hardening contributions. $R_s$ can for example be used to model dislocations based hardening. $R_{cum}$ can for instance be used to introduce an additional phenomenological hardening. The term $\rho_\sharp/\rho_0(\mu_\chi \gamma_{cum} - \Delta_\chi)$ corresponds to the strain gradient

contribution. It follows the evolution laws for void growth

$$\underset{\sim}{\boldsymbol{L}}{}^{p}_{s} = -\frac{\mathrm{d}\Lambda}{\mathrm{d}\tilde{\phi}^{s}}\frac{\partial\tilde{\phi}^{s}}{\partial\left(-\frac{\underset{\sim}{\boldsymbol{\Pi}}{}^{M}}{\rho_{\sharp}}\right)} = -(1-f)\dot{\gamma}^{s}\left(\frac{\partial\phi^{s}}{\partial\tau^{s}_{*}}\right)^{-1}\frac{\partial\phi^{s}}{\partial\left(\frac{\underset{\sim}{\boldsymbol{\Pi}}{}^{M}}{\rho_{\sharp}}\right)} = (1-f)\dot{\gamma}^{s}\underset{\sim}{\boldsymbol{N}}{}^{s}_{*} \tag{6.83}$$

$$\dot{r}_{s} = -\frac{\mathrm{d}\Lambda}{\mathrm{d}\tilde{\phi}^{s}}\frac{\partial\tilde{\phi}^{s}}{\partial\left(\frac{R_{s}}{\rho_{\sharp}}\right)} = -\dot{\gamma}^{s}\frac{\partial\tilde{\phi}^{s}}{\partial\left(\frac{R_{s}}{\rho_{\sharp}}\right)} \tag{6.84}$$

where the normal tensor $\underset{\sim}{\boldsymbol{N}}{}^{s}_{*}$ already derived in Ling et al. (2016) is introduced as

$$\underset{\sim}{\boldsymbol{N}}{}^{s}_{*} = \frac{\partial\tau^{s}_{*}}{\partial\left(-\frac{\underset{\sim}{\boldsymbol{\Pi}}{}^{M}}{\rho_{\sharp}}\right)} = -\left(\frac{\partial\phi^{s}}{\partial\tau^{s}_{*}}\right)^{-1}\frac{\partial\phi^{s}}{\partial\left(\frac{\underset{\sim}{\boldsymbol{\Pi}}{}^{M}}{\rho_{\sharp}}\right)} \tag{6.85}$$

where

$$\begin{aligned}\frac{\partial\phi^{s}}{\partial\tau^{s}_{*}} &= -2\frac{\tau^{s2}}{\tau^{s3}_{*}} - \frac{4}{45}\alpha f\frac{\Pi^{M^{2}}_{eq}}{\tau^{s3}_{*}} \\ &\quad - 2\sqrt{\frac{3}{20}}q_{1}q_{2}f\frac{\Pi^{M}_{m}-(1-f)R_{f}}{\tau^{s2}_{*}}\sinh\left(q_{2}\sqrt{\frac{3}{20}}\frac{\Pi^{M}_{m}-(1-f)R_{f}}{\tau^{s}_{*}}\right)\end{aligned} \tag{6.86}$$

and

$$\begin{aligned}\frac{\partial\phi^{s}}{\partial\left(\frac{\underset{\sim}{\boldsymbol{\Pi}}{}^{M}}{\rho_{\sharp}}\right)} &= 2\frac{\tau^{s}}{\tau^{s2}_{*}}(\underline{\boldsymbol{m}}^{s}\otimes\underline{\boldsymbol{n}}^{s}) + \frac{2}{15}\alpha f\frac{1}{\tau^{s2}_{*}}\underset{\sim}{\boldsymbol{\Pi}}{}^{M'} \\ &\quad + \frac{2}{3}\sqrt{\frac{3}{20}}\frac{q_{1}q_{2}f}{\tau^{s}_{*}}\sinh\left(q_{2}\sqrt{\frac{3}{20}}\frac{\Pi^{M}_{m}-(1-f)R_{f}}{\tau^{s}_{*}}\right)\underset{\sim}{\boldsymbol{1}}\end{aligned} \tag{6.87}$$

#### 6.3.4.2 Void coalescence

A criterion to detect coalescence by intervoid necking in single crystals was proposed by Yerra et al. (2010). Their criterion is based on the well known criterion by Thomason (1985) which can be expressed with the function

$$\phi^{c} = \sigma_{I} - C_{f}\sigma^{g}_{*} \tag{6.88}$$

$\sigma_{I}$ is the stress orthogonal to the coalescence plane defined by its normal vector $\underline{\boldsymbol{e}}_{I}$. In general, the plane in which coalescence takes place is unkown *a priori*. Therefore it is usually necessary to test the criterion over a wide range of directions in order to determine the plane in which coalescence will initiate at first. As this work proceeds it is assumed that the normal to the coalescence plane coincides with the direction of the largest eigenvalue of the symmetric Cauchy stress tensor $\underset{\sim}{\boldsymbol{\sigma}}$. The scalar $\sigma_{I}$ is therefore interpreted as the maximum principal Cauchy stress and $\underline{\boldsymbol{e}}_{I}$ is the associated eigenvector. Such an assumption was already successfully used by Nguyen et al. (2020). The principal stress $\sigma_{I}$ satisfies $\sigma_{I} = \underset{\sim}{\boldsymbol{\sigma}} : (\underline{\boldsymbol{e}}_{I}\otimes\underline{\boldsymbol{e}}_{I})$. The coefficient $C_{f}$ is a concentration factor which is a function of homogenization cell and void geometries. To characterize these geometries the cell aspect ratio $\lambda_{c}$, void aspect ratio $W$ and normalized intervoid ligament size $\chi$ are often introduced. For a spheroidal void of semi-axes $a_{1}$ and $a_{2}$ in a tetragonal unit-cell of dimensions $L_{1}$ and $L_{2}$ they are respectively expressed

$$\lambda_{c} = \frac{L_{1}}{L_{2}} \qquad W = \frac{a_{1}}{a_{2}} \qquad \chi = \frac{2a_{2}}{L_{2}} \tag{6.89}$$

The porosity can be expressed in terms of these geometrical quantities

$$f = \frac{\frac{4}{3}\pi a_1 a_2^2}{L_1 L_2^2} = \frac{\pi}{6}\frac{W\chi^3}{\lambda_c} \tag{6.90}$$

Since $C_f$ depends on these quantities, equations characterizing their evolutions with loading are needed. Deriving an accurate evolution equation for the void aspect ratio $W$ in porous single crystals is out of the scope of the present study. A first proposal based on variational limit analysis was provided by Mbiakop et al. (2015a). However, for the sake of simplicity, as this work proceeds the void aspect ratio $W$ will be fixed to 1, which corresponds to voids remaining spherical. For an arbitrary small porous unit-cell, the cell aspect ratio $\lambda_c$ can be expressed with respect to its initial value $\lambda_c^0$, initial porosity $f_0$ and the cell normalized elongation $L_1/L_1^0$ which depends upon the deformation gradient tensor $\underset{\sim}{\boldsymbol{F}}$ as follows

$$\underset{\sim}{\boldsymbol{F}}^{-1}.\underline{\boldsymbol{L}}_1 = \underline{\boldsymbol{L}}_1^0 \tag{6.91}$$

$$L_1 \underset{\sim}{\boldsymbol{F}}^{-1}.\underline{\boldsymbol{e}}_I = L_1^0 \underline{\boldsymbol{e}}_I \tag{6.92}$$

$$\frac{L_1}{L_1^0} = \frac{1}{\sqrt{(\underset{\sim}{\boldsymbol{F}}^{-1}.\underline{\boldsymbol{e}}_I).(\underset{\sim}{\boldsymbol{F}}^{-1}.\underline{\boldsymbol{e}}_I)}} \tag{6.93}$$

$$\lambda_c = \lambda_c^0 \left(\frac{L_1}{L_1^0}\right)^{\frac{3}{2}} \sqrt{\frac{1-f}{1-f_0}} \tag{6.94}$$

To derive this expression it was assumed that the principal direction of the unit-cell coincides with the direction of the maximum principal Cauchy stress oriented by the eigenvector $\underline{\boldsymbol{e}}_I$. It appears from Eq. (6.90) that, assuming $W = 1$, applying equation (6.94) and having an evolution equation for $f$ allows to compute $\chi$ with

$$\chi = \left(\frac{6}{\pi}\lambda_c f\right)^{\frac{1}{3}} \tag{6.95}$$

In Eq. (6.88) $\sigma_*^g$ represents the effective flow stress of the matrix during void growth. In (Yerra et al., 2010) the authors account for hardening of the matrix by determining an effective flow stress in the vicinity of the void in the intervoid coalescence plane. They propose to perform an auxiliary computation on a single Gauss point with an identical crystal orientation and under an equibiaxial straining loading state which is representative of the loading during coalescence in the coalescence plane. The effective flow stress is then derived as the equivalent stress when the actual equivalent plastic deformation is reached in the auxiliary computation. Such a method is an elegant way to introduce hardening in Thomason's coalescence criterion. Nevertheless, the computational cost of performing these auxiliary simulations in order to determine the effective flow stress of the crystal matrix can become significant. In principle, at each iteration of the constitutive integration such a simulation should be done. Therefore a new approach is proposed. The main ingredient of this new method is to consider that at initiation of intervoid necking many slip systems are activated in the intervoid ligament. The Thomason criterion is reformulated as

$$\sigma_*^c \quad | \quad \phi^c = \Sigma_I - C_f \sigma_*^c \overset{\text{def}}{=} 0 \tag{6.96}$$

$$\tilde{\phi}^c = (1-f)\left(\sigma_*^c - R_{cum} - \frac{\rho_\sharp}{\rho_0}\left(\mu_\chi \gamma_{cum} - \Delta_\chi\right) - \sigma_*^g\right) \tag{6.97}$$

where $\Sigma_I$ is the maximum eigenvalue of the Cauchy stress $\underset{\sim}{\boldsymbol{\Sigma}}$

$$\underset{\sim}{\boldsymbol{\Sigma}} = \frac{1}{\det\left(\underset{\sim}{\boldsymbol{F}}\right)} \underset{\sim}{\boldsymbol{F}}^{-T}.\left(\underset{\sim}{\boldsymbol{\Pi}}^M - (1-f)R_f \underset{\sim}{\mathbf{1}}\right).\underset{\sim}{\boldsymbol{F}}^T \tag{6.98}$$

Eq (6.96) defines an equivalent coalescence stress $\sigma_*^c$, while Eq. (6.97) is the effective coalescence flow potential. These equations are the coalescence counterpart of Eq. (6.81) and (6.82) defined previously for void growth. Since many slip systems are active, the effective flow stress $\sigma_*^g$ of the crystal matrix can hence be approximated by the effective flow stress of an isotropic matrix. The latter can for instance be defined implicitly by a GTN-like equation

$$\sigma_*^g \quad | \quad \phi^g = \left(\frac{\Sigma_{eq}}{\sigma_*^g}\right)^2 + 2q_1^c f \cosh\left(q_2^c \frac{3}{2}\frac{\Sigma_m}{\sigma_*^g}\right) - 1 - (q_1^c f)^2 \overset{\text{def}}{=} 0 \tag{6.99}$$

where $q_1^c$ and $q_2^c$ are parameters to be calibrated. $\sigma_*^g$ represents the effective flow stress of the matrix during void growth, thus it must be updated while coalescence is not taking place. However once coalescence sets on $\sigma_*^g$ is a constant. It follows the evolution laws for void coalescence

$$\underset{\sim}{\boldsymbol{L}}_c^p = -\frac{\mathrm{d}\Lambda}{\mathrm{d}\tilde{\phi}^c}\frac{\partial\tilde{\phi}^c}{\partial\left(-\frac{\underset{\sim}{\boldsymbol{\Pi}}^M}{\rho_\sharp}\right)} = -(1-f)\dot{\gamma}^c\left(\frac{\partial\phi^c}{\partial\sigma_*^c}\right)^{-1}\frac{\partial\phi^c}{\partial\left(\frac{\underset{\sim}{\boldsymbol{\Pi}}^M}{\rho_\sharp}\right)} = (1-f)\dot{\gamma}^c\underset{\sim}{\boldsymbol{N}}_*^c \tag{6.100}$$

where the normal $\underset{\sim}{\boldsymbol{N}}_*^c$ is introduced such that

$$\underset{\sim}{\boldsymbol{N}}_*^c = \frac{\partial\sigma_*^c}{\partial\left(-\frac{\underset{\sim}{\boldsymbol{\Pi}}^M}{\rho_\sharp}\right)} = -\left(\frac{\partial\phi^c}{\partial\sigma_*^c}\right)^{-1}\frac{\partial\phi^c}{\partial\left(\frac{\underset{\sim}{\boldsymbol{\Pi}}^M}{\rho_\sharp}\right)} \tag{6.101}$$

where

$$\frac{\partial\phi^c}{\partial\sigma_*^c} = -C_f \tag{6.102}$$

and

$$\frac{\partial\phi^c}{\partial\left(\frac{\underset{\sim}{\boldsymbol{\Pi}}^M}{\rho_\sharp}\right)} = \frac{\partial\phi^c}{\partial\left(\frac{\underset{\sim}{\boldsymbol{\Sigma}}}{\rho_\sharp}\right)} : \frac{\partial\left(\frac{\underset{\sim}{\boldsymbol{\Sigma}}}{\rho_\sharp}\right)}{\partial\left(\frac{\underset{\sim}{\boldsymbol{\Pi}}^M}{\rho_\sharp}\right)} = \frac{\partial\Sigma_I}{\partial\underset{\sim}{\boldsymbol{\Sigma}}} : \left(\frac{1}{\det\left(\underset{\sim}{\boldsymbol{E}}\right)}\underset{\sim}{\boldsymbol{E}}^{-T}\underline{\otimes}\underset{\sim}{\boldsymbol{E}}\right) \tag{6.103}$$

$$= \left(\underline{\boldsymbol{e}}_I \otimes \underline{\boldsymbol{e}}_I\right) : \left(\frac{1}{\det\left(\underset{\sim}{\boldsymbol{E}}\right)}\underset{\sim}{\boldsymbol{E}}^{-T}\underline{\otimes}\underset{\sim}{\boldsymbol{E}}\right) \tag{6.104}$$

One has by construction

$$\dot{f} = (1-f)\mathrm{tr}\left(\underset{\sim}{\boldsymbol{L}}^p\right) \tag{6.105}$$

Therefore, the overall macroscopic plastic dissipation becomes

$$\begin{aligned}\left(\underset{\sim}{\boldsymbol{\Pi}}^M - (1-f)R_f\underset{\sim}{\boldsymbol{1}}\right) : \left(\dot{\underset{\sim}{\boldsymbol{P}}}.\underset{\sim}{\boldsymbol{P}}^{-1}\right) &= (1-f)\sum_{s=1}^{N}\dot{\gamma}^s\left(\underset{\sim}{\boldsymbol{\Pi}}^M - (1-f)R_f\underset{\sim}{\boldsymbol{1}}\right) : \underset{\sim}{\boldsymbol{N}}_*^s \\ &+ (1-f)\dot{\gamma}^c\left(\underset{\sim}{\boldsymbol{\Pi}}^M - (1-f)R_f\underset{\sim}{\boldsymbol{1}}\right) : \underset{\sim}{\boldsymbol{N}}_*^c \qquad (6.106)\\ &= (1-f)\sum_{s=1}^{N}\dot{\gamma}^s\tau_*^s + (1-f)\dot{\gamma}^c\sigma_*^c \qquad (6.107)\end{aligned}$$

This equation is in fact the Hill-Mandel lemma. It states the equivalence between macroscopically and microscopically dissipated energies. Then the mechanical dissipation can eventually be

Table 6.1 Summary of equilibrium equations, state laws and evolution equations.

| equilibrium equations | state laws | evolution equations |
|---|---|---|
| $\mathrm{Div}\,\underset{\sim}{\boldsymbol{S}} = \underline{\mathbf{0}} \quad \forall \underline{\boldsymbol{X}} \in D_0$ | $\underset{\sim}{\boldsymbol{\Pi}}^e = \underset{\approx}{\boldsymbol{C}} : \underset{\sim}{\boldsymbol{E}}^e_{GL}$ | $\underset{\sim}{\dot{\boldsymbol{E}}} = \underset{\sim}{\dot{\boldsymbol{F}}}.\underset{\sim}{\boldsymbol{F}}^{-1}.\underset{\sim}{\boldsymbol{E}} - \underset{\sim}{\boldsymbol{E}}.\left(\sum_{k\in\{s;c\}} \dot{\gamma}^s \underset{\sim}{\boldsymbol{N}}^k_*\right)$ |
| $\mathrm{Div}\,\underline{\boldsymbol{M}} - S = 0 \quad \forall \underline{\boldsymbol{X}} \in D_0$ | $\underline{\boldsymbol{M}} = (1-f)A\underline{\boldsymbol{K}}_\chi$ | $\dot{\gamma}^k = \dot{\gamma}_0 \left\langle \frac{\tilde{\phi}^k}{\tau_0(1-f)} \right\rangle^n$ with $k \in \{s;c\}$ and $s = 1..N$ |
| $\underline{\boldsymbol{T}} = \underset{\sim}{\boldsymbol{S}}.\underline{\boldsymbol{n}}_0 \quad \forall \underline{\boldsymbol{X}} \in \partial D_0$ | $S = (1-f)(\Delta_\chi - \mu_\chi \gamma_{cum})$ | $\dot{r}^s = g_s(r_s)\lvert\dot{\gamma}^s\rvert$ with $s = 1..N$ |
| $M = \underline{\boldsymbol{M}}.\underline{\boldsymbol{n}}_0 \quad \forall \underline{\boldsymbol{X}} \in \partial D_0$ | | $\dot{\gamma}_{cum} = \sum_{k\in\{s;c\}} \lvert\dot{\gamma}^k\rvert$ |

formulated as a sum over all deformation mechanisms

$$d = \frac{1-f}{\rho_\sharp} \sum_{s=1}^{N} \left( \tau^s_* - \frac{\rho_\sharp}{\rho_0} \left( \mu_\chi \gamma_{cum} - \Delta_\chi \right) - R_s - R_{cum} \right) |\dot{\gamma}^s| + \frac{1-f}{\rho_\sharp} \left( \sigma^c_* - \frac{\rho_\sharp}{\rho_0} \left( \mu_\chi \gamma_{cum} - \Delta_\chi \right) - R_{cum} \right) |\dot{\gamma}^c| \tag{6.108}$$

$$= \frac{1}{\rho_\sharp} \sum_{s=1}^{N} \left( \tilde{\phi}^s + (1-f)\tau_0 \right) |\dot{\gamma}^s| + \frac{1}{\rho_\sharp} \left( \tilde{\phi}^c + (1-f)\sigma^g_* \right) |\dot{\gamma}^c| \tag{6.109}$$

### 6.3.5 Viscoplastic flow rules

A viscoplastic flow rule is adopted for each deformation mechanism (void growth mechanisms and void coalescence mechanism). In that way evolution of the plastic slip variables $\dot{\gamma}^s$ and $\dot{\gamma}^c$ are indistinguishably governed by the following Norton type flow rule

$$\dot{\gamma}^k = \dot{\gamma}_0 \left\langle \frac{\tilde{\phi}^k}{\tau_0(1-f)} \right\rangle^n \qquad k \in \{s;c\} \tag{6.110}$$

where $\dot{\gamma}_0$ and $n$ are materials parameters controlling the rate sensitivity of the material behaviour. Distinct values of these viscosity parameters can be selected for growth and coalescence, if necessary. Note that the term $(1-f)$ at the denominator accounts for the fact that the slip rates $\dot{\gamma}^k$ are power conjugate to the effective matrix stresses $\tau^s_*$ and $\sigma^c_*$ as depicted in Eq. (6.107).

### 6.3.6 Summary of constitutive equations and material parameters

Equilibrium equations, state laws and evolution equations are summarized in Table 6.1. Four categories of material parameters can be identified:

1. Material parameters for elasto-plasticity
2. Initial void characteristics
3. Porous criteria GTN-like parameters
4. Strain gradient parameters

They are listed in Table 6.2 with their corresponding unit and signification.

Table 6.2 Summary of material parameters involved in the strain gradient porous crystal plasticity model.

| Category | Parameter | Unit | Signification |
|---|---|---|---|
| 1 | $C_{ijkl}$ | MPa | Elastic moduli |
| | $\tau_0$ | MPa | Initial critical resolved shear stress |
| | $\dot{\gamma}_0$ | $s^{-1}$ | Reference slip rate |
| | $n$ | - | Viscosity exponent |
| | $\psi_h$ / $R_s$, $R_{cum}$ | MPa | Hardening potential / Hardening functions |
| | $g_s$ | - | Hardening variables evolution functions |
| 2 | $f_0$ | - | Initial porosity |
| | $\lambda_c^0$ / $\chi_0$ | - | Initial cell aspect ratio / intervoid distance |
| 3 | $q_1$, $q_2$, $\alpha$ | - | Void growth GTN-like parameters |
| | $q_1^c$, $q_2^c$ | - | Void coalescence GTN-like parameters |
| 4 | $A$ | $MPa.mm^2$ | Strain gradient modulus |
| | $\mu_\chi$ | MPa | Penalization modulus |

## 6.4 Validation of the coalescence criterion

In order to validate the capability of the criterion given by Eq. (6.97) to detect onset of coalescence the following procedure is proposed. Porous unit-cell finite element simulations are performed for several crystal orientations, stress triaxiality ratios and hardening behaviour. Onset of void coalescence can then be identified in each unit-cell simulation. Finally, the value of $\sigma_I$ at onset of coalescence ($\sigma_I^{num}$) is compared to the theoretical value ($\sigma_I^{th}$) predicted by the proposed criterion.

### 6.4.1 Single crystal porous unit-cell simulations

Periodic porous unit-cell finite element simulations are performed by prescribing a macroscopic deformation gradient $\overline{\underset{\sim}{\boldsymbol{F}}}$ to a cubic cell containing an initially centered spherical void such that initial porosity $f_0 = 1\%$. Periodic displacement boundary conditions are applied

$$\underline{\boldsymbol{u}} = \overline{\underset{\sim}{\boldsymbol{F}}}.\underline{\boldsymbol{x}} + \underline{\boldsymbol{v}} \qquad \underline{\boldsymbol{v}}\,(\underline{\boldsymbol{x}}^+) = \underline{\boldsymbol{v}}\,(\underline{\boldsymbol{x}}^-) \tag{6.111}$$

where $\underline{\boldsymbol{u}}$ is the displacement field and $\underline{\boldsymbol{v}}$ the periodic fluctuation. The vectors $\underline{\boldsymbol{x}}^+$ and $\underline{\boldsymbol{x}}^-$ denote homologous nodes on opposite faces of the unit-cell. In keeping with Ling et al. (2016) the macroscopic deformation gradient $\overline{\underset{\sim}{\boldsymbol{F}}}$ and first Piola-Kirchhoff stress $\overline{\underset{\sim}{\boldsymbol{S}}}$ are related to their microscopic counterpart by volume averages

$$\overline{\underset{\sim}{\boldsymbol{F}}} = \frac{1}{V_0^{tot}} \int_{D_0} \underset{\sim}{\boldsymbol{F}} \mathrm{d}V \qquad \overline{\underset{\sim}{\boldsymbol{S}}} = \frac{1}{V_0^{tot}} \int_{D_0} \underset{\sim}{\boldsymbol{S}} \mathrm{d}V \tag{6.112}$$

where $V_0^{tot}$ denotes the total volume (including the void) of the unit-cell domain $D_0$ in the reference configuration. It follows that the macroscopic Cauchy stress is given by

$$\overline{\underset{\sim}{\boldsymbol{\sigma}}} = \frac{1}{V^{tot}} \int_D \underset{\sim}{\boldsymbol{\sigma}} \mathrm{d}V = \frac{1}{\det\left(\overline{\underset{\sim}{\boldsymbol{F}}}\right)} \overline{\underset{\sim}{\boldsymbol{S}}}.\overline{\underset{\sim}{\boldsymbol{F}}}^T \tag{6.113}$$

where $V^{tot}$ denotes the total volume (void included) of the unit-cell domain $D$ in the current configuration. Macroscopic hydrostatic ($\overline{\sigma}_m$), equivalent ($\overline{\sigma}_{eq}$) stresses are defined by

$$\overline{\sigma}_m = \frac{\mathrm{tr}\left(\overline{\underset{\sim}{\boldsymbol{\sigma}}}\right)}{3} \qquad \overline{\sigma}_{eq} = \sqrt{\frac{3}{2}\overline{\underset{\sim}{\boldsymbol{\sigma}}}' : \overline{\underset{\sim}{\boldsymbol{\sigma}}}'} \qquad \overline{\underset{\sim}{\boldsymbol{\sigma}}}' = \overline{\underset{\sim}{\boldsymbol{\sigma}}} - \sigma_m \underset{\sim}{\mathbf{1}} \tag{6.114}$$

Only axisymmetric loading conditions are considered for which the macroscopic stress tensor and stress triaxiality ratio can be written

$$\overline{\underset{\sim}{\boldsymbol{\sigma}}} = \begin{pmatrix} \overline{\sigma}_{11} & 0 & 0 \\ 0 & \eta\overline{\sigma}_{11} & 0 \\ 0 & 0 & \eta\overline{\sigma}_{11} \end{pmatrix} \qquad T = \frac{\overline{\sigma}_m}{\overline{\sigma}_{eq}} = \frac{1+2\eta}{3(1-\eta)} \tag{6.115}$$

The simulations are performed at fixed macroscopic Cauchy stress triaxialities $T \in \{1; 1.5; 2; 3\}$. The reader is referred to (Ling et al., 2016) for the numerical implementation of such a condition. The hardening behaviour considered is this study is a standard dislocation density based law following (Kubin et al., 2008). The critical resolved shear stress of a given system $s$ is composed of a thermal component due to lattice friction $\tau_0$ and an athermal component $R_s$ due to dislocations interactions

$$\tau_c^s = \tau_0 + R_s = \tau_0 + \mu\sqrt{\sum_{u=1}^{N} a^{su} r^u} \tag{6.116}$$

where $\mu$ is the shear modulus and $a^{su}$ a matrix describing interactions between dislocations. $r^u$ denotes the adimensional dislocation density ($r^u/b^2 = \rho^u$ is the usual dislocation density, *i.e.* the length of dislocation lines per unit volume, $b$ being the norm of the dislocation Burgers vector $\underline{\boldsymbol{b}}$). Two sets $\mathcal{O}_1$ and $\mathcal{O}_2$ of crystal orientations (given with respect to the unit-cell lattice periodicity directions $\underline{\boldsymbol{X}}_1 - \underline{\boldsymbol{X}}_2 - \underline{\boldsymbol{X}}_3$) are considered

$$\mathcal{O}_1 = \left\{ \begin{array}{l} [100] - [010] - [001] \\ [\bar{1}25] - [1\bar{2}1] - [210] \\ [110] - [\bar{1}10] - [001] \\ [111] - [\bar{2}11] - [0\bar{1}1] \end{array} \right\} \qquad \mathcal{O}_2 = \left\{ \begin{array}{l} [210] - [\bar{1}20] - [001] \\ [\bar{1}25] - [0\bar{5}2] - [29\ 25] \\ [100] - [01\bar{1}] - [011] \\ [100] - [02\bar{1}] - [012] \end{array} \right\} \tag{6.117}$$

For the first set $\mathcal{O}_1$ unit-cell simulations were performed in (Ling et al., 2016) with the material parameters listed in Table 6.3. In this study additional unit-cell simulations are performed for all orientations in $\mathcal{O}_1$ and $\mathcal{O}_2$ with the same materials parameters but $\mu = 0$, *i.e.* in the absence of hardening.

### 6.4.2 Coalescence onset

Onset of coalescence means here the transition to a uniaxial straining mode (extension) during which plastic deformation localizes in the intervoid ligament. This transition is marked by the saturation of transverse (in the coalescence plane) deformation. In other words if the coalescence plane is normal to $\underline{\boldsymbol{X}}_1$ the components $\overline{F}_{22}$ and $\overline{F}_{33}$ of the deformation gradient will saturate. Therefore, for an increment $\Delta\overline{\underset{\sim}{\boldsymbol{F}}}$ of the macroscopic deformation gradient, onset of void coalescence can be detected when the ratios $\Delta\overline{F}_{22}/\Delta\overline{F}_{11}$ and $\Delta\overline{F}_{33}/\Delta\overline{F}_{11}$ become lower than an

Table 6.3 Numerical values of material parameters for the simulation of unit-cell simulations for crystal orientations in $\mathcal{O}_1$.

| $C_{11}$ | $C_{12}$ | $C_{44}$ | $\tau_0$ | $n$ | $\dot{\gamma}_0$ |
|---|---|---|---|---|---|
| 200 GPa | 136 GPa | 105 GPa | 88 MPa | 15 | $10^{14}\,\mathrm{s}^{-1}$ |

| $\mu$ | $G_c$ | $\kappa$ | $r_0^s$ | $b^{su}$ $(s \neq u)$ | $b^{uu}$ |
|---|---|---|---|---|---|
| 65.6 GPa | 10.4 | 42.8 | $5.38 \times 10^{-11}$ | 1 | 0 |

| $a_1$ | $a_2$ | $a_3$ | $a_4$ | $a_5$ | $a_6$ |
|---|---|---|---|---|---|
| 0.124 | 0.124 | 0.07 | 0.625 | 0.137 | 0.122 |

arbitrary low value. As this work proceeds onset of coalescence will be considered when these two ratios are simultaneously lower than 5%. During the post-processing of a unit-cell simulation, the lowest time $t_c$ at which this condition is met, is considered as the onset of coalescence and the maximum principal Cauchy stress at coalescence is recorded as $\sigma_I^{num} = \overline{\sigma}_{11}(t_c)$. At the same time the value of $C_f\sigma_*^c$ is computed. For that purpose, the original form of $C_f$ derived by Thomason (1985) is adopted

$$C_f(\chi, W) = (1-\chi^2)\left(0.1\left(\frac{1-\chi}{\chi W}\right)^2 + 1.2\sqrt{\frac{1}{\chi}}\right) \tag{6.118}$$

where $\chi$ and $W$ respectively represent effective normalized intervoid distance and void aspect ratio. To estimate $\chi$ and $W$ it is assumed for simplicity that the initially cubic cell remains orthorombic and that the initially spherical voids remain ellipsoidal when deforming. Although these assumptions might be crude for highly deformed cells at coalescence, especially at low triaxialities, it is the simplest way to obtain estimates. With these assumptions a deformed unit-cell is characterized by $L_1$, $L_2$ and $L_3$ which are respectively computed by following the displacements of the nodes initially located at the middle of each face of the unit-cell. The void is characterized by three semi-axes $r_1$, $r_2$ and $r_3$ which are respectively computed by following the displacements of the nodes initially located at the intersection of the void with the three major axis of the cube. The geometrical parameters $\chi$ and $W$ are then computed as follows

$$\chi = \sqrt{\chi_2\chi_3} = \sqrt{\frac{2r_2}{L_2}\frac{2r_3}{L_3}} \qquad W = 2\frac{W_{12}W_{13}}{W_{12}+W_{13}} = 2\frac{\frac{r_1}{r_2}\frac{r_1}{r_3}}{\frac{r_1}{r_2}+\frac{r_1}{r_3}} \qquad \lambda_c = \frac{L_1}{\sqrt{L_2L_3}} \tag{6.119}$$

which correspond to their usual definition when the void is a sphere and the cell a cube ($\chi = 2R/L$ and $W = 1$). Yet, the choice made in Eq. (6.119) to define $\chi$, $W$ and $\lambda_c$ is not unique. The value of $\sigma_*^c$ should be equal to $\sigma_*^g$ at onset of coalescence, hence $\sigma_*^g$ is computed by solving Eq. (6.99) where $q_1^c = 1.5$ and $q_2^c = 1$ are chosen. The theoretical coalescence stress is therefore $\sigma_I^{th} = C_f(\chi, W)\sigma_*^g$. In Figure 6.1, the numerical coalescence stresses are plotted against the theoretical coalescence stresses for all the simulations for which coalescence was attained. If the criterion were to be exact the points would be located on the '$y = x$' bisector. As it is only an approximation the points may not exactly lay on this line. Almost all the predicted coalescence stress values are less than $\pm$%20 apart from the values predicted by the unit-cell simulation. It

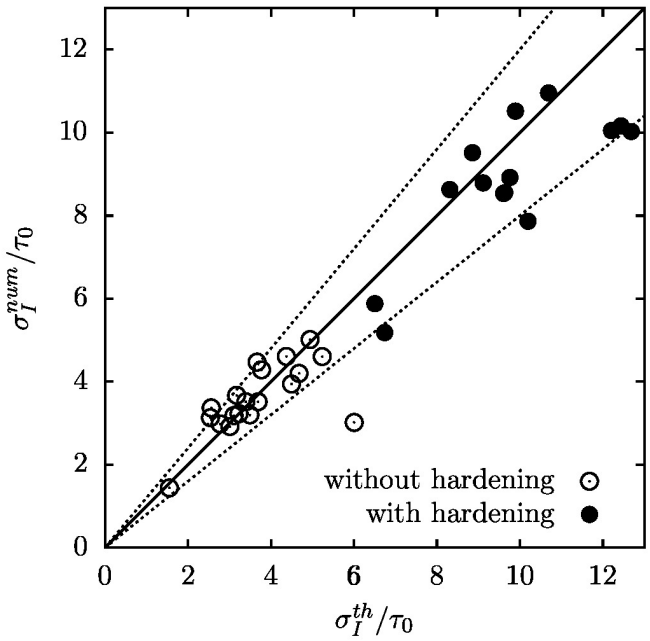


Figure 6.1 Numerically computed principal Cauchy stress in unit-cell simulations *vs* theoretical prediction of the principal Cauchy stress at onset of coalescence. Dashed lines represent the ±20% error from the case were the theoretical prediction matches the numerical value.

can be seen that the criterion is capable of well predicting the coalescence onset with or without hardening of the matrix material surrounding the void. A more refined tuning of the function $C_f$ in Eq. (6.119) and the parameters in Eq. (6.99) could lead to a more precise prediction of coalescence onsets. This is however beyond the scope of the present study.

### 6.4.3 Alternative formulation for modeling void coalescence

Void coalescence was described in previous sections as an individual plastic mechanism having its own yield surface. This approach is comfortable from a modeling point of view. However, from a numerical perspective the implementation effort and computational costs associated to this approach can be significant. Another common approach in the literature consists in modeling void coalescence without extending the set of yield criteria. The method proposed by Tvergaard and Needleman (1984) introduces an effective definition of the porosity $f^*$ once a critical porosity $f_c$ is reached

$$f^* = \begin{cases} f & \text{for} \quad f \leq f_c \\ f_c + \frac{f_u^* - f_c}{f_R - f_c}(f - f_c) & \text{for} \quad f > f_c \end{cases} \tag{6.120}$$

where $f_c$, $f_R$ and $f_u^*$ are material parameters. $f_c$ describes the porosity at the onset of void coalescence. $f_R$ denotes the standard porosity at fracture, while $f_u^*$ is the effective porosity at fracture. With adequate numerical values of material parameters, Eq. (6.120) allows to artificially provoke acceleration of effective porosity growth once coalescence sets on. As a consequence, the yield surface(s) associated to void growth shrink at a greater rate leading to an accelerated stress drop. The advantage of utilizing Eq. (6.120) is that void coalescence can straightforwardly be incorporated in a numerical implementation of a void growth model. On the other hand, some drawbacks are the lack of physical foundation for the effective porosity and the necessity to know *a priori* the critical porosity at coalescence $f_c$. Furthermore, in such a formulation this parameter is assumed no to depend on the loading state.

Table 6.4 Numerical values of material parameters for void growth and coalescence mechanisms and $f^*$-type coalescence.

| $f_0$ | $\lambda_c^0$ | $q_1$ | $q_2$ | $\alpha$ | $q_1^c$ | $q_2^c$ | $f_R$ | $f_u^*$ |
|---|---|---|---|---|---|---|---|---|
| 0.1% | 1 | 1.471 | 1.325 | 6.456 | 1 | 1.5 | 0.35 | 0.67 |

In order to alleviate these two last drawbacks an hybrid formulation was proposed by Zhang et al. (2000). Their idea was to combine a coalescence criterion based on the stress state with the efficient treatment of void coalescence by the use of an effective porosity $f^*$. To do so, they proposed to revoke the *ad hoc* choice of $f_c$ and proposed to define it as the porosity reached when Thomason's coalescence onset criterion is met. In that manner, $f_c$ is continuously updated upon loading and becomes constant when void coalescence is reached. As this chapter proceeds, $f^*$-type void coalescence will rely on the coalescence criterion defined at Eq. (6.97) in order to obtain $f_c$ locally. The summary of material parameters given in Table 6.2 has its third category extended by two additional material parameters, namely $f_R$ and $f_u^*$.

In the context of the strain gradient crystal plasticity model presented in Section 6.3, assuming an effective porosity as in Eq. (6.120) does not involve major difficulties. The main point consists in replacing $f$ by $f^*$ in each equation, but one. The only equation in which $f$ is not replaced by $f^*$ is the evolution law of the porosity Eq. (6.4). However, it should be noted that since void coalescence is not treated as an independent plastic mechanism, $\gamma^c$ is not defined anymore. As a consequence the auxiliary variable $\gamma_\chi$ does not account for void coalescence directly. Since void growth criteria are affected by $f^*$, void coalescence still has an indirect effect on $\gamma_\chi$.

### 6.4.4 Void growth mechanisms and $f^*$-type coalescence *vs* void growth and void coalescence mechanisms

Several variations of the model presented above are compared in this section. Ductile fracture by void growth only is compared to ductile fracture by void growth and void coalescence, with either the $f^*$-type treatment of coalescence or its yield mechanism based treatment. A single hexahedral element with eight nodes and reduced integration with one Gauss point is loaded with a constant stress triaxiality similarly to the periodic porous unit-cells in Section 6.4. Triaxialities of 1 and 3 are applied. Four different crystal orientations are considered and correspond to the orientations in set $\mathcal{O}_1$. Numerical values of material parameters used are listed in Tables 6.3 and 6.4. Since a single Gauss point is used, no gradients of accumulated plastic slip can form and therefore the non-local moduli $A$ and $\mu_\chi$ do not influence the results presented hereafter. Furthermore, for simplicity, the force conjugate to porosity $R_f$ is neglected. Stress-strain responses and porosity evolutions are plotted in Figure 6.2. Solid lines correspond to cases at a triaxiality $T = 1$ and dashed lines to cases at $T = 3$. Reference behaviours of the pristine void-free single crystal are plotted in black. Red curves correspond to the model with void growth mechanisms only, *i.e.* without accounting for void coalescence. Orange and blue curves correspond to the model with $f^*$-type coalescence and void coalescence mechanism respectively. Since only their treatment of coalescence differ, curves with different colors depart from one another once coalescence sets on. In addition, since the same coalescence criterion is used for $f^*$-type coalescence and void coalescence mechanism, blue and orange curves start deviating from the red curve at the same moment. When only void growth mechanisms are accounted for, stress and porosity evolutions with strain are smooth all the way until fracture. However, if coalescence is taken into account, a corner appears at onset of void coalescence. That corner marks a fast acceleration of porosity increase which simultaneously triggers a sharp stress drop. In all cases presented in Figure 6.2 but one, with the parameters in Table 6.4, the acceleration of porosity increase is more pronounced

with the void coalescence mechanism than with the $f^*$-type treatment of coalescence. As a consequence, stresses also sink faster. In order to fully break the material, a failure condition on $f$, $f^*$ and $\chi$ is introduced. The material is considered broken if $f$ reaches 99.9% of $1/q_1$ or if $f^*$ reaches 99.9% of $f_u^*$ or if $\chi$ reaches 0.999. If at least one of these conditions is met the stress tensor is fixed to 0 and the tangent matrix is set to $\varepsilon \underset{\approx}{\boldsymbol{C}}$, where $\varepsilon = 10^{-6}$ and where $\underset{\approx}{\boldsymbol{C}}$ is the elastic stiffness tensor.

It is well established in the literature that $f_u^*$ can be adjusted in order to obtain an adequate acceleration of the porosity when a $f^*$-type coalescence model is used (Zhang et al., 2000). In Figure 6.2, the numerical value chosen for $f_u^*$, namely 67%, leads to a relatively weak acceleration of porosity increase. Increasing $f_u^*$ would result in a sharper acceleration of porosity and thus result in a faster drop of the stress. When coalescence is treated as an additional yielding mechanism (orange curves) it is less straightforward to control the slopes of porosity increase and decrease of stress in the coalescence regime. In the model presented in Section 6.3.4.2, the flow stress for void coalescence noted $\sigma_*^g$ was considered constant once coalescence has set on. Here an extended formulation is proposed in order to be able to control the acceleration of porosity and stress decrease in the spirit of the work of Brepols et al. (2017). The coalescence flow stress now writes

$$\sigma_*^g \leftarrow \sigma_*^g + \omega \left(1 - \exp\left(-\frac{\gamma^c}{\beta}\right)\right) \tag{6.121}$$

where $\omega$ and $\beta$ are additional material parameters that can be adjusted to control the rate of void coalescence. Alternative approaches to account for hardening were proposed by (Scheyvaerts et al., 2011; Vishwakarma and Keralavarma, 2019). Their respective influence is brought to light in Figure 6.3 in which $\omega$ and $\beta$ were independently varied. $\omega$ is taken in the range 1.5 to 100 GPa, while $\beta$ is in the range 0.1 to 10. In the present example the coalescence flow stress $\sigma_*^g$ was equal to 615 MPa. Increasing $\omega$ results in a slower porosity growth and stress softening. On the contrary increasing $\beta$ has opposite effects, namely a faster porosity augmentation and a sharper stress drop. Figure 6.4 shows how $\omega$ affects the void growth and coalescence plastic slip variables after coalescence. As $\omega$ increases void growth plastic variables increase more and more in the coalescence regime, whereas for $\omega = 0$ void growth mechanisms are completely inactive in the coalescence regime. In contrast, as $\omega$ increases, the contribution of void coalescence $\gamma^c$ to the plastic activity decreases in the post-coalescence regime. The role of Eq. (6.121) is thus to introduce strain hardening associated to the void coalescence mechanism. In that way, the softening rate can be calibrated from experiments or computational unit cell results.

## 6.5 Numerical applications

The model was discretized using an Euler-backward (implicit) scheme and implemented in the finite element software Z-set (Besson and Foerch, 1998). Details on the finite element implementation of the Lagrange multiplier formulation were described in Chapter 5.

### 6.5.1 Plane strain tension

#### 6.5.1.1 Mesh convergence analysis

First, a mesh convergence analysis is carried out in order to demonstrate the regularization capacity of the model. A thin rectangular plate of initial length $L_0$, width $W_0 = L_0/5$ and thickness $T_0 = W_0/10$, as depicted in Figure 6.5, is loaded in tension by applying the following

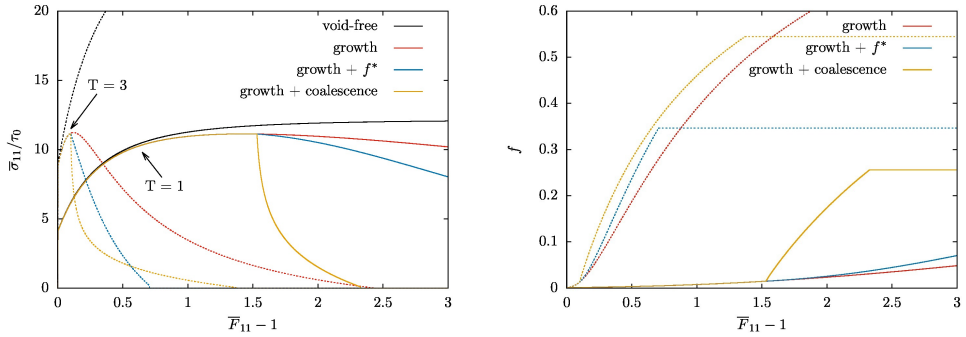


(a) <100>




(b) <100>

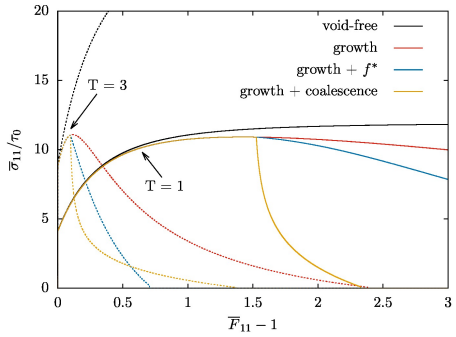


(c) <110>

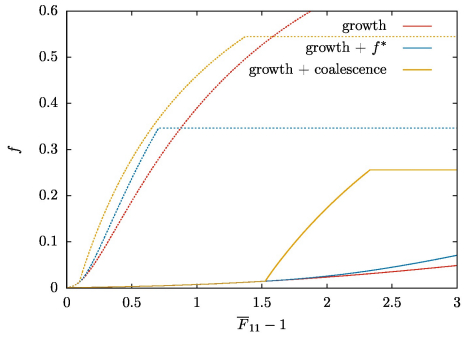


(d) <110>

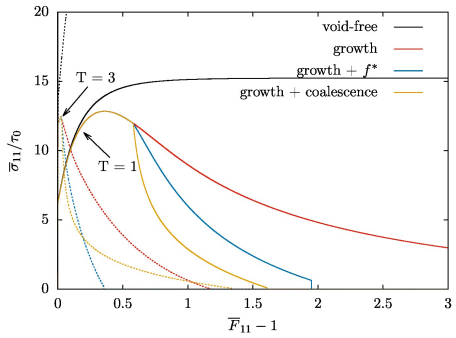


(e) <111>

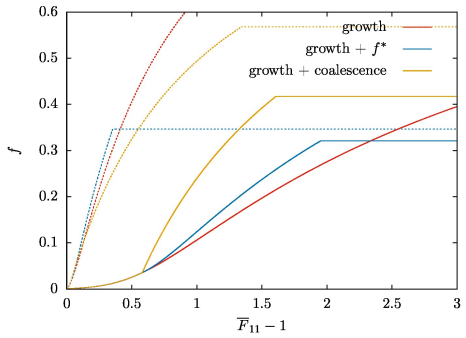


(f) <111>

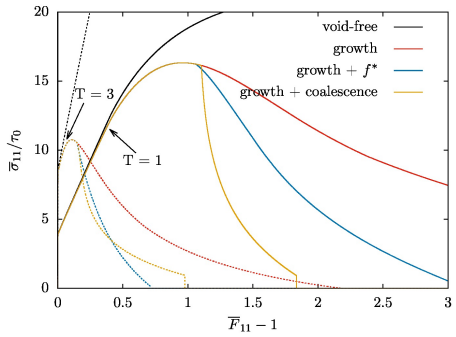


(g) <125>

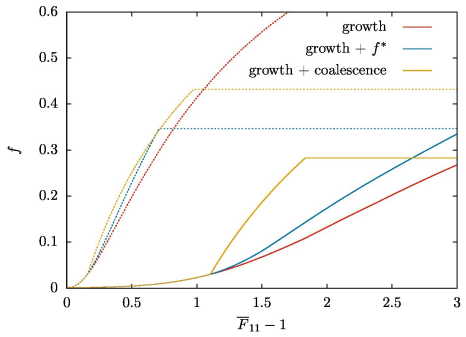


(h) <125>

Figure 6.2 Stress-strain behaviour and porosity evolution at imposed stress triaxialities of 1 (solid lines) and 3 (dashed lines) on a single Gauss point with three different variants of the porous single crystal ductile failure model: void growth mechanisms only (red), void growth mechanisms and $f^*$-type coalescence (blue), and void growth and void coalescence mechanisms (orange).

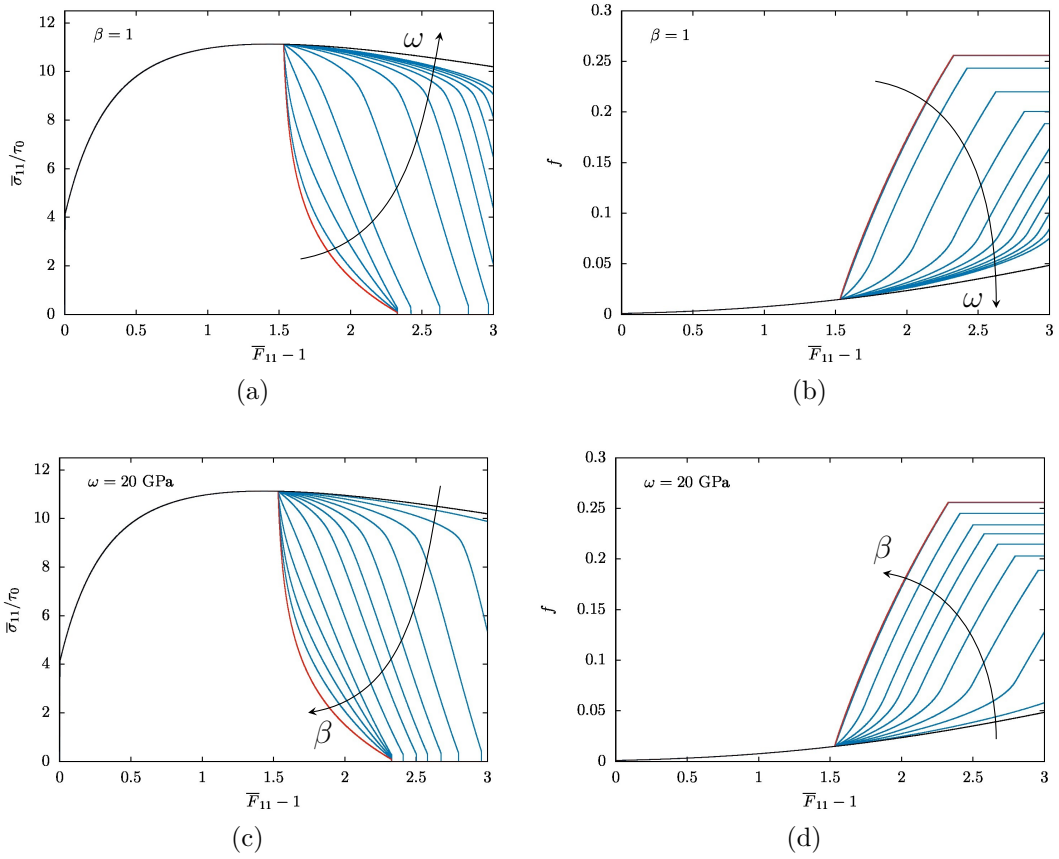


Figure 6.3 Influence of material parameters $\omega$ and $\beta$ from Eq. (6.121) on the post-coalescence regime of the tensile stress and the porosity. $\sigma_*^g = 615\,\mathrm{MPa}$ in this example.

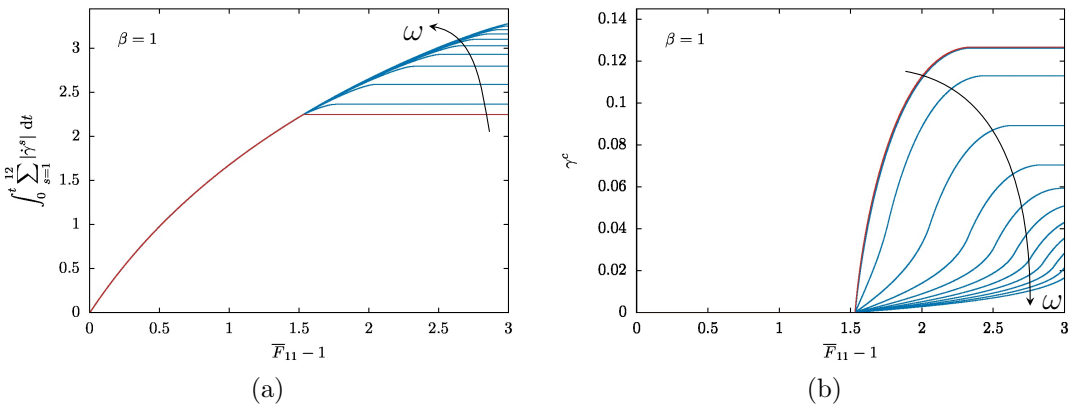


Figure 6.4 Influence of material parameter $\omega$ on the post-coalescence regime of void growth and void coalescence plastic slip variables.

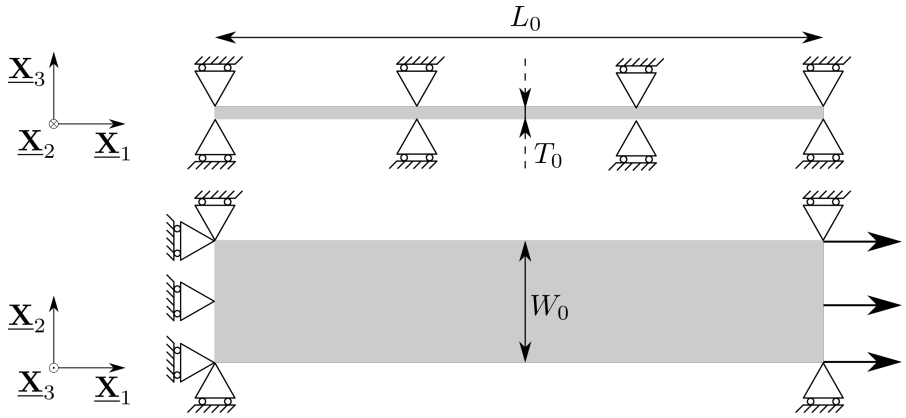


Figure 6.5 Sketch of the geometry and boundary conditions used in the mesh convergence analysis.

boundary conditions

$$U_1(X_1 = 0, X_2, X_3) = 0 \qquad U_1(X_1 = L_0, X_2, X_3) = U_1(t) \tag{6.122}$$

$$U_2(X_1 = 0, X_2, X_3) = 0 \qquad U_2(X_1 = L_0, X_2, X_3) = 0 \tag{6.123}$$

$$U_3(X_1, X_2, X_3) = 0 \tag{6.124}$$

The plate is discretized with $m$ finite elements in width, $5m$ finite elements in length and one element in thickness. The total number of elements is hence $5m^2$. The 20-node brick elements used have quadratic shape functions for displacement degrees of freedom and linear shape functions for the Lagrange multiplier $\lambda$ and micro-slip $\gamma_\chi$ degrees of freedom. Elements with reduced integration with eight Gauss points are used. The mesh convergence analysis is performed on a single crystal with the crystal directions [100], [010] and [001] initially oriented along the orthonormal basis vectors $\underline{\boldsymbol{X}}_1$, $\underline{\boldsymbol{X}}_2$ and $\underline{\boldsymbol{X}}_3$ respectively. The connection between the standard hardening law at Eq. (6.116) and a hardening free energy potential $\psi_h$ is still an open question in literature. For the sake of simplicity a simplified hardening behaviour is used

$$\tau_c^s = \tau_0 + Q \sum_{u=1}^{N} H^{su} \left(1 - \exp\left(-\frac{|\gamma^u|}{\gamma_0}\right)\right) \tag{6.125}$$

in which interactions are neglected by taking the interaction matrix $H^{su} = \delta_{su}$, with $\delta_{su}$ the Kronecker delta. The hardening potential associated to such a hardening is

$$\psi_h\left(\gamma^1, ..., \gamma^N\right) = Q \sum_{s=1}^{N} \left(\gamma^s + \gamma_0 \exp\left(-\frac{|\gamma^s|}{\gamma_0}\right)\right) \tag{6.126}$$

Values of material parameters are listed in Table 6.5.

Figure 6.6 plots the engineering stress $F/S_0$ against the normalized elongation $\Delta L/L_0$ and normalized width extension $-\Delta W/W_0$. The predictions of the model without regularization (solid lines) are compared to the predictions with regularization (dashed lines). With and without regularization four mesh discretizations with $m \in \{4, 8, 16, 32\}$ are computed. At small strains all meshes produce identical results regardless of regularization. This is due to the fact that prior to necking, no gradients of plastic strain exist, hence no size effects due to gradients arise. However, as expected, no convergence is attained when mesh size is decreased in the post-localization regime in the absence of gradient contributions. This is due to the fact that in the post-localization regime strain gradients build up and self-perpetuate by provoking damage localization. Therefore the finer the mesh, the lower the energy necessary to reach failure and the earlier the sharp stress drop starts. On the contrary, when regularization is active, the

Table 6.5 Numerical values of material parameters used for the mesh convergence analysis.

| $C_{11}$ | $C_{12}$ | $C_{44}$ | $\tau_0$ | $n$ | $\dot{\gamma}_0$ | $Q$ | $\gamma_0$ | $f_0$ | $\lambda_c^0$ |
|---|---|---|---|---|---|---|---|---|---|
| 200 GPa | 136 GPa | 105 GPa | 88 MPa | 15 | $10^{29}\,\mathrm{s}^{-1}$ | 100 MPa | 0.05 | 1% | 1 |

| $q_1$ | $q_2$ | $\alpha$ | $q_1^c$ | $q_2^c$ | $A$ | $\mu_\chi$ | $\omega$ | $\beta$ |
|---|---|---|---|---|---|---|---|---|
| 1.471 | 1.325 | 6.456 | 1 | 1.5 | 1 N | 500 MPa | 20 GPa | 1 |

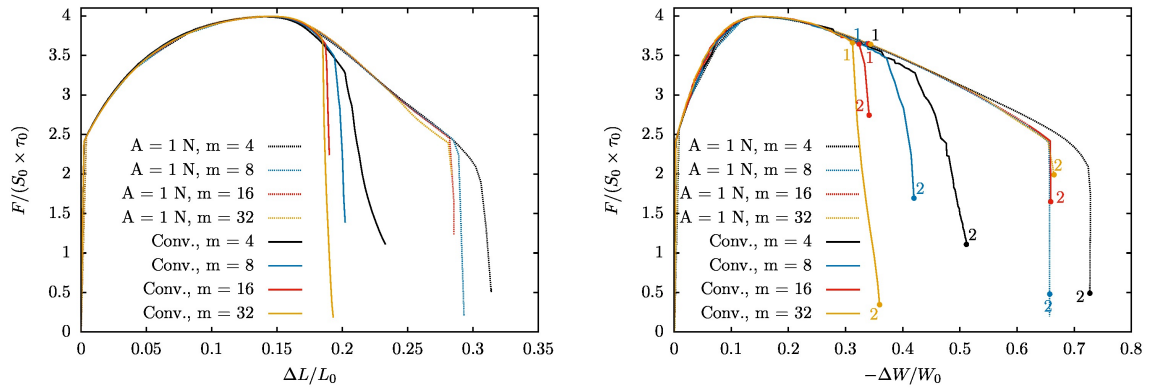


(a) (b)

Figure 6.6 Stress *vs* normalized elongation (a) and normalized width reduction (b) for conventional and gradient porous single crystal plasticity for several mesh refinements $m \in \{4, 8, 16, 32\}$.

apparition of plastic strain gradients are balanced by gradient-induced hardening. This has two effects. First, the sharp stress drop leading to failure occurs at larger strains. Second, the discrepancy between the four meshes on the strain at onset of failure is much smaller.

Figure 6.7 displays, at locations denoted by number '1' in Figure 6.6b, the fields of the normalized intervoid distance $\chi$ which is the relevant damage variable during coalescence. It can be noted that with a conventional plasticity theory, *i.e.* not accounting for strain gradients, the more refined the mesh is, the more localized the damage variable is. When mesh size is decreased a smaller volume needs thus to be completely damaged to reach failure. This explains why less energy is required for failure when mesh size is decreased and the absence of convergence with mesh size reduction. In contrast, with the strain gradient regularization, the damage variable spans over a similar volume for the four different meshes. This explains why macroscopic stress-strain curves are nearly mesh-size independent. Figure 6.7 shows the same fields at the last converged step for each simulation, denoted by number '2' in Figure 6.6b. It can be noted that $\chi$ strongly localizes in the necked region, for both conventional and strain gradient porous crystal plasticity. Even though the macroscopic stress *vs* strain curve seems to be almost mesh-size independent (for $m = 16$ and $m = 32$) with the strain gradient model, the local field of the damage variable $\chi$ still localizes eventually to the thickness of one Gauss point.

#### 6.5.1.2 Effect of thermodynamic force conjugate to porosity

The impact of the thermodynamic force conjugate to porosity noted $R_f$ defined at Eq. (6.78) is assessed by performing tensile tests on a porous single crystal plate. The same geometry, initial

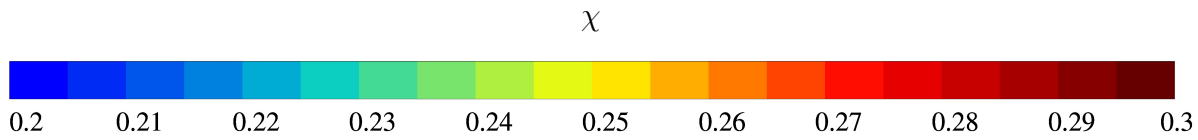


Conventional porous crystal plasticity | Strain gradient porous crystal plasticity

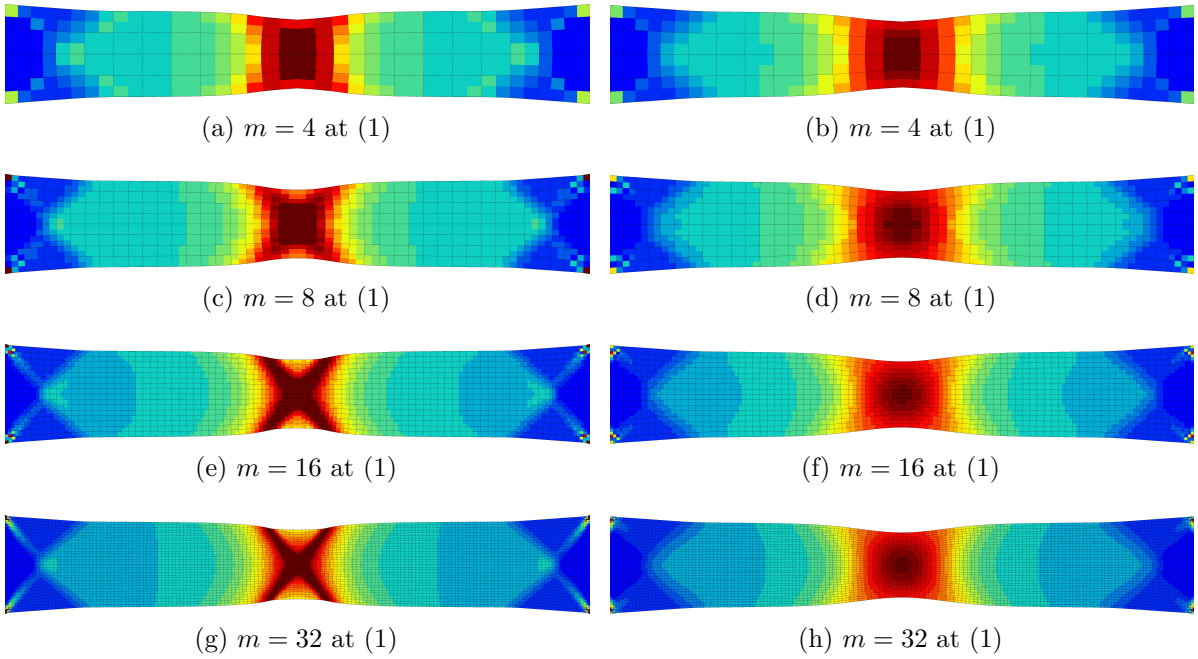

(a) $m = 4$ at (1) (b) $m = 4$ at (1)

(c) $m = 8$ at (1) (d) $m = 8$ at (1)

(e) $m = 16$ at (1) (f) $m = 16$ at (1)

(g) $m = 32$ at (1) (h) $m = 32$ at (1)

Figure 6.7 Field of damage variable $\chi$ at location (1) in Figure 6.6b for conventional (left) and gradient (right) porous single crystal plasticity for several mesh refinements $m \in \{4, 8, 16, 32\}$.

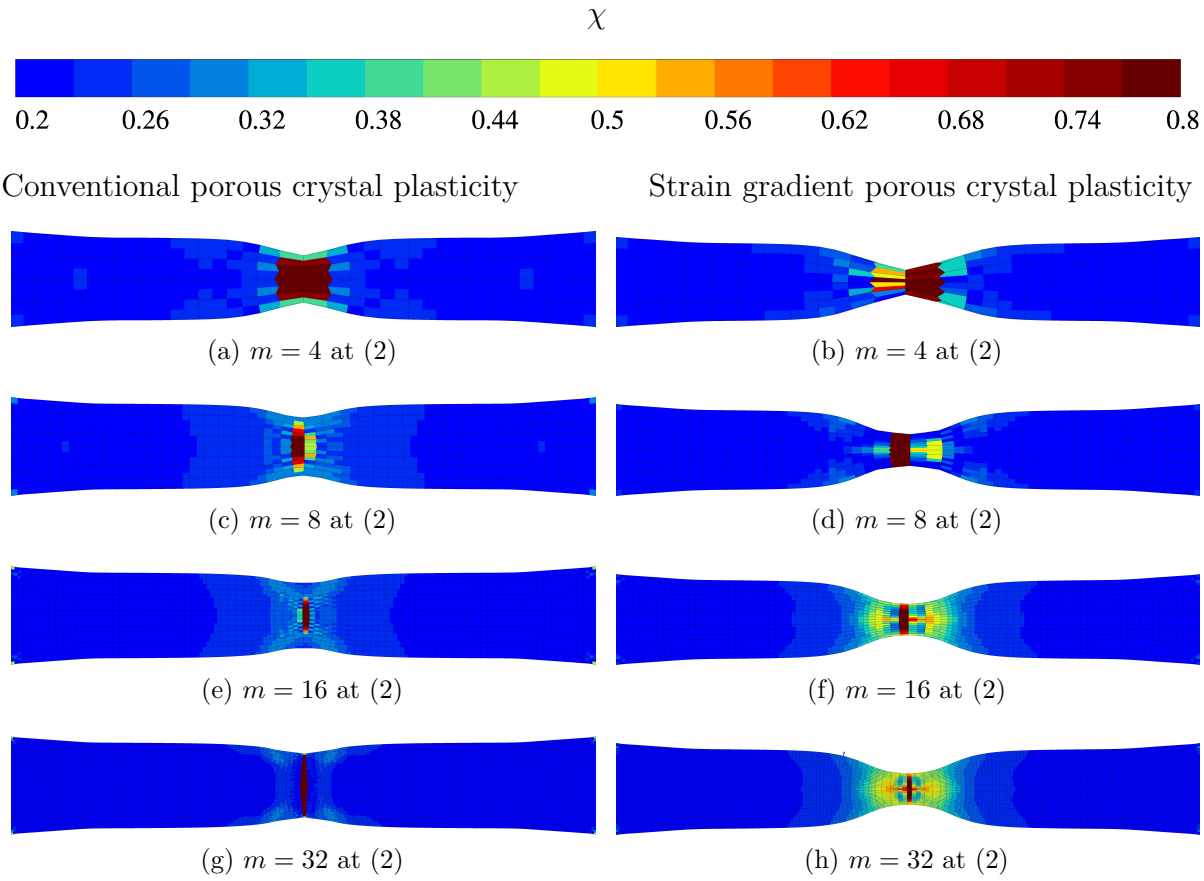


(a) $m = 4$ at (2)

(b) $m = 4$ at (2)

(c) $m = 8$ at (2)

(d) $m = 8$ at (2)

(e) $m = 16$ at (2)

(f) $m = 16$ at (2)

(g) $m = 32$ at (2)

(h) $m = 32$ at (2)

Figure 6.8 Field of damage variable $\chi$ at location (2) in Figure 6.6b for conventional (left) and strain gradient (right) porous single crystal plasticity for several mesh refinements $m \in \{4, 8, 16, 32\}$.

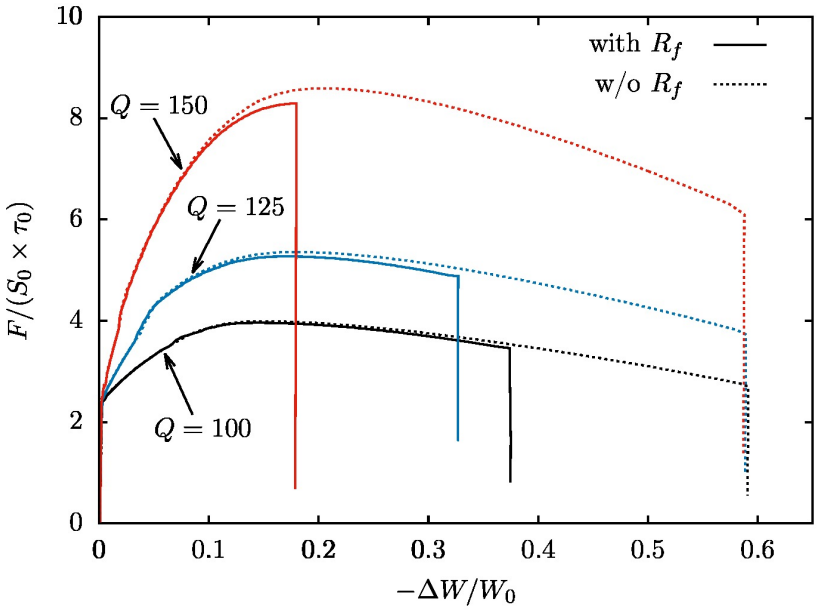


Figure 6.9 Influence of the presence or absence of the force $R_f$ in the yield criteria for several hardening behaviours $Q = 100\,\text{MPa}$ (black), $Q = 125\,\text{MPa}$ (blue) and $Q = 150\,\text{MPa}$ (red).

porosity and boundary conditions as the one used for the mesh convergence analysis are used to assess the influence of $R_f$ on the results. $A$ is taken equal to 1 N. The mesh corresponding to $m = 16$ is used to perform simulations where $R_f$ is neglected or not. Figure 6.9 plots the stress-strain curves obtained when $R_f$ is not neglected (solid lines) and is neglected (dashed lines). Several hardening laws with $Q \in \{100; 125; 150\}$ are considered in order to vary the magnitude of $R_f$. It is observed that, for all hardening laws considered, $R_f$ does not affect the macroscopic stress-strain behaviour at small strains, from 0 to almost 0.2 strain. However once the macroscopic engineering stress reached a maximum the influence of $R_f$ becomes visible. Simulations in which $R_f$ was neglected display a slightly harder response in the softening regime. This is more pronounced for the case with significant hardening, because in this case $R_f$, defined at Eq. (6.78) takes larger values due to the hardening stored energy $\psi_h$. Moreover the onset of the sharp stress drop prior to failure is significantly postponed when $R_f$ is neglected. The force conjugate to porosity contributes indeed to increasing the largest eigenvalue of $\underset{\sim}{\boldsymbol{\Sigma}}$ which enters in the coalescence criterion Eq. (6.96) and (6.97). Therefore void coalescence occurs at larger strains when it is omitted.

Figure 6.10 compares the mean stress field $\sigma_m$ to the fields of each term in the following decomposition: $R_f = R_f^{elas} + R_f^{hard} + R_f^{grad}$. It can be noted that $R_f$ is mostly determined by the energy stored due to hardening in the example considered here. The contribution of elastic stored energy and gradient related energy contribution in $R_f$ are indeed small compared to the latter.

### 6.5.2 Periodic perforated plate

The behaviour of a perforated periodic plate submitted to a triaxial stress field is now analyzed. Periodic boundary conditions are applied and a mean deformation gradient is imposed simultaneously to a fixed stress triaxiality $T = 2$ in the same manner as in Section 6.4. Several variations of the porous single crystal model are investigated. In particular, results accounting for void growth only are compared to results accounting for void growth and coalescence with an $f^*$-type implementation of coalescence as described in Section 6.4.3. Conventional crystal plasticity and strain gradient crystal plasticity are considered.

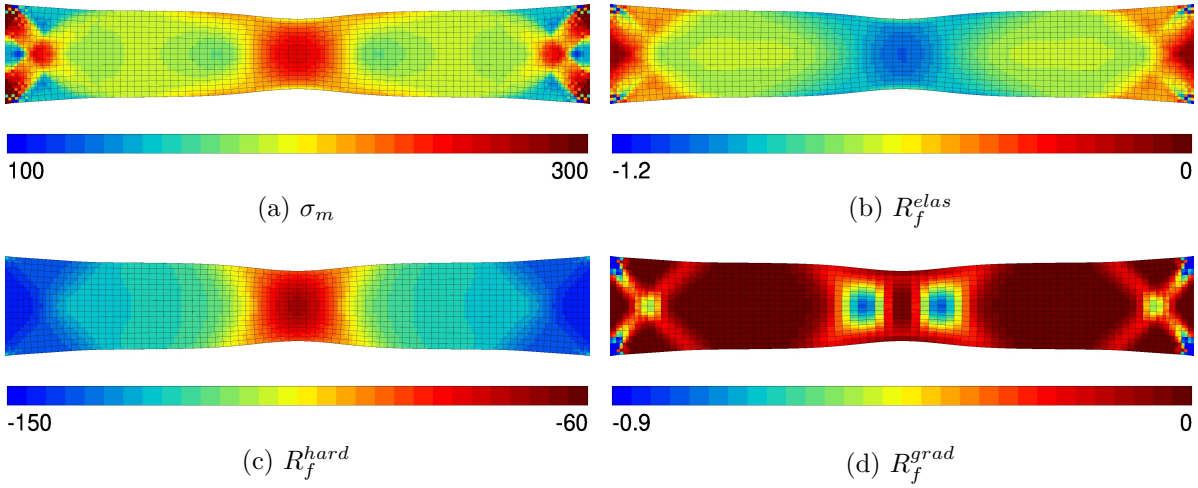


(a) $\sigma_m$ (b) $R_f^{elas}$

(c) $R_f^{hard}$ (d) $R_f^{grad}$

Figure 6.10 Comparison between the mean stress $\sigma_m$ and three different contributions to $R_f$ related respectively to elasticity, hardening and gradient effects for $Q = 100\,\text{MPa}$ and at $-\Delta W/W_0 = 0.3$. Stresses are expressed in MPa.

Table 6.6 Numerical values of material parameters for the simulation of periodic perforated porous single crystal plates.

| $f_0$ | $\lambda_c^0$ | $q_1$ | $q_2$ | $\alpha$ | $f_u^*$ |
|---|---|---|---|---|---|
| 0.1% | 1 | 1.471 | 1.325 | 6.456 | 0.667 |

| $f_R$ | $q_1^c$ | $q_2^c$ | $\mu_\chi$ | $A$ |
|---|---|---|---|---|
| 0.35 | 1 | 1.5 | 1000 MPa | 0 ; $10^{-3}$ ; $10^{-1}$ ; 1 N |

#### 6.5.2.1 Results and discussion

The single crystal surrounding the center hole is oriented such that the crystal orientations triplet $([100], [010], [001])$ coincide with the orthonormal basis $(\underline{\boldsymbol{X}}_1, \underline{\boldsymbol{X}}_2, \underline{\boldsymbol{X}}_3)$ parallel to the edges of the plate. The dislocation densities based hardening law presented in Chapter 3 is used with the material parameters of Table 6.3. Additional material parameters regarding the (strain gradient) porous single crystal model are listed in Table 6.6. The force $R_f$ conjugate to the porosity evolution is not accounted for in the simulations.

The macroscopic stress-strain curves of the periodic perforated porous single crystal plates are plotted in Figure 6.11. First of all, size effects can be observed on the hardening behaviour already at early stages of straining, when only void growth plastic mechanisms are active. However, for the smallest characteristic length, *i.e.* $A = 10^{-3}$ N, the hardening part of the curve is very close to the conventional crystal plasticity behaviour. Then, at larger strains, size effects become even more predominant. When only void growth is accounted for (solid lines) two main effects can be noted. First, increasing the characteristic length postpones the onset of the stress drop. Second, the softening rate decreases when increasing the higher order modulus $A$ (*i.e.* the intrinsic length). When void coalescence is taken into account with an effective porosity $f^*$ (dashed lines) the same observations can be made except for $A = 1$ N. In that case, the onset of softening occurs earlier than with $A = 10^{-1}$ N. This behaviour is associated to a modification of the failure mode and will be explained in light of the accumulated plastic strain fields presented

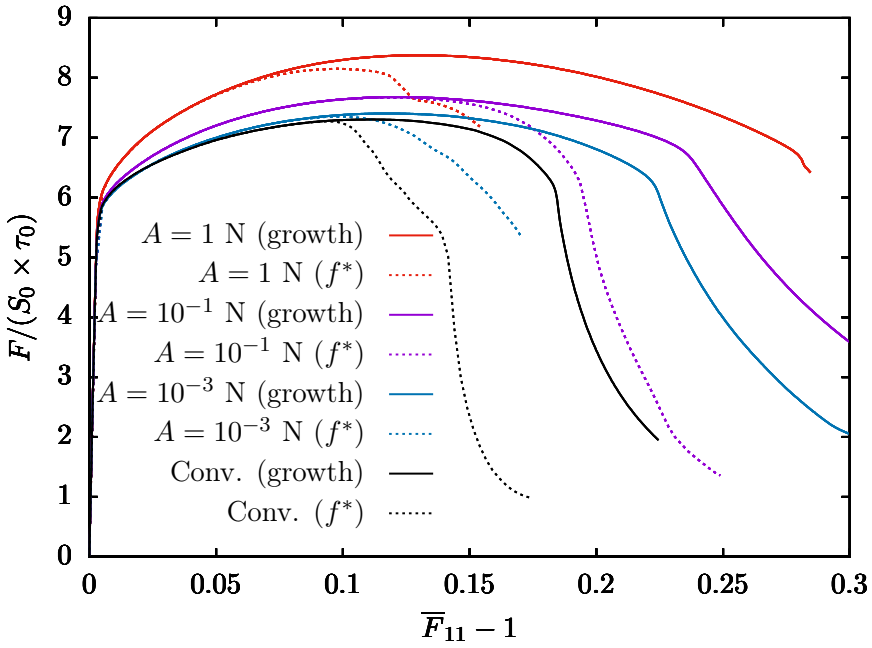


Figure 6.11 Macroscopic normalized stress *vs* macroscopic strain $\overline{F}_{11} - 1$ for conventional and strain gradient perforated porous single crystal plates oriented along [100] – [010] – [001] crystal directions.

in Figure 6.12. A common feature of the results presented in Figure 6.11 is that, for a given value of $A$, taking void coalescence into account provokes an earlier transition to macroscopic softening. Such a behaviour is in fact due to the acceleration of porosity increase when the coalescence criterion is met.

Accumulated plastic strain fields are shown in 6.12 for void growth in Figure 6.12(a-d) and void growth combined with $f^*$-type void coalescence in Figure 6.12(e-h). Plastic strain fields are plotted on meshes deformed by the periodic fluctuation $\underline{\boldsymbol{v}}$ only (*i.e.* the homogeneous part $\underset{\sim}{\overline{\boldsymbol{F}}}.\underline{\boldsymbol{x}}$ is omitted). It can be noted that, for both cases, as the material length scale increases (from left to right) the plastic strain fields become more homogeneous as expected according to Ling et al. (2018). The conventional crystal plasticity simulation displays indeed a very localized plastic strain field, in particular in the case for which coalescence is accounted for. Localization of plastic slip is in that case due to softening induced by porosity increase. Since this phenomenon is unregulated in conventional plasticity, damage and plastic strains localize eventually in a one-Gauss point thick band and results are mesh-size dependent. On the other hand, the predicted plastic strain fields in the case of the strain gradient porous crystal plasticity model are more diffuse and smoother, even when void coalescence is considered. In all cases but one, the plastic strain field is the most intense in the vicinity of the void and propagates along two symmetric directions inclined with respect to the main loading direction. However, a remarkable behaviour is observed at $A = 1$ N, when a $f^*$-type coalescence model is used. In that case, plastic strains are also maximum close to the void, but the maxima are located on the horizontal symmetry axis of the unit-cell instead of the vertical symmetry axis. The line crossing both maxima is therefore aligned with the main loading direction instead of being orthogonal to it as in all other cases. The peculiar positions of these maxima is due to the fact that porosity is also maximum at these locations. Such a behaviour arises, because of the stress redistributions induced by gradient effects which cause stress triaxiality to be greater at non-standard locations.

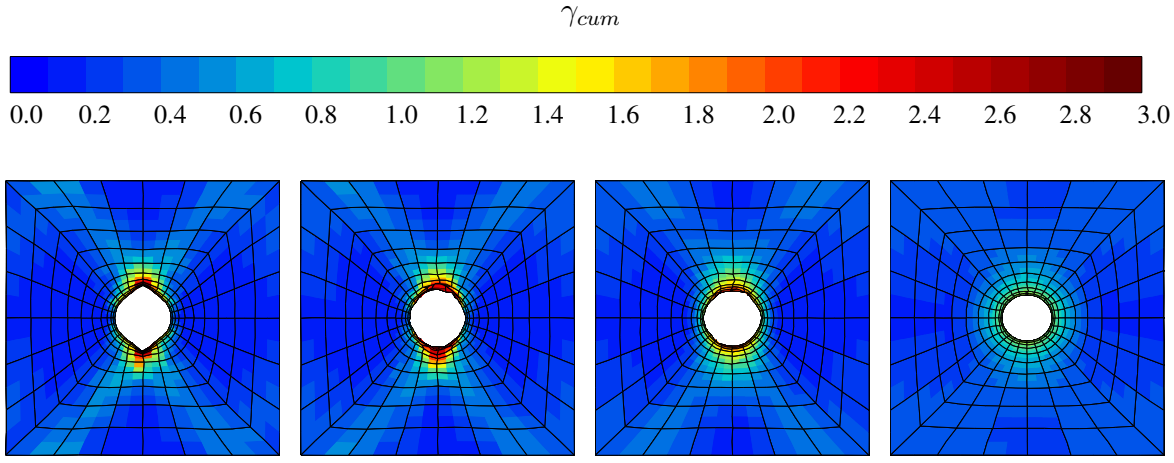


(a) Conv. - growth (b) $A = 10^{-3}$ N - growth (c) $A = 10^{-1}$ N - growth (d) $A = 1$ N - growth

(e) Conv. - $f^*$ (f) $A = 10^{-3}$ N - $f^*$ (g) $A = 10^{-1}$ N - $f^*$ (h) $A = 1$ N - $f^*$

Figure 6.12 Accumulated plastic strain fields at $\overline{F}_{11} - 1 = 0.15$ for conventional and strain gradient periodic perforated porous single crystal plates oriented along $[100] - [010] - [001]$ crystal directions.

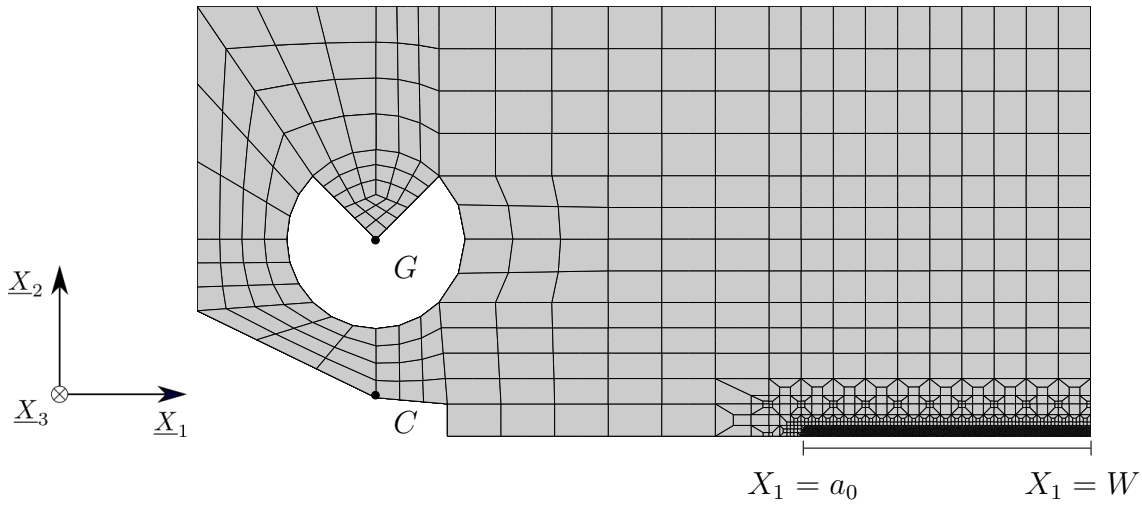


Figure 6.13 Finite element mesh of a half CT specimen geometry.

## 6.6 Application to ductile fracture simulation of single crystal CT specimen

### 6.6.1 Single crystal CT specimen geometry, mesh and boundary conditions

A half CT specimen geometry is meshed with finite elements which are quadratic with respect to displacements and linear with respect to micro-slip $\gamma_\chi$ and Lagrange multiplier $\lambda$ degrees of freedom. The mesh is one-element thick along $\underline{\boldsymbol{X}}_3$. The notch front of the CT specimen is located at $X_1 = a_0$. The notch is supposed infinitely sharp, so that the notch radius is considered to be zero. Symmetry conditions are imposed on the bottom face of the geometry at $X_2 = 0$, from $X_1 = a_0$ to $X_1 = W$, such that $U_2(X_1 \in [a_0, W], X_2 = 0, X_3) = 0$. A vertical displacement $U_2^G(t)$ is applied to the node denoted by the letter $G$ in Figure 6.13. Plane strain conditions are imposed by enforcing $U_3 = 0$ to all nodes of the finite element mesh. Numerical values of material parameters used for the simulation of the CT specimen are listed in Tables 6.3 and 6.4. The regularization capability of the model is investigated by performing simulations with the conventional and the strain gradient versions of the porous single crystal. $f^*$-type void coalescence is compared to void growth only. For sake the of simplicity, the force conjugate to porosity $R_f$ is neglected in these simulations.

Only one half of the complete geometry is used in order to save computation time. The symmetry condition entails two main assumptions. First of all it supposes that the plane defined by $X_2 = 0$ is a symmetry plane for the crystal in the specimen. Therefore, it restricts the utilization of the mesh to specific crystal orientations that satisfy this condition. Then, it assumes than upon loading the symmetry persists despite the rotation of the crystal, and that mechanical fields also remain symmetric with respect to the plane $X_2 = 0$. With this constraint, crack bifurcation in the post-localization regime is replaced by crack branching.

### 6.6.2 Results and discussion

Figure 6.14 shows the porosity fields in the vicinity of the notch front of the CT specimen for several variants of the porous single crystal model. As expected, the porosity field appears intensely localized when the conventional model is used (see Figure 6.14a and 6.14c). Ahead of the notch, mainly a single band of the thickness of one Gauss point concentrates most of the damage, while the rest of the structure retains a porosity close to the initial value $f_0 = 0.1\%$.

Such a result is evidently mesh size dependent, and decreasing the element size would result in a thinner damage localization band. It is also interesting to note that the first finite element located ahead of the notch is less damaged than its neighbour on its right-hand side. The origin of that phenomenon lies in the fact that the stress triaxiality is much larger in the latter bulk element than in the former which is closer to a free-boundary. Taking void coalescence into account with the $f^*$-type coalescence model results in an even more localized field of porosity. In fact, the faster increase of porosity in the coalescence regime is responsible for a stronger softening and thus a more intense localization. On the other hand, the strain gradient porous single crystal model is once more proven to be able to regularize porosity localization, since, with identical loading conditions, the porosity field localization spans over several Gauss point layers. Similarly to what is observed with the conventional model, when void coalescence is accounted for in the strain gradient model, the porosity is localized in a narrower region than when only void growth is taken into account. However, even though the porosity is more confined with the $f^*$-type coalescence than with void growth only, the localized region still remains larger than the mesh size.

Figure 6.15 displays the curves of applied load $F$ at point $G$ against the crack mouth opening displacement (CMOD) computed as the vertical displacement of the point denoted by letter $C$ in Figure 6.13. For comparison, the load *vs* CMOD curves predicted without porosity are also displayed. Loading curves obtained with the conventional porous model (black lines) are evidently mesh size dependent and reducing mesh size would result in an even less ductile apparent behaviour. However, it is observed that $f^*$-type coalescence results in a fast decrease of the load which is due to the sharp acceleration of porosity increase ahead of the notch tip. Taking strain gradients into account postpones the load drop. As pictured in Figure 6.14, damage is indeed smeared over several Gauss point layers, thus requiring a larger amount of energy to be supplied in order to drive the crack forward. Similarly to the conventional case, $f^*$-type coalescence is responsible for more localized and intense damage which translates into a sharper drop of the stress as compared to the model accounting only for void growth.

## 6.7 Conclusions

The main conclusions of this chapter can be listed as follows:

- It was shown how several thermodynamical approaches to ductile fracture available in the literature are based on distinct simplifying hypotheses and how they can be reconciled in an unifying framework. A key aspect of the discussion is the distinction between void volume fraction, regarded as the relative volume of empty spaces in the material, and the porosity, treated as a damage variable.

- A multi-mechanism framework is settled in order to account for multiple plastic processes that can be simultaneously or successively activated upon loading. The setting allows to treat void growth and void coalescence mechanisms concomitantly and is also tailored to porous crystal plasticity for which several void growth plastic processes can coexist.

- The thermodynamical framework was then extended to strain gradient crystal plasticity. The chosen formulation is based on a Lagrange multiplier based extension of the free energy potential in order to account for gradients of an accumulated plastic slip scalar field.

- A new criterion for void coalescence onset detection in single crystals was proposed and validated by means of porous unit-cell simulations. The criterion relies on a revisited version of Thomason's criterion, in which the effective coalescence flow stress is implicitly defined by the stress satisfying the GTN criterion. The main motivation of such a criterion is based on the experimental observation that incipient failure in single crystals is associated with activation of many slip systems and thus a quasi-isotropic behaviour.

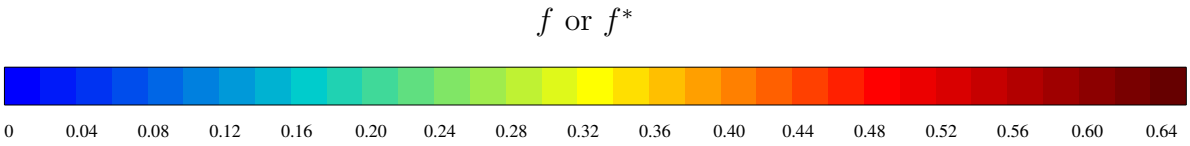


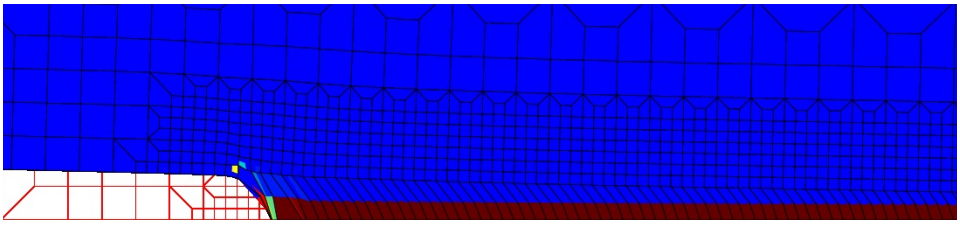

(a) Conv. - growth

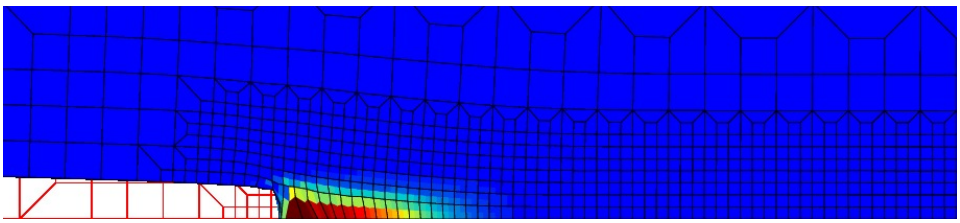

(b) $A = 0.5$ N - growth

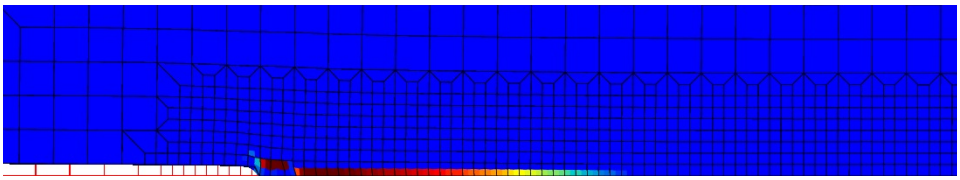

(c) Conv. - $f^*$

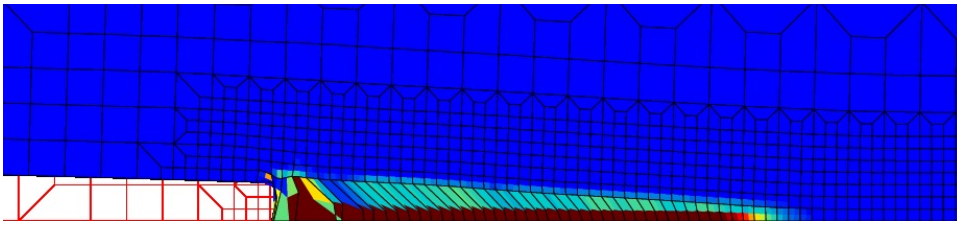

(d) $A = 0.5$ N - $f^*$

Figure 6.14 Porosity fields in the vicinity of the CT specimen notch front, *i.e.* close to $X_1 = a_0$ at CMOD=2 mm in (a), (b) and (d). The last computed time step is used in (c). Initial (undeformed) mesh is displayed in solid red lines.

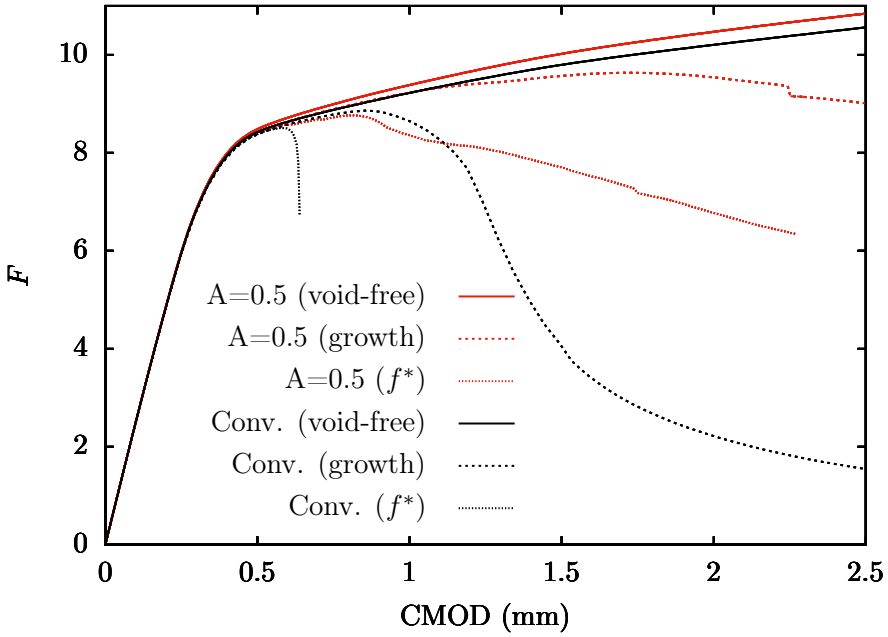


Figure 6.15 Load $F$ *vs* CMOD for conventional and strain-gradient porous single crystal CT specimens oriented along $[100] - [010] - [001]$ crystal directions.

- An alternative formulation to model void coalescence involving an effective porosity $f^*$ was compared to the plastic mechanism based void coalescence model. Both approaches were tested on single Gauss point simulations at fixed triaxiality and up to failure. An extension of the plastic mechanism based model was shown to enable control of the softening rate in the post-coalescence regime.

- Multiple variants of the strain gradient porous crystal plasticity model were tested on finite element numerical applications. The convergence with respect to mesh size when gradient terms are accounted for is demonstrated. Smoothing of damage fields is observed as the material characteristic length is increased.

- First of a kind simulations of ductile fracture in porous single crystal plane strain CT-like geometries were performed. The strain gradient model allows to regularize the width of the damaged zone, while the crack propagates in a one Gauss point thick layer with the conventional model.

# 7

# Conclusions and prospects


## Résumé

Cette thèse porte sur la localisation de la déformation et les mécanismes de rupture ductile dans les monocristaux. Les résultats obtenus au cours de ce travail s'inscrivent dans le contexte des matériaux pour le nucléaire, mais peuvent également bénéficier à d'autres secteurs, comme les transports ou la santé. Une des principales motivations de cette étude est la chute de ténacité en fonction de l'accroissement de la dose d'irradiation observée dans les aciers austénitiques utilisés dans l'industrie nucléaire. Celle-ci est couramment attribuée à l'apparition de défauts induits par irradiation tels que des boucles de dislocation de Frank en conditions d'un réacteur à eau légère ou encore des nano-cavités dans les conditions d'un réacteur à neutrons rapides. Ces défauts étant formés à l'échelle de quelques dizaines de nanomètres, l'étude de leur influence sur les propriétés mécaniques de ces matériaux peut être réalisée à l'échelle du grain, c'est à dire du monocristal, qui les contient. Or, la caractérisation mécanique de monocristaux d'aciers austénitiques n'a été que très rarement étudiée d'un point de vu expérimental dans la littérature. Les premiers résultats de cette thèse ont donc porté sur l'acquisition de données expérimentales à cette échelle. Puis, leur traitement a permis la calibration d'un modèle de plasticité cristalline en procédant à l'identification de différents paramètres associés à l'écrouissage. Ensuite, l'existence de phénomènes de localisation de la déformation plastique dans certains matériaux irradiés nous a conduit au développement d'un modèle de plasticité cristalline capable de décrire ce type de mécanisme. Basé sur un formalisme à gradient de déformation, ce modèle a été enrichi afin de limiter l'élargissement de bandes de localisation lorsque l'adoucissement du matériau sature. De plus, deux versions du modèle, l'une basée sur l'approche micromorphe, la seconde sur une formulation faisant intervenir un multiplicateur de Lagrange, ont été implémentées dans un code de calcul aux éléments finis. Leur mise en œuvre dans différentes simulations a montré la meilleure efficacité numérique de cette deuxième approche. Enfin, un modèle original de rupture ductile par croissance et coalescence de cavités dans une matrice cristalline a été développé. Ce modèle est fondé sur une approche thermodynamique, dont le cadre théorique

nous a permis d'introduire une contribution non-locale du gradient du glissement plastique cumulé. Ainsi, des premières simulations de rupture ductile régularisée ont pu être réalisées dans des structures monocristallines. Les perspectives possibles de ces travaux concernent à la fois les aspects expérimentaux et les aspects théoriques et numériques. La caractérisation mécanique de monocristaux d'aciers austénitiques pourra être poursuivi, notamment en suivant la voie d'essais mécaniques *in situ* dans un microscope électronique à balayage afin de décrire les mécanismes de déformation avec une plus grande résolution. De plus, des essais mécaniques sur monocristaux irradiés aux protons est entrevu afin d'identifier les paramètres matériaux relatifs aux défauts d'irradiation dans un modèle de plasticité cristalline. Par ailleurs, l'amélioration des fondements physiques et de l'efficacité numérique de modèles de plasticité cristalline à gradient pourra être poursuivi. Les axes d'amélioration possibles portent aussi bien sur la formulation théorique de ce type de modèle, que sur la méthode d'implémentation de la plasticité cristalline et le traitement des effets non-locaux d'un point de vue numérique. Enfin, le modèle de rupture ductile régularisée à l'échelle cristalline pourra être mis en œuvre dans des simulations de structure mono- et polycristallines afin d'en valider sa capacité à décrire l'influence de l'anisotropie induite par la plasticité cristalline sur la rupture. *In fine* ce modèle pourra être envisagé afin de prédire la chute de ténacité avec l'augmentation de la dose d'irradiation observée dans les aciers irradiés.

## Contents

## 7.1 Conclusions

The present work deals with strain localization and ductile failure in single crystals. Both phenomena are of utmost interest in the context of metallic alloys, and for instance, in their use by the nuclear industry. Focus was geared towards the behaviour of austenitic stainless steels which are widely employed as structural materials in nuclear reactors. Many conclusions drawn in this work are however not limited to nuclear materials, or even austenitic steels, and can benefit to a wide range of engineering fields, as varied as transports or medicine. In the specific case of nuclear reactor internal structures, experimental studies have demonstrated that neutron irradiation can significantly alter the mechanical properties of austenitic stainless steels. A major potential concern is the drop of fracture toughness as irradiation dose increases. In the literature, it is well established that fracture toughness is linked to deformation and failure mechanisms. As a consequence, modifications of the latter with irradiation were extensively studied in order to explain and predict evolution of toughness with neutron exposure. Depending on the temperature and neutron flux conditions, radiation-induced defects were observed that can cause toughness to decrease. In Light Water Reactor (LWR) conditions, dislocation Frank loops can be nucleated during irradiation and can, upon loading, lead to strain localization. In Fast Neutron Reactor (FNR) conditions, nanometric voids and bubbles can be formed under irradiation and contribute to void driven ductile failure. Both kinds of defects are nucleated at scales much lower than the grain size. Their environment can therefore relevantly be modeled by a single crystal.

Crystal plasticity constitutive equations are standard in the literature. Their validity is often assessed on experiments involving polycrystals or by coarse graining results from lower scale simulations such as discrete dislocation dynamics (DDD) or molecular dynamics (MD). In fewer cases, validation upon comparison to mechanical tests on single crystals is proposed. In the specific case of austenitic stainless steels the latter approach is almost nonexistent.

Furthermore, modeling strain localization is a hot topic of the present-day literature. Numerous theoretical and numerical tools such as integral and gradient methods have flourished in order to be able to capture such phenomena in simulations. Nevertheless, available approaches are often cumbersome and suffer from important numerical costs preventing their use for large scale applications.

In addition, modeling the behaviour of voids embedded in single crystals is a much more nascent topic. However, an abundant literature is available on the modeling of ductile nucleation, growth and coalescence of voids in plastic isotropic, or even anisotropic, materials. Recent advances have taken advantage of several decades of separate research on crystal plasticity on the one hand, and ductile fracture on the other hand, in order to bring together both realms. At dawn of predicting material failure at the single crystal scale, significant efforts are still required in order to obtain quantitatively predictive, robust and efficient constitutive models and numerical implementations.

In the present work, a literature review of the mechanical behaviour of irradiated stainless steels and the modeling of strain localization and ductile fracture was conducted in Chapter 2. Experimental investigation of the mechanical behaviour of austenitic stainless steel single crystals was carried out and presented in Chapter 3. Then, some theoretical and numerical limitations of gradient regularization of strain localization were addressed in Chapter 4 and Chapter 5 respectively. At last, enhanced modeling and simulation of single crystal ductile failure was proposed in Chapter 6.

Tensile experiments conducted on austenitic stainless steel single crystals presented in Chapter 3 have led to original observations and conclusions which can be listed as follows:

- Heterogeneous strain patterns are formed on the tensile specimen surface. These patterns are composed of bands, themselves composed of bundles of slip lines, whose orientations coincide with activated slip plane traces as predicted by the Schmid criterion.

- The yield strength and hardening behaviour highly depends on the crystal orientation with respect to the tensile direction. When pulled along <111> directions 316L single

crystals display a harder and more pronounced strain hardening response than along <110> directions. Both directions display an almost linear strain hardening behaviour.

- Crystal plasticity simulations have shown that available sets of material parameters, identified on polycrystals (Ling, 2017; Monnet and Mai, 2019), predict unrealistic strain hardening behaviours when single crystals are considered. A new set of material parameters was therefore identified in order to fit single crystals and polycrystals experimental data.

Note that no strain gradient plasticity effects were introduced at this stage due to the rather macroscopic nature of the tests and measurements. A review of available constitutive hardening laws that account for irradiation defects was then presented. As an introduction to a future study, the conditions of a proton-irradiation experiment performed on 316L single crystal were then presented.

Then, light was shed on some theoretical limitations of a reduced micromorphic strain gradient crystal plasticity model at finite strains and an enhanced model was derived. The main outcomes of this study can be summarized as follows:

- Numerical finite element predictions were shown to fit remarkably well with analytical solutions in single slip. Linear hardening, absence of hardening and linear softening were shown to trigger boundary layers, parabolic profile or cosine-shaped localization band of plastic slip in a periodic bar loaded in simple shear, depending on the sign of the hardening modulus.

- Progressive, unlimited broadening of the localization band was demonstrated as a saturating softening behaviour was considered.

- An evolving material length scale was thus proposed. It was shown by approximate analytical solutions and finite element simulations to be able to prevent broadening of strain localization.

- The model was finally applied to investigate interactions between localization bands and cylindrical voids for several ratios between the band width and void's radius. Smaller voids were shown to preserve elliptical shapes, while larger voids deform in peanut-like shapes. Larger void volume fractions were responsible for wider localization bands.

Improvements of the strain gradient crystal plasticity model were implemented and are available in the finite element software Z-set.

An alternative to the micromorphic approach was proposed in order to relax the reduced strain gradient crystal plasticity model. This innovative approach takes advantage of a Lagrange multiplier and an additional penalization (Zhang et al., 2018). Micromorphic and Lagrange multiplier formulations were compared, leading to the following state-of-the-art results:

- Micromorphic and Lagrange multiplier approaches are conceptually very similar, since they share the idea of duplicating the non-local variable whose gradients are accounted for. The micromorphic theory allows to recover the original gradient theory by using a large penalization modulus acting on the difference between both instances of the non-local variable. On the other hand, the Lagrange multiplier formulation enforces weakly equality between both instances by the means of a Lagrange multiplier and an additional penalization.

- The Lagrange multiplier approach was shown analytically to be strictly equivalent to the micromorphic approach in the specific case of strain localization in a periodic bar in simple shear with a single slip system. Analytical solutions display the discontinuity of the Lagrange multiplier at the elastic-plastic interfaces of the localization band. The additional penalization term was shown to be fundamental when predicting that discontinuity without spurious oscillations in the context of finite elements. Accounting for discontinuities of the Lagrange multiplier will be possible in the future using discontinuous Galerkin

methods (Cockburn et al., 2012) or recent Hybrid High-Order (HHO) elements (Di Pietro et al., 2016).

- A detailed presentation of the finite element implementation of the Lagrange multiplier formulation was made. In particular, tangent and Jacobian matrices were derived analytically.

- A drastic reduction of computational cost was obtained in general with the Lagrange multiplier implementation as compared to the micromorphic implementation. A speedup of up to two order of magnitude was reached in some cases.

- Further numerical comparisons of predicted size effects were performed on single crystal wires in torsion and cubic porous unit-cells under imposed stress triaxiality. Micromorphic and Lagrange multiplier approaches were shown to be almost equivalent at small length scales. As material length scale rises (or specimen size decreases) the micromorphic approach displays a saturation of enhanced hardening. On the contrary, size effects predicted by the Lagrange multiplier formulation are unbounded.

Additionally, rate-dependent and rate-independent (Forest and Rubin, 2016) crystal plasticity settings were compared from a computational cost perspective. Both formulations were shown to have overall similar computational performance. Implementation of the Lagrange multiplier formulation was done and is available in the finite element software Z-set. Further developments were concomitantly implemented. A finite element, including displacement degrees of freedom and micro-slip and associated Lagrange multiplier degrees of freedom was established. Periodic finite elements for both micromorphic and Lagrange multiplier formulations were implemented. In addition, a micromorphic and Lagrange multiplier formulation of von Mises plasticity were set up with the equivalent plastic deformation as non-local variable.

Eventually, a first-of-its-kind ductile fracture model for single crystals was formulated in a strain-gradient plasticity setting. It is composed of the following essential building blocks:

- A thermodynamical framework for porous homogenized models was proposed. It aims at unifying and generalizing several available approaches in the literature (Besson, 2009; Bouby and Kondo, 2017; Enakoutsa et al., 2007; Rousselier, 2001). The fundamental ingredient of the formulation lies in the treatment of the void volume fraction as an independent state variable. It is shown how a well chosen condition on the dissipation potential can be formulated in order to recover the usual evolution law for porosity.

- The thermodynamical setting serves as a foundation for the formulation of a strain gradient porous crystal plasticity model. A Lagrange multiplier approach is followed similarly as in Chapter 5. The porous crystal plasticity model accounts for void growth with a modified, pressure dependent, Schmid yield criterion for each slip system. It also takes into account the mechanism of void coalescence in an original way.

- The newly formulated void coalescence criterion is validated upon comparison to single crystal porous unit-cell simulations. It is shown to predict satisfactorily the critical stress at coalescence in absence or presence of strain hardening.

The model was then tested on several geometries in order to assess its capacity of predicting regularized ductile fracture in single crystals.

## 7.2 Prospects

The present work raised and left behind many open questions. As follows is a non-exhaustive list of suggestions for research to be conducted in future studies. First of all, experimental data gathered in this work are unique and thereby require to be validated and complemented by

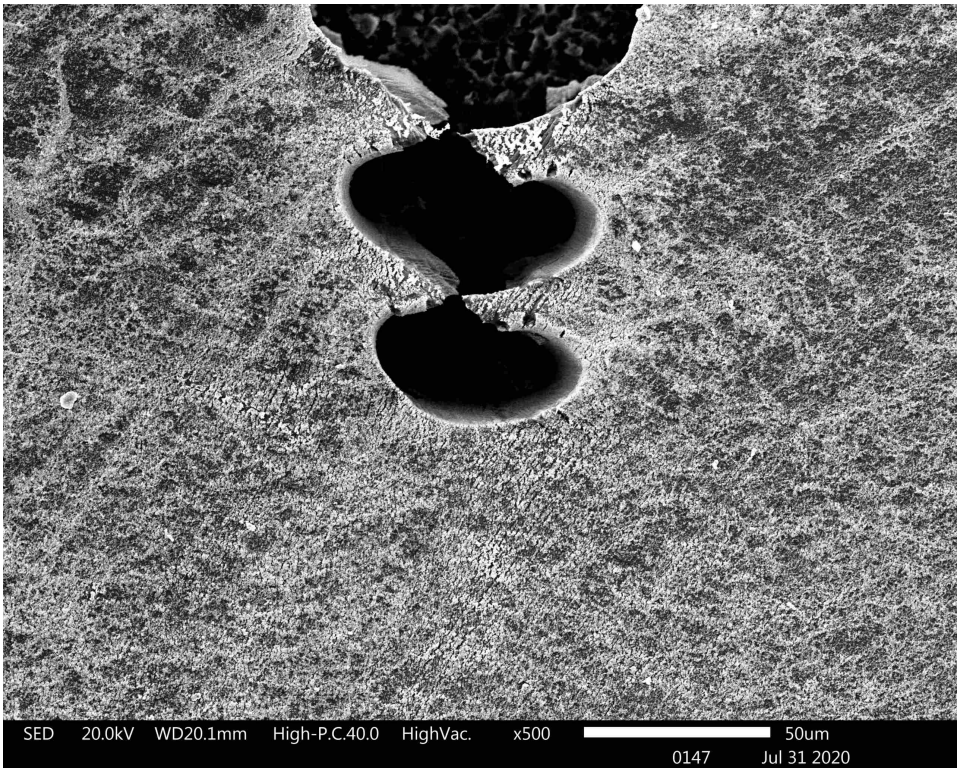


Figure 7.1 Notched and perforated single crystal specimen tested *in situ* with SEM imaging to perform DIC displacements fields measurements on the gold nanoparticles pattern laid down on its surface.

additional studies. Experimental investigations of stainless steel single crystals remain indeed very scarce and the present work only scratched the surface of a territory which should be further explored. The following investigations are proposed:

- SEM *in situ* tests appear particularly promising to further study the behaviour of these materials. A first experiment conducted in situ on a notched and perforated specimen shown in Figure 7.1 has proven encouraging possibilities in that way. Tensile tests, but also, for instance, micro-indentation tests or micro-pillar indentation, can be considered to further validate or adjust identified parameters.

- In a near future, experimental characterization of proton-irradiated stainless steel single crystals could be pursued. Data obtained on irradiated materials would allow to calibrate more precisely material parameters used in constitutive equations accounting for irradiation-induced defects at the single crystal scale.

Then, modeling size effects and strain localization in single crystal is a promising topic. Major lines of development are the enhancement of the physical foundation of the corresponding models and in addition the improvement of numerical tools to implement them.

- Rate-independent and quasi-rate-independent viscoplastic crystal plasticity flow rules were compared from a computational viewpoint. Both settings were shown to have advantages and drawbacks. Results not shown here suggest that alternative algorithms available in the literature could lead to a more efficient numerical integration of crystal plasticity flow rules. The Lagrange multiplier based formulation by Schmidt-Baldassari (2003), for instance, has shown promising results.

- Micromorphic and Lagrange multiplier based strain gradient formulations were also compared from a computational perspective. If a significant gain was obtained with the latter,

the numerical efforts associated to gradient models remain a serious drawback. Further attention could be given to computational aspects in order to continuously enhance the efficiency of such kind of models.

- The Lagrange multiplier formulation developed in the context of strain gradient (porous) crystal plasticity appears promising from a computational point of view. However absence of saturation of the size-effects predicted by the Lagrange multiplier formulation may seem unrealistic in some cases. This lack is due to the simple quadratic form of the non-local free-energy potential adopted. Investigating more refined potentials could be envisaged to adapt the predictions in order to obtain desired asymptotic size-dependence.

Finally, investigations concerning ductile fracture mechanisms at the single crystal scale should be continued. Among the research pathways which could be followed, the following aspects appear to be promising:

- The single crystal void growth and coalescence model is still very nascent. A thorough investigation of its predictions compared to porous unit-cell simulations could be carried out. Such a study would lead to improve the calibration of void growth and void coalescence criteria, but also reveal necessary improvements in order to capture mechanisms not yet taken into account. For instance, accounting for coalescence in shear as in (Hure, 2019) could be considered as a first step.

- Effects of crystal plastic anisotropy on void growth and void coalescence could be further assessed. Parametric studies on relevant geometries (NT, CT specimen for instance) could be considered. In the longer term, the model could be used as a part of a workflow devoted to microstructure optimization.

- Numerical results obtained with the porous single crystal plasticity model should be correlated and compared to experimental data. Mechanical tests on specimen containing a few number of grains could be performed to this end. For instance, aluminum with large grains could be used as a model FCC material for such experiments.

- Continuation of the present work could eventually reach the ultimate objective of predicting, for a given microstructure, the evolution of relevant mechanical properties with irradiation dose. In particular, being able to predict quantitatively evolution of toughness with neutron exposure from numerical methods is a key target of the present project.

# References


Acharya, A., Bassani, J., 2000. Lattice incompatibility and a gradient theory of crystal plasticity. Journal of the Mechanics and Physics of Solids 48, 1565–1595.

Achouri, M., Germain, G., Dal Santo, P., Saidane, D., 2013. Experimental characterization and numerical modeling of micromechanical damage under different stress states. Materials & Design 50, 207–222.

Aifantis, E.C., 1984. On the microstructural origin of certain inelastic models. Journal of Engineering Materials and technology 106, 326–330.

Aifantis, E.C., 1987. The physics of plastic deformation. International journal of plasticity 3, 211–247.

Al Kotob, M., 2019. Compétition entre instabilités globales et locales lors de la ruine de structures aéronautiques. Ph.D. thesis. Université PSL. URL: http://www.theses.fr/2019PSLEM002/document. Thèse de doctorat dirigée par Forest, Samuel et Maziere, Matthieu.

Alexander, D.J., Pawel, J.E., Grossbeck, M.L., Rowcliffe, A.F., Shiba, K., 1996. Fracture toughness of irradiated candidate materials for ITER first wall/blanket structures, in: Effects of Radiation on Materials: 17th International Symposium, ASTM International. pp. 945–970.

Anand, L., Aslan, O., Chester, S.A., 2012. A large-deformation gradient theory for elastic–plastic materials: strain softening and regularization of shear bands. International Journal of Plasticity 30, 116–143.

Anand, L., Kothari, M., 1996. A computational procedure for rate-independent crystal plasticity. Journal of the Mechanics and Physics of Solids 44, 525–558.

Anoukou, K., Pastor, F., Dufrenoy, P., Kondo, D., 2016. Limit analysis and homogenization of porous materials with Mohr–Coulomb matrix. Part I: Theoretical formulation. Journal of the Mechanics and Physics of Solids 91, 145–171.

Arminjon, M., 1991. A regular form of the Schmid law. Application to the ambiguity problem. Texture, Stress, and Microstructure 14, 1121–1128.

Arsenlis, A., Rhee, M., Hommes, G., Cook, R., Marian, J., 2012. A dislocation dynamics study of the transition from homogeneous to heterogeneous deformation in irradiated body-centered cubic iron. Acta Materialia 60, 3748–3757.

Asaro, R.J., Rice, J., 1977. Strain localization in ductile single crystals. Journal of the Mechanics and Physics of Solids 25, 309–338.

Ashby, M.F., 1970. The deformation of plastically non-homogeneous materials. The Philosophical Magazine: A Journal of Theoretical Experimental and Applied Physics 21, 399–424.

Ask, A., Forest, S., Appolaire, B., Ammar, K., Salman, O.U., 2018. A Cosserat crystal plasticity and phase field theory for grain boundary migration. Journal of the Mechanics and Physics of Solids 115, 167–194.

Aslan, O., Cordero, N., Gaubert, A., Forest, S., 2011. Micromorphic approach to single crystal plasticity and damage. International Journal of Engineering Science 49, 1311 – 1325.

ASTM Standard A240/A240M, 2012. Standard specification for chromium and chromium-nickel stainless steel plate, sheet, and strip for pressure vessels and for general applications. https://www.astm.org/.

ASTM Standard E521-96, 2009. Standard pratice for neutron radiation damage simulation by charged-particle irradiation. https://www.astm.org/.

Audoly, B., Hutchinson, J.W., 2019. One-dimensional modeling of necking in rate-dependent materials. Journal of the Mechanics and Physics of Solids 123, 149–171.

Avramovic-Cingara, G., Saleh, C., Jain, M., Wilkinson, D., 2009. Void nucleation and growth in dual-phase steel 600 during uniaxial tensile testing. Metallurgical and Materials Transactions A 40, 3117.

Babout, L., Brechet, Y., Maire, E., Fougeres, R., 2004. On the competition between particle fracture and particle decohesion in metal matrix composites. Acta materialia 52, 4517–4525.

Bagley, K., Little, E., Levy, V., Alamo, A., Ehrlich, K., Anderko, K., Calzabini, A., 1987. Materials for nuclear reactor core applications, in: Proceedings of the International Conference held at Bristol, England, 27-29 Oct. 1987 and Organized by the British Nuclear Energy Society, pp. 37–46.

Bailat, C., Almazouzi, A., Baluc, N., Schäublin, R., Gröschel, F., Victoria, M., 2000. The effects of irradiation and testing temperature on tensile behaviour of stainless steels. Journal of nuclear materials 283, 446–450.

Bapna, M., Mori, T., Meshii, M., 1968. The observation of slip channels in quenched gold. The Philosophical Magazine: A Journal of Theoretical Experimental and Applied Physics 17, 177–184.

Bardella, L., 2006. A deformation theory of strain gradient crystal plasticity that accounts for geometrically necessary dislocations. Journal of the Mechanics and Physics of Solids 54, 128–160.

Bardella, L., Segurado, J., Panteghini, A., Llorca, J., 2013. Latent hardening size effect in small-scale plasticity. Modelling and Simulation in Materials Science and Engineering 21, 055009.

Barrioz, P., Hure, J., Tanguy, B., 2019. Effect of dislocation channeling on void growth to coalescence in FCC crystals. Materials Science and Engineering: A 749, 255–270.

Barrioz, P.O., 2019. Rupture ductile des matériaux CFC irradiés. Ph.D. thesis. Université Paris-Saclay.

Barton, N.R., Arsenlis, A., Marian, J., 2013. A polycrystal plasticity model of strain localization in irradiated iron. Journal of the Mechanics and Physics of Solids 61, 341–351.

Bassani, J.L., Wu, T.Y., 1991. Latent hardening in single crystals. II. Analytical characterization and predictions. Proceedings of the Royal Society of London. Series A: Mathematical and Physical Sciences 435, 21–41.

Bayerschen, E., 2016. Single-crystal gradient plasticity with an accumulated plastic slip: Theory and applications. Phd thesis. KIT, Karlsruhe, Germany.

Bažant, Z.P., Belytschko, T.B., Chang, T.P., 1984. Continuum theory for strain-softening. Journal of Engineering Mechanics 110, 1666–1692.

Bažant, Z.P., Jirásek, M., 2002. Nonlocal integral formulations of plasticity and damage: survey of progress. Journal of engineering mechanics 128, 1119–1149.

Beao, 2014. Sodium-cooled fast reactor schemata. https://commons.wikimedia.org/wiki/File:Sodium-Cooled_Fast_Reactor_Schemata.svg.

de Bellefon, G.M., Van Duysen, J., 2016. Tailoring plasticity of austenitic stainless steels for nuclear applications: review of mechanisms controlling plasticity of austenitic steels below 400 C. Journal of Nuclear Materials 475, 168–191.

Belytschko, T., Ong, J.S.J., Liu, W.K., Kennedy, J.M., 1984. Hourglass control in linear and nonlinear problems. Computer Methods in Applied Mechanics and Engineering 43, 251–276.

Benzerga, A., Leblond, J.B., 2014. Effective yield criterion accounting for microvoid coalescence. Journal of Applied Mechanics 81.

Benzerga, A.A., Besson, J., 2001. Plastic potentials for anisotropic porous solids. European Journal of Mechanics-A/Solids 20, 397–434.

Benzerga, A.A., Besson, J., Batisse, R., Pineau, A., 2001. Synergistic effects of plastic anisotropy and void coalescence on fracture mode in plane strain. Modelling and Simulation in Materials Science and Engineering 10, 73.

Benzerga, A.A., Leblond, J.B., 2010. Ductile fracture by void growth to coalescence, in: Advances in applied mechanics. Elsevier. volume 44, pp. 169–305.

Besson, J., 1990. Simulation numérique de la mise en forme des céramiques. Application à la compaction isostatique à chaud. Ph.D. thesis. URL: http://www.theses.fr/1990ENMP0193. 1990ENMP0193.

Besson, J., 2009. Damage of ductile materials deforming under multiple plastic or viscoplastic mechanisms. International Journal of Plasticity 25, 2204–2221.

Besson, J., 2010. Continuum models of ductile fracture: a review. International Journal of Damage Mechanics 19, 3–52.

Besson, J., Cailletaud, G., Chaboche, J.L., Forest, S., 2009. Non-linear mechanics of materials. volume 167. Springer Science & Business Media.

Besson, J., Foerch, R., 1997. Large scale object–oriented finite element code design. Computer Methods in Applied Mechanics and Engineering 142, 165–187.

Besson, J., Foerch, R., 1998. Object-oriented programming applied to the finite element method part I. general concepts. Revue Européenne des Eléments Finis 7, 535–566.

Besson, J., Guillemer-Neel, C., 2003. An extension of the Green and Gurson models to kinematic hardening. Mechanics of materials 35, 1–18.

Blaber, J., Adair, B., Antoniou, A., 2015. Ncorr: open-source 2d digital image correlation matlab software. Experimental Mechanics 55, 1105–1122.

Bloom, E., 1976. Irradiation strengthening and embrittlement, in: Radiation damage in metals, pp. 295–329.

Borg, U., Kysar, J.W., 2007. Strain gradient crystal plasticity analysis of a single crystal containing a cylindrical void. International Journal of Solids and Structures 44, 6382–6397.

Borg, U., Niordson, C.F., Kysar, J.W., 2008. Size effects on void growth in single crystals with distributed voids. International Journal of Plasticity 24, 688–701.

Bouby, C., Kondo, D., 2017. Sur le cadre thermodynamique d'une classe de modèles de plasticité de milieux poreux ductiles, in: Congrès français de mécanique, AFM, Association Française de Mécanique.

Brager, H., Straalsund, J., Holmes, J., Bates, J., 1971. Irradiation-produced defects in austenitic stainless steel. Metallurgical Transactions 2, 1893–1904.

Bragg, W.L., Nye, J., 1947. A dynamical model of a crystal structure. Proceedings of the Royal Society of London. Series A. Mathematical and Physical Sciences 190, 474–481.

Brepols, T., Wulfinghoff, S., Reese, S., 2017. Gradient-extended two-surface damage-plasticity: micromorphic formulation and numerical aspects. International Journal of Plasticity 97, 64–106.

Bruemmer, S.M., Simonen, E.P., Scott, P.M., Andresen, P.L., Was, G.S., Nelson, J.L., 1999. Radiation-induced material changes and susceptibility to intergranular failure of light-water-reactor core internals. Journal of Nuclear Materials 274, 299–314.

Busso, E.P., Cailletaud, G., 2005. On the selection of active slip systems in crystal plasticity. International Journal of Plasticity 21, 2212–2231.

Byun, T., Farrell, K., 2004a. Irradiation hardening behavior of polycrystalline metals after low temperature irradiation. Journal of Nuclear Materials 326, 86 – 96.

Byun, T., Farrell, K., 2004b. Plastic instability in polycrystalline metals after low temperature irradiation. Acta Materialia 52, 1597–1608.

Byun, T., Hashimoto, N., 2006. Strain localization in irradiated materials. Nuclear Engineering and technology 38, 619–638.

Byun, T., Hashimoto, N., Farrell, K., 2004. Temperature dependence of strain hardening and plastic instability behaviors in austenitic stainless steels. Acta Materialia 52, 3889–3899.

Byun, T., Hashimoto, N., Farrell, K., 2006. Deformation mode map of irradiated 316 stainless steel in true stress–dose space. Journal of nuclear materials 351, 303–315.

Caesar, A.G., 2019. Iron-carbon phase diagram under atmospheric pressure. https://commons.wikimedia.org/wiki/File:Iron_carbon_phase_diagram.svg#filelinks [CC BY-SA 4.0 (https://creativecommons.org/licenses/by-sa/4.0)].

Cailletaud, G., Forest, S., Jeulin, D., Feyel, F., Galliet, I., Mounoury, V., Quilici, S., 2003. Some elements of microstructural mechanics. Computational Materials Science 27, 351–374.

Canadinc, D., Sehitoglu, H., Maier, H., Chumlyakov, Y., 2005. Strain hardening behavior of aluminum alloyed Hadfield steel single crystals. Acta Materialia 53, 1831 – 1842.

Cao, T.S., Mazière, M., Danas, K., Besson, J., 2015. A model for ductile damage prediction at low stress triaxialities incorporating void shape change and void rotation. International Journal of Solids and Structures 63, 240–263.

Castañeda, P.P., 1991. The effective mechanical properties of nonlinear isotropic composites. Journal of the Mechanics and Physics of Solids 39, 45–71.

Castañeda, P.P., Suquet, P., 1997. Nonlinear composites, in: Advances in applied mechanics. Elsevier. volume 34, pp. 171–302.

Cawthorne, C., Fulton, E., 1967. Voids in irradiated stainless steel. Nature 216, 575–576.

Cazacu, O., Revil-Baudard, B., Chandola, N., Kondo, D., 2014. New analytical criterion for porous solids with Tresca matrix under axisymmetric loadings. International Journal of Solids and Structures 51, 861–874.

Chaboche, J.L., 1988. Continuum Damage Mechanics: Part I—General Concepts. Journal of Applied Mechanics 55, 59–64.

Chang, H., Segurado, J., de la Fuente, O.R., Pabón, B., LLorca, J., 2013. Molecular dynamics modeling and simulation of void growth in two dimensions. Modelling and Simulation in Materials Science and Engineering 21, 075010.

Chaouadi, R., 2008. Effect of irradiation-induced plastic flow localization on ductile crack resistance behavior of a 9% Cr tempered martensitic steel. Journal of Nuclear Materials 372, 379–390.

Chen, Y., 2019. Modélisation de la rupture ductile par approche locale: simulation robuste de la déchirure. Ph.D. thesis. Paris Sciences et Lettres.

Chopra, O., Rao, A., 2011a. A review of irradiation effects on LWR core internal materials – IASCC susceptibility and crack growth rates of austenitic stainless steels. Journal of Nuclear Materials 409, 235 – 256.

Chopra, O., Rao, A., 2011b. A review of irradiation effects on LWR core internal materials – neutron embrittlement. Journal of Nuclear Materials 412, 195 – 208.

Chopra, O., Shack, W., 2008. Crack growth rates and fracture toughness of irradiated austenitic stainless steels in BWR environments. Technical Report. Argonne National Lab.(ANL), Argonne, IL (United States).

Choyke, W., McGruer, J., Townsend, J., Spitznagel, J., Doyle, N., Venskytis, F., 1979. Helium effects in ion-bombarded 304 stainless steel. Journal of Nuclear Materials 85, 647–651.

Clarke, W., White, M., Ranganath, S., 1990. Evaluation of the fracture toughness of irradiated stainless steel using short rod specimens, in: Effects of Radiation on Materials: 14th International Symposium (Volume II), ASTM International. pp. 470–486.

Cockburn, B., Karniadakis, G.E., Shu, C.W., 2012. Discontinuous Galerkin methods: theory, computation and applications. volume 11. Springer Science & Business Media.

Conermann, J., 2005. Irradiation effects in a highly irradiated cold worked stainless steel removed from a commercial PWR, in: Proc. 12th Int. Conf. on Environmental Degradation of Materials in Nuclear Power Systems-Water Reactors, 2005, TMS.

Considère, M., 1885. L'emploi du fer et de l'acier dans les constructions. Annales des Ponts et Chaussées 9, 574–775.

Cordero, N., Forest, S., Busso, E., Berbenni, S., Cherkaoui, M., 2012a. Grain size effects on plastic strain and dislocation density tensor fields in metal polycrystals. Computational Materials Science 52, 7 – 13.

Cordero, N., Gaubert, A., Forest, S., Busso, E.P., Gallerneau, F., Kruch, S., 2010. Size effects in generalised continuum crystal plasticity for two-phase laminates. Journal of the Mechanics and Physics of Solids 58, 1963–1994.

Cordero, N.M., Forest, S., Busso, E.P., 2012b. Generalised continuum modelling of grain size effects in polycrystals. Comptes Rendus Mécanique 340, 261–274.

Courcelle, A., Jublot, M., Bisor, C., Séran, J., Turque, I., Rabouille, O., Azera, M., Mallet, C., Verhaeghe, B., Desserouer, C., et al., 2018. Grain-boundary embrittlement in highly irradiated 15-15ti austenitic steel, in: NUMAT-2018.

Coussy, O., 2004. Poromechanics. John Wiley & Sons.

Crépin, J., Bretheau, T., Caldemaison, D., 1996. Cavity growth and rupture of $\beta$-treated zirconium: a crystallographic model. Acta materialia 44, 4927–4935.

Cui, Y., Po, G., Ghoniem, N., 2018. Suppression of localized plastic flow in irradiated materials. Scripta Materialia 154, 34–39.

Cuitino, A., Ortiz, M., 1996. Three-dimensional crack-tip fields in four-point-bending copper single-crystal specimens. Journal of the Mechanics and Physics of Solids 44, 863–904.

Dahlberg, C.F.O., Boasen, M., 2019. Evolution of the length scale in strain gradient plasticity. International Journal of Plasticity 112, 220 – 241.

Dai, Y., Victoria, M., 1996. Defect cluster structure and tensile properties of copper single crystals irradiated with 600 MeV protons. MRS Online Proceedings Library Archive 439.

Daly, M., Burnett, T., Pickering, E., Tuck, O., Léonard, F., Kelley, R., Withers, P., Sherry, A., 2017. A multi-scale correlative investigation of ductile fracture. Acta Materialia 130, 56 – 68.

Danas, K., Aravas, N., 2012. Numerical modeling of elasto-plastic porous materials with void shape effects at finite deformations. Composites Part B: Engineering 43, 2544–2559.

Danas, K., Castañeda, P.P., 2009. A finite-strain model for anisotropic viscoplastic porous media: I–theory. European Journal of Mechanics-A/Solids 28, 387–401.

Demir, E., Raabe, D., 2010. Mechanical and microstructural single-crystal Bauschinger effects: Observation of reversible plasticity in copper during bending. Acta Materialia 58, 6055–6063.

Devincre, B., Kubin, L., Hoc, T., 2006. Physical analyses of crystal plasticity by DD simulations. Scripta Materialia 54, 741–746.

Di Gioacchino, F., Quinta da Fonseca, J., 2013. Plastic strain mapping with sub-micron resolution using digital image correlation. Experimental Mechanics 53, 743–754.

Di Pietro, D.A., Ern, A., Lemaire, S., 2016. A review of hybrid high-order methods: formulations, computational aspects, comparison with other methods, in: Building bridges: connections and challenges in modern approaches to numerical partial differential equations. Springer, pp. 205–236.

Dormieux, L., Kondo, D., 2010. An extension of Gurson model incorporating interface stresses effects. International Journal of Engineering Science 48, 575–581.

Edwards, D.J., Simonen, E.P., Bruemmer, S.M., 2003. Evolution of fine-scale defects in stainless steels neutron-irradiated at 275 C. Journal of nuclear materials 317, 13–31.

Ehrnstén, U., Toivonen, A., Ivanchenko, M., Nevdacha, V., Yagozinskyy, Y., Hanninen, H., 2007. Dynamic strain ageing of deformed nitrogen-alloyed aisi 316 stainless steels. EUROPEAN FEDERATION OF CORROSION PUBLICATIONS 51, 103.

Enakoutsa, K., Leblond, J., Perrin, G., 2007. Numerical implementation and assessment of a phenomenological nonlocal model of ductile rupture. Computer Methods in Applied Mechanics and Engineering 196, 1946–1957.

Enakoutsa, K., Leblond, J.B., 2009. Numerical implementation and assessment of the GLPD micromorphic model of ductile rupture. European Journal of Mechanics-A/Solids 28, 445–460.

Encyclopædia Britannica, 2019. Stainless steel: nickel and chromium content. https://www.britannica.com/technology/stainless-steel#/media/1/562558/233265.

Erdle, H., Böhlke, T., 2017. A gradient crystal plasticity theory for large deformations with a discontinuous accumulated plastic slip. Computational Mechanics 60, 923–942.

Eringen, A.C., Suhubi, E., 1964. Nonlinear theory of simple micro-elastic solids—I. International Journal of Engineering Science 2, 189–203.

Essmann, U., Seeger, A., 1964. Verfestigungsverhalten neutronenbestrahlter Metalle. II. Temperaturwechselversuche und Gleitlinienbeobachtungen an Kupfereinkristallen. physica status solidi (b) 4, 177–197.

Etienne, A., 2009. Etude des effets d'irradiations et de la nanostructuration dans des aciers austénitiques inoxydables. Ph.D. thesis. Université de Rouen. URL: http://www.theses.fr/2009ROUES010/document. Thèse de doctorat dirigée par Pareige, Philippe Physique.

Evers, L., Brekelmans, W., Geers, M., 2004. Non-local crystal plasticity model with intrinsic SSD and GND effects. Journal of the Mechanics and Physics of Solids 52, 2379–2401.

Fabrègue, D., Pardoen, T., 2008. A constitutive model for elastoplastic solids containing primary and secondary voids. Journal of the Mechanics and Physics of Solids 56, 719–741.

Farooq, H., Cailletaud, G., Forest, S., Ryckelynck, D., 2020. Crystal plasticity modeling of the cyclic behavior of polycrystalline aggregates under non-symmetric uniaxial loading: Global and local analyses. International Journal of Plasticity 126, 102619.

Farrell, K., Byun, T., Hashimoto, N., 2003. Mapping flow localization processes in deformation of irradiated reactor structural alloys—final report. ORNL/TM-2003/63 .

Farrell, K., Byun, T., Hashimoto, N., 2004. Deformation mode maps for tensile deformation of neutron-irradiated structural alloys. Journal of Nuclear Materials 335, 471–486.

Feaugas, X., Haddou, H., 2003. Grain-size effects on tensile behavior of nickel and AISI 316L stainless steel. Metallurgical and materials transactions A 34, 2329–2340.

Fish, R., Hunter, C., 1976. Tensile properties of fast reactor irradiated type 304 stainless steel, in: Irradiation Effects on The Microstructure and Properties of Metals. ASTM International, pp. 119–138.

Fish, R., Straalsund, J., Hunter, C., Holmes, J., 1973. Swelling and tensile property evaluations of high-fluence EBR-II thimbles, in: Effects of Radiation on Substructure and Mechanical Properties of Metals and Alloys. ASTM International, pp. 149–164.

Fleck, N., Hutchinson, J., 1997. Strain gradient plasticity. Advances in Applied Mechanics 33, 296–361.

Forest, S., 1998. Modeling slip, kink and shear banding in classical and generalized single crystal plasticity. Acta Materialia 46, 3265–3281.

Forest, S., 2005. Generalized continua, in: Buschow, K.J., Cahn, R.W., Flemings, M.C., Ilschner, B., Kramer, E.J., Mahajan, S., Veyssière, P. (Eds.), Encyclopedia of Materials: Science and Technology. Elsevier, Oxford, pp. 1 – 7.

Forest, S., 2006. Milieux continus généralisés et matériaux hétérogènes. Presses des MINES.

Forest, S., 2008. Some links between Cosserat, strain gradient crystal plasticity and the statistical theory of dislocations. Philosophical Magazine 88, 3549–3563.

Forest, S., 2009. Micromorphic approach for gradient elasticity, viscoplasticity, and damage. Journal of Engineering Mechanics 135, 117–131.

Forest, S., 2016a. Nonlinear regularisation operators as derived from the micromorphic approach to gradient elasticity, viscoplasticity and damage. Proc. R. Soc. A 472, 20150755.

Forest, S., 2016b. Nonlinear regularization operators as derived from the micromorphic approach to gradient elasticity, viscoplasticity and damage. Proc. R. Soc. A 472, 20150755.

Forest, S., Barbe, F., Cailletaud, G., 2000. Cosserat modelling of size effects in the mechanical behaviour of polycrystals and multiphase materials. International Journal of Solids and Structures 37, 7105–7126.

Forest, S., Bertram, A., 2011. Formulations of strain gradient plasticity, in: Mechanics of Generalized Continua. Springer, pp. 137–149.

Forest, S., Boubidi, P., Sievert, R., 2001. Strain localization patterns at a crack tip in generalized single crystal plasticity. Scripta Materialia 44, 953–958.

Forest, S., Olschewski, J., Ziebs, J., Kühn, H.J., Meersmann, J., Frenz, H., 1996. The elastic/plastic deformation behaviour of various oriented SC16 single crystals under combined tension/torsion fatigue loading, in: Lütjering, G., Nowack, H. (Eds.), Sixth International Fatigue Congress, Pergamon. pp. 1087–1092.

Forest, S., Rubin, M., 2016. A rate-independent crystal plasticity model with a smooth elastic–plastic transition and no slip indeterminacy. European Journal of Mechanics-A/Solids 55, 278–288.

Forest, S., Sedláček, R., 2003. Plastic slip distribution in two-phase laminate microstructures: dislocation-based versus generalized-continuum approaches. Philosophical Magazine 83, 245–276.

Forest, S., Sievert, R., 2003. Elastoviscoplastic constitutive frameworks for generalized continua. Acta Mechanica 160, 71–111.

Forest, S., Sievert, R., Aifantis, E.C., 2002. Strain gradient crystal plasticity: thermomechanical formulations and applications. Journal of the Mechanical Behavior of Materials 13, 219–232.

Fortin, M., Glowinski, R., 1983. Chapter III on decomposition-coordination methods using an augmented lagrangian, in: Studies in Mathematics and Its Applications. Elsevier. volume 15, pp. 97–146.

Franciosi, P., 1985. The concepts of latent hardening and strain hardening in metallic single crystals. Acta Metallurgica 33, 1601–1612.

Franciosi, P., Berveiller, M., Zaoui, A., 1980. Latent hardening in copper and aluminium single crystals. Acta Metallurgica 28, 273–283.

Frémond, M., Nedjar, B., 1996. Damage, gradient of damage and principle of virtual power. International Journal of Solids and Structures 33, 1083–1103.

Fukuya, K., Fujii, K., Nishioka, H., Kitsunai, Y., 2006. Evolution of microstructure and microchemistry in cold-worked 316 stainless steels under PWR irradiation. Journal of nuclear science and technology 43, 159–173.

Fukuya, K., Nishioka, H., Fujii, K., Kamaya, M., Miura, T., Torimaru, T., 2008. Fracture behavior of austenitic stainless steels irradiated in PWR. Journal of nuclear materials 378, 211–219.

Gallican, V., Hure, J., 2017. Anisotropic coalescence criterion for nanoporous materials. Journal of the Mechanics and Physics of Solids 108, 30–48.

Gambin, W., 1992. Refined analysis of elastic-plastic crystals. International journal of solids and structures 29, 2013–2021.

Gan, J., Was, G., 2001. Microstructure evolution in austenitic Fe–Cr–Ni alloys irradiated with rotons: Comparison with neutron-irradiated microstructures. Journal of nuclear materials 297, 161–175.

Gan, Y.X., Kysar, J.W., Morse, T.L., 2006. Cylindrical void in a rigid-ideally plastic single crystal II: Experiments and simulations. International Journal of Plasticity 22, 39–72.

Gao, H., Huang, Y., 2001. Taylor-based nonlocal theory of plasticity. International Journal of Solids and Structures 38, 2615 – 2637.

Garner, F., 2012. 4.02 radiation damage in austenitic steels. Comprehensive nuclear materials 4, 33–95.

Garner, F., 2018. The challenge of using ion irradiation to develop and test advanced alloys for application to very high neutron exposures in future reactor concepts. chapter 2, in: Accelerator Simulation and Theoretical Modelling of Radiation Effects in Structural Materials, pp. 4–22.

Garner, F., Edwards, D., Bruemmer, S., Porollo, S., Konobeev, Y.V., Neustroev, V., Shamardin, V., Kozlov, A., 2002. Recent developments concerning potential void swelling of PWR internals constructed from austenitic stainless steels, in: Contribution of materials investigation to the resolution of problems encountered in pressurized water reactors, pp. 393–404.

Garner, F., Hamilton, M., Panayotou, N., Johnson, G., 1981. The microstructural origins of yield strength changes in AISI 316 during fission or fusion irradiation. Journal of nuclear materials 104, 803–807.

Garnier, J., 2009. Déformation sous flux des aciers austénitiques des structures internes des réacteurs à eau pressurisée. Ph.D. thesis. CEA Saclay, Direction des systèmes d'information.

Geers, M., de Borst, R., Brekelmans, W., Peerlings, R., 1998. Strain-based transient-gradient damage model for failure analyses. Computer Methods in Applied Mechanics and Engineering 160, 133 – 153.

Germain, N., Besson, J., Feyel, F., 2007. Simulation of laminate composites degradation using mesoscopic non-local damage model and non-local layered shell element. Modelling and Simulation in Materials Science and Engineering 15, S425.

Germain, P., 1973. The method of virtual power in continuum mechanics. Part 2: Microstructure. SIAM Journal on Applied Mathematics 25, 556–575.

Germain, P., Nguyen, Q.S., Suquet, P., 1983. Continuum Thermodynamics. Journal of Applied Mechanics 50, 1010–1020.

Ghosh, G., Olson, G.B., 2002. The isotropic shear modulus of multicomponent Fe-base solid solutions. Acta materialia 50, 2655–2675.

Gilman, J., 1954. Mechanism of ortho kink-band formation in compressed zinc monocrystals. JOM 6, 621–629.

Gologanu, M., Leblond, J.B., Devaux, J., 1993. Approximate models for ductile metals containing non-spherical voids—case of axisymmetric prolate ellipsoidal cavities. Journal of the Mechanics and Physics of Solids 41, 1723–1754.

Gologanu, M., Leblond, J.B., Perrin, G., 1995. A micromechanically based Gurson-type model for ductile porous metals including strain gradient effects. Net Shape Processing of Powder Materials , 47–56.

Gologanu, M., Leblond, J.B., Perrin, G., Devaux, J., 1997. Recent extensions of Gurson's model for porous ductile metals, in: Continuum micromechanics. Springer, pp. 61–130.

Green, R., 1972. A plasticity theory for porous solids. International Journal of Mechanical Sciences 14, 215–224.

Greenfield, I., Crivelli-Visconti, I., 1966. Interaction between dislocation loops and glide dislocations in a solid solution Al-Mg alloy, in: Proc. Int. Conf. Electron Microscopy (Kyoto), pp. 351–352.

Greenfield, I., Wilsdorf, H., 1961. Effect of neutron irradiation on the plastic deformation of copper single crystals. Journal of Applied Physics 32, 827–839.

Greer, J.R., Oliver, W.C., Nix, W.D., 2005. Size dependence of mechanical properties of gold at the micron scale in the absence of strain gradients. Acta Materialia 53, 1821 – 1830.

Gudmundson, P., 2004. A unified treatment of strain gradient plasticity. Journal of the Mechanics and Physics of Solids 52, 1379–1406.

Guo, S., He, Y., Lei, J., Li, Z., Liu, D., 2017. Individual strain gradient effect on torsional strength of electropolished microscale copper wires. Scripta Materialia 130, 124 – 127.

Gurovich, B., Kuleshova, E., Frolov, A., Maltsev, D., Prikhodko, K., Fedotova, S., Margolin, B., Sorokin, A., 2015. Investigation of high temperature annealing effectiveness for recovery of radiation-induced structural changes and properties of 18Cr–10Ni–Ti austenitic stainless steels. Journal of Nuclear Materials 465, 565–581.

Gurson, A.L., 1977. Continuum theory of ductile rupture by void nucleation and growth: Part I—Yield criteria and flow rules for porous ductile media. Journal of Engineering Materials and Technology 99, 2–15.

Gurtin, M.E., 2000. On the plasticity of single crystals: free energy, microforces, plastic-strain gradients. Journal of the Mechanics and Physics of Solids 48, 989–1036.

Gurtin, M.E., 2002. A gradient theory of single-crystal viscoplasticity that accounts for geometrically necessary dislocations. Journal of the Mechanics and Physics of Solids 50, 5–32.

Gurtin, M.E., 2006. The Burgers vector and the flow of screw and edge dislocations in finite-deformation single-crystal plasticity. Journal of the Mechanics and Physics of Solids 54, 1882–1898.

Gurtin, M.E., 2008. A finite-deformation, gradient theory of single-crystal plasticity with free energy dependent on densities of geometrically necessary dislocations. International Journal of Plasticity 24, 702–725.

Gurtin, M.E., Anand, L., 2009. Thermodynamics applied to gradient theories involving the accumulated plastic strain: the theories of Aifantis and Fleck and Hutchinson and their generalization. Journal of the Mechanics and Physics of Solids 57, 405–421.

Gussev, M.N., Field, K.G., Busby, J.T., 2015. Deformation localization and dislocation channel dynamics in neutron-irradiated austenitic stainless steels. Journal of Nuclear Materials 460, 139–152.

Gélébart, L., 2020. Amitex. http://www.maisondelasimulation.fr/projects/amitex/general/_build/html/index.html.

Ha, S., Kim, K., 2010. Void growth and coalescence in fcc single crystals. International Journal of Mechanical Sciences 52, 863–873.

Hadamard, J., 1903. Leçons sur la propagation des ondes et les équations de l'hydrodynamique. Paris, Librairie Scientifique A. Hermann .

Håkansson, P., Wallin, M., Ristinmaa, M., 2006. Thermomechanical response of non-local porous material. International journal of plasticity 22, 2066–2090.

Halphen, B., Nguyen, Q.S., 1975. Sur les matériaux standard généralisés. J. Mécanique , 39–63.

Hamilton, M., Cannon, N., Johnson, G., 1982. Mechanical properties of highly irradiated 20 percent cold worked type 316 stainless steel, in: Effects of Radiation on Materials. ASTM International, pp. 636–647.

Hamilton, M.L., Huang, F.H., Yang, W.J., Garner, F.A., 1987. Mechanical properties and fracture behavior of 20% cold-worked 316 stainless steel irradiated to very high neutron exposures, in: Influence of Radiation on Material Properties: 13th International Symposium (Part II), ASTM International. pp. 245–270.

Han, X., 2012. Modélisation de la fragilisation due au gonflement dans les aciers inoxydables austénitiques irradiés. Ph.D. thesis. Paris, ENMP.

Han, X., Besson, J., Forest, S., Tanguy, B., Bugat, S., 2013. A yield function for single crystals containing voids. International Journal of Solids and Structures 50, 2115–2131.

Hanriot, F., Cailletaud, G., Remy, L., 1991. Mechanical behaviour of a nickel-based superalloy single crystal. A. Freed, K. Walker, Editeurs: High temperature constitutive modelling-Theory and application, ASME, New-York , 139–150.

Haque, M., Saif, M., 2003. Strain gradient effect in nanoscale thin films. Acta Materialia 51, 3053 – 3061.

Hart, E., 1967. Theory of the tensile test. Acta Metallurgica 15, 351 – 355.

Hashimoto, N., Byun, T., 2007. Deformation-induced martensite formation and dislocation channeling in neutron-irradiated 316 stainless steel. Journal of Nuclear Materials 367-370, 960 – 965. Proceedings of the Twelfth International Conference on Fusion Reactor Materials (ICFRM-12).

Hill, R., 1958. A general theory of uniqueness and stability in elastic-plastic solids. Journal of the Mechanics and Physics of Solids 6, 236–249.

Hill, R., 1962. Acceleration waves in solids. Journal of the Mechanics and Physics of Solids 10, 1–16.

Hojná, A., 2017. Overview of intergranular fracture of neutron irradiated austenitic stainless steels. Metals 7, 392.

Holmes, J., Bobbins, R., Brimhall, J., 1969. Effect of fast reactor irradiation on the tensile properties of 304 stainless steel. Journal of Nuclear Materials 32, 330–339.

Holmes, J.J., Straalsund, J.L., 1977. Effects of fast reactor exposure on the mechanical properties of stainless steels, in: Radiation effects in breeder reactor structural materials, pp. 53–63.

Hori, M., Nemat-Nasser, S., 1988a. Dynamic response of crystalline solids with microcavities. Journal of applied physics 64, 856–863.

Hori, M., Nemat-Nasser, S., 1988b. Mechanics of void growth and void collapse in crystals. Mechanics of Materials 7, 1–13.

Huang, F., 1984. The fracture characterization of highly irradiated type 316 stainless steel. International Journal of Fracture 25, 181–193.

Huang, F., 1992. Comparison of fracture behavior for low-swelling ferritic and austenitic alloys irradiated in the fast flux test facility (FFTF) to 180 dpa. Engineering fracture mechanics 43, 733–748.

Hughes, T.J., Scovazzi, G., Bochev, P.B., Buffa, A., 2006. A multiscale discontinuous galerkin method with the computational structure of a continuous Galerkin method. Computer Methods in Applied Mechanics and Engineering 195, 2761–2787.

Hunter, C., Fish, R., Holmes, J., 1972. Channel fracture in irradiated EBR-II type 304 stainless steel. Trans. Amer. Nucl. Soc 15, 254–255.

Hure, J., 2019. A coalescence criterion for porous single crystals. Journal of the Mechanics and Physics of Solids 124, 505–525.

Hure, J., Barrioz, P., Tanguy, B., 2020. Assessing size effects on the deformation of nanovoids in metallic materials. Scripta Materialia 177, 54–57.

Hure, J., El Shawish, S., Cizelj, L., Tanguy, B., 2016. Intergranular stress distributions in polycrystalline aggregates of irradiated stainless steel. Journal of Nuclear Materials 476, 231–242.

Hussein, M., Borg, U., Niordson, C.F., Deshpande, V., 2008. Plasticity size effects in voided crystals. Journal of the Mechanics and Physics of Solids 56, 114–131.

Hutchinson, J., Fleck, N., 1997. Strain gradient plasticity. Advances in applied mechanics 33, 295–361.

Idiart, M.I., 2008. Modeling the macroscopic behavior of two-phase nonlinear composites by infinite-rank laminates. Journal of the Mechanics and Physics of Solids 56, 2599–2617.

Jaoul, B., (1965, 2008). Etude de la plasticité et application aux métaux. Presses des MINES.

Jiao, Z., Was, G., 2010. The role of irradiated microstructure in the localized deformation of austenitic stainless steels. Journal of Nuclear Materials 407, 34–43.

Jitsukawa, S., Ioka, I., Hishinuma, A., 1999. Post-irradiation mechanical properties of austenitic alloys at temperatures below 703 K. Journal of nuclear materials 271, 167–172.

Joëssel, L., 2018. Modélisation micromécanique du comportement viscoplastique d'un polycristal poreux: application à un acier inoxydable austénitique irradié. Ph.D. thesis. Université d'Aix-Marseille.

Kachanov, L., 2013. Introduction to continuum damage mechanics. volume 10. Springer Science & Business Media.

Kacher, J., Liu, G., Robertson, I., 2012. In situ and tomographic observations of defect free channel formation in ion irradiated stainless steels. Micron 43, 1099–1107.

Kaiser, T., Menzel, A., 2019a. A dislocation density tensor-based crystal plasticity framework. Journal of the Mechanics and Physics of Solids 131, 276 – 302.

Kaiser, T., Menzel, A., 2019b. An incompatibility tensor-based gradient plasticity formulation-Theory and numerics. Computer Methods in Applied Mechanics and Engineering 345, 671 – 700.

Kammers, A., Daly, S., 2011. Small-scale patterning methods for digital image correlation under scanning electron microscopy. Measurement Science and Technology 22, 125501.

Karaman, I., Sehitoglu, H., Gall, K., Chumlyakov, Y., Maier, H., 2000. Deformation of single crystal Hadfield steel by twinning and slip. Acta Materialia 48, 1345 – 1359.

Karaman, I., Sehitoglu, H., Maier, H., Chumlyakov, Y., 2001. Competing mechanisms and modeling of deformation in austenitic stainless steel single crystals with and without nitrogen. Acta Materialia 49, 3919–3933.

KBS, C., 2020. https://www.kbs-coatings.com/.

Keh, A.S., Nakada, Y., 1967. Plasticity of iron single crystals. Canadian Journal of Physics 45, 1101–1120.

Keralavarma, S., Chockalingam, S., 2016. A criterion for void coalescence in anisotropic ductile materials. International Journal of Plasticity 82, 159–176.

Kocks, U., Mecking, H., 2003. Physics and phenomenology of strain hardening: the FCC case. Progress in Materials Science 48, 171 – 273.

Koplik, J., Needleman, A., 1988. Void growth and coalescence in porous plastic solids. International Journal of Solids and Structures 24, 835–853.

Kothari, M., Anand, L., 1998. Elasto-viscoplastic constitutive equations for polycrystalline metals: application to tantalum. Journal of the Mechanics and Physics of Solids 46, 51–83.

Krishna, S., De, S., 2011. A temperature and rate-dependent micromechanical model of molybdenum under neutron irradiation. Mechanics of materials 43, 99–110.

Krishna, S., Zamiri, A., De, S., 2010. Dislocation and defect density-based micromechanical modeling of the mechanical behavior of FCC metals under neutron irradiation. Philosophical magazine 90, 4013–4025.

Krug, M., Shogan, R., 2005. Materials Reliability Program: Fracture Toughness Testing of Decommissioned PWR Core Internals Material Samples (MRP-160) Non-Proprietary Version. Technical Report. Electric Power Research Institute.

Kubin, L., Devincre, B., Hoc, T., 2008. Modeling dislocation storage rates and mean free paths in face-centered cubic crystals. Acta materialia 56, 6040–6049.

Kuhlmann-Wilsdorf, D., 1999. The theory of dislocation-based crystal plasticity. Philosophical Magazine A 79, 955–1008.

Kulcinski, G.L., Laidler, J., Doran, D., 1971. Simulation of high fluence fast neutron damage with heavy ion bombardment. radiation effects 7, 195–202.

Leblond, J.B., Perrin, G., Devaux, J., 1995. An improved Gurson-type model for hardenable ductile metals. European journal of mechanics. A. Solids 14, 499–527.

Lee, E., Byun, T., Hunn, J., Yoo, M., Farrell, K., Mansur, L., 2001. On the origin of deformation microstructures in austenitic stainless steel: Part I–microstructures. Acta Materialia 49, 3269 – 3276.

Lehtinen, A., Laurson, L., Granberg, F., Nordlund, K., Alava, M.J., 2018. Effects of precipitates and dislocation loops on the yield stress of irradiated iron. Scientific reports 8, 6914.

Lewandowski, M., Stupkiewicz, S., 2018. Size effects in wedge indentation predicted by a gradient-enhanced crystal-plasticity model. International Journal of Plasticity 109, 54–78.

Lewis, M., Packan, N., Wells, G., Buhl, R., 1979. Improved techniques for heavy-ion simulation of neutron radiation damage. Nuclear Instruments and Methods 167, 233–247.

Li, D., Zbib, H., Sun, X., Khaleel, M., 2014. Predicting plastic flow and irradiation hardening of iron single crystal with mechanism-based continuum dislocation dynamics. International Journal of Plasticity 52, 3–17.

Lindroos, M., Laukkanen, A., Andersson, T., Vaara, J., Mäntylä, A., Frondelius, T., 2019. Micromechanical modeling of short crack nucleation and growth in high cycle fatigue of martensitic microstructures. Computational Materials Science 170, 109185.

Ling, C., 2017. Simulation de la rupture ductile intragranulaire des aciers irradiés. Effets de l'anisotropie cristalline et du gradient de déformations. Ph.D. thesis. Paris Sciences et Lettres.

Ling, C., Besson, J., Forest, S., Tanguy, B., Latourte, F., Bosso, E., 2016. An elastoviscoplastic model for porous single crystals at finite strains and its assessment based on unit cell simulations. International Journal of Plasticity 84, 58–87.

Ling, C., Forest, S., Besson, J., Tanguy, B., Latourte, F., 2018. A reduced micromorphic single crystal plasticity model at finite deformations. application to strain localization and void growth in ductile metals. International Journal of Solids and Structures 134, 43–69.

Ling, C., Tanguy, B., Besson, J., Forest, S., Latourte, F., 2017. Void growth and coalescence in triaxial stress fields in irradiated fcc single crystals. Journal of Nuclear Materials 492, 157–170.

Little, E., 1986. Fracture mechanics evaluations of neutron irradiated type 321 austenitic steel. Journal of Nuclear Materials 139, 261–276.

Liu, W., He, Z., Tang, J., Hu, Z., Cui, D., 2012. The effects of load condition on void coalescence in FCC single crystals. Computational Materials Science 60, 66–74.

Liu, Y., Ngan, A., 2001. Depth dependence of hardness in copper single crystals measured by nanoindentation. Scripta Materialia 44, 237–241.

Lorentz, E., Benallal, A., 2005. Gradient constitutive relations: numerical aspects and application to gradient damage. Computer Methods in Applied Mechanics and Engineering 194, 5191 – 5220.

Lorentz, E., Besson, J., Cano, V., 2008. Numerical simulation of ductile fracture with the Rousselier constitutive law. Computer Methods in Applied Mechanics and Engineering 197, 1965–1982.

Luft, A., Richter, J., Schlaubitz, K., Loose, C., Mühlhaus, C., 1975. Work softening and microstructural instability of predeformed molybdenum single crystals. Materials Science and Engineering 20, 113–122.

Madec, R., Devincre, B., Kubin, L., Hoc, T., Rodney, D., 2003. The role of collinear interaction in dislocation-induced hardening. Science 301, 1879–1882.

Mandel, J., 1966. Conditions de stabilité et postulat de Drucker, in: Rheology and Soil Mechanics/Rhéologie et Mécanique des Sols. Springer, pp. 58–68.

Marano, A., Gélébart, L., Forest, S., 2019. Intragranular localization induced by softening crystal plasticity: Analysis of slip and kink bands localization modes from high resolution FFT–simulations results. Acta Materialia 175, 262 – 275.

Margolin, B., Sorokin, A., Shvetsova, V., Minkin, A., Potapova, V., Smirnov, V., 2016. The radiation swelling effect on fracture properties and fracture mechanisms of irradiated austenitic steels. Part I. ductility and fracture toughness. Journal of Nuclear Materials 480, 52–68.

Marshall, P., 1984. Austenitic stainless steels: microstructure and mechanical properties. Springer Science & Business Media.

Mastel, B., Kissinger, H., Laidler, J., Bierlein, T., 1963. Dislocation channeling in neutron-irradiated molybdenum. Journal of Applied Physics 34, 3637–3638.

Mbiakop, A., Constantinescu, A., Danas, K., 2015a. An analytical model for porous single crystals with ellipsoidal voids. Journal of the Mechanics and Physics of Solids 84, 436–467.

Mbiakop, A., Constantinescu, A., Danas, K., 2015b. A model for porous single crystals with cylindrical voids of elliptical cross-section. International Journal of Solids and Structures 64, 100–119.

McClintock, F.A., 1968. A Criterion for Ductile Fracture by the Growth of Holes. Journal of Applied Mechanics 35, 363–371.

McMurtrey, M., Was, G., Patrick, L., Farkas, D., 2011. Relationship between localized strain and irradiation assisted stress corrosion cracking in an austenitic alloy. Materials Science and Engineering: A 528, 3730 – 3740.

Mear, M.E., Hutchinson, J., 1985. Influence of yield surface curvature on flow localization in dilatant plasticity. Mechanics of Materials 4, 395–407.

Mecking, H., Kocks, U., 1981. Kinetics of flow and strain-hardening. Acta Metallurgica 29, 1865–1875.

Méric, L., Poubanne, P., Cailletaud, G., 1991. Single Crystal Modeling for Structural Calculations: Part 1—Model Presentation. Journal of Engineering Materials and Technology 113, 162–170.

Michel, D., Gray, R., 1987. Effects of irradiation on the fracture toughness of FBR structural materials. Journal of Nuclear Materials 148, 194–203.

MicroMecha, 2020. http://micromecha.fr/.

Miehe, C., Hofacker, M., Welschinger, F., 2010. A phase field model for rate-independent crack propagation: Robust algorithmic implementation based on operator splits. Computer Methods in Applied Mechanics and Engineering 199, 2765–2778.

Miehe, C., Kienle, D., Aldakheel, F., Teichtmeister, S., 2016. Phase field modeling of fracture in porous plasticity: A variational gradient-extended eulerian framework for the macroscopic analysis of ductile failure. Computer Methods in Applied Mechanics and Engineering 312, 3–50.

Mills, W., 1988. Fracture toughness of irradiated stainless steel alloys. Nuclear technology 82, 290–303.

Mills, W., 1997. Fracture toughness of type 304 and 316 stainless steels and their welds. International Materials Reviews 42, 45–82.

Mindlin, R.D., 1964. Micro-structure in linear elasticity. Archive for Rational Mechanics and Analysis 16, 51–78.

Mindlin, R.D., 1965. Second gradient of strain and surface-tension in linear elasticity. International Journal of Solids and Structures 1, 417–438.

Monnet, G., 2015. New insights into radiation hardening in face-centered cubic alloys. Scripta Materialia 100, 24 – 27.

Monnet, G., 2018. Multiscale modeling of irradiation hardening: Application to important nuclear materials. Journal of Nuclear Materials 508, 609 – 627.

Monnet, G., Domain, C., Queyreau, S., Naamane, S., Devincre, B., 2009. Atomic and dislocation dynamics simulations of plastic deformation in reactor pressure vessel steel. Journal of nuclear materials 394, 174–181.

Monnet, G., Mai, C., 2019. Prediction of irradiation hardening in austenitic stainless steels: Analytical and crystal plasticity studies. Journal of Nuclear Materials 518, 316–325.

Morgeneyer, T.F., Besson, J., 2011. Flat to slant ductile fracture transition: Tomography examination and simulations using shear-controlled void nucleation. Scripta Materialia 65, 1002–1005.

Morgeneyer, T.F., Helfen, L., Sinclair, I., Proudhon, H., Xu, F., Baumbach, T., 2011. Ductile crack initiation and propagation assessed via in situ synchrotron radiation-computed laminography. Scripta Materialia 65, 1010–1013.

Mori, T., Meshii, M., 1969. Plastic deformation of quench-hardened aluminum single crystals. Acta Metallurgica 17, 167–175.

Morin, L., 2015. Influence of void shape and size effects, and plastic anisotropy on ductile fracture. Theses. Université Pierre et Marie Curie - Paris VI. URL: https://tel.archives-ouvertes.fr/tel-01233531.

Morin, L., Leblond, J.B., Benzerga, A.A., 2015. Coalescence of voids by internal necking: theoretical estimates and numerical results. Journal of the Mechanics and Physics of Solids 75, 140–158.

Morin, L., Michel, J.C., Leblond, J.B., 2017. A Gurson-type layer model for ductile porous solids with isotropic and kinematic hardening. International Journal of Solids and Structures 118, 167–178.

Muhamed, G.A., Gündüz, S., Erden, M.A., Taştemur, D., 2017. Dynamic strain aging behaviour in aisi 316l austenitic stainless steel under as-received and as-welded conditions. Metals 7, 362.

Nahshon, K., Hutchinson, J., 2008. Modification of the Gurson model for shear failure. European journal of mechanics. A, Solids 27, 1.

Needleman, A., 1988. Material rate dependence and mesh sensitivity in localization problems. Computer Methods in Applied Mechanics and Engineering 67, 69 – 85.

Neff, P., Ghiba, I., Madeo, A., Placidi, L., Rosi, G., 2014. A unifying perspective: the relaxed linear micromorphic continuum. Continuum Mechanics and Thermodynamics 26, 639–681.

Nellemann, C., Niordson, C., Nielsen, K., 2017. An incremental flow theory for crystal plasticity incorporating strain gradient effects. International Journal of Solids and Structures 110-111, 239 – 250.

Nellemann, C., Niordson, C., Nielsen, K., 2018. Hardening and strengthening behavior in rate-independent strain gradient crystal plasticity. European Journal of Mechanics - A/Solids 67, 157 – 168.

Nelson, R., Mazey, D., Hudson, J., 1970. The use of ion accelerators to simulate fast neutron-induced voidage in metals. Journal of Nuclear Materials 37, 1–12.

Neuhäuser, H., 1983. Dislocations in Solids, Vol. 6, F.R.N. Nabarro, Editor. North-Holland Publishing Company, Amsterdam. chapter The dynamics of slip band formation in single crystals. pp. 319–440.

Neuhäuser, H., 1988. The dynamics of slip band formation in single crystals. Res Mech. 23, 113–135.

Neustroev, V., Garner, F., 2009. Severe embrittlement of neutron irradiated austenitic steels arising from high void swelling. Journal of nuclear materials 386, 157–160.

Nguyen, Q.S., 2000. Stability and nonlinear solid mechanics. Wiley.

Nguyen, V.D., Pardoen, T., Noels, L., 2020. A nonlocal approach of ductile failure incorporating void growth, internal necking, and shear dominated coalescence mechanisms. Journal of the Mechanics and Physics of Solids 137, 103891.

Niordson, C.F., Kysar, J.W., 2014. Computational strain gradient crystal plasticity. Journal of the Mechanics and Physics of Solids 62, 31–47.

Nix, W.D., Gao, H., 1998. Indentation size effects in crystalline materials: A law for strain gradient plasticity. Journal of the Mechanics and Physics of Solids 46, 411 – 425.

Noell, P.J., Carroll, J.D., Boyce, B.L., 2018. The mechanisms of ductile rupture. Acta Materialia 161, 83–98.

Nogaret, T., Rodney, D., Fivel, M., Robertson, C., 2008. Clear band formation simulated by dislocation dynamics: Role of helical turns and pile-ups. Journal of nuclear materials 380, 22–29.

Nouailhas, D., Cailletaud, G., 1995. Tension-torsion behavior of single-crystal superalloys - Experiment and finite-element analysis. Int. J. Plasticity 8, 451–470.

Nye, J., 1953. Some geometrical relations in dislocated crystals. Acta metallurgica 1, 153–162.

Odette, G., Lucas, G., 1989. Effects of low temperature neutron irradiation on the properties of 300 series stainless steels. Fusion Reactor Materials Semiannual Progress Report for Period Ending March 31 , 313.

Odette, G., Lucas, G., 1991. The effects of intermediate temperature irradiation on the mechanical behavior of 300-series austenitic stainless steels. Journal of nuclear materials 179, 572–576.

Paccou, E., Tanguy, B., Legros, M., 2019. Micropillar compression study of Fe-irradiated 304l steel. Scripta Materialia 172, 56–60.

Packan, N.H., Farrell, K., 1983. Radiation-induced swelling in an austenitic alloy: Observations and interpretation of the effects of helium. Nuclear Technology-Fusion 3, 392–404.

Panteghini, A., Bardella, L., 2016. On the finite element implementation of higher-order gradient plasticity, with focus on theories based on plastic distortion incompatibility. Computer Methods in Applied Mechanics and Engineering 310, 840–865.

Papasidero, J., Doquet, V., Mohr, D., 2015. Ductile fracture of aluminum 2024-T351 under proportional and non-proportional multi-axial loading: Bao–Wierzbicki results revisited. International Journal of Solids and Structures 69-70, 459 – 474.

Pardoen, T., Hutchinson, J., 2000. An extended model for void growth and coalescence. Journal of the Mechanics and Physics of Solids 48, 2467–2512.

Pardoen, T., Hutchinson, J., 2003. Micromechanics-based model for trends in toughness of ductile metals. Acta Materialia 51, 133–148.

Paux, J., Brenner, R., Kondo, D., 2018. Plastic yield criterion and hardening of porous single crystals. International Journal of Solids and Structures 132, 80–95.

Paux, J., Morin, L., Brenner, R., Kondo, D., 2015. An approximate yield criterion for porous single crystals. European Journal of Mechanics-A/Solids 51, 1–10.

Pawel, J., Rowcliffe, A., Lucas, G., Zinkle, S., 1996. Irradiation performance of stainless steels for ITER application. Journal of nuclear materials 239, 126–131.

Payet, S.F., Besson, J., Feyel, F., Chiaruttini, V., 2012. Crack initiation and propagation in nonlocal ductile media, in: ICDM, p. 117.

Peerlings, R., de Borst, R., Brekelmans, W., Geers, M., 2002. Localisation issues in local and nonlocal continuum approaches to fracture. European Journal of Mechanics - A/Solids 21, 175 – 189.

Peirce, D., Asaro, R., Needleman, A., 1983. Material rate dependence and localized deformation in crystalline solids. Acta Metallurgica 31, 1951 – 1976.

Petryk, H., Stupkiewicz, S., 2016. A minimal gradient-enhancement of the classical continuum theory of crystal plasticity. Part I: The hardening law. Archives of Mechanics 68, 459–485.

Pineau, A., Benzerga, A.A., Pardoen, T., 2016. Failure of metals I: Brittle and ductile fracture. Acta Materialia 107, 424–483.

Poh, L.H., Sun, G., 2017. Localizing gradient damage model with decreasing interactions. International Journal for Numerical Methods in Engineering 110, 503–522.

Pokor, C., 2002. Caractérisation microstructurale et modélisation du durcissement des aciers austénitiques irradiés des structures internes des réacteurs à eau pressurisée. Ph.D. thesis. Grenoble INPG.

Pokor, C., Averty, X., Brechet, Y., Dubuisson, P., Massoud, J., 2004a. Effect of irradiation defects on the work hardening behavior. Scripta materialia 50, 597–600.

Pokor, C., Brechet, Y., Dubuisson, P., Massoud, J.P., Averty, X., 2004b. Irradiation damage in 304 and 316 stainless steels: experimental investigation and modeling. Part II: Irradiation induced hardening. Journal of nuclear materials 326, 30–37.

Potirniche, G., Hearndon, J., Horstemeyer, M., Ling, X., 2006a. Lattice orientation effects on void growth and coalescence in fcc single crystals. International Journal of Plasticity 22, 921–942.

Potirniche, G., Horstemeyer, M., Wagner, G., Gullett, P., 2006b. A molecular dynamics study of void growth and coalescence in single crystal nickel. International Journal of Plasticity 22, 257–278.

Princeton Scientific Corporation, 2020. https://princetonscientific.com.

Quilici, S., Forest, S., Cailletaud, G., 1998. On size effects in torsion of multi- and polycrystalline specimens. Journal de Physique IV 8, Pr8–325–332.

Raffaitin, A., Monceau, D., Crabos, F., Andrieu, E., 2007. The effect of thermal cycling on the high-temperature creep behaviour of a single crystal nickel-based superalloy. Scripta Materialia 56, 277–280.

Ramaswamy, S., Aravas, N., 1998. Finite element implementation of gradient plasticity models Part II: Gradient-dependent evolution equations. Computer methods in applied mechanics and engineering 163, 33–53.

Rao, V.K., Taplin, D., Rao, P.R., 1975. The grain size dependence of flow and fracture in a Cr-Mn-N austenitic steel from 300 to 1300 K. Metallurgical Transactions A 6, 77–86.

Rashid, M., Nemat-Nasser, S., 1992. A constitutive algorithm for rate-dependent crystal plasticity. Computer Methods in Applied Mechanics and Engineering 94, 201–228.

Renault-Laborne, A., Hure, J., Malaplate, J., Gavoille, P., Sefta, F., Tanguy, B., 2018. Tensile properties and deformation microstructure of highly neutron-irradiated 316 stainless steels at low and fast strain rate. Journal of Nuclear Materials 508, 488 – 504.

Rice, J., 1976. Theoretical and applied mechanics, in: Proc. of the 14th IUTAM Congress, North-Holland, Amsterdam, Netherlands, 1976, pp. 207–220.

Rice, J.R., Tracey, D.M., 1969. On the ductile enlargement of voids in triaxial stress fields. Journal of the Mechanics and Physics of Solids 17, 201–217.

Ridley, N., Dyson, D., Holmes, B., 1971. Effect of alloying addition on the lattice parameter of austenite. Transactions of the Iron and Steel Institute of Japan 209, 396.

Rodchenkov, B., Kalinin, G., Strebkov, Y.S., Shamardin, V., Prokhorov, V., Bulanova, T., 2009. Irradiation behavior of Ti-stabilized 316l type steel. Journal of Nuclear Materials 386, 277–280.

Roters, F., Eisenlohr, P., Hantcherli, L., Tjahjanto, D., Bieler, T., Raabe, D., 2010. Overview of constitutive laws, kinematics, homogenization and multiscale methods in crystal plasticity finite-element modeling: Theory, experiments, applications. Acta Materialia 58, 1152 – 1211.

Rousselier, G., 1981. Finite deformation constitutive relations including ductile fracture damage. IUTAM symposium, in: Nemat-Nasser, S., (Ed.), Three-dimensional constitutive relations and ductile fracture. North-Holland, Amsterdam, pp. 319–343.

Rousselier, G., 1987. Ductile fracture models and their potential in local approach of fracture. Nuclear engineering and design 105, 97–111.

Rousselier, G., 2001. Dissipation in porous metal plasticity and ductile fracture. Journal of the Mechanics and Physics of Solids 49, 1727–1746.

Ryś, M., Forest, S., Petryk, H., 2020. A micromorphic crystal plasticity model with the gradient-enhanced incremental hardening law. International Journal of Plasticity , 102655.

Sabnis, P., Mazière, M., Forest, S., Arakere, N.K., Ebrahimi, F., 2012. Effect of secondary orientation on notch-tip plasticity in superalloy single crystals. International Journal of Plasticity 28, 102–123.

Scherer, J., Besson, J., Forest, S., Hure, J., Tanguy, B., 2019. Strain gradient crystal plasticity with evolving length scale: Application to voided irradiated materials. European Journal of Mechanics-A/Solids 77, 103768.

Scheyvaerts, F., Onck, P., Tekoğlu, C., Pardoen, T., 2011. The growth and coalescence of ellipsoidal voids in plane strain under combined shear and tension. Journal of the Mechanics and Physics of Solids 59, 373–397.

Schmidt-Baldassari, M., 2003. Numerical concepts for rate-independent single crystal plasticity. Computer Methods in Applied Mechanics and Engineering 192, 1261–1280.

Seeger, A., 1958. On the theory of radiation damage and radiation hardening. Proceedings of the Second United Nation International Conference on Peaceful uses of Atomic Energy 6, 250–273.

Segurado, J., Llorca, J., 2009. An analysis of the size effect on void growth in single crystals using discrete dislocation dynamics. Acta Materialia 57, 1427–1436.

Segurado, J., LLorca, J., 2010. Discrete dislocation dynamics analysis of the effect of lattice orientation on void growth in single crystals. International journal of plasticity 26, 806–819.

Selvarajou, B., Joshi, S.P., Benzerga, A.A., 2019. Void growth and coalescence in hexagonal close packed crystals. Journal of the Mechanics and Physics of Solids 125, 198–224.

Sensy, 2020. https://www.sensy.com/en/.

Shabrov, M., Briant, C., Needleman, A., Kim, S., Sylven, E., Sherman, D., Chuzhoy, L., 2004. Void nucleation by inclusion cracking. Metallurgical and Materials Transactions A 35, 1745–1755.

Sharp, J., 1974. Deformation of neutron irradiated copper alloys. Acta Metallurgica 22, 449–457.

Shin, P., Meshii, M., 1963. Electron microscopic and mechanical study of quenched aluminium. J. Metals 15, 80.

Shu, J.Y., 1998. Scale-dependent deformation of porous single crystals. International Journal of Plasticity 14, 1085–1107.

Simone, A., Askes, H., Sluys, L.J., 2004. Incorrect initiation and propagation of failure in non-local and gradient-enhanced media. International Journal of Solids and Structures 41, 351 – 363.

Smidt Jr, F.A., 1970a. Comments on dislocation structures in irradiated and strained iron. Scripta Metallurgica 4, 517–520.

Smidt Jr, F.A., 1970b. Dislocation channeling in irradiated metals. Technical Report. Naval Research Lab Washington DC.

Song, D., Xiao, X., Xue, J., Chu, H., Duan, H., 2015. Mechanical properties of irradiated multi-phase polycrystalline BCC materials. Acta Mechanica Sinica 31, 191–204.

Steinmann, P., Stein, E., 1996. On the numerical treatment and analysis of finite deformation ductile single crystal plasticity. Computer Methods in Applied Mechanics and Engineering 129, 235–254.

Stelmashenko, N., Walls, M., Brown, L., Milman, Y.V., 1993. Microindentations on W and Mo oriented single crystals: A STM study. Acta Metallurgica et Materialia 41, 2855–2865.

Struers, 2020. https://www.struers.com.

Stölken, J., Evans, A., 1998. A microbend test method for measuring the plasticity length scale. Acta Materialia 46, 5109 – 5115.

Svendsen, B., Bargmann, S., 2010. On the continuum thermodynamic rate variational formulation of models for extended crystal plasticity at large deformation. Journal of the Mechanics and Physics of Solids 58, 1253–1271.

Syed, B., Geng, J., Mishra, R., Kumar, K., 2012. [0001] compression response at room temperature of single-crystal magnesium. Scripta Materialia 67, 700 – 703.

Tabourot, L., Fivel, M., Rauch, E., 1997. Generalised constitutive laws for FCC single crystals. Materials Science and Engineering: A 234, 639–642.

Tanguy, B., Besson, J., 2001. An extension of the Rousselier model to predict viscoplastic temperature dependant materials. International Journal of Fracture .

Tanguy, B., Han, X., Besson, J., Forest, S., Robertson, C., Rupin, N., 2013. Dislocations and irradiation defects-based micromechanical modelling for neutron irradiated austenitic stainless steels, in: International Symposium on Plasticity, pp. 3–8.

Taylor, G.I., Elam, C.F., 1925. The plastic extension and fracture of aluminium crystals. Proceedings of the Royal Society of London. Series A, Containing Papers of a Mathematical and Physical Character 108, 28–51.

Tekoğlu, C., Leblond, J.B., Pardoen, T., 2012. A criterion for the onset of void coalescence under combined tension and shear. Journal of the Mechanics and Physics of Solids 60, 1363–1381.

Teodosiu, C., 1975. A physical theory of the finite elastic-viscoplastic behaviour of single crystals. Engineering Transaction 23, 151–184.

Thomas, T.Y., 1961. Plastic Flow and Fracture in Solids. volume 2. Elsevier.

Thomason, P., 1985. Three-dimensional models for the plastic limit-loads at incipient failure of the intervoid matrix in ductile porous solids. Acta Metallurgica 33, 1079–1085.

Torimaru, T., Kodama, M., Tanaka, S., Nakamura, T., Kumagai, K., Asano, K., 2010. Fracture toughness of austenitic stainless steels after BWR irradiation. Proceedings of Fontevroud 7.

Torki, M., Benzerga, A., Leblond, J.B., 2015. On void coalescence under combined tension and shear. Journal of Applied Mechanics 82.

Toupin, R., 1962. Elastic materials with couple-stresses. Archive for Rational Mechanics and Analysis 11, 385–414.

Traiviratana, S., Bringa, E.M., Benson, D.J., Meyers, M.A., 2008. Void growth in metals: atomistic calculations. Acta Materialia 56, 3874–3886.

Trinkaus, H., Singh, B., Foreman, A., 1997a. Mechanisms for decoration of dislocations by small dislocation loops under cascade damage conditions. Journal of Nuclear Materials 249, 91–102.

Trinkaus, H., Singh, B., Foreman, A., 1997b. Segregation of cascade induced interstitial loops at dislocations: possible effect on initiation of plastic deformation. Journal of Nuclear Materials 251, 172–187.

Tucker, R.P., Wechsler, M.S., Ohr, S.M., 1969. Dislocation channeling in neutron-irradiated niobium. Journal of Applied Physics 40, 400–408.

Tvergaard, V., Needleman, A., 1984. Analysis of the cup-cone fracture in a round tensile bar. Acta metallurgica 32, 157–169.

Uchic, M., Dimiduk, D., Florando, J., Nix, W., 2004. Sample dimensions influence strength and crystal plasticity. Science (New York, N.Y.) 305, 986–9.

USNRC, H., 2020. Westinghouse technology systems manual, section 3.1, reactor vessel and internals. https://www.nrc.gov/docs/ML1122/ML11223A212.pdf.

Vandoren, B., Simone, A., 2018. Modeling and simulation of quasi-brittle failure with continuous anisotropic stress-based gradient-enhanced damage models. Computer Methods in Applied Mechanics and Engineering 332, 644–685.

Vignjevic, R., Djordjevic, N., Vuyst, T.D., Gemkow, S., 2018. Modelling of strain softening materials based on equivalent damage force. Computer Methods in Applied Mechanics and Engineering 335, 52 – 68.

Vishwakarma, V., Keralavarma, S.M., 2019. Micromechanical modeling and simulation of the loading path dependence of ductile failure by void growth to coalescence. International Journal of Solids and Structures 166, 135–153.

Volterra, V., 1907. Sur l'équilibre des corps élastiques multiplement connexes, in: Annales scientifiques de l'École normale supérieure, pp. 401–517.

Voyiadjis, G.Z., Al-Rub, R.K.A., 2005. Gradient plasticity theory with a variable length scale parameter. International Journal of Solids and Structures 42, 3998 – 4029.

Voyiadjis, G.Z., Song, Y., 2019. Strain gradient continuum plasticity theories: theoretical, numerical and experimental investigations. International Journal of Plasticity .

Weaver, J.S., Pathak, S., Reichardt, A., Vo, H.T., Maloy, S.A., Hosemann, P., Mara, N.A., 2017. Spherical nanoindentation of proton irradiated 304 stainless steel: A comparison of small scale mechanical test techniques for measuring irradiation hardening. Journal of Nuclear Materials 493, 368–379.

Wechsler, M., 1973. Dislocation channeling in irradiated and quenched metals. The Inhomogeneity of Plastic Deformation URL: https://ci.nii.ac.jp/naid/10017531930/en/.

Wechsler, M., Tucker, R., Bode, R., 1969. Radiation hardening in single crystal niobium—the temperature dependence of yielding. Acta Metallurgica 17, 541–551.

Wei, X., Theaker, J., Griffiths, M., 2007. Deformation anisotropy of annealed zircaloy-2 as a function of fast neutron fluence. Journal of ASTM International 5, 1–11.

Wen, J., Huang, Y., Hwang, K., Liu, C., Li, M., 2005. The modified Gurson model accounting for the void size effect. International Journal of Plasticity 21, 381–395.

Whelan, M.J., Hirsch, P.B., Horne, R., Bollmann, W., 1957. Dislocations and stacking faults in stainless steel. Proceedings of the Royal Society of London. Series A. Mathematical and Physical Sciences 240, 524–538.

Wintle, J.B., Hayes, B., Goldthorpe, M.R., 2004. Adimew test: Assessment of a cracked dissimilar metal weld assembly, in: ASME Pressure Vessels and Piping Conference, pp. 21–36.

Wulfinghoff, S., Bayerschen, E., Böhlke, T., 2013. A gradient plasticity grain boundary yield theory. International Journal of Plasticity 51, 33–46.

Wulfinghoff, S., Böhlke, T., 2012. Equivalent plastic strain gradient enhancement of single crystal plasticity: theory and numerics. Proc. R. Soc. A 468, 2682–2703.

Wulfinghoff, S., Forest, S., Böhlke, T., 2015. Strain gradient plasticity modeling of the cyclic behavior of laminate microstructures. Journal of the Mechanics and Physics of Solids 79, 1–20.

Xu, H., Fyfitch, S., 2004. Materials reliability program: A review of radiation embrittlement for stainless steels (mrp-79).

Xu, X.P., Needleman, A., 1993. Void nucleation by inclusion debonding in a crystal matrix. Modelling and Simulation in Materials Science and Engineering 1, 111.

Xue, Z., Pontin, M., Zok, F., Hutchinson, J.W., 2010. Calibration procedures for a computational model of ductile fracture. Engineering Fracture Mechanics 77, 492–509.

Yalcinkaya, T., Brekelmans, W., Geers, M., 2012. Non-convex rate dependent strain gradient crystal plasticity and deformation patterning. International Journal of Solids and Structures 49, 2625–2636.

Yerra, S., Tekoğlu, C., Scheyvaerts, F., Delannay, L., Van Houtte, P., Pardoen, T., et al., 2010. Void growth and coalescence in single crystals. International Journal of Solids and Structures 47, 1016–1029.

Z–set package, 2020. Non-linear material & structure analysis suite, www.zset-software.com.

Zbib, H.M., Aifantis, E.C., 1988. On the structure and width of shear bands. Scripta Metallurgica 22, 703–708.

Zhang, X., Xu, C., Wang, L., Chen, Y., Li, M., Almer, J.D., Benda, E., Kenesei, P., Mashayekhi, A., Park, J.S., et al., 2017. iradmat: A thermo-mechanical testing system for in situ high-energy x-ray characterization of radioactive specimens. Review of Scientific Instruments 88, 015111.

Zhang, Y., Lorentz, E., Besson, J., 2018. Ductile damage modelling with locking-free regularised gtn model. International Journal for Numerical Methods in Engineering 113, 1871–1903.

Zhang, Z., Thaulow, C., Ødegård, J., 2000. A complete Gurson model approach for ductile fracture. Engineering Fracture Mechanics 67, 155–168.

Zhao, K., Chen, C., Shen, Y., Lu, T., 2009. Molecular dynamics study on the nano-void growth in face-centered cubic single crystal copper. Computational Materials Science 46, 749–754.

Ziegler, J.F., Ziegler, M., Biersack, J., 2010. Srim – the stopping and range of ions in matter (2010). Nuclear Instruments and Methods in Physics Research Section B: Beam Interactions with Materials and Atoms 268, 1818 – 1823. 19th International Conference on Ion Beam Analysis.

Zinkle, S., Maziasz, P., Stoller, R., 1993. Dose dependence of the microstructural evolution in neutron-irradiated austenitic stainless steel. Journal of Nuclear materials 206, 266–286.

Zinkle, S.J., Matsukawa, Y., 2004. Observation and analysis of defect cluster production and interactions with dislocations. Journal of nuclear materials 329, 88–96.

Zybell, L., Hütter, G., Linse, T., Mühlich, U., Kuna, M., 2014. Size effects in ductile failure of porous materials containing two populations of voids. European Journal of Mechanics-A/Solids 45, 8–19.

# A

# Single crystal tensile specimens sampling plans

Single- an bi-crystal tensile specimens were cut by electrical discharge machining with a wire diameter of $\phi = 100\,\mu m$. The geometry and positioning of the specimen in the plate were optimized in order to maximize the number of single crystal specimens and the number of different orientations. Figure A.1 shows the sampling plans used for the recto and verso parts of the initial plate purchased from Princeton Scientific. The background grayscale represents crystallographic orientation. Mainly two grains misoriented by about 10° composed the whole plate. The specimens contours are denoted by solid blue lines. Lengths are expressed in millimeters. From the recto part R, a smaller plate, delimited by dashed green lines in Figure A.1a, was collected in order to perform a proton irradiation experiment.

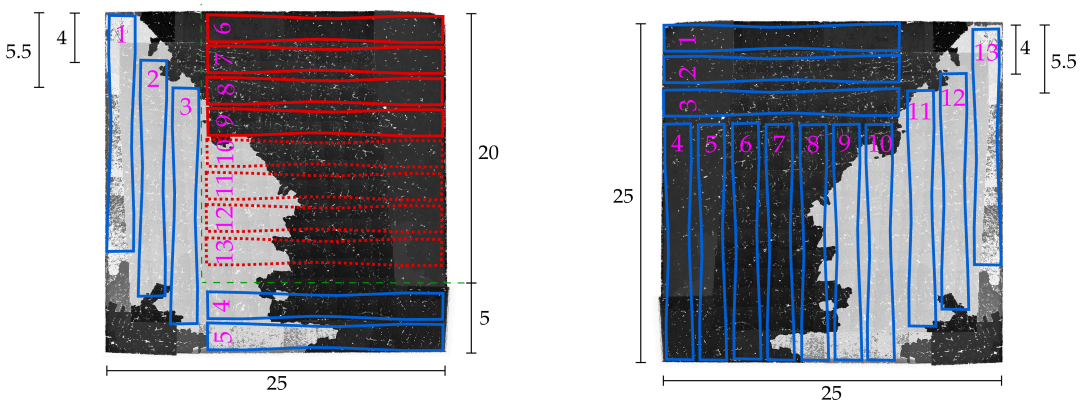


(a) recto ($R$)

(b) verso ($V$)

Figure A.1 Sampling plans of single- or bi-crystal tensile specimens.

# B

# Single crystal tensile specimens preparation

## B.1 Specimen thickness reduction

The specimen geometry was designed in order to maximize the number specimens that could be cut from the initial plate. The chosen geometry does not have wide heads as in common tensile specimen geometries. Therefore, during tensile tests on this geometry, both ends of the specimen need to be gripped. In order to avoid any sliding, specimens were thinned down by mechanical hand-polishing to a thickness of ∼140 µm. A stainless steel disk as shown in Figure B.1 was used as specimen holder during polishing. The specimen is stuck in the middle of the disk by using a hot melt adhesive (or hot glue). As shown in Figure B.1, the disk has a crown on its outer boundary. That crown is polished simultaneously to the specimen. The height of the crown is measured periodically in multiple locations in order to ensure the horizontality of the polished surface. Specimens were mirror-polished on both sides in order to remove any surface imperfections. The last polishing step was performed with a 0.25 µm colloidal silica suspension from Struers (Struers, 2020) in order to remove the hard surface layer induced by previous polishing operations.

## B.2 Heat resistant paint speckle pattern

A heat paint speckle pattern was deposited onto the surface of the single crystal tensile specimens in order to perform displacement field measurements by DIC. An in-house airbrush system, depicted in Figure B.2, was used to lay a first coating of white heat resistant paint on the whole specimen surface. The airbrush nozzle was then cleaned up and mounted again on the airbrush. The nozzle was tightened in order to reduce the airbrush outlet aperture to its lowest level. The distance between the specimen and the airbrush head was then maximized by moving the airbrush on its rail. Finally black heat resistant paint droplets were projected on the white coated surface of the specimen. This procedure allowed to obtain very small black spots (∼50 µm) and therefore a very fine DIC pattern ideal for high resolution field measurements.

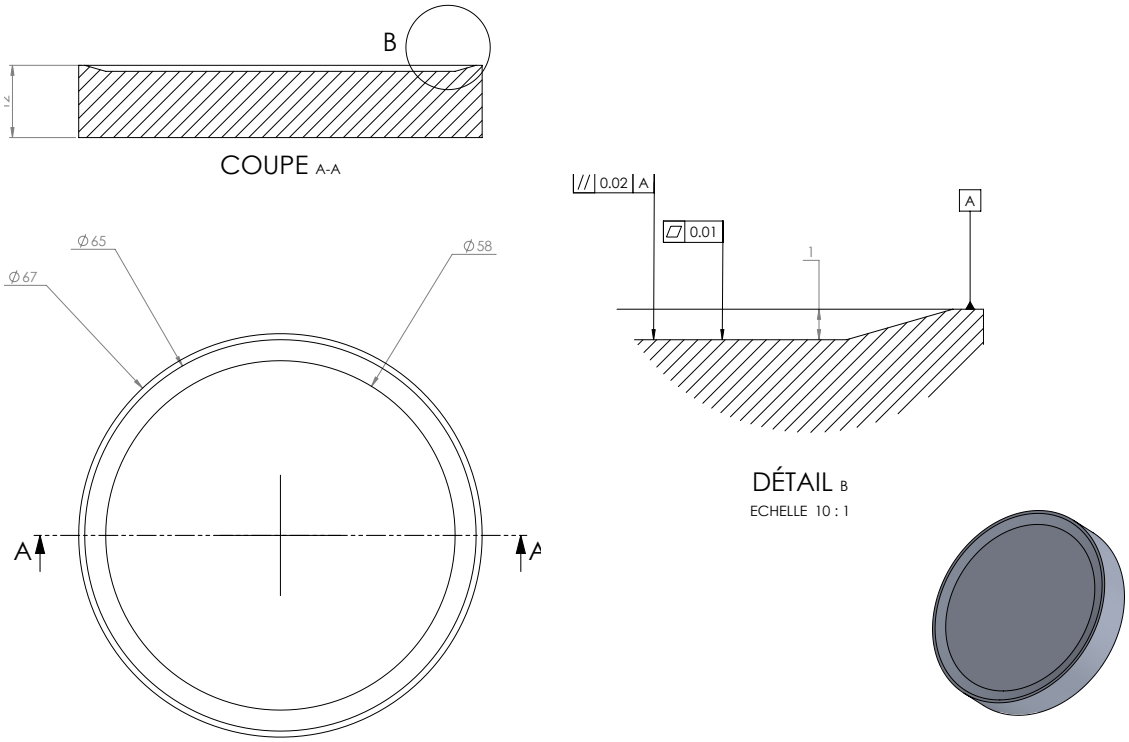


Figure B.1 Geometry of the specimen holder used for hand-polishing single crystal specimens. The outer crown is used to guarantee horizontality of the polished surface.

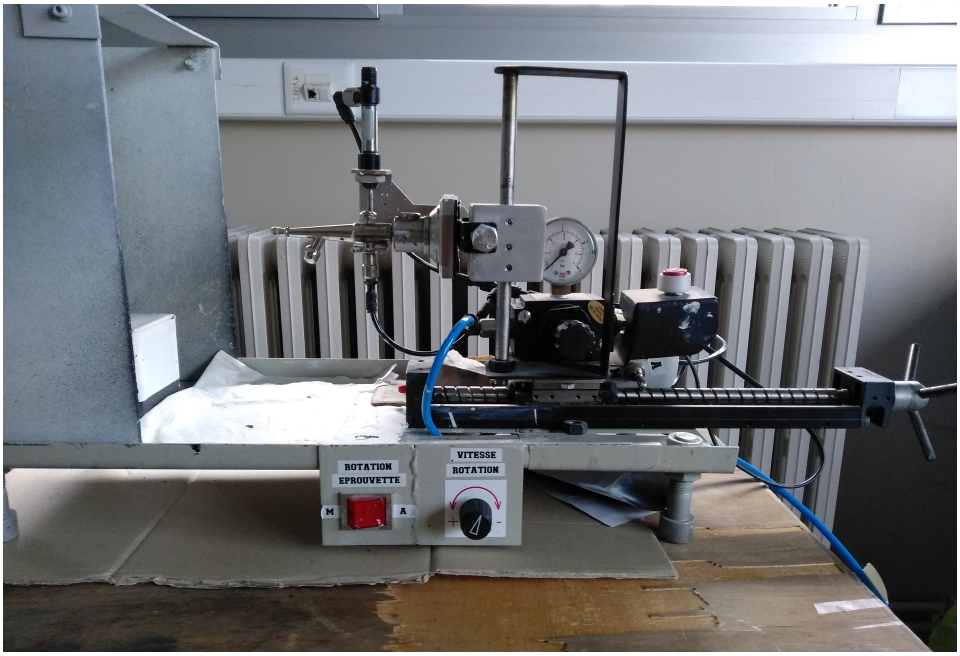


Figure B.2 Airbrush device used to make heat resistant paint speckle DIC patterns.

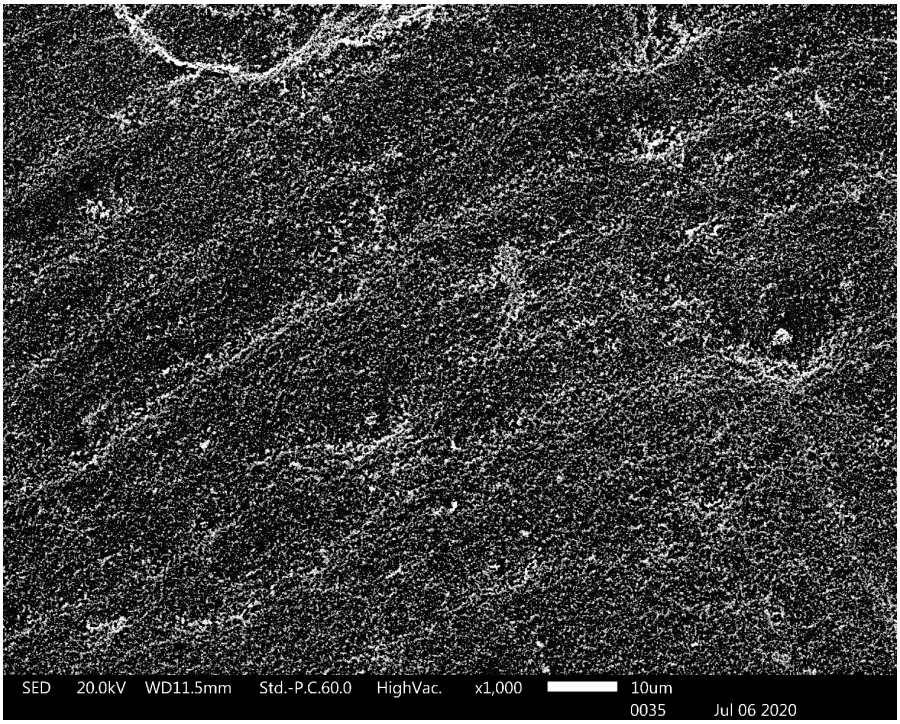


Figure B.3 SEM micrography of a DIC pattern suited for *in situ* testing obtained by deposition of gold nanoparticles on a mirror-polished specimen.

## B.3 Heat resistant gold nanoparticles pattern

As a perspective of the present work is to perform SEM *in situ* tensile experiments, a methodology was elaborated in order to create patterns suited for DIC with secondary electron images. Based on a technique presented in (Kammers and Daly, 2011) gold nanoparticle temperature resistant pattern were formed. A Milli-Q water solution containing $100\pm15$ nm wide gold nanoparticles, with a concentration of $0.053\,\mathrm{mg\,\mu L^{-1}}$, *i.e.* $5.0 \times 10^9$ particles/mL, was purchased from Ted Pella (Ref.: NanoXact$^{TM}$ 100 nm T. Cap. Gold). 10 µL droplets of the nanoparticle solution are laid with a micro-pipette on the mirror-polished specimen so as to cover the whole surface. After sufficient time water evaporates and nanoparticles remain on the specimen surface. To accelerate the evaporation process the specimen is heated to a temperature of 150 °C when depositing the droplets. Several depositions are needed in order to obtain a sufficiently dense and homogeneously distributed population of nanoparticles. About 15 successive depositions results in an adequate pattern as presented in Figure B.3. Evaporation of the solution can result in the formation of halos having a denser quantity of nanoparticles. Such an aureole is visible in the top left corner of Figure B.3. This phenomenon, known as the 'coffee ring' effect (Kammers and Daly, 2011), is imputed to a capillary fluid flow conveying nanoparticles to the droplet outer boundary. According to Kammers and Daly (2011) the 'coffee ring' effect can be mitigated by decreasing the drying time. Alternative methods to heating the sample could be considered, such as angling the sample, spin-coating or layering. The major drawback related to the elaboration of gold nanoparticles patterns lies in the difficulty of obtaining an ideal pattern at the desired location. However, the fact that such patterns can be elaborated in minutes and easily removed with purified water and a soft polishing film makes it a very lean and reliable technique.

# C

# Temperature gradient along single crystal tensile specimens

The heating device devoted for tensile tests at high temperatures provided with the MicroMecha micro-tensile machine consist in a 8 mm wide heating unit getting in contact with the bottom face of the specimen. Since tensile specimens are longer than the width of the heating unit, specimens heads are only heated by heat conduction and to some extent by heat convection. A FLIR infrared thermographic camera was used in order to characterize the temperature gradient along the specimen surface, in particular at the edge of the heating unit. The camera was calibrated by measuring the temperature on the specimen surface by using a welded thermocouple. Figure C.1a shows the thermographic image obtained after waiting a sufficient time to reach a steady state. Two profile lines Li1 and Li2 were plotted on the specimen surface and the heating unit surface respectively. Figure C.1b shows the temperature profile along both profile lines. It is not necessarily inconsistent that the specimen appears warmer than the heating unit, because both elements have possibly very different emissivity. In the contact-heated region the specimen temperature is rather homogeneous, while out of the contact-heated region a gradient of about -60 °C /mm is measured. As a consequence, the center part of the specimen, with lowest cross section sees also the highest temperature. Despite the fact that the specimen geometry is exempt of wide heads, the softer response induced by a higher temperature guarantees that the specimen will predominantly deform in its middle section.

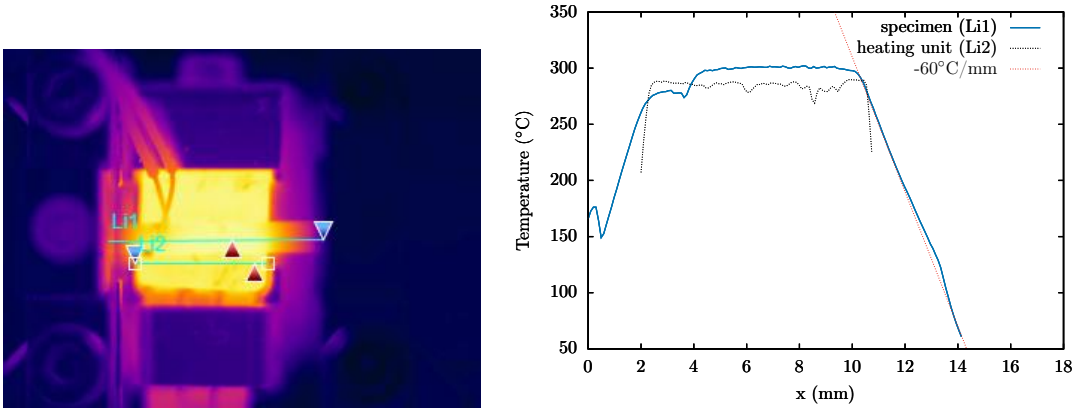


(a) (b)

Figure C.1 (a) Infrared thermographic image of a tensile specimen heated by contact with a heating unit. Li1 and Li2 are profile lines located along the specimen and the heating unit respectively. On each line, hot spots and cold spots are denoted by red and blue triangles respectively. (b) Temperature profiles along Li1 and Li2.

# D

# Crystal plasticity material parameters sensitivity analysis

In order to describe the effect of material parameters $\kappa$, $G_c$, $\rho_0^s$ and $A_i$ on the hardening behaviour, a sensitivity analysis is conducted. Each material parameter is varied independently and several different numerical values are used for each variable. Numerical values identified by Ling (2017) are used as the set of reference. The sensitivity analysis is performed for two different crystal orientations, namely orientations of specimen R4 and R2 presented in Table 3.2.

Figure D.1 shows the dependence of the hardening behaviour on the values taken by the interaction matrix coefficients $A_1$, $A_2$ and $A_3$. Generally speaking, increasing one of the $A_i$ parameter leads to an increase of the hardening rate. Both orientations have a greater sensitivity to the value taken by $A_1$. For $A_1$ orientation R4 is slightly more sensitive than $R2$. While orientation $R4$ is almost insensitive to $A_2$, orientation R2 displays a slender dependency to the same parameter. Orientation R2 and R4 have a very limited sensitivity to parameter $A_3$.

Figure D.2 shows the results of the sensitivity analysis for parameters $\kappa$ and $G_c$ involved in the evolution law of dislocation densities. $\kappa$ characterizes the number of obstacles a dislocation can cross before being immobilized, while $bG_c$ represents the annihilation distance between two dislocations belonging to the same slip system. Increasing $\kappa$ or $G_c$ leads thereby to a reduction of the strain hardening rate. In the domain considered for each parameter, the sensitivity of the hardening behaviour to $\kappa$ is more important than the sensitivity to $G_c$. Orientation $R4$ is slightly more sensitive than orientation $R2$ to the values taken by $\kappa$ and $G_c$.

Figure D.3 shows the influence of the initial dislocation density per slip system $\rho_0^s$ and the evolution of coefficients $A_i$ on the hardening behaviour. Increasing the initial dislocation density results in a larger yield stress. However the asymptotic hardening behaviour at large strains does not depend on $\rho_0^s$. Therefore the rate of strain hardening is lower for the largest $\rho_0^s$ values. When the evolution law for the interaction matrix coefficients Eq. (3.7) proposed by Monnet and Mai (2019) is adopted, the density of obstacles $\rho_{obs}$ to dislocation motion increases, thereby the interaction coefficients decrease and as a consequence the rate of strain hardening decreases and a softer asymptotic behaviour is predicted.

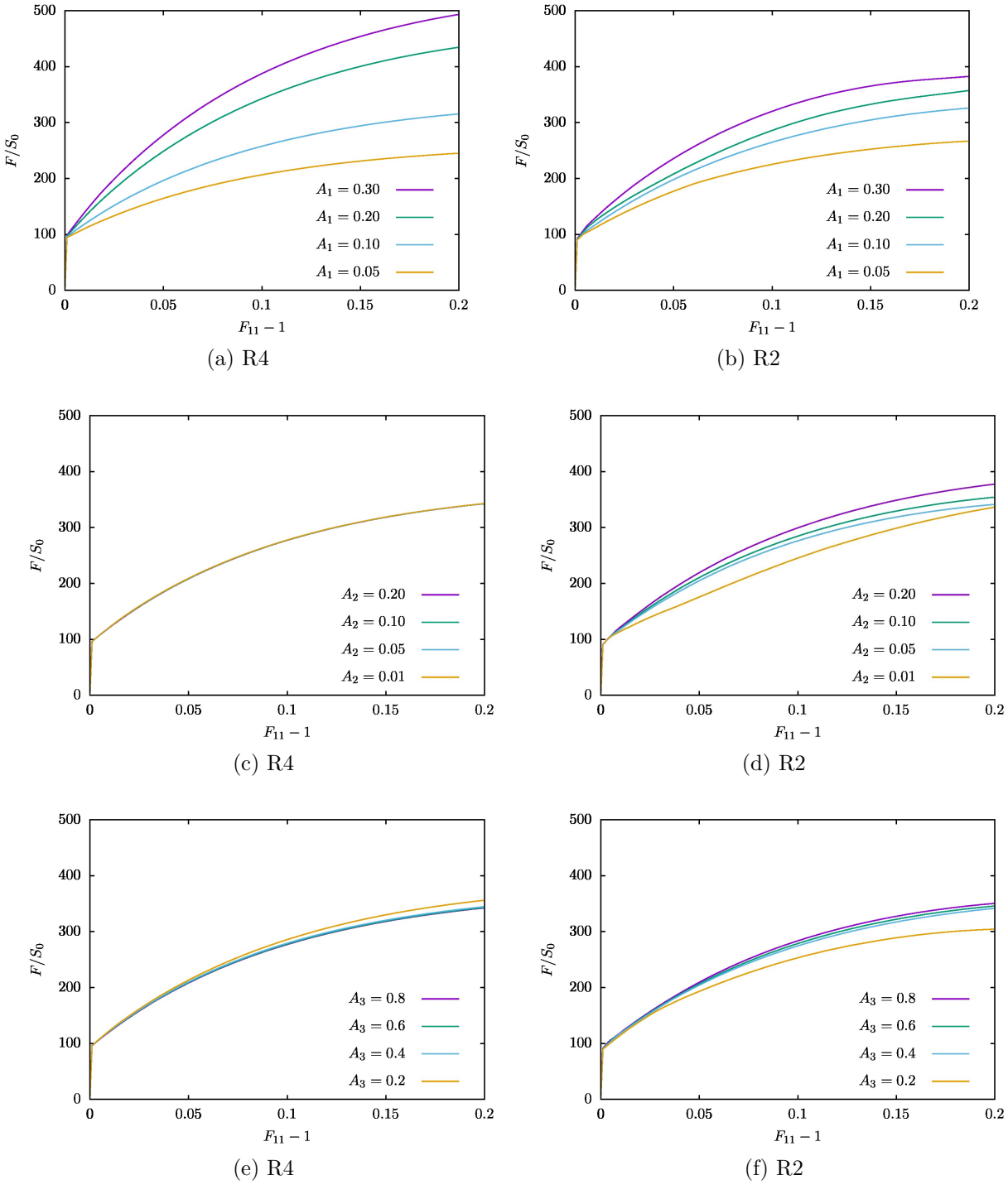


(a) R4 (b) R2

(c) R4 (d) R2

(e) R4 (f) R2

Figure D.1 Sensitivity analysis to the parameters $A_1$, $A_2$ and $A_3$ for orientations R4 in (a,c,e) and R2 in (b,d,f) (The other simulation parameters were assigned the values given in Table 3.3 from Ling (2017))

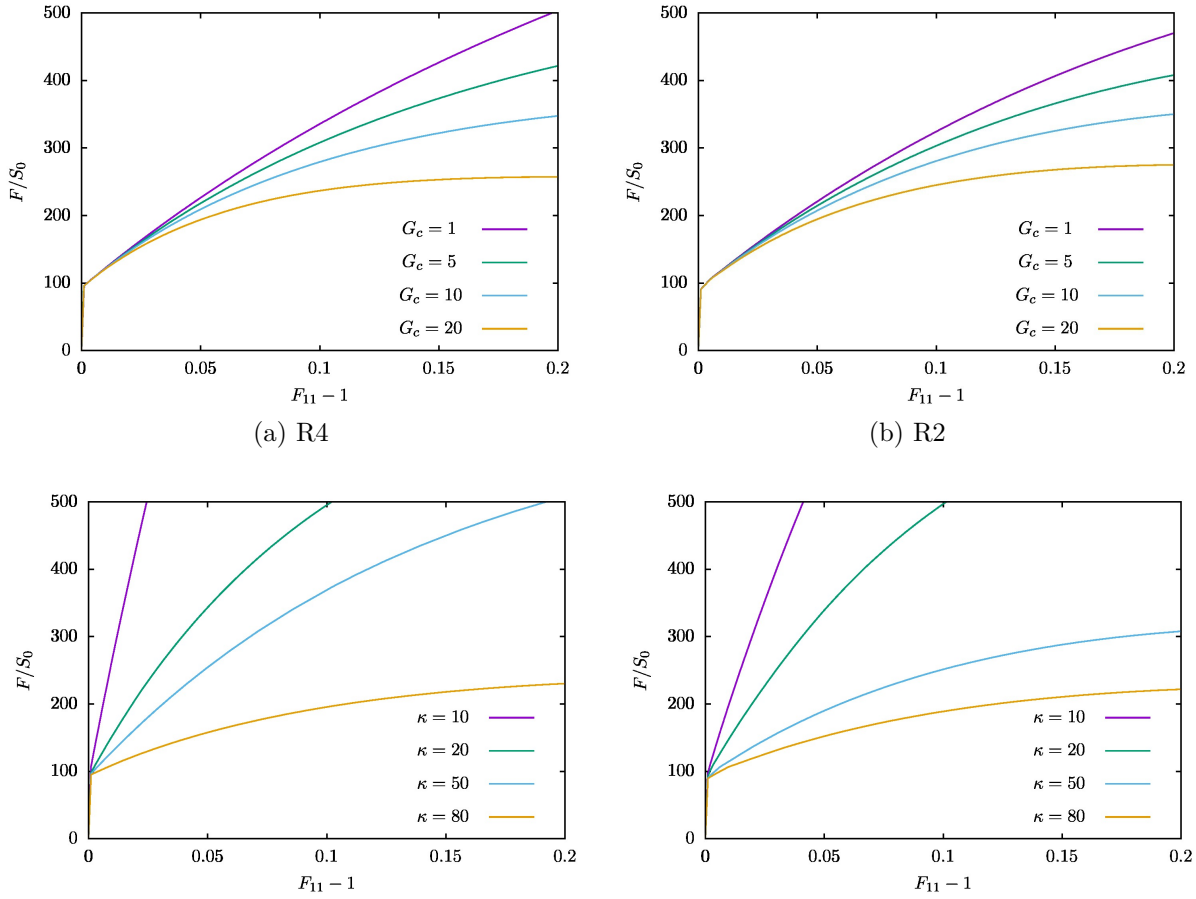


(a) R4 (b) R2

(c) R4 (d) R2

Figure D.2 Sensitivity analysis to the parameters $\kappa$, $G_c$ for orientations R4 in (a,c) and R2 in (b,d) (The other simulation parameters were assigned the values given in Table 3.3 from Ling (2017)).

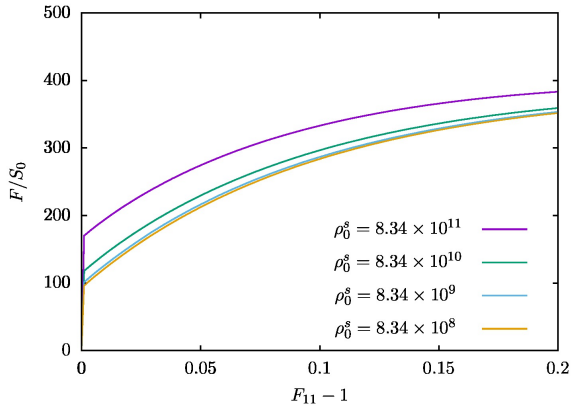


(a) R4

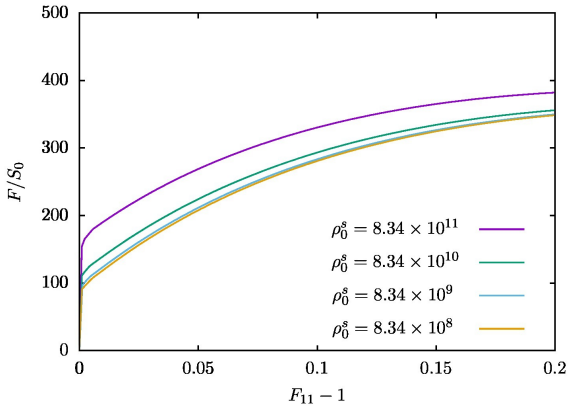


(b) R2

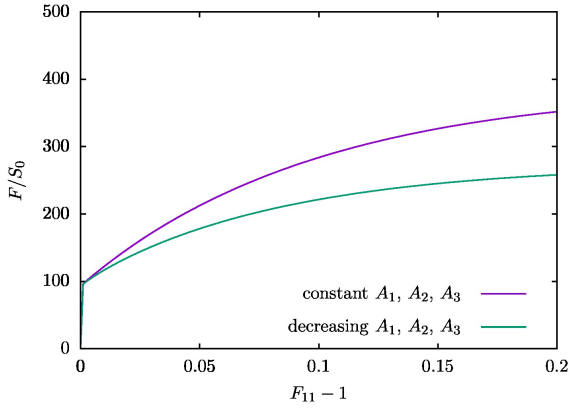


(c) R4

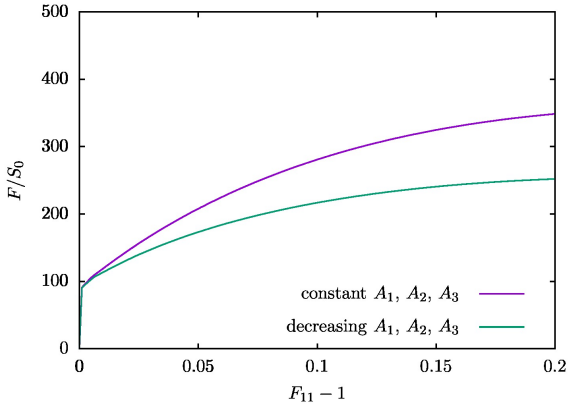


(d) R2

Figure D.3 Sensitivity analysis to the parameter $\rho_0^s$ and evolutions chosen for $A_i$ for orientations R4 in (a,b,c) and R2 in (d,e,f) (The other simulation parameters were assigned the values given in Table 3.3 from Ling (2017))

# E

# Influence of hard inclusions on local strains

In Chapter 3 it was shown that strain fields computed numerically are much more homogeneous than strain fields measured from experiments with DIC analysis. In order to explain this discrepancy, the track of strain heterogeneities caused by hard inclusions is investigated. Such hard inclusions can for example model the influence of ferrite inclusions present in the tensile specimens. Finite element simulations of tensile experiments presented in Chapter 3 are repeated, but with a modification of the local material behaviour in a few areas. 1% of all elements of the finite element mesh are selected randomly and assigned a purely elastic behaviour. The elastic constants are set the same as the rest of specimen, but plastic slip cannot occur in these elements. Figure E.1 shows the equivalent Hencky strain fields obtained numerically and experimentally for crystal orientations corresponding to specimen R4 and R2 at $\Delta L/L_0 = 0.10$. The stress redistribution due to hard elastic inclusions affects greatly the equivalent Hencky strain field. Instead of a smooth deformation profile, strain heterogeneities are nucleated in the vicinity of these inclusions. As the macroscopic deformation increases, heterogeneities become more and more intense. However, areas of intense plastic activity remain located near hard inclusions. This observation can be put in parallel with the intensely deformed bands observed experimentally. It was noted that these bands were indeed more prone to have their intensity increase, instead of having new bands nucleated. A more quantitative analysis could be performed by obtaining a more realistic morphology of a single ferrite inclusion (*e.g.* by EBSD) and measuring the local strain field in the vicinity of it during an SEM *in situ* tensile test. The same ferrite inclusion could then be simulated embedded in an austenite matrix in a finite element simulation in order to validate or disprove the hypothesis that ferrite inclusions are responsible for the apparition on strain heterogeneities in the form of bands. This is out of the scope of the present study.

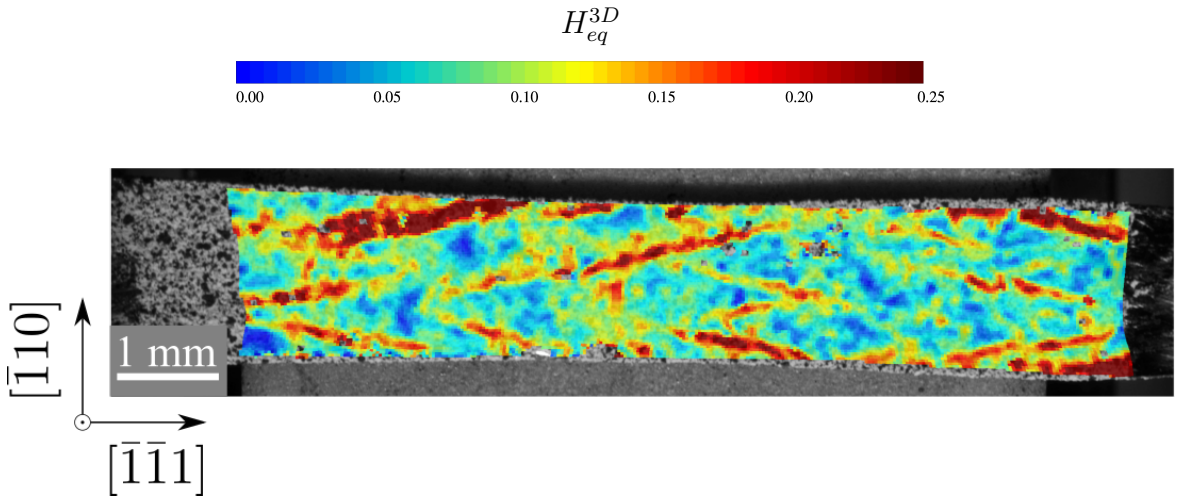


(a) R4 experimental

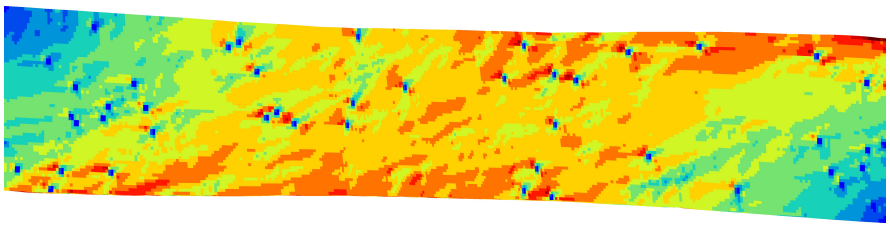

(b) R4 numerical

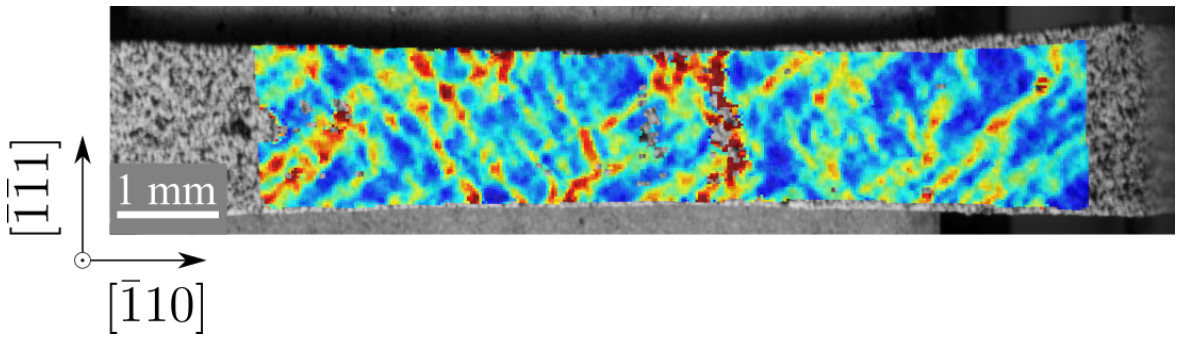


(c) R2 experimental

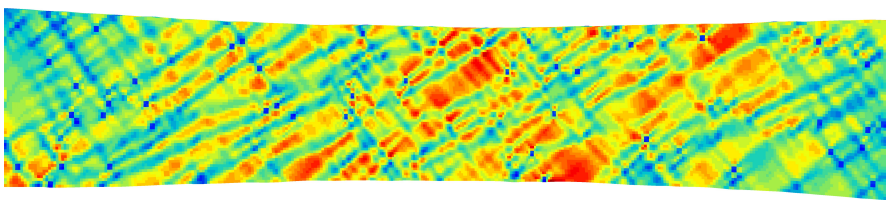

(d) R2 numerical

Figure E.1 DIC measured three-dimensional equivalent Hencky strain fields compared to numerical fields at a macroscopic strain of $\Delta L/L_0 = 0.10$ for specimen R4 in (a) and (b) and specimen R2 in (c) and (d). Elements appearing as blue in numerical strain fields were assigned an elastic behaviour to model hard inclusions.

# F

# Jacobian matrix $\partial\mathcal{R}/\partial v_{\text{int}}$

The Jacobian matrix is needed to integrate the constitutive equations at the Gauss point level. The block form of the Jacobian matrix writes

$$\mathcal{J} = \frac{\partial \mathcal{R}}{\partial \Delta v_{\text{int}}} = \begin{pmatrix} \frac{\partial \mathcal{R}_{\underset{\sim}{\boldsymbol{E}}}}{\partial \Delta \underset{\sim}{\boldsymbol{E}}} & \frac{\partial \mathcal{R}_{\underset{\sim}{\boldsymbol{E}}}}{\partial \Delta \gamma^p} & \frac{\partial \mathcal{R}_{\underset{\sim}{\boldsymbol{E}}}}{\partial \Delta r^q} & \frac{\partial \mathcal{R}_{\underset{\sim}{\boldsymbol{E}}}}{\partial \Delta \gamma_{cum}} \\ \frac{\partial \mathcal{R}_{\gamma^s}}{\partial \Delta \underset{\sim}{\boldsymbol{E}}} & \frac{\partial \mathcal{R}_{\gamma^s}}{\partial \Delta \gamma^p} & \frac{\partial \mathcal{R}_{\gamma^s}}{\partial \Delta r^q} & \frac{\partial \mathcal{R}_{\gamma^s}}{\partial \Delta \gamma_{cum}} \\ \frac{\partial \mathcal{R}_{r^s}}{\partial \Delta \underset{\sim}{\boldsymbol{E}}} & \frac{\partial \mathcal{R}_{r^s}}{\partial \Delta \gamma^p} & \frac{\partial \mathcal{R}_{r^s}}{\partial \Delta r^q} & \frac{\partial \mathcal{R}_{r^s}}{\partial \Delta \gamma_{cum}} \\ \frac{\partial \mathcal{R}_{\gamma_{cum}}}{\partial \Delta \underset{\sim}{\boldsymbol{E}}} & \frac{\partial \mathcal{R}_{\gamma_{cum}}}{\partial \Delta \gamma^p} & \frac{\partial \mathcal{R}_{\gamma_{cum}}}{\partial \Delta r^q} & \frac{\partial \mathcal{R}_{\gamma_{cum}}}{\partial \Delta \gamma_{cum}} \end{pmatrix} \tag{F.1}$$

- Derivatives of $\mathcal{R}_{\underset{\sim}{\boldsymbol{E}}}$

$$\mathcal{R}_{\underset{\sim}{\boldsymbol{E}}} = \Delta \underset{\sim}{\boldsymbol{E}} - \Delta \underset{\sim}{\boldsymbol{F}} . \underset{\sim}{\boldsymbol{F}}^{-1} . \underset{\sim}{\boldsymbol{E}} + \underset{\sim}{\boldsymbol{E}} . \left( \sum_{s=1}^{N} \Delta \gamma^s \underset{\sim}{\boldsymbol{N}}^s \right) \tag{F.2}$$

$$\frac{\partial \mathcal{R}_{\underset{\sim}{\boldsymbol{E}}}}{\partial \Delta \underset{\sim}{\boldsymbol{E}}} = \underset{\approx}{\mathbf{1}} - (\Delta \underset{\sim}{\boldsymbol{F}} . \underset{\sim}{\boldsymbol{F}}^{-1}) \underline{\otimes} \underset{\approx}{\mathbf{1}} + \underset{\approx}{\mathbf{1}} \underline{\otimes} \left( \sum_{s=1}^{N} \Delta \gamma^s \underset{\sim}{\boldsymbol{N}}^s \right)^T \tag{F.3}$$

$$\frac{\partial \mathcal{R}_{\underset{\sim}{\boldsymbol{E}}}}{\partial \Delta \gamma^p} = \underset{\sim}{\boldsymbol{E}} . \underset{\sim}{\boldsymbol{N}}^p \qquad \frac{\partial \mathcal{R}_{\underset{\sim}{\boldsymbol{E}}}}{\partial \Delta r^q} = 0 \qquad \frac{\partial R_{\underset{\sim}{\boldsymbol{E}}}}{\partial \Delta \gamma_{cum}} = 0 \tag{F.4}$$

- Derivatives of $\mathcal{R}_{\gamma^s}$

$$\mathcal{R}_{\gamma^s} \quad = \Delta \gamma^s - \Delta \Gamma \Phi^s \left( |\tau^s| - \left\langle \tau_c^s - \frac{\rho_\sharp}{\rho_0} \left( \Delta_\chi - \mu_\chi \gamma_{cum} \right) \right\rangle \right) \text{sign} \left( \tau^s \right) \tag{F.5}$$

$$\frac{\partial \mathcal{R}_{\gamma^s}}{\partial \Delta \underset{\sim}{\boldsymbol{E}}} = -\Delta\Gamma \frac{\partial \Phi^s}{\partial \tau^s} \frac{\partial \tau^s}{\partial \underset{\sim}{\boldsymbol{\Pi}}^M} : \frac{\partial \underset{\sim}{\boldsymbol{\Pi}}^M}{\partial \underset{\sim}{\boldsymbol{C}}^e} : \frac{\partial \underset{\sim}{\boldsymbol{C}}^e}{\partial \underset{\sim}{\boldsymbol{E}}} : \frac{\partial \underset{\sim}{\boldsymbol{E}}}{\partial \Delta \underset{\sim}{\boldsymbol{E}}} \text{sign}\left(\tau^s\right) \qquad \underset{\sim}{\boldsymbol{C}}^e = \underset{\sim}{\boldsymbol{E}}^T . \underset{\sim}{\boldsymbol{E}} \tag{F.6}$$

with

$$\frac{\partial \Phi^s}{\partial \tau^s} = \frac{\partial \Phi^s}{\partial f^s} \frac{\partial f^s}{\partial \tau^s} = \text{sign}\left(\tau^s\right) \Phi^{s'} \qquad \Phi^{s'} = \begin{cases} \Phi^{s'}_{RD} = \dfrac{n}{\tau_0^n} \left\langle \dfrac{f^s}{\tau_0} \right\rangle^{n-1} \\ \Phi^{s'}_{RI} = 1/R \end{cases} \qquad \frac{\partial \tau^s}{\partial \underset{\sim}{\boldsymbol{\Pi}}^M} = \underset{\sim}{\boldsymbol{N}}^s \tag{F.7}$$

$$\frac{\partial \underset{\sim}{\boldsymbol{\Pi}}^M}{\partial \underset{\sim}{\boldsymbol{C}}^e} = \frac{\partial \left[ \underset{\sim}{\boldsymbol{C}}^e . \left( \underset{\approx}{\boldsymbol{C}} : \frac{1}{2} (\underset{\sim}{\boldsymbol{C}}^e - 1) \right) \right]}{\partial \underset{\sim}{\boldsymbol{C}}^e} = (\underset{\sim}{\boldsymbol{1}} \underline{\otimes} \underset{\sim}{\boldsymbol{\Pi}}^{eT}) + \frac{1}{2} (\underset{\sim}{\boldsymbol{C}}^e \underline{\otimes} \underset{\sim}{\boldsymbol{1}}) : \underset{\approx}{\boldsymbol{C}} \tag{F.8}$$

$$\frac{\partial \underset{\sim}{\boldsymbol{C}}^e}{\partial \underset{\sim}{\boldsymbol{E}}} = \underset{\sim}{\boldsymbol{1}} \overline{\otimes} \underset{\sim}{\boldsymbol{E}}^T + \underset{\sim}{\boldsymbol{E}}^T \underline{\otimes} \underset{\sim}{\boldsymbol{1}} \qquad \frac{\partial \underset{\sim}{\boldsymbol{E}}}{\partial \Delta \underset{\sim}{\boldsymbol{E}}} = \underset{\approx}{\boldsymbol{1}} \tag{F.9}$$

$$\frac{\partial \mathcal{R}_{\gamma^s}}{\partial \Delta \underset{\sim}{\boldsymbol{E}}} = -\Delta\Gamma \Phi^{s'} \underset{\sim}{\boldsymbol{N}}^s : \left[ (\underset{\sim}{\boldsymbol{1}} \underline{\otimes} \underset{\sim}{\boldsymbol{\Pi}}^e) + \frac{1}{2} (\underset{\sim}{\boldsymbol{C}}^e \underline{\otimes} \underset{\sim}{\boldsymbol{1}}) : \underset{\approx}{\boldsymbol{C}} \right] : (\underset{\sim}{\boldsymbol{1}} \overline{\otimes} \underset{\sim}{\boldsymbol{E}}^T + \underset{\sim}{\boldsymbol{E}}^T \underline{\otimes} \underset{\sim}{\boldsymbol{1}}) \tag{F.10}$$

$$\frac{\partial \mathcal{R}_{\gamma^s}}{\partial \Delta \gamma^p} = \delta_{sp} \tag{F.11}$$

$$\frac{\partial \mathcal{R}_{\gamma^s}}{\partial \Delta r^q} = -\Delta\Gamma \frac{\partial \Phi^s}{\partial f^s} \frac{\partial f^s}{\partial \tau_c^s} \frac{\partial \tau_c^s}{\partial \Delta r^q} \text{sign}\left(\tau^s\right) = \text{sign}\left(\tau^s\right) \Delta\Gamma \Phi^{s'} \frac{1}{2} \mu \left( \sum_{u=1}^{N} a^{su} r^u \right)^{-\frac{1}{2}} a^{sq} \tag{F.12}$$

$$\frac{\partial \mathcal{R}_{\gamma^s}}{\partial \Delta \gamma_{cum}} = -\Delta\Gamma \frac{\partial \Phi^s}{\partial f^s} \frac{\partial f^s}{\partial \gamma_{cum}} \text{sign}\left(\tau^s\right) = \Delta\Gamma \Phi^{s'} \mu_\chi \text{sign}\left(\tau^s\right) \tag{F.13}$$

- Derivatives of $\mathcal{R}_{r^s}$

$$\mathcal{R}_{r^s} = \Delta r^s - |\Delta \gamma^s| \left( \frac{\sqrt{\sum_{u=1}^{N} b^{su} r^u}}{\kappa} - G_c r^s \right) \tag{F.14}$$

$$\frac{\partial \mathcal{R}_{r^s}}{\partial \Delta \underset{\sim}{\boldsymbol{E}}} = 0 \qquad \frac{\partial \mathcal{R}_{r^s}}{\partial \Delta \gamma^p} = -\text{sign}\left(\Delta \gamma^s\right) \delta_{sp} \left( \frac{\sqrt{\sum_{u=1}^{N} b^{su} r^u}}{\kappa} - G_c r^s \right) \tag{F.15}$$

$$\frac{\partial \mathcal{R}_{r^s}}{\partial \Delta r^q} = \delta_{sq} - |\Delta \gamma^s| \left( \frac{1}{2} \frac{\left( \sum_{u=1}^{N} b^{su} r^u \right)^{-\frac{1}{2}} b^{sq}}{\kappa} - G_c \delta_{sq} \right) \qquad \frac{\partial \mathcal{R}_{r^s}}{\partial \Delta \gamma_{cum}} = 0 \tag{F.16}$$

- Derivatives of $R_{\gamma_{cum}}$

$$R_{\gamma_{cum}} = \Delta\gamma_{cum} - \sum_{s=1}^{N} |\Delta\gamma^s| \tag{F.17}$$

$$\frac{\partial\mathcal{R}_{\gamma_{cum}}}{\partial\Delta\underset{\sim}{\boldsymbol{E}}} = 0 \qquad \frac{\partial\mathcal{R}_{\gamma_{cum}}}{\partial\Delta\gamma^p} = -\text{sign}\left(\Delta\gamma^p\right) \qquad \frac{\partial\mathcal{R}_{\gamma_{cum}}}{\partial\Delta r^q} = 0 \qquad \frac{\partial\mathcal{R}_{\gamma_{cum}}}{\partial\Delta\gamma_{cum}} = 1 \tag{F.18}$$

# G

# Details on the finite element implementation

In order to facilitate the numerical implementation in a finite element code, equations are now written in vector and matrix form. The rates of nodal degrees of freedom $\dot{\tilde{u}}^a$, $\dot{\tilde{\gamma}}^b_\chi$ and $\dot{\tilde{\lambda}}^b$ are arranged in vector form as

$$\{\dot{\tilde{u}}^a_i\} = \{\dot{\tilde{\mathbf{u}}}^e\} = \begin{Bmatrix} \dot{\tilde{u}}^1_1 \\ \dot{\tilde{u}}^1_2 \\ \dot{\tilde{u}}^1_3 \\ \vdots \\ \dot{\tilde{u}}^p_1 \\ \dot{\tilde{u}}^p_2 \\ \dot{\tilde{u}}^p_3 \end{Bmatrix} \qquad \{\dot{\tilde{\gamma}}^b_\chi\} = \{\dot{\tilde{\boldsymbol{\gamma}}}^e_{\boldsymbol{\chi}}\} = \begin{Bmatrix} \dot{\tilde{\gamma}}^1_\chi \\ \dot{\tilde{\gamma}}^2_\chi \\ \vdots \\ \dot{\tilde{\gamma}}^q_\chi \end{Bmatrix} \qquad \{\dot{\tilde{\lambda}}^b\} = \{\dot{\tilde{\boldsymbol{\lambda}}}^e\} = \begin{Bmatrix} \dot{\tilde{\lambda}}^1 \\ \dot{\tilde{\lambda}}^2 \\ \vdots \\ \dot{\tilde{\lambda}}^q \end{Bmatrix} \tag{G.1}$$

Here, superscripts $a$ and $b$ used for summation over the nodes of one element are dropped and a superscript $e$ is added, in order to indicate that the vector is for one individual element and to distinguish it from vectors for the entire finite element mesh. Recall that $p$ is the number of nodes possessing displacement degrees of freedom and $q$ is that for $\Delta_\chi$ and microslip $\gamma_\chi$. Voigt's notation is used for writing tensors in the form of vectors and matrices. Especially, the second-order non-symmetric tensor $\underset{\sim}{\boldsymbol{F}}$ is arranged in the form:

$$\{\underset{\sim}{\boldsymbol{F}}\} = \begin{Bmatrix} F_{11} \\ F_{22} \\ F_{33} \\ F_{12} \\ F_{23} \\ F_{31} \\ F_{21} \\ F_{32} \\ F_{13} \end{Bmatrix} \tag{G.2}$$

Thus, shape functions ${}^{u}N_i^a$ and ${}^{\chi}N^b$ can be written as

$$[{}^{\mathbf{u}}\mathbf{N}] = \begin{bmatrix} {}^{u}N^1 & 0 & 0 & \cdots & {}^{u}N^p & 0 & 0 \\ 0 & {}^{u}N^1 & 0 & \cdots & 0 & {}^{u}N^p & 0 \\ 0 & 0 & {}^{u}N^1 & \cdots & 0 & 0 & {}^{u}N^p \end{bmatrix} \tag{G.3}$$

and

$$[{}^{\chi}\mathbf{N}] = \begin{bmatrix} {}^{\chi}N^1 & {}^{\chi}N^2 & {}^{\chi}N^3 & \cdots & {}^{\chi}N^q. \end{bmatrix} \tag{G.4}$$

Accordingly, ${}^{u}B_{ij}^a$ and ${}^{\chi}B_i^a$ can also be written in matrix form denoted by $[{}^{\mathbf{u}}\mathbf{B}]$ and $[{}^{\chi}\mathbf{B}]$:

$$[{}^{\mathbf{u}}\mathbf{B}] = \begin{bmatrix} \frac{\partial {}^{u}N^1}{\partial X_1} & 0 & 0 & \cdots & \frac{\partial {}^{u}N^p}{\partial X_1} & 0 & 0 \\ 0 & \frac{\partial {}^{u}N^1}{\partial X_2} & 0 & \cdots & 0 & \frac{\partial {}^{u}N^p}{\partial X_2} & 0 \\ 0 & 0 & \frac{\partial {}^{u}N^1}{\partial X_3} & \cdots & 0 & 0 & \frac{\partial {}^{u}N^p}{\partial X_3} \\ \frac{\partial {}^{u}N^1}{\partial X_2} & 0 & 0 & \cdots & \frac{\partial {}^{u}N^p}{\partial X_2} & 0 & 0 \\ 0 & \frac{\partial {}^{u}N^1}{\partial X_3} & 0 & \cdots & 0 & \frac{\partial {}^{u}N^p}{\partial X_3} & 0 \\ 0 & 0 & \frac{\partial {}^{u}N^1}{\partial X_1} & \cdots & 0 & 0 & \frac{\partial {}^{u}N^p}{\partial X_1} \\ 0 & \frac{\partial {}^{u}N^1}{\partial X_1} & 0 & \cdots & 0 & \frac{\partial {}^{u}N^p}{\partial X_1} & 0 \\ 0 & 0 & \frac{\partial {}^{u}N^1}{\partial X_2} & \cdots & 0 & 0 & \frac{\partial {}^{u}N^p}{\partial X_2} \\ \frac{\partial {}^{u}N^1}{\partial X_3} & 0 & 0 & \cdots & \frac{\partial {}^{u}N^p}{\partial X_3} & 0 & 0 \end{bmatrix} \tag{G.5}$$

and

$$[{}^{\chi}\mathbf{B}] = \begin{bmatrix} \frac{\partial {}^{\chi}N^1}{\partial X_1} & \frac{\partial {}^{\chi}N^2}{\partial X_1} & \frac{\partial {}^{\chi}N^3}{\partial X_1} & \cdots & \frac{\partial {}^{\chi}N^q}{\partial X_1} \\ \frac{\partial {}^{\chi}N^1}{\partial X_2} & \frac{\partial {}^{\chi}N^2}{\partial X_2} & \frac{\partial {}^{\chi}N^3}{\partial X_2} & \cdots & \frac{\partial {}^{\chi}N^q}{\partial X_2} \\ \frac{\partial {}^{\chi}N^1}{\partial X_3} & \frac{\partial {}^{\chi}N^2}{\partial X_3} & \frac{\partial {}^{\chi}N^3}{\partial X_3} & \cdots & \frac{\partial {}^{\chi}N^q}{\partial X_3} \end{bmatrix} \tag{G.6}$$

The interpolation of increment of the displacements $\dot{u}_i$, microslip $\dot{\gamma}_\chi$ and Lagrange multiplier $\dot{\lambda}$ in one element thus write

$$\{\underline{\dot{\boldsymbol{u}}}\} = [{}^{\mathbf{u}}\mathbf{N}].\{\dot{\tilde{\mathbf{u}}}^e\} \quad \{\dot{\boldsymbol{\gamma}}_{\boldsymbol{\chi}}\} = [{}^{\chi}\mathbf{N}].\{\dot{\tilde{\boldsymbol{\gamma}}}_{\boldsymbol{\chi}}^e\} \tag{G.7}$$

$$\{\dot{\boldsymbol{\lambda}}\} = [{}^{\chi}\mathbf{N}].\{\dot{\tilde{\boldsymbol{\lambda}}}^e\} \quad \text{thus} \quad \{\dot{\boldsymbol{\Delta}}_{\boldsymbol{\chi}}\} = [{}^{\chi}\mathbf{N}].\left[\{\dot{\tilde{\boldsymbol{\lambda}}}^e\} + \mu_\chi\{\dot{\tilde{\boldsymbol{\gamma}}}_{\boldsymbol{\chi}}^e\}\right] \tag{G.8}$$

and therefore it follows

$$\{\underset{\sim}{\dot{\boldsymbol{F}}}\} = [{}^{\mathbf{u}}\mathbf{B}].\{\dot{\tilde{\mathbf{u}}}^e\} \qquad \{\underline{\dot{\boldsymbol{K}}}_{\boldsymbol{\chi}}\} = [{}^{\chi}\mathbf{B}].\{\dot{\tilde{\boldsymbol{\gamma}}}_{\boldsymbol{\chi}}^e\}. \tag{G.9}$$

With stress and strain variables expressed with Voigt's notation, Eqs. (5.62), (5.63), (5.64) and (5.65) follow

$$\{\mathbf{R}^e_{\text{int(u)}}\} = \int_{D^e_0} [{}^{\mathbf{u}}\mathbf{B}]^T.\{\underset{\sim}{\boldsymbol{S}}\}\mathrm{d}V^e_0 \tag{G.10}$$

$$\{\mathbf{R}^e_{\text{int}(\gamma_\chi)}\} = \int_{D^e_0} A[{}^{\chi}\mathbf{B}]^T.[{}^{\chi}\mathbf{B}].\{\boldsymbol{\gamma}_{\boldsymbol{\chi}}\} + [{}^{\chi}\mathbf{N}]^T.\left(\{\boldsymbol{\Delta}_{\boldsymbol{\chi}}\} - \mu_\chi\{\boldsymbol{\gamma}_{\boldsymbol{M}}\}\right)\mathrm{d}V^e_0 \tag{G.11}$$

$$\{\mathbf{R}^e_{\text{int}(\lambda)}\} = \int_{D^e_0} [{}^{\chi}\mathbf{N}]^T.\left(\{\boldsymbol{\gamma}_{\boldsymbol{\chi}}\} - \{\boldsymbol{\gamma}_{\boldsymbol{M}}\}\right)\mathrm{d}V^e_0 \tag{G.12}$$

$$\{\mathbf{R}^e_{\text{ext(u)}}\} = \int_{\partial D^e_0} [{}^{\mathbf{u}}\mathbf{N}]^T.\{\underline{\boldsymbol{T}}\}\mathrm{d}S^e_0 \tag{G.13}$$

$$\{\mathbf{R}^e_{\text{ext}(\gamma_\chi)}\} = \int_{\partial D^e_0} [{}^{\chi}\mathbf{N}]^T.\{\mathbf{M}\}\mathrm{d}S^e_0 \tag{G.14}$$

$$\{\mathbf{R}^e_{\text{ext}(\lambda)}\} = \{\mathbf{0}\} \tag{G.15}$$

where $[{}^{\mathbf{u}}\mathbf{B}]^T$ is the transpose of the matrix $[{}^{\mathbf{u}}\mathbf{B}]$ and the same notation is used for other matrices. In practice the integrals are approximated in each element by a Gaussian quadrature rule. The global finite element set of equations is obtained by applying an assembly operator $\mathcal{A}$ on internal reactions and external reactions:

$$\{\mathbf{R}_{\text{int(u)}}\} = \mathcal{A}(\{\mathbf{R}^e_{\text{int(u)}}\}) \quad \{\mathbf{R}_{\text{int}(\gamma_\chi)}\} = \mathcal{A}(\{\mathbf{R}^e_{\text{int}(\gamma_\chi)}\}) \quad \{\mathbf{R}_{\text{int}(\lambda)}\} = \mathcal{A}(\{\mathbf{R}^e_{\text{int}(\lambda)}\}) \tag{G.16}$$

$$\{\mathbf{R}_{\text{ext(u)}}\} = \mathcal{A}(\{\mathbf{R}^e_{\text{ext(u)}}\}) \quad \{\mathbf{R}_{\text{ext}(\gamma_\chi)}\} = \mathcal{A}(\{\mathbf{R}^e_{\text{ext}(\gamma_\chi)}\}) \quad \{\mathbf{R}_{\text{ext}(\lambda)}\} = \mathcal{A}(\{\mathbf{R}^e_{\text{ext}(\lambda)}\}) \tag{G.17}$$

The reader is referred to (Besson et al., 2009) for the description of the assembly procedure. Thus, the global finite element set of equations Eqs. (5.66), (5.67) and (5.68) to be solved can be written as

$$\begin{Bmatrix} \{\mathbf{R}_{\text{int(u)}}\} \\ \{\mathbf{R}_{\text{int}(\gamma_\chi)}\} \\ \{\mathbf{R}_{\text{int}(\lambda)}\} \end{Bmatrix} . \begin{Bmatrix} \{\dot{\tilde{\mathbf{u}}}\} \\ \{\dot{\tilde{\boldsymbol{\gamma}}}_{\boldsymbol{\chi}}\} \\ \{\dot{\tilde{\boldsymbol{\lambda}}}\} \end{Bmatrix} = \begin{Bmatrix} \{\mathbf{R}_{\text{ext(u)}}\} \\ \{\mathbf{R}_{\text{ext}(\gamma_\chi)}\} \\ \{\mathbf{R}_{\text{ext}(\lambda)}\} \end{Bmatrix} . \begin{Bmatrix} \{\dot{\tilde{\mathbf{u}}}\} \\ \{\dot{\tilde{\boldsymbol{\gamma}}}_{\boldsymbol{\chi}}\} \\ \{\dot{\tilde{\boldsymbol{\lambda}}}\} \end{Bmatrix} \tag{G.18}$$

Since the system is nonlinear, it can be solved by Newton's method which requires the calculation of the Jacobian matrix with respect to the internal reactions (Besson et al., 2009). The Jacobian matrix of an individual element, split into nine blocks, writes

$$\begin{bmatrix} [\mathbf{K}^e_{\text{(uu)}}] & [\mathbf{K}^e_{\text{(ug)}}] & [\mathbf{K}^e_{\text{(ul)}}] \\ [\mathbf{K}^e_{\text{(gu)}}] & [\mathbf{K}^e_{\text{(gg)}}] & [\mathbf{K}^e_{\text{(gl)}}] \\ [\mathbf{K}^e_{\text{(lu)}}] & [\mathbf{K}^e_{\text{(lg)}}] & [\mathbf{K}^e_{\text{(ll)}}] \end{bmatrix} = \begin{bmatrix} \left[\dfrac{\partial\{\mathbf{R}^e_{\text{int(u)}}\}}{\partial\{\tilde{\mathbf{u}}^e\}}\right] & \left[\dfrac{\partial\{\mathbf{R}^e_{\text{int(u)}}\}}{\partial\{\tilde{\boldsymbol{\gamma}}^e_{\boldsymbol{\chi}}\}}\right] & \left[\dfrac{\partial\{\mathbf{R}^e_{\text{int(u)}}\}}{\partial\{\tilde{\boldsymbol{\lambda}}^e\}}\right] \\ \left[\dfrac{\partial\{\mathbf{R}^e_{\text{int}(\gamma_\chi)}\}}{\partial\{\tilde{\mathbf{u}}^e\}}\right] & \left[\dfrac{\partial\{\mathbf{R}^e_{\text{int}(\gamma_\chi)}\}}{\partial\{\tilde{\boldsymbol{\gamma}}^e_{\boldsymbol{\chi}}\}}\right] & \left[\dfrac{\partial\{\mathbf{R}^e_{\text{int}(\gamma_\chi)}\}}{\partial\{\tilde{\boldsymbol{\lambda}}^e\}}\right] \\ \left[\dfrac{\partial\{\mathbf{R}^e_{\text{int}(\lambda)}\}}{\partial\{\tilde{\mathbf{u}}^e\}}\right] & \left[\dfrac{\partial\{\mathbf{R}^e_{\text{int}(\lambda)}\}}{\partial\{\tilde{\boldsymbol{\gamma}}^e_{\boldsymbol{\chi}}\}}\right] & \left[\dfrac{\partial\{\mathbf{R}^e_{\text{int}(\lambda)}\}}{\partial\{\tilde{\boldsymbol{\lambda}}^e\}}\right] \end{bmatrix} \tag{G.19}$$

Using the assembly operation $\mathcal{A}$, one can calculate the global Jacobian matrix $[\mathbf{K}]$

$$[\mathbf{K}] = \mathcal{A}\begin{bmatrix} [\mathbf{K}^e_{\text{(uu)}}] & [\mathbf{K}^e_{\text{(ug)}}] & [\mathbf{K}^e_{\text{(ul)}}] \\ [\mathbf{K}^e_{\text{(gu)}}] & [\mathbf{K}^e_{\text{(gg)}}] & [\mathbf{K}^e_{\text{(gl)}}] \\ [\mathbf{K}^e_{\text{(lu)}}] & [\mathbf{K}^e_{\text{(lg)}}] & [\mathbf{K}^e_{\text{(ll)}}] \end{bmatrix} \tag{G.20}$$

One calculates the blocks for an individual element and obtains the so-called element stiffness matrix:

$$[\mathbf{K}^e_{(\mathrm{uu})}] = \frac{\partial\{\mathbf{R}^e_{\mathrm{int(u)}}\}}{\partial\{\widetilde{\mathbf{u}}^e\}} = \int_{D^e_0} [{}^{\mathrm{u}}\mathbf{B}]^T . \frac{\partial\{\underset{\sim}{\boldsymbol{S}}\}}{\partial\{\underset{\sim}{\boldsymbol{F}}\}} . \frac{\partial\{\underset{\sim}{\boldsymbol{F}}\}}{\partial\{\widetilde{\mathbf{u}}^e\}} \,\mathrm{d}V^e_0$$

$$= \int_{D^e_0} [{}^{\mathrm{u}}\mathbf{B}]^T . \frac{\partial\{\underset{\sim}{\boldsymbol{S}}\}}{\partial\{\underset{\sim}{\boldsymbol{F}}\}} . [{}^{\mathrm{u}}\mathbf{B}] \,\mathrm{d}V^e_0 \tag{G.21}$$

$$[\mathbf{K}^e_{(\mathrm{ug})}] = \frac{\partial\{\mathbf{R}^e_{\mathrm{int(u)}}\}}{\partial\{\widetilde{\boldsymbol{\gamma}}^e_{\boldsymbol{\chi}}\}} = \int_{D^e_0} \left( [{}^{\mathrm{u}}\mathbf{B}]^T . \frac{\partial\{\underset{\sim}{\boldsymbol{S}}\}}{\partial\{\boldsymbol{\gamma}_{\boldsymbol{\chi}}\}} . \frac{\partial\{\boldsymbol{\gamma}_{\boldsymbol{\chi}}\}}{\partial\{\widetilde{\boldsymbol{\gamma}}^e_{\boldsymbol{\chi}}\}} + [{}^{\mathrm{u}}\mathbf{B}]^T . \frac{\partial\{\underset{\sim}{\boldsymbol{S}}\}}{\partial\{\boldsymbol{\Delta}_{\boldsymbol{\chi}}\}} . \frac{\partial\{\boldsymbol{\Delta}_{\boldsymbol{\chi}}\}}{\partial\{\widetilde{\boldsymbol{\gamma}}_{\boldsymbol{\chi}}\}} . \frac{\partial\{\widetilde{\boldsymbol{\gamma}}_{\boldsymbol{\chi}}\}}{\partial\{\widetilde{\boldsymbol{\gamma}}^e_{\boldsymbol{\chi}}\}} \right) \mathrm{d}V^e_0$$

$$= \int_{D^e_0} \left( [{}^{\mathrm{u}}\mathbf{B}]^T . \frac{\partial\{\underset{\sim}{\boldsymbol{S}}\}}{\partial\{\boldsymbol{\gamma}_{\boldsymbol{\chi}}\}} . [{}^{\chi}\mathbf{N}] + \mu_\chi [{}^{\mathrm{u}}\mathbf{B}]^T . \frac{\partial\{\underset{\sim}{\boldsymbol{S}}\}}{\partial\{\boldsymbol{\lambda}\}} . [{}^{\chi}\mathbf{N}] \right) \mathrm{d}V^e_0 \tag{G.22}$$

$$[\mathbf{K}^e_{(\mathrm{ul})}] = \frac{\partial\{\mathbf{R}^e_{\mathrm{int(u)}}\}}{\partial\{\widetilde{\boldsymbol{\lambda}}^e\}} = \int_{D^e_0} \left( [{}^{\mathrm{u}}\mathbf{B}]^T . \frac{\partial\{\underset{\sim}{\boldsymbol{S}}\}}{\partial\{\boldsymbol{\Delta}_{\boldsymbol{\chi}}\}} . \frac{\partial\{\boldsymbol{\Delta}_{\boldsymbol{\chi}}\}}{\partial\{\boldsymbol{\lambda}\}} . \frac{\partial\{\boldsymbol{\lambda}\}}{\partial\{\widetilde{\boldsymbol{\lambda}}^e\}} \right) \mathrm{d}V^e_0$$

$$= \int_{D^e_0} \left( [{}^{\mathrm{u}}\mathbf{B}]^T . \frac{\partial\{\underset{\sim}{\boldsymbol{S}}\}}{\partial\{\boldsymbol{\Delta}_{\boldsymbol{\chi}}\}} . [{}^{\chi}\mathbf{N}] \right) \mathrm{d}V^e_0 \tag{G.23}$$

$$[\mathbf{K}^e_{(\mathrm{gu})}] = \frac{\partial\{\mathbf{R}^e_{\mathrm{int}(\gamma_\chi)}\}}{\partial\{\widetilde{\mathbf{u}}^e\}} = \int_{D^e_0} \left( -\mu_\chi [{}^{\chi}\mathbf{N}]^T . \frac{\partial\{\gamma_M\}}{\partial\{\underset{\sim}{\boldsymbol{F}}\}} . \frac{\partial\{\underset{\sim}{\boldsymbol{F}}\}}{\partial\{\widetilde{\mathbf{u}}^e\}} \right) \mathrm{d}V^e_0$$

$$= \int_{D^e_0} \left( -\mu_\chi [{}^{\chi}\mathbf{N}]^T . \frac{\partial\{\gamma_M\}}{\partial\{\underset{\sim}{\boldsymbol{F}}\}} . [{}^{\mathrm{u}}\mathbf{B}] \right) \mathrm{d}V^e_0 \tag{G.24}$$

$$[\mathbf{K}^e_{(\mathrm{gg})}] = \frac{\partial\{\mathbf{R}^e_{\mathrm{int}(\gamma_\chi)}\}}{\partial\{\widetilde{\boldsymbol{\gamma}}^e_{\boldsymbol{\chi}}\}} = \int_{D^e_0} \left( A [{}^{\chi}\mathbf{B}]^T . [{}^{\chi}\mathbf{B}] . \frac{\partial\{\boldsymbol{\gamma}_{\boldsymbol{\chi}}\}}{\partial\{\widetilde{\boldsymbol{\gamma}}^e_{\boldsymbol{\chi}}\}} + \mu_\chi [{}^{\chi}\mathbf{N}]^T . \frac{\partial\{\boldsymbol{\gamma}_{\boldsymbol{\chi}}\}}{\partial\{\widetilde{\boldsymbol{\gamma}}^e_{\boldsymbol{\chi}}\}} \right.$$

$$\left. -\mu_\chi [{}^{\chi}\mathbf{N}]^T . \frac{\partial\{\gamma_M\}}{\partial\{\boldsymbol{\Delta}_{\boldsymbol{\chi}}\}} . \frac{\partial\{\boldsymbol{\Delta}_{\boldsymbol{\chi}}\}}{\partial\{\widetilde{\boldsymbol{\gamma}}_{\boldsymbol{\chi}}\}} . \frac{\partial\{\widetilde{\boldsymbol{\gamma}}_{\boldsymbol{\chi}}\}}{\partial\{\widetilde{\boldsymbol{\gamma}}^e_{\boldsymbol{\chi}}\}} \right) \mathrm{d}V^e_0$$

$$= \int_{D^e_0} \left( A [{}^{\chi}\mathbf{B}]^T . [{}^{\chi}\mathbf{B}] . [{}^{\chi}\mathbf{N}] + \mu_\chi [{}^{\chi}\mathbf{N}]^T . [{}^{\chi}\mathbf{N}] - \mu^2_\chi [{}^{\chi}\mathbf{N}]^T . \frac{\partial\{\gamma_M\}}{\partial\{\boldsymbol{\Delta}_{\boldsymbol{\chi}}\}} . [{}^{\chi}\mathbf{N}] \right) \mathrm{d}V^e_0 \tag{G.25}$$

$$[\mathbf{K}^e_{(\mathrm{gl})}] = \frac{\partial\{\mathbf{R}^e_{\mathrm{int}(\gamma_\chi)}\}}{\partial\{\widetilde{\boldsymbol{\lambda}}^e\}} = \int_{D^e_0} \left( [{}^{\chi}\mathbf{N}]^T . \frac{\partial\{\boldsymbol{\lambda}\}}{\partial\{\widetilde{\boldsymbol{\lambda}}^e\}} - \mu_\chi [{}^{\chi}\mathbf{N}]^T . \frac{\partial\{\gamma_M\}}{\partial\{\boldsymbol{\Delta}_{\boldsymbol{\chi}}\}} . \frac{\partial\{\boldsymbol{\Delta}_{\boldsymbol{\chi}}\}}{\partial\{\boldsymbol{\lambda}\}} \frac{\partial\{\boldsymbol{\lambda}\}}{\partial\{\widetilde{\boldsymbol{\lambda}}^e\}} \right) \mathrm{d}V^e_0$$

$$= \int_{D^e_0} \left( [{}^{\chi}\mathbf{N}]^T . [{}^{\chi}\mathbf{N}] - \mu_\chi [{}^{\chi}\mathbf{N}]^T . \frac{\partial\{\gamma_M\}}{\partial\{\boldsymbol{\Delta}_{\boldsymbol{\chi}}\}} . [{}^{\chi}\mathbf{N}] \right) \mathrm{d}V^e_0 \tag{G.26}$$

$$[\mathbf{K}^e_{(\mathrm{lu})}] = \frac{\partial\{\mathbf{R}^e_{\mathrm{int}(\lambda)}\}}{\partial\{\widetilde{\mathbf{u}}^e\}} = \int_{D^e_0} \left( -[{}^{\chi}\mathbf{N}]^T . \frac{\partial\{\gamma_M\}}{\partial\{\underset{\sim}{\boldsymbol{F}}\}} . \frac{\partial\{\underset{\sim}{\boldsymbol{F}}\}}{\partial\{\widetilde{\mathbf{u}}^e\}} \right) \mathrm{d}V^e_0$$

$$= \int_{D^e_0} \left( -[{}^{\chi}\mathbf{N}]^T . \frac{\partial\{\gamma_M\}}{\partial\{\underset{\sim}{\boldsymbol{F}}\}} . [{}^{\mathrm{u}}\mathbf{B}] \right) \mathrm{d}V^e_0 \tag{G.27}$$

$$[\mathbf{K}^e_{(\mathrm{lg})}] = \frac{\partial\{\mathbf{R}^e_{\mathrm{int}(\lambda)}\}}{\partial\{\widetilde{\boldsymbol{\gamma}}^e_{\boldsymbol{\chi}}\}} = \int_{D^e_0} \left( [{}^{\chi}\mathbf{N}]^T . \frac{\partial\{\boldsymbol{\gamma}_{\boldsymbol{\chi}}\}}{\partial\{\widetilde{\boldsymbol{\gamma}}^e_{\boldsymbol{\chi}}\}} - [{}^{\chi}\mathbf{N}]^T . \frac{\partial\{\gamma_M\}}{\partial\{\boldsymbol{\Delta}_{\boldsymbol{\chi}}\}} . \frac{\partial\{\boldsymbol{\Delta}_{\boldsymbol{\chi}}\}}{\partial\{\boldsymbol{\gamma}_{\boldsymbol{\chi}}\}} . \frac{\partial\{\boldsymbol{\gamma}_{\boldsymbol{\chi}}\}}{\partial\{\widetilde{\boldsymbol{\gamma}}^e_{\boldsymbol{\chi}}\}} \right) \mathrm{d}V^e_0$$

$$= \int_{D^e_0} \left( [{}^{\chi}\mathbf{N}]^T . [{}^{\chi}\mathbf{N}] - \mu_\chi [{}^{\chi}\mathbf{N}]^T . \frac{\partial\{\gamma_M\}}{\partial\{\boldsymbol{\Delta}_{\boldsymbol{\chi}}\}} . [{}^{\chi}\mathbf{N}] \right) \mathrm{d}V^e_0 \tag{G.28}$$

$$[\mathbf{K}^e_{(\mathrm{ll})}] = \frac{\partial\{\mathbf{R}^e_{\mathrm{int}(\lambda)}\}}{\partial\{\widetilde{\boldsymbol{\lambda}}^e\}} = \int_{D^e_0} \left( -[{}^{\chi}\mathbf{N}]^T . \frac{\partial\{\gamma_M\}}{\partial\{\boldsymbol{\Delta}_{\boldsymbol{\chi}}\}} . \frac{\partial\{\boldsymbol{\Delta}_{\boldsymbol{\chi}}\}}{\partial\{\boldsymbol{\lambda}\}} . \frac{\partial\{\boldsymbol{\lambda}\}}{\partial\{\widetilde{\boldsymbol{\lambda}}^e\}} \right) \mathrm{d}V^e_0$$

$$= \int_{D^e_0} \left( -[{}^{\chi}\mathbf{N}]^T . \frac{\partial\{\gamma_M\}}{\partial\{\boldsymbol{\Delta}_{\boldsymbol{\chi}}\}} . [{}^{\chi}\mathbf{N}] \right) \mathrm{d}V^e_0 \tag{G.29}$$

In the element stiffness matrix, one can find four derivatives which will be evaluated by consistent tangent matrix $\{\mathbf{J}^*\}$ in the next section. The consistent tangent matrix $\{\mathbf{J}^*\}$ is defined as:

$$\mathbf{J}^* = \frac{\delta \Delta v_{\mathrm{OUT}}}{\delta \Delta v_{\mathrm{IN}}} \tag{G.30}$$

# H

# Details on the consistent tangent matrix

It is shown in (Ling et al., 2018) that the consistent tangent matrix is

$$\mathbf{J}^* = \left\{ \frac{\partial \Delta v_{\text{OUT}}}{\partial \Delta v_{\text{INT}}} \left[ - \left( \frac{\partial \mathcal{R}}{\partial \Delta v_{\text{INT}}} \right)^{-1} \frac{\partial \mathcal{R}}{\partial \Delta v_{\text{IN}}} \right] + \frac{\partial \Delta v_{\text{OUT}}}{\partial \Delta v_{\text{IN}}} \right\} \tag{H.1}$$

which involves the inverse of the (local) Jacobian matrix $\mathcal{J} = \partial \mathcal{R} / \partial v_{\text{INT}}$.

- $\frac{\partial \Delta v_{\text{OUT}}}{\partial \Delta v_{\text{INT}}}$

$$\frac{\partial \Delta \underset{\sim}{\boldsymbol{S}}}{\partial \Delta \underset{\sim}{\boldsymbol{E}}} = \frac{\partial \underset{\sim}{\boldsymbol{S}}}{\partial \underset{\sim}{\boldsymbol{E}}} = \frac{\partial \underset{\sim}{\boldsymbol{S}}}{\partial \underset{\sim}{\boldsymbol{\sigma}}} : \frac{\partial \underset{\sim}{\boldsymbol{\sigma}}}{\partial \underset{\sim}{\boldsymbol{E}}} \tag{H.2}$$

$$\frac{\partial \underset{\sim}{\boldsymbol{S}}}{\partial \underset{\sim}{\boldsymbol{\sigma}}} = J \underset{\sim}{\mathbf{1}} \underline{\otimes} \underset{\sim}{\boldsymbol{F}}^{-1} \tag{H.3}$$

$$\begin{aligned} \frac{\partial \underset{\sim}{\boldsymbol{\sigma}}}{\partial \underset{\sim}{\boldsymbol{E}}} &= -\frac{1}{J_e} (\underset{\sim}{\boldsymbol{E}} . \underset{\sim}{\boldsymbol{\Pi}}^e . \underset{\sim}{\boldsymbol{E}}^T) \otimes \underset{\sim}{\boldsymbol{E}}^{-T} + \frac{1}{J_e} \underset{\sim}{\mathbf{1}} \underline{\otimes} (\underset{\sim}{\boldsymbol{\Pi}}^e . \underset{\sim}{\boldsymbol{E}}^T)^T \\ &\quad + \frac{1}{J_e} (\underset{\sim}{\boldsymbol{E}} \underline{\otimes} \underset{\sim}{\boldsymbol{E}}) : \frac{\partial \underset{\sim}{\boldsymbol{\Pi}}^e}{\partial \underset{\sim}{\boldsymbol{E}}} + \frac{1}{J_e} \left[ (\underset{\sim}{\boldsymbol{E}} . \underset{\sim}{\boldsymbol{\Pi}}^e) \underline{\otimes} \underset{\sim}{\mathbf{1}} \right] : (\underset{\sim}{\mathbf{1}} \overline{\otimes} \underset{\sim}{\mathbf{1}}) \end{aligned} \tag{H.4}$$

$$\frac{\partial \underset{\sim}{\boldsymbol{\Pi}}^e}{\partial \underset{\sim}{\boldsymbol{E}}} = \frac{\partial \underset{\sim}{\boldsymbol{\Pi}}^e}{\partial \underset{\sim}{\boldsymbol{E}}^e_{GL}} : \frac{\partial \underset{\sim}{\boldsymbol{E}}^e_{GL}}{\partial \underset{\sim}{\boldsymbol{E}}} \tag{H.5}$$

$$\frac{\partial \underset{\sim}{\boldsymbol{\Pi}}^e}{\partial \underset{\sim}{\boldsymbol{E}}^e_{GL}} = \underset{\approx}{\boldsymbol{C}} \tag{H.6}$$

$$\frac{\partial \underset{\sim}{\boldsymbol{E}}^e_{GL}}{\partial \underset{\sim}{\boldsymbol{E}}} = \frac{1}{2} (\underset{\sim}{\mathbf{1}} \overline{\otimes} \underset{\sim}{\boldsymbol{E}}^T + \underset{\sim}{\boldsymbol{E}}^T \underline{\otimes} \underset{\sim}{\mathbf{1}}) \tag{H.7}$$

$$\frac{\partial \Delta \underset{\sim}{\boldsymbol{S}}}{\partial \Delta \gamma^s} = 0 \qquad \frac{\partial \Delta \underset{\sim}{\boldsymbol{S}}}{\partial \Delta r^s} = 0 \qquad \frac{\partial \Delta \underset{\sim}{\boldsymbol{S}}}{\partial \Delta \gamma_{cum}} = 0 \tag{H.8}$$

$$\frac{\partial \Delta \gamma_M}{\partial \Delta \underset{\sim}{\boldsymbol{E}}} = 0 \qquad \frac{\partial \Delta \gamma_M}{\partial \Delta \gamma^s} = 0 \qquad \frac{\partial \Delta \gamma_M}{\partial \Delta r^s} = 0 \qquad \frac{\partial \Delta \gamma_M}{\partial \Delta \gamma_{cum}} = 1 \tag{H.9}$$

- $\frac{\partial \mathcal{R}}{\partial \Delta v_{\mathrm{IN}}}$

$$\frac{\partial R_{\underset{\sim}{\boldsymbol{E}}}}{\partial \Delta \Delta_\chi} = 0 \qquad \frac{\partial R_{\underset{\sim}{\boldsymbol{E}}}}{\partial \Delta \underset{\sim}{\boldsymbol{F}}} = -\frac{\partial (\Delta \underset{\sim}{\boldsymbol{F}}.\underset{\sim}{\boldsymbol{F}}^{-1}.\underset{\sim}{\boldsymbol{E}})}{\partial \Delta \underset{\sim}{\boldsymbol{F}}} \tag{H.10}$$

$$= -\underset{\sim}{\mathbf{1}} \underline{\otimes} \left( \underset{\sim}{\boldsymbol{F}}^{-1}.\underset{\sim}{\boldsymbol{E}} \right)^T - (\Delta \underset{\sim}{\boldsymbol{F}} \underline{\otimes} \underset{\sim}{\boldsymbol{E}}^T) : \frac{\partial \underset{\sim}{\boldsymbol{F}}^{-1}}{\partial \underset{\sim}{\boldsymbol{F}}} : \frac{\partial \underset{\sim}{\boldsymbol{F}}}{\partial \Delta \underset{\sim}{\boldsymbol{F}}} \tag{H.11}$$

$$= -\underset{\sim}{\mathbf{1}} \underline{\otimes} \left( \underset{\sim}{\boldsymbol{E}}^T.\underset{\sim}{\boldsymbol{F}}^{-T} \right)^T - (\Delta \underset{\sim}{\boldsymbol{F}} \underline{\otimes} \underset{\sim}{\boldsymbol{E}}^T) : (-\underset{\sim}{\boldsymbol{F}}^{-1} \underline{\otimes} \underset{\sim}{\boldsymbol{F}}^{-T}) : \underset{\approx}{\mathbf{1}} \tag{H.12}$$

$$= -\underset{\sim}{\mathbf{1}} \underline{\otimes} \left( \underset{\sim}{\boldsymbol{E}}^T.\underset{\sim}{\boldsymbol{F}}^{-T} \right) + (\Delta \underset{\sim}{\boldsymbol{F}} \underline{\otimes} \underset{\sim}{\boldsymbol{E}}^T) : (\underset{\sim}{\boldsymbol{F}}^{-1} \underline{\otimes} \underset{\sim}{\boldsymbol{F}}^{-T}) \tag{H.13}$$

For the rate-dependent formulation

$$\frac{\partial R_{\gamma^s}}{\partial \Delta \underset{\sim}{\boldsymbol{F}}} = 0 \tag{H.14}$$

For the rate-independent formulation

$$\frac{\partial R_{\gamma^s}}{\partial \Delta \underset{\sim}{\boldsymbol{F}}} = -\mathrm{sign}\left(\tau^s\right) \Phi^s \frac{\partial \Delta \varepsilon_{eq}}{\partial \Delta \underset{\sim}{\boldsymbol{F}}} \tag{H.15}$$

$$\frac{\partial \Delta \varepsilon_{eq}}{\partial \Delta \underset{\sim}{\boldsymbol{F}}} = \frac{\partial \Delta \varepsilon_{eq}}{\partial \Delta \underset{\sim}{\boldsymbol{D}}'} : \frac{\partial \Delta \underset{\sim}{\boldsymbol{D}}'}{\partial \Delta \underset{\sim}{\boldsymbol{D}}} : \frac{\partial \Delta \underset{\sim}{\boldsymbol{D}}}{\partial \Delta \underset{\sim}{\boldsymbol{L}}} : \frac{\partial \Delta \underset{\sim}{\boldsymbol{L}}}{\partial \Delta \underset{\sim}{\boldsymbol{F}}} \tag{H.16}$$

$$= \frac{2}{3} \frac{\Delta \underset{\sim}{\boldsymbol{D}}'}{\Delta \varepsilon_{eq}} : \frac{\partial (\Delta \underset{\sim}{\boldsymbol{F}} \underset{\sim}{\boldsymbol{F}}^{-1})}{\partial \Delta \underset{\sim}{\boldsymbol{F}}} \tag{H.17}$$

$$\frac{\partial (\Delta \underset{\sim}{\boldsymbol{F}}.\underset{\sim}{\boldsymbol{F}}^{-1})}{\partial \Delta \underset{\sim}{\boldsymbol{F}}} = \underset{\sim}{\mathbf{1}} \underline{\otimes} \underset{\sim}{\boldsymbol{F}}^{-T} + \Delta \underset{\sim}{\boldsymbol{F}} \frac{\partial \underset{\sim}{\boldsymbol{F}}^{-1}}{\partial \underset{\sim}{\boldsymbol{F}}} : \frac{\partial \underset{\sim}{\boldsymbol{F}}}{\partial \Delta \underset{\sim}{\boldsymbol{F}}} \tag{H.18}$$

$$= \underset{\sim}{\mathbf{1}} \underline{\otimes} \underset{\sim}{\boldsymbol{F}}^{-T} + (\Delta \underset{\sim}{\boldsymbol{F}} \underline{\otimes} \underset{\sim}{\mathbf{1}}) : (-\underset{\sim}{\boldsymbol{F}}^{-1} \underline{\otimes} \underset{\sim}{\boldsymbol{F}}^{-T}) : \underset{\approx}{\mathbf{1}} \tag{H.19}$$

$$\frac{\partial R_{\gamma^s}}{\partial \Delta \Delta_\chi} = -\mathrm{sign}\left(\tau^s\right) \Delta\Gamma \frac{\partial \Phi^s}{\partial f^s} \frac{\partial f^s}{\partial \Delta \Delta_\chi} = -\mathrm{sign}\left(\tau^s\right) \Delta\Gamma \Phi^{s'} \ \frac{\rho_\sharp}{\rho_0} \tag{H.20}$$

$$\frac{\partial R_{r^s}}{\partial \Delta \underset{\sim}{\boldsymbol{F}}} = 0 \qquad \frac{\partial R_{r^s}}{\partial \Delta \Delta_\chi} = 0 \qquad \frac{\partial R_{\gamma_{cum}}}{\partial \Delta \underset{\sim}{\boldsymbol{F}}} = 0 \qquad \frac{\partial R_{\gamma_{cum}}}{\partial \Delta \Delta_\chi} = 0 \tag{H.21}$$

- $\frac{\partial \Delta v_{\mathrm{OUT}}}{\partial \Delta v_{\mathrm{IN}}}$

$$\frac{\partial \Delta \underset{\sim}{\boldsymbol{S}}}{\partial \Delta \underset{\sim}{\boldsymbol{F}}} = \frac{\partial \underset{\sim}{\boldsymbol{S}}}{\partial \underset{\sim}{\boldsymbol{F}}} = (\underset{\sim}{\boldsymbol{\sigma}}.\underset{\sim}{\boldsymbol{F}}^{-T}) \otimes \frac{\partial J}{\partial \underset{\sim}{\boldsymbol{F}}} + J \frac{\partial \underset{\sim}{\boldsymbol{\sigma}}.\underset{\sim}{\boldsymbol{F}}^{-T}}{\partial \underset{\sim}{\boldsymbol{F}}^{-T}} : \frac{\partial \underset{\sim}{\boldsymbol{F}}^{-T}}{\partial \underset{\sim}{\boldsymbol{F}}} \tag{H.22}$$

$$= J(\underset{\sim}{\boldsymbol{\sigma}}.\underset{\sim}{\boldsymbol{F}}^{-T}) \otimes \underset{\sim}{\boldsymbol{F}}^{-T} + J(\underset{\sim}{\boldsymbol{\sigma}} \underline{\otimes} \underset{\sim}{\mathbf{1}}) : (-\underset{\sim}{\boldsymbol{F}}^{-T} \overline{\otimes} \underset{\sim}{\boldsymbol{F}}^{-1}) \tag{H.23}$$

$$\frac{\partial \Delta \underset{\sim}{\boldsymbol{S}}}{\partial \Delta \Delta_\chi} = 0 \qquad \frac{\partial \Delta \gamma_M}{\partial \Delta \underset{\sim}{\boldsymbol{F}}} = 0 \qquad \frac{\partial \Delta \gamma_M}{\partial \Delta \Delta_\chi} = 0 \tag{H.24}$$

# I

# A small strain thermodynamical formulation of Gurson's model

Gurson's model is revisited here in a simplified version of the framework proposed in Chapter 6. Small perturbations are assumed such that the symmetric small strain tensor $\underset{\approx}{\boldsymbol{\varepsilon}} = (1/2)(\nabla \underline{\boldsymbol{u}} + \nabla \underline{\boldsymbol{u}}^T)$ is additively decomposed into an elastic and a plastic part

$$\underset{\approx}{\boldsymbol{\varepsilon}} = \underset{\approx}{\boldsymbol{\varepsilon}}^e + \underset{\approx}{\boldsymbol{\varepsilon}}^p \tag{I.1}$$

In that context the evolution of the total volume can be neglected and thereby $\rho_0$, $\rho_\sharp$ and $\rho$ become the same quantity. The porosity $f$ is still defined by its initial value $f_0$ and the following evolution law

$$\dot{f} = (1-f)\mathrm{tr}\,(\dot{\underset{\approx}{\boldsymbol{\varepsilon}}}^p) \tag{I.2}$$

The set of state variables is supposed to consist of the elastic strain tensor $\underset{\approx}{\boldsymbol{\varepsilon}}^e$, the porosity $f$ and a hardening scalar variable $p$. The specific free energy density is assumed to take the following form

$$\psi(\underset{\approx}{\boldsymbol{\varepsilon}}^e, f, p) = (1-f)\left(\frac{1}{2\rho}\underset{\approx}{\boldsymbol{\varepsilon}}^e : \underset{\approx}{\boldsymbol{C}} : \underset{\approx}{\boldsymbol{\varepsilon}}^e + \psi_h(p)\right) \tag{I.3}$$

According to the 1-st and 2-nd law of thermodynamics, in the isothermal case, the Clausius-Duhem inequality is written

$$\begin{aligned} d &= \dot{e} - \dot{\psi} \geq 0 && \text{(I.4)}\\ &= \frac{\underset{\approx}{\boldsymbol{\sigma}}}{\rho} : \dot{\underset{\approx}{\boldsymbol{\varepsilon}}} - \frac{\partial \psi}{\partial \underset{\approx}{\boldsymbol{\varepsilon}}^e} : \dot{\underset{\approx}{\boldsymbol{\varepsilon}}}^e - \frac{\partial \psi}{\partial f}\dot{f} - \frac{\partial \psi}{\partial p}\dot{p} \geq 0 && \text{(I.5)}\\ &= \left(\frac{\underset{\approx}{\boldsymbol{\sigma}}}{\rho} - \frac{\partial \psi}{\partial \underset{\approx}{\boldsymbol{\varepsilon}}^e}\right) : \dot{\underset{\approx}{\boldsymbol{\varepsilon}}}^e + \frac{\underset{\approx}{\boldsymbol{\sigma}}}{\rho} : \dot{\underset{\approx}{\boldsymbol{\varepsilon}}}^p - \frac{\partial \psi}{\partial f}\dot{f} - \frac{\partial \psi}{\partial p}\dot{p} \geq 0 && \text{(I.6)} \end{aligned}$$

where $\underset{\sim}{\boldsymbol{\sigma}}$ is the Cauchy stress tensor. The quantities $R_f/\rho = \partial\psi/\partial f = -((1/2)\underset{\sim}{\boldsymbol{\varepsilon}}^e : \underset{\approx}{\boldsymbol{C}} : \underset{\sim}{\boldsymbol{\varepsilon}}^e + \psi_h(p))$ and $R_p/\rho = \partial\psi/\partial p$ are introduced. The following state law is postulated

$$\underset{\sim}{\boldsymbol{\sigma}} = \rho \frac{\partial \psi}{\partial \underset{\sim}{\boldsymbol{\varepsilon}}^e} = \underset{\approx}{\boldsymbol{C}} : \underset{\sim}{\boldsymbol{\varepsilon}}^e \tag{I.7}$$

As a result, the residual mechanical dissipation can be written

$$d = \frac{\underset{\sim}{\boldsymbol{\sigma}}}{\rho} : \dot{\underset{\sim}{\boldsymbol{\varepsilon}}}^p - \frac{R_f}{\rho}\dot{f} - \frac{R_p}{\rho}\dot{p} \geq 0 \tag{I.8}$$

Evolution laws for $\dot{\underset{\sim}{\boldsymbol{\varepsilon}}}^p$, $\dot{f}$ and $\dot{p}$ can be obtained from the definition of a dissipation pseudo-potential $\Omega$ taking for instance the form

$$\Omega\left(\frac{\underset{\sim}{\boldsymbol{\sigma}}}{\rho}, \frac{R_f}{\rho}, \frac{R_p}{\rho}; \underset{\sim}{\boldsymbol{\varepsilon}}^e, p, f\right) = \Lambda(\phi) = \Lambda\left(\phi_{eq}\left(\frac{\sigma_{eq}}{\rho}, \frac{R_p}{\rho}\right) + \phi_m\left(\frac{\sigma_m}{\rho}, \frac{R_f}{\rho}, \frac{R_p}{\rho}; f\right)\right) \tag{I.9}$$

Evolution equations than formally write

$$\dot{\underset{\sim}{\boldsymbol{\varepsilon}}}^{p'} = -\frac{\partial\Omega}{\partial\left(-\frac{\underset{\sim}{\boldsymbol{\sigma}}'}{\rho}\right)} \qquad \mathrm{tr}\,(\dot{\underset{\sim}{\boldsymbol{\varepsilon}}}^p) = -\frac{\partial\Omega}{\partial\left(-\frac{\sigma_m}{\rho}\right)} \tag{I.10}$$

$$\dot{f} = -\frac{\partial\Omega}{\partial\left(\frac{R_f}{\rho}\right)} \qquad \dot{p} = -\frac{\partial\Omega}{\partial\left(\frac{R_p}{\rho}\right)} \tag{I.11}$$

where $\dot{\underset{\sim}{\boldsymbol{\varepsilon}}}^{p'} = \dot{\underset{\sim}{\boldsymbol{\varepsilon}}}^p - \frac{\mathrm{tr}\,(\dot{\underset{\sim}{\boldsymbol{\varepsilon}}})}{3}\underset{\sim}{\mathbf{1}}$. As in Chapter 6 it is assumed that $\phi_m$ can be written in the following form

$$\phi_m\left(\frac{\sigma_m}{\rho}, \frac{R_f}{\rho}, \frac{R_p}{\rho}; f\right) = h\left(\frac{R_f}{\rho}; f\right) g\left(\frac{\sigma_m}{\rho} + k\left(\frac{R_f}{\rho}; f\right), \frac{R_p}{\rho}; f\right) \tag{I.12}$$

Here $h = 1$ is assumed. In order to satisfy simultaneously Eq. I.2 and I.11 the following equality must hold

$$-\frac{\partial\Omega}{\partial\left(\frac{R_f}{\rho}\right)} = (1-f)\left(-\frac{\partial\Omega}{\partial\left(-\frac{\sigma_m}{\rho}\right)}\right) \tag{I.13}$$

That equality holds with the condition that

$$\frac{\partial k}{\partial\left(\frac{R_f}{\rho}\right)}\left(\frac{R_f}{\rho}; f\right) = (1-f)\frac{\partial g}{\partial\left(\frac{\sigma_m}{\rho}\right)}\left(\frac{\sigma_m}{\rho} + k\left(\frac{R_f}{\rho}; f\right), \frac{R_p}{\rho}; f\right) \tag{I.14}$$

In the context of Gurson's model, the functions $g$ and $k$ are such that

$$g\left(\frac{\sigma_m}{\rho} + k\left(\frac{R_f}{\rho}; f\right), \frac{R_p}{\rho}; f\right) = 2f\cosh\left(\frac{\frac{\sigma_m}{\rho} + k\left(\frac{R_f}{\rho}; f\right)}{\frac{R_p}{\rho}}\right) \tag{I.15}$$

$$k\left(\frac{R_f}{\rho}; f\right) = -(1-f)\frac{R_f}{\rho} \tag{I.16}$$

The revisited Gurson criterion can thereby be written

$$\phi = \left(\frac{\Sigma_{eq}}{R_0 + R_p}\right)^2 + 2f\cosh\left(\frac{3}{2}\frac{\Sigma_m}{R_0 + R_p}\right) - 1 - f^2 \tag{I.17}$$

where $\underset{\sim}{\boldsymbol{\Sigma}} = \underset{\sim}{\boldsymbol{\sigma}} - (1-f)R_f\underset{\sim}{\mathbf{1}}$ is the relevant stress. Eq. (I.17) can then be interpreted as an implicit definition of an effective stress $\sigma_*\left(\underset{\sim}{\boldsymbol{\Sigma}}; f\right)$ homogeneous of degree one in $\underset{\sim}{\boldsymbol{\Sigma}}$, with the yield criterion being then expressed as

$$\left\{\begin{array}{l|l} \sigma_* & \phi\left(\dfrac{\Sigma_{eq}}{\sigma_*}\right)^2 + 2f\cosh\left(\dfrac{3}{2}\dfrac{\Sigma_m}{\sigma_*}\right) - 1 - f^2 \overset{\text{def}}{=} 0 \\ & \tilde{\phi} = (1-f)(\sigma_* - R_p - R_0) \end{array}\right. \tag{I.18}$$

In fine, the residual mechanical dissipation becomes

$$d = \frac{\underset{\sim}{\boldsymbol{\Sigma}}}{\rho} : \dot{\underset{\sim}{\boldsymbol{\varepsilon}}}^p - \frac{R_p}{\rho}\dot{p} \tag{I.19}$$

$$= \frac{\underset{\sim}{\boldsymbol{\Sigma}}}{\rho} : \left(\frac{\partial\Lambda}{\partial\phi}\frac{\partial\phi}{\partial\tilde{\phi}}\frac{\partial\tilde{\phi}}{\partial\sigma_*}\frac{\partial\sigma_*}{\partial\underset{\sim}{\boldsymbol{\Sigma}}}\right) - \frac{R_p}{\rho}\frac{\partial\Lambda}{\partial\phi}\frac{\partial\phi}{\partial\tilde{\phi}}\frac{\partial\tilde{\phi}}{\partial R_p} \tag{I.20}$$

$$= \frac{(1-f)}{\rho}\dot{\lambda}(\sigma_* - R_p) \tag{I.21}$$

where $\dot{\lambda} = \partial\Lambda/\partial\phi$. Noting that $\sigma_* - R_p \geq \sigma_* - R_p - R_0 \geq 0$ proves the positivity of the dissipation.

## RÉSUMÉ

Pour leurs excellentes propriétés mécaniques et d'oxydation, les aciers austénitiques inoxydables sont largement utilisés dans l'industrie nucléaire, en particulier pour les structures internes de cœur des réacteurs. Toutefois, les niveaux d'irradiation neutronique importants auxquels ces matériaux sont exposés peuvent nuire à leurs propriétés mécaniques. Une forte baisse de la ténacité est en effet observée à mesure que la dose d'irradiation augmente. Selon les conditions d'irradiation (température, dose), on distingue principalement deux types de défauts induits par l'irradiation pouvant être responsables de ce comportement : des boucles de dislocations de Frank à basse température d'irradiation ($\sim 300\,^{\circ}\mathrm{C}$) et des nano-cavités à haute température ($\sim 600\,^{\circ}\mathrm{C}$). Comme ces défauts existent et agissent à des échelles inférieures à la taille de grain, leurs effets peuvent être étudiés à l'échelle du monocristal. Tout d'abord, ce travail vise à obtenir des données expérimentales sur le comportement mécanique des monocristaux d'acier inoxydable austénitique. Ensuite, la modélisation de la localisation de la déformation plastique induite par l'adoucissement survenant dans les aciers irradiés est étudiée. Les limites d'un modèle de plasticité cristalline à gradient sont exposées sur la base de solutions analytiques de l'apparition de bandes de localisation. Une théorie étendue tenant compte de l'évolution de la longueur interne est proposée. Une attention particulière est alors accordée à l'efficacité numérique de la mise en œuvre par éléments finis du modèle de plasticité à gradient susmentionné. Des formulations basées sur l'approche micromorphe ou sur une approche à multiplicateur de Lagrange sont décrites et comparées à l'aide de simulations par éléments finis. Enfin, un modèle de rupture ductile de monocristaux poreux est proposé – incluant à la fois la croissance et la coalescence des cavités – afin d'étudier l'impact des nano-cavités induites par irradiation sur le comportement mécanique des aciers austénitiques inoxydables. Le modèle est mis en place dans un formalisme à gradient afin de régulariser la rupture ductile.

## MOTS CLÉS

Plasticité cristalline, rupture ductile, localisation, plasticité à gradient, aciers austénitiques irradiés.

## ABSTRACT

For their excellent mechanical and oxidation properties, austenitic stainless steels are widely used in the nuclear industry, in particular for structural applications inside the core of reactors. However the substantial neutron irradiation levels these materials can be exposed to can detrimentally affect their mechanical properties. A sharp drop of toughness is indeed observed as the irradiation dose increases. Depending on the irradiation conditions (temperature, dose), mainly two kinds of radiation-induced defects can be responsible for this behaviour: dislocation Frank loops at low irradiation temperature ($\sim 300\,^{\circ}\mathrm{C}$) and nano-voids at higher temperature ($\sim 600\,^{\circ}\mathrm{C}$). Since these defects exist and act at the subgrain level, it motivates to study their effects at the single crystal scale. First of all, this work aims at obtaining experimental data on the mechanical behaviour of austenitic stainless steel single crystals. Then, modeling of softening induced strain localization phenomena, as those taking place in irradiated materials, is investigated. The limitations of a reduced strain gradient crystal plasticity model regarding shear bands predictions are exposed on the grounds of analytical solutions and an enhanced theory accounting for internal length evolution is proposed. Thereupon attention is given to the numerical efficiency of the finite element implementation of the aforementionned strain gradient plasticity model. Micromorphic and Lagrange multiplier based formulations of the original theory are described and compared upon finite element simulations. Eventually, one of a kind ductile fracture model of porous single crystals is proposed – including both void growth and void coalescence – in order to investigate impact of radiation-induced nano-voids on the mechanical behavior of irradiated austenitic stainless steels. The model is set up in a strain gradient framework in order to regularize ductile fracture.

## KEYWORDS

Crystal plasticity, ductile fracture, localization, strain gradient plasticity, irradiated austenitic steels.